AES 2024 Rome - Italy

The 10th International Conference on Antennas and Electromagnetic Systems

June 25 – 28, 2024

Rome - Italy

Proceedings

ISSN 2491-2417

aesconference.org

AES 2024 Rome - Italy

The 10th International Conference on Antennas and Electromagnetic Systems

Edited by

Stefan Wabnitz | Sapienza Università di Roma, Italy
Said Zouhdi | Paris-Saclay University, France

TABLE OF CONTENT

ORGANIZATION I COMMITTEES 4

SPONSORS I EXHIBITORS 6

PLENARY SPEAKERS 8

KEYNOTE SPEAKERS 12

TUTORIALS 21

GUIDELINES FOR PRESENTERS 22

USEFUL INFORMATION 23

TABLE OF CONTENTS 27

ORGANIZATION I COMMITTEES

Conference Chairs

Stefan Wabnitz
Sapienza Università di Roma (Italy)

Said Zouhdi
Paris–Saclay University (France)

Organizing Committee

Rita Asquini, Italy
Mario Ferraro, Italy
Fabio Mangini, Italy

International Advisory Committee

Christos Christopoulos, UK
Tie Jun Cui, China
Costantino De Angelis, Italy
Peter de Maagt, Netherlands
Dave.V. Giri, USA
Xun Gong, USA
Nathan Ida, USA
Koichi Ito, Japan
Ahmed Kishk, Canada
Giuseppe Leo, France
Kwai Man Luk, Hong Kong
Andrea Massa, Italy
Alain Sibille, France
Ari Sihvola, Finland
Paul Smith, Australia
Stefano Trillo, Italy
Junhong Wang, China

Technical Program Committee

Christos Argyropoulos, USA
Rita Asquini, Italy
Silvio Ernesto Barbin, Brazil
Xavier Begaud, France
Yangjian Cai, China
Pai-Yen Chen, USA
Renato Cicchetti, Italy
Christophe Craeye, Belgium
Tian Sen Jason Horng, Taiwan
Zhirun Hu, UK
Ruey-Bing Hwang, Taiwan
Sungtek Kahng, Korea
Ali Khenchaf, France
Sebastien Lallechere, France
Allen M. Larar, USA
Howard Lee, USA
Jensen Li, Hong Kong
Jean-Marc Lopez, France
Ozlem Ozgun, Turkey
Oscar Quevedo-Teruel, Sweden
Eva Rajo-Iglesias, Spain
Blaise Ravelo, China
Junsuk Rho, Korea
Orlandino Testa, Italy
Josaphat T. Sri Sumantyo, Japan
Van Yem Vu, Viet Nam
Kaikai Xu, China
Amir I. Zaghloul, USA
Kuang Zhang, China
Qi-Jun Zhang, Canada
Linjie Zhou, China
Arkady Zhukov, Spain

Special Sessions Organizers

Ryszard Buczynski, Poland
Kaveh Delfanazari, UK
Mario Ferraro, Italy
Angelo Freni, Italy
Walter Fuscaldo, Italy
Tatjana Gric, Lithuania
Mercedeh Khajavikhan, USA
Konstantinos Makris, Greece
Fabio Mangini, Italy
Ziad Musslimani, USA
Paola Pirinoli, Italy
Edik U. Rafailov, UK
Sergey Saveliev, UK

Special Symposia Organizers

Andrea Fratalocchi
KAUST (Saudi Arabia)

Maha Ben Rhouma
Gustave Eiffel University (France)

SPONSORS I EXHIBITORS

Partners

Sapienza University of Rome Founded in 1303, Sapienza is the oldest university in Rome and the largest in Europe. Its mission is to contribute to the development of a knowledge society through research, excellence, quality education and international cooperation.
The world most important university rankings place Sapienza at the national top for quality of research, education and international dimension ; moreover, Sapienza excels and leads as a benchmark in many subject areas.

Université Paris-Saclay is a research university based in Paris, France. Université Paris-Saclay offers a comprehensive and varied range of Undergraduate, Master's and PhD degrees, renowned internationally thanks to the University's reputation for research excellence and the commitment of its academic staff. The University's constituent faculties, institutes and component institutions all contribute to the curricula with cutting-edge specialised courses in Science and Engineering, Life Sciences and Health, and Social Sciences and Humanities.
Université Paris-Saclayis ranked 1st in France and 16th in the world according to the Academic Ranking of World Universities (ARWU).

DIET the Department of Information Engineering, Electronics and Telecommunications was established on 1st of July 2010 by joining the former Department of Electronic Engineering and the Department of Information Science and Technique (known with its acronym INFOCOM) in the frame of reorganization of Sapienza University. Research at DIET is carried out in the frame of several national and international projects focussed on the development of both cabled and wireless transmission systems and networks, radar systems, remote sensing systems, electronic measurements, sensors, multimedia and bioengineering applications.

AEM - Advanced Electromagnetics is a free, peer-reviewed, Gold Open Access journal. It covers recent international research results in the general field of Electromagnetic Waves, Antennas and Propagation. Authors of articles published in Advanced Electromagnetics retain the copyright of their articles and are free to reproduce and disseminate their work (under a Creative Commons Attribution License). AEM is widely indexed and has a Scopus CiteScore of 2.3 (2023).

Silver Sponsor

The IEEE Antennas and Propagation Society (AP-S) strives for advancement of the theory and practice of electrical and electronics engineering. The field of interest includes analysis, design, measurement and testing of antennas, radiation, propagation, and the interaction of electromagnetic waves with various applications.

IEEE AP-S Young Professionals is a vibrant group with various activities to encourage young professionals to pursue research in antennas and propagation as well as nurture them to be future leaders of AP Society. Learn more about IEEE AP-S Young Professionals at :
https ://ieeeaps.org/committees/yp.

PLENARY SPEAKERS

Andrea Alù

City University of New York, USA

Extreme Wave Control with Space-Time Metamaterials

Andrea Alù is a Distinguished Professor at the City University of New York (CUNY), the Founding Director of the Photonics Initiative at the CUNY Advanced Science Research Center, and the Einstein Professor of Physics at the CUNY Graduate Center. He received his Laurea (2001) and PhD (2007) from the University of Roma Tre, Italy, and, after a postdoc at the University of Pennsylvania, he joined the faculty of the University of Texas at Austin in 2009, where he was the Temple Foundation Endowed Professor until Jan. 2018. Dr. Alù is a Fellow of the National Academy of Inventors (NAI), the American Association for the Advancement of Science (AAAS), the Institute of Electrical and Electronic Engineers (IEEE), the Materials Research Society (MRS), Optica, the International Society for Optics and Photonics (SPIE) and the American Physical Society (APS). He is the President of Metamorphose, a Highly Cited Researcher since 2017, a Simons Investigator in Physics, the director of the Simons Collaboration on Extreme Wave Phenomena Based on Symmetries, and the Editor in Chief of Optical Materials Express. He has received several scientific awards, including the NSF Alan T. Waterman award, the Blavatnik National Award for Physical Sciences and Engineering, the IEEE Kiyo Tomiyasu Award, the ICO Prize in Optics, the OSA Adolph Lomb Medal, and the URSI Issac Koga Gold Medal.

Extreme Wave Control with Space-Time Metamaterials
Metamaterials offer a powerful platform to manipulate wave propagation and gain control over waves, from radio-frequencies to light and sound. In this talk, I will discuss our recent progress in developing new metamaterial technologies, introducing time as an additional dimension for wave control.

Alexandra Boltasseva

Purdue University, USA

Tailorable Materials for Dynamic Photonics : From Metasurfaces to New Physical Phenomena

Alexandra Boltasseva is a Professor at the School of Electrical and Computer Engineering at Purdue University. She received her PhD in electrical engineering at Technical University of Denmark, DTU in 2004. Boltasseva specializes in nanophotonics, nanofabrication, optical materials, plasmonics and metamaterials. She is 2018 Blavatnik National Award for Young Scientists Finalist and received the 2013 IEEE Photonics Society Young Investigator Award, 2013 Materials Research Society (MRS) Outstanding Young Investigator Award, the MIT Technology Review Top Young Innovator (TR35), the Young Researcher Award in Advanced Optical Technologies from the University of Erlangen-Nuremberg, Germany, and the Young Elite-Researcher Award from the Danish Council for Independent Research. She is a Fellow of the Optical Society of America (OSA) and Fellow of SPIE. She served on MRS Board of Directors and is Editor-in-Chief for OSA's Optical Materials Express.

Tailorable Materials for Dynamic Photonics : From Metasurfaces to New Physical Phenomena
Transparent conducting oxides and transition metal nitrides have attracted attention for photonic applications as they exhibit enhanced light-matter interactions, particularly in their metallic/plasmonic regime and near the so-called epsilon near zero (ENZ) region. Here, we explore the static and dynamic tailorability and tunability of optical properties in TCOs and TMNs.

Stefano Maci

University of Siena, Italy

The New Generation of Metasurface Antennas

Stefano Maci received the Laurea Degree cum Laude at University of Florence in 87 and from '97 is a Professor at the University of Siena. His research interest includes high-frequency and beam representation methods, computational electromagnetics, large phased arrays, planar antennas, reflector antennas and feeds, metamaterials and metasurfaces. Since 2000 he was member the Technical Advisory Board of 12 international conferences, member of the Review Board of 6 International Journals. He organized 25 special sessions in international conferences, and he held 10 short courses in the IEEE Antennas and Propagation Society (AP-S) Symposia about metamaterials, antennas and computational electromagnetics. In 2004-2007 he was WP leader of the Antenna Center of Excellence (ACE, FP6-EU) and in 2007-2010 he was International Coordinator of a 24-institution consortium of a Marie Curie Action (FP6). He has been Principal Investigator from 2010 of 6 cooperative projects financed by European Space Agency. In 2004 he was the founder of the European School of Antennas (ESoA), a post graduate school that presently comprises 34 courses on Antennas, Propagation, Electromagnetic Theory, and Computational Electromagnetics and 150 teachers coming from 15 countries. Since 2004 is the Director of ESoA.

Professor Maci is IEEE Fellow since 2004, he has been a former member of the AdCom of IEEE Antennas and Propagation Society (AP-S), associate editor of AP-Transaction, Chair of the Award Committee of IEEE AP-S, and member of the Board of Directors of the European Association on Antennas and Propagation (EurAAP). From 2008 to 2015 he has been Director of the PhD program in Information Engineering and Mathematics of University of Siena, and from 2013 to 2015 he was member of the National Italian Committee for Qualification to Professor. He has been former member of the Antennas and Propagation Executive Board of the Institution of Engineering and Technology (IET, UK). He is presently the director of the consortium FORESEEN, presently involving 48 European Institutions, and principal investigator of the Future Emerging Technology project "Nanoarchitectronics" of the 8th EU Framework program. He was co-founder of 2 Spin-off Company. He is a Distinguished Lecturer of the IEEE Antennas and Propagation Society (AP-S), and recipient of the EurAAP Award in 2014, of the IEEE Shelkunoff Transaction Prize 2015, and of the Chen-To Tai Distinguished Educator award 2016. In 2020 will be TPC Chair of the METAMATERIAL conference. In the last ten years he has been invited 25 times as key-note speaker in international conferences. The research activity of Professor Maci is documented in 150 papers published in international journals, (among which 100 on IEEE journals), 10 book chapters, and about 400 papers in proceedings of international. These papers have received around 6800 citations with h index 41.

The New Generation of Metasurface Antennas

This presentation will focus on the control of surface waves, showcasing examples such as the design of high-gain, low cross-polarization antennas, multibeam antennas, and scanning beam flat lenses. Emphasis will be given to space applications. The presentation will also concern the third generation of adaptive metasurfaces (MTSs).

Oscar Quevedo-Teruel

KTH Royal Institute of Technology, Sweden

Geodesic Lens Antennas for 5G/6G and Satellite Communications

Oscar Quevedo-Teruel received his Telecommunication Engineering and Ph.D. Degrees from Carlos III University of Madrid, Spain in 2005 and 2010. From 2010-2011, he joined the Department of Theoretical Physics of Condensed Matter at Universidad Autonoma de Madrid as a research fellow and went on to continue his postdoctoral research at Queen Mary University of London from 2011-2013. In 2014, he joined the KTH Royal Institute of Technology (Stockholm, Sweden), where he is presently a Full Professor in the Division of Electromagnetic Engineering and Fusion Science. He is also the Responsible for the Antenna Laboratory and Director of the Master Programme in Electromagnetics Fusion and Space Engineering.

He was an Associate Editor of the IEEE Transactions on Antennas and Propagation (IEEE TAP) since 2018-2022, and he acts as Track Editor in IEEE TAP since 2022. He was a distinguished lecturer of the IEEE Antennas and Propagation Society for the period of 2019-2022. He is an IEEE Fellow for his contributions to glide symmetry based metasurfaces and lens antennas. He has been a member of the European Association on Antennas and Propagation (EurAAP) Board of Directors since January 2021. Since January 2022, he is the vice-chair of EurAAP. He is the co-author of more than 140 papers in international journals and more than 240 at international conferences.

Geodesic Lens Antennas for 5G/6G and Satellite Communications

In this talk, we present the development of massive MIMO antenna technologies for the emerging 6G and associated challenges. The overall system performance and antenna design-choice in terms of spectrum and channel propagation properties are discussed. We explore the centimeter wave spectrum for the 6G massive MIMO. The candidate frequency range is from 7GHz to 15GHz, we discuss the new propagation properties and ultra-large antenna element array architecture, namely, the 1K-element-array paradigm for both base-station and user-equipment.

KEYNOTE SPEAKERS

Che Ting Chan

HKUST, Hong Kong

Scalar wave solutions to a 3D electromagnetic vector wave problem

Che Ting Chan received his PhD degree from the University of California at Berkeley in 1985. He is currently serving as the Associate Vice-President for Research and Development at HKUST. He is also concurrently the Daniel C K Yu Professor of Science, Chair Professor of Physics, and the Director of Research Office of HKUST. He has been elected a Fellow of the American Physical Society and the Physical Society of Hong Kong and a member of the Hong Kong Academy of Sciences.

Scalar wave solutions to a 3D electromagnetic vector wave problem
We showed that some 3D photonic crystals have scalar-wave-like band dispersions. These crystals feature topological surface states with high-Q within the light cone continuum. As such, the surface states in our 3D nested crystals can be exposed directly to air, making such systems well-suited for practical applications.

Tommaso Isernia

Università Mediterranea di Reggio Calabria, Italy

A X-Words Play into 2-D Phase Retrieval Problems

Tommaso Isernia is a Full Professor of Electromagnetic Fields at Università Mediterranea di Reggio Calabria (Italy) where he leads the "LEMMA" Group, ranked amongst the best research groups in Italy according to the last national evaluation of the quality of research (all "class A" products). From October 2018 to January 2023 he has been the Head of "Dipartimento di Ingegneria dell'Informazione, delle Infrastrutture e della Energia Sostenibile" (DIIES), which has been included in the restricted list of "Dipartimenti di eccellenza" by the Italian Ministry for Research. The scientific activities of Tommaso Isernia have considered non linear inverse scattering problems in electromagnetics, with particular reference to the problem of the possible occurrence of false solutions when solving the considered non-linear retrieval problems. He is an IEEE Fellow since 2022 for contributions to Antenna Synthesis and inverse scattering solution methods. Main research results include definitive solution procedures for a number of antenna synthesis problems, for the 2D phase retrieval problem, as well as the introduction of a number of effective approaches for the solution of inverse scattering problems.

A X-Words Play into 2-D Phase Retrieval Problems

Phase retrieval is a challenging problem of interest in very many electromagnetic problems. We report about a recent approach, emulating the solution of crosswords puzzles, which, opposite to common schemes, is able to use a single set of data, and still avoid false solutions.

Mona Jarrahi

University of California Los Angeles, USA

Chip-scale terahertz optoelectronics

Mona Jarrahi is a Professor of Electrical and Computer Engineering at the University of California Los Angeles. She has made significant contributions to the development of ultrafast electronic and optoelectronic devices and integrated systems for terahertz, infrared, and millimeter-wave sensing, imaging, computing, and communication systems by utilizing novel materials, nanostructures, and innovative plasmonic concepts. Her scientific achievements have been recognized by several prestigious awards including the Presidential Early Career Award for Scientists and Engineers ; Friedrich Wilhelm Bessel Research Award from Alexander von Humboldt Foundation ; Moore Inventor Fellowship from the Gordon and Betty Moore Foundation ; Kavli Fellowship by the USA National Academy of Sciences, Grainger Foundation Frontiers of Engineering Award from the USA National Academy of Engineering ; Breakthrough Award from Popular Mechanics Magazine ; Research Award from Okawa Foundation ; Early Career Award in Nanotechnology from the IEEE Nanotechnology Council ; Outstanding Young Engineer Award from the IEEE Microwave Theory and Techniques Society ; Booker Fellowship from the USA National Committee of the International Union of Radio Science ; Lot Shafai Mid-Career Distinguished Achievement Award from the IEEE Antennas and Propagation Society ; Early Career Award from the USA National Science Foundation ; Young Investigator Awards from the USA Office of Naval Research, the Army Research Office, and the Defense Advanced Research Projects Agency. Prof. Jarrahi is a Fellow of IEEE, OSA and SPIE societies and has served as a distinguished lecturer of IEEE, traveling lecturer of OSA, and visiting lecturer of SPIE societies.

Chip-scale terahertz optoelectronics

We introduce a new scheme for realizing chip-scale terahertz optoelectronics, enabling the scalable implementation of complex terahertz imaging, spectroscopy, and communication systems through a compact platform.

Yongmin Liu

Northeastern University, USA

Accelerating Photonic Design by Deep Learning

Yongmin Liu obtained his Ph.D. from the University of California, Berkeley in 2009. He joined the faculty of Northeastern University in Boston in fall 2012, and currently he is an associate professor in the Department of Mechanical and Industrial Engineering and the Department of Electrical and Computer Engineering. Dr. Liu's research interests include nano optics, nanoscale materials and engineering, plasmonics, metamaterials/metasurfaces, biophotonics, and artificial intelligence for photonic design. He has authored and co-authored more than 120 journal papers, including Science, Nature, Nature Photonics, Nature Nanotechnology, Advanced Materials, Physical Review Letters and Nano Letters. Dr. Liu was a recipient of NSF CAREER Award, Office of Naval Research Young Investigator Award, SPIE DCS Rising Researcher Award, 3M Non-Tenured Faculty Award, as well as the Faculty Fellow of College of Engineering and Søren Buus Outstanding Research Award at Northeastern University. He has served as an editorial board member for Nano Convergence, PhotoniX, EPJ Applied Metamaterials, and Scientific Reports. He is a Fellow of Optica (formerly OSA) and SPIE.

Accelerating Photonic Design by Deep Learning

Deep learning is instrumental in computational electromagnetics as it excels at capturing intricate patterns and complex relationships within vast datasets, enabling more efficient and accurate modeling of electromagnetic phenomena. This capability is particularly beneficial in photonics design, leading to the discovery of innovative and optimized configurations for desired functionalities.

Junsuk Rho

POSTECH, Korea

Low-cost and scalable manufacturing of optical metasurfaces in the visible using engineering optical materials

Junsuk Rho is a Mu-Eun-Jae Endowed Chair Professor at Pohang University of Science and Technology (POSTECH), Korea, with a double appointment in the Department of Chemical Engineering and the Department of Mechanical Engineering. He received his Ph.D. at the University of California, Berkeley (2013), M.S. at the University of Illinois, Urbana-Champaign (2008) and B.S. at Seoul National University, Korea (2007) all in Mechanical Engineering. Prior joining POSTECH, he conducted postdoctoral research in Materials Sciences Division and Molecular Foundry at Lawrence Berkeley National Laboratory, and also worked as a principal investigator (Ugo Fano Fellow) in Nanoscience and Technology Division and the Center for Nanoscale Materials at Argonne National Laboratory.

Prof. Rho has authored and co-authored more than 300 high-impact journal papers including Science, Nature, Nature Nanotechnology, Nature Materials, Nature Photonics and Chemical Reviews. He is also the recipients of several notable honors and awards such as Samsung Lee Kun-Hee fellowship (2008-2013), US Department of Energy Argonne Named fellowship (2013-2016), Korean Presidential Early Career Award for Scientists and Engineers (2019), Springer-Nature MINE Young Scientist Award (2020), Elsevier MEE/MNE Young Investigator Award and Lectureship (2020), MDPI Micromachines Young Investigator Award (2020), Member of the Young Korean Academy of Science and Technology (2020), Associate Member of the National Academy of Engineering of Korea (2022), NAEK Young Engineers Award (2022), Hong Jin-Ki Creator Award (2022), Fulbright Visiting Scholar Fellowship (2022), Simpson Fellowship (2022) and Eshbach Fellowship (2023), Clarivate Highly Cited Researcher (2023). He serves 14 editorial positions including Light : Science and Applications (Springer-Nature), Microsystems and Nanoengineering (Springer-Nature), npj Nanophotonics (Springer-Nature) and Nanophotonics (De Gruyter).

Low-cost and scalable manufacturing of optical metasurfaces in the visible using engineering optical materials

Here, we demonstrate low-cost, scalable manufacturing of optical metasurfaces with three approaches : increasing a refractive index of resin with dielectric particle embedding for single-step nanoimprinting, 2) suppressing optical losses of hydrogenated amorphous silicon (a-Si :H) to apply complementary-metal-oxide-semiconductor technologies, and 3) high-index atomic layer deposited (ALD) structural resin.

Vladimir M. Shalaev

Purdue University, USA

Extreme Space-Time Optics and Quantum Meta-Photonics

Vladimir M. Shalaev, Scientific Director for Nanophotonics at Birck Nanotechnology Center and Distinguished Professor of Electrical and Computer Engineering at Purdue University, specializes in nanophotonics, plasmonics, and optical metamaterials. Vladimir M. Shalaev has received several awards for his research in the field of nanophotonics and metamaterials, including the Max Born Award of the Optical Society of America for his pioneering contributions to the field of optical metamaterials, the Willis E. Lamb Award for Laser Science and Quantum Optics, IEEE Photonics Society William Streifer Scientific Achievement Award, Rolf Landauer medal of the ETOPIM (Electrical, Transport and Optical Properties of Inhomogeneous Media) International Association, the UNESCO Medal for the development of nanosciences and nanotechnologies, OSA and SPIE Goodman Book Writing Award. He is a Fellow of the IEEE, APS, SPIE, MRS and OSA. Prof. Shalaev has authored three books, thirty invited book chapters and over 500 research publications.

Extreme Space-Time Optics and Quantum Meta-Photonics

We discuss all-optical modulation with single photons using electron avalanche, resulting in record-high nonlinearities. Then we show that transparent conducting oxides (TCOs) operating in the near-zero index regime can provide strong single-cycle modulation, enabling novel photonic time crystals. Finally, we discuss scalable quantum photonics with single-photon emitters in silicon nitride.

David R. Smith

Duke University, USA

Large-Area, Reconfigurable Metasurface Apertures for Synthetic Aperture Radar and Other Applications

David R. Smith is the James B. Duke Distinguished Professor of the Electrical and Computer Engineering Department at Duke University, where he also serves as Director for the Center for Metamaterial and Integrated Plasmonics. Dr. Smith is also the Founding Director of the Metamaterials Commercialization Center at Intellectual Ventures in Bellevue, Washington. Dr. Smith received his Ph.D. in 1994 in Physics from UCSD. Dr. Smith's research interests include the theory, simulation and characterization of unique electromagnetic structures, including photonic crystals, metamaterials and plasmonic nanostructures. Smith and his colleagues demonstrated the first left-handed (or negative index) metamaterial at microwave frequencies in 2000, and also demonstrated a metamaterial "invisibility cloak" in 2006. In 2005, Dr. Smith was part of a five-member team that received the Descartes Research Prize, awarded by the European Union, for their contributions to metamaterials and other novel electromagnetic materials. In 2006, Dr. Smith was selected as one of the "Scientific American 50." Since 2009, Dr. Smith has continually been named a "Citation Laureate" by ISI Web of Knowledge for having among the most number of highly cited papers in the field of Physics. Dr. Smith is a co-recipient of the McGroddy Prize for New Materials, awarded by the American Physical Society, for "the discovery of metamaterials" (2013). In 2016, Dr. Smith was elected to the National Academy of Inventors. Dr. Smith has recently been active in transitioning metamaterial concepts for commercialization, being a co-founder of Evolv Technology, Echodyne Corporation, Pivotal Commware, and advisor to Kymeta Corporation—all companies devoted to developing metamaterial products.

Large-Area, Reconfigurable Metasurface Apertures for Synthetic Aperture Radar and Other Applications

Metasurfaces are an excellent fit for large-area, reconfigurable apertures due to their use of passive tuning components rather than the active (externally powered) phase shifters and amplifiers integrated into traditional phased arrays. We discuss the advantages of metasurfaces for extremely large, reconfigurable antennas in the context of space-based systems.

Marin Soljačić

MIT, USA

Nanophotonic scintillators and various topics in AI for topology

Marin Soljačić is a Professor of Physics at MIT. He is a founder of a few companies, including WiTricity Corporation (2007) and Lightelligence (2017). His main research interests are in artificial intelligence as well as electromagnetic phenomena, focusing on nanophotonics, non-linear optics, and wireless power transfer. He is a co-author of more than 300 scientific articles, more than 100 issued US patents, and he has been invited to give more than 100 invited talks at conferences and universities around the world. He is a recipient of the Adolph Lomb medal from the Optical Society of America (2005), and the TR35 award of the Technology Review magazine (2006). In 2008, he was awarded a MacArthur fellowship “genius” grant. He is an international member of the Croatian Academy of Engineering since 2009. In 2011 he became a Young Global Leader (YGL) of the World Economic Forum. In 2014, he was awarded Blavatnik National Award, as well as Invented Here ! (Boston Patent Law Association). In 2017, he was awarded "The Order of the Croatian Daystar, with the image of Ruđer Bošković", the Croatian President’s top medal for Science. In 2017, the Croatian President also awarded him with "The Order of the Croatian Interlace" medal. He was a Highly Cited Researcher according to WoS for 2019, 2020, 2021, 2022 and 2023. In 2023, he was awarded Max Born award of Optica.

Nanophotonic scintillators and various topics in AI for topology

Nanophotonic methods provide intriguing options for manipulating scintillation phenomena. We will outline recent developments in this domain, along with our general theoretical framework for modeling these occurrences, supported by our experimental findings. We will also cover novel numerical techniques for discovery of topological phenomena in photonics.

Jelena Vuckovic

Stanford University, USA

Scalable semiconductor photonic systems

Jelena Vuckovic (PhD Caltech 2002) is the Jensen Huang Professor in Global Leadership in the School of Engineering, and Professor of Electrical Engineering and by courtesy of Applied Physics at Stanford, where she leads the Nanoscale and Quantum Photonics Lab. She is also the Fortinet Founders Chair of the Electrical Engineering Department at Stanford, and was the inaugural director of Q-FARM, the Stanford-SLAC Quantum Science and Engineering Initiative. Vuckovic has received many awards and honors including recently the Vannevar Bush Faculty Fellowship (2022), the Mildred Dresselhaus Lectureship from MIT (2021), the James Gordon Memorial Speakership from the OSA (2020), the IET A. F. Harvey Engineering Research Prize (2019), Distinguished Scholarship of the Max Planck Institute for Quantum Optics (2019), the Hans Fischer Senior Fellowship from the Institute for Advanced Studies in Munich (2013), and Humboldt Prize (2010). She is a Fellow of the APS, of the Optica (OSA), and of the IEEE, and an associate editor of the ACS Photonics.

Scalable semiconductor photonic systems

Recent breakthroughs in photonics design, along with new nanofabrication approaches and heterogeneous integration play crucial roles in building photonics for applications including optical interconnects and quantum technologies.

TUTORIALS

Lorenzo Crocco

National Research Council, Italy

Wednesday 26th June
14:00 - 15:00 — Room1

Virtual experiments and alternative formulations for effective solution of inverse scattering problems

Lorenzo Crocco is a Research Director at the Institute for the Electromagnetic Sensing of the Environment, National Research Council of Italy (IREA-CNR), Naples. His scientific interests mainly concern electromagnetic scattering, with a focus on diagnostic and therapeutic uses of EM fields, non-invasive electromagnetic inspections, through-the-wall radar and GPR. On these topics, he has published more than 120 papers, given keynote talks and lectures, and led or participated to national and international research projects. He is associate editor for the IEEE Journal of Electromagnetics, RF and Microwaves in Medicine and Biology (IEEE J-ERM) and has edited two books on medical electromagnetic technologies. He is member of the board for the European School of Antennas (ESOA), member of the Scientific Board of the Italian Electromagnetic Society (SIEm) and a member of the Italian URSI Commission (International Union of Radio Science). Since 2019, he is member of the Scientific Board of the Engineering Department (DIITET) of CNR. Since 2024, he has been elected in the EurAAP Delegate Assembly (Delegate Group 3 : Italy, San Marino, Vatican City). Dr. Crocco is a fellow of the Electromagnetic Academy (TEA) and a URSI Senior Member.

Virtual experiments and alternative formulations for effective solution of inverse scattering problems
Description : Electromagnetic inverse scattering problems are one of the most exciting topics in applied electromagnetics, due to the broad range of applications in which they are involved and the methodological challenges they pose. In this tutorial, an overview of the difficulties inherent to the non-linear and ill-posed nature of the inverse scattering problems will be given first. Then, some recent results aiming at addressing the challenges posed by the non-linearity will be reviewed. The focus will be on the use of alternative formulations of the basic equations and on the virtual experiments framework, which allow to deal with “simpler” problems by means of simple – but tailored - manipulations of the scattering equations and of the data, respectively.

GUIDELINES FOR PRESENTERS

Oral Presentations

Each session room is equipped with a stationary computer connected to a LCD projector. Presenters must load their presentation files in advance onto the session computer. Technician personnel will be available to assist you.

Scheduled time slots for oral presentations are 15 mn for regular, 20 mn for invited presentations, 30 mn for keynote talks and 35 mn for plenary talks, including questions and discussions. Presenters are required to report to their session room and to their session Chair at least 15 minutes prior to the start of their session.

The session chair must be present in the session room at least 15 minutes before the start of the session and must strictly observe the starting time and time limit of each paper.

Poster Presentations

Presenters are requested to stand by their posters during their session. One poster board, A0 size (118.9 x 84.1 cm), in portrait orientation, will be available for each poster. Pins or thumbtacks are provided to mount your posters on the board. All presenters are required to mount their papers 30mn before the session and remove them at the end of their sessions. Posters must prepared using the standard AES poster template (available on the conference website).

USEFUL INFORMATION

Venue

AES 2024 will be held at :
Faculty of Civil and Industrial Engineering, Sapienza University of Rome
Via Eudossiana 18, 00184 Rome (Italy)

https://www.ing.uniroma1.it/

Housed in the former convent of San Pietro in Vincoli, the Faculty is positioned on the Esquiline Hill, offering breathtaking views of the Colosseum and the Imperial Forum. It is adjacent to the Basilica di San Pietro in Vincoli (St Peter in Chains), which houses one of Michelangelo's magnificent sculptures, the tomb of pope Julius II, including the marble statue of Moses (1513-1515).

Floor maps

Ground floor map

First floor map

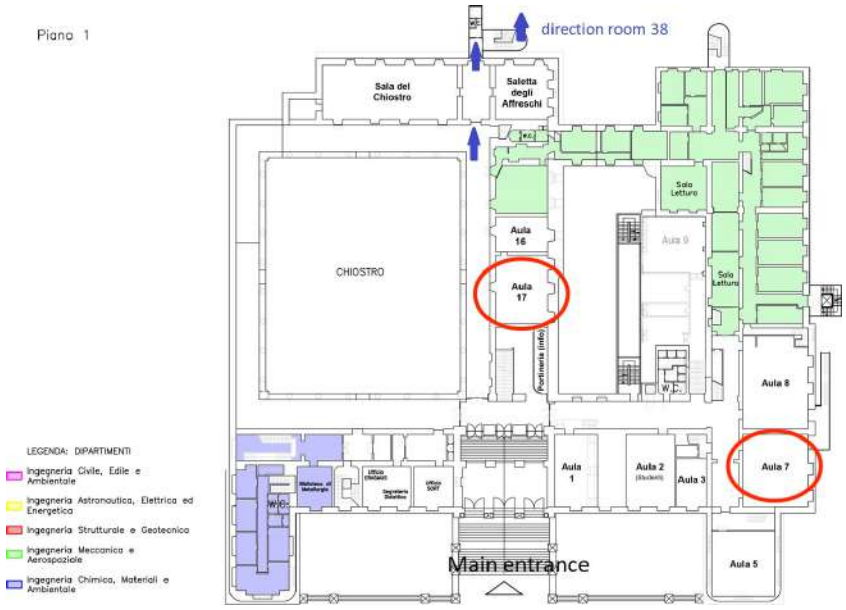

Second floor map

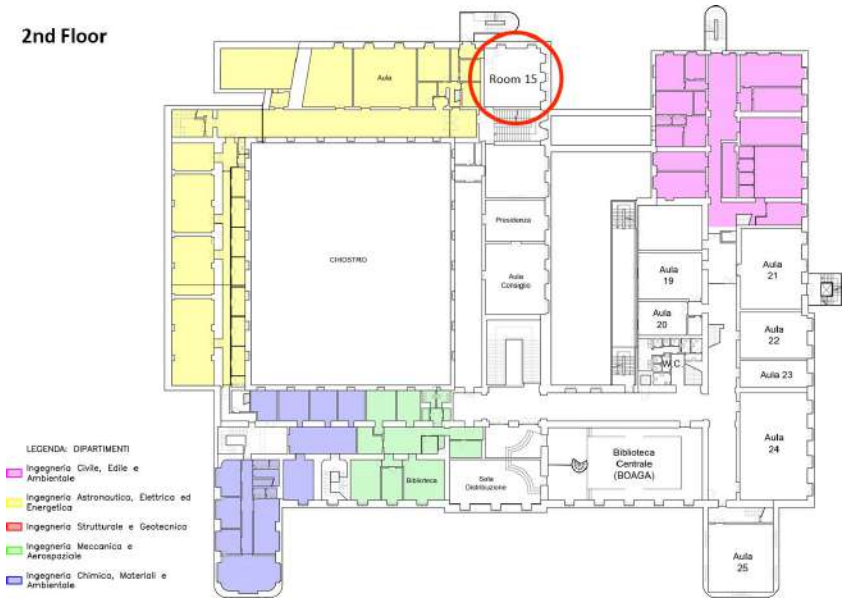

Getting to Venue

How to reach the venue

The site is less than 20 minutes walking distance from Roma Termini rail Station and a few minutes walking distance from the metro stations of “Cavour” and “Colosseo” (Blue line B).

How to reach Rome

Rome is served by two airports : Leonardo Da Vinci Airport (also known as Fiumicino Airport) and G. B. Pastine Airport (also known as Ciampino Airport).

Arriving at Fiumicino Airport

Leonardo Da Vinci is the main italian hub and it has direct flights to more than 200 destinations, including all the european capitals and major european cities, major cities of the US, Canada, Brazil, Mexico, Japan, Middle-east and Asia.

Train “Leonardo Express” (see here for further information) that has a direct connection to Rome Termini Station (Rome main railways station), where you can take the underground Line A (direction Anagnina), exit to Manzoni station and then walk for some meters (approximately 45 min). The train schedule is frequent and the entire trip takes around 30 minutes, tickets can be bought near the train departure site at the airport. Leonardo Da Vinci Airport is connected to Rome also by frequent busses.

Arriving at Ciampino Airport

G. B. Pastine Airport is a smaller airport used mainly by low cost companies, it has connections to many european cities. Terravision shuttle bus from Ciampino Airport to Rome Termini Station (Rome main railways station) where you can take the underground Line A (direction Anagnina), exit to Manzoni station and then walk for some meters (the time depends on the traffic, because Rome is a city with a lot of traffic, but approximately 60 min).

Taxi

The official cabs of the City of Rome are white, with the word “TAXI” on the roof and the symbol of the City of Rome and the license number clearly visible on the doors. You will find cabs both at Terminal 1

and Terminal 3 arrivals at Fiumicino Airport.

From Fiumicino airport to Rome Center, i.e. inside the Aurelian Walls (including Rome Termini station), and back there is a fixed cost rate of €50,00.

If you intend to reach Fiumicino airport by cab from Rome, know that all trips departing from inside the Grande Raccordo Anulare, can not and will never exceed the amount of €73,00.

From Ciampino airport to Rome Center, i.e. inside the Aurelian Walls (including Rome Termini station), and back there is a fixed cost rate of €31,00.

TABLE OF CONTENTS

Plenary presentations

Extreme Wave Control with Space-Time Metamaterials (pp. 43)
Andrea Alu

Geodesic Lens Antennas for 5G/6G and Satellite Communications (pp. 44)
Oscar Quevedo Teruel

Tailorable Materials for Dynamic Photonics: From Metasurfaces to New Physical Phenomena (pp. 45)
Alexandra Boltasseva

Metasurface antennas and RIS in Space and 6G Scenarios (pp. 46)
Stefano Maci

Keynote presentations

Scalar wave solutions to a 3D electromagnetic vector wave problem (pp. 48)
Che Ting Chan

A X-Words Play into 2-D Phase Retrieval Problems (pp. 49)
Tommaso Isernia, Giada Maria Battaglia, Andrea Francesco Morabito, Roberta Palmeri

Accelerating Photonic Design by Deep Learning (pp. 51)
Yongmin Liu

Scalable semiconductor photonic systems: Jelena Vuckovic (pp. 53)
Jelena Vuckovic

Low-cost and scalable manufacturing of optical metasurfaces in the visible using engineering optical materials (pp. 55)
Junsuk Rho

Nanophotonic scintillators and various topics in AI for topology (pp. 57)
Marin Soljacic

Chip-scale terahertz optoelectronics (pp. 58)
Y. Zhao, Mona Jarrahi

Large-Area, Reconfigurable Metasurface Apertures for Synthetic Aperture Radar and Other Applications (pp. 59)
David R. Smith

Extreme Space-Time Optics & Quantum Meta-Photonics (pp. 60)
Vladimir Shalaev

Tutorials

Virtual experiments and alternative formulations for effective of solution inverse scattering problems (pp. 62)
Lorenzo Crocco

Smart Electromagnetic Skins for the Next Generation of Wireless Network

On the Features of Curved Passive Electromagnetic Skins (pp. 64)
Michele Beccaria, Michele Beccaria, Agnese Mazzinghi, Angelo Freni, Paola Pirinoli

An Approach for the Estimation of The Impact of Technological Constraints on Information at the Deep Physical Layer (pp. 66)
Marco Donald Migliore, Marco Di Renzo

Introduction to fewer known properties of glide symmetry (pp. 68)

Oscar Quevedo Teruel

Design and Optimization of Active and Passive Quasi-Periodic Structures for Beam Steering (pp. 70)
Pasquale Nicolaci, M. M. Bilgic, M. Zhou

A scattering matrix approach for the inverse design of smart devices (pp. 77)
Andrea Francesco Morabito, Renat Abdullin, Giada Maria Battaglia, Tommaso Isernia, Roberta Palmeri

Liquid Crystal Technology for Implementing Smart Electromagnetic Skins in Next Generations of mm-Waves Wireless Systems (pp. 79)
Eduardo Carrasco, Roberto Guirado, Gerardo Pérez-Palomino, Pablo de la Rosa, Morten A. Geday

Metasurfaces for Enhanced Wireless Communications (pp. 80)
Andrea Alu

Design of a Dual-Band Dual-Polarized Smart Electromagnetic Skin with Shaped Anomalous Reflection Considering Phase Shift Constraints in the Unit Cell (pp. 82)
Alvaro F. Vaquero, Eduardo Martinez-de-Rioja, Manuel Arrebola

Advanced antenna systems: modelling and experiments

On the use of the parabolic wave equation to model the electromagnetic propagation in maritime environment (pp. 85)
Thomas Bonnafont, Ali Khenchaf

Controllable polarization emission laser based on chiral metasurfaces (pp. 88)
Ioannis Katsantonis, Anna Tasolamprou, Thomas Koschny, Maria Kafesaki

Physics-embedded machine learning method for the prediction of long-range electromagnetic field propagation (pp. 90)
Thomas Bonnafont, Abdelmalek Toumi

Reconfigurable Intelligent Surface as a MIMO (pp. 93)
Sotiris Droulias, Giorgos Stratidakis, Angeliki Alexiou

Non-Hermitian Metasurfaces for Sensitive THz Systems (pp. 95)
Teun-Teun Kim

Real-time Spectroscopy of Broadband THz-wave with High Frequency Resolution (pp. 97)
Sota Mine, Kodo Kawase, Chiko Otani, François Blanchard

Excitation of out-of-plane resonances at normal incidence (pp. 99)
Juan R. Deop-Ruano, Juan J. Alvarez-Serrano, Vincenzo Aglieri, Andrea Toma, Alejandro Manjavacas

Tuneable plasmonics and nanoantennas based on in-plane hyperbolic conducting polymers (pp. 100)
Yulong Duan, Aiman Rahmanudin, Shangzhi Chen, Nara Kim, Klas Tybrandt, Magnus P. Jonsson

Nano-thermoelectric infrared detectors (pp. 102)
A. Varpula, A. Murros, O. Merchiers, K. Sovanto, J. Tiira, K. Tappura, P.-O. Chapuis, Mika Prunnila

Frontiers in Nonlinear Photonics: Optical Thermodynamics of Complex Systems

Thermalization and Non-Equilibrium Transport in Multimoded Nonlinear Photonic Circuits (pp. 104)
Tsampikos Kottos

Optical entropy growth accompanies beam clean-up in multimode fibers (pp. 105)
Fabio Mangini, Mario Ferraro, Wasyhun Gemechu, Yifan Sun, Vincent Couderc, Stefan Wabnitz

Optical Thermalization and Applications to High-Power Lasers (pp. 107)
Frank Wise, Demetrios Christodoulides

Thermalization and condensation of light waves: Wave turbulence theory and experiments in multimode optical fibers (pp.

108)

Kilian Baudin, Lucas Zanaglia, Josselin Garnier, Nicolas Berti, Adrien Fusaro, Katarzyna Krupa, Valerie Doya, Claire Michel, Guy Millot, Antonio Picozzi

Spatial localization induced by coupled transport processes (pp. 110)

Stefano Iubini, M. Giusfredi, G. Gotti, A. Politi, P. Politi

Pressure in optical thermodynamics (pp. 112)

Nikolaos Efremidis, Demetrios Christodoulides

Optical Thermodynamics of Nonlinear Highly Multimode Systems (pp. 113)

Demetrios Christodoulides

Nonlinear Fiber Optics Towards Applications

Femtosecond Regenerative Amplifiers Based on Optical Fiber (pp. 115)

Henry Haig, Nicholas Bender, Yishai Eisenberg, Frank Wise

Soliton Self-Frequency Shift in Nitrogen-Filled Hollow Fiber (pp. 116)

Yishai Eisenberg, Yi-Hao Chen, Henry Haig, Enrique Antonio-Lopez, Rodrigo Amezcua-Correa, Frank Wise

Fundamental vibration dynamics of soliton complexes in ultrafast fiber laser (pp. 118)

Anastasiia Sheveleva, Christophe Finot, Pierre Colman

Relocation of a Townes soliton dedicated to ultrafast 3D imaging (pp. 120)

Nick Bagley, Tigran Mansuryan, Lucie Chretien, Remy Boulesteix, Yago Arosa Lobato, Mario Ferraro, Mario Zitelli, Fabio Mangini, Yifan Sun, Katarzyna Krupa, Benjamin Wetzel, Vincent Couderc, Stefan Wabnitz, Alejandro Aceves, Alessandro Tonello

Nonlinear Interactions of Ultrafast Pulses between Higher Order Modes in Step-Index Optical Fibers (pp. 122)

Lars Rishøj, Andrea Arduin, Jesper Lægsgaard

Development of soft glass nonlinear optical fibers based on 3D preform printing (pp. 124)

Ryszard Buczynski, Pawel Wienclaw, Przemyslaw Golebiewski, Pawel Socha, Dariusz Pysz, Adam Filipkowski, Grzegorz Stepniewski, Irenesz Kujawa, Olga Czerwinska, Andrzej Burgs, Rafal Kasztelanic

Extension of the fundamental four wave-mixing model to large bandwidth systems (pp. 127)

Anastasiia Sheveleva, Pierre Colman, Christophe Finot

Application of supercontinuum laser system for a χ(2) and χ(3) characterization of biomedical structure (pp. 129)

Claire Lefort, M. Nafa, T. Mansuryan, C. Carrion, A. Tonnello, Jean-René Duclère, V. Couderc

Unexpected phase-locked Brillouin Kerr Frequency comb in fiber Fabry Perot resonators (pp. 130)

Thomas Bunel, Matteo Conforti, Julien Lumeau, Antonin Moreau, Arnaud Fernandez, Olivier Llopis, Julien Roul, Auro M. Perego, Arnaud Mussot

Control and Optimization of Nonlinear Dynamics using Machine Learning (pp. 131)

Goery Genty, M. Hary, L. Salmela, M. Mabed, A. Ermolaev, D. Bruner, J. M. Dudley

Breathing Soliton Dynamics in Laser Cavities (pp. 132)

Sonia Boscolo, Junsong Peng, Xiuqi Wu, Ying Zhang, Christophe Finot, Heping Zeng

Optical fiber-based devices for sensing torsion, temperature and refractive index: from kW- to micro- and nano- scale applications (pp. 134)

L. F. Granados-Zambrano, J. Korterijk, Tommie Verouden, F. Segerink, D. Jauregui-Vazquez, H. L. Offerhaus, Jose Alfredo Alvarez-Chavez

Electromagnetic Metasurfaces for Microwave, Terahertz, and Optical Applications

Reflective Moiré Metasurfaces: A Frontier of Innovation and Technical Challenges (pp. 137)

Shuo Liu, Lei Zhang, Xiaoqing Chen

Terahertz characterization of thin resistive films and homogenized reactive metasurfaces via reflection time-domain spectroscopy (pp. 139)

Dimitrios Zografopoulos, Francesco Maita, Luca Maiolo, Irnik Dionisiev, Nikolay Minev, Gaetana Petrone, Silvia Tofani, Tiziana Ritacco, Dimitre Dimitrov, Vera Marinova, Andrea Liscio, Valentina Mussi, Romeo Beccherelli, Walter Fuscaldo

An overview of advanced techniques for design and synthesis of nondiffractive Bessel beams in near-field (pp. 141)

Santi Concetto Pavone

Gain and Impedance Bandwidth Enhancement in Fabry-Perot Cavity Leaky-Wave Antennas Based on Metasurfaces (pp. 143)

Edoardo Negri, Walter Fuscaldo, Paolo Burghignoli, Alessandro Galli

Metasurfaces enhanced with 2D photonic materials: Analysis based on quasinormal modes (pp. 145)

Thomas Christopoulos, Georgios Nousios, Emmanouil Kriezis, Odysseas Tsilipakos

Modal Analysis Glide-Symmetric Open Structure (pp. 147)

Davide Comite, Guido Valerio, Yuhuan Tong

Gradient and Modulated Metasurfaces for Sub-Terahertz Antenna Systems (pp. 148)

David Gonzalez Ovejero, Malo Robin, Xavier Morvan, Olivier de Sagazan

Specialty Optical Fibers

Gas sensing inside negative curvature hollow-core fibers (pp. 151)

Grzegorz Gomółka, Patrycja Gronowicz, Ryszard Buczynski, Michal Nikodem

Dispersion properties of highly birefringent microstructured fibers with germanium doped cores (pp. 153)

Tadeusz Martynkien, Karol Tarnowski, Karolina Stefanska, Pawel Mergo

Pedestal-free structured-core thulium-doped fibers for applications in eye-safer fiber lasers (pp. 155)

Pavel Peterka, Ivan Kašík, Adam Filipkowski, Michal Kamrádek, Dariusz Pysz, Marcin Franczyk, Jan Aubrecht, Martin Grábner, Bára Švejkarová, Pavel Honzátko

Linear and nonlinear optics in hollow-core photonic crystal fibres (pp. 157)

Francesco Tani

4D optical fibers thermally drawn from shape-memory polymers (pp. 158)

Clément Strutynski, Frédéric Désévédavy, Grégory Gadret, Claire-Hélène Brachais, Bertrand Kibler, Frédéric Smektala

X-ray-based techniques for the characterization of specialty optical fibers (pp. 160)

Mario Ferraro, Maria Caterina Crocco, Raffaele Filosa, Riccardo Cristoforo Barberi, Raffaele Giuseppe Agostino, Vincenzo Formoso

Superconducting and high-frequency neuromorphic devices

Bifurcation Phenomena in a Circuit with a Three-Level Quantum Memristor (pp. 163)

Finlay J. Potter, Alexandre Zagoskin, Sergey Saveliev, Alexander G. Balanov

Superconducting systems for quantum and neuromorphic AI and reservoir computing (pp. 164)

Sergey Saveliev

Study of aspect ratio effect on radiation characteristics of rectangular shape of high-temperature superconductor Bi2212 terahertz wave emitters (pp. 165)

Takanari Kashiwagi, Ryuta Kikuchi, Shungo Nakagawa, Shotaro Yamada, Yuki Enomoto, Yuuki Yamauchi, Yoshihiko Kuzumi, Kentaro Maeshima, Hidetoshi Minami

Josephson transmission lines employing granular aluminum (pp. 167)

Alexey Ustinov

Frequency modulated terahertz radiation from Josephson plasma emitters of a cuprate superconductor (pp. 168)

Itsuhiro Kakeya

Artificial Neuron Circuit with a Two-Level Quantum Memristor (pp. 169)
Finlay Potter, Alexandre Zagoskin, Sergey Saveliev, Alexander G. Balanov

Superconductor plasmonic nanoantenna array metasurfaces (pp. 170)
Kaveh Delfanazari

New trends in nanophotonics

Applications on demand with engineered composites (pp. 172)
Dorota A. Pawlak, P. Piotrowski, M. Tomczyk, K. Sadecka, K. Bandopadhay, N. Aghad, K. Markus, A. Abbas, S. Saha, A. Materna, A. Bellardini, C. Sibilia

Limits and opportunities for nonlinear nanophotonics (pp. 173)
Alejandro Rodriguez

Recent Advances in Nanophotonics and Metamaterials

Noise-resilient exceptional-point sensors enabled by oscillation quenching phenomena (pp. 175)
Arunn Suntharalingam, Lucas Fernandez-Alcazar, Rodion Kononchuk, Tsampikos Kottos

Large-area photonic emitters with full spatial control of intensity, phase and polarization compatible with batch fabrication by optical lithography (pp. 176)
Vladimir Aksyuk, Chad Ropp, Alexei Azarov, Dhriti Maurya, Alexander Yulaev, Daron Westly

Metamaterials: A Review from the Perspectives of the Effective Properties and Applications (pp. 178)
Tatjana Gric, Vladimir Mityushev, Edik Rafailov

Soliton formation in an exciton-polariton condensate at a bound state in the continuum (pp. 184)
I. Septembre, I. Fudjo, V. Develay, T. Guillet, S. Bouchoule, J. Zuniga-Perez, G. Malpuech, Dmitry Solnyshkov

Imaging chirality of optical fields near nano-/micro-structured materials (pp. 186)
Hiromi Okamoto, Junsuke Yamanishi

Visualization of photonic band structures of topological and non-Hermitian photonic crystals (pp. 188)
Yuto Moritake, Taiki Yoda, Masaya Notomi

Dielectric cylindrical and ring resonators: hot spots and photonic resonances (pp. 190)
Kirill Bronnikov, N. S. Solodovchenko, M. F. Limonov

Algorithm-driven Design of Metasurfaces for Multi-dimensional Light Manipulation (pp. 192)
Wei Ma, Bo Xiong

Perfect absorption and thermal radiation control of MIM metasurfaces (pp. 194)
Yoshiaki Nishijima, Tsuyoshi Kawaida, Megumi Tanaka, Kazuma Sekiya

Inverse Design for wavelength and polarization multiplexing in optical metasurfaces (pp. 197)
Bo Xiong, Wei Ma

Plasmonic/Excitonic hybrid systems for nanoscale thermometry (pp. 198)
Lorenzo Ramò, Valentina Venturino, Ermes Peci, Emma Spotorno, M. Magnozzi, Maria Caterina Giordano, Domenica Convertino, Giorgio Orlandini, Camilla Coletti, Maurizio Canepa, Francesco Bisio

Integrated Photonics for Quantum Information Processing and Artificial Neural Networks (pp. 200)
Imtiaz Alamgir, Luigi Di Lauro, Stefania Sciara, Abdul Rahim Aadhi, Celine Mazoukh, Hao Yu, Bennet Fischer, Nicolas Perron, Nicola Montaut, Mario Chemnitz, Brent E. Little, Sai T. Chu, David J. Moss, Zhiming Wang, Roberto Morandotti

Anisotropic polaritons in van der Waals layered crystals (pp. 202)
Andrea Mancini, Nicola Melchioni, Giacomo Venturi, Stefano Chiodini, Antonio Ambrosio

Integrated Phased Array Antenna Using Phase Change Material (pp. 204)

Rahuldas Kutteeri, Martino De Carlo, Francesco De Leonardis, Richard Soref, Vittorio Passaro

Liquid Crystal Thin Films for Low-Cost Large-Area Diffractive Optical Gratings with Excellent Efficiency (pp. 208)
Kristiaan Neyts, M. Stebryte, F. Van Acker, S. Liu, X. Ke, I. Nys

Redox-tunable conducting polymer plasmonics and metasurfaces (pp. 210)
Magnus Jonsson

Precision Unleashed: Coherence-Moderated Sensing for Simultaneous Accuracy and High Bandwidth (pp. 211)
Johannes Dickmann

Hybridized Silicon Metasurface with Two-Dimensional Nanomaterials for Perfect Absorption (pp. 213)
Junichi Takahara

Transparent Materials with Low Radiative Cooling Efficiency (pp. 214)
Kotaro Kajikawa

Mid-infrared dielectric antennas on epsilon-near-zero material for sensing (pp. 215)
Paolo Biagioni, Francesco Rusconi, Pierre Felhen, Fernando Gonzalez-Posada, Laurent Cerutti, Giovanni Pellegrini, Marco Finazzi, Thierry Taliercio

Crystallization of Induce Optical Vortex by Bessel Beams (pp. 217)
Sahil Sahoo, Yuri Gorodetski

Tunable Bound States in the Continuum in Magneto-Optic and Graphene Metasurfaces (pp. 219)
Jose L. Pura, Juan R. Deop-Ruano, Diego R. Abujetas, Alejandro Manjavacas, V. Giannini, Antonio Garcia-Martin, Jose A. Sanchez-Gil

Magnetic control of electrically uncharged magneto-optical particles (pp. 221)
Manuel Marques, Shulamit Edelstein, Pedro A. Serena, Beatriz Castillo Lopez de Larrinzar, Antonio Garcia Martin

Pushing the Limit of Multiplexing Capacity in Optical Metasurfaces (pp. 223)
Yongmin Liu

Tailoring the emission and the photodynamics of quantum emitters with simple and optimized high-index dielectric nanostructures (pp. 225)
Mélodie Humbert, Romain Hernandez, Peter R. Wiecha, Jonas Muller, Etienne Palleau, Frank Fournel, Vincent Larrey, Aurélie Lecestre, Guilhem Larrieu, Christian Girard, Vincent Paillard, Laurence Ressier, Aurelien Cuche

Cylindrical vector beams for control of light emission of quantum emitters coupled to silicon nanoantennas (pp. 227)
M. Montagnac, J-M. Poumirol, A. Cuche, Y. Brûlé, G. Colas des Francs, J. Müller, G. Larrieu, V. Larrey, F. Fournel, O. Boisron, B. Masenelli, G. Agez, Vincent Paillard

Enhancing Electric and Magnetic Light-Matter Interactions with Plasmonic Nanoantennas (pp. 229)
Sebastien Bidault

Moderate-refractive-index nanoantennas for QD fluorescence enhancement (pp. 230)
Rafael Ramos, Angela Barreda, Braulio Garcia-Camara

Gain-controlled nonlinearity and interactions in wave-based neuromorphic photonic systems (pp. 232)
Giulia Marcucci, Luana Olivieri, Juan Sebastian Totero Gongora

Photonic Neuromorphic Computing (pp. 234)
Frank Brueckerhoff-Plueckelmann, Jelle Dijkstra, Ivonne Bente, Wolfram Pernice

Wafer-scale structural coloration using gray-scale lithographic nanofabrication (pp. 236)
Wen-Di Li, Z. F. Gan, C. W. Liang, Z. Sun, S. B. Huang

Low-index nonlinear optics (pp. 238)
Wallace Jaffray, Sven Stengel, Alexandra Boltasseva, Vladimir Shalaev, Andrea Di Falco, Marcello Ferrera

THz metamaterial-based devices and ultrafast modulators (pp. 240)

Stelios Tzortzakis

Electrochemically-tunable and light-emitting metasurfaces (pp. 242)
Vivian Ferry

Dispersion tuning of spoof surface plasmon polaritons by MEMS-integrated metasurfaces (pp. 244)
Lars Franke, Steffen Klingel, Steffen Klingel, Marco Rahm

Elastic Wave Focusing and Optomechanical Coupling in a Nano-Opto-Electro-Mechanical Device (pp. 246)
A. Gueddida, L. Carpentier, G. Lévêque, Y. Pennec, Bahram Djafari Rouhani

Energy transfer mechanisms in nanophotonic systems for pulsed photocatalysis (pp. 248)
Alessandro Alabastri

Nanophotonic paths to enhance the open circuit voltage in perovskite and organic photovoltaic cells (pp. 250)
Francisco Bernal Texca, Martina D'andrea, Jordi Martorell

Infrared radiation from sub-l antennas and high mobility graphene devices (pp. 251)
L. Abou-Hamdan, A. Schmitt, S. Rossetti, R. Bretel, S. Bidault, V. Krachmalnicoff, J.-P. Hugonin, C. Voisin, R. Haidar, P. Bouchon, J.-J. Greffet, E. Baudin, Yannick De Wilde

Nanoresonators and Metasurfaces for Enhanced Infrared/Terahertz Light-Matter Interaction (pp. 253)
Luca Razzari

Towards a full quantum photonics platform (pp. 254)
Christophe Couteau, Roy Konnoth Ancel, Surena Fatemi, Christoph Becher, Régis Deturche, Sylvain Blaize

Nanophotonics on the Tip of a Fiber: Membrane-on-Fiber Technology (pp. 256)
Andrea Fiore, Arthur L. Hendriks, Luca Picelli, Mildred S. Cano-Velázquez, Daan Rabelink, Paco Dreverman, Mathias Dolci, René van Veldhoven, Peter Zijlstra, Ewold Verhagen

Recent Advances in the Research of Graphene-based 2D Heterostructures for THz Plasmonic Device Applications (pp. 258)
Taiichi Otsuji

Light-modulated van der Waals Force Microscopy (pp. 259)
Benfeng Bai

Near-field heat transfer in many-body systems: application to thermal management and energy harvesting (pp. 260)
Philippe Ben Abdallah

Electron-Plasmon Interactions in Nanoplasmonics: Fundamentals and Applications (pp. 261)
P. André D. Gonçalves, F. Javier García de Abajo

Two-photon plasmon induced polymerization for the deterministic integration of single photon sources (pp. 262)
Abdelrahman Abdelaal, Ali Issa, Dandan Ge, Aurélie Broussier, Christophe Couteau, Sylvain Blaize, Renaud Bachelot, Safi Jradi

Enhanced Light-Matter Interactions by engineered metal nanoantennas: Applications in Advanced Biosensing (pp. 263)
Maria Grazia Manera, A. Colombelli, D. Lospinoso, R. Rella

Sustainable photocatalysis with scalable plasmonic metasurfaces (pp. 265)
Alberto Naldoni

Micro-thermo-mechanical devices for THz detection (pp. 266)
B. Bertoni, L. Vicarelli, S. Zanotto, S. Roddaro, Alessandro Tredicucci, A. Pitanti

Achieving Non-Local Optical Response in Planar Metamaterials (pp. 267)
Vassili Fedotov

Efficient nonlinearities in metasurfaces enabled by bound states in the continuum (pp. 268)
Hayk Harutyunyan

Chip-scale Nanophotonic Technologies and Applications (pp. 269)
Yeshaiahu Fainman

Backward terahertz-wave parametric oscillation and its innovation (pp. 271)
Hiroaki Minamide

Nonlinear generation of optical beams with orbital angular momentum on chi(2) dielectric films and metasurfaces (pp. 273)
Laure Coudrat, Domenico De Ceglia, Rana Tanos, Jean-Michel Gérard, Costantino De Angelis, Aloyse Degiron, Giuseppe Leo

Metasurfaces in Laser Cooling and Trapping of Neutral Atoms Towards Quantum Information Processing & Quantum Sensing (pp. 274)
Thu H. H. Le, R. Takei, S. Kagami, A. Takamizawa, Y. Kurashima

Enabling new life science tools through visible integrated nanophotonics (pp. 276)
Pol Van Dorpe

Strong termination dependence of quasi-BIC's lifetime and frequency in plasmonic double-nets (pp. 277)
Cedric Schumacher, Bilel Abdennadher, Ullrich Steiner, Matthias Saba

Spin and lattice dynamics of FePt nanoparticles at fundamental time and lengthscales (pp. 278)
Hermann Durr

Optical Spin Waves (pp. 279)
Vage Karakhanyan, Roland Salut, Miguel Suarez, Nicolas Martin, Thierry Grosjean

System bath approach in nonlinear optical thermodynamics (pp. 280)
Konstantinos Makris, Georgios Pyrialakos, Demetrios Christodoulides

Photonic filter in the 300 GHz band with SiN microresonator frequency comb (pp. 282)
Takasumi Tanabe, Koya Tanikawa, Manto Imamura, Ayaka Yomoda, Satoki Kawanishi, Shun Fujii

Finite Difference Numerical Package for Multiphysics Simulations of Nanophotonic Systems (pp. 284)
M. Tamagnone, H. Gupta, T. Contino, M. A. Yaqub, M. W. Ashraf

Hybrid low loss integrated photonics: from chipscale frequency combs, frequency agile lasers, erbium amplifiers to cryogenic quantum interconnects (pp. 285)
Tobias Kippenberg

Functional UV metalenses (pp. 286)
Thomas Krauss, Augusto Martins, Roxanne Guenette, Kezheng Li, Emiliano R. Martins

Programmable Nanophotonics with Phase-Change Materials: Towards Multilevel Tunability and Low-Loss devices (pp. 288)
F. Bentata, C. Laprais, N. Baboux, P. Genevet, S. Monfray, G. Saint-Girons, X. Letartre, L. Berguiga, Sébastien Cueff

Disorder as a degree of freedom for photonic nanomaterials (pp. 289)
Rémi Carminati, Romain Pierrat

Compact terahertz harmonic generation in the Reststrahlenband in nanophotonic graphene resonators (pp. 290)
Miriam Serena Vitiello

Topological phenomena and OAM manipulation in photonic graphene (pp. 291)
Zhigang Chen

Plasmon-Driven Photografting of Molecularly Imprinted Polymers onto Metal Nanostructures for Enhanced SERS Sensor Performance (pp. 292)
A. Khitous, C. Molinaro, K. Haupt, S. Gree, Olivier Soppera

Advances in optically-tunable metasurfaces (pp. 293)
Dmitrii Pidgaiko, I. Staude

Linear Frequency Generation in Time-Varying Dispersive Interfaces (pp. 295)

Carlo Rizza, M. A. Vincenti, A. Contestabile, G. Castaldi, V. Galdi, M. Scalora

Quantum metric and non-Hermitian Berry curvature in a plasmonic lattice (pp. 297)
Javier Cuerda

Layered Metal-Dielectric-Metal Nanocavities with Vanishing Permittivity: Resonance Coupling and Strong Light-Matter Interaction (pp. 298)
Aniket Patra, V. Caligiuri, Bruno Zappone, Antonio De Luca, Roman Krahne

Advanced Techniques for Computational Electromagnetics, by Maha Ben Rhouma

An efficient method for calculating resonant modes in biperiodic photonic structures (pp. 301)
Nan Zhang, Y. Y. Lu

Simulating photoemission performance of a nanostructured photocathode with a coupled finite difference time domain - Monte Carlo technique (pp. 303)
Mikhail Popov, Ilya Valuev, Sergei Belousov

Controlling thermal state in many-body systems (pp. 305)
Philippe Ben Abdallah

Excitation engineering-based fault diagnosis of phased antenna arrays (pp. 306)
Uday K Khankhoje, Prajosh K P, Sreekar Sai Ranganathan, Francesco Ferranti

A FEM-IE and FEM-FEM domain decomposition approach to solve non-matching multi-scale domains (pp. 307)
Juliano Mologni, Kezhong Zhao

New generation of photonic simulation with hardware accelerated FDTD and automatic differentiation (pp. 309)
Zongfu Yu

The optimal dielectric near-field antenna (pp. 310)
Owen Miller

Ubiquitous Analog Reservoir Computing: Modelling, Optimising, and Controlling Dynamics-Driven Hardware AI (pp. 311)
Giulia Marcucci

Novel Machine-learning Techniques for Inverse Design and Knowledge Discovery in Electromagnetics (pp. 313)
Mohammadreza Zandehshahvar, Mahmoodreza Marzban, mohammad Hadighehjavani, Ali Adibi

Inevitable radiation decay of surface plasmon at any metal-dielectric interface (pp. 314)
Arkadii Krokhin, Kevin Rocapricone, Andrey Bozhko, Gleb Nazarikov, Vladimir Drachev

Connecting antenna and diffraction theory with the radiation of Fisher information in scattering experiments (pp. 316)
Jakob Hüpfl, F. Russo, L. M. Rachbauer, D. Bouchet, J. Lu, U. Kuhl, S. Rotter

Chiral waveguides and exceptional points (pp. 318)
Alice De Corte, Mondher Besbes, Henri Benisty, Stefanos Koufidis, Martin McCall, Bjorn Maes

Concepts for oblique semi-guided waves: integrated optics with negative effective permittivity (pp. 320)
Manfred Hammer, Lena Ebers, Henna Farheen, Samer Alhaddad, Andre Hildebrandt, Jens Förstner

Variational approaches for light bullets characterization in nonlinear optics (pp. 322)
Pedro Parra-Rivas, Yifan Sun, Stefan Wabnitz

An overview of spatial spectral methods with complex-plane deformations for the representation of waves in homogeneous and layered media without absorbing boundary conditions (pp. 324)
Roeland Dilz

Time domain topology optimization for dispersive nanophotonics inverse design (pp. 326)
Johannes Gedeon, Emadeldeen Hassan, Antonio Calà Lesina

Optimal design of sub-relativistic dielectric particle accelerators (pp. 328)
Roberta Palmeri, Giorgio Sebastiano Mauro, Giuseppe Torrisi, Nunzio Salerno, Gino Sorbello

Long-range super-Planckian heat transfer between nano-emitters in a resonant cavity (pp. 330)
Kiryl Asheichyk, Philippe Ben-Abdallah, Matthias Krüger, Riccardo Messina

Observation of multipole-type excitations through nanoscale spatial structure of light: from mesoscopic systems to single molecules (pp. 332)
Hajime Ishihara

All-dielectric epsilon-near-zero Bragg-wall microcavities with tailored coupling efficiency and figure of merit (pp. 334)
Mikko Huttunen, Ali Panahpour, Jussi Kelavuori

Perfect absorption with electric and magnetic lattice resonances (pp. 336)
Luis Cerdán, Juan Ramón Deop-Ruano, Juan José Alvarez-Serrano, Alejandro Manjavacas

Implementing Inhomogeneous Broadening in Time Domain Photonic Simulations (pp. 338)
Ludmila Prokopeva, Alexander V. Kildishev

2D Quantitative Inverse Scattering via Suitable Reformulations as an Effective Way to Reduce Non-linearity (pp. 340)
Martina Teresa Bevacqua, Tommaso Isernia

Computational Electromagnetics in Atomic Scale: First-Principles Approach (pp. 342)
Takashi Takeuchi, Mitsuharu Uemoto, Kazuhiro Yabana

Calculating free-electron nonlinearities in nonclassical plasmonic heavily doped semiconductor systems (pp. 344)
Huatian Hu, Cristian Ciracì

Metasurfaces with Angular Invariant Scattering (pp. 345)
Karim Achouri

Green's functions for electromagnetism on a lattice (pp. 347)
Bastiaan Pieter de Hon

Efficient FEM simulation of resonance modes of VCSELs (pp. 349)
Lilli Kuen, Martin Hammerschmidt, Philipp-Immanuel Schneider, Lin Zschiedrich, Sven Burger

Efficient simulation and design of large-scale metasurfaces (pp. 351)
Dan-Nha Huynh, Jens Niegemann, Han-Hsiang (Michael) Cheng, Thibault Leportier, Federico Duque Gomez, Shin-Sung Kim, Adam Reid

A few recent developments in nanophotonic scintillators (pp. 352)
Charles Roques-Carmes

Extreme Dielectric Confinement of Light Inverse Design, Experimental Realization, Applications. Going Beyond the Second Dimension (pp. 353)
Rasmus Christiansen, Jesper Mørk, Ole Sigmund

Fast and Efficient Design-by-Optimization of Complex Microwave Devices Using Novel FEM Techniques (pp. 354)
Michał Baranowski, Adam Lamecki, Lukasz Balewski, Michal Mrozowski

Fluctuational electrodynamics effects in graphene-based nanosystems (pp. 356)
Mauro Antezza

Wave propagation in four-dimensional media: effective media in space and time and cascaded frequency conversion (pp. 357)
Victor Pacheco-Peña, Nader Engheta

Plasmonic Mid Infrared Photothermal Microscopy (pp. 359)
Sahil Sharma, Joby Joseph, Qammer Abbasi, Hasan Abbas

Existence of accidental bound states in the continuum in periodically perturbed slabs (pp. 361)

Amgad Abdrabou, Wangtao Lu, Ya Yan Lu

The Dawn of global optimization in photonics and electromagnetics ? (pp. 363)
Pauline Bennet, Abdourahman Khaireh-Walieh, Denis Langevin, Olivier Teytaud, Peter Wiecha, Antoine Moreau

Probing Terahertz pulses with nonclassical radiation (pp. 365)
Dionysis Adamou, Lennart Hirsch, Taylor Shields, Seungjin Yoon, Adetunmise Dada, Jonathan Weaver, Daniele Faccio, Lucia Caspani, Marco Peccianti, Matteo Clerici

Hybrid Simulation Techniques Combining Finite Difference and Fourier expansions for Nanophotonic Devices (pp. 366)
Mondher Besbes, Christophe Sauvan, Henri Benisty

Advanced optical metasurface design for imaging and sensing (pp. 368)
Tian Gu

Programmable Photonic Processor for Chaotic Signal Recovery in the Presence of Atmospheric Turbulence (pp. 369)
Heming Huang, Sara Zaminga, Andres Martinez, Francesco Morichetti, Andrea Meloni, Frederic Grillot

Analog computing with nonlinear flat optics (pp. 371)
Costantino De Angelis

Multi-channel optics: thickness bound, efficiency bound, and designs that reach them (pp. 372)
Chia Wei Hsu

From machine learning for design to fabrication of nanophotonic structures (pp. 373)
Francesco Ferranti

Design and simulation of phase-gradient metasurfaces for antenna applications (pp. 374)
Alessio Monti, Stefano Vellucci, Michela Longhi, Mirko Barbuto, Mohsen Karamirad, Davide Ramaccia, Luca Stefanini, Alessandro Toscano, Filiberto Bilotti

Antenna theory and design

Design of an Antipodal Vivaldi Antenna with upper shell (pp. 377)
S. Rudys, Olga Suvorova

The Effective wearable camouflaged UHF antenna (pp. 379)
Saulius Rudys, Juras Banys

Bi-CMOS Design of Miniature BP-NGD Circuit with RLC-Parallel Network (pp. 381)
M. Guerin, S. Ngoho, F. Haddad, H. Du, F. Wan, W. Rahajandraibe, Blaise Ravelo

Unfoldable fully textile antenna using memory form technology mechanism (pp. 383)
Benoit Agnus, Y. Herve, L. Mercier, S. Carras

Array antennas, active, adaptive and reconfigurable antennas

A Variable 60 GHz Liquid Crystal Phase Shifter (pp. 386)
Shreya Menon, Shahin Salarian, Dariush Mirshekar-Syahkal

Review of 3D Printed Beam-Steering Dielectric Lens Antennas for Millimeter-Wave Applications (pp. 390)
Jose Luis Masa Campos, M. H. Rasekhmanesh, A. Piroutiniya, J. Melendro-Jimenez, E. García Marín, P. Sanchez-Olivares, A. Tamayo-Dominguez, J. M. Fernandez-Gonzalez

A Performance Analysis of Partial LIS for 6G Systems (pp. 392)
Mário Marques da Silva, Rui Dinis

Millimeter/Terahertz and nano-optical antennas

THz Near-field Molecular Fingerprint Sensor for glucose detection (pp. 395)
Hyeji Son, Jeong-Sik Jo, Hyunwoo Park, Jae-Won Jang, Teun-Teun Kim

Electromagnetically coupled on-chip antenna in CMOS technology for multi-color sensing applications (pp. 397)
Alexander Chernyadiev, Dmytro But, Kęstutis Ikamas, Wojciech Knap, Alvydas Lisauskas

Low-loss Functional Waveguide Devices Fabricated with a UV-Curable Resin Type 3D Printer, RECILS, and Metal Plating in 200-400 GHz Band (pp. 399)
Junji Yumoto

Real-time Spectroscopy Using Terahertz Parametric Generator and Detector (pp. 401)
Kosuke Murate, Sota Mine, Kodo Kawase

Photonics-based millimeter- and THz wave visualization and its applications (pp. 403)
Shintaro Hisatake

Advances in ultrafast terahertz scanning tunneling microscopy (pp. 405)
Frank Hegmann

Analytical, Computational and numerical techniques

Shortened Conical Horn Antennas Loaded by Lenses (pp. 408)
Jose M. Gil, M. A. González, R. Gómez, J. Rubio, J. García

The Impact of 5G on Human Health (pp. 410)
Yahya Khraisat, 2024-03-01 03:31:02 2024-03-01 03:31:02

New expression for the resonant frequency of rectangular microstrip antenna using genetic algorithm and effective parameters (pp. 418)
Tarek Fortaki, Siham Benkouda, Ahmed Mahamdi, Sami Bedra

Resonant Characteristics of a Superconducting Thin Film Resonator Using the Two-Fluid Model and Artificial Neural Networks (pp. 422)
Siham Benkouda, Tarek Fortaki, Abdelkrim Gadda, Sami Bedra

Optimization of transient electromagnetic problems using discontinuous Galerkin methods (pp. 429)
Fengwen Wang, Tim Warburton, Niels Aage

Electromagnetic interaction and coupling

Enhanced Electromagnetic Interference Shielding of Self-Supporting and Ultrathin Ferrite-Decorated Carbon Nanotube Film (pp. 432)
Nilufer Cakmakci, Youngjin Jeong

Observation of tunable topological phases of polaritons in a cavity waveguide (pp. 434)
Yan Meng, Zhen Gao

Electric Near-Field Probe Calibration for PCB Emission Scanning (pp. 436)
H. Jia, F. Wan, J. Rossignol, V. Mordachev, G. Fontgalland, D-T. Do, Blaise Ravelo

Role of Decoupling Techniques in MIMO Antnna Systems (pp. 438)
Mohammed Bait-Suwailam

Generalizing the Yagi-Uda Antenna: Multi-scale inverse design of disordered metamaterials for radiation pattern shaping (pp. 439)
James Capers, Leanne Stanfield, John Sambles, Stephen Boyes, Alex Powell, Alastair Hibbins, Simon Horsley

Spin wave amplification through superradiance (pp. 441)
X. R. Wang

Metamaterials, metasurfaces, FSS and EBG

Broadband dispersion compensation with ultrathin multiresonant metasurfaces (pp. 443)
Odysseas Tsilipakos, Thomas Koschny

Magnetic permeability investigation of AL800 ferrite by different methods (pp. 445)
Saulius Rudys, Christine Vollinger, Juras Banys, Vidmantas Kalendra

Non-contact Bio-molecules Sensing via Exceptional Transitions on Non-Hermitian Metasurfaces (pp. 447)
Hyunwoo Park, Sodam Jeong, Heiji Son, Soojeong Baek, Teun-Teun Kim

Temporal metastructures enabling multi-mode generation and continuous spectrum radiation (pp. 449)
Davide Ramaccia, Luca Stefanini, Alessio Monti, Mirko Barbuto, Stefano Vellucci, Michela Longhi, Mohsen Karamirad, Alessandro Toscano, Filiberto Bilotti

Local Design of Phase-gradient Metasurfaces robust to Mutual Coupling and Fabrication Errors (pp. 451)
Davide Ramaccia, Luca Stefanini, Alessio Monti, Mirko Barbuto, Stefano Vellucci, Michela Longhi, Mohsen Karamirad, Alessandro Toscano, Filiberto Bilotti

Planar Wideband Metamaterials Energy Harvester (pp. 453)
Mohammed M. Bait-Suwailam, Hassan Al-Lawati, Thamer Almoneef

Electromagnetic Routing using a 6-Port Topological Valley Junction (pp. 455)
Christian Johnson-Richards, Alex Yakovlev, Victor Pacheco-Peña

The nanofabrication and unique properties of 3D metamaterials (pp. 457)
Changzhi Gu

Nanophotonics, plasmonics and quantum optics

Emission Line Selective Optical Manipulation Using Stimulated Recoil Force (pp. 460)
Takao Horai, Takudo Wada, Yoshiki Saito, Masaaki Ashida, Hajime Ishihara

Theoretical study of optical manipulation using electronic resonant light by controlling the triplet state populations (pp. 462)
Yoshiki Umekawa, Takao Horai, Roger Bresolí-Obach, Hajime Ishihara

Combined thermal and mechanical phenomena induced by the fluctuations of the electromagnetic field (pp. 464)
Juan R. Deop-Ruano, Alejandro Manjavacas

Efficient hot-carrier-generation supported by the localization of hybridized plasmon in Au nanoparticle arrays (pp. 466)
Soshun Inoue, Tomohiro Yokoyama, Keiji Sasaki, Hiroaki Misawa, Hajime Ishihara

Superfluorescence-induced optical force in metallic nanofiber systems (pp. 468)
Hideki Arahari, Hajime Ishihara, Nobuhiko Yokoshi

Antenna and interference effects in plasmon-assisted metal photoluminescence (pp. 470)
Tigran Shahbazyan

Plasmonic-enhanced Fabry-Pérot cavity for photocatalysis application (pp. 472)
Ning Lyu, Anjalie Edirisooriya, Zelio Fusco, Fiona Beck, Christin David

Plasmonic effects in composites fabricated by crystal growth techniques (pp. 474)
Piotr Piotrowski, Piotr Paszke, Rafał Nowaczyński, Hańcza Surma, Katarzyna Sadecka, Nuttawut Kongsuwan, Johann Toudert, Ortwin Hess, Dorota A. Pawlak

Optics and Photonics

Fabry-Pérot and Friedrich-Wintgen bound states in the continuum in photonic triple-stub cavity (pp. 476)

Y. Rezzouk, S. Khattou, M. El Ghafiani, M. Amrani, E. H. El Boudouti, A. Talbi, Bahram Djafari Rouhani

Optical Coherence Tomography vs. X-ray imaging for biomedical applications (pp. 478)
Virgil-Florin Duma, Ralph-Alexandru Erdelyi

Direct generation of terahertz cylindrical vector beams in nonlinear crystals (pp. 480)
Seigo Ohno, Hiroaki Iwase

High-order terahertz Bessel beams with an orbital angular momentum (pp. 482)
Katsuhiko Miyamoto

Large-area van der Waals heterostructures for photon harversting (pp. 484)
Maria Giordano, M. Barelli, M. Gardella, G. Zambito, G. Ferrando, F. Buatier de Mongeot

Nanostructures for Photonic Functionalities and Medical Physics Applications (pp. 485)
Mauro Pereira, Humaira Zafar, V. Vaks, A. Ganguly, G. Das

Planarized Terahertz quantum cascade frequency combs with inverse-designed reflectors and integrated antennas for far field control (pp. 486)
Giacomo Scalari, U. Senica, S. Gloor, P. Micheletti, D. Stark, M. Beck, J. Faist

Flexible holographic metasurfaces in the visible and mm-wave range (pp. 488)
Jianling Xiao, Tomasz Plaskocinski, Mohammad Biabanifard, Andrea Di Falco

Radar systems, target detection, localization, and tracking

An Intermodulation Radar for Sensing Applications (pp. 491)
Stefano Pisa, Pietro Monsurrò, Pasquale Tommasino, Alessandro Trifiletti

A Drone Mounted Ground Probing Radar for the Characterization of the Buried Ice Deposits on Mars (pp. 493)
Orlandino Testa, Stefano Pisa, Renato Cicchetti, Andrea Cicchetti, Paolo d'Atanasio, Alessandro Zambotti

Progress on Upgrading the HUSIR Radar for Deep-space Satellite Imaging (pp. 495)
Michael MacDonald, Donna Grimes, Roy Lee, David Gordon, Mohamed Abouzahra, Melissa Schoenfeld

Range Unlimited Coherent Lidar and Autonomous Self-Localization (pp. 496)
Ozdal Boyraz, Ataberk Atalar, Christian Margison, Mustafa Mert Bayer, Xun Li, Ozan Boyraz

Material Characterization and non-destructive testing

Giant Magnetoimpedance Effect at GHz Frequencies in Amorphous Microwires (pp. 499)
Arcady Zhukov, Mihail Ipatov, Paula Corte-Leon, Juan Maria Blanco, Valentina Zhukova

Temperature-dependent properties of amorphous oxide thin films for high-performance distributed Bragg reflectors (pp. 501)
Michele Magnozzi, Stefano Colace, Shima Samandari, Massimo Granata, Alex Amato, Michael Caminale, Christophe Michel, Gianluca Gemme, Laurent Pinard, Maurizio Canepa

Development of Carbon Fiber Composites with Ferromagnetic Microwire Inclusions for Free Space Microwave Sensing (pp. 503)
Valentina Zhukova, Mihail Ipatov, Johan Malm, Christer Johansson, Rafael Garcia-Etxabe, Francisco Javier Vallejo, Peio Olaskoaga, Arcady Zhukov

Plenary presentations

AES 2024, ROME - ITALY, 25 –28 JUNE 2024

Extreme Wave Control with Space-Time Metamaterials

A. Alù[1,2]

[1]Advanced Science Research Center, City University of New York, USA
[2]Graduate Center, City University of New York, USA
[*]corresponding author: aalu@gc.cuny.edu

Abstract: Metamaterials offer a powerful platform to manipulate wave propagation and gain control over waves, from radio-frequencies to light and sound. In this talk, I will discuss our recent progress in developing new metamaterial technologies, introducing time as an additional dimension for wave control.

The field of metamaterials, artificial engineered materials, has been rapidly evolving in the past two decades, demonstrating extreme optical phenomena and unprecedented control over wave propagation. In this talk, I discuss recent developments in this field of research, with an emphasis on the role of symmetries in establishing emerging electromagnetic responses for metamaterials based on otherwise simple constituents. Geometrical rotations, suitably tailored perturbations, and broken time reversal symmetry can be carefully engaged to tailor waves in robust and efficient ways, control their propagation, break Lorentz reciprocity and enable topological order and phase transitions. In my talk, I will discuss the underlying physical principles that span over a wide range of frequencies in the design of metamaterials, and focus on the relevance of the temporal dimension as an additional knob for wave control. I will also discuss the impact of metamaterials on practical technologies, from imaging, energy and sensing to computing and wireless communications.

AES 2024, ROME - ITALY, 25 –28 JUNE 2024

Geodesic Lens Antennas for 5G/6G and Satellite Communications

O. Quevedo-Teruel

KTH Royal Institute of Technology, Stockholm, Sweden.
corresponding author: oscarqt@kth.se

Abstract: In this talk, I will introduce the theory and operation of geodesic lenses. These lenses have attracted the attention of the antenna community due to two of their advantageous properties: low cost and high efficiency. Geodesic lenses make use of a physical path that mimics an equivalent graded refractive index. Therefore, differently to conventional lenses, they can be implemented in a fully-metallic configuration using parallel plate waveguides. This makes these lenses ideal for high-frequency applications, where dielectric materials have significant losses. These lenses are an excellent candidate for new applications in the millimeter frequency regime, especially for antennas with low-scan losses. For example, they are being considered for antenna solutions in 5G/6G, satellite communications in Low-Earth Orbit constellations and automotive radars.

AES 2024, ROME - ITALY, 25 –28 JUNE 2024

Tailorable Materials for Dynamic Photonics: From Metasurfaces to New Physical Phenomena

Alexandra Boltasseva

Purdue University, USA

Abstract: Transparent conducting oxides (TCOs) and transition metal nitrides (TMNs) have attracted attention for photonic applications as they exhibit enhanced light-matter interactions, particularly in their metallic/plasmonic regime and near the so-called epsilon near zero (ENZ) region. Here, we explore the static and dynamic tailorability and tunability of optical properties in TCOs and TMNs, accompanying shifts of their ENZ points. Both homogeneous TCOs and TMNs, as well as structured devices made from them, were investigated for tunability of their nonlinear optical interactions such as harmonic generation and optical modulation. TCO's potential to realize the emerging and novel idea of photonic time crystals has increased their popularity. This research also contributes to understanding novel physical phenomena in ultra-thin TMN films in the so-called transdimensional regime.

AES 2024, ROME - ITALY, 25 –28 JUNE 2024

Metasurface antennas and RIS in Space and 6G Scenarios

Stefano Maci

Department of Information Engineering and Mathematics, University of Siena, Italy
macis@dii.unisi.it

Abstract

Metasurfaces belong to the category of thin metamaterials and find applications across a wide frequency range, from microwaves to optical frequencies, for developing innovative electromagnetic engineering devices. These surfaces are created by densely arranging with a weakly aperiodic distribution small elements ina background environment. By adjusting the dimensions of these elements while maintaining sub-wavelength 2D periodicity, a pixelated visual appearance impedance boundary conditions (IBC) is achieved, which perform the modulation of the electromagnetic incident surface wave. The manipulation of IBC allows for localized modifications in the dispersion equation, influencing the local wavevector while maintaining a constant operating frequency. This capability enables the transformation of surface or guided waves into various wavefield configurations with specified properties. This presentation will focus on the control of surface waves, showcasing examples such as the design of high-gain, low cross-polarization antennas, multibeam antennas, and scanning beam flat lenses. Emphasis will be given to space applications. The presentation will also concern the third generation of adaptive metasurfaces (MTSs), featuring dynamically reconfigurable boundary conditions. This advancement opens possibilities for exploring new perspectives in the development of next-generation wireless communication systems. The presentation will touch upon the concept of a Smart Radio Environment (SRE) as a new paradigm, analyzing the potential of utilizing Reconfigurable Intelligent Surfaces as an enabling technology for 6G networks.

Keynote presentations

AES 2024, ROME - ITALY, 25 –28 JUNE 2024

Scalar wave solutions to a 3D electromagnetic vector wave problem

C.T. Chan[1*]

[1]Physics Department, Hong Kong University of Science and Technology, Hong Kong, China

[*]corresponding author: phchan@ust.hk

Abstract: We showed that some 3D photonic crystals have scalar-wave-like band dispersions. These crystals feature topological surface states with high-Q within the light cone continuum. As such, the surface states in our 3D nested crystals can be exposed directly to air, making such systems well-suited for practical applications.

It is widely acknowledged that solving for the electromagnetic (EM) modes in three-dimensional (3D) systems necessitates the explicit consideration of vector waves, rendering the scalar wave approximation inapplicable. This stands in stark contrast to condensed matter physics, where the scalar approach, which disregards spin, often provides a satisfactory approximation. In condensed matter systems, incorporating the spin degree of freedom can be regarded as a perturbation to the scalar wave band dispersion. However, in the case of EM waves, there is no scalar counterpart to Maxwell's equations in 3D systems. The inherent vector nature of EM waves consistently poses a challenge in the design of topological photonic systems in 3D, as the presence of topologically trivial bands tends to overshadow the emergence of topological bands resulting from symmetry considerations. The realization of "scalar photonic topological phases" in 3D would be highly desirable. In this study, we demonstrate that this can be achieved by constructing a meta-crystal with a nested crystal structure defined by connectivity [1]. The resulting low frequency band structure exhibits a strong resemblance to scalar waves. Through experimental means, we validate this approach by constructing a meta-crystal that hosts spin-1 Weyl points, accomplished solely through considerations of the space group. The scalar approach is straightforward and can be extended to other frequency regimes. Similar methodologies can be employed to realize other photonic topological phases. More importantly, the topological surface wave states exhibit skyrmion-like electric field distributions, resulting in a complete band of high-Q surface states within the light cone continuum. This unique characteristic enables the direct exposure of the topological surface states in our 3D metacrystals to air, making these systems highly suitable for practical applications. Our ideas have been validated through experimental demonstrations.

Acknowledgements: This work is supported by RGC Hong Kong.

References

1. Yang, B. *et al.*, "Scalar topological photonic nested meta-crystals and skyrmion surface states in the light cone continuum", Nature Materials 22, 1203–1209, 2023.

AES 2024, ROME - ITALY, 25 –28 JUNE 2024

A X-Words Play into 2-D Phase Retrieval Problems

T. Isernia[1,2*], G. M. Battaglia[1], A. F. Morabito[1], and R. Palmeri[1,2]

[1] DIIES, Università Mediterranea di Reggio Calabria, Italy {tommaso.isernia@unirc.it}
[2] IREA/CNR, Consiglio Nazionale delle Ricerche, Napoli, Italy

Abstract: Phase retrieval is a challenging problem of interest in very many electromagnetic problems. We report about a recent approach, emulating the solution of crosswords puzzles, which, opposite to common schemes, is able to use a single set of data, and still avoid false solutions.

The Phase Retrieval (PR) problem is a very long-standing challenging problem which is of interest in very many branches of applied science, including optics, inverse scattering, electron microscopy, antenna measurements and synthesis, and many others. Roughly speaking it amounts to recover the phase of a complex field distribution starting from measurements of its amplitude (plus some additional information). Then, the knowledge of the overall complex signal allows to infer properties of the field at hand (such as for example in phaseless near field/far field transformation) or even the recover/synthesize of the source generating such a field.

By the sake of simplicity, let us focus on the case where the signal at hand is the Fourier transform of an aperture field/source, which include the cases of reflectors, lenses, planar arrays, and many others. In this scenario, the far field is related to the 2-D Fourier Transform of the source distribution, so that the signal of interest is spatially bandlimited.

In such a situation, theoretical results are available in the 2-D case which prove that the signal is univocally determined, except for a zero-measure set of cases and trivial ambiguities. These latter correspond to the complex conjugate field, a linear phase, or a combination of the two. Notably, as a linear phase correspond to a translation of the source, the linear phase ambiguity can be fixed by the a-priori knowledge of the support of the source, so that one ends up (apart from a zero-measure set of cases) with just the ground field truth solution and its complex conjugate. The residual zero-measure set of cases arise from factorable fields, because the set of factorable 2-D polynomials has a zero measure in the space of polynomials. This notwithstanding, any current solution procedure for such a problem requires the availability of a substantially larger set of data, such as two different sets of amplitude measurements under defocusing of the feed for reflectors, or measurements on two different near field planes, or other. This is due to the non-linearity of the problem, which implies that solution procedures may be easily ‘trapped’ into false solutions by using the theoretically minimal quantity of data.

A widespread class of solution procedure include many variants of the general ‘alternating projections onto non-convex sets’ strategy, the most popular being probably the ‘Hybrid Input Output’ procedure by Fienup [1].

A more recent class of solution procedures use instead the so-called ‘matrix completion trick’ [2]. In this latter, auxiliary variables are introduced (in such a way that the number of new unknowns is equal to the square of the original ones) in such a way that the problem becomes linear in these new variables.

More specifically the new unknowns are all the possible products amongst the original unknowns (linearly representing the unknown field) and the complex conjugate of this latter. Notably, these unknowns can be then organized into a matrix, and in order to ensure that one can go back to the original unknowns, such a matrix should be enforced to have a rank 1. Unfortunately, this is still a non-convex problem, so that some relaxation related to Compressive Sensing kind of reasoning is introduced. But one is not ensured about the overall effectiveness, as a single solution is eventually found (see below), and because of the enlarged dimensionality

the approach becomes rapidly unusable.

Opposite to the 2-D case, in case of 1-D signals the PR problem has (beyond the trivial ambiguities) very many solutions, which derive from the fact that the power pattern can be expressed as a 1-D polynomial, and then one can play with ('flip') the coupled zeroes of this polynomial in order to generate different solutions. Interestingly, one is able to compute all of these different solutions by the factorization of the polynomial representing the data, and subsequent pairing and flipping of these zeroes [3].

By starting from all the above, an interesting (and in our view) very effective way to proceed to solve in a reliable and accurate fashion a 2-D PR problem with a single set of data can be given, in its initial form [4], as follows.

- First, solve 1-D PR problems along rows and columns, and take note of the possible 'words', that is to say, of the possible phase behaviors;
- second, cross-check horizontal and vertical possible words, so that you can prune the set of possibilities, just like in solving crosswords puzzles.

By so doing, one will keep track (and find) the actual ground truth (and its complex conjugate), but a problem is still there. In fact, large sources imply to deal with polynomials along rows and columns which have a very large order, so that factorization, coupling, and pruning become very difficult.

Such a last problem has been finally solved in our last contribution [5]. In this latter, we solve 1-D PR problems along intersecting small circles (organized according to a hexagonal lattice) and then check for congruence amongst the field solutions on the different circles. In such a way, we are always able to deal with low dimensional polynomials.

A review of main results previously available in 2-D PR, details on the new strategy, and a number of applications will be given at the conference.

Acknowledgements

This work was partially supported by the European Union under the Italian National Recovery and Resilience Plan (NRRP) of NextGenerationEU, partnership on "Telecommunications of the Future" (PE00000001 - program "RESTART").

References

1. J. R. Fienup, "Phase retrieval algorithms: A comparison," *Appl. Opt.*, vol. 21, no. 15, pp. 2758–2769, Aug. 1982.
2. E. J. Candes, Y. C. Eldar, T. Strohmer, and V. Voroninski, "Phase retrieval via matrix completion," *SIAM Rev.*, vol. 57, no. 2, pp. 225–251, 2015.
3. T. Isernia, O. M. Bucci, and N. Fiorentino, "Shaped beam antenna syn- thesis problems: Feasibility criteria and new strategies," *J. Electromagn. Waves Appl.*, vol. 12, no. 1, pp. 103–138, Jan. 1998.
4. G. M. Battaglia, R. Palmeri, A. F. Morabito, P. G. Nicolaci, and T. Isernia, "A non-iterative crosswords-inspired approach to the recovery of 2-D discrete signals from phaseless Fourier trans- form data," *IEEE Open J. Antennas Propag.*, vol. 2, pp. 269–280, 2021.
5. G. M. Battaglia, A. F. Morabito, R. Palmeri and T. Isernia, "Effective Non-Iterative Phase Retrieval of 2-D Bandlimited Signals With Applications to Antenna Characterization and Diagnostics," *IEEE Transactions on Antennas and Propagation*, vol. 71, no. 8, pp. 6444-6453, 2023.

AES 2024, ROME - ITALY, 25 –28 JUNE 2024

Accelerating Photonic Design by Deep Learning

Yongmin Liu[1,2,*]

[1]Department of Mechanical and Industrial Engineering, Northeastern University, Boston, Massachusetts, USA
[2]Department of Electrical and Computer Engineering, Northeastern University, Boston, Massachusetts, USA
[*]corresponding author: y.liu@northeastern.edu

Abstract: Deep learning is instrumental in computational electromagnetics as it excels at capturing intricate patterns and complex relationships within vast datasets, enabling more efficient and accurate modeling of electromagnetic phenomena. This capability is particularly beneficial in photonics design, leading to the discovery of innovative and optimized configurations for desired functionalities.

Novel photonic structures, devices and systems have played a pivotal role in advancing fundamental science and technology development. For example, by tailoring the geometry of the building blocks of metamaterials and engineering their spatial distribution, we can control the amplitude, polarization state, phase and trajectory of electromagnetic waves or light waves in an almost arbitrary manner.[1-3] However, the conventional physics- or rule-based approaches are insufficient for designing multi-functional and multi-dimensional metamaterials, since the degrees of freedom in the design space become extremely large. Deep learning, a subset of machine learning that learns multilevel abstraction of data using hierarchically structured layers, could substantially accelerate the development of complex metamaterials and other photonic structures with high efficiency, accuracy and fidelity.[4-5]

In this talk, I will show that deep learning can help to unveil the highly nonintuitive and nonlinear structure-property relationships in metamaterials. The developed deep learning models, after training, can simultaneously realize the forward prediction and inverse design of 2D and 3D metamaterials that exhibit pronounced chiral or anisotropic responses.[6-7] Using the data-driven approach, we demonstrate multifunctional meta-devices, such as flat lenses and holograms, which exhibit up to eight controllable responses subjected to different combinations of working frequencies and polarization states.[8] We also demonstrate multiwavelength infrared image sensors based on dielectric freeform metasurfaces, which can separate the mixed near-infrared light into distinct wavelengths.[9] The deep-learning approach can be combined with physics-guided methods to further push the functionality-multiplexing capacity. More exciting advancements are expected when researchers with different backgrounds collectively contribute to this emerging field where photonics and artificial intelligence merge.

Acknowledgements: The work was supported by the National Science Foundation under grants 2202268 and ECCS-1916839.

References

1. Smith, D.; Pendry, J.; Wiltshire, M., Metamaterials and negative refractive index. *Science* **2004,** *305* (5685), 788-792.
2. Liu, Y.; Zhang, X., Metamaterials: a new frontier of science and technology. *Chemical Society Reviews* **2011,** *40* (5), 2494-2507.
3. Kildishev, A. V.; Boltasseva, A.; Shalaev, V. M., Planar Photonics with Metasurfaces. *Science* **2013,** *339* (6125), 1232009.

4. Ma, W.; Liu, Z.; Kudyshev, Z. A.; Boltasseva, A.; Cai, W.; Liu, Y., Deep learning for the design of photonic structures. *Nature Photonics* **2021,** *15*, 77-90.

5. Xu, Y.; Xiong, B.; Ma, W.; Liu, Y., Software-defined nanophotonic devices and systems empowered by machine learning. *Progress in Quantum Electronics* **2023**, 100469.

6. Ma, W.; Cheng, F.; Liu, Y., Deep-Learning Enabled On-Demand Design of Chiral Metamaterials. *ACS nano* **2018,** *12*, 6326-6334.

7. Ma, W.; Cheng, F.; Xu, Y.; Wen, Q.; Liu, Y., Probabilistic Representation and Inverse Design of Metamaterials Based on a Deep Generative Model with Semi‐Supervised Learning Strategy. *Advanced Materials* **2019,** *31* (35), 1901111.

8. Ma, W.; Xu, Y.; Xiong, B.; Deng, L.; Peng, R. W.; Wang, M.; Liu, Y., Pushing the limits of functionality‐multiplexing capability in metasurface design based on statistical machine learning. *Advanced Materials* **2022,** *34* (16), 2110022.

9. Xiong, B.; Xu, Y.; Li, W.; Ma, W.; Chu, T.; Liu, Y., Deep Learning Design for Multiwavelength Infrared Image Sensors Based on Dielectric Freeform Metasurface. *Advanced Optical Materials* **2023**, 2302200.

AES 2024, ROME - ITALY, 25 –28 JUNE 2024

Scalable semiconductor photonic systems

Jelena Vuckovic
Ginzton Laboratory, Stanford University, Stanford, CA 94305, USA
*corresponding author: jela@stanford.edu

Abstract: Recent breakthroughs in photonics design, along with new nanofabrication approaches and heterogeneous integration play crucial roles in building photonics for applications including optical interconnects and quantum technologies.

Novel computational techniques such as photonics inverse design, along with new nanofabrication approaches, play a crucial role in building scalable integrated photonics. While initial inverse design demonstrations focused on individual small footprint devices, recent developments enable rapid optimization of large footprint structures in 3D, with linear dimensions over 100 microns, and fully compatible with foundry fabrication. We illustrate this with recent demonstrations of powerful integrated photonic systems for application such as optical interconnects [1].

The implementation of scalable quantum systems is the most dramatic example of this effort, as it requires new photonic materials and device functionalities, together with stringent device performances. Towards this goal, the platforms based on color centers in diamond and silicon carbide have been considered promising candidates, because of their high quality optically interfaced spin qubits, and high quality photonics [2,3].

To enable all necessary functionalities, future photonic systems also require integration of traditional and non-traditional photonic materials, including silicon, silicon-carbide, diamond, sapphire, and strong electro-optic materials such as lithium niobate, strontium and barium titanate. We show that a compact and efficient lasers, isolators, electro-optic modulators, and detectors can all be integrated on silicon platform. Following the same advances in design, fabrication, and heterogenous integration, even Titanium:sapphire laser, the workhorse of optics laboratories, can be miniaturized into sub-cubic centimeter volume together with its pump. We demonstrate such a laser, and show how it can replace commercial tabletop Ti:sapphire lasers in our quantum optics experiments without any loss in performance [4]. We also show how CMOS compatible photonics can be used to achieve on chip isolation simultaneously with laser frequency stabilization [5].

References

1. K.Y.Yang, C.Shirpurkar, A.D.White, J. Zhang, L.Chang, F.Ashtiani, M. A. Guidry, D. M. Lukin, S.V.Pericherla, J. Yang, H. Kwon, J. Lu, G.H. Ahn, K. Van Gasse, Y. Jin, S.P. Yu, T.C. Brilles, J. R. Stone, D.R.Calson, H.Song, K.Zou, H.Zhou, K.Pang, H. Hao, L. Trask, M. Li, A.Netherton, L. Rechtman, J. S. Stone, J.Skarda, L.Su, D.Vercruysse, J.P. W. MacLean, S.Aghaeimeibodi, M. J. Li, D.A.B.Miller, D. Marom, A.E.Willner, J.E.Bowers, S.B. Papp, P. J. Delfyett, F.Aflatouni, and J.Vuckovic, “Multi-dimensional data transmission using inverse-designed silicon photonics and microcombs,” *Nature Communications,* vol. 13, 7862 (2022)
2. Eric I. Rosenthal, Christopher P. Anderson,1 Hannah C. Kleidermacher, Abigail Stein, Hope Lee, Jakob Grzesik, Giovanni Scuri, Alison E. Rugar, Daniel Riedel, Shahriar Aghaeimeibodi, Geun Ho Ahn, Kasper Van Gasse, and Jelena Vuckovic, “Microwave Spin Control of a Tin-Vacancy Qubit in Diamond,” *Physical Review X, vol. 13,* article 031022 (2023)

3. Daniil M. Lukin, Melissa A. Guidry, Joshua Yang, Misagh Ghezellou, Sattwik Deb Mishra, Hiroshi Abe, Takeshi Ohshima, Jawad Ul-Hassan, and Jelena Vuckovic, “Two-emitter multi-mode cavity quantum electrodynamics in thin film silicon carbide photonics,” *Physical Review X,* vol. 13, 011005 (2023)

4. Joshua Yang, Kasper Van Gasse, Daniil Lukin, Melissa Guidry, Geun Ho Ahn, Jelena Vuckovic, “Titanium:sapphire on insulator photonics for brodband, tunable lasers and amplifiers on chip,” Joshua arxiv:2312.00256 (2023)

5. Alexander D. White, Geun Ho Ahn, Kasper Van Gasse, Ki Youl Yang, Lin Chang, Theodore J. Morin, John E. Bowers, Jelena Vuckovic, “Integrated Passive Nonlinear Optical Isolators,” *Nature Photonics,* DOI: 10.1038/s41566-022-01110-y (2022)

AES 2024, ROME - ITALY, 25 –28 JUNE 2024

Low-cost and scalable manufacturing of optical metasurfaces in the visible using engineering optical materials

Junsuk Rho*[1,2,3,4]

[1]Department of Mechanical Engineering, Pohang University of Science and Technology (POSTECH), Pohang, Republic of Korea 37673

[2]Department of Chemical Engineering, Pohang University of Science and Technology (POSTECH), Pohang, Republic of Korea 37673

[3]Department of Chemical Engineering, Pohang University of Science and Technology (POSTECH), Pohang, Republic of Korea 37673

[4]POSCO-POSTECH-RIST Convergence Research Center for Flat Optics and Metaphotonics, Pohang, Republic of Korea 37673

E-mail: jsrho@postech.ac.kr

Abstract: Here, we demonstrate low-cost, scalable manufacturing of optical metasurfaces with three approaches: increasing a refractive index of resin with dielectric particle embedding for single-step nanoimprinting, 2) suppressing optical losses of hydrogenated amorphous silicon (a-Si:H) to apply complementary-metal-oxide-semiconductor technologies, and 3) high-index atomic layer deposited (ALD) structural resin.

Here, we demonstrate low-cost, scalable manufacturing of optical metasurfaces with three approaches: 1) increasing a refractive index of resin with dielectric particle embedding for single-step nanoimprinting [1-5, 7], 2) suppressing optical losses of hydrogenated amorphous silicon (a-Si:H) to apply complementary-metal-oxide-semiconductor technologies [6,7], and 3) high-index atomic layer deposited (ALD) structural resin [7]. We demonstrate the effectiveness of these materials in creating optical metasurfaces operating at different wavelengths in the infrared, visible, and ultraviolet spectra. Firstly, we achieve high efficiencies of up to 90.6%, 47%, and 60% with a-Si [1,7], TiO_2 [2-4], and ZrO_2 PER [5] at wavelengths of 940, 532, and 325 nm, respectively. Furthermore, we obtain a measured efficiency of 30% at a wavelength of 248 nm using ZrO_2 PER metasurfaces [5]. Secondly, by adjusting the deposition conditions of plasma-enhanced chemical vapor deposition, we engineer the bandgap of a-Si:H to enable low-loss operation, with minimum extinction coefficients as low as 0.082 at 450 nm [6]. Using low-loss a-Si:H, we demonstrate efficient beam-steering metasurfaces with measured efficiencies of 42%, 65%, and 75% at 450, 532, and 635 nm, respectively, marking the first Si-typed metasurfaces working at the full visible, as well as demonstrating high-efficiency near-infrared metalenses [7]. Finally, we manufacture highly efficient metalenses using hybrid ALD structural resin with deep-ultraviolet lithography in the visible [8] and ultraviolet [9]. Their measured efficiencies approach 60.9%, 77.8%, and 64.8% at 450, 532 and 635 nm, making them suitable for ultrathin virtual reality devices. Our approaches using PER [1-5], low-loss a-Si:H [6,7], and hybrid ALD structural resin [8,9] enables the low-cost, large-area manufacturing of efficient optical metasurfaces across different wavelengths, facilitating the commercialization of metasurface-based photonic devices [10-16].

References

[1] Yoon, G.; Kim, K.; Kim, S.-U.; Han, S.; Lee, H.; Rho, J.; "Printable Nanocomposite Metalens for High-Contrast Near-Infrared Imaging" ACS Nano 2021 15(1) 698-706.

[2] Kim, K.; Yoon, G.; Baek, S.; Rho, J.; Lee, H.; "Facile Nanocasting of Dielectric Metasurfaces with Sub-100 nm Resolution" ACS Appl. Mater. Interfaces 11(29) 26109-26115.

[3] Yoon, G.; Kim, K.; Huh, D.; Lee, H.; Rho, J.; "Single-step Manufacturing of Hierarchical Dielectric Metalens in the Visible" Nat. Commun. 2020 11 2268.

[4] Kim, J.; Oh, D. K.; Kim, H.; Yoon, G.; Jung, C.; Kim, J.; Badloe, T.; Kang H.; Kim, S.; Yang, Y.; Lee, J.; Ko, B.; Ok, J.G.; Rho, J.; "Metasurface Holography Reaching the Highest Efficiency Limit in the Visible via One-step Nanoparticle-Embedded-Resin Printing" Laser Photonics Rev. 2022 16(8) 2200098.

[5] Kim, J.; Kim, W.; Oh, D.K.; Kang, H.; Kim, H.; Badloe, T.; Kim, S.; Park, C.; Choi, H.; Lee, H.; Rho, J.; "One-step Printable platform for High-Efficiency Metasurfaces Down to the Deep-Ultraviolet Region" Light Sci. Appl. 2023 12 68.

[6] Yang, Y.; Yoon, G.; Park, S.; Namgung, S.D.; Badloe, T.; Nam, K.T.; Rho, J.; "Revealing Structural Disorder in Hydrogenated Amorphous Silicon for a Low-loss Photonic Platform at Visible Frequencies" Adv. Mater. 2021 33(9) 2005893.

[7] S.-W. Moon et al., "Wafer-scale manufacturing of near-infrared metalenses", Laser Photonic Rev. 2024 18 2300929

[8] Kim, J.; Seong, J.; Kim, W.; Lee, G.-Y.; Kim, S.; Kim, H.; Moon, S.-W.; Oh, D.K.; Yang, Y.; Park, J.; Jang, J.; Kim, Y.; Jeong, M.; Park, C.; Choi, H.; Jeon, G.; Lee, K.-I.; Park, N.; Lee, B.; Lee, H.; Rho, J.; "Scalable Manufacturing of High-Index Atomic Layer-Polymer Hybrid Metaphotonics in the Visible" Nat. Mater. 2023 22 474-481.

[9] Kim, J. et al., ""

[10] Kim, G.; Kim, Y.; Yun J.; Moon, S.-W.; Kim, S.; Kim, J.; Park, J.; Badloe, T.; Kim, I.; Rho, J.; "Metasurface-Driven Full-Space Structured Light for Three-Dimensional Imaging" Nat. Commun. 2022 13 5920.

[11] Choi, E. and Kim, G. et al., "360° structured light with learned metasurfaces", Nat. Photon 2024 (in press)

[12] Kim, I.; Kim, W.-S.; Ansari, M.A.; Mehmood, M.Q.; Badloe T.; Kim, Y.; Gwak, J.; Lee, H.; Kim, Y.K.; Rho, J.; "Holographic Metasurface Gas Sensors for Instantaneous Visual Alarms" Sci. Adv. 2021 7(15) eabe9943.

[13] Kim, I.; Ansari, M.A.; Mehmood, M.Q.; Kim, W.-S.; Jang, J.; Zubair, M.; Kim, Y.-K.; Rho, J.; "Stimuli-Responsive Dynamic Metaholographic Display with Designer Liquid Crystal Modulators" Adv. Mater. 2020 32(5) 2004664.

[14] Jung, C.; Kim, G.; Jeong, M.; Jang, J.; Dong, Z.; Badloe, T.; Yang, J.K.W.; Rho, J.; "Metasurface-Driven Optically Variable Devcies" Chem. Rev. 2021 121(21) 13013-13050.

[15] Kim, I.; Martins, R.J.; Jang, J.; Badloe, T.; Khadir, S.; Jung, H.-Y.; Kim, H.; Kim, J.; Genevet, P.; Rho, J.; Nat. Nanotechol. 2021 16 508-524.

[16] Kim, J. et al., "Metasurfaces: Subwavelength Nanostructure Arrays for Ultrathin Flat Optics and Photonics" Nat. Food 2024 (in press).

Nanophotonic scintillators and various topics in AI for topology

Marin Soljačić

Physics Department, Massachusetts Institute of Technology, Cambridge, MA, USA
soljacic@mit.edu

Abstract: Nanophotonic methods provide intriguing options for manipulating scintillation phenomena. We will outline recent developments in this domain, along with our general theoretical framework for modeling these occurrences, supported by our experimental findings. We will also cover novel numerical techniques for discovery of topological phenomena in photonics, as well as AI techniques for discovery of topological phenomena in materials.

AES 2024, ROME - ITALY, 25 –28 JUNE 2024

Chip-scale terahertz optoelectronics

Y. Zhao[1] **and M. Jarrahi**[1*]

[1]Electrical and Computer Engineering, University of California Los Angeles, USA
[*]corresponding author: mjarrahi@ucla.edu

Abstract: We introduce a new scheme for realizing chip-scale terahertz optoelectronics, enabling the scalable implementation of complex terahertz imaging, spectroscopy, and communication systems through a compact platform.

AES 2024, ROME - ITALY, 25 –28 JUNE 2024

Large-Area, Reconfigurable Metasurface Apertures for Synthetic Aperture Radar and Other Applications

David R. Smith

Duke University, USA

Abstract: Metasurfaces are an excellent fit for large-area, reconfigurable apertures due to their use of passive tuning components rather than the active (externally powered) phase shifters and amplifiers integrated into traditional phased arrays. We discuss the advantages of metasurfaces for extremely large, reconfigurable antennas in the context of space-based systems.

Extreme Space-Time Optics & Quantum Meta-Photonics

Vladimir M. Shalaev

Purdue University
West Lafayette, Indiana, USA
corresponding author: shalaev@purdue.edu

Abstract: We first discuss all-optical modulation with single photons using electron avalanche, resulting in record-high nonlinearities. Then we show that transparent conducting oxides (TCOs) operating in the near-zero index (NZI) regime can provide strong single-cycle modulation, thus enabling novel photonic time crystals. Finally, we discuss scalable quantum photonics with single-photon emitters in silicon nitride that we recently discovered as well as the intriguing possibility to generate indistinguishable single photons by using plasmonic speedup that could enable important quantum photonics applications, including quantum communication and quantum computing.

Tutorials

AES 2024, ROME - ITALY, 25 –28 JUNE 2024

Virtual experiments and alternative formulations for effective of solution inverse scattering problems

Lorenzo Crocco

Institute for the Electromagnetic Sensing of the Environment, National Research Council of Italy (IREA-CNR), Italy

*corresponding author: crocco.l@irea.cnr.it

Electromagnetic inverse scattering problems are one of the most exciting topics in applied electromagnetics, due to the broad range of applications in which they are involved and the methodological challenges they pose. In this tutorial, an overview of the difficulties inherent to the non-linear and ill-posed nature of the inverse scattering problems will be given first. Then, some recent results aiming at addressing the challenges posed by the non-linearity will be reviewed. The focus will be on the use of alternative formulations of the basic equations and on the virtual experiments framework, which allow to deal with "simpler" problems by means of simple – but tailored - manipulations of the scattering equations and of the data, respectively.

Smart Electromagnetic Skins for the Next Generation of Wireless Network

On the Features of Curved Passive Electromagnetic Skins

M. Beccaria[1], S. Ayaz[1], A. Mazzinghi[2], A. Freni[2], and P. Pirinoli[1]

[1] Politecnico di Torino, Turin, Italy
[2] University of Florence, Florence, Italy
*corresponding author: machele.beccaria@polito.it

Abstract: In this communication, the features of curved passive smart electromagnetic skins working at millimeter waves to be mounted on street lights or stop light poles are presented and compared to those of the classic planar solution.

The foreseen characteristics of the next-generation communication systems make it necessary to define new paradigms for the network. While the use of mm-waves or sub-THz frequencies seems to be very promising due to the extremely high bandwidth that their use can guarantee, they suffer from higher losses, that are responsible for the degradation of the coverage. To address this issue while maintaining network simplicity, cost-effectiveness, and low power consumption, it becomes fundamental to consider the propagation environment as an additional design parameter. This is possible thanks to the introduction of Smart Electromagnetic Skins (SESs), i.e., very thin surfaces able to provide a not specular reflection to reach blind spots or cover desired areas. Although conventional solutions consist of the use of planar reflecting surfaces [1], recently an alternative configuration that makes use of curved passive electromagnetic skin has been introduced [2]. One of the advantages of such a configuration is the possibility of integration into light or traffic light poles which makes its installation simpler. Furthermore, the SES can be rotated on the pole to maximize the link with the base station. The field re-radiated by the SES is not affected by the contribution of the walls, which could be not negligible [3]. Finally, several SESs, with different orientations, can be mounted on the same pole to cover different areas, with the incident signal arriving from the same direction, or to redirect in the same area the field radiated by different base stations.

With reference to the configuration shown in [2], a new reradiating element (see Fig. 1) that incorporates the radome is here investigated with the aim of reducing the SES manufacturing complexity and mounting. The new element combined with the curved geometry of the SES reduces the presence of higher-order Floquet modes.

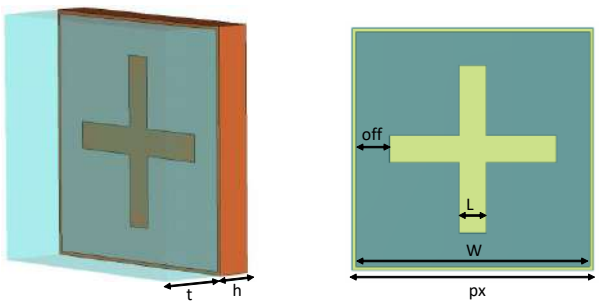

Fig. 1 - Reradiating element geometry (Diclad527 substrate $\varepsilon_r = 2.55$, $\tan\delta = 0.0022$, $h = 0.508\text{mm}$, Lexan radome $\varepsilon_r = 2.8$, $\tan\delta = 0.01$, $t = 1\text{mm}$, $px = 3.6\text{mm}$, $1.5\text{mm} < W < 3.5\text{mm}$, $L = 0.4\text{mm}$, $\text{off} = 0.2\text{mm}$)

The SES is then designed in such a way that it can cover different 5G millimeter wave bands with a simple small rotation. Thus it allows the use of the same SES in different Countries.

This research was carried out in the framework of the Italian National Recovery and Resilience Plan (NRRP) of NextGenerationEU, partnership on "Telecommunications of the Future" (PE0000001—program "RESTART")..

References

1. Martinez-de-Rioja, E.; Vaquero, ÁF.; Arrebola, M.; Carrasco, E.; Encinar, J.A.; Achour, M. Passive intelligent reflecting surfaces based on reflectarray panels to enhance 5G millimeter-wave coverage. Int. J. Microw. Wirel. Tech. 2022, 15, 1–12.
2. Freni A, Beccaria M, Mazzinghi A, Massaccesi A, Pirinoli P. Low-Profile and Low-Visual Impact Smart Electromagnetic Curved Passive Skins for Enhancing Connectivity in Urban Scenarios. Electronics. 2023; 12(21):4491.
3. Vaquero, A.F.; Martinez-de-Rioja, E.; Arrebola, M.; Encinar, J.A. Study on the Effect of theWall in the Performance of an Intelligent Reflective Surface for Providing Coverage in mm-Wave Frequencies. In Proceedings of the European Conference on Antennas and Propag. (EuCAP), Florence, Italy, 26–31 March 2023.

AES 2024, ROME - ITALY, 25 –28 JUNE 2024

An Approach for the Estimation of The Impact of Technological Constraints on Information at the Deep Physical Layer

M.D. Migliore[1*] and M. Di Renzo[2]

[1]DIEI, University of Cassino and Southern Lazio, Italy
[2] Universite´Paris-Saclay, CNRS, CentraleSupe´lec Laboratoire des Signaux et Syste`mes, France
[*]corresponding author: mdmiglio@unicas.it

Abstract:
This contribution proposes an approach to estimate the impact of different technological solutions of radiating/scattering systems. The method is based on the ε-Kolmogorov capacity and can be implemented using a statistical approach.

The relationship between the degrees of freedom of the electromagnetic field and the channel capacity of telecommunications systems is a topic of great interest [1], which is known under the acronym EIT (Electromagnetic Information Theory). Recently, the introduction of innovative ideas regarding the control of the spatial communication channel, such as the use of Reflecting Intelligent Surfaces (SIRs) [2] or Spatial Information Lenses (SILs) [3], has led to a new discipline, known by the acronym ESIT (Electromagnetic Signal and Information Theory) [4], that introduces information processing carried out directly onto the spatial configurations of the electromagnetic field within the physical communication channel, i.e. at the level of the Deep Physical Layer [2].

The goal of ESIT is ambitious and challenging: to combine information theory, signal processing and electromagnetic theory to identify practically implementable solutions that improve the performance of wireless communication systems. The final goal is to obtain novel solutions that are able to increase the reliability and capacity of communication systems, including a reduction of radiated power in the environment with beneficial effects in terms of electromagnetic exposure [5].

Research activity in the electromagnetic community is extremely active and explores various technological solutions [4]. However, achieving the challenging goals of new generations of cellular systems requires a deep understanding of the impact of different technological solutions on the amount of information that can be transmitted. i.e., looking at the communication system from an ESIT perspective.

From an information point of view, using specific architectures introduces further constraints imposed not by fundamental limits imposed by nature but by the technological solutions necessary to implement the systems using the currently available technology. To compare different technological solutions, a preliminary step is introducing a measure of information in the Deep Physical Layer. In [6], the Kolmogorov ε-capacity was proposed as a possible measure of information. In simple terms, the amount of information is given by the cardinality of the set of distinguishable spatial configurations (i.e. whose distance is larger than the noise level) on the domain in which the receiving system is placed. Technological constraints limit set to a subset of the field configurations that are obtainable in an “ideal” system without technological constraints (but verifying the fundamental principles of physics), limiting the ε-capacity. From a functional point of view, information is given by a sphere-packing problem limited to the set of “technological constraints” that determine the radiated fields.

This approach, originally proposed in [7] for information-optimized antenna synthesis, is a possible way to compare different technological solutions. Solving the sphere-packing problem in high dimensions is a formidable task, but statistical approaches allow us to make the problem manageable.

As a simple example, Figure 1 shows the CDF of the distance between the functional points representing the field configuration radiated by a 0.5 λ linear array compared to a continuous aperture, evaluated considering 2000 random excitations having unit norm. According to the theoretical results in [6], the figure shows similar performance for the two solutions.

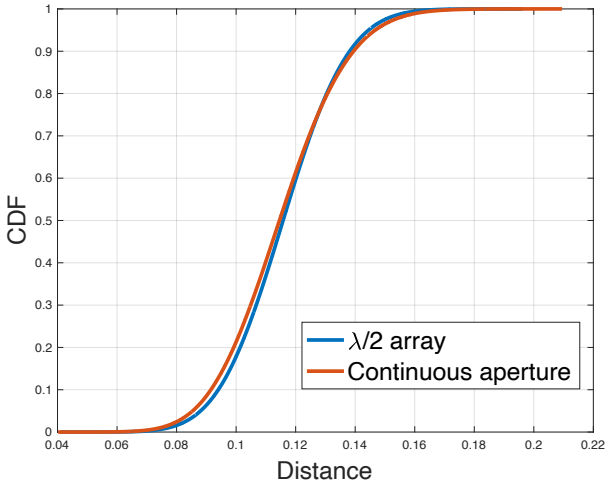

Figure 1: distance between the functional points representing the field configuration radiated by a 0.5 λ linear array compared to a continuous aperture, evaluated considering 2000 random excitations having unit norm

References

1. Zhu, J., Wan, Z., Dai, L., Debbah, M. and Poor, H.V. "Electromagnetic information theory: Fundamentals, modeling, applications, and open problems", IEEE Wireless Communications, doi: 10.1109/MWC.019.2200602, 2024
2. Liu, Y., Liu, X., Mu, X., Hou, T., Xu, J., Di Renzo, M., & Al-Dhahir, N. "Reconfigurable intelligent surfaces: Principles and opportunities. IEEE communications surveys & tutorials", 23(3), 1546-1577, 2021.
3. Migliore, M.D., "Classical and Quantum Processing in the Deep Physical Layer". IEEE Access, 2023
4. Di Renzo, M. and Migliore, M.D., 2023. "Electromagnetic Signal and Information Theory-On Electromagnetically Consistent Communication Models for the Transmission and Processing of Information" IEEE BITS the Information Theory Magazine, Early access, doi: 10.1109/MBITS.2024.3359523, 2024
5. Petroulakis, N., Mattsson, M. O., Chatziadam, P., Simko, M., Gavrielides, A., Yiorkas, A. M., ... & Bogdanova, A. "NextGEM: Next-Generation Integrated Sensing and Analytical System for Monitoring and Assessing Radiofrequency Electromagnetic Field Exposure and Health. International Journal of Environmental Research and Public Health", 20(12), 6085, 2006.
6. Migliore, M. D. "On electromagnetics and information theory." IEEE transactions on antennas and propagation, 56(10), 3188-3200, 2008.
7. Migliore, M. D. "Horse (electromagnetics) is more important than horseman (information) for wireless transmission. IEEE Transactions on Antennas and Propagation", 67(4), 2046-2055, 2018

AES 2024, ROME - ITALY, 25 –28 JUNE 2024

Introduction to fewer known properties of glide symmetry

Oscar Quevedo-Teruel[1*]

[1] Division of Electromagnetic Engineering and Fusion Science, KTH, Stockholm, Sweden
[*]corresponding author: oscarqt@kth.se

Abstract: In this talk, I will introduce the concept of glide symmetry and its application for periodic structures. The use of glide symmetries is popular due to their ability to enhance electromagnetic band gaps in metallic holey structures, as well as their ability to reduce the dispersion of periodic structures, which is beneficial for example for increasing the bandwidth or alleviating the manufacturing difficulties of graded-index lenses. However, other attractive properties of glide symmetries, such their ability to produce composite magnetic-dielectric materials, or to enhance the levels of anisotropy were not sufficiently noticed. In this presentation, I will explain these two properties and their interest for reducing the size of lenses with transformation optics, as well as to reduce the reflections in the borders of lenses.

A periodic structure possesses glide symmetry if it is invariant after a translation and a mirroring [1]. This simple geometric condition can produce significant changes in the electromagnetic properties of a unit cell specially in highly coupled sub-unit cells [2]. Among the most popular exploited properties of glide symmetries are the following two:

- Increasing the bandwidth and attenuation constant of periodic structures [3]. These properties have been employed, for example, to avoid the leakage between parallel plate transitions, such as flanges [4], or for producing cost-effective designs of gap-wave guide technology [5].
- Reducing the dispersion of periodic structures, increasing their effective refractive index, and improving their isotropy [6], which is beneficial for the design of lens antennas [7].

Multiple variants of these two properties have been broadly reported in the literature and applied to multiple use cases. However, there are another two attractive properties associated to glide symmetries, which have been less studied.

The first one is the ability to enhance the anisotropy and bandwidth of periodic structures. This property was first demonstrated in [8] for the propagation in a dielectric slab with metallic patterns in the top and bottom. In [8], glide-symmetric elliptical holes were employed to produce a compressed Luneburg lens designed with the use of transformation optics. Later, in [9], glide-symmetric holes were used to produce a compressed Maxwell fish-eye lens. In the latter, the propagation was in the air, and the holes were filled with dielectric in a parallel plate waveguide configuration. More recently, a compressed Luneburg lens was proposed in [10]. In this case, the chosen technology was substrate-integrated-holes with a propagation in the air, with a designed aimed at being both cost-effective and low lossy.

The second property is the ability of glide symmetry to increase the permeability in a dielectric slab (surrounded by metal), by using glide-symmetric holes in the top and bottom. This property was first demonstrated in [11] and employed to reduce the reflections in a different refractive index in normal and oblique incidence. The concept was experimentally demonstrated in a substrate integrated waveguide filled with two different dielectric materials. In addition, the concept was proposed to avoid the reflections at the contour of a two-dimensional dielectric hyperbolic lens, although his was only demonstrated with simulations. No further

studies have been conducted in this topic, despite of the potential use in conventional lens antennas for avoiding reflections and enhancing their radiation efficiency.

In this talk, I will discuss these cases, and open a discussion of possible new demonstrations, which could be potentially interesting for ground and satellite communications, radar and sensing.

References

1. A. Hessel, M. H. Chen, R. C. M. Li, and A. A. Oliner, "Propagation in periodically loaded waveguides with higher symmetries," *Proc. IEEE*, vol. 61, no. 2, pp. 183–195, Feb. 1973.
2. O. Quevedo-Teruel, Q. Chen, F. Mesa, N. J. G. Fonseca, G. Valerio, "On the benefits of glide symmetries for microwave devices," *IEEE J. Microw.*, vol. 1, no. 1, pp. 457-469, winter 2021.
3. Q. Chen, F. Mesa, X. Yin, O. Quevedo-Teruel, "Accurate Characterization and Design Guidelines of Glide-Symmetric Holey EBG", *IEEE Trans. Microw. Theory Techn.*, vol. 68, no. 12, pp. 4984-4994, Dec. 2020.
4. M. Ebrahimpouri, A. A. Brazalez, L. Manholm, and O. Quevedo-Teruel, "Using glide-symmetric holes to reduce leakage between waveguide flanges," *IEEE Microw. Wireless Compon. Lett.*, vol. 28, no. 6, pp. 473–475, Jun. 2018.
5. M. Ebrahimpouri, E. Rajo-Iglesias, Z. Sipus, and O. Quevedo-Teruel, "Cost-effective gap waveguide technology based on glide-symmetric holey EBG structures," *IEEE Trans. Microw. Theory Techn.*, vol. 66, no. 2, pp. 927–934, Feb. 2018.
6. O. Quevedo-Teruel, M. Ebrahimpouri, and M. N. M. Kehn, "Ultrawideband metasurface lenses based on off-shifted opposite layers," *IEEE Antennas Wireless Propag. Lett.*, vol. 15, pp. 484–487, Dec. 2016.
7. O. Quevedo-Teruel, J. Miao, M. Mattsson, A. Algaba-Brazalez, M. Johansson, and L. Manholm, "Glide-symmetric fully metallic Luneburg lens for 5G communications at Ka-band,"2*IEEE Antennas Wireless Propag. Lett.*, vol. 17, no. 9, pp. 1588–1592, Sep. 2018.
8. M. Ebrahimpouri and O. Quevedo-Teruel, "Ultrawideband anisotropic glide-symmetric metasurfaces," *IEEE Antennas Wireless Propag. Lett.*, vol. 18, no. 8, pp. 1547–1551, Aug. 2019.
9. A. Alex-Amor, F. Ghasemifard, G. Valerio, M. Ebrahimpouri, P. Padilla, J. M. Fernandez-Gonzalez, O. Quevedo-Teruel, "Glide-Symmetric Metallic Structures With Elliptical Holes for Lens Compression", *IEEE Trans. Microw. Theory Techn.*, vol. 68, no. 10, pp. 4236-4248, Oct. 2020.
10. Q. Chen, F. Giusti, G. Valerio, F. Mesa, O. Quevedo-Teruel, "Anisotropic Glide-Symmetric Substrate-Integrated-Holey Metasurface for a Compressed Ultrawideband Luneburg Lens", *Appl. Phys. Lett.*, vol. 118, number 8, 2021. I
11. M. Ebrahimpouri, L. F. Herran, and O. Quevedo-Teruel, "Wide angle impedance matching using glide-symmetric metasurfaces," *IEEE Microw. Wireless Compon. Lett.*, vol. 30, no. 1, pp. 8–11, Jan. 2020.

Design and Optimization of Active and Passive Quasi-Periodic Structures for Beam Steering

Pasquale Giuseppe Nicolaci *, Mustafa Murat Bilgic, Min Zhou

[1]TICRA, Denmark

*corresponding author, E-mail: pgn@ticra.com

Abstract

This paper presents the direct optimization of active and passive reconfigurable quasi-periodic structures for beam steering. Two configurations are considered, an active reconfigurable reflectarray working between 24.5-27.5 GHz for 5G application, and a passive mechanical steered low profile transmitarray working between 19.7-20.2 GHz.

1. Introduction

In the last decade the interest in quasi-periodic structure antennas has grown producing a lot of solutions based on active or passive configurations. In this work, we will name quasi-periodic antenna systems that achieve beam steering via electronic control as active quasi-periodic structures and reflectarray/transmitarray antennas with static beams patterns that achieve beam steering via mechanical control will be named passive quasi-periodic structures.

One of the emerging areas where active quasi-periodic structures can provide an affordable and efficient solution are applications that require beam collimation and adaptive pattern scanning. With the application of 5G technology, it has been found that traditional means of adapting to the wireless propagation environment, such as enhancing the capabilities of base stations and terminals, and optimizing the networking structure, are all ineffective due to the easily blocked characteristics of millimetre waves [1]. Recently, there is a lot of work published in the literature where reconfigurable intelligent surfaces (RIS) and reconfigurable reflectarray antennas (RRA) are demonstrated to overcome the issues with communication channels. Extensive comparative studies and definitions regarding RISs and RRAs, and their applications can be found in [1] – [3].

By changing the reflection phase of each unit cell in a reflectarray it is possible to collimate or shape the antenna far-field pattern to a desired specification. An arbitrary phase shift between 0° and 360° will help achieve perfect phase correction hence full control on optimizing the beam shape. For pattern scanning, ideally, it would be desired to have the same arbitrary phase shift to actively steer the beam in the desired direction. However, active quasi-periodic structure with continuous 0° - 360° phase range-controlled unit cells are technically and practically very challenging.

To overcome bandwidth, linearity and complexity issues of beam-steerable active quasi-periodic structures, discreate phase quantization schemes have been adopted. In [4], [5], a general overview of the existing designs that have implemented 1-bit, 2-bit and 3-bit quantization schemes have been discussed with comparisons from the literature and how they also can be applied for polarisation conversions have also been given. A wide range of research is focused on 2-bit phase quantization and the work in the literature shows that a good beam-steering in a wide band and range can be achieved, some examples of these works can be found in [6], [7] and [8].

Despite the flexibility given by the active solutions, the passive mechanical solution for beam steering can provide advantages for the cases where large apertures are needed which entails that the complexity and cost of an active antenna can drastically grow.

In the last years several publications on the use of rotating lens to implement the steering of the beam have been presented. These solutions represent the evolution of the Risley prism concept. The typical optical system Risley Prism consists of two independently rotatable prisms which deflect a beam via refraction. Some drawbacks of the Risley prism include bulky and heavy dielectric wedges and high reflections at the interfaces, which significantly degrade the antenna radiation performance. However, this antenna configuration doesn’t2 need2 any active component or complex beamforming network and it is able to cover wide beam scanning angles.

The new solutions based on the optical Risley prism were focused on overcoming the main drawback related to the thickness and weight which lead to the phase shifting surface where the phase shifting is achieved by thin conductive layered constituted by several etched patches on dielectric slab. Despite the simplicity of the antenna concept, a drawback which is difficult to deal with is to achieve an optimal solution where all the sidelobes are under control.

In section 2 and 3 we will present the initial designs of both an active and a passive quasi-periodic structure intended for

beam steering applications using a direct optimization approach for optimizing the quasi-periodic surfaces.

The conventional method for designing such quasi-periodic surfaces is to employ the phase-only optimization approach, as described in [9]. This approach involves first determining the necessary phase and subsequently calculating the individual mode for each array element. However, due to its two-step nature, it lacks complete control over the far-field pattern. This limitation makes it challenging to design reflectarrays with intricate beam shapes, such as shaped beams or pencil beams with stringent side lobe suppression requirements. In contrast, by adopting a direct optimization approach, as described in [10], where the individual modes for all array elements are optimized simultaneously based on the desired far-field pattern, it becomes easier to precisely control the shape of the far-field pattern and achieve complex beam shapes.

To accomplish these designs, we employed the commercial software tool QUPES [11], which is specifically tailored for the design and analysis of quasi-periodic surfaces, including reflectarrays and transmitarrays. Final conclusions are made in the last section.

2. Active Reflectarray Design

The active quasi-periodic structure is intended for operation within the 24.5 - 27.5 GHz frequency band, utilizing a five-step phase quantization scheme. The selected band is to be used to bring low-cost wideband solution for base station extensions based on indoor, urban macro and dense urban deployment scenarios.

2.1. Antenna Architecture

2.1.1. PUC Design

In this work, we consider an array element based on aperture coupled stacked patch antenna topology. Figure 1 shows the aperture coupled stacked patch setup with some of the widely used aperture shapes. By varying the stub length (L_{stub}), it is possible to achieve a wide reflection phase variation angle control. The proposed array element geometry is shown in Figure 2. The array element has a stack up of five layers. The SP4T switch is placed below the ground plane at the very bottom. The switch inputs and outputs are connected to phase quantization striplines in the mid copper layer by vias. Confining main RF paths in the mid-layer gives us the ability to reduce losses and isolate the RF layer from the DC circuitry and the discrete circuit components required to operate the switch, which can degrade performance due coupling.

The SP4T switch intended to be implemented in the PUC operated by connecting the input to one of the four outputs using two control bits. A single bit is used to enable and disable the switch device. The two control bits together with the enable/disable bit will conclude to five possible phase modes.

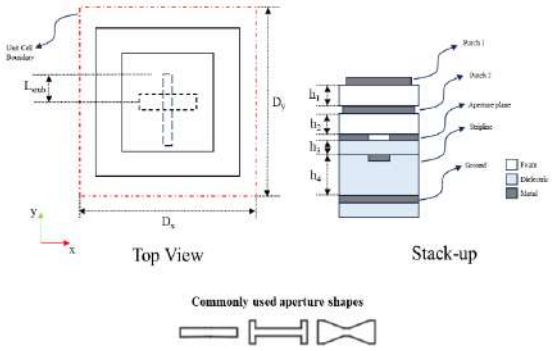

Figure 1: Aperture coupled stacked patch element.

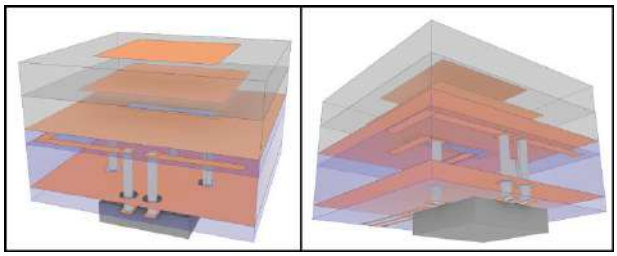

Figure 2: Proposed reconfigurable array element geometry.

The model has been built using QUPES. The preliminary design will incorporate the array element as simplified version. The switch is not included in the model, but the switching function is implemented in the mid layer. The simplified model and the five possible switching states implemented in the mid layer are shown in Figure 3.

The design has been optimized to have linear phase variation and low reflection loss. It can be seen from Figure 4 that the phase variation of the optimized unit cell is almost linear throughout the 24.5-27.5 GHz band. At each frequency, the five modes can provide a phase quantization in the dynamic range of 320° and the peak reflection loss is below 0.6 dB for all modes.

2.1.2. Reflectarray Design

As application example, we consider the design of a reconfigurable reflectarray, with a focus on a practical 5G application case, were the reflectarray shall redirect incoming waves originating from a telecommunications source. These incoming waves may be obstructed by obstacles, e.g., by a wall, and the reflectarray is utilized to steer the incoming wave towards the intended reception area as depicted in Figure 5.

The reflectarray has a dimension of 25x25 cm^2 and is illuminated by a plane wave source symbolising a source as a base station stationed far away. There are 2601 array elements in the reflectarray, and the entire antenna is modelled using QUPES. The optimization variables are the discrete modes of the array elements, resulting in a total of 2601 optimization variables. As optimization goal, the reflectarray is optimized to redirect the peak for each scan

angle individually. Furthermore, a side lobe suppression has been enforced to be 25 dB below peak.

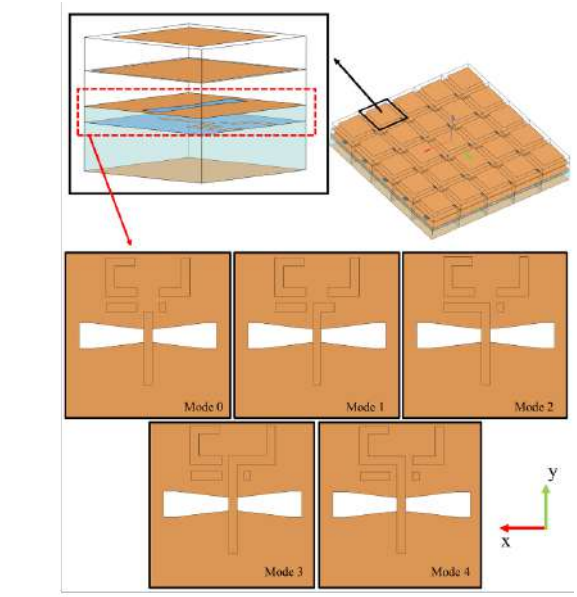

Figure 3: Simulation model of preliminary reconfigurable array element together with the five discreate operation modes.

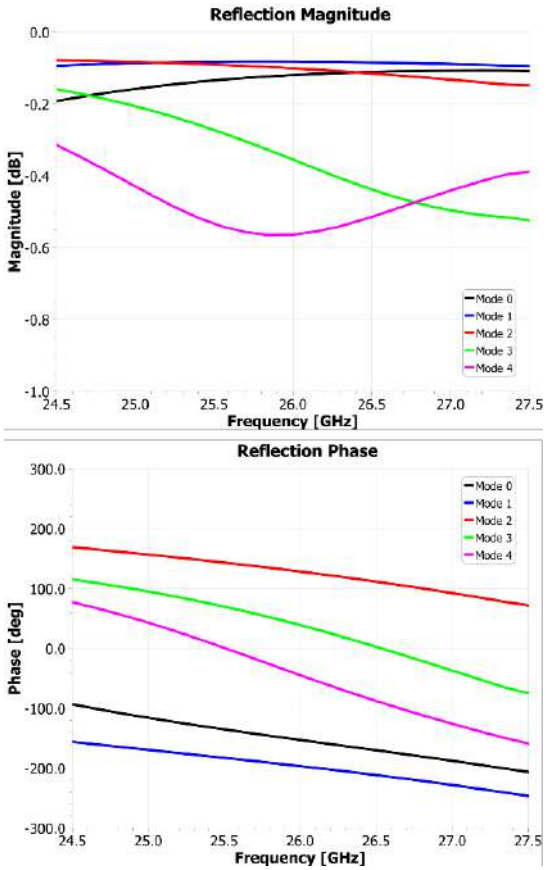

Figure 4: Electrical properties of optimized unit cell.

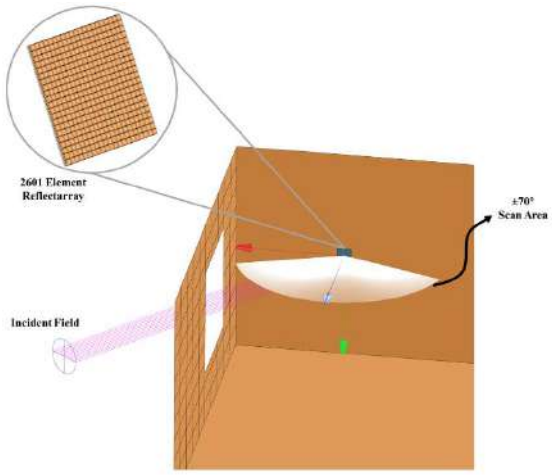

Figure 5: Application case where the reflectarray redirects the incoming plane wave to the intended reception area.

2.2. Antenna Performance

In Figure 6, the radiation pattern of the reflectarray, which has been optimized for redirecting the incident plane wave to 20° (the specular direction), is presented. The discrete modes of each individual array element, along with the optimization template marked by red lines, are visible in this figure. In a conventional reflectarray designed to redirect a plane wave to the specular direction, the phase variation across the reflectarray surface remains constant. However, in our case, all five modes are utilized in a somewhat irregular fashion. This is a direct consequence of the imposed side lobe suppression requirements. The result shows that we achieve a directive beam directed towards -20°, with side lobes measuring more than 20 dB below the peak value.

In Figure 7, we show far-field radiation pattern of all the optimized reflectarrays for scanned beam between ±70°. It is seen that it is indeed possible to scan within this range, albeit significant scan loss at the higher scanning angles, as expected.

In addition to scanned beams, other pattern shapes can be achieved, depending on the intended reception area. The design process is identical to that of the scanned beams, but as optimization goal, the reflectarray is optimized to reshape the incidence field into a fan shape, i.e, wide beam in one plane and a narrower beam in the orthogonal plane.

Fig. 8 shows the radiation pattern of an optimized design that can create a wide beam between ±50°, together with colour codes of the discrete modes of each individual array element over the reflectarray surface. It is seen here that the reflectarray radiates in a wide beam between ±50°. Obviously, there are some ripples in the beam pattern, but this is expected since the reflectarray only operates with 5 modes. Contrary to the pencil beam cases, it is seen in the colour codes that mode 4 is employed to a larger extent, indicating that additional bits are required if one is interested in reducing the ripples in the pattern.

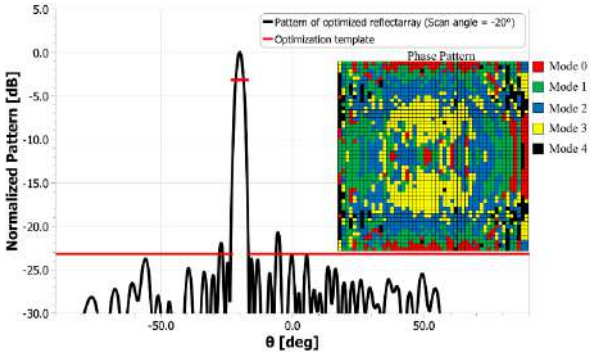

Figure 6: Far-field radiation pattern of the optimized reflectarray for θ = -20°.

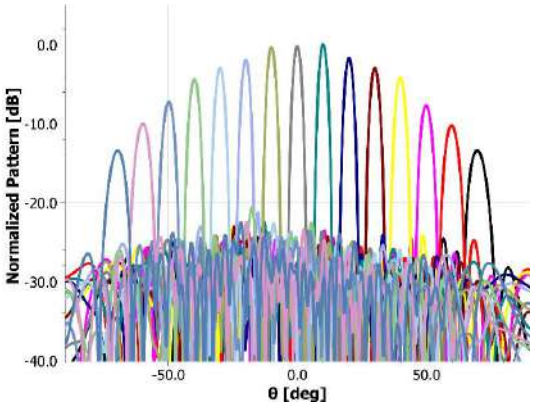

Figure 7: Far-field radiation pattern of the optimized reflectarrays for scanned beams between ±70°. (All beams have been optimized for 26 GHz).

All the simulations presented in this section were carried out on an Intel(R) Core (TM) i9-12900F 2.4 GHz computer and the time to complete one optimization for a certain scan angle requires only approximately two minutes.

3. Passive Transmitarray Design

This section is focused on the design of passive antenna for beam steering. The antenna is designed to cover the Ka band frequency range from 19.7 GHz to 20.2 GHz with a beam steering range of [90°, 30°] in elevation plane and [0°, 360°] in the azimuth plane. The beam steering is achieved by mechanically rotating the dual passive transmitarrays system while the primary source is fixed. This allows us to avoid rotary joint which introduces unwanted losses in the antenna system.

In the proposed design the primary source is a dual reflector system where the main reflector is a reflectarray. This optical subsystem feeds the transmitarrays which are placed on top of the sub reflector of the primary source, see Figure 9.

The overall antenna swept volume is 400 mm x 400 mm x 100 mm and the dual orthogonal circular polarizations are achieved by means of a septum polarizer connected with the waveguide section of the primary source.

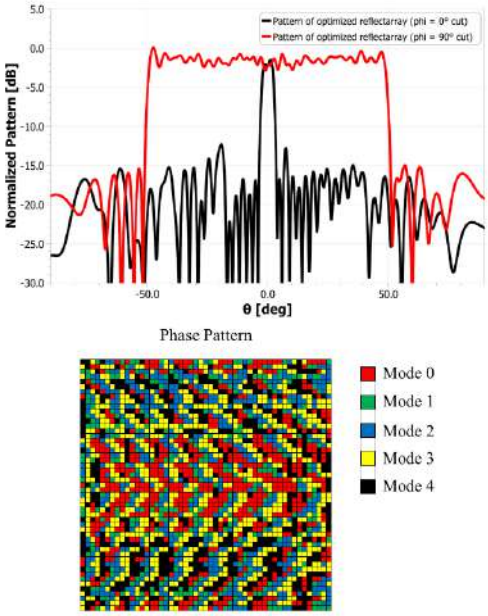

Figure 8: Far-field radiation pattern of the optimized reflectarray for ±50°. fan beam.

Figure 9: Antenna system architecture for the passive antenna configuration.

The role of the primary source is to provide a plane wave which feeds the rotating transmitarray. In the literature there are many different flat planar sources based on RLSA array, patch cavities, leaky wave antennas, etc. The proposed solution in this section has many advantages, such as: easy handling of the dual polarization, good cross-polarization purity, and a good phase illumination of the transmitarrays.

3.1. Antenna Design

3.1.1. Primary Source Design and Optimization

The antenna optics is an axial displaced ellipse with a stepped subreflector which was optimized to provide the best illumination to the reflectarray. The optics focal length over the diameter is around 0.17 and a dielectric cone is designed to support the subreflector which has a diameter of 40 mm.

The reflectarray is a single layer structure of Roger Duroid 5880 with a thickness of 0.787 mm. The unit cell is a simple square patch with an inter-elements distance of $\lambda/2$.

The primary source antenna was optimized with a direct multilevel optimization task where the subreflector steps and the size of patches are optimized to achieve a pencil beam pattern pointing at the boresight with suppressed sidelobe and cross-polarization level. Figure 10 shows the geometry of the optimized reflectarray and subreflector.

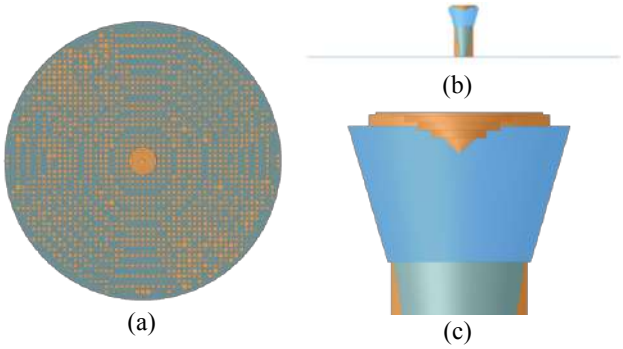

Figure 10: Top view of the optimized reflectarray (a), lateral view (b), zoom of the sub reflector and supporting structure (c).

Figure 11 depicts the radiation pattern of the primary source antenna for the planes passing through ϕ = (0, 45, 90) degrees at the frequency of 19.95 GHz. It can be noted that the multi-level optimization allows to get a pattern with well controlled sidelobes and cross-polarization.

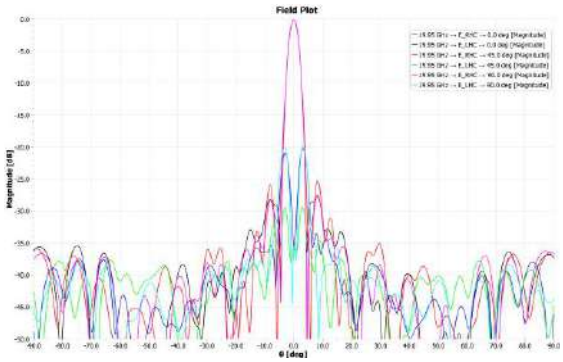

Figure 11: Radiation pattern of the primary antenna source.

3.1.2. Transmit Array Design and Optimization

The role of the two rotating transmitarray is to steer the incoming beam towards a desired direction. The two transmitarrays act like phase shifting surface (PSS) and each one introduce a gradient phase shift to the transmitted wave. The two transmitarrays or PSSs are equal, and each one is optimized to steer the beam at the angle (θ, ϕ) = (35, 0) degrees. Combining the relative counter rotations of the two PSSs it is possible to control the beam steering along the elevation plane for a desired azimuth plane, and rotating both PSSs with respect to the primary source with the same angle it is possible to change the azimuth pointing.

The are different strategies reported to achieve a gradient phase shift. All these strategies work at the unit cell level where some geometrical parameters are used to insert a desired phase. A phase variation can be achieved by changing the size of the patches [12] - [14] or rotating the unit cell [15] - [17].

The second strategy has an important advantage because the unit cell can be optimized to minimize the insertion loss which is independent of the rotation angle allowing to have a uniform amplitude distribution on the PSS.

In this paper the transmitarray unit cell geometry is based on the rotated element strategy and the design was inspired by [16]. The unit cell geometry was optimized in QUPES to work in the desired Ka- band. As depicted in Figure 12, the unit cell has four dielectric layers where patches and a ground plane with a crossed slot are accommodated. The crossed slot is optimized to provide circular polarization, while the rectangular patches are optimized to get a 180 degrees phase difference between the x and y components of the transmitted wave. The unit cell has a side length of $\lambda/2$ and an overall thickness of 6.3 mm.

Figure 13 reports the unit cell performance in terms of amplitude and phase variation of the transmitted wave as function of the rotating angle in the operative bandwidth. It is evident that the insertion loss variation with the rotating angle is less than 0.15 dB in the full band, and the phase spans the full [0°, 360°] range.

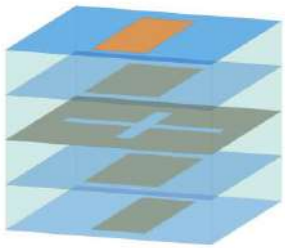

Figure 12: Unit cell geometry of the transmitarray.

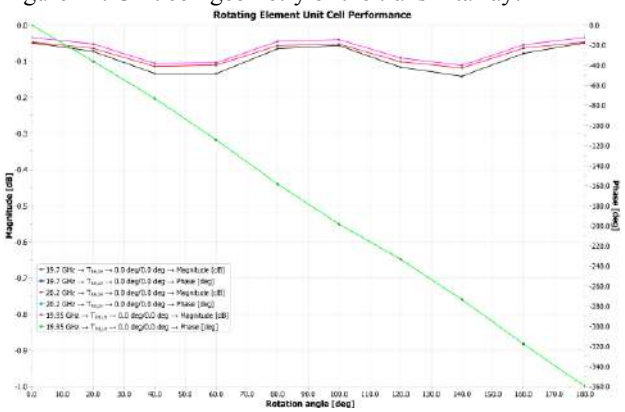

Figure 13: Amplitude and phase variation vs rotating angle.

The next step of the optimization foresees the optimization of the full transmitarray. As said before, the two shifting surfaces are identical, and each one is optimized to steer the

beam at the angle of 35 degrees along the plane ϕ = 0°. Figure 14 and Figure 15 show the normalized cut pattern and *uv* pattern of a single transmitarray fed by the primary source. All the lobes in the scanning plane are below 25 dB with respect to the pattern peak.

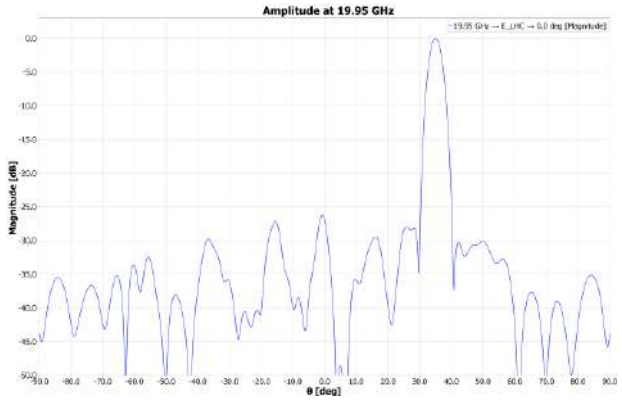

Figure 14: Normalized pattern of the single transmitarray fed by the primary source.

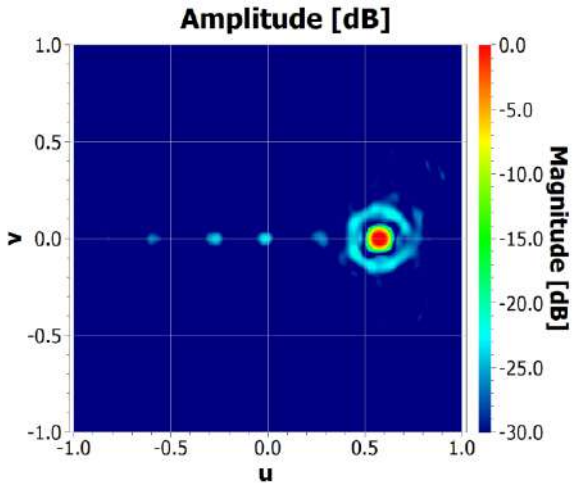

Figure 15: Normalized *uv* pattern of the single transmitarray fed by the primary source.

3.2. Antenna Performance

In this section the expected performances of the full antenna system achieved by means simulations in QUPES are reported.

Figure 16 shows the radiation patterns for different scanning angles along the plane phi = 90°. It can be noticed that the scan loss is in accordance with the $cos(\theta)^{1.2}$ law, the lobes are below -25 dB with respect to the peak in the scanning plane.

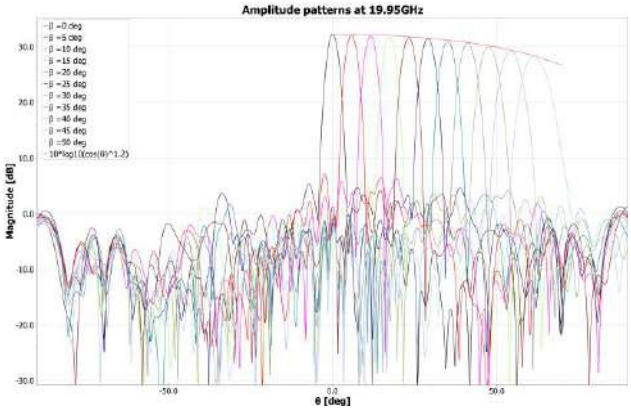

Figure 16: Normalized pattern cuts of the full antenna system.

Figure 17 depicts the patterns in the uv plane for different scanning angle along the plane u=0. In the plots there are some spurious lobes, but their level is under -18 dB in the worst case. This is an important achievement because grating lobes are one of the major issues for this kind of antenna based on phase shifting surfaces, but the optimization at the unit cell level and the direct optimization of the full antenna system are able to get a good amplitude and phase for the TE and the TM modes which implies that the grating lobe are under control.

4. Conclusions

This paper presents the preliminary design of an active and a passive quasi-periodic structure-based antennas intended for beam steering applications using the commercial software QUPES, utilizing the direct optimization approach.

In the first design, by employing a five-state switch-controlled unit cell for discreate phase quantization, various reflectarray optimizations for beam steering and fan beam patterns have been optimized The active quasi-periodic structure was built within the context of a 5G application, where the reflectarray is to facilitate beam scanning over an angular range of ±70° and dan shaped patterns, all while subject to stringent side lobe suppression requirements. The second design, which is the passive quasi-periodic structure, can steer the beam by using a mechanical rotation of the two identical transmitarray. The transmitarray unit cell is based on the phase rotation principle which allows to get large phase variation range and very low insertion losses. The direct optimization allows to optimize the primary source and the two transmitarrays to get the desired pattern and reducing the sidelobe level.

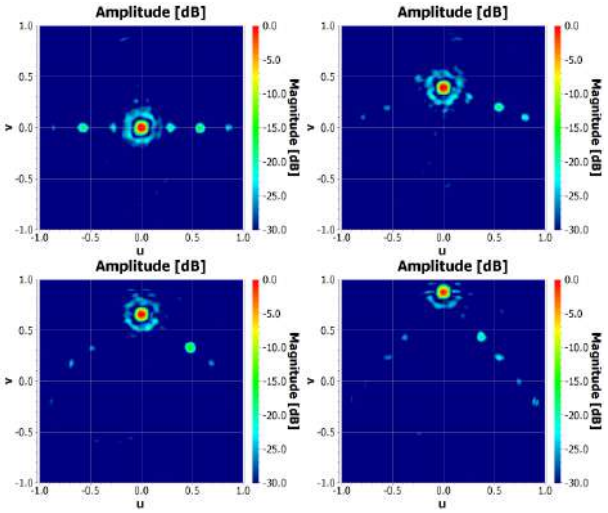

Figure 17: Normalized *uv* pattern of the full antenna system

References

[1] X. Zou, J. Yao, K. L. Chung, G. Lai, W. Zeng, and W. Gu, "A comparative study between reconfigurable intelligent surface and reflectarray antenna," in Proc. 5th ICEICT, 2022.

[2] Z. Fu, X. Zou, Y. Liao, G. Lai, Y. Li, and K. L. Chung, "A brief review and comparison between transmitarray antennas, reflectarray antennas and reconfigurable intelligent surfaces," in Proc. 3rd ITOCS, 2022.

[3] L. Chen, K. L. Chung, G. Lai, J. Yao, X. Zou, X. Cheng, K. Zheng, and Y. Li, "Cross deployment of active and passive reconfigurable intelligent surfaces (riss) for next-generation communications," in Proc. 25th ICEICT, 2022.

[4] H. Luyen, J. H. Booske, and N. Behdad, "2-bit phase quantization using mixed polarization-rotation/non-polarization-rotation reflection modes for beam-steerable reflectarrays," IEEE Trans. Antennas Propag., vol. 68, no. 12, 2020.

[5] H. Yu, Z. Zhang, J. Su, M. Qu, Z. Li, S. Xu, and F. Yang, "Quadpolarization reconfigurable reflectarray with independent beam-scanning and polarization switching capabilities," IEEE Trans. Antennas Propag., vol. 71, no. 9, pp. 7285–7298, 2023.

[6] C. C. Cheng and A. Abbaspour-Tamijani, "Design and experimental verification of steerable reflect-arrays based on two-bit antenna filterantenna elements," IEEE MTT-S Int. Microw. Symp. Dig., pp. 1181–1184, 2009.

[7] R. Sorrentino, "Mems-based reconfigurable reflectarrays," Proc. 2nd Eur. Conf. Antennas Propag. (EuCAP), Edinburgh, pp. 1–7, 2007.

[8] B. Xi, Y. Xiao, K. Zhu, Y. Liu, H. Sun, and Z. Chen, "1-bit wideband reconfigurable reflectarray design in Ku-band," IEEE Access, vol. 10, pp. 4340–4348, 2022.

[9] J. Huang and J. A. Encinar, Reflectarray Antennas. IEEE Press, 2008.

[10] M. Zhou, S. B. Sørensen, O. S. Kim, E. Jørgensen, P. Meincke, and O. Breinbjerg, "Direct optimization of printed reflectarrays for contoured beam satellite antenna applications," IEEE Trans. Antennas Propag., vol. 61, no. 4, pp. 1995–2004, 2013.

[11] "QUPES Software," TICRA, Denmark.

[12] N. Gagnon and A. Petosa, "Using Rotatable Planar Phase Shifting Surfaces to Steer a High-Gain Beam," in IEEE Transactions on Antennas and Propagation, vol. 61, no. 6, pp. 3086-3092, June 2013.

[13] M. U. Afzal and K. P. Esselle, "Steering the Beam of Medium-to-High Gain Antennas Using Near-Field Phase Transformation," in IEEE Transactions on Antennas and Propagation, vol. 65, no. 4, pp. 1680-1690, April 2017.

[14] Sérgio Matos, João Felício, Jorge Costa, Carlos Fernandes, Nelson J. G. Fonseca "Dielectric versus patch-based implementations of Risley Prism transmit-arrays in Ka-band" EURAAP 17th European Conference on Antennas and Propagation (EuCAP), 2023

[15] F. Caminita et al., "Low-profile Steerable Antennas for User Terminals," 2023 17th European Conference on Antennas and Propagation (EuCAP), Florence, Italy, 2023, pp. 1-5.

[16] R. H. Phillion and M. Okoniewski, "Lenses for Circular Polarization Using Planar Arrays of Rotated Passive Elements," in IEEE Transactions on Antennas and Propagation, vol. 59, no. 4, pp. 1217-1227, April 2011.

[17] J. Wang and Y. Rahmat-Samii, "A Simplified Configuration of Beam-Steerable Risley Prism Antennas: Principles and Validation," in IEEE Antennas and Wireless Propagation Letters, vol. 21, no. 11, pp. 2288-2292, Nov. 2022.

AES 2024, ROME - ITALY, 25-28 JUNE 2024

A scattering matrix approach for the inverse design of smart devices

A. F. Morabito[1*], R. Abdullin[1], G. M. Battaglia[1], T. Isernia[1,2], and R. Palmeri[1,2]

[1] DIIES, Università Mediterranea di Reggio Calabria, Reggio Calabria, Italy

[2] Istituto per il Rilevamento Elettromagnetico dell'Ambiente, IREA/CNR, Napoli, Italy

[*] corresponding author: andrea.morabito@unirc.it

Abstract: The present contribution deals with the synthesis of smart skin and anomalously reflecting devices by exploiting a new 'inverse design' procedure exploiting the scattering matrix approach.

In 'inverse design' approaches, the shape and internal electromagnetic features of the antennas and guiding devices are identified by solving an inverse scattering problem in such a way that, for a given incident field, the scattered field fulfills some desired requirements (e.g., a given power-pattern shape, beamwidth, and sidelobe level) [1].

When the design of smart devices like smart skin, anomalously reflecting devices, and Reconfigurable Intelligent Surfaces (RIS) must be dealt with, recasting the synthesis problem as an inverse design one allows achieving effective and flexible solutions [1]. From an electromagnetic scattering point of view, these devices can often be conceived as the result of the interaction of properly arranged inclusions/scatterers that can be located above a Perfect Electric Conductor (PEC) (plus a supporting dielectric layer) [2]. In this respect, the design problem can be cast as an inverse scattering one aimed at determining some optimal parameters of the scatterers (e.g., position, shape, dimension, material) such that the overall reflected field obeys assigned specifications.

As a step towards inverse design, we consider herein the forward problem, establishing an effective method to compute the field scattered by a given configuration of scatterers subject to a given incident field in a half-space above a PEC. To take this problem, we exploit the so-called 'scattering matrix' associated to each scatterer, which encodes the relationship amongst the coefficients of the expansions of the incident and scattered fields [3], and we extend the overall analysis method to embed the additional field contributions due to the presence of the PEC.

Acknowledgements

This work was partially supported by the European Union under the Italian National Recovery and Resilience Plan (NRRP) of NextGenerationEU, partnership on "Telecommunications of the Future" (PE000000012 - program "RESTART").

References

1. R. Palmeri, M. T. Bevacqua, A. F. Morabito, and T. Isernia, "Design of artificial-material-based antennas using inverse scattering techniques," *IEEE Trans. on Antennas and Propagation*, 66(12), pp. 7076-7090, 2018.
2. T. E. Rimpiläinen and R. Jäntti, "Multiple Scattering Model for Beam Synthesis With Reconfigurable Intelligent

Surfaces," *IEEE Transactions on Antennas and Propagation*, 71(6), pp. 4990-5000, 2023.

3. D. Felbacq, G. Tayeb, D. Maystre, "Scattering by a random set of parallel cylinders," *J. Opt. Soc. Am. A*, vol. 11, no. 9, pp. 2526-2538, Sept. 1994.

AES 2024, ROME - ITALY, 25 –28 JUNE 2024

Liquid Crystal Technology for Implementing Smart Electromagnetic Skins in Next Generations of mm-Waves Wireless Systems

E. Carrasco*, R. Guirado, G. Pérez-Palomino, P. de la Rosa, M. A. Geday
Information Processing and Telecommunications Center, Universidad Politécnica de Madrid
*corresponding author: eduardo.carrasco@upm.es

Abstract: Reflective phase-shifting surfaces bases on liquid crystal (LC) technology allow implementing efficient and low-cost, smart electromagnetic skins. By locally controlling a low-frequency voltage, the coverage of a reflected wave can be dynamically optimized. This is a powerful solution for improving the capabilities of next generation air interface design, in mm-waves.

Acknowledgment: This work has been supported by MCIN/AEI/10.13039/501100011033 within project ENHANCE-5G (PID2020-114172RB-C22)

AES 2024, ROME - ITALY, 25 –28 JUNE 2024

Metasurfaces for Enhanced Wireless Communications

A. Alù[1,2]

[1]Advanced Science Research Center, City University of New York, USA
[2]Graduate Center, City University of New York, USA
[*]corresponding author: aalu@gc.cuny.edu

Abstract: Metasurfaces offer a powerful platform to address the challenges of modern wireless communications, especially when considering the opportunity to integrate conventional metasurface elements with active, nonlinear and time-varying components suitably tailored and controlled in real-time to respond to changes in the background.

Metasurfaces are formed by planarized two-dimensional arrays of subwavelength tailored constituent elements, which control locally the amplitude, phase and polarization features of the outgoing electromagnetic wave and enable extreme wavefront engineering. The conventional technologies underlying these engineered surfaces is passive, static, linear and time-invariant, hence it has limited opportunities for wireless communication systems, and it suffers from inherent challenges, including limited efficiency, loss and bandwidth constraints. At microwave and mm-wave frequencies, however, the metasurface elements can be quite straightforwardly integrated with tailored circuits, enabling real-time reconfigurability, feedback, amplification, nonlinear responses, parametric phenomena and temporal modulations. Metasurfaces loaded with active, time-varying and nonlinear elements indeed have been recently explored in a variety of settings, including to realize largely nonreciprocal responses [1], frequency conversion and mixing [2-4], active cloaking [5], and self-induced topological features associated with robust response [6]. In turn, these functionalities may open interesting opportunities when combined together and applied to wireless communication systems.

Time-varying metasurfaces can be rapidly modulated in time and programmed as a function of the impinging signals and of the changing environment, reacting to these changes and tailored to optimize the scattering matrix connecting a multitude of users operating at different frequencies and with vastly diverse service requirements. Such surfaces may tailor and steer the reflection wavefront pattern in its spatial distribution, polarization, frequency content and dispersion to maximize interference among multiple paths for all users. The real-time programmability of its elements may enable the implementation of a dynamic environment in which changes in the user positions and in the background can be dynamically monitored, and the information may be used to program the metasurface response in real-time. Large nonlinearities in metasurfaces have been demonstrated in a variety of settings [7-9], yielding efficient spectrum transformations, intensity-dependent responses, limiting [10], with opportunities for signal multiplexing and frequency generation and conversion. Active elements, such as transistors and amplifiers, integrated in metasurfaces can provide programmable amplification of the impinging signals to suppress decay loss, especially at high frequencies, and tailor with flexibility their amplitudes and phases, overcoming the limitations of passive metasurfaces in terms of energy conservation and bandwidth. Temporal variations can also induce parametric phenomena, which may be leveraged for mixing [11], to compensate for Doppler shifts [12], to break reciprocity [13], to boost the impinging signals through parametric amplification, and even to realize true-time delay beyond the delay-bandwidth limitations of passive systems [14]. Nonlinearities and/or time modulation can also be

leveraged to break electromagnetic reciprocity [15].

These functionalities can largely enhance the degrees of freedom available to manipulate the overall scattering response of metasurfaces, and they are instrumental in enhancing spectrum efficiency of wireless networks towards enabling a better use of frequency channels. As an additional opportunity, metasurfaces may offer an agile platform for analog signal processing, leveraging advanced dispersion engineering through their nonlocal response to impart on the impinging signals mathematical operations of choice [16], hence enabling the calculation of the Fourier transform of the input signals over an efficient and ultralow-energy platform.

References

1. Hadad, Y., Soric, J. C. & Alu, A. Breaking temporal symmetries for emission and absorption. Proc Natl Acad Sci USA 113, 3471–3475 (2016).
2. Yuan, J., De Carvalho, E., Williams, R. J., Bjornson, E. & Popovski, P. Frequency-Mixing Intelligent Reflecting Surfaces for Nonlinear Wireless Propagation. IEEE Wireless Commun. Lett. 1–1 (2021) doi:10.1109/LWC.2021.3077085.
3. Wu, Z. & Grbic, A. Serrodyne Frequency Translation Using Time-Modulated Metasurfaces. IEEE Trans. Antennas Propagat. 68, 1599–1606 (2020).
4. Wu, Z., Scarborough, C. & Grbic, A. Space-Time-Modulated Metasurfaces with Spatial Discretization: Free-Space N -Path Systems. Phys. Rev. Applied 14, 064060 (2020).
5. Selvanayagam, M. & Eleftheriades, G. V. Experimental Demonstration of Active Electromagnetic Cloaking. Phys. Rev. X 3, 041011 (2013).
6. Hadad, Y., Soric, J. C., Khanikaev, A. B. & Alù, A. Self-induced topological protection in nonlinear circuit arrays. Nat Electron 1, 178–182 (2018).
7. Lee, J. et al. Giant nonlinear response from plasmonic metasurfaces coupled to intersubband transitions. Nature 511, 65–69 (2014).
8. Lee, J. et al. Ultrathin Second‐Harmonic Metasurfaces with Record‐High Nonlinear Optical Response. Advanced Optical Materials 4, 664‐670 (2016).
9. Tymchenko, M., Gomez-Diaz, J. S., Lee, J., Belkin, M. A. & Alù, A. Highly-efficient THz generation using nonlinear plasmonic metasurfaces. J. Opt. 19, 104001 (2017).
10. Mann, S. A. et al. Ultrafast optical switching and power limiting in intersubband polaritonic metasurfaces. Optica 8, 606-613 (2021).
11. Qin, C. et al. Spectrum Control through Discrete Frequency Diffraction in the Presence of Photonic Gauge Potentials. Phys. Rev. Lett. 120, 133901 (2018).
12. Ramaccia, D., Sounas, D. L., Alù, A., Toscano, A. & Bilotti, F. Doppler cloak restores invisibility to objects in relativistic motion. Phys. Rev. B 95, 075113 (2017).
13. Hadad, Y., Soric, J. C. & Alu, A. Breaking temporal symmetries for emission and absorption. Proc Natl Acad Sci USA 113, 3471–3475 (2016).
14. Tymchenko, M., Sounas, D., Nagulu, A., Krishnaswamy, H. & Alù, A. Quasielectrostatic Wave Propagation Beyond the Delay-Bandwidth Limit in Switched Networks. Phys. Rev. X 9, 031015 (2019).
15. Kord, A., Sounas, D. L. & Alu, A. Microwave Nonreciprocity. Proc. IEEE 108, 1728–1758 (2020).
16. Kwon, H., Sounas, D., Cordaro, A., Polman, A. & Alù, A. Nonlocal Metasurfaces for Optical Signal Processing. Phys. Rev. Lett. 121, 173004 (2018).

AES 2024, ROME - ITALY, 25 –28 JUNE 2024

Design of a Dual-Band Dual-Polarized Smart Electromagnetic Skin with Shaped Anomalous Reflection Considering Phase Shift Constraints in the Unit Cell

Álvaro F. Vaquero[1*], Eduardo Martinez-de-Rioja[2], and Manuel Arrebola[1]

[1]Dept. Electrical Engineering, Group of Signal Theory and Communications, Universidad de Oviedo, Spain
[2]Dept. of Signal Theory and Communications and Telematic Systems and Computing, Universidad Rey Juan Carlos, Madrid, Spain
[*]Corresponding author: fernandezvalvaro@uniovi.es

Abstract: This work analyzes the design of a Smart Electromagnetic Skin (SES) to enhance millimeter-wave (mm-Wave) communications, working on dual band, at 28 and 39 GHz, as well as in dual-linear polarization. The design is carried out considering a phase-shift limitation in the phase response of the unit cell.

The deployment of mm-Wave communications entails tackling new challenges in communications systems, particularly those related to signal propagation. This frequency range is characterized by high propagation and penetration losses [1]. In certain scenarios, such as some outdoor urban areas or indoor locations like malls, auditoriums or airports, the blind zones are so common. A blind zone refers to an area within the coverage region where the signal level is extremely low, disrupting the link between users and base station.

To overcome, or at least, alleviate this problem, Reflective Intelligent Surfaces (RIS) have been proposed, which can be classified into four groups (from RIS-1 to RIS-4) based on their capabilities [2]. Here, our focus lies on RIS-1, also known as Smart Electromagnetic Skins (SES), as they are entirely passive and intended to improve urban wireless coverage [3]. SES are particularly useful to overcome blind zones, since they can capture a portion of the radiated power of a base station and redirect it towards the blind zone, either in specular or anomalous direction. Furthermore, SES not only reflects a focused beam in the desired direction but also shapes the reflected beam according to the blind zone requirements, thereby preventing disruption of the mm-Wave link. Recently, reflectarray-based panels have been proposed to enhance the SES performance, yielding successful results in shaped blind-zone coverage in dual-linear polarization [4]-[6].

In this work, the design of a dual-band dual-linear-polarized reflectarray-based SES is presented to generate a shaped coverage for a blind zone. The SES operates at 28 and 39 GHz, considering that incident field in each band is provided by an independent base station in different locations. Moreover, at each operating frequency, the reflected beam is independently controlled for each linear polarization. To do so, the SES is composed of a 40 x 40 cm^2 reflective panel, formed by an array of 89 x 89 unit cells which are comprised of sets of orthogonal coplanar dipoles, as Figure 1 depicts. The reflected beam in each polarization and frequency is redirected towards the same direction, applying beamforming to cover the desired angular range of the blind zone. The beamforming is reached by using a Phase-Only Synthesis (POS) based on the Intersection Approach framework [7]. However, in this case, a phase-shift constraint in the unit cell is introduced, ensuring that the dipoles physically fit within the cell size being used. The electromagnetic simulation results show the successful performance in both polarizations, as well as both frequency bands, as Figure 2 depicts.

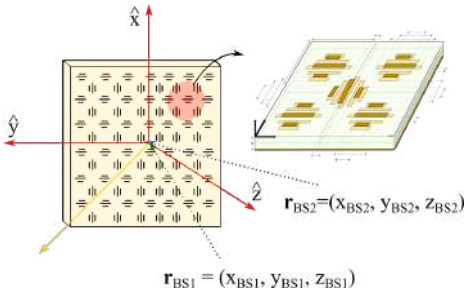

Figure 1. Scenario proposed to deploy the SES and its unit cell.

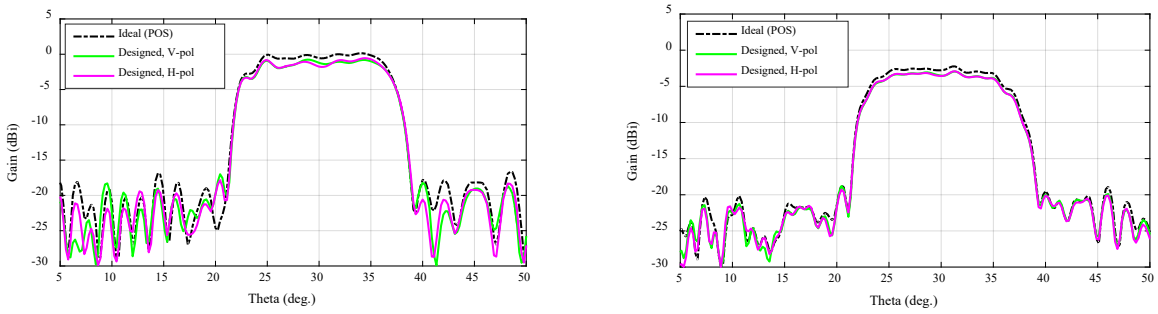

(a) (b)

Figure 2. Simulated radiation patterns: azimuth cut at (a) 28 GHz and (b) 39 GHz.

This work was supported in part by MCIN/AEI/10.13039/501100011033 under grants PID2020-114172RB-C21-2, TED2021-131975A-I00 and TED2021-130650B-C22, the last two cofounded by UE (European Union) "NextGenerationEU"/PRTR; by the Spanish Ministry of Universities and European Union (NextGenerationEU/PRTR) under grant MU-21-UP2021-03071895621J; and by Comunidad de Madrid within the Multiannual Agreement Framework with Universidad Rey Juan Carlos, Line of Action 1, Young Researchers R&D Project INCREASE-5G (Ref. F858).

References

1. S. Salous *et al.*, "Millimeter-wave propagation: Characterization and modeling toward fifth-generation systems," IEEE Antennas Propag. Mag., vol. 58, no. 6, pp. 115-127, Dec. 2016.
2. S. Maci, "Reflective Intelligent Surfaces and metasurface antennas," IEEE Radio Antenna Days Indian Ocean (RADIO), Balaclava, Mauritius, 2023.
3. P. Rocca *et al.*, "On the Design of Modular Reflecting EM Skins for Enhanced Urban Wireless Coverage," IEEE Transactions on Antennas and Propagation, vol. 70, no. 10, pp. 8771-8784, Oct. 2022.
4. Á. F. Vaquero, B. Imaz-Lueje, M. R. Pino and M. Arrebola, "Reflectarray Antenna for Simultaneous NEar-Field Fronthaul and Far-Field Backhaul Links in Next 5G FR2 Femtocells," IEEE Open Journal of Antennas and Propagation.
5. E. Martinez-de-Rioja *et al.*, "Enhancement of 5G millimter-wave coverage in indoor scenarios by passive shaped-beam reflectarray panels," 2022 16th Eur. Conf. Antennas Propag. (EuCAP), Madrid, Spain, 2022, pp. 1-5.
6. E. Martinez-de-Rioja *et al.*, "Passive dual-polarized shaped-beam reflectarrays to improve coverage in millimeter-wave 5G networks," 2021 15th Eur. Conf. Antennas Propag. (EuCAP), Dusseldorf, Germany, 2021, pp. 1-5.

Advanced antenna systems: modelling and experiments

AES 2024, ROME - ITALY, 25-28 JUNE 2024

On the use of the parabolic wave equation to model the electromagnetic propagation in maritime environment

T. Bonnafont[1], A. Khenchaf[1*]

[1]Lab-STICC, UMR CNRS 6285, ENSTA Bretagne, 29806, Brest, France
[*]corresponding author: ali.khenchaf@ensta-bretagne.fr

Abstract: Modeling the long-range propagation in a maritime environment is a challenging problem since many physical phenomena shall be accounted for, such as refraction, or waves. Here a model based on the parabolic wave equation solved with split-step wavelet that allows obtaining accurate simulations is proposed.

Modeling the tropospheric long-range propagation is very important for predicting the coverage of systems or optimizing the placement of antennas. In this work, we are interested in the propagation in the maritime environment, where local phenomena, such as sea waves or surface ducts, shall be accounted for.

In this context, a widely used model is the parabolic wave equation (PWE) [1]. Indeed, it allows fast computational simulations while accounting for the refraction, the relief, and the ground composition. In particular, a low complexity method, i.e., split-step wavelet (SSW), has been developed [2,3] for tropospheric propagation applications. The latter has been modified to account for the sea, using a hybrid approach [4,5]. In this approach, the sea spectrum is cut in half, the lowest part is used to generate random sea surface, while the highest allows computing a new roughness coefficient. We improve this method by modifying this coefficient to account for the shadowing effect of the waves, as in [6]. Using this approach, we are also able to model the propagation above polluted sea surfaces [7]. In Figures 1 and 2, we plot the propagation computed with SSW. Different models are used: a plane sea is considered with either the Ament or Miller-Brown roughness coefficient, the usual hybrid approach is used, or the shadowed hybrid approach. For the last two, which are stochastic methods, a Monte Carlo simulation is performed and the mean and 99% confidence intervals are plotted. In Figure 1, we considered a 10 m/s wind speed, while a 15 m/s wind speed is considered for 3.

As expected, the results are quite different considering the waves or not. Indeed, the extremum are not at the same position, mostly due to the effect of the relief (sea waves), in particular when higher wind speeds are considered, as expected. Also, introducing the shadowed coefficient in the hybrid approach introduced a slight modification of the maxima and minima values.

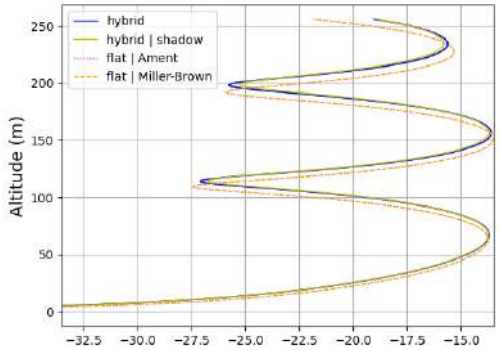

Figure 1: Field (in dB) computed with SSW with different approaches considering a wind speed of 10 m/s.

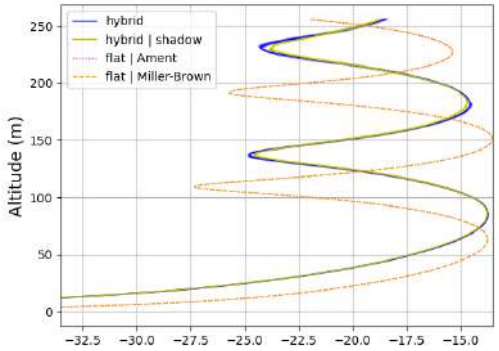

Figure 2: Field (in dB) computed with SSW with different approaches considering a wind speed of 15 m/s

In the maritime environment, we also need to consider tropospheric ducts that are very common. Among the

various models available to understand evaporation ducts, the log-normal model stands out. Remarkably, it relies on just four parameters: duct height, surface parameter, roughness, and refractive index at sea level. However, accurately setting these parameters for simulation poses challenges due to inherent errors in meteorological measurements. To address this, we conduct a statistical study employing a Latin hypercube sampling and Sobol' indices strategy, we can explore the influence of different parameter sets on the predicted field, thereby showing their respective impacts on the predicted field. In Figure 4, we plot some samples of the field computed with some set of parameters, but also the mean value and the 99% confidence interval computed over the samples. In red, we also plot the case when no error is assumed.

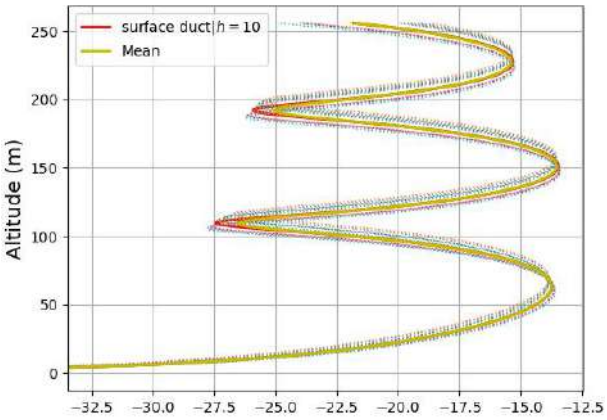

Figure 3: Statistical analysis of the parameters of log-normal model duct.

In this figure, we can see that the measurement errors influence on the result. Indeed, the position and values of maxima and minima are different. Therefore, it shall be accounted for. Furthermore, the Sobol' indices strategy has shown that the key parameters of the model are the duct height and the surface parameter. Therefore, more accuracy is needed on these two for better predictions.

In this work, we proposed a PWE/SSW method to model the propagation in the maritime environment. The propagation above the sea is considered through a shadowed hybrid approach. Furthermore, we proposed a statistical study to explore the influence of measurement error on the parameters of the log-normal model for evaporation ducts.

Acknowledgment

The authors wish to thank the DGA-AID (Direction Générale de l'Armement / Agence de l'Innovation de Défense, France) for its support of the MEPOM project, where this work is in progress.

References

1. Levy, M. "Parabolic equation methods for electromagnetic wave propagation," IET, 2000.
2. Zhou, H., R. Douvenot, and A. Chabory, "Modeling the long-range wave propagation by a split-step wavelet method," *Journal of Computational Physics*, 402, 109042, 2020.
3. Bonnafont, T., Douvenot, R., & Chabory, A. (2021). "A local split-step wavelet method for the long-range propagation simulation in 2D," *Radio science*, 56(2), 1-11.
4. Benhmammouch, O., Khenchaf, A., & Caouren, N. (2011). "Modelling roughness effects on propagation of electromagnetic waves in a maritime environment: A hybrid approach," *IET radar, sonar & navigation*, 5(9), 1018-1025.
5. Bonnafont, T., Benhmammouch, O., & Khenchaf, A. (2022). "A two-way split-step wavelet scheme for tropospheric long-range propagation in various environments," *Remote Sensing*, 14(11), 2686.

6. Pinel, N., Bourlier, C., & Saillard, J. (2007). "Forward radar propagation over oil slicks on sea surfaces using the Ament model with shadowing effect," *Progress In Electromagnetics Research*, 76, 95-126.
7. Bonnafont, T., & Khenchaf, A. (2023, June). A hybrid wavelet-based method to model the electromagnetic propagation above a polluted sea surface. In *9th International Conference on Antennas and Electromagnetic Systems, AES 2023*.

AES 2024, ROME - ITALY, 25 –28 JUNE 2024

Controllable polarization emission laser based on chiral metasurfaces

I. Katsantonis[1,2], A. Tasolamprou[1,3], Th. Koschny[4], and M. Kafesaki[1,2*]

[1]Institute of Electronic Structure and Laser, Foundation for Research and Technology Hellas (FORTH), Heraklion, Crete, Greece
[2]Dept. of Materials Science and Technology, Univ. of Crete, Greece.
[3]Dept. of Physics, National and Kapodistrian University of Athens, Athens, Greece
[4]Ames Lab and Dept. of Physics and Astronomy, Iowa State University, Ames, Iowa, US
[*]corresponding author: kafesaki@iesl.forth.gr

Abstract: We present an ultracompact lasing structure able to provide dynamically controllable polarization emission, ranging from linear to circular and from left-handed circular to right-handed circular. The structure is based on a properly designed chiral metasurface combined with a gain material (dye molecules).

Compact, polarization-controllable lasers, particularly those emitting circularly polarized (CP) light, have garnered significant attention in recent years due to their potential advancements across various applications, such as spectroscopy, sensing, and display technology [1-4]. Additionally, CP emission lasers offer a valuable tool for comprehending and manipulating chiral light-matter interactions, critical across different scientific disciplines, including chemistry, pharmacology, biophysics, and quantum optics [1-4].

One approach to achieve CP emission lasers involves integrating a gain medium with a chiral system. Chiral metamaterials and metasurfaces hold great promise in this regard, as they can exhibit a strong chiral response (typically 4-5 orders of magnitude greater than natural chiral media) within ultra-compact structures. However, while significant efforts have been made to achieve CP emission lasers using this approach [5-6], the resulting emitted waves often lack purity in circular polarization. Moreover, existing structures struggle to provide dynamic control over the laser field.

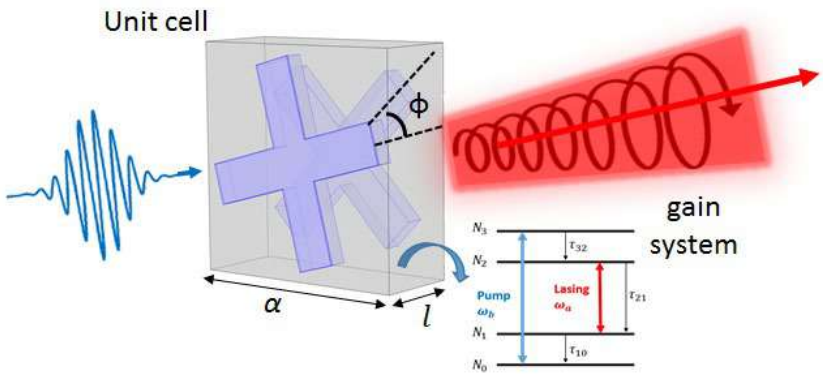

Figure 1: Illustration of the unit cell of the proposed structure. The structure comprises pairs of mutually twisted metallic crosses, embedded in a dielectric medium dopped with a gain material (dye molecules). The gain material is modelled as a 4-level atomic system [7], as shown also in the figure. The structure unit cell lateral size is

a=300 nm, with thickness l=100 nm.

Here, we propose an ultra-compact lasing configuration achieved through the fusion of a chiral metasurface with a gain medium (dye molecules) [8]. The metasurface unit-cell is illustrated in Fig. 1; it is composed of a pair of mutually twisted metallic crosses embedded in a gain-dopped host material. As our detailed numerical simulations demonstrate [8], our structure exhibits the capability to generate an emission laser with nearly pure circular polarization (with emitted wave ellipticity close to 45 degrees). The polarization characteristics of this emission can be highly tailored by adjusting the geometry of the structure, enabling transition between left-handed circular polarization (LCP) and right-handed circular polarization (RCP), as well as between linear and circular polarization states. More importantly though, our structure is able to provide dynamically controllable laser emission, by varying the polarization of the linearly-polarized pump wave. By altering the polarization of the pump wave, the laser emission can be switched between LCP and RCP and vice versa.

Being ultra-compact, dynamically controllable and with possibility to generate almost pure circular polarization, our structure provides a promising path for the practical realization of controllable circularly polarized emission laser, with great prospects in all applications related with chiral light-mater interactions.

Acknowledgments: The work is supported by the EU Project CHARTIST

References

1. T. J. Wenzel, Prasad I. Polavarapu (ed.), “Chiral analysis: advances in spectroscopy, chromatography, and emerging methods”, 2nd ed, Analytical and bioanalytical chemistry, Vol. 410, 7261, 2018.
2. R. Naaman, Y. Paltiel, and D. H. Waldeck, “Chiral induced spin selectivity and its implications for biological functions”, Annual Review of Biophysics, Vol. 51, 99, 2022.
3. I. Thanopoulos, E. Paspalakis, and Z. Kis, “Laser-driven coherent manipulation of molecular chirality”, Chemical Physical Review, Vol. 390, 228, 2004.
4. H. Hubener, U. De Giovannini, C. Sch2afer, J. Andberger, M. Ruggenthaler, J. Faist, and A. Rubio, “Engineering quantum materials with chiral optical cavities”, Nature Materials, Vol. 20, 438, 2021.
5. K. Konishi, M. Nomura, N. Kumagai, S. Iwamoto, Y. Arakawa, M. Kuwata-Gonokami, “Circularly Polarized Light Emission from Semiconductor Planar Chiral Nanostructures”. Phys. Rev. Lett., Vol. 106, 057402, 2011.
6. X. Zhang, Y. Liu, J. Han, Y. Kivshar, Q. Song, “Chiral emission from resonant metasurfaces”. Science, Vol. 377, 1215, 2022.
7. A. Fang, T. Koschny, and C. M. Soukoulis, “Lasing in metamaterial nanostructures”, Journal of Optics A: Pure and Applied Optics, Vol. 12, 024013, 2010.
8. I. Katsantonis, A. Tasolamprou, E.N. Economou, Th. Koschny, and M. Kafesaki, “Dynamically controllable circularly polarized emission lasing based on chiral metasurfaces”, in preparation.

AES 2024, ROME - ITALY, 25-28 JUNE 2024

Physics-embedded machine learning method for the prediction of long-range electromagnetic field propagation

T. Bonnafont[1*], A. Toumi[1]

[1]Lab-STICC, UMR CNRS 6285, ENSTA Bretagne, 29806 Brest, France
[*]corresponding author: thomas.bonnafont@ensta-bretagne.fr

Abstract: We propose a sequential physics-embedded machine learning method to predict propagation over rural terrain. The training process uses artificial data computed by solving the parabolic wave equation. A fine-tuning strategy is also proposed, rendering the method versatile. Numerical simulations are provided to validate the proposed approach.

Fast and accurate computational methods are necessary to model the tropospheric electromagnetic long-range propagation to predict, for example, the coverage of antenna systems, such as for 5G applications. In this context, numerous physical phenomena such as *the terrain* shall be considered

For such applications, the *knife-edge model* [1] is widely used since it allows a first estimation in almost real-time, but its accuracy is low when real-life reliefs are studied. For better prediction, can based on the accelerated surface integral equation [2], the ray tracing method [3], or the *parabolic wave equation model* (PWE) [4,5]. Indeed, they trade computational time for better accuracy. This is why *machine learning* methods have recently received a lot more attention from the community; see [6] for an overview. In particular, in [7] they proposed a U-Net-based architecture trained from artificial data computed using a ray-tracing method. The latter model allows good predictions in almost real-time for indoor propagation. Based on the same architecture, Brennan *et al.* [8] proposed a machine-learning model to predict the long-range propagation over rural terrain. Nonetheless, this method uses data that resemble rural terrains, which leads to good results when the relief has a similar shape.

In this work, we propose to use the same architecture, *i.e.*, a U-Net, because it has shown good results in the domain. However, we propose a different training method that proves to be more versatile. Indeed, artificially labeled training data are created using the PWE model solved with split-step wavelet [5], which allows one to account for the terrain through a staircase model [4]. With that physical *a priori* we propose to construct a data set with rectangular and triangular obstacles placed randomly in the domain using a *Latin Hypercube Sampling* (LHS) method to precisely sample the associated manifold. We used 4000 terrain samples that contain between 2 and 5 random obstacles of different sizes. It shall be noted that the set is equidistributed and that this construction method is completely generalizable to add the effect of ground composition or refraction for example. The proposed U-Net architecture, with 4 levels of encoding and decoding, is then trained with a proper loss function, i.e., a weighted combination of an L2 and L1 norm, using 80% of the dataset. The other 20% are used as test dataset. The trained predictor allows us to obtain good results on the validation dataset, consisting of terrain with 6 random obstacles, and even on real-life terrain data obtained with the IGN dataset [9]. Nonetheless, for very specific applications, such as propagation over the sea, the terrain can be very different, and the predictor accuracy reduces drastically. Therefore, to render the method versatile, we propose a *fine-tuning strategy*, where only the decoding layers are trained again with a reduced dataset that resembles the studied terrain to improve the accuracy and adapt the predictor for the desired application. To the author's knowledge, this strategy has not yet been proposed for tropospheric propagation.

To conclude this summary, we present two simulations in Figures 1 and 2. First, the proposed machine-learning method is used to predict the propagation between Paris and Chartres accounting for the real terrain, and shows very good results, since the overall behavior of the field is well retrieved. Furthermore, the prediction is performed in almost real-time, with a computation time below 0.07 s. It thus allows a first glance at the field propagation with better accuracy than a conventional knife-edge model. Second, the advantage of the fine-tuning strategy is shown when a random Gaussian terrain is accounted for. Indeed, it allows to drastically improve the accuracy of the prediction. In both cases, we show the mean square error (MSE) in the legend. One can note that for the IGN landscape, we have an MSE of 1.01, which is low considering 4000 samples of very general terrain are used for the training. In the second case, we can note that the error has been divided by more than 6 using the fine-tuning strategy with 1500 samples of Gaussian terrain.

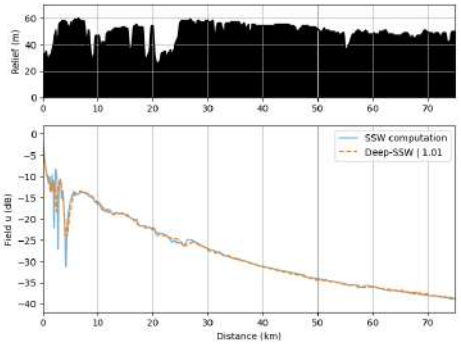

Figure 1: Prediction of the field (dB) over a real landscape.

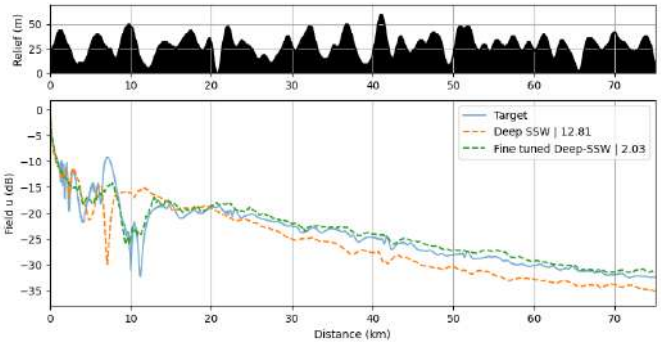

Figure 2: Prediction of the field (dB) over a Gaussian terrain.

In the full version of the article, a thorough study of the error with the number of samples and the fine-tuning strategy will be proposed.

Acknowledgment

The authors wish to thank the DGA-AID (Direction Générale de l'Armement / Agence de l'Innovation de Défense, France) for its support of the MEPOM project, where this work is in progress.

References

1. Deygout, J., "Multiple knife-edge diffraction of microwaves," IEEE Transactions on Antennas and Propagation, Vol. 14, No. 4, 480-489, 1966.
2. Brennan, C., and P.J. Cullen, "Application of the fast far-field approximation to the computation of UHF pathloss over irregular terrain", IEEE Transactions on Antennas and Propagation, Vol. 46, No 6, 881-890, 1998.
3. Green, D., Z. Yun, and M.F. Iskander, "Path loss characteristics in urban environments using ray-tracing methods," IEEE Antennas and Wireless Propagation Letters, Vol. 16, 3063-3066, 2017.
4. Levy, M. Parabolic Equation Methods for Electromagnetic Wave Propagation, IET, 2000.
5. Bonnafont T., R. Douvenot, and A. Chabory, "A local split-step wavelet method for the long range propagation simulation in 2D," Radio Science, Vol. 56, No. 2, 1-11, 2021.
6. Seretis, A., and C.D. Sarris, "An overview of machine learning techniques for radiowave propagation modeling," IEEE Transactions on Antennas and Propagation, Vol. 70, No. 6, 3970-3985, 2021.
7. Bakirtzis, S., K. Qiu, J. Zhang, and I. Wassel, "DeepRay: Deep learning meets ray-tracing," in proc. 16th European Conference on Antennas and Propagation (EuCAP), 1-5, 2022.

8. Brennan, C., and K. McGuinness, "Site-specific deep learning path loss models based on the method of moments", in proc. 17th European Conference on Antennas and Propagation (EuCAP), 1-5, 2023.
9. Elevation lines data of the Institut Nationale de l'informations Géographique et Forestière (IGN), https://geoportail.gouv.fr/, Accessed : 03-05-2023.

AES 2024, ROME - ITALY, 25 –28 JUNE 2024

Reconfigurable Intelligent Surface as a MIMO

S. Droulias*, G. Stratidakis and A. Alexiou

Department of Digital Systems, University of Piraeus, Piraeus 18534, Greece

*corresponding author: sdroulias@unipi.gr

Abstract: The Reconfigurable Intelligent Surface (RIS) is often treated as a collection of point scatterers or as a continuous radiating surface. In this work we explore the connection between the two approaches, for applications in near-field wavefront engineering with large apertures, including holographic MIMO technologies and large antenna arrays.

A Reconfigurable Intelligent Surface (RIS) redirects and possibly modifies the properties of incident waves, in order to restore non-line-of-sight communication links. Usually, the RIS is treated as a continuous radiating surface that locally satisfies the boundary conditions, ensuring that an incident plane wave is reflected towards the desired direction [1,2]. Alternatively, due to the inherently discrete nature of the RIS elements, the RIS is commonly treated as a planar distribution of point scatterers that bear the properties of conventional antennas, such as gain and directivity [3,4], in an equivalent MIMO communication link. On the one hand, the continuous approach involves a radiating sheet of infinite extent that is subsequently discretized; therefore, the question here is how well the local RIS elements retain the properties prescribed by the continuous infinite radiating sheet upon discretization and what is the effect of the finite RIS size. On the other hand, the discrete (or MIMO) approach involves the collective response of individual scatterers, therefore by definition implementing a finite-sized RIS; here the question is how well the properties of the individual antenna-like scatterers can reproduce the actual field radiated from the RIS.

In this work, we demonstrate the equivalence between the two approaches. We analyze each approach separately and we find the connection between the two, on the basis that they must both account for elements with the same properties, i.e. polarizabilities, guaranteeing the same scattered wave. We investigate how the properties of the continuous sheet are related to the properties of point scatterers that bear characteristics consistent with the antenna theory, and we discuss commonly used models in recent theoretical works. We find that, overall, the treatment of the RIS as point scatterers may overestimate the scattered field and, therefore, a correction factor must be taken into account [5]. We analyze the correction factor using realistic radiation patterns, and we demonstrate how the RIS performance is affected by design properties of the RIS elements, such as gain, directivity and inter-element coupling, and we discuss the implications on the predicted power at the receiver. Our findings are applicable to general large intelligent surfaces, holographic MIMO technologies, and large antenna arrays.

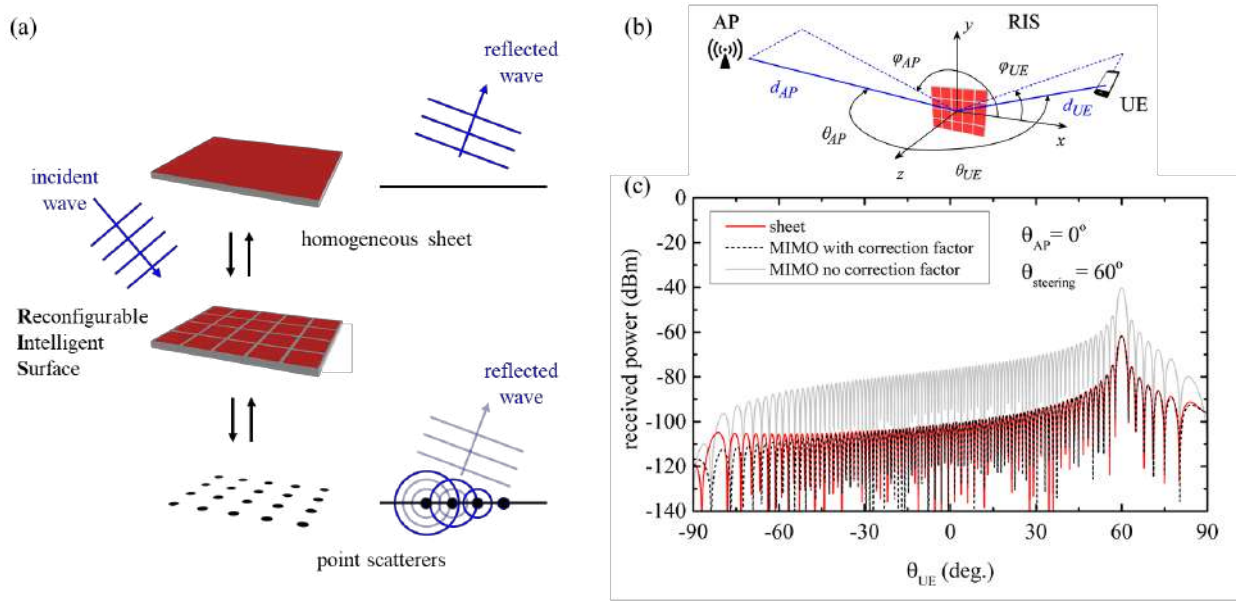

Figure 1. RIS as a radiating sheet and as a MIMO scatterer. (a) Schematic representation of a RIS as a homogeneous radiating surface and as a distribution of point scatterers that bear the properties of conventional antennas. (b) System model of RIS-aided link, illustrating the positions and relative angles between the Access Point (AP), RIS and User Equipment (UE). (c) Equivalence between the two approaches for RIS elements modeled as antennas with radiation pattern $U_0(\theta,\varphi) = \cos^2\theta$. The AP transmitts a TE-polarized wave with amplitude 1 V/m, which impinges normally on a lossless RIS ($\theta_{AP} = 0^o$). The RIS steers the wave on the *xz* plane at angle $\theta_{steering} = 60^o$, maximizing the received power when $\theta_{UE} = 60^o$. Without the correction factor (solid gray line) the antenna model overestimates the analytically predicted power (solid red line); the sheet-MIMO equivalence is restored upon incorporating the correction factor (dashed black line). The RIS is operating at 150 GHz and consists of 250×250 elements with periodicity $\lambda/5$, forming a reflecting surface of total size 10 × 10 cm^2. The received power is calculated at distance 20 m from the RIS, as a function of the angle θ_{UE} that marks the UE position.

Acknowledgements

This work was supported by the European Commission's Horizon Europe Programme under the Smart Networks and Services Joint Undertaking INSTINCT project (Grant Agreement 101139161).

References

1. Tang, W. et al., "Wireless Communications With Reconfigurable Intelligent Surface: Path Loss Modeling and Experimental Measurement," in IEEE Transactions on Wireless Communications, vol. 20, no. 1, 421-439, 2021.
2. Boulogeorgos, A. -A. A. and Alexiou, A., "Coverage Analysis of Reconfigurable Intelligent Surface Assisted THz Wireless Systems," in IEEE Open Journal of Vehicular Technology, vol. 2, 94-110, 2021.
3. Stratidakis, G., Droulias, S. and Alexiou, A., "Analytical performance assessment of beamforming efficiency in reconfigurable intelligent surface-aided links," IEEE Access, vol. 9, 115922–115 931, 2021.
4. Di Renzo, M., Danufane, F. H. and Tretyakov, S., "Communication Models for Reconfigurable Intelligent Surfaces: From Surface Electromagnetics to Wireless Networks Optimization," in Proceedings of the IEEE, vol. 110, no. 9,1164-1209, 2022
5. Droulias, S. and Alexiou, A., "Reconfigurable Intelligent Surface: MIMO or radiating sheet?," in IEEE Transactions on Wireless Communications, doi: 10.1109/TWC.2023.3302577, 2023.

AES 2024, ROME - ITALY, 25 –28 JUNE 2024

Non-Hermitian Metasurfaces for Sensitive THz Systems

Teun-Teun Kim[1*]

[1]Department of Semiconductor Physics & Engineering, University of Ulsan, Republic of Korea

[*]corresponding author: ttkim@ulsan.ac.kr

Abstract: We introduce highly sensitive THz systems, comprising non-Hermitian THz active polarization diodes and ultra-sensitive biochemical sensors. These systems are realized by combining graphene and microfluidic channels with non-Hermitian metallic metasurfaces with a complex refractive index.

In recent years, the study of non-Hermitian degeneracies, known as exceptional points (EPs), has expanded across various physical systems, with optics emerging as a particularly fruitful field []. This area benefits from the ability to manipulate gain and loss structures, making it an ideal platform for delving into non-Hermitian physics. Most research has focused on one-dimensional structures, such as micro-resonators, optical fibers, and waveguides, leading to a relative neglect of studies on light polarization, which becomes significant due to phase delay in two-dimensional spaces. Near EPs, the heightened sensitivity to minor perturbations highlights the potential for experimental and fabrication inaccuracies. Traditional research methods, involving the continuous fabrication of varied structural samples, fall short in providing straightforward experimental access to EPs, raising critical challenges in feasibility and scalability within non-Hermitian optics. Here, we demonstrate the observation of exceptional points and phase singularities within a non-Hermitian metasurface. By engineering a metasurface with hybrid meta-atoms characterized by anisotropic radiation loss and employing graphene to adjust the intrinsic coupling among meta-atom components, we achieve control over the polarization eigenstates by2altering2the2radiation2frequency2and2graphene's2optical2conductivity.2Our2research2uncovers2a2polarization2 phase singularity at the exceptional point during transmission through an anisotropic metasurface.

We first developed a non-Hermitian metasurface using meta-atoms that have the same resonance frequency but exhibit different losses, as shown in Figure 1 [2,3]. To demonstrate the merging behavior of eigenstates, we depict the polarization eigenstates on a Poincaré sphere, varying with gate voltages. Figure 1a illustrates that these eigenstates appear in pairs, symmetrically positioned around the south pole of the sphere, except at the chiral exceptional point (EP). Nearing the chiral EP in the parameter space causes these paired eigenstates to move towards the south pole, eventually m0erging into a single left circularly polarized state. Figure 1b outlines three distinct scenarios and their associated representations on the Poincaré sphere for the input and output polarization states: (i) Right-handed circularly polarized (RCP) incident light is converted into a mix of left and right circularly polarized light (LCP/RCP). (ii) An LCP input remains as LCP in the output. (iii) With mixed polarization input, the RCP component is reliably transmitted. Our adaptable metasurface framework offers a crucial means for investigating dynamic events related to non-Hermitian chiral degeneracies and could facilitate the creation of novel polarization-based devices and highly sensitive sensors.

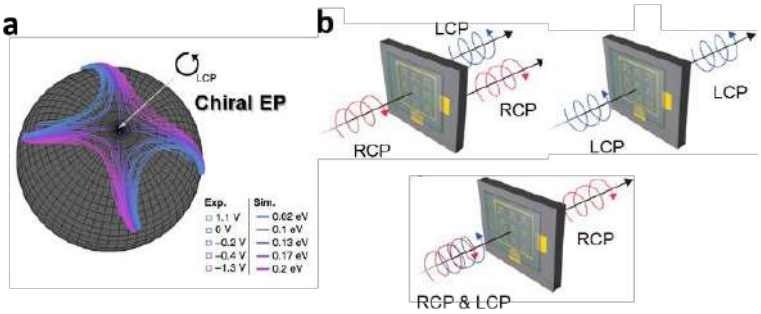

Fig. 1. (a) Chiral EP represented on the Poincaré sphere. (b) Circularly polarized light transmission at the chiral EPs.

Acknowledgements, this work was supported by National Research Foundation of Korea (NRF) through the government of Korea (NRF-2021R1C1C100631612).

References

1. Chen, W., Ş.K.Özdemir, G.Zhao, J.Wiersig, and L.Yang, "Exceptional points enhance sensing in an optical microcavity.," Nature Vol. 548, 192–196, 2017
2. Park, S. H., S.-G. Lee, S. Baek, T. Ha, S. Lee, B. Min, S. Zhang, M. Lawrence, and T.-T. Kim, "Observation of an exceptional point in a non-Hermitian metasurface," Nanophotonics, Vol 9, 1031–1039, 2020
3. Baek, S., S. H. Park, D. Oh, K. Lee, S. Lee, H. Lim, T. Ha, H. S. Park, S. Zhang, L. Yang, B. Min, and T.-T. Kim, "Non-Hermitian chiral degeneracy of gated graphene metasurfaces," Light Sci Appl, Vol 12, 87 2023

AES 2024, ROME - ITALY, 25 –28 JUNE 2024

Real-time Spectroscopy of Broadband THz-wave with High Frequency Resolution

S. Mine[1*], K. Kawase[1], C. Otani[2], K. Murate[1] and F. Blanchard[3]

[1]Nagoya University, Japan
[2]RIKEN, Japan
[3]École de technologie supérieure (ÉTS), Canada
[*]corresponding author: mine.sota.e8@s.mai.nagoya-u.ac.jp

Abstract: By implementing THz parametric detection, wherein THz-waves are converted to a near-infrared beam, we have facilitated the realization of one-shot spectroscopy of broadband THz-waves. The precision of frequency resolution has been augmented significantly via the non-collinear phase matching condition.

Terahertz time-domain spectroscopy (THz-TDS) has been instrumental in the advancement of THz applications throughout this century. However, THz-TDS encounters obstacles in enhancing real-time and frequency resolution due to the inherent trade-off between measurement duration and sampling quantity. On the other hand, THz frequency-domain spectroscopy, using a widely tunable THz parametric generator/detector, has been reported to have high real-time performance [1]. Assuming the broadband THz-waves generated by a femtosecond (fs) laser pump utilized in THz-TDS could be detected in the frequency domain, it would represent an ideal THz spectroscopy system. One strategy involves the wavelength conversion (up-conversion) of broadband THz-waves to a near-infrared (NIR) beam through difference-frequency optical mixing. However, detecting broadband THz-waves generated by a fs laser pump requires, similarly, a broadband fs probe beam. Given that both the THz-wave to be detected and the probe beam are broadband, complex difference-frequency optical mixing occurs, making it difficult to recover the spectral information of the THz-wave. For example, using a 40-fs probe beam results in a frequency resolution of approximately 11 THz. The aforementioned method present challenges in spectroscopically analyzing broadband THz-waves with high frequency resolution in real-time, necessitating the development of new spectroscopic techniques. In this context, the current study proposes a novel approach—THz spectroscopy by wavenumber measurement. By observing the wavenumber of THz-waves—a vector quantity—rather than the frequency—a scalar quantity, this method achieves THz spectroscopy with high frequency resolution while retaining the real-time performance of frequency measurements.

In this study, we leveraged THz parametric detection [2] toward the realization of THz spectroscopy by wavenumber measurement. In THz parametric detection, both the pump and THz-wave to be detected are injected into a lithium niobate ($LiNbO_3$) crystal, which generates an NIR Stokes beam by up-conversion. The Stokes beam is generated at an angle that satisfies the non-collinear phase matching condition. Consequently, by observing the generation angle of the Stokes beam, the wavenumber of the THz-wave can be obtained. Given that the wavenumber of THz-waves is substantially smaller (by two orders of magnitude) than that of the pump, the angle of Stokes generation predominantly depends on the wavenumber of the THz-waves, even when using a fs laser pump. This dependency significantly mitigates the reduction in frequency resolution that was a challenge in frequency measurements. Figure 1 illustrates the experimental setup for broadband THz parametric detection. The pump laser employed was a Ti:sapphire laser with a regenerative amplifier (800 nm, 3 mJ/pulse, 40 fs, 1 kHz). The source was a broadband THz-wave (approximately 0.1–2.0 THz) generated by optical rectification under the Cherenkov phase-matching condition in an $LiNbO_3$ crystal (dimensions: 20 mm × 4 mm × 5 mm) [3]. Subsequently, the generated THz-waves were injected into a detection $LiNbO_3$ crystal (dimensions: 62.5 mm × 4 mm × 5 mm) at an angle satisfying the non-collinear phase matching condition, converting the THz-waves into

Stokes beams that were then observed with an NIR camera. Broadband THz parametric detection relies on observing the wavenumbers of THz-waves by the generation angle of Stokes beams. However, due to the indeterminate generation location of the Stokes beam within the $LiNbO_3$ crystal, absolute evaluation of the generation angle is difficult. Therefore, a delay stage was introduced to the detection pump, allowing for time domain spectroscopy to calibrate the generation angle (i.e., camera pixels) with THz frequency.

Figure 2 depicts the observed Stokes beams. The generation of Stokes beams confirmed the one-shot detection of broadband THz-waves. Time domain spectroscopy at each camera pixel was conducted by sweeping the delay of the pump to calibrate the camera pixels with the THz wavenumbers. Here, the output from the camera, as shown in Fig. 2, was vertically integrated to convert the Stokes intensity into a one-dimensional profile, after which the data for each delay time were vertically aligned for display (Fig. 3(a)). The results of the Fourier transform are presented in Fig. 3(b), where the horizontal axis represents the camera pixels, and the vertical axis indicates the frequency of the THz-waves captured by those pixels. For instance, the Stokes beam observed at the horizontal axis of 1750 pixels in Fig. 2 contained intensity and phase information at approximately 0.7 THz. From Fig. 3(b), a frequency resolution of 60 GHz was achieved across the entire range of approximately 0.25–1.5 THz. The spectroscopic information in the range of 0.25–1.5 THz (Fig. 2) was obtained from a single pulse of the pump, marking the successful one-shot detection of broadband THz-waves with high frequency resolution by wavenumber measurement.

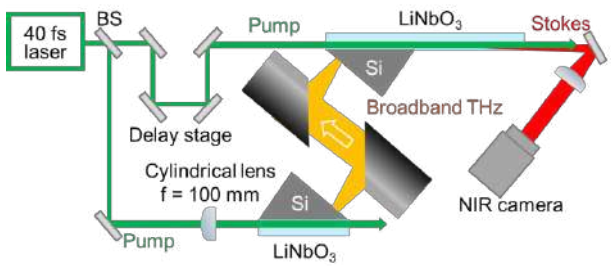

Fig. 1 Experimental setup of broadband THz parametric detection.

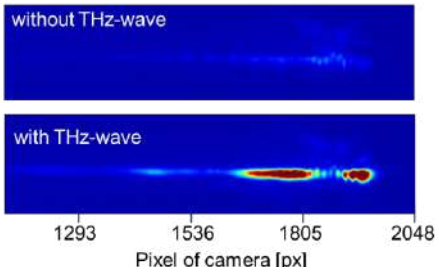

Fig. 2 One-shot detection of broadband THz-wave.

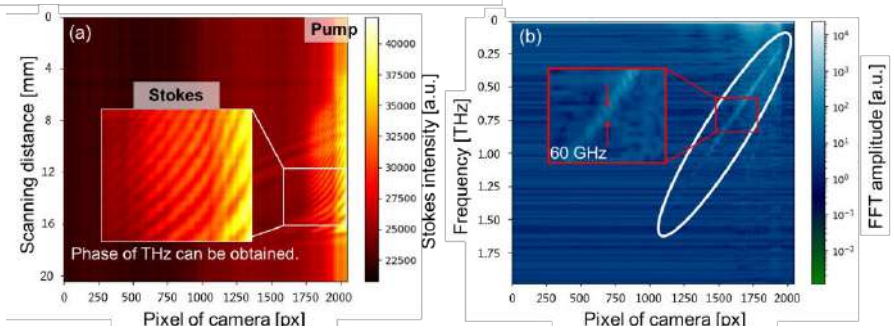

Fig. 3 (a) Time waveform of each camera pixel. (b) Result of fast Fourier transform (FFT) for each camera pixel.

References

[1] K. Murate, S. Mine, and K. Kawase, "Terahertz Parametric Generators and Detectors for Nondestructive Testing Through High-Attenuation Packaging Materials," IEEE J. Quantum Electron., Vol. 29, No. 5, 1-13, 2023.

[2] R. Guo, S. Ohno, H. Minamide, T. Ikari, and H.Ito, "Highly sensitive coherent detection of terahertz waves at room temperature using a parametric process," Appl. Phys. Lett., Vol. 93, No. 2, 021106, 2008.

[3] D. H. Auston, K. P. Cheung, J. A. Valdmanis, and D. A. Kleinman, "Cherenkov Radiation from Femtosecond Optical Pulses in Electro-Optic Media," Phys. Rev. Lett., Vol. 53, No. 16, 1555-1558, 1984.

AES 2024, ROME - ITALY, 25 –28 JUNE 2024

Excitation of out-of-plane resonances at normal incidence

J. R. Deop-Ruano[1]*, J. J. Alvarez-Serrano[1], V. Aglieri[2], A. Toma[2], and A. Manjavacas[1]*

[1]Instituto de Óptica "Daza de Valdés" (IO-CSIC), Spain
[2]Istituto Italiano di Tecnologia
*corresponding author: juan.deop@csic.es
*corresponding author: a.manjavacas@csic.es

Abstract: Out-of-plane resonances are characterized by minimum radiative losses, high quality factors and strong electric field enhancements. Due to their nature, their excitation at normal incidence is elusive. Here, we explore the excitation of out-of-plane lattice resonances at normal incidence in periodic arrays of metallic nanostructures.

Localized surface plasmons are excitations of the free electrons in metallic nanostructures. Thanks to their strong optical response and field enhancement, these modes are excellent candidates for optical manipulation at the nanoscale. Nevertheless, the high losses of metals limit their operability. A well-known approach to mitigate losses and enhance the properties of metallic nanostructures is to arrange them in a periodic array [1-3]. These systems present extraordinary properties, which are being exploited in a wide range of applications, including nanoscale laser emission and biosensing.

Periodic arrays can sustain resonances with a dominant component of the polarization perpendicular to the plane of the array. Because of their polarization, these modes, which are commonly known as out-of-plane lattice resonances, inhibit radiative losses. In that way, they behave as quasi-bound states in the continuum, with a quality factor only limited by the non-radiative losses of the constituents of the array. However, due to the transversality property of the electromagnetic radiation, it is extremely challenging to excite them.

Here [4], we explore different methods of exciting out-of-plane lattice resonances in periodic arrays of nanostructures at normal incidence. In particular, we explore the excitation of the out-of-plane lattice resonance as the symmetry of the array is broken by the addition of a second particle to the unit cell. Furthermore, we analyze the response under different sources of structured light. In doing so, we determine the optimal conditions for the excitation of the mode.

References

1. Kravets, V. G.; Kabashin, A. V.; Barnes, W. L.; and Grigorenko, A. N., "Plasmonic Surface Lattice Resonances: A Review of Properties and Applications", Chem. Rev., Vol. 118, No. 12, 5912−5951, 2018.
2. Baur, S.; Sanders, S.; and Manjavacas, A., "Hybridization of Lattice Resonances", ACS Nano 2018, Vol. 12, No. 2, 1618, 2018.
3. Cuartero-González, A.; Sanders, S.; Zundel, L., Fernández-Domínguez, A. I.; and A. Manjavacas, "Super- and Subradiant Lattice Resonances in Bipartite Nanoparticle Arrays", ACS Nano, Vol. 14, No. 9, 11876−11887, 2020.
4. Alvarez-Serrano, J. J.; Deop-Ruano, J. R.; Aglieri, V.; Toma, A.; and Manjavacas, A., "Normal Incidence Excitation of Out-of-Plane Lattice Resonances in Bipartite Arrays of Metallic Nanostructures," ACS Photonics, Vol. 11, No. 1, 301−309, 2024.

AES 2024, ROME - ITALY, 25 –28 JUNE 2024

Tuneable plasmonics and nanoantennas based on in-plane hyperbolic conducting polymers.

Yulong Duan, Aiman Rahmanudin, Shangzhi Chen,

Nara Kim, Klas Tybrandt, and Magnus P. Jonsson*

Laboratory of Organic Electronics, Department of Science and Technology (ITN), Linköping University, SE-601 74 Sweden

*corresponding author: magnus.jonsson@liu.se

Abstract: Plasmonic nanoantennas with polarization-dependent resonances have widespread application in photonics, yet their design has been limited to antennas with anisotropic shapes such as nanorods. We proposed an alternative approach to overcome this limitation, wherein shape-symmetric nanoantennas are fabricated from aligned conductive polymer materials possessing anisotropic permittivity.

Conventional plasmonic metals, like gold and silver, possess highly cubic symmetry and exhibit isotropic permittivity. Although researchers can artificially induce anisotropy in various isotropic metallic materials using nanoscale lateral gratings which results in hyperbolic metasurfaces, materials with naturally in-plane hyperbolic permittivity or in-plane anisotropic negative permittivity, along with in-situ tunability, are rare. We have recently introduced a new type of tunable plasmonic material based on conducting polymers of PEDOT:Sulf (poly[3,4-ethylenedioxythiophene]:sulfate) (1). The unique capability to switch the material between metallic and dielectric states via its redox state enables the reversible operation of plasmonic nanoantennas, as validated both chemically and electrically (2, 3). Moreover, research in the field of stretchable electronics has shown that adding strain to these materials can align the polymer chains in certain directions, resulting in different conductivities in different in-plane directions. The molecular alignment of the conducting polymer not only influences anisotropic charge mobility but also induces anisotropy in the effective mass of the charge carriers. Consequently, we achieve a material with polarization-dependent plasma frequency and an accompanying region of in-plane hyperbolic permittivity (4).

Utilizing this unique characteristic, we present the design of circularly symmetric nanoantennas capable of exhibiting anisotropic localized plasmonic resonances in parallel and perpendicular orientations to the polymer alignment direction. The anisotropic nanoantennas are further tuneable via the redox state of the polymer. Notably, the polymer alignment can blue-shift the plasma wavelength by several hundreds of nanometers, thereby forming a novel approach towards reaching the goal of redox-tunable conducting polymer nanoantennas for visible light.

References

1. S. Chen *et al.*, Conductive polymer nanoantennas for dynamic organic plasmonics. *Nature Nanotechnology* **15**, 35-40 (2020).
2. A. Karki *et al.*, Doped semiconducting polymer nanoantennas for tunable organic plasmonics. *Communications Materials* **3**, 48 (2022).
3. A. Karki *et al.*, Electrical Tuning of Plasmonic Conducting Polymer Nanoantennas. *Advanced Materials* **34**, 2107172 (2022).
4. Duan, Y. *et al.* Tuneable Anisotropic Plasmonics with Shape‐Symmetric Conducting Polymer Nanoantennas. *Advanced Materials* **35**, 2303949 (2023).

AES 2024, ROME - ITALY, 25 –28 JUNE 2024

Nano-thermoelectric infrared detectors

A. Varpula[1], A. Murros[1], O. Merchiers[2], K. Sovanto[1], J. Tiira[1], K. Tappura[1], P.-O. Chapuis[2] and M. Prunnila[1,*]

[1] VTT Technical Research Centre of Finland, Tietotie 3, FI-02150 Espoo, Finland
[2] Université de Lyon, CNRS, Lyon, France
[*]corresponding author: mika.prunnila@vtt.fi

Abstract: Infrared (IR) radiation detection is required in numerous applications from spectroscopic gas sensing to thermal imaging. Obtaining high speed and sensitivity, low-power operation, and cost-effectiveness with a single technology remains to be a challenge in the field of IR sensing. By combining nano-thermoelectric heat-to-voltage transduction and sub-wavelength absorbers, we demonstrate uncooled IR bolometer technology that provides fast and high sensitivity response to long-wavelength IR (LWIR) around 8 - 12 μm and is material-compatible with large-scale CMOS fabrication.

Nano-thermoelectrics has been mainly driven by applications in thermal energy harvesting with very little attention to detectors until recently when it was postulated [1] and demonstrated [2] that nano-thermoelectrics can provide an attractive low noise transduction method for bolometers. When nano-thermoelectric beams are combined with nanomembrane IR absorbers with inherently low thermal mass, they can be utilized as fast and sensitive infrared detectors [2]. The nano-thermoelectric transducer-support approach benefits from enhanced phonon scattering in the beams, which enhances the sensitivity. We have demonstrated different size nano-thermoelectric bolometric photodetector pixels with LWIR responsitivities, specific detectivities, and time constants in the ranges 179 V/W–2930 V/W, 1.5×10^7 cm $Hz^{1/2}$/W–3.1×10^8 cm $Hz^{1/2}$/W, and 66 μs–3600 μs, respectively [2]. We benchmark the technology against different LWIR detector solutions and show how nano-thermoelectric detector technology can reach the fundamental sensitivity limits posed by phonon and photon thermal fluctuation noise.

[1] A. Varpula et al., Appl. Phys. Lett. 110, 262101 (2017).

[2] A. Varpula, K. Tappura, J. Tiira, K. Grigoras, O.-P. Kilpi, K. Sovanto, J. Ahopelto, and M. Prunnila, APL Photonics 6, 036111 (2021).

Frontiers in Nonlinear Photonics: Optical Thermodynamics of Complex Systems

AES 2024, ROME - ITALY, 25 –28 JUNE 2024

Thermalization and Non-Equilibrium Transport in Multimoded Nonlinear Photonic Circuits

T. Kottos*

Wave Transport in Complex Systems Lab, Department of Physics, Wesleyan University, Middletown CT-06459, USA
*corresponding author: tkottos@wesleyan.edu

Abstract: We analyze the beam thermalization process in multimode photonic circuits when one nonlinear defect enforces thermalization. Furthermore, using a combination of Landauer and kinematics approach, we present a non-equilibrium transport theory of multimode nonlinear photonic circuits attached to optical reservoirs.

We show that even a single nonlinear defect, can enforces the thermalization of a beam in multimode photonic circuits [1]. In the presence of disorder, the thermalization process involves the formation of prethermal states whose power distributions can differ dramatically from the final thermal Rayleigh-Jeans (RJ). The presence of disorder controls the density of these prethermal modes. We develop a theory that predicts their density and relaxation rate statistics which depends on a single scaling variable given by the ratio of the localization length to the system size.

Furthermore, we develop a universal transport theory that describes the nonequilibrium steady states generated in multimode nonlinear photonic circuits (MMNPC) when are in contact with two optical reservoirs at different optical temperatures and/or chemical potentials [2]. The proposed theory allows us to define and calculate various kinetic coefficients like optical power and thermal conductivities in full analogy with physical kinetics in condensed matter.

We acknowledge support from Simons Foundation via grant No. 733698.

References

1. Kabat, E., Ramos, A., Fernandez-Alcazar, Kottos, T., “Nonlinear Defect Theory of Thermaliation in Complex Multimoded Systems”, in preparation (2024).
2. Kurnosov, A., Fernandez-Alcazar, L., Ramos, A., Shapiro, B., Kottos, T., “Opyical Kinetic Theory of Nonlinear Multi-mode Photonic Networks,” arXiv:2310.16784.

AES 2024, ROME - ITALY, 25 –28 JUNE 2024

Optical entropy growth accompanies beam clean-up in multimode fibers

F. Mangini[1], M. Ferraro[2], W. A. Gemechu[1], Y. Sun[1], V. Couderc[3], S. Wabnitz[1,*]

[1]DIET, Sapienza University of Rome, Via Eudossiana 18, 00184 Rome, Italy
[2]Department of Physics, University of Calabria, Via P. Bucci, 87069 Rende, Italy
[3]Université de Limoges, XLIM, UMR CNRS 7252, 123 Avenue A. Thomas, 87060 Limoges, France

[*]Corresponding author: stefan.wabnitz@uniroma1.it

Abstract: We experimentally demonstrate that the beam self-cleaning effect in multimode optical fibers is driven by the growth of entropy, in agreement with the second principle of thermodynamics.

The spatial beam self-cleaning (BSC) effect consists of the nonlinear transformation of a speckled beam at the output of a graded-index multimode fiber into a bell shape when its input power overcomes a certain threshold value [1]. BSC has shown its potential across a wide range of application fields, from telecommunications and medical imaging to industrial sensing and defense technologies. However, the physical mechanisms that lay at the basis of BSC are under debate.

One of the descriptions of this phenomenon which is more and more taking place in the community is based on thermodynamic considerations: the beam self-cleaning effect is seen as the irreversible evolution of a gas of photon from a disordered state (the speckles) into its thermal equilibrium state (the bell-shape beam) [2,3]. In the latter, the beam power is distributed among the multitude of guided modes according to the Rayleigh-Jeans law. This has been verified in several independent experimental works [4-6].

As is well known from thermodynamic principles, thermalization effects are driven by the principle of entropy maximization. Early experiments have shown that, indeed, BSC is somehow consistent with the growth of entropy. In particular, some of us demonstrated the validity of the second principle of thermodynamics within an optical calorimetry experiment [7], where two beams exchange “heat” while simultaneously undergoing BSC. Whereas, the entropy variation associated to BSC was studied in Ref.[8], by keeping constant both the input power (P) and the beam internal energy (U). Nonetheless, in conventional experiments, BSC is achieved by increasing P and keeping U/P constant.

Here, we verified that BSC is consistent with the second principle of thermodynamics: this requires measuring the entropy of a single beam during the evolution from an out-of-equilibrium to the equilibrium state. In our experiments, we combine state-of-the-art mode decomposition techniques with a cut-back approach. This allowed us to demonstrate the growth of entropy during BSC both with the increase of the input power and the fiber length. Hence, the thermalization of a single beam undoubtedly is an adiabatic process that occurs in the absence of energy exchanges with the environment. In this regard, our results dispel the idea that the thermodynamic approach to BSC contrasts with the second law of thermodynamics, i.e., that beam cleanup is due to the presence of possible nonlinear dissipative effects [9].

We acknowledge financial support from THE EU HORIZON 2020 ERC PROJECT 740355, EU HORIZON EUROPE MSCA (101064614,101023717), Sapienza University (RG12117A84DA7437), EU under the NRRP of NextGenerationEU, partnership on “Telecommunications of the Future” (PE00000001 - “RESTART”), and French research national agency (ANR-18-CE080016-01, ANR-10-LABX-0074-01), the Italian Ministerial grant PRIN2022 "SAFE" (2022ESAC3K).

References

1. Krupa, K., et al. "Spatial beam self-cleaning in multimode fibres." Nature Photonics 11.4 (2017): 237-241.
2. Wu, F.O., et al. "Thermodynamic theory of highly multimoded nonlinear optical systems." Nature Photonics 13.11 (2019): 776-782.
3. Ferraro, M., et al. "On spatial beam self-cleaning from the perspective of optical wave thermalization in multimode graded-index fibers." Advances in Physics: X, 8.1 (2023): 2228018.
4. Garnier, J., et al. "Wave condensation with weak disorder versus beam self-cleaning in multimode fibers." Physical Review A 100.5 (2019): 053835.
5. Pourbeyram, H., et al. "Direct observations of thermalization to a Rayleigh–Jeans distribution in multimode optical fibres." Nature Physics 18.6 (2022): 685-690.
6. Mangini, F., et al. "Statistical mechanics of beam self-cleaning in GRIN multimode optical fibers." Optics Express 30.7 (2022): 10850-10865.
7. Ferraro, M., et al. "Calorimetry of photon gases in nonlinear multimode optical fibers." arXiv preprint arXiv:2212.12781 (2022).
8. Baudin, K., et al. "Classical Rayleigh-Jeans condensation of light waves: Observation and thermodynamic characterization." Physical Review Letters 125.24 (2020): 244101.
9. Steinmeyer, G.. "Generalized thermodynamics of optical multimode systems and the breach of the second law of thermodynamics." 2023 Conference on Lasers and Electro-Optics Europe & European Quantum Electronics Conference (CLEO/Europe-EQEC). IEEE, 2023.

AES 2024, ROME - ITALY, 25 –28 JUNE 2024

Optical Thermalization and Applications to High-Power Lasers

Frank Wise[1*] and Demetrios Christodoulides[2]

[1]Cornell University, USA
[2]University of Southern California, USA
[*]corresponding author: frank.wise@cornell.edu

Abstract: Experimental measurements of optical thermalization in multimode fibers[1] will be reviewed briefly, and efforts to exploit optical thermodynamics to design short-pulse lasers with enhanced performance will be described.

References

1. H. Pourbeyram *et al.*, "Direct observations of thermalization to a Rayleigh-Jeans distribution in multimode optical fiber," *Nature Phys.* **18**, 685 (2022).

AES 2024, ROME - ITALY, 25 –28 JUNE 2024

Thermalization and condensation of light waves: Wave turbulence theory and experiments in multimode optical fibers

K. Baudin[1], L. Zanaglia[2], J. Garnier[3], N. Berti[1], A. Fusaro[4], K. Krupa[5], V. Doya[2], C. Michel[2], G. Millot[1], A. Picozzi[1]

[1]Laboratoire Interdisciplinaire Carnot de Bourgogne, CNRS, Université de Bourgogne, Dijon, France
[2] Université Côte d'Azur, CNRS, Institut de Physique de Nice, Nice, France
[3] CMAP, CNRS, Ecole Polytechnique, Institut Polytechnique de Paris, 91128 Palaiseau Cedex, France
[4] CEA, DAM, DIF, F-91297 Arpajon Cedex, France
[5] Institute of Physical Chemistry Polish Academy of Sciences, Warsaw, Poland
[*]corresponding author: Antonio.Picozzi@u-bourgogne.fr

Abstract: We review recent progress on the observation of light thermalization to the Rayleigh-Jeans equilibrium in multimode optical fibers. We develop a nonequilibrium thermodynamic description of light thermalization in multimode fibers on the basis of the wave turbulence theory by taking into account the impact of weak and strong disorder.

Different studies on wave turbulence revealed that purely classical waves can exhibit a process of condensation that originates from the thermalization of the waves toward the Rayleigh-Jeans (RJ) equilibrium distribution [1]. Although this phenomenon of condensation of classical waves differs from the quantum Bose-Einstein condensation, the underlying mathematical origin is formally analogous because of the common singular behavior (vanishing denominator) of the equilibrium Bose distribution for quantum particles and the equilibrium Rayleigh-Jeans distribution for classical waves [1-2]. However, the observation of condensation of optical waves in a conservative (e.g., cavity-less) configuration is hindered by the prohibitive large propagation lengths required to achieve RJ thermalization. Recently, the observation of the RJ condensation and thermalization of light waves has been reported in multimode optical fibers [2-5]. The experiments are based on a phenomenon of spatial beam cleaning recently discovered in multimode optical fibers [6-9]. As a matter of fact, light propagation in multimode optical fibers is affected by a structural disorder of the material. We have formulated a wave turbulence kinetic description of the random waves that account for the presence of structural disorder. The theory unveils a significant acceleration of the process of thermalization and condensation that is induced by the disorder [10], which can explain the fast process of thermalization observed in the experiments.

Our experiments in multimode fibers evidence the transition to light condensation: By decreasing the kinetic energy ('temperature') below the critical value, we observe a transition from the incoherent thermal RJ distribution to wave condensation [2]. The experimental results show that the chemical potential reaches the lowest energy level at the critical value of the energy to condensation, which leads to the macroscopic population of the fundamental mode of the optical fiber. The condensate fraction across the transition to condensation is in quantitative agreement with the RJ theory. We have also characterized the thermodynamics [11] of classical condensation through the analysis of the specific heat: In opposition to quantum Bose-Einstein condensation, the heat capacity takes a constant value in the condensed state and tends to vanish above the transition in the normal state [2]. More recently, RJ thermalization has been extended to non-Hermitian optical lattices [12] or by including the conservation of orbital angular momentum [13-14].

We will present recent developments about the development of a wave turbulence theory accounting for the impact of strong disorder [15]. The theory unveils the interplay of disorder and nonlinearity. It reveals that a nonequilibrium process of condensation and thermalization can take place in the regime where disorder effects dominate over nonlinear effects. We validate the theory by numerical simulations of the nonlinear Schrödinger equation and the derived kinetic equation, which are found in quantitative agreement without using adjustable parameters. Experiments realized in multimode optical fibers with an applied external stress evidence the process of thermalization in the presence of strong disorder [15]. More generally, the observation of RJ thermalization in disordered optical fibers has stimulated the study of the interplay of nonlinearity and disorder in multimode optical systems [16-17].

Finally, we report the observation of Rayleigh-Jeans thermalization to negative temperature equilibrium states through its propagation in a multimode optical fiber [18]. The bounded energy spectrum of the optical fiber enables negative temperature equilibriums with high energy levels (high order fiber modes) more populated than low energy levels (low order modes). Bringing negative temperatures to the field of optics opens the door to the investigation of fundamental issues of negative temperature states in a flexible experimental environment.

References:

[1] P. Aschieri, J. Garnier, C. Michel, V. Doya, A. Picozzi, PRA 83, 033838 (2011)

[2] K. Baudin, A. Fusaro, K. Krupa, J. Garnier, S. Rica, G. Millot, A. Picozzi, PRL 125, 244101 (2020)

[3] H. Pourbeyram, P. Sidorenko, F. Wu, L. Wright, D. Christodoulides, F. Wise, Nature Physics 18, 685 (2022)

[4] F. Mangini, M. Gervaziev, M. Ferraro, D. S. Kharenko, M. Zitelli, Y. Sun, V. Couderc, E.V. Podivilov, S. A. Babin, and S. Wabnitz, Optics Express 30, 10850 (2022)

[5] M. Ferraro, F. Mangini, F.O. Wu, M. Zitelli, D.N. Christodoulides, S. Wabnitz, arXiv:2212.12781.

[6] K. Krupa, K. Krupa, A. Tonello, B.M. Shalaby, M. Fabert, A. Barthélémy, G. Millot, S. Wabnitz, V. Couderc, Nature Photonics 11, 237 (2017)

[7] L.G. Wright, Z. Liu, D.A. Nolan, M.-J. Li, D.N. Christodoulides, F.W. Wise, Nature Photonics 10, 771 (2016)

[8] E. Podivilov F. Mangini, O.S. Sidelnikov, M. Ferraro, M. Gervaziev, D.S. Kharenko, M. Zitelli, M.P. Fedoruk, S.A. Babin, S. Wabnitz, PRL 122, 103902 (2019)

[9] L.G. Wright, F.O. Wu, D.N. Christodoulides, F.W. Wise, Nat. Phys. 18, 1018 (2022)

[10] A. Fusaro, J. Garnier, K. Krupa, G. Millot, A. Picozzi, PRL 122, 123902 (2019)

[11] F. O. Wu, A.U. Hassan, D.N. Christodoulides, Nature Photonics 13, 776 (2019)

[12] G. G. Pyrialakos, H. Ren, P.S. Jung, M. Khajavikhan, D.N. Christodoulides, PRL 128, 213901 (2022)

[13] F.O. Wu, Q. Zhong, H. Ren, P.S. Jung, K.G. Makris, D.N. Christodoulides, PRL 128, 123901 (2022)

[14] E.V. Podivilov, F. Mangini, O.S. Sidelnikov, M. Ferraro, M. Gervaziev, D.S. Kharenko, M. Zitelli, M.P. Fedoruk, S.A. Babin, S. Wabnitz, PRL 128, 243901 (2022)

[15] N. Berti, K. Baudin, A. Fusaro, G. Millot, A. Picozzi, J. Garnier, PRL 129, 063901 (2022)

[16] A. Ramos , L. Fern\'andez-Alcazar, T. Kottos, B. Shapiro, Phys. Rev. X 10, 031024 (2020).

[17] G.G. Pyrialakos, F.O. Wu, P.S. Jung, H. Ren, K.G. Makris, Z.H. Musslimani, M. Khajavikhan, T. Kottos, D. Christodoulides, Phys. Rev. Research 6, 013072 (2024)

[18] K. Baudin, J. Garnier, A. Fusaro, N. Berti, C. Michel, K. Krupa, G. Millot, A. Picozzi, PRL 130, 063801 (2023)

AES 2024, ROME - ITALY, 25 –28 JUNE 2024

Spatial localization induced by coupled transport processes

S. Iubini[1,4,*], M. Giusfredi[2,1,4], G. Gotti[2,1], A. Politi[3,1] and P. Politi[1,4]

[1]Istituto dei Sistemi Complessi, Consiglio Nazionale delle Ricerche, via Madonna del Piano 10, I-50019 Sesto Fiorentino, Italy
[2]Dipartimento di Fisica e Astronomia, Università di Firenze, via G. Sansone 1, I-50019 Sesto Fiorentino, Italy
[3]Institute for Complex Systems and Mathematical Biology, University of Aberdeen, Aberdeen AB24 3UE, United Kingdom
[4]Istituto Nazionale di Fisica Nucleare, Sezione di Firenze Via G. Sansone 1, I-50019 Sesto Fiorentino, Italy
[*]corresponding author: stefano.iubini@cnr.it

Abstract: A novel phenomenon of spatial localization occurring in nonlinear lattices and in steady out-of-equilibrium conditions is discussed. This mechanism has no analogs in thermal equilibrium and requires the transport of at least two independent quantities.

Several nonlinear lattice systems display a localization transition in space when the density of a suitable order parameter exceeds a critical value. In the localized phase, a finite fraction of the total energy is localized in few lattice sites while the remaining sites host a homogeneous, low-density background. To observe localization it is not necessary to require thermal equilibrium. I will present a recently discovered mechanism [1,2,3] in which localization emerges spontaneously in transport conditions, when thermal and “chemical” unbalances are imposed at the system's boundaries, see Fig. 1. The related phenomenology is qualitatively different from the equilibrium one and requires the presence of at least two independent transported quantities (coupled transport). Moreover, absolute negative temperature states are steadily reached in the bulk of the system. Connections with nonlinear multimode photonic systems [4] will be discussed, also with reference to the dynamics of a Discrete Nonlinear Schroedinger Equation [5].

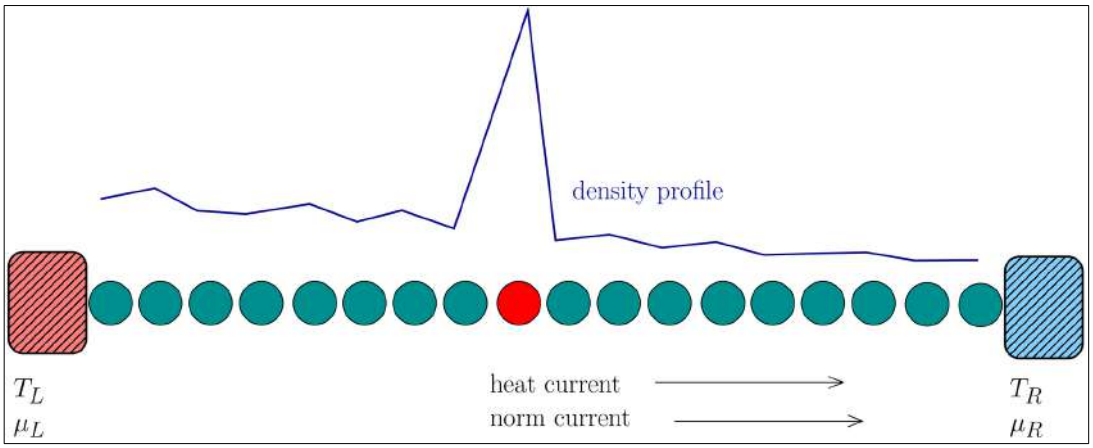

Figure 1. The nonequilibrium localization regime for a one-dimensional lattice in contact with two external reservoirs fixing temperature T and chemical potential μ. The red site hosts a localized state.

References

1. Gotti, G., Iubini, S. and Politi, P. “Condensation induced by coupled transport processes”. Physical Review E,

106(5), 054158, 2022.

2. Iubini, S., Politi, A. and Politi, P. “Onsager coefficients in a coupled-transport model displaying a condensation transition”. New Journal of Physics, 25(6), 063020, 2023.

3. Giusfredi, M., Iubini S. and Politi P. “Condensation in nonequilibrium steady states”. In preparation.

4. Kurnosov, A., Fernández-Alcázar, L. J., Ramos, A. Y., Shapiro, B. and Kottos, T. “Optical Kinetic Theory of Nonlinear Multi-mode Photonic Networks”. arXiv preprint arXiv:2310.16784, 2023.

5. Iubini, S., Lepri, S., Livi, R., Oppo, G. L. and Politi, A. “A chain, a bath, a sink, and a wall”. Entropy, 19(9), 445, 2017.

AES 2024, ROME 2-4 ITALY, 25-28 JUNE 2024

Pressure in optical thermodynamics

Nikolaos K. Efremidis[1,2,*] **and Demetrios N. Christodoulides**[3]

[1]Department of Mathematics and Applied Mathematics, University of Crete, Heraklion 70013 Crete, Greece.
[2]Institute of Applied and Computational Mathematics, Foundation for Research and Technology-Hellas (FORTH), Heraklion 70013 Crete, Greece.
[3]Ming Hsieh Department of Electrical and Computer Engineering, University of Southern California, Los Angeles, California 90089, USA.
[*]corresponding author: nefrem@uoc.gr

Abstract: We examine the thermodynamics, and the exerted optomechanical pressure of weakly nonlinear multimoded optical systems. We extend our analysis to the investigation of composite systems comprising different frequencies and/or polarizations. Our results can be applied to a variety of settings including fibers, waveguides, resonators and their configurations.

A supermodal thermodynamic theory of multimoded weakly nonlinear optical settings has recently been developed to account for the collective behavior of such utterly complex systems [1]. Optical thermodynamics has been utilized to explain the effect of beam self-cleaning in graded-index multimode fibers [2], [3].

In contrast to classical thermodynamics, in optical thermodynamics the entropy is considered to be extensive with respect to the power N the energy U and the number of modes M. Since, in classical thermodynamics, the pressure is the conjugate variable of the volume, the introduction of the system dimensions is important in order to compute the actual optomechanical pressures in optical thermodynamics. This can be done using the theory developed in [4], which accounts for additional system parameters. In this respect in [5] the optomechanical pressure was analytically computed. We have verified the validity of our results by comparing with more complicated energy expressions [6].

We also extend our results for composite systems. In this case, the type of the nonlinearity determines the power conservation laws of the system, and thus the resulting thermal equilibrium. Furthermore, the find that the total optomechanical pressure is the sum of the partial pressure exerted by each component.

References

[1] F. O. Wu, A. U. Hassan, and D. N. Christodoulides, "Thermodynamic theory of highly multimoded nonlinear optical systems," *Nat. Photonics*, vol. 13, no. 11, pp. 776–782, Nov. 2019, doi: 10.1038/s41566-019-0501-8.

[2] H. Pourbeyram *et al.*, "Direct observations of thermalization to a Rayleigh–Jeans distribution in multimode optical fibres," *Nat. Phys.*, vol. 18, no. 6, pp. 685–690, Jun. 2022, doi: 10.1038/s41567-022-01579-y.

[3] F. Mangini *et al.*, "Statistical mechanics of beam self-cleaning in GRIN multimode optical fibers," *Opt. Express*, vol. 30, no. 7, p. 10850, Mar. 2022, doi: 10.1364/OE.449187.

[4] N. K. Efremidis and D. N. Christodoulides, "Fundamental entropic processes in the theory of optical thermodynamics," *Phys. Rev. A*, vol. 103, no. 4, p. 043517, Apr. 2021, doi: 10.1103/PhysRevA.103.043517.

[5] N. K. Efremidis and D. N. Christodoulides, "Thermodynamic optical pressures in tight-binding nonlinear multimode photonic systems," *Commun Phys*, vol. 5, no. 1, p. 286, Nov. 2022, doi: 10.1038/s42005-022-01067-y.

[6] M. L. Povinelli *et al.*, "Evanescent-wave bonding between optical waveguides," *Opt. Lett.*, vol. 30, no. 22, p. 3042, Nov. 2005, doi: 10.1364/OL.30.003042.

AES 2024, ROME - ITALY, JUNE 25 – 28, 2024

Optical Thermodynamics of Nonlinear Highly Multimode Systems

Demetrios Christodoulides

Dept. of Electrical Engineering, University of Southern California, Los Angeles, CA 90089-2565, USA
*corresponding author: demetri@usc.edu

Abstract: The past few years have witnessed a resurgence of interest in multimode structures, predominantly driven by the ever-increasing demand for higher information capacities. This renaissance, in turn, incited a flurry of activities in the general area of nonlinear multimode optics. The sheer complexity associated with the presence of hundreds or thousands of nonlinearly interacting modes that collectively act as a many-body system, has led to new opportunities in observing a multitude of novel optical effects that would have been otherwise impossible in single-mode settings. In this talk, a thermodynamic theory capable of describing complex, highly multimoded, nonlinear optical systems is presented. It is shown that the mode occupancies in such nonlinear multimode arrangements follow a universal behavior that always tends to maximize the system's entropy at steady-state. This thermodynamic response takes place irrespective of the type of nonlinearities involved and can be utilized to either heat or cool an optical multimode system. Aspects associated with adiabatic compressions and expansions will be discussed along with the possibility for all-optical Carnot cycles.

Nonlinear Fiber Optics Towards Applications

AES 2024, ROME - ITALY, 25 –28 JUNE 2024

Femtosecond Regenerative Amplifiers Based on Optical Fiber

Henry Haig[1], Nicholas Bender[1], Yishai Eisenberg[1], and Frank Wise[1*]
[1]Cornell University, USA
[*]corresponding author: frank.wise@cornell.edu

Abstract: Single-transverse-mode operation of a regenerative amplifier based on highly-multimode fiber is described. This approach to short-pulse generation achieves high performance and offers multiple opportunities for scaling to much higher peak power. In addition, it opens new opportunities to control pulse propagation and generation.

Regenerative amplification is a standard approach to generation of high-peak-power short pulses from solid-state gain media. Short-pulse sources based on optical fiber are typically limited by excessive nonlinear phase accumulation, rather than by gain or amplified spontaneous emission, and as a result it is understood that regenerative amplification will not offer benefits to fiber systems. However, the availability of fibers with very large modes areas changes this calculus.

The first demonstration of regenerative amplification of femtosecond pulses in fiber was based on highly-multimode fiber with a 100-μm core diameter.[1] The amplifier achieves very high (57 dB) gain while completely suppressing amplified spontaneous emission. This allows 50-μJ and 300-fs pulses, with excellent beam quality, to be generated from a single amplifier stage (Fig. 1).

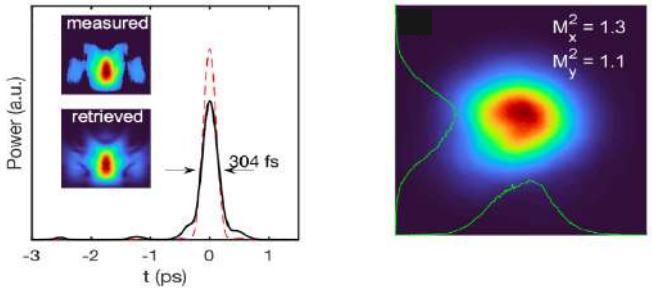

Figure 1. Left: Pulse generated by regenerative amplifier. The dashed red line indicates the transform-limited pulse. Insets show measured and retrieved FROG traces. Right: Output beam, with centered cross-sections in green.

Theoretical and experimental results of work to scale the performance by engineering the pulse propagation in the regenerative amplifier will be described.

This work was funded by the National Science Foundation (ECCS-1912742), the Office of Naval Research (N00014-20-1-2789) and the National Institutes of Health (U01NS128660 and R01EB033179).

Reference

1. H. Haig, N. Bender, Y. Eisenberg, and F. Wise, “Single-mode regenerative amplification in multimode fiber,” *Optica* **10**, 1417 (2023).

AES 2024, ROME - ITALY, 25 –28 JUNE 2024

Soliton Self-Frequency Shift in Nitrogen-Filled Hollow Fiber

Yishai Eisenberg[1], Yi-Hao Chen[1], Henry Haig[1], Enrique Antonio-Lopez[2], Rodrigo Amezcua-Correa[2], and Frank Wise[1*]

[1]Cornell University, USA

[2]University of Central Florida, USA

[*]corresponding author: frank.wise@cornell.edu

Abstract: Theoretical and experimental results of femtosecond pulse propagation in anti-resonant hollow-core fiber filled with nitrogen in the anomalous-dispersion regime are presented.

The soliton self-frequency shift is an effective way to generate tunable short pulses, but it is limited to about 100-nJ pulse energy in solid glass fiber. One possible approach to scaling to higher pulse energy is to use gas-filled hollow-core fiber, and initial experiments based on hydrogen have yielded megawatt peak powers, with clear room for improvement [1,2]. For the broadest application of this technique, it is desirable to demonstrate it in gases such as nitrogen that avoid the safety issues associated with handling hydrogen. Diatomic molecules have both vibrational and rotational modes that can be excited, and a challenge is to isolate the Raman transition(s) of interest. The dense rotational Raman spectrum of nitrogen presents a possible obstacle to the desired pulse evolution. Prior work has investigated short-pulse propagation in nitrogen-filled capillaries with normal dispersion [3,4], but there is no prior work in the anomalous-dispersion regime.

Experiments were performed with anti-resonant hollow-core fiber with a core diameter of 30 μm (Fig. 1), which has anomalous dispersion for the pressures investigated in this work. Linearly-polarized 300-fs pulses from a Yb fiber amplifier were coupled into the fiber, and experiments were performed with varying gas pressure and pulse energy. The results of numerical simulations with an input pulse energy of 7 μJ are shown in Fig. 1. The experimental spectrum observed with 2 bar pressure is also shown in Fig. 1. Similar degrees of spectral broadening to longer wavelengths are observed in simulations and experiments. However, while the simulations exhibit clear Raman soliton formation, in the experiments a spectrally-isolated soliton is not observed. Similar results are found with a range of pressures.

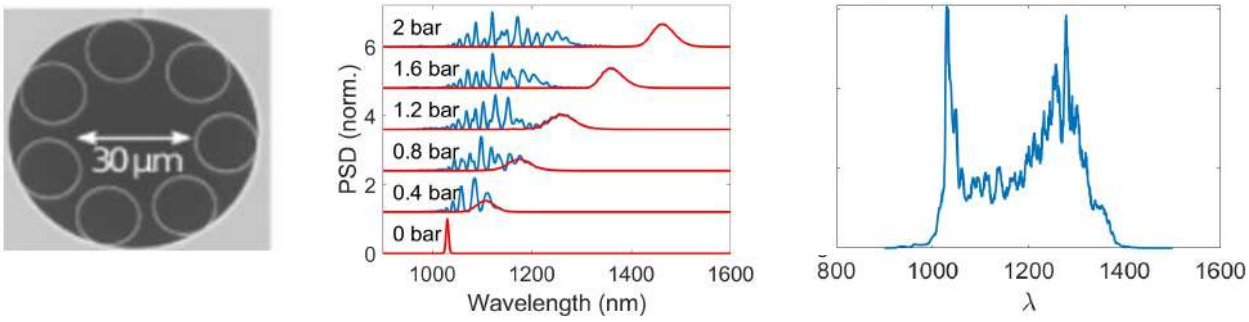

Figure 1. Left: cross section of hollow fiber. Center: simulated spectra with 7-μJ input pulses and the indicated nitrogen pressures. Right: output spectrum with 2 bar of nitrogen for input pulse energy of 5 μJ.

Results of filtering to isolate light with wavelengths longer than 1250 nm are shown in Fig. 2. Approximately 200 nJ is contained in the presented portion of the spectrum, and frequency-resolved optical gating (FROG) measurements indicate a pulse duration of 100 fs. While further systematic understanding of the process is needed, these initial results are encouraging and suggest that peak powers well above 1 MW will be achievable at 1300 nm. Such pulses would be valuable for deep-tissue imaging by multiphoton microscopy, for example.

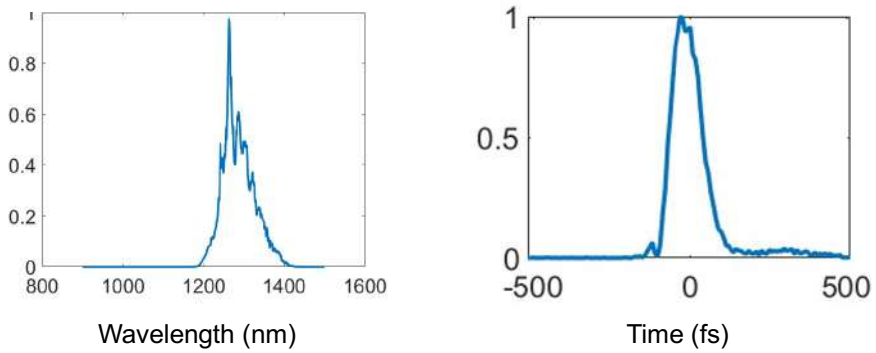

Figure 2. Spectral (left) and temporal (right) profiles retrieved by FROG for a pulse at 1300 nm with 6-μJ input pulses and 2 bar of nitrogen.

This work was funded by the National Institutes of Health (U01NS128660 and R01EB033179).

References

1. Y.-H. Chen *et al*., "Efficient soliton self-frequency shift in hydrogen-filled hollow-core fiber," *Opt. Lett.* **47**, 285 (2022).
2. F. Tani, J. Lampen, M. Butryn, M. H. Frosz, J. Jiang, M. E. Fermann, and P. St. J. Russell, *Phys. Rev. Appl.* **18**, 064069 (2022).
3. G. Fan *et al.*, "High energy redshifted and enhanced spectra broadening by molecular alignment," *Opt. Lett.* **45**, 3013 (2020).
4. P.A. Carpeggiani *et al.*, "Extreme Raman red shift: ultrafast multimode nonlinear space-time dynamics, pulse compression, and broadly tunable frequency conversion," *Optica* **7**, 1349 (2020).

Fundamental vibration dynamics of soliton complexes in ultrafast fiber laser

A. Sheveleva[1], C. Finot[1], and P. Colman[1*]

[1]Laboratoire Interdisciplinaire Carnot de Bourgogne, UMR 6303 CNRS-Université de Bourgogne, Dijon 21000, France
[*]corresponding author: pierre.colman@u-bourgogne.fr

Abstract: Mode decomposition techniques allow decomposing the Dispersive Fourier Transform signal of a soliton molecule in terms of elementary vibration modes. This technique based on correlation permits to aggregate into a global mode the individual evolutions of the pulses which constitute the soliton complexes, hence revealing a much richer dynamics.

In an ultrafast fiber laser ring cavity, several co-propagating dissipative solitons can interact to form firmly bind complexes of pulses called a soliton molecule (SM) [1]. Soliton molecules exhibit interesting analogy with their chemical counterparts as they can also manifest oscillatory and vibrating dynamics. The existence of the SM, its organization, and its dynamics, are directly related to the internal state of the cavity laser that defines the features of the limit cycle attractor which the SM is attached to [2]. On a practical aspect, the analysis of SM containing more than two solitons becomes much more complex. Indeed it becomes then quite ambiguous to attribute the relative motion of each possible soliton pair to a given oscillator involving the whole molecule. As a result the investigation of large (starting from N>2) soliton complexes remains mainly thus far purely descriptive.

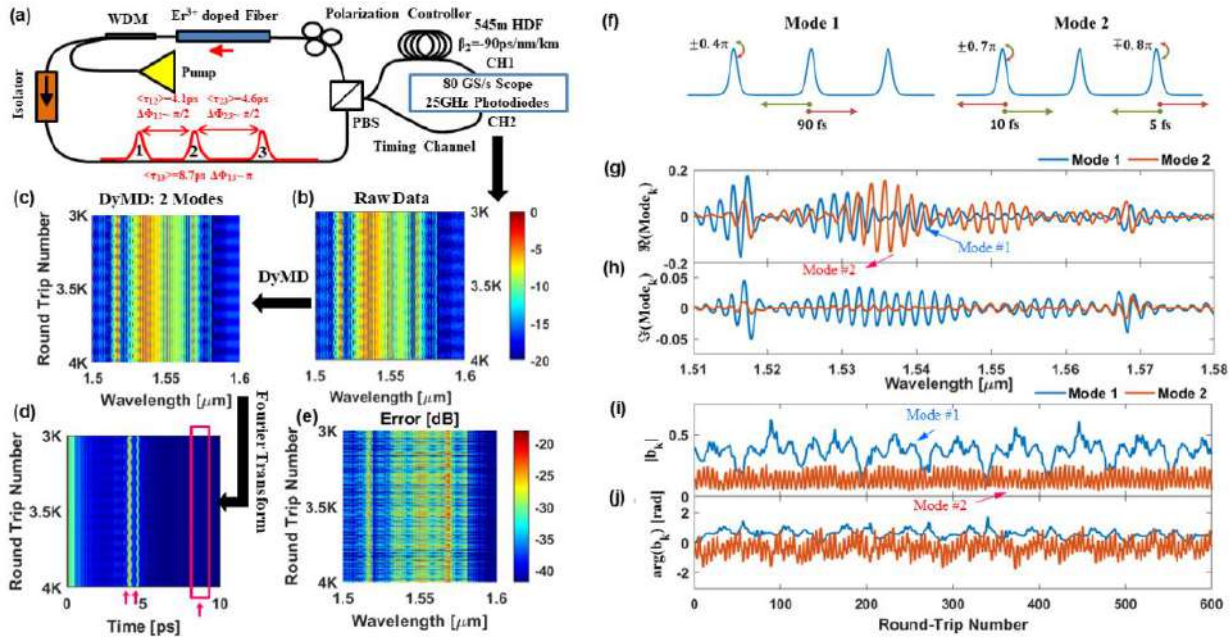

Figure 1 (a) *Experimental setup. PBS: Polarization Beam Splitter.* ***(b)*** *Raw DFT spectra (log scale).* ***(c)*** *DyMD reconstruction of (b) using two Modes.* ***(d)*** *Fourier Transform of (c) showing the three pulses separations (purple arrows).* ***(e)*** *Reconstruction error (in dB) of the DyMD decomposition (-24dB is lossless reconstruction).* ***(f)*** *Fundamental vibration mode extracted from the DyMD.* ***(g-h)*** *Relative phase and amplitude evolution between the two modes (b_k coefficients).*

Consequently we decided to perform a Dynamic Mode Decomposition (DyMD [3]) of the DFT spectra (Fig.

1-(d)). It consists in decomposing the instantaneous snapshot spectra $S(\lambda,n)$ at round trip n as $S(\lambda,n) = \Sigma_k Mode_k(\lambda) b_k(n)$. The temporal dynamics of the laser system is then encoded in the b_k coefficients (Fig. 1-(i-j)), while the $Mode_k(\lambda)$ contains the spectral information related to vibration mode k (Fig. 1-(g-h)).

As an example, we consider here a three-soliton molecule propagating round a 5-m long fiber ring laser cavity comprising 3 meters of Erbium doped fiber and a polarizer (see Fig. 1-(a)). Mode-locking is ensured by nonlinear polarization rotation followed by discrimination through a polarization beam splitter, also acting as an output coupler. After dispersion of the laser output in a -50 ps/nm Highly Dispersive Fiber (HDF), the DFT spectra are recorded by an 80GS/s, 40GHz electrical bandwidth, 8-bit depth oscilloscope. This laser architecture can support the propagation of a 3-soliton molecule, characterized by the distinct interferometric fringes seen on the DFT spectra (Fig. 1-(b)).

Instead of describing the evolution in term of variation of the individual soliton distance (Fig. 1(d)), the DyMD permits now to describe the dynamics as the interplay of two vibrational modes. The two modes identified within the dataset are presented in Fig. 1-(f): Mode 1 and 2 are odd and even symmetry vibration modes, respectively. Confirming theory regarding soliton interaction, we observe here that for each mode the solitons tend to get out of phase when getting closer, resulting then in a repulsive interaction. Interaction becomes then progressively more attractive (solitons in phase) as the pulses are going away from each other. In addition to the possibility to investigate qualitatively the dynamical features of the soliton molecules, it is also possible to get a more quantitative description. Indeed the amplitudes of each elementary vibration and their relative evolution are encoded in the b_k coefficients (Fig. 1-(i,j)), which are provided by the DyMD along with the modes' shape. We see that the two modes have radically different oscillation frequency and magnitude. In particular, Mode 2 has a period of about 5 Round-Trips and is of low intensity, making it hard to infer without resorting to a proper mode decomposition technics. Regarding Mode 1, its intensity evolves anharmonically with alternated flaring-up and damping burst around an average value of about 0.5. Much fine analysis (not shown here) reveals that the two elementary modes can influence each other, but are otherwise each driven by radically different intrinsic dynamics.

The dynamic mode decomposition (DyMD) allows the unambiguous decomposition of vibration modes of complex soliton molecules that involve more than 2 solitons and multiple oscillatory patterns. It also permits a denoising of the raw DFT data with minimal loss of information. In the present proof of concept, we managed to show that a soliton molecule can support two vibration modes in interaction with each other. This tends to indicate that the soliton molecule is under influence of radically different attractors. On a more general prospect the current example clearly demonstrates the suitability of the DyMD technique for the analysis of recurring phenomena, which are typical in ultrafast fiber ring cavity lasers**.**

References

1. M. Stratmann, et al. ,"Experimental observation of temporal soliton molecules," PRL 95, 143902 (2005)
2. P. Grelu and N. Akhmediev, "Dissipative solitons for mode-locked lasers," Nat. Photonics 6, 84 (2012).
3. P. J. Schmid, "Dynamic mode decomposition of numerical and experimental data," J. Fluid Mech. 656, 5–28 (2010)
4. A. Sheveleva et al, "Analysis of the dispersive Fourier transform dataset using dynamic mode decomposition: evidence of multiple vibrational modes and their interplay in a three-soliton molecule", Opt. Let. **48**(11), 3015-3018 (2023)

AES 2024, ROME - ITALY, 25 –28 JUNE 2024

Relocation of a Townes soliton dedicated to ultrafast 3D imaging

N. Bagley[1], T. Mansuryan[2], L. Chretien[3], R. Boulesteix[3], Y. Arosa Lobato[4], M. Ferraro[5], M. Zitelli[5], F. Mangini[5], Y. Sun[5], K. Krupa[6], B. Wetzel[2], V. Couderc[2,*], S.Wabnitz[5], A. Aceves[1], and A. Tonello[2]

[1] Southern Methodist University, 6425 Boaz Lane, 75205, Dallas, Texas, USA
[2] XLIM, Université de Limoges, UMR 7252, 123 Avenue A. Thomas, 87060 Limoges, France
[3] IRCER, Université de Limoges, UMR 7315, 12 Rue Atlantis, 87068 Limoges, France
[4] University of Santiago de Compostela, Praza do Obradoiro S/N, Santiago de Compostela, 15782 Coruna, Spain
[5] DIET, Sapienza University of Rome Via Eudossiana 18, 00184 Rome, Italy
[6] Institute of Physical Chemistry, Polish Academy of Sciences, ul. Kasprzaka 44/52, 01-224 Warsaw, Poland
*Corresponding author's email: Vincent.couderc@xlim.fr

Abstract: By leveraging the power dependent behavior of the spatial self-focusing, we realize an ultrafast focusing adjustment in a nonlinear microspectroscopy system. Temporal shaping and encoding of incident pulse enable us to construct a 3D image of an object by implementing a single 2D scan.

Optical spatial solitons result from the compensation of the linear spatial phase introduced by diffraction through a nonlinear spatial phase generally resulting from light-matter interaction involving cubic or quadratic processes [1-2]. The spatial soliton is usually generated by focusing a strong pump wave in a nonlinear medium: the focusing points generally identifies the origin of the trapped beam. In materials with cubic nonlinearity the nonlinear lensing effect can (Townes soliton) overcomes diffraction when the power exceed a given threshold leading to a self-focusing effect called catastrophic wave collapse. In the real world, mathematical catastrophes are smoothed out by physical processes such as plasma defocusing and nonlinear absorption [1] [3]. Due to the localized effect of plasma defocusing, the beam shape can fluctuate multiple times along the propagation resulting in a series of focusing-defocusing cycles [5]. The location of each light filament or the self-focusing length is power-dependent, and the beam quality of a self-focused beam well matches the requirements of practical applications such as nonlinear microspectroscopy. Spatial self-focusing is also an interesting mechanism for spectral broadening and supercontinuum generation, such that a sample object can be analysed by a large palette of wavelengths ranging from the visible to the infrared domain.

In this work, we show experimentally and numerically that the intensity dependent self-focusing length obtained in a Nd:YAG ceramic [6] can be used as a longitudinal modulator capable of shifting the longitudinal focus in an ultrafast speed microscope system. Additionally, the simultaneous emission of multiple Townes solitons with different peak intensities can provide different focus points, leading to acquire images at different depths in the sample through a common 2D scan of the transverse domain. This demonstration paves the way towards ultrafast temporal control of a nonlinear 3D imaging system for microscopy.

The propagation of an ultrashort spatio-temporal pulsed beam envelope E(x,y,z,t) under the pararaxial approximation in YAG can be described by the Nonlinear Envelope Equation (NEE) with Kerr nonlinearity, nonlinear absorption, and plasma effects [3], [4]… Our experimental setup is based on a femtosecond laser focused in a Nd:YAG ceramic rod using a 50 mm focal lens. The output beam is collimated and sent into a microscope, which

focuses the light on a biological sample with an Olympus XLUMPLFN20XW objective. A filter (FL-1064-10), placed in front of the microscope, allows to select the wavelength of the incident beam. Under the high incident peak power, the self-focusing process starts at a given position in the ceramic rod and can be shifted by varying the input beam power. At the output of the ceramic rod, the self-focusing point can be shifted accordingly along the depth axis of the sample (Figure 1).

In a second step, we modified our setup to generate several Townes solitons by replicating the input pump pulse with different amplitudes and temporal delays. This feature was achieved by splitting the pulse in an unbalanced Michelson interferometer at the YAG rod input facet. In particular we obtained two different light filaments in the Nd:YAG ceramic and, consequently, two foci at different depths in the biological sample. By time demultiplexing, we obtained then two different images at two depths of the same sample.

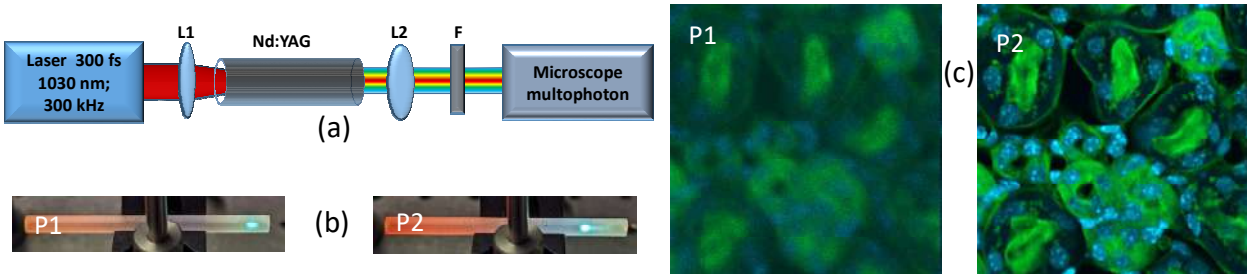

Figure 1: (a) experimental setup; (b) Townes soliton in Nd:YAG ceramic at two different input peak powers, P1=1.5 MW, P2 = 1.7 MW; (c) Nonlinear imaging (two-photon fluorescence of kidney mouse with P1: blurred image/no focus, P2: sharp image/exact focus).

This work demonstrates the utilization of the power dependence of the self-focusing length in a Nd:YAG ceramic for ultrafast focus adjustment in a nonlinear microspectroscopy imaging system. The maximum defocus amplitude was 40 µm. By splitting and delaying the initial pump beam, it was possible to time multiplex beam pulses at different powers and record a 3D image using a unique and common 2D scan.

References:

1. R. Y. Chiao, E. Garmire, C. H. Townes, "Self-trapping of optical beam," Phys. Rev. Lett. 13, 479 (1964).
2. Y. N. Karamzin and A.P. Sukhorukov, "Mutual focusing of high-power light beams in media with quadratic nonlinearity," Sov. Phys.-JETP. 41,414 (1975).
3. A. Couairon, A. Mysyrowicz. "Femtosecond filamentation in transparent media," Phys. Rep., 441, 47-187, 2007.
4. Mlejnek, M., Wright, et al. "Dynamic spatial replenishment of femtosecond pulses propagating in air," Opt. Lett. 23 (5), 382–384, 1998.
5. F. Silva et. al. "Multi-octave supercontinuum generation from mid-infrared filamentation in a bulk crystal," Nat. Commun., 3:807. 28, 2012.
6. R. Boulesteix et. al. "Manufacturing of Large Size and Highly Transparent Nd:YAG Ceramics by Pressure Slip-Casting and Post-Sintering by HIP: An Experimental and Simulation Study," Materials, 13 [9], 2199 (2020).

AES 2024, ROME - ITALY, 25 –28 JUNE 2024

Nonlinear Interactions of Ultrafast Pulses between Higher Order Modes in Step-Index Optical Fibers

L. Rishøj[1*], A. Arduin[1], and J. Lægsgaard[1]

[1]DTU Electro, Ørsteds Plads 343, Technical University of Denmark, 2800 Kgs. Lyngby, Denmark.
[*]Corresponding author: lris@dtu.dk

Abstract: We demonstrate high-energy frequency conversion of ultrafast pulses from an Yb-doped fiber laser by utilizing higher order modes in a simple step-index fiber. Using a combination of soliton self-frequency shifting, soliton self-mode conversion, and dispersive wave generation we generate pulses with wavelengths ranging from 560 nm to 1587 nm.

The wavelength range accessible with high-power fiber lasers is typically constrained by the available rare-earth dopants. However, by employing various frequency-conversion processes, it is possible to extend the spectral coverage [1]. Unfortunately, many of these nonlinear processes necessitate anomalous dispersion at the pump wavelength. In the 1 µm region of Yb-doped fiber lasers, achieving such dispersion is challenging with conventional solid-core single modes fibers. Nevertheless, this hurdle is overcome by photonic crystal fibers (PCFs). However, PCFs come with a drawback: anomalous dispersion is achieved by reducing the core diameter. Consequently, this limits the power-handling capabilities of the fiber in high-power applications. Alternatively, using higher order modes (HOMs) in simple step-index fibers offers a solution, since it offers anomalous dispersion without compromising the effective area of the mode. Here we utilize HOMs to demonstrate frequency conversion in the range 560 to 1587 nm. On the anti-Stokes side of the pump few nJs are generated using dispersive wave generation (DWG) [2]. On the Stokes side of the pump tens of nJs is demonstrated using a combination of soliton self-frequency shifting (SSFS) and soliton self-mode conversion (SSMC) [3].

The schematic of the experimental setup is shown in Fig. 1. Ultrafast pump pulses are launched in the desired LP_{0m} mode [4] of step-index fibers with a numerical aperture of 0.34 (manufactured by OFS Denmark). For the DWG experiments, the mode excitation is realized using an axicon, the pulse duration of the laser is 150 fs, and the core diameter of the fiber is 50 µm. For the SSFS/SSMC experiments, a spatial light modulator (SLM) was used for the mode excitation, the pump pulses were 100 fs, and the core diameter of the fiber was 87 µm. The output from the HOM fiber is characterized using a camera, OSA, or a combination of spectral filters and a power meter.

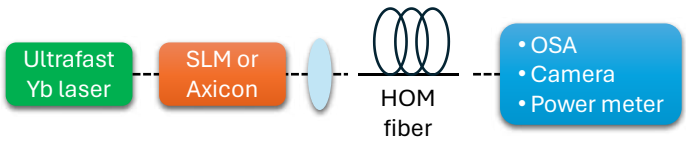

Figure 1: Sketch of the experimental setup.

Figure 2a) shows the output spectra of intramodal DWG in 50 cm of the HOM fiber with a core diameter of 50 µm. A dispersive wave (DW) is generated on the short-wavelength side of the pump from 850 nm down to 560 nm as the chosen pump mode order is increased from $LP_{0,8}$ to $LP_{0,13}$. The spectra are normalized with the power of the short wavelength DWs. The pulse energy of the DW ranges from approximately 2 nJ for the $LP_{0,8}$ DW with a decreasing trend down to 0.5 nJ for the $LP_{0,13}$ DW. On the Stokes side of the pump, red-shifting solitons are observed along with narrow DWs when pumping in the $LP_{0,12}$ and $LP_{0,13}$ modes since the dispersion of the mode becomes normal as it approaches modal cut-off. Decreasing the fiber length and increasing the pump power can increase the DW pulse energy, and in [2] 14 nJ was demonstrated at 710 nm using a similar

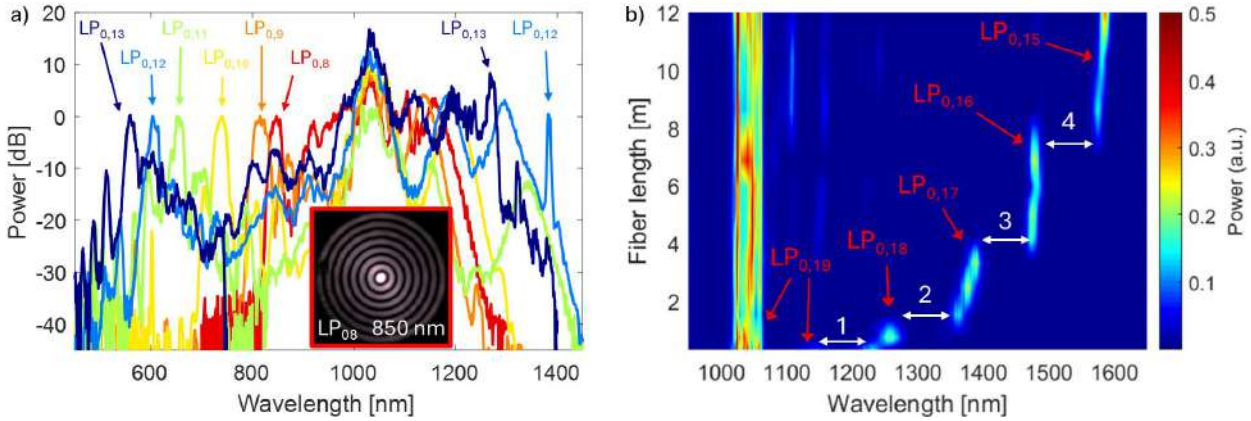

Figure 2 a) Spectra of intramodal DWG. B) Spectra as a function of fiber lengths showing SSFS and SSMC.

DWG approach. The modes of the different DW peaks were identified by spectrally filtering the fiber output and imaging on a camera. For example, the inset shows the intramodal DW pulse at 850 nm in the $LP_{0,8}$ mode.

A fiber cutback measurement for a different experiment, relying on the Raman-based effects of SSFS and SSMC, is shown in Fig. 2b). A 72 nJ pump pulse is launched in the $LP_{0,19}$ mode. Initially, a red shifting soliton is formed in the $LP_{0,19}$ mode, after 33 cm of propagation the soliton reaches 1141 nm where it is group index matched with the $LP_{0,18}$ mode at 16 THz of frequency separation. Since this separation is close to a Raman Stoke's2shift,2all2energy2is2transferred2to2a2newly2generated2pulse in the $LP_{0,18}$ mode. After complete power transfer, conventional SSFS continues to shift the newly formed pulse in the $LP_{0,18}$ mode. This pattern repeats itself, and in the 12 m fiber sample, a total of four SSMC processes occur (marked on the plot), eventually leading to a soliton in the $LP_{0,15}$ mode at 1587 nm with a pulse energy of 27 nJ. Theoretically, 34 % of the decrease in pulse energy is attributed to Raman being a dissipative process, whereas the remaining energy of the launched pump pulse remains at the pump wavelength. In [5] 80 nJ was demonstrated using SSMC in the biologically important wavelength window at 1300 nm, and further utilized for nonlinear biological imaging.

In summary, we demonstrated frequency conversion of 1030 nm ultrafast pulses via various nonlinear processes, such as SSFS, SSMC, and DWG. Ultrafast pulses were generated in the wavelength range from 560 to 1587 nm, with pulse energies ranging from a few nJ up to several tens of nJs depending on the wavelength.

Acknowledgments: This work was supported by a research grant (42100) from VILLUM FONDEN and a research grant (1032-00115B) from the Danish Council for Independent Research (DFF).

References

1. Krupa, K., Tonello, A., Barthélémy, A., Couderc, V., Shalaby, B. M., Bendahmane, A., Millot, G., and S. Wabnitz, "Observation of Geometric Parametric Instability Induced by the Periodic...", Phys. Rev. Lett., Vol. 116, 183901, 2016.
2. Arduin, A., Rishøj, L. and J. Lægsgaard, "High Energy Visible Dispersive Wave Generation in LP0m Modes of a Large-Core Step-Index-Fiber,"2CLEO, p. SM1F. 6, 2023.
3. Rishøj, L., Tai, B., Kristensen, P. and S. Ramachandran, "Soliton self-mode conversion: Revisiting Raman scattering of ultrashort pulses," Optica Vol. No. 6, 304-308, 2019.
4. Demas. J., Rishøj, L. and S. Ramachandran, "Free-space beam shaping for precise control and conversion of modes in optical fiber," Opt. Express, Vol. 23, No. 22, 28531-28545, 2015.
5. Rishøj, L., Hernández, I. C., Ramachandran, S. and N. Jowett, "Multiphoton microscopy for label-free multicolor imaging of peripheral nerve," J. Biomed. Opt., Vol. 27, No. 5, 056501-056501-11, 2022.

Development of soft glass nonlinear optical fibers based on 3D preform printing

R. Buczyński[1,2*], P. Wiencław[1,3], P. Gołebiewski[2], P. Socha[2], D. Pysz[2], A. Filipkowski[2], G. Stępniewski[2], I. Kujawa[2], O Czerwińska[3], A. Burgs[3], R. Kasztelanic[1,2]

[1]University of Warsaw, Faculty of Physics, Warsaw 02-093, Poland
[2] Lukasiewicz - Institute of Microelectronics and Photonics, Warsaw 02-668, Poland
[3]Sygnis S.A. al. Grunwaldzka 472, 80-309 Gdansk, Poland
[*]corresponding author: ryszard.buczynski@fuw.edu.pl

Abstract: We report on the development of highly nonlinear microstructured optical fibers using the 3D printing system devoted to soft glass processing. We used a 3D printer to construct a preform of the fiber based on the deposition of straight, horizontally oriented lines to replace the manual stack-and-draw fiber assembly process.

The stack-and-draw method is commonly utilized in the development of highly nonlinear microstructured fibers [1]. This approach necessitates the manual assembly of numerous rods and capillaries into an array, following a preliminarily calculated pattern to create a fiber preform. However, this process is time-consuming, not scalable, and prone to operator errors during manual assembly [2]. Therefore, automating this process could represent a significant innovation in the efficient development of complex preforms for structured optical fibers.

Recently, various methods for 3D printing glass have been explored, yet only a few are applicable to optical fiber development [3, 4]. We propose horizontal printing of fiber preforms as an alternative to manual assembly, utilizing a set of individual rods and capillaries [5]. To this end, the dedicated 3D glass printer, SYGLASS, was developed. In this approach, fiber preforms are directly printed from bulk glass through extrusion from the crucible, which is regulated by temperature and pressure (Fig.1).

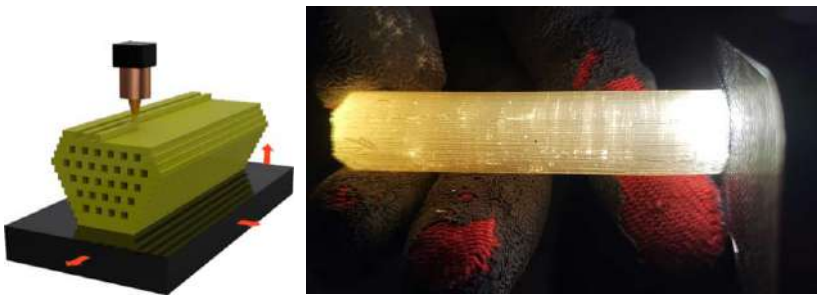

Figure 1. Horizontal 3D glass printing of optical fiber preforms using line-by-line printing approach: a schematic of the set-up (a) and printed glass preform (b).

For fiber development, we have used synthesized in-house lead borate glass with composition $5{\cdot}SiO_2 - 15{\cdot}B_2O_3 - 71{\cdot}PbO - 3{\cdot}ZnO - 6{\cdot}CdO2$(in2mass%), labeled as CD-16. The CD-16 glass is thermally stable, has good optical properties (DTA measurements), and high nonlinear refractive index, The synthesized glass was cut and polished to the shape of circular rods 35 mm in diameter and 70 mm long to create blocks for printing.

The printing setup comprises a heated crucible and a printing bed, both situated within a thermally controlled chamber. It features a combination of lateral (XY) and vertical (Z) translation stages, enabling the printing of glass elements up to a size of 10x10x10 cm. The crucible, cylindrical in shape and equipped with an integrated

cone-shaped nozzle featuring an exit hole 0.4 mm in diameter, is constructed from stainless steel. The system is capable of operating at temperatures up to 800°C and can apply pressures within the crucible of up to 10 bar. As a proof of concept, we printed a preform for a photonic crystal fiber (PCF) with a solid core and three rings of air holes in the cladding, arranged in a hexagonal lattice (Fig. 2a). The drawing process utilized a standard fiber drawing tower. As a result, we successfully developed a fiber with a maintained structure, although defects in the photonic crystal cladding, which formed during the subpreform processing, are visible.

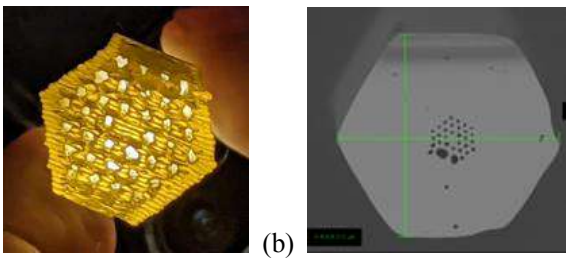

(a) (b)

Figure 2. Cross-section of fiber structure made of heavy metal oxide glass CD16 at different stages of fabrication: the preform of the core (a), and final photonic crystal fiber structure.

The fiber has a core diameter d_c=5.62 µm, lattice constant Λ=4.42 µm, and averaged hole diameter d=2.62 µm. The measured numerical aperture (NA) of the fabricated fiber was NA=0.5, which confirms a multimode characteristic of the fiber. The fiber becomes a single-mode at the wavelength of 1550 nm, which is crucial for supercontinuum generation when pumped with this wavelength. We have characterized optical properties of the developed fiber and verified its performance for supercontinuum generation in the femtosecond regime (Fig. 3).

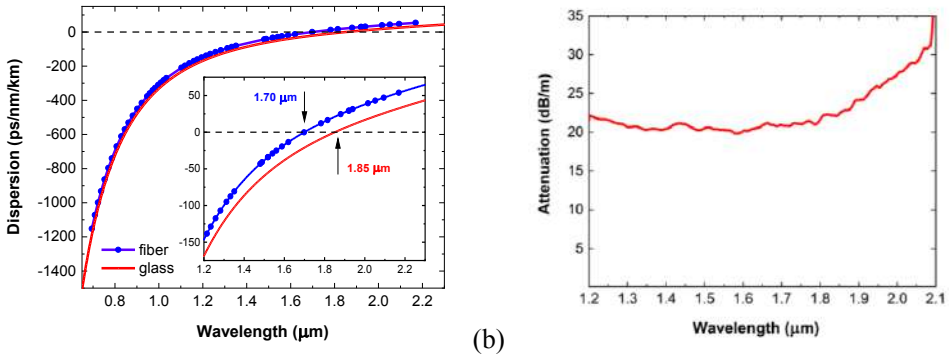

(a) (b)

Figure 3. Characterization of the microstructured fiber: chromatic dispersion (a) and fiber losses(b).

The authors acknowledge the financial support of MAESTRO UMO-2022/46/A/ST7/00238 grant National Science Centre, Poland) and POIR.01.01.01-00-1326/17 grant (the European Regional Development Fund).

References

1. "The Supercontinuum Laser Source," ed. Robert R Alfano, Edition IV, Springer, 2023
2. D. Pysz, I. Kujawa, R. Stępień, et al., "Stack and draw fabrication of soft glass microstructured fiber optics," Bull. Pol. Acad. Sci. Tech. Sci., Vol. 62, No. 4, 667-682, 2014.
3. . Carcreff, F. Cheviré, E. Galdo, et al., "Mid-infrared hollow core fiber drawn from a 3D printed chalcogenide glass preform," Opt. Mater. Express. Vol. 11, No. 1, 198-209, 2021.
4. P. Golebiewski, P. Wienclaw, J. Cimek, et al., "3D soft glass printing of preforms for microstructured optical fibers,"

Addit. Manuf., Vol. 79, 103899, 2024.

Extension of the fundamental four wave-mixing model to large bandwidth systems

A. Sheveleva[1*], P. Colman[1], and C. Finot[1]

[1]Laboratoire Interdisciplinaire Carnot de Bourgogne, UMR 6303 CNRS-Université de Bourgogne, Dijon 21000, France
[*]corresponding author: anastasiia.sheveleva@u-bourgogne.fr

Abstract: While retaining the nominal three-wave framework used for the fundamental four-wave mixing dynamics, we extend it using second order perturbation theory in order to include the impact of higher order sidebands. We discuss then the mechanisms at the origin of the divergence of intermediate systems from the ideal model.

Waves dynamics in optical fiber is governed by the nonlinear Schrödinger equation (NLSE) which describes the impact of dispersion and nonlinearity on phases and amplitudes of the involved waves. For the system containing only three waves $\sum_{n=-1}^{1}\psi_n e^{-in\omega_m t+i\phi_n}$, where ω_m is the modulation angular frequency, ψ_n and ϕ_n are spectral amplitude and phase of n^{th} spectral line, the process can be referred to as the four-wave mixing (FWM) in its degenerate case. Then the complete dynamics can be described using a Hamiltonian framework by a set of coupled equations in terms of reduced variables $\eta = {\psi_0}^2/\sum_{n=-1}^{1}{\psi_n}^2$ and $\varphi = \phi_{-1} + \phi_1 - 2\phi_0$ [1].

However, this fundamental FWM process is valid only if the system is strictly limited to three spectral lines. Nevertheless, we have recently demonstrated it experimentally [2] by implementing an original setup relying on iterated initial conditions as depicted in Figure 1 (a). The idea is to limit light propagation to a small segment of fiber and filter-out the higher-order sidebands at each iteration while continuously updating the input conditions, hence preventing the growth of any extra-sidebands, as well as other detrimental mechanisms (e.g. Raman and Brillouin effect, propagation loss).

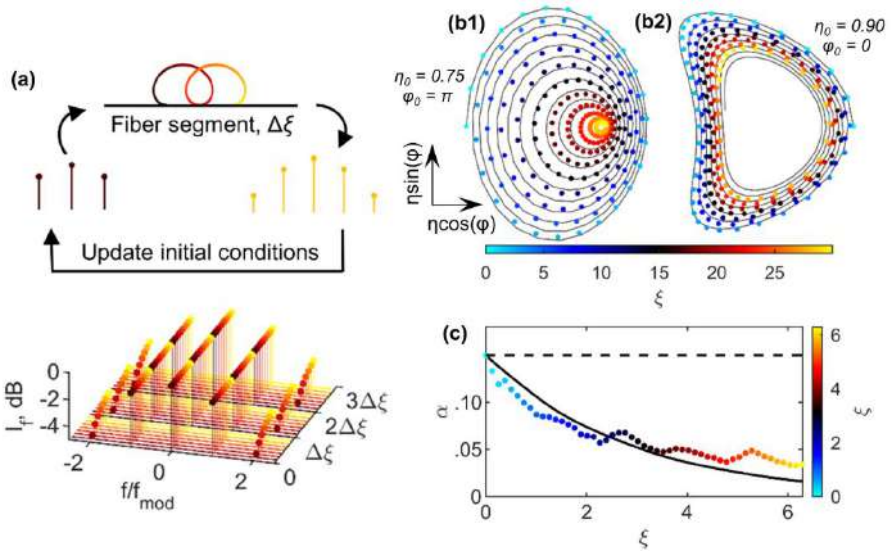

Figure 1 (a) *Simplified sketch of the experimental concept [2]. The bottom panel displays growth and filtering of the second-order sidebands over each segment length* $\Delta\xi$. ***(b)*** *FWM dynamics over long propagation distance* $\boldsymbol{\xi = z\gamma P_0 = 30 = 236\Delta\xi}$ *and* $\boldsymbol{\kappa = \beta_2\omega_m^2/\gamma P_0 = -2}$ *(where* $\boldsymbol{\beta_2}$ *is the second-order dispersion,* $\boldsymbol{\gamma}$ *– nonlinear coefficient,* $\boldsymbol{P_0}$ *– average power,* $\boldsymbol{z}$ *– fiber length in m): numerical simulation of the segmented propagation - black, updated model - colored dots.* ***(c)*** *Experimental recording of the asymmetry parameter (colored dots) is compared to numerical data (black solid line)*

and the fundamental FWM (black dashed line). The parameters are: $\boldsymbol{\kappa = -1.2,\ \alpha_0 = 0.15, \eta_0 = 0.75, \varphi_0 = 0}$.

In this case, the fundamental dynamics is reproduced over short propagation lengths (100Δξ, about 50km in fiber); but gradually degrades at longer propagation distances exhibiting a gradual spiraling toward a fix point (of a limit cycle) visible when looking at the phase-portrait $(\eta\cos\varphi, \eta\sin\varphi)$. It happens because in the real fiber propagation, unlike in the perfect mathematical model, it's impossible to eliminate fundamental photons exchange processes between the main three lines and the higher-order harmonics. Even if these extra photonics states are not populated, their very existence opens up new interactions paths which eventually results into small (less than 1% of energy is transferred to the extra sidebands) but alas cumulative effect which drives the system off its idealized dynamics.

To improve the ideal FWM model we include the effect of the second-order sidebands. Because their resulting impact is small, it is actually possible to include them as an adiabatic perturbation. This leads to development of average values of $\psi_{\pm 2}, \phi_{\pm 2}$ expressed solely in terms of the idealized three-wave parameters η, φ which are accumulated over Δξ. After developing the reduced set of equations while taking into account extra photon exchange process paths, we obtain a modified model which retains the initial two-equation description:

$$\begin{cases} \dfrac{d\eta}{d\xi} = -2\eta(1-\eta)\sin\varphi + \Delta\xi f_1(\eta,\varphi) \\ \dfrac{d\varphi}{d\xi} = (\kappa - 1) + 3\eta - 2(1-2\eta)\cos\varphi + \Delta\xi f_2(\eta,\varphi) \end{cases} \quad (1)$$

where $f_{1,2}(\eta,\varphi)$ are modifications to the fundamental model which is depicted in the first part of the equations.

Solving numerically Eq. (1), we obtain a close agreement with numerical results imitating experimental iterated propagation (Figure 1 (b)). After analyzing the Eq. (1), we conclude that the non-conserved dynamics and the spiraling behavior are directly linked to the dissipations of the Hamiltonian whose energy no longer a constant for each orbit.

Another propagation invariant in the ideal FWM is the asymmetry parameter defined as $\alpha = {\psi_{-1}}^2 - {\psi_1}^2$. However, in our experimental configuration we observe its gradual decay towards zero (colored dots in Figure 1 (c)). This behavior is again attributed to the impact of the second-order harmonics, as confirmed by our improved model. We can quantify the decay rate of the asymmetry parameter depending on the initial conditions and parameters of the system [3].

In this work, we investigate changes in the FWM invariants that are observed during experimental and numerical simulation of the iterated propagation. These changes are attributed to the impact of the second-order sidebands. Even though their spectral amplitudes are kept almost negligible, even the very existence of extra open passages for photons interactions is enough to disturb the system. By taking the perturbative approach, we can quantify these impacts, and we demonstrate a detailed study and a derivation of a modified FWM model operating the same reduced variables. Hence, our approach can be generalized to other systems where the dynamics of a closed system becomes sensitive to the impact of its external environment.

References

1. Cappellini G. and Trillo S., "Third-order three-wave mixing in single-mode fibers : exact solutions and spatial instability effects," J. Opt. Soc. Am. B, vol. 8, no. 4, pp. 824–838, 1991.
2. Sheveleva A., Andral U., Kibler B., Colman P., Dudley J. M., and Finot C., "Idealized four-wave mixing dynamics in a nonlinear Schrödinger equation fiber system," Optica, vol. 9, no. 6, pp. 656–662, 2022.
3. Sheveleva A., Colman P., Dudley J.M., and Finot C., "Conservation of a spectral asymmetry invariant in optical fiber four-wave mixing," Annalen der Physik, p. 2300489, 2024.

AES 2024, ROME - ITALY, 25 –28 JUNE 2024

Application of supercontinuum laser system for a $\chi^{(2)}$ and $\chi^{(3)}$ characterization of biomedical structure

C. Lefort[1], M. Nafa[1], T. Mansuryan[1], C. Carrion[2], A. Tonnello[1], Jean-René Duclère[3], V. Couderc[1]

[1]Université de Limoges, XLIM, UMR CNRS 7252, Limoges, France

[2]Université de Limoges, BISCEm, Microscopy core Facility, Limoges, France

[3]Université de Limoges, IRCER, UMR CNRS 7315, Limoges, France
[*]corresponding author: Claire.lefort@xlim.fr

Abstract: Supercontinuum laser sources are already well established for characterization in the life sciences. In the XLIM laboratory, we are using supercontinuum sources produced by spectral broadening in optical fibers in nonlinear microscopy to characterize second and third order non-linearities in biomedical structures. The main biomedical characterization results are presented.

Unexpected phase-locked Brillouin Kerr Frequency comb in fiber Fabry Perot resonators

Thomas Bunel[1], Matteo Conforti[1*], Julien Lumeau[2], Antonin Moreau[2], Arnaud Fernandez[3], Olivier Llopis[3], Julien Roul[3], Auro M. Perego[4], and Arnaud Mussot[1]

1. Université de Lille, CNRS, UMR 8523-PhLAM–Physique des Lasers Atomes et Molécules, F-59000 Lille, France

2. LAAS-CNRS, Université de Toulouse, CNRS, 7 avenue de Colonel Roche, 31031 Toulouse, France

3. Aix Marseille Univ, CNRS, Centrale Marseille, Institut Fresnel, Marseille, France

4. Aston Institute of Photonic Technologies, Aston University, Birmingham, B4 7ET, United Kingdom

**matteo.conforti@univ-lille.fr*

Stimulated Brillouin scattering (SBS) is the first nonlinear effect to be triggered when a powerful continuous wave laser interacts with a nonlinear waveguide. This effect is further exacerbated in resonators due to the multiple round trips in the cavity. SBS has proven to be extremely interesting for building ultra-stable microwave photonic synthesizers [1], to trigger broadband cavity solitons [2], or to balance thermo-optical effects to obtain ultra-stable sources [3]. Whatever the cavity architecture, the only requirement is to obtain a spectral overlap between the SBS gain ($\nu_B = 10$ GHz, $\Delta\nu = 50$ MHz), and the cavity resonances. This condition is automatically verified in fiber ring cavities, which have free spectral ranges (FSRs) typically between 1 and 100 MHz, or can be met by fine-tuning the cavity lengths in microresonators with FSRs in the GHz range [2-3]. In this paper we evidence an original mode-locking phenomena to generate a stable Brillouin Kerr frequency comb in fiber Fabry Perot resonators. The surprising feature of our work is illustrated in Fig. 1 (a). While there is a spectral overlap between the 8^{th} cavity resonance (dashed lines) and the SBS gain curve (red curve) at 9.416 GHz, we observed a Brillouin Kerr frequency comb with a line-to-line spacing equals to 10.593 GHz (exactly 9 times the cavity FSR, blue line in Fig. 1 (a)) where there is no spectral overlap. The cavity is pumped by an ultra-narrow CW laser of 1.3 W. It is swept from

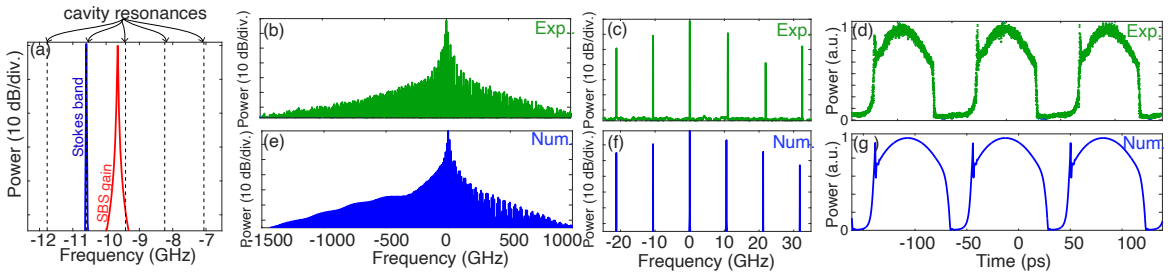

Figure 1 : (a) Scheme representing the SBS gain curve (red curve, SBS shift is 9.655 GHz), the cavity resonance positions (vertical dashed lines) and the first Stokes band (blue curve). (b) and (e) output spectra, (c) and (f) zoom on the central part, and (d) and (g) temporal traces. (b)-(d) Experiments and (e)-(g) numerics. Parameters : length 8.78 cm, FSR=1.177 GHz, cavity detuning $\Delta = -0.0891$ rad, highly nonlinear fiber with group velocity dispersion $\beta_2 = +0.38$ ps^2 km^{-1} and nonlinearity $\gamma = 10.8$ W^{-1}.km^{-1}, and a cavity factor of 65 millions. Spectra had been recorded with a high resolution (20 MHz) optical spectrum analyser and time traces with a high bandpass (700 GHz) optical sampling oscilloscope.

blue to red to reach a cavity detuning of $\Delta = -0.0891$ rad, in order to jump onto the upper branch of the cavity CW response. In the early steps of the process, a Stokes band at 10.593 GHz (9 times the cavity FSR) is generated, and many others through four-wave mixing processes cascade (Fig. 1 (c)). Finally, a broadband frequency comb of 2 THz (Fig. 1 (b) and (c)) is obtained corresponding to a stable pulse train (Fig. 1 (d)). Numerical simulations, including forward and backward fields [5], without any fitting parameters reproduce perfectly these experimental observations (Fig. 1 (e)-(g)). We explain this unexpected feature by performing a linear stability analysis of a mean-field reduction of the governing equations. We found a maximum of the parametric gain exactly at 10.593 GHz, revealing the parametric origin of the Stokes band at this unexpected position.

To conclude, we discovered and explained a new nonlinear mechanism in fiber Fabry Perot cavities. It enables the generation of phase-locked stable Brillouin Kerr frequency combs which could find great interest in microwave photonic synthesizers.

References

[1] Lucas, E., Brochard, P., Bouchand, R. et al. "Ultralow-noise photonic microwave synthesis using a soliton microcomb-based transfer oscillator," Nat Commun 11, 374 (2020).

[2] Yan Bai, Menghua Zhang, Qi Shi, Shulin Ding, Yingchun Qin, Zhenda Xie, Xiaoshun Jiang, and Min Xiao, "Brillouin-Kerr Soliton Frequency Combs in an Optical Microresonator" Phys. Rev. Lett. 126, 063901 (2021).

[3] K . Jia, X. Wang, D. Kwon, J. Wang, E. Tsao, H. Liu, X. Ni, J. Guo, M. Yang, X. Jiang, J. Kim, S. Zhu, Z. Xie, and S.-W. Huang, "Photonic Flywheel in a Monolithic Fiber Resonator," Phys. Rev. Lett. 125, 143902 (2020).

[4] E. Lucas, M. Deroh, and B. Kibler, "Dynamic Interplay Between Kerr Combs and Brillouin Lasing in Fiber Cavities," ArXiV 2212.08534 (2022)

[5] M. Dong and H. G. Winful, "Unified approach to cascaded stimulated Brillouin scattering and frequency-comb generation," Phys. Rev. A 93, 1–5 (2016).

AES 2024, ROME - ITALY, 25 –28 JUNE 2024

Control and Optimization of Nonlinear Dynamics using Machine Learning

G. Genty[1], M. Hary[1], L. Salmela[1], M. Mabed[2], A. Ermolaev[2], D. Bruner[2] and J. M. Dudley[2]

[1]Laboratory of Photonics, Tampere University, Tampere, Finland
[2]Institut Femto-St, University of Franche-Comté, Besançon France
*corresponding author: goery.genty@tuni.fi

Abstract: We review our recent work on the control and optimization of nonlinear dynamics in optical fiber systems using machine learning.

AES 2024, ROME - ITALY, 25 –28 JUNE 2024

Breathing Soliton Dynamics in Laser Cavities

S. Boscolo[1*], J. Peng[2], X. Wu[2], Y. Zhang[2], C. Finot[3], and H. Zeng[2]

[1]Aston Institute of Photonic Technologies, Aston University, Birmingham B4 7ET, United Kingdom
[2]State Key Laboratory of Precision Spectroscopy, East China Normal University, Shanghai 200062, China
[3]Laboratoire Interdisciplinaire Carnot de Bourgogne, UMR 6303 CNRS-Université de Bourgogne, 21078 Dijon, France
[*]Corresponding author: s.a.boscolo@aston.ac.uk

Abstract: We review our recent work on the dynamics of breathing solitons in ultrafast fibre lasers, including single breathers and breather molecular complexes, breather explosions, the synchronisation and de-synchronisation of breather complexes, the fractal dynamics of breathers, their transition to chaos, and their control by genetic algorithms.

Mode-locked fibre lasers are well-known to display a rich landscape of "dissipative soliton" dynamics, resulting from the interplay of the nonlinearity with dispersion and dissipation. Breathing solitons, manifesting themselves as localised temporal/spatial structures that exhibit periodic oscillatory behavior, are fundamental modes of many nonlinear physical systems and relate to a wide range of important nonlinear dynamics. First studied experimentally in fibre Kerr cavities and optical micro-resonators, optical breathers have also emerged as a ubiquitous ultra-short pulse regime of passively mode-locked fibre lasers [1-3] thanks to the recent development of real-time measurements. In the present paper, we review our recent experimental and numerical modelling results and advances in this fast-growing research area.

Breathing solitons in mode-locked lasers feature synchronous periodic variations of their spectrum and temporal intensity over cavity round trips. In [1], we have captured such a fast evolutionary behaviour in real time using time-stretch dispersive Fourier transform-based single-shot spectral measurements and spatio-temporal intensity measurements. One of the remarkable properties of dissipative solitons, which are mostly absent in integrable systems, is the ability to form stable multi-soliton bound states, also termed "soliton molecules", and showing similar dynamics to matter molecules. For the first time in experiments with mode-locked fibre lasers, breather-pair molecules have been also generated in the cavity [1]. While soliton pairs constitute the central soliton molecule case, soliton molecules can exist in various isomers, and a large population of solitons can self-assembly into macromolecules and soliton crystals. In [2], we have demonstrated various types of breather molecular complexes (BMCs), including multi-breather molecules, and complexes formed by the binding of two diatomic molecules, or a diatomic and a monoatomic molecule. We have also observed non-equilibrium dynamics of breathers, including collisions and annihilation of an elementary breather within a complex. Soliton explosions are among the most striking nonlinear dissipative phenomena that can manifest in mode-locked lasers. In this regime, a dissipative soliton circulating in the laser cavity experiences an abrupt structural collapse, but within a few round trips returns to its original quasi-stable state. By pushing the analogy in dynamics between stationary and breathing solitons further, we have demonstrated the explosive dynamics of breathers in a mode-locked fibre laser [3].

A laser working in the breather generation regime shows competition between the frequency of the breather oscillations f_b and the cavity repetition frequency f_r. In [4], we have reported frequency locking at Farey fractions of a breather laser by demonstrating for the first time that the winding numbers f_b/f_r show the hierarchy of the Farey tree and the structure of a devil's staircase, in accordance with the predictions from the theory of nonlinear systems with

two competing frequencies [5]. The fractal dimension of 0.906 determined from the measured staircase indicates the universal nature of this nonlinear system. The locked breathing frequencies feature narrow linewidth and high signal-to-noise ratio (SNR) and give rise to dense radiofrequency (RF) combs with a line spacing that is not constrained by the cavity length and can reach the sub-megahertz range. The subharmonic breather entrainment is a generalised form of synchronisation wherein a harmonic of the breathing frequency synchronises with the cavity frequency. Our further study [6] has shown for the first time the subharmonic synchronisation and de-synchronisation of breather molecules in a laser cavity, thus opening the possibility to study the dynamics of nonlinear systems with three or more interacting frequencies. In the de-synchronised phase, while the breather molecule as whole is not synchronised to the cavity, lag synchronisation among the constituent breathers is observed. The existence of an intermediate regime between the synchronised and de-synchronised phases is also unveiled, featuring a subharmonic breathing frequency with non-subharmonic sidebands. Furthermore, we have demonstrated that the modulated subharmonic phase of breathing solitons can trigger the onset of chaos in a mode-locked laser, thereby unfolding a new route from solitons to chaos in nonlinear systems [7].

Reaching a specific mode-locked regime in a laser generally involves adjusting multiple control parameters in a high-dimensional space, which is a laborious task if addressed via trial and error. In [8], we have demonstrated, for the first time, the use of genetic algorithms (GAs) for searching and optimising the breather regime in ultrafast lasers. We have designed merit functions relying on the characteristic features of the RF spectrum of the laser output, which are capable to locate various self-starting breather states in the laser, including single breathers with controllable breathing ratio and period, and BMCs with a controllable number of elementary constituents. The use of a GA with a merit function designed to exploit the distinguishing trait of frequency-locked breather states, i.e., a high SNR of the breathing frequency, has been the key to tailoring the frequency locking process in [4].

In conclusion, our work further demonstrates that mode-locked fibre lasers are an ideal test bed for the study of complex nonlinear wave dynamics relevant to a large variety of physical systems.

References

1. Peng, J., S. Boscolo, Z. Zhao *et al.*, "Breathing dissipative solitons in mode-locked fiber lasers," Sci. Adv., Vol. 5, eaax1110, 2019.
2. Peng, J., Z. Zhao, S. Boscolo *et al.*, "Breather molecular complexes in a passively mode-locked fibre laser," Laser Photon. Rev., Vol. 15, 2000132, 2021.
3. Peng, J. and H. Zeng, "Experimental observations of breathing dissipative soliton explosions," Phys. Rev. Appl., Vol. 12, 034052, 2019.
4. Wu, X., Y. Zhang, J. Peng *et al.*, "Farey tree and devil's staircase of frequency-locked breathers in ultrafast lasers," Nat. Commun., Vol. 13, 5784, 2022.
5. Jensen, M. H., P. Bak and T. Bohr, "Complete devil's staircase, fractal dimension, and universality of mode-locking structure in the circle map," Phys. Rev. Lett., Vol. 50, 1637, 1983.
6. Wu, X., J. Peng, S. Boscolo *et al.*, "Synchronization, desynchronization, and intermediate regime of breathing solitons and soliton molecules in a laser cavity," Phys. Rev. Lett., Vol. 131, 263802, 2023.
7. Wu, X., J. Peng, S. Boscolo *et al.*, "Observation of optical chaotic solitons and modulated subharmonic route to chaos in mode-locked laser," Submitted, 2024.
8. Wu, X., J. Peng, S. Boscolo *et al.*, "Intelligent breathing soliton generation in ultrafast fibre lasers," Laser Photon. Rev., Vol. 16, 2100191, 2022.

Optical fiber-based devices for sensing torsion, temperature and refractive index: from kW- to micro- and nano- scale applications

L. F. Granados-Zambrano[1,2], J. Korterijk[1], Tommie Verouden[1], F. Segerink[1], D. Jauregui-Vazquez[3], H.L. Offerhaus[1], and J.A. Alvarez-Chavez[1,*]

[1]Optical Sciences group at University of Twente, Enschede The Netherlands
[2]Facultad de Ingenieria at Universidad de Guanajuato, Mexico
[3]CICESE, Ensenada Baja California, Mexico
[*]Corresponding author: j.a.alvarezchavez@utwente.nl

Abstract: Active and passive optical fiber-based devices are the core of research and development for a wide range of sensing applications. Results from our scientific developments on strain, temperature and refractive index in these areas will be presented and discussed, using both tapered and non-tapered optical fiber sections.

Since Kao and Hockham in the UK proposed cylindrical glass waveguide for light propagation [1], optical fiber-based devices using both active and passive dopants have been studied for decades [2]. Fiber lasers and amplifiers are at the heart of scientific and industrial discoveries and developments every day. For the last 5 years, a line of work at the Optical Sciences group has focused on probably the lowest rated of devices in glass: the taper [3].

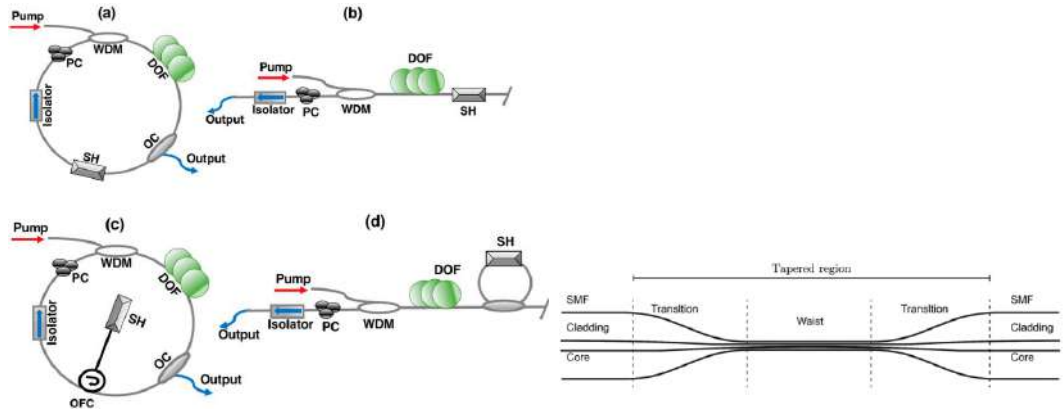

Figure 1. A) Traditional optical fiber-based sensors, (a) ring, and (b) linear, fiber laser cavities proposed for continuous wave (CW) fiber laser sensors. Alternative (c) ring, and (d) linear, configurations using a sensing head (SH) in reflection and bi-directional mode, taken from [5] and B) Typical taper structure, taken from [3].

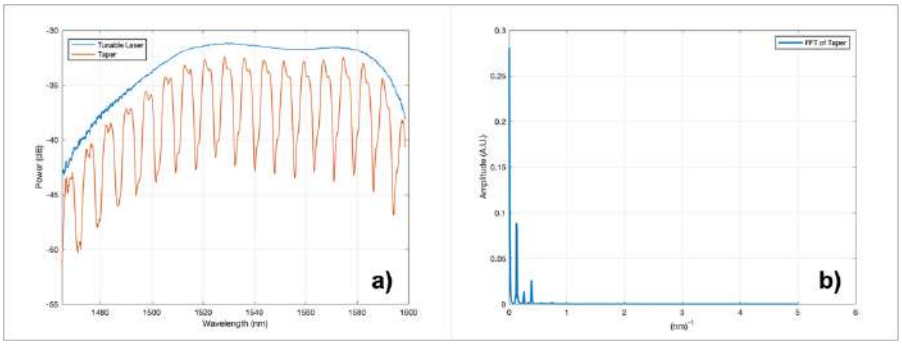

Figure 2 a) Spectral response of un-tapered and tapered fibres, and b) Fast Fourier Transform of the tapered fibre spectrum.

In this talk, besides the relevant concepts of fiber amplifiers and lasers, we will present results from our groups work on the development of tapering rigs [4]. Besides the technical description of the development of 2 novel tapering rigs, the talk will include relevant results on fiber-based strain, temperature, and refractive index. As part of the of the concrete applications of the developed tapers, we will discuss the prospects of our devices for applications at the interface with micro- and nano photonics, super continuum generation, integrated photonics and the medical areas [5].

Acknowledgements: The authors are grateful to CONAHCYT, Universidad de Guanajuato and CICESE in Mexico, and the Optical Sciences group at University of Twente, for the support towards their projects.

References

1. K.C. Kao and G.A. Hockham, “Dielectric-fibre surface waveguides for optical frequencies,” Proc. IEE, Volume 113, Issue 7, July 1966, p. 1151 – 1158, DOI: 10.1049/piee.1966.0189, Print ISSN 0020-3270, Online ISSN 2053-7891
2. G. Brambilla, “Optical fibre nanowires and microwires: a review”, 2010 J. Opt. 12 043001.
3. J.R. Ek-Ek, D. Jauregui-Vazquez, J.P. Korterik, M. Benedictus, F. Martinez-Pinon, H.L. Offerhaus, and J.A. Alvarez-Chavez, “Dual tapered optical fiber for simultaneous detection of curvature and strain”, Optical Fiber Technology journal, Volume 69, March 2022, 102843. https://doi.org/10.1016/j.yofte.2022.102843
4. L.F. Granados-Zambrano, J.P. Korterik, J.M. Estudillo-Ayala, R. Rojas Laguna, D. Jauregui-Vazquez, H.L. Offerhaus and J.A. Alvarez-Chavez, “Optimized Plasma-based Optical Fibre Tapering Rig”, Submitted for publication.
5. D. Jauregui-Vazquez, J. A. Alvarez-Chavez, T. Lozano-Hernandez, J. M. Estudillo-Ayala, J. M. Sierra-Hernandez, and H. L. Offerhaus, “Fiber Laser Sensor Configurations for Refractive Index, Temperature and Strain: A Review”, Photonics 2023, 10(5), 495; https://doi.org/10.3390/photonics10050495

Electromagnetic Metasurfaces for Microwave, Terahertz, and Optical Applications

Reflective Moiré Metasurfaces: A Frontier of Innovation and Technical Challenges

Shuo Liu[1*], Lei Zhang[1], and Xiaoqing Chen[1]

[1]State Key Laboratory of Millimeter Waves, Southeast University, Nanjing 210096, China
[*]corresponding author: liushuo.china@seu.edu.cn

Abstract: Reflective Moiré metasurface provides an economical approach for dynamic beamforming in RIS applications, introducing novel methods for far-field scattering synthesis through compact, ultrathin metallic patterns with diverse symmetries. This breakthrough is expected to have widespread impact across the fields of electromagnetics, antenna development, and wireless communication.

Dynamic beamforming plays a pivotal role in various technological applications, including radar systems, holographic imaging, and the development of reconfigurable intelligent surfaces (RIS).[1-3] Traditional methods for achieving this dynamic control rely heavily on active electronic components, such as pin-diodes and varactor diodes. This reliance significantly escalates costs for large-scale implementations, a challenge that becomes even more pronounced at millimeter-wave and sub-terahertz frequencies where these components are notably costly or may not be readily available.

Recently, the fascinating physical properties of moiré patterns created by overlaying two differently twisted two-dimensional (2D) materials have drawn renewed attention. In this context, we introduce a novel approach for dynamic beam steering using two closely attached metasurfaces. By adjusting the in-plane rotation of these two metasurfaces relative to each other, we can continuously manipulate the direction of reflected beams [4], as demonstrated in **Figure 1**. This method allows for a variety of beam configurations, directions, and paths by varying the twist angle and designing different patterns for each metasurface layer. In this work, we design and experimentally demonstrate two different moiré metasurfaces, the chessboard-type and triangular-type, which produce four-beam and six-beam radiations, respectively. Remarkably, the beam efficiency achieved by our moiré metasurfaces is even greater than the conventional metasurface designed with super unit cell configuration. Note that the design of moiré metasurfaces is fundamentally different from all previously reported moiré metasurfaces, in which the separation between the two metasurfaces is designed large enough to ensure linear combination of the functionality of each individual layer.

Our design offers a cost-effective solution for dynamic beamforming in RIS applications and unveils a novel approach to exploring new physics in programmable metasurfaces. Their compact profile makes them highly adaptable for use in a variety of applications, effortlessly blending into indoor environments as part of walls, ceilings, and decorative art, as well as enhancing outdoor infrastructures like building facades, streetlights, and advertising boards to extend signal reach. Beyond the cost-saving advantage, our fully passive reflective moiré metasurface architecture boasts several remarkable features, including zero static power consumption, no receiver noise, and a high capacity for handling power, showcasing its vast potential for applications in RIS and electronic warfare.

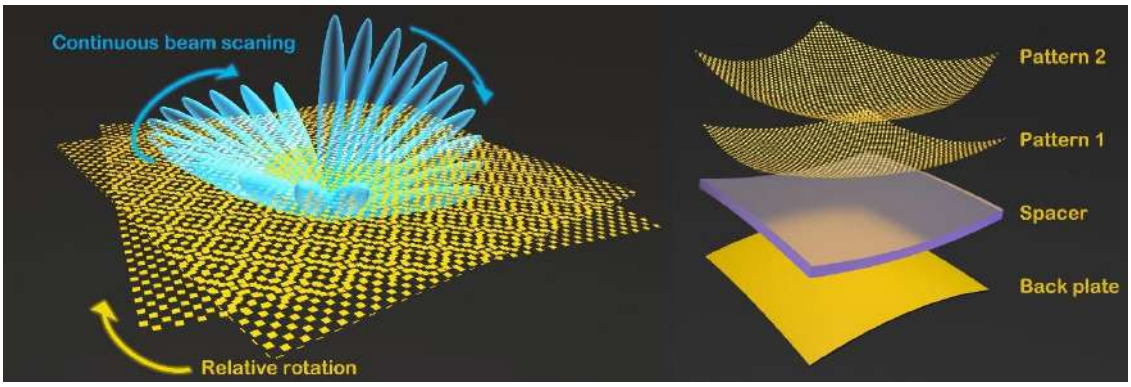

Figure 1 Schematic illustration and composition of a moiré metasurface.

However, the exploration of reflective moiré metasurfaces presents unique challenges and issues across various aspects, diverging significantly from the traditional design paradigms of conventional metasurfaces. Unlike their conventional counterparts, which rely on the repetitive nature of unit cells with locally periodic boundary conditions, reflective moiré metasurfaces cannot be described using a similar approach. This is because the moiré patterns, although periodically perceivable by the human eye under most conditions, do not exhibit true two-dimensional crystallinity except at certain discrete twist angles where the overlaid grid lattices of the two patterns align exactly.

Further complicating the design and understanding of moiré metasurfaces is their inherent high anisotropy. Traditional metasurface designs often leverage straightforward geometric shapes arranged in square or hexagonal lattices, resulting in predictable electromagnetic (EM) responses. Reflective moiré metasurfaces, however, introduce an additional layer of complexity due to the complex moiré pattern that changes with the twist angle. The moiré pattern not only complicates the polarization state of reflected waves, which may contain both co-polarized and cross-polarized components, but also leads to a shift in moiré periodicity across various lattice types as the twist angle changes. Such changes significantly affect the radiation pattern, making the design process more intricate.

Our research paves the way for novel methods of engineering far-field scattering by closely aligning ultra-thin metal patterns from different symmetry groups, a breakthrough with significant theoretical and practical implications. This innovation is expected to have widespread impact across the fields of electromagnetics, antenna development, and wireless communication, marking a significant step forward in these disciplines.

References

[1] T. J. Cui, S. Liu, and L. Zhang, Information metamaterials and metasurfaces, J. Mater. Chem. C 5, 3644-3668 (2017).

[2] T. J. Cui, L. Li, S. Liu, Q. Ma, L. Zhang, X. Wan, W. X. Jiang, and Q. Cheng, Information Metamaterial Systems, iScience 23, 101403 (2020).

[3] W. Tang, M. Z. Chen, X. Chen, J. Y. Dai, Y. Han, M. D. Renzo, Y. Zeng, S. Jin, Q. Cheng, and T. J. Cui, Wireless communications with reconfigurable intelligent surface: path loss modeling and experimental measurement, IEEE Trans. Wirel. Commun. 20, 421-439 (2021).

[4] S. Liu, S. Ma, R. Shao, L. Zhang, T. Yan, Q. Ma, S. Zhang, and T. J. Cui, Moiré metasurfaces for dynamic beamforming, Sci. Adv. 8, abo1511 (2022).

Terahertz characterization of thin resistive films and homogenized reactive metasurfaces via reflection time-domain spectroscopy

D. C. Zografopoulos[1*], F. Maita[1], L. Maiolo[1], I. Dionisiev[2], N. Minev[2], G. Petrone[1,3], S. Tofani[1], T. Ritacco[1], D. Dimitrov[2,4], V. Marinova[2], A. Liscio[1], V. Mussi[1], R. Beccherelli[1], and W. Fuscaldo[1]

[1]Consiglio Nazionale delle Ricerche, Istituto per la Microelettronica e Microsistemi, Rome, 00133, Italy
[2]Bulgarian Academy of Sciences, Institute of Optical Materials and Technologies, Sofia, 1133, Bulgaria
[3]Sapienza University of Rome, Department of Astronautics, Electrical, and Energy Engineering, Rome, 00185, Italy
[4]Bulgarian Academy of Sciences, Institute of Solid State Physics, Sofia, 1784, Bulgaria
[*]corresponding author: dimitrios.zografopoulos@cnr.it

Abstract: We present a detailed analytical and experimental study of a protocol for the broadband terahertz characterization of thin films and homogenized metasurfaces based on the Gires–Tournois étalon configuration. Particular emphasis is given to two generic case studies, namely, purely resistive or purely reactive films, and the sensitivity and overall performance of measuring their sheet resistance and reactance, respectively. Experimental verification is provided through the measurement of a series of thin film samples for both categories, such as transparent conducting oxides, reduced graphene oxide, and transition metal dichalcogenides in the first, and fishnet, patch, and strip grating metasurfaces in the second scenario.

Terahertz time-domain spectroscopy (THz-TDS) is a widespread technique for material and device characterization in the low THz spectrum, providing significant advantages, such as fast, broadband measurements providing both amplitude and phase information [1]. It is mostly operated in transmission mode, although reflection measurements have also been employed for particularly reflective or lossy samples. Here, we provide a thorough analysis of the technique for the characterization of thin films, continuous or consisting of homogenized metallic metasurfaces, on a grounded dielectric slab configuration, i.e., the so-called Gires–Tournois étalon (see Fig. 1a). The system is analytically described by an equivalent transmission-line circuit, where the film is characterized by its generally complex surface admittance $Y_s=G_s+jB_s$ (as in Fig. 1b) [3].

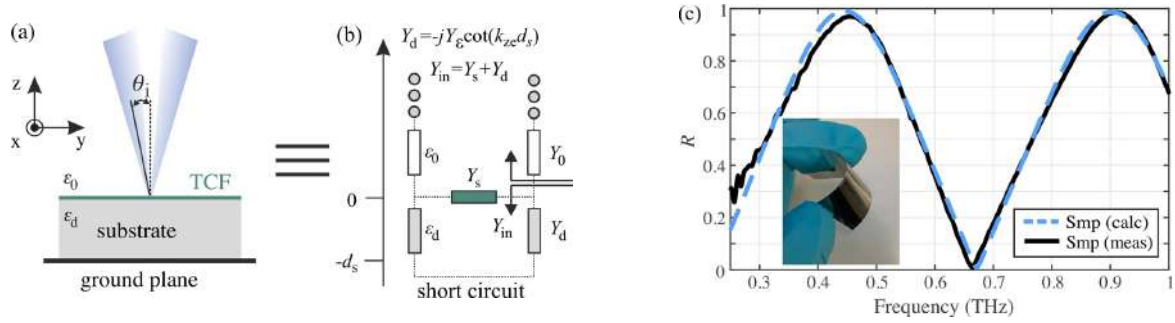

Figure 1: a) Schematic of the investigated one-dimensional electromagnetic problem and b) equivalent transmission-line circuit model. c) Calculated and measured reflection spectra for a thin titanium film on a 188-μm thick Zeonor substrate backed by an aluminum mirror. The inset shows a photo of the flexible sample.

First, the complex dielectric constant and dispersion of the dielectric slab are investigated, by assuming relevant dispersive models (e.g., Debye and Lorentz), and fitting their reflection spectrum to the analytically predicted values [4]. Such models intrinsically ensure the fulfillment of Kramers–Kronig relations. Once the

properties of the substrate are established, the surface admittance of the thin film is calculated by a similar fitting optimization algorithm.

We focus on two complementary scenarios, namely purely resistive (B_s=0) and purely reactive (G_s=0) films. In the first case, the performance of the THz-TDS technique as a sheet resistance sensor is studied in detail, as well as particular aspects that naturally arise such as critically coupled Salisbury screens, an example of which, based on a nanometric titanium film, is showed in Fig. 2c. Overall, a large series of emerging thin film samples were used to provide experimental demonstration: transparent conducting oxides, reduced graphene, titanium films, and 2D transition metal dichalcogenide layers.

Subsequently, a series of metallic metasurfaces were fabricated by photolithography with a pitch of 200 μm (λ/5 at 300 GHz) targeting three archetypal geometries: patch arrays, strip gratings, and fishnet structures. Such metasurfaces behave as almost purely reactive sheets with capacitive or inductive behaviour depending on their geometry, thereby inducing a spectral shift of the étalon resonances. This shift was experimentally verified by the proposed technique, which was assessed in terms of its sensitivity in estimating the value of sheet reactance.

Overall, the presented results corroborate the efficiency of the technique for the fast and non-destructive characterization of emerging thin resistive and reactive films. Potential emerging THz applications, such as metasurface-based leaky-wave antennas are briefly discussed.

This work was supported by the project ECS00000024 “Ecosistemi dell’Innovazione”- Rome Technopole – (B83C22002890005) of the Italian Ministry of University and Research, public call n. 3277, PNRR-Mission 4, Component 2, Investment 1.5, financed by the European Union, Next Generation EU. D. C. Z. and V. M. acknowledge the bilateral project between the Consiglio Nazionale delle Ricerche and the Bulgarian Academy of Sciences “Two-dimensional nanomaterials toward terahertz optoelectronic applications” (B83C23000610005). W. F. acknowledges the project PRIN 2022 “SAFE” (Spiral and Focused Electromagnetic fields) 2022ESAC3K, Italian Ministry of University and Research (MUR), financed by the European Union, Next Generation EU. V. M and D. D. acknowledge the Bulgarian Science Fund project number КП-06-Н-68/1, and the European Regional Development Fund within the “Science and Education for Smart Growth 2014–2020” under the Project CoE “National Center of Mechatronics and Clean Technologies” BG05M2OP001-1.001-0008.

References

1. Withayachumnankul, W. and M. Naftaly, “Fundamentals of measurement in terahertz time-domain spectroscopy,” J. Infrared Milli. Terahz. Waves, Vol. 35, pp. 610–637, 2014.
2. Jepsen, P. U., U. Møller and H. Merbold, “Investigation of aqueous alcohol and sugar solutions with reflection terahertz time-domain spectroscopy,” Opt. Express, Vol. 15, No. 22, 14717–14737, 2007.
3. Fuscaldo, W., S. De Simone, D. Dimitrov, V. Marinova, V. Mussi, R. Beccherelli and D. C. Zografopoulos, “Terahertz characterization of graphene conductivity via time-domain reflection spectroscopy on metal-backed dielectric substrates,” J. Phys. D., Vol. 55, art. no. 365101, 2022.
4. Fuscaldo, W., F. Maita, L. Maiolo, R. Beccherelli and D. C. Zografopoulos, “Broadband dielectric characterization of high-permittivity Rogers substrates via terahertz time-domain spectroscopy in reflection mode,” Appl. Sci., Vol. 12, art. no. 8259, 2022.
5. Zografopoulos, D. C., I. Dionisiev, N. Minev, G. Petrone, F. Maita, L. Maiolo, D. Dimitrov, V. Marinova, A. Liscio, V. Mussi, R. Beccherelli and W. Fuscaldo, “Terahertz time-domain characterization of thin conducting films in reflection mode,” submitted, 2024.

AES 2024, ROME - ITALY, 25 –28 JUNE 2024

An overview of advanced techniques for design and synthesis of nondiffractive Bessel beams in near-field

Santi C. Pavone[1]

[1]Department of Electrical, Electronics, and Computer Engineering (DIEEI), University of Catania,
Via S. Sofia 64, 95123 Catania, Italy.
[*]*corresponding author: santi.pavone@unict.it*

Abstract: In this contribution, an overview of the techniques and methods to synthesize and radiate nondiffractive Bessel beams is presented, spanning from solutions in the optical regime to others at microwaves and millimeter waves, by considering also applications.

In some applications belonging to electrical engineering and applied physics, it is required to mitigate as much as possible the physical phenomenon of beam diffraction. Indeed, the spatial spreading of electromagnetic energy unfortunately reduces the signal-to-noise ratio of near-field radio-links, the ability to detect scatterers in GPR, in through-the-wall imaging, and also in wireless power transfer applications [1], [2]. To mitigate these issues, in the last decades, localized waves in near-field [3], [4] deserved increasing importance [5]-[9], due to their interesting field structure, among which it should be mentioned the invariance of their transverse field profile when propagating in free-space.

Among localized waves, Bessel beams deserve research interest both from historical and scientific viewpoints, since their early formalization by Durnin [10]–[11]. Indeed, Bessel beams are an exact beam-wave solution of homogeneous scalar Helmholtz equation in cylindrical coordinates, namely

$$\left(\nabla^2 + k^2\right)\varphi_n\left(\mathbf{r}\right) = 0 \qquad (1)$$

being $\varphi_n\left(\mathbf{r}\right)$ a suitable auxiliary potential derived from electromagnetic field scalarization procedure. The general solution to (1) can be written in the form $\varphi_n\left(\mathbf{r}\right) = J_n\left(k_{\rho a}\rho\right)e^{-jk_{za}z}e^{jn\varphi}$, from which it is possible to distinguish zeroth order ($n = 0$) and higher-order Bessel beams ($n \neq 0$).

Zeroth order Bessel beams, on which we mainly focus in this contribution, are characterized by a maximum of radiation for $\rho = 0$, and exhibit a spatially invariant transverse field profile, that inherently prevents diffraction along the longitudinal axis. However, it should be noted that pure Bessel beams, intended as theoretical solutions, require infinite power to be radiated, like plane waves. Nevertheless, in the last decades truncated Bessel beam launchers, characterized by very-high radiation efficiency, were successfully optimized and characterized both at microwaves/millimeter waves, and in optics [12]–[14].

Another really interesting feature of Bessel beams is the so-called *self-healing* property, that is the ability of beam reconstruction beyond obstacles that are quite small in terms of its main lobe. Such a feature allows using Bessel beam launchers also in some noisy environments, in which beam scattering occurs.

The aim of this contribution is to critically analyze and discuss pros and cons of the techniques developed for the synthesis and optimization of Bessel beams, spanning from optics to Terahertz, from microwaves to

millimeter waves. Moreover, particular attention will be paid to launcher optimization techniques. Indeed, the techniques proposed to achieve high-performance beam launchers can be sometimes computationally heavy, especially by exploiting refined aperture synthesis methods. Suitable optimization procedures require to clearly state physics-based functionals [13], by avoiding blind algorithms which would dramatically increase the computational burden, especially for applications at microwaves and millimeter waves.

In addition to more standard technologies for beam launcher development, metasurface-based Bessel beam launchers represent undoubtedly a good trade-off between aperture synthesis flexibility and the possibility to formalize design techniques that can be profitably adopted from microwaves to Terahertz. In this sense, partially-reflective metasurfaces placed on top of prescribed dielectric layered structures (like Fabry-Perot cavities) represent an attractive alternative for Bessel beam launcher design, that will be exploited and discussed.

Finally, a detailed analysis of recent Bessel beam applications in electrical and electronics engineering will be reported and investigated, by carefully considering the problem of Bessel-beam power-transfer maximization through planar multilayer structures, obtained by defining appropriate figures of merit to quantify the amount of beam power that is effectively delivered beyond the stratification. The presented analysis paves the way to novel applications of Bessel beams in several research fields and frequency ranges, spanning from imaging to efficient power delivery, from RADARs to field focusing.

References

1. S.2C.2Pavone2and2M.2Albani,2"Design2of2a2wireless2link2at2microwaves2in2the2radiative2near-field by using RLSA Bessel beam2launchers,"2019 PhotonIcs & Electromagn. Research Symp. (PIERS), 2019, pp. 289–294.
2. S.2Paković,2S.2Zhou,2D.2González-Ovejero, S. C. Pavone, A. Grbic and M. Ettorre, "Bessel–Gauss Beam Launchers for Wireless Power Transfer," IEEE Open Journ. Antennas Propag., vol. 2, pp. 654-663, 2021.
3. H. E. Hernandez-Figueroa, M. Zamboni-Rached, and E. Recami, "Localized waves", J. Wiley & Sons, 2008, vol. 194.
4. H. E. Hernandez-Figueroa, M. Zamboni-Rached, and E. Recami, "Non-diffracting waves", J. Wiley & Sons, 2013.
5. T. A. Planchon, L. Gao, D. E. Milkie, M.2W.2Davidson,2J.2A.2Galbraith,2C.2G.2Galbraith,2and2E.2Betzig,2"Rapid2three-dimensional2isotropic2imaging2of2living2cells2using2Bessel2beam2plane2illumination,"2Nat.2meth.,2vol.28,2no.25,2pp.2417–423, 2011.
6. W. Williams, J.2Pendry,2"Generating2Bessel2beams2by2use2of2localized2modes,"2JOSA2A,2v. 22, n. 5, p. 992–997, 2005.
7. D. McGloin, K.2Dholakia,2"Bessel2beams:2diffraction2in2a2new2light,"2Contem. Physics, vol. 46, no. 1, pp. 15–28, 2005.
8. S. C. Pavone, G. Sorbello, and L. Di Donato, "Improving2Physical2Optics2approximation2through2Bessel2beam2scattering,"2IEEE2Antennas2Wireless2Propag.2Lett.,2vol.220,2no.26,2pp.2993–997, 2021.
9. S.2C.2Pavone,2G.2Sorbello,2and2L.2Di2Donato,2"Forward2and2inverse2scattering2of2metallic2objects2through2focused2Bessel-shaped2fields,"2IEEE2Open2Journ.2Antennas2Propag.,2vol.23,2pp.2911–916, 2022.
10. J.2Durnin,2"Exact2solutions2for2nondiffracting2beams.2I.2The2scalar2theory,"2JOSA2A,2vol.24,2no.24,2pp.2651–654, 1987.
11. J.2Durnin,2J.2Miceli2Jr,2and2J.2Eberly,2"Diffraction-free2beams,"2Phys.2Rev.2Lett.,2vol.258,2no.215,2p.21499,21987.
12. S.2Monk,2J.2Arlt,2D.2Robertson,2J.2Courtial,2and2M.2Padgett,2"The2generation2of2Bessel2beams2at2millimetre-wave frequencies2by2use2of2an2axicon,"2Optics2Communications,2vol.2170,2no.24-6, pp. 213–215, 1999.
13. S.2C.2Pavone,2M.2Ettorre,2M.2Casaletti,2and2M.2Albani,2"Analysis2and2design2of2Bessel2beam2launchers:2Transverse2polarization,"2IEEE2Trans.2Antennas2Propag.,2vol.269,2no.28,2pp.25175–5180, 2021.
14. W.2Fuscaldo,2G.2Valerio,2A.2Galli,2R.2Sauleau,2A.2Grbic,2and2M.2Ettorre,2"Higher-order leaky-mode Bessel-beam launcher,"2IEEE2Trans.2Antennas Propag., vol. 64, no. 3, pp. 904–913, 2015.

AES 2024, ROME - ITALY, 25 –28 JUNE 2024

Gain and Impedance Bandwidth Enhancement in Fabry–Perot Cavity Leaky-Wave Antennas Based on Metasurfaces

E. Negri[1*], W. Fuscaldo[2], P. Burghignoli[1], and A. Galli[1]

[1]Department of Information Engineering, Electronics and Telecommunications, Sapienza University of Rome, Rome, Italy
[2]Istituto per la Microelettronica e Microsistemi, Consiglio Nazionale delle Ricerche, Rome, Italy
[*]corresponding author: edoardo.negri@uniroma1.it

Abstract: Recently the gain bandwidth of Fabry–Perot cavity antennas (FPCAs) has been greatly enhanced by using metasurfaces with dielectric covers. To ensure the wideband behavior, the impedance bandwidth must be enlarged as well. Thus, an efficient technique is here proposed to design an FPCA with enhanced gain and impedance bandwidths.

Fabry–Perot cavity antennas (FPCAs) are radiating devices able to generate a broadside pencil beam. They typically consist of a grounded dielectric slab with an isotropic metasurface on top. The latter is commonly realized through a *thin* sub-wavelength metallic lattice, and represented by a scalar, purely imaginary, impedance sheet $Z_s = jX_s$ [1]. The thin metasurface generates a Foster-like phase contribution, which is responsible for the narrowband behavior of typical FPCAs [2]. To give some numbers, the –3 dB gain fractional bandwidth rarely exceeds a few percents, thus ensuring a -10 dB S_{11} impedance bandwidth rarely represents an issue.

As shown in [2], the gain bandwidth can be enhanced by using a *thick* metasurface, i.e., a thin metasurface with a cover dielectric layer [see Fig. 1(a)]. By properly choosing the dielectric superstrate height h_{sup} and its relative dielectric permittivity ε_r, it is indeed possible to achieve broadside radiation over gain bandwidths as large as about 20%. Under this condition, an ad hoc matching network needs to be designed to ensure an adequate impedance bandwidth.

The bandwidth performance of FPCAs can easily be predicted by means of a leaky-wave interpretation [2]. Indeed, broadside radiation in FPCAs is obtained when the *leaky* phase and attenuation constants (β and α, respectively) of the dominant transverse-electric (TE) and transverse-magnetic (TM) leaky modes are small and close to each other [2, 3]. This aspect is evident in Fig. 1(b) where β and α are reported normalized with respect to the vacuum wavenumber k_0 (the2hat2‘^’2represents2this normalization) for the case of an air-filled FPCA (whose thickness is h_{sub} = 0.5 mm for an application around f_0 = 300 GHz) with either a *thin* metasurface (X_s =2852Ω) or a properly designed *thick* metasurface. It is clear that, while for *thin* metasurfaces the condition $\beta \approx 2\alpha$ occurs only at a single frequency, the same constraint is closely satisfied over a wider frequency range for a *thick* metasurface with h_{sup} = 0.2825 mm and ε_r = 6.15, enlarging the theoretically expected –3 dB gain fractional bandwidth up to 17% (computed using the same approach as in [2]).

Once the modal solutions are found, both the desired TE and TM modes have to be excited in the FPCA in order to achieve a broadside radiation pattern. As shown in [1], a pair of TE and TM leaky modes can easily be excited by feeding an FPCA with a horizontal magnetic/electric dipole (HMD/HED). A practical HMD source can be realized by etching a rectangular quasi-resonant slot in the antenna ground plane [4]. The slot can be fed either through free-space coupling or by a rectangular waveguide (RWG). As shown in Fig. 1(a), the latter configuration is here examined (choosing a RWG with height $a = 2\lambda_0/3$ and width $b = \lambda_0/3$, being λ_0 the vacuum wavenumber), as it allows for a straightforward method to enhance the impedance bandwidth, for instance by designing reactive loads within the RWG section. As shown in [5], this task is performed by analytically representing two waveguide discontinuities through two equivalent susceptances in a transmission-line model

(TLM) [see Fig. 1(c)]. The distinctive feature of the proposed approach is to retrieve the FPCA input admittance Y_{in} through a single full-wave simulation (without capacitive irises and de-embedding the waveguide port up to the FPCA ground plane), thus avoiding a computationally expensive software parameter optimization. In particular, by considering two capacitive irises it is possible to exploit closed-form expressions for their equivalent susceptances B_1 and B_2 in terms of their physical dimensions (the distances d_1 and d_2 and the gap heights g_1 and g_2); then, the best matching-configuration is found through a fast and accurate numerical approach [5] obtaining: $g_1 = 0.175b$, $g_2 = 0.375b$, $d_1 = 0.275\lambda_0$, and $d_2 = 0.155\lambda_0$ [see Fig. 1(a)]. The results of this analysis for an efficiently designed matching network are reported in Fig. 1(d), where a remarkable agreement is found between a numerical full-wave simulation and the theoretical performance based on the proposed technique (also note the matching improvement with respect to the case without irises).

W.2 F.2 acknowledges2 the2 project2 PRIN2 20222 “SAFE”2 (Spiral2 and2 Focused2 Electromagnetic2 fields)2 2022ESAC3K, Italian Ministry of University and Research (MUR), financed by the European Union, Next Generation EU. A. G. thanks for the support of the European Union under the Italian National Recovery and Resilience2 Plan2 (NRRP)2 of2 NextGenerationEU,2 partnership2 on2 “Telecommunications2 of2 the2 Future”2 (PE00000001 - program2‘RESTART”).

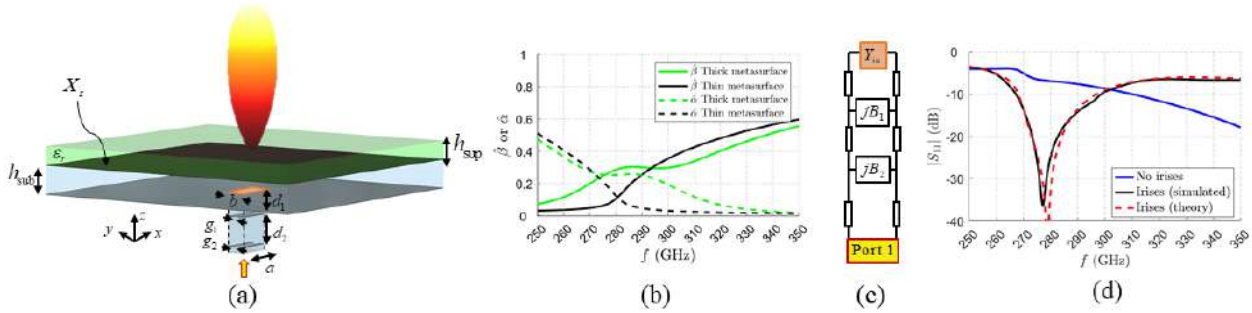

Figure 1: (a) Pictorial representation of a thick-metasurface-based FPCA with its far-field radiation pattern at broadside. (b) Leaky-mode dispersion curves for the same FPCA with either a *thin* (black) or a *thick* (green) metasurface. (c) Equivalent TLM of the waveguide matching network. (d) Full-wave results for the S_{11} in dB vs. frequency f of the FPCA without (blue) and with the matching network (black). Numerical results obtained with the TLM are reported through a red dashed line.

References

1. P. Burghignoli, W. Fuscaldo,2and2A.2Galli,2‘Fabry–Perot cavity antennas: The leaky-wave2perspective,”2*IEEE Antennas Propag. Mag.*, vol. 63, no. 4, pp. 116–145, Aug. 2021.
2. A. T. Almutawa, A. Hosseini, D. R. Jackson, and F.2Capolino,2‘Leaky-wave analysis of wideband planar Fabry–Pérot cavity2antennas2formed2by2a2thick2PRS,”2*IEEE Trans. Antennas Propag.*, vol. 67, no. 8, pp. 5163–5175, Aug. 2019.
3. G.2Lovat,2P.2Burghignoli,2and2D.2R.2Jackson,2‘Fundamental2properties2and2optimization of broadside radiation from uniform leaky-wave antennas,”2*IEEE Trans. Antennas Propag.*, vol. 54, no. 5, pp. 1442–1452, May 2006.
4. E.2Negri,2W.2Fuscaldo,2P.2Burghignoli,2and2A.2Galli,2“Leaky-wave analysis of TM-, TE-, and hybrid-polarized aperture-fed Bessel-beam2launchers2for2wireless2power2transfer2links,”2*IEEE Trans. Antennas Prop.*, vol. 71, no. 2, pp. 1424–1436, Feb. 2023.
5. E.2Negri,2W.2Fuscaldo,2S.2Tofani,2P.2Burghignoli,2and2A.2Galli,2‘An2efficient2and2accurate2semi-analytical matching technique for waveguide-fed2antennas,”2*Sci. Rep.*, vol. 14, no. 3892, Feb. 2024.

AES 2024, ROME - ITALY, 25 –28 JUNE 2024

Metasurfaces enhanced with 2D photonic materials: Analysis based on quasinormal modes

T. Christopoulos,[1] Georgios Nousios,[2] Emmanouil E. Kriezis,[2] and O. Tsilipakos[1,*]

[1]Theoretical and Physical Chemistry Institute, National Hellenic Research Foundation, 11635 Athens, Greece
[2]School of Electrical and Computer Engineering, Aristotle University of Thessaloniki, 54124 Thessaloniki, Greece
[*]corresponding author: otsilipakos@eie.gr

Abstract: Two-dimensional photonic materials exhibit tunable linear and nonlinear properties. They can be incorporated in metasurfaces to enable novel functionalities. Here, we study 2D-material-enhanced metasurfaces for THz and near-infrared frequencies. The analysis is performed with a novel multimode framework based on the quasinormal modes supported by these non-Hermitian systems.

Metasurfaces (MSs), ultrathin structures composed of a periodic arrangement of resonant meta-atoms on a plane, have attracted considerable research interest [1,2]. By engineering the geometry and material composition of the constituent meta-atoms, MSs can be designed to control the amplitude, phase, wavefront, and polarization of impinging electromagnetic waves. As a result, they have provided a platform for observing a broad range of linear (e,g., perfect absorption, wavefront manipulation, polarization control) and nonlinear (e.g., saturable absorption, frequency generation) phenomena at frequencies ranging from microwaves and THz to the near infrared (NIR) and visible. In order to enable reconfigurable and nonlinear response, materials with tunable and intensity-dependent properties can be integrated within the MS. In this context, two-dimensional (2D) photonic materials (e.g., graphene, transition metal dichalcogenides, black phosphorus, MXenes, etc.) are recently being incorporated in MS structures. Their ultrathin nature is naturally compatible with MSs and they can offer electrically-tunable properties, strong nonlinearity, and broadband and tunable gain.

In this work, we study two cases of 2D-material-enhanced metasurfaces, with important practical application: (i) a multiresonant graphene-based MS that supports tightly-confined graphene surface plasmon (GSP) resonances and can be utilized for third-harmonic generation at THz frequencies [3,4,5] and (ii) a strongly-resonant dielectric metasurface overlaid with a transition metal dichalcogenide (TMD) layer, which can emit light at optical frequencies [6]. In order to analyze and design such multiresonant resonant free-space structures, we develop a theoretical framework based on the concept of quasinormal modes (QNMs) [7,5], i.e., the natural modes supported by non-Hermitian (leaky and/or lossy) systems. More specifically, the scattered field is expanded in terms of the supported QNMs, which are numerically computed via the finite element method (FEM). Both the linear and nonlinear spectral response can be retrieved and both specular reflection/transmission and higher diffraction orders can be accommodated by the framework. Full wave FEM simulations are used to verify the validity of the obtained results. We find the framework to be very efficient and extremely accurate. In addition, probing the resonant structure of the system under study provides important physical insight into the design process.

To highlight the capabilities of the proposed framework, we focus on the example of the graphene-based MS. Graphene exhibits strong third-order nonlinearity at THz frequencies and the ability to support surface plasmons with ultra-short plasmon wavelengths tight confinement, thus further boosting the inherently strong material nonlinearity. We consider a MS made of periodically arranged graphene strips on a metal-backed substrate to

operate in reflection [Fig. 1(a)]. The results of Fig. 1(b),(c) show excellent agreement between the framework and full-wave simulations both in the linear and nonlinear regimes and even under oblique incidence.

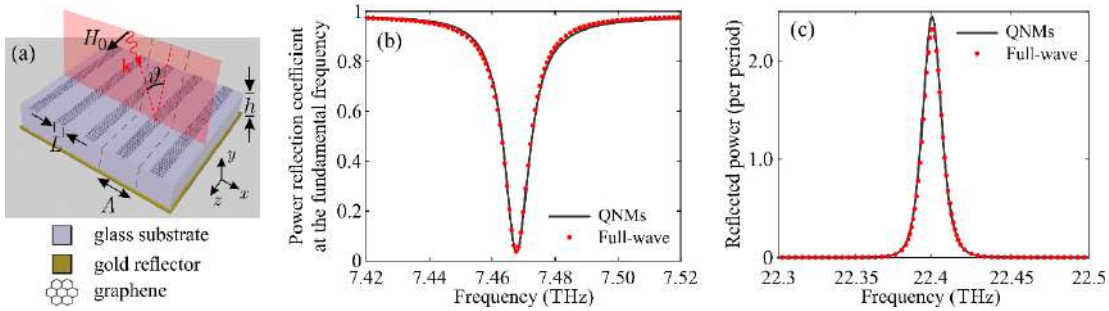

Fig. 1: (a) Graphene-strip metasurface on a metal-backed glass substrate ($L = 5\ \mu m, \Lambda = 10\ \mu m, h = 19.5\ \mu m$). (b) Linear (power reflection coefficient) and (c) nonlinear response (reflected power in W/m for $P_{inc} = 100\ W/m$) of a graphene metasurface under TM-polarized ($\mathbf{H} = H_z\hat{z}$) oblique incidence ($\theta = 20°$). QNM expansion (solid lines) and full-wave simulations (red markers) show excellent agreement.

Acknowledgments

This work was supported by the Hellenic Foundation for Research and Innovation (H.F.R.I.) under the "2nd Call for H.F.R.I. Research Projects to support Post-doctoral Researchers" (Project Number: 2916, PHOTOSURF).

References

1. D. C. Zografopoulos and O. Tsilipakos, "Recent advances in strongly-resonant and gradient all-dielectric metasurfaces," Materials Advances, Vol. 4, 11-34, 2023.
2. T. Gu, H. J. Kim, C. Rivero-Baleine, and J. Hu, "Reconfigurable metasurfaces towards commercial success," Nat. Photon., Vol. 17, 48–58, 2023.
3. J. W. You and N. C. Panoiu, "Tunable and dual-broadband giant enhancement of second-harmonic and third-harmonic generation in an optimized graphene-insulator-graphene metasurface," Phys. Rev. B, Vol. 102, 121403, 2020.
4. A. Theodosi, O. Tsilipakos, C. M. Soukoulis, E. N. Economou. and M. Kafesaki, "2D-patterned Graphene Metasurfaces for Efficient Third Harmonic Generation at THz Frequencies," Opt. Express, Vol. 30, 460-472, 2022.
5. T. Christopoulos, E. Kriezis, and O. Tsilipakos, "Multimode non-Hermitian framework for third-order nonlinear photonic systems comprising two-dimensional materials," Phys. Rev. B, Vol. 107, 035413, 2023.
6. G. Nousios, T. Christopoulos, O. Tsilipakos and E. Kriezis, "Integrated Lasers with Transition Metal Dichalcogenide Heterostructures: Analysis and Design Utilizing Coupled-Mode Theory for Two-Dimensional Materials," Phys. Rev. Appl., Vol. 19, 064027, 2023.
7. C. Gigli, T. Wu, G. Marino, A. Borne, G. Leo, and P. Lalanne, "Quasinormal-mode non-hermitian modeling and design in nonlinear nano-optics," ACS Photonics, Vol. 7, 1197, 2020.

Modal Analysis Glide-Symmetric Open Structure

Davide Comite[1*], Guido Valerio[2], Yuhuan Tong[2]

[1]Sapienza University, via Eudossiana 18, 00184, Rome, Italy
[2]Sorbonne Université, CNRS, Laboratoire GeePs, 75252 Paris, France
[*]corresponding author: davide.comite@uniroma1.it

Abstract: Periodic structure are broadly used to design antenna and electromagnetic devices in general. Higher symmetries, glide-symmetric structures included, are a class of periodic structures recently studied for their interesting guided-waves dispersion features [1]. Due to the suppression of frequency dispersion and the presence of sharp stopband, ultra-wideband antennas, planar lenses in particular, can be designed using glide symmetry, as well as electromagnetic bandgap materials. Many works have been proposed in the last decade based on glide symmetry, but no attempt have been made to study the properties of open waveguides offering glide-symmetric configurations.

We propose dispersive study of an all-metal glide-symmetric corrugated waveguide open with thin slots (see Fig. 1). The presence of the slots transform the guided mode of the waveguide into a leaky mode [2], whose complex propagation constant is here rigorously computed with a periodic method-of-moment formulation. The backward-to-forward leaky transition is studied and the results compared with full-wave .

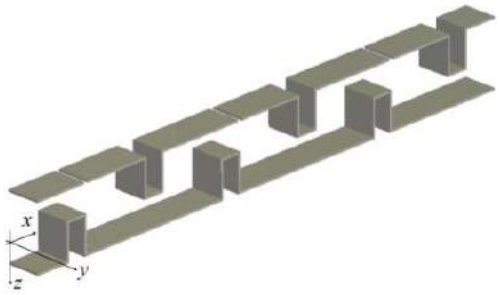

Figure 1. Geometry of the glide-symmetric structure under analysis. One slot per cell is present.

This work is partially supported by the Air Force Office of Scientific Research under award number FA8655-23-1-7018, by the European Union under the Italian National Recovery and Resilience Plan (NRRP) of NextGenerationEU, partnership on "Telecommunications of the Future", PE00000001 - program "RESTART", CUP B53C22004050001, and by the Horizon Europe Research and Innovation Program under the GENIUS Project, Marie Skłodowska-Curie Grant under Agreement 101072560. It is also based upon work from COST Action SyMat (CA18223), supported by COST (European Cooperation in Science and Technology).

References

1. A. Hessel, M. H. Chen, R. C. M. Li, and A. A. Oliner, "Propagation in periodically loaded waveguides with higher symmetries," Proceedings of the IEEE, vol. 61, no. 2, pp. 183–195, Feb. 1973.
2. P. Baccarelli, et al., "Modal properties of surface and leaky waves propagating at arbitrary angles along a metal strip grating on a grounded slab," IEEE Trans. Antennas Propag., vol. 53, no. 1, pp. 36–46, 2005.

AES 2024, ROME - ITALY, 25 –28 JUNE 2024

Gradient and Modulated Metasurfaces for Sub-Terahertz Antenna Systems

D. González Ovejero[1*], M. Robin[1], X. Morvan[1], and O. de Sagazan[1]

[1]Univ Rennes, CNRS, Institut d'Électronique et des Technologies du numéRique (IETR), UMR 6164, 35000 Rennes, France.

[*]corresponding author: david.gonzalez-ovejero@univ-rennes.fr

Abstract: This paper discusses the application of modulated metasurfaces in the sub-THz range, presenting the motivation for adopting this solution, addressing some of its drawbacks, and exploring possible solutions. In particular, we focus on multi-port architectures for enhancing the bandwidth. The architecture and technological solutions for its implementation are succinctly introduced.

One of the key challenges in exploiting millimeter-wave and sub-terahertz systems for wireless communications lies in compensating for the free-space path loss, which is proportional to frequency and thus very high for these bands. To overcome this issue, high-gain antennas are needed to minimize the amount of power radiated into directions in which it will not be received [1]. Besides satisfying the link budget, front-ends must also be amenable for integration on the chassis of vehicles, in smart cities and buildings. Therefore, individual sensors and instruments must be replaced by ultra-thin, surface-based, functional systems equivalent to smart skins. Currently, this change of paradigm is impeded by the use of spatially fed antennas, such as reflectors or lenses [1], where the source or sources are placed at a focal distance f from the optics. Although one can replace reflectors and lenses with lighter and flat reflect-arrays [1] and transmit-arrays [3] with a diameter D, the ratio f/D typically remains around 1 in these cases, so the required volume is still large.

This is where gradient and modulated metasurfaces (MTSs) come into play. They consist of ultra-thin surfaces comprising a texture of sub-wavelength elements, such as patches printed on a grounded substrate or conductive pins protruding out of a metallic ground. Owing to the sub-wavelength size of these constitutive elements, one can homogenize the surface as an impedance boundary condition (IBC) [4]. An appropriate design of these electrically small elements confers advanced electromagnetic functionalities to such surfaces. One can use gradient MTSs in parallel plate waveguides to design beam-formers [5] or periodically modulate the IBC to achieve directive radiation [4]. In the latter case, an inductive IBC supports the propagation dominantly transverse magnetic (TM) surface-wave (SW). This SW is gradually radiated owing to the IBC modulation, tailored in such a way that the -1 Floquet mode in the field expansion becomes a leaky-wave (LW).

The main difference and advantage compared to spatially fed antennas is that instead of a space wave, a surface wave (SW) is used to illuminate the antenna aperture, and the source and the MTS coexist in the same plane, yielding truly planar structures. This feature allows us to address the aforementioned compactness and integration issues of spatially-fed arrays, albeit at the expense of a reduced gain bandwidth. Although it is possible to radially chirp the period of the modulation to enlarge the bandwidth of modulated MTS antennas, this solution leads to an active region antenna with limited aperture efficiency [6]. We will discuss how one can increase the bandwidth without impacting the aperture efficiency (hence the gain) by dividing the total aperture into sub-apertures with smaller radii, each one fed by its own source. In this context, compact SW launchers well-suited to the sub-THz range are required; different topologies based on over-moded circular waveguides will be presented.

Finally, from a technological perspective, while it is feasible to manufacture MTS structures using standard printed circuit board (PCB) technology [3] or additive manufacturing [8] in the microwave and mm-wave range, these methods are no longer suitable for achieving the strict tolerances required in the sub-terahertz range. Hence, we are currently investigating fabrication processes for sub-THz modulated MTS. Among the technologies being explored are Si micromachining and the multi-spin process for Su8 photoresist on Si wafers. Each solution has its own advantages and drawbacks. For example, the Bosch process used for deep reactive ion etching (DRIE) of Si wafers provides robust structures with good accuracy, but it is a costly and relatively time-consuming process. Conversely, rapid and accurate prototyping may be obtained by Su8 multi-spin, but the resin may be sensitive to temperature and may not withstand harsh environments, such as in space applications. These advantages and disadvantages will be discussed in more detail during the presentation.

Acknowledgements: This work has received support from the French National Research Agency (ANR) through the project AROMA with reference ANR-22-CE24-0013 and the project FUNTERA with reference ANR-22-PEEL-0006. This work has also received support from the French Government through the Labex CominLabs Excellence Laboratory, managed by ANR in the Investing for the Future Program under Reference ANR-10-LABX-07-01.

References

1. T. Nagatsuma, G. Ducournau, and C. C. Renaud, "Advances in terahertz communications accelerated by photonics," *Nature Photon.*, vol. 10, no. 6, pp. 371–379, Junc. 2016.
2. X. You, R. T. Ako, W. S. L. Lee, M. X. Low, M. Bhaskaran, S. Sriram, C. Fumeaux, W. Withayachumnankul, "Terahertz reflectarray with enhanced bandwidth," *Adv. Optical Mater.*, 2019, 7, 1900791.
3. F. F. Manzillo, A. Clemente and J. L. González-Jiménez, "High-gain D-band transmitarrays in standard PCB technology for beyond-5G communications", *IEEE Trans. Antennas Propag.*, vol. 68, no. 1, pp. 587-592, Jan. 2020.
4. M. Faenzi, G. Minatti, David González-Ovejero, F. Caminita, E. Martini, C. Della Giovampaola and S. Maci, "Metasurface Antennas: New models, applications and realizations," *Sci. Rep.*, vol. 9, pp. 10178, 2019.
5. A. Mahmoud, J. Ruiz-García, O. de Sagazan, M. Ettorre, R. Sauleau and D. González-Ovejero, "Low-cost and low-profile sub-terahertz Luneburg lens beamformer on polymer," *IEEE Antennas Wireless Propag. Lett.*, vol. 22, no. 6, pp. 1411-1415, Jun. 2023.
6. M. Faenzi, D. González-Ovejero and S. Maci, "Wideband active region metasurface antennas," *IEEE Trans. Antennas Propag.*, vol. 68, no. 3, pp. 1261-1272, Mar. 2020.
7. D. Gonzalez-Ovejero, J. Taillieu, C. Bilitos, R Sauleau, O. de Sagazan, "Modulated metasurface antennas and arrays for millimeter wave and sub-terahertz applications," *13th Int. Conf. Metamaterials, Photon. Crystals Plasmonics (META 2023)*, Jul 2023, Paris, France. pp.858-859.
8. D. González-Ovejero, N.Chahat, R. Sauleau, G. Chattopadhyay, S. Maci and M. Ettorre, "Additive manufactured metal-only modulated metasurface antennas," *IEEE Trans. Antennas Propag.*, vol. 66, no. 11, pp. 6106-6114, Nov. 2018.

Specialty Optical Fibers

AES 2024, ROME - ITALY, 25 –28 JUNE 2024

Gas sensing inside negative curvature hollow-core fibers

G. Gomolka[1], P. Gronowicz[1,2], and R. Buczynski[3,4], and M. Nikodem[1*]

[1]Wroclaw University of Science and Technology, Poland
[2]Whitecarbon/Nanores Ltd., Poland
[3]Łukasiewicz Research Network - Institute of Microelectronics and Photonics, Poland
[4]University of Warsaw, Poland
[*]corresponding author: Michal.nikodem@pwr.edu.pl

Abstract: Application of negative curvature hollow-core fibers (HCF) as gas cells in gas sensing systems will be discussed. We will present experiments in which laser spectroscopy inside silica-based fibers is performed in various spectral regions, from visible to mid-infrared. Novel sensing configuration with HCF-based reflective probe will be demonstrated.

In the past few decades the utilization of semiconductor lasers as sources for trace-gas detection has evolved into a valuable tool across various fields, from environmental research to industrial process control and monitoring. While near-infrared laser diodes offer practical advantages, like fiber-coupled sources and cost-effective fiber-based components, the mid-infrared spectral range that holds the potential for the highest sensitivity (it is mid-infrared where the strongest, fundamental ro-vibrational transitions are located). Using infrared spectroscopy, relatively simple sensing techniques such as direct absorption spectroscopy (DAS) or wavelength modulation spectroscopy (WMS), detection limits down to parts-per-million (ppm) or even parts-per-billion (ppb) levels can be achieved for numerous molecules. However, achieving such sensitivities typically requires increasing the sensing path length to several meters or several tens of meters, which is usually accomplished with multi-pass cells of various designs. Unfortunately, although multi-pass cells have become a standard element of trace-gas detection systems, they have some limitations concerning weight, size, and cost. Additionally, dense multi-pass cells may introduce opto-mechanical drifts, affecting long-term sensor performance. In light of these challenges, hollow-core fibers (HCFs) emerge as a promising alternative to traditional gas cells. HCFs offer solutions to limitations of multi-pass cells related to size, weight and mechanical stability, but they also provide some additional benefits, such as, for example, low volume and possibilities for endoscope-like probe development.

Various types of HCFs have been investigated for gas detection purposes in the past. Recently, negative-curvature hollow-core fibers (NC-HCFs) [1] have gained attention due to their advantageous properties in gas sensing applications, such as single-mode propagation (that limits multimodal interferences), low bending losses (that allow to use long fibers while keeping setup size small), and relatively large core sizes (which simplify gas filling procedures). Over the past few years, numerous gas sensing systems utilizing NC-HCFs have been reported, detecting various molecules across different spectral regions. Near-infrared sensing demonstrations include, for example, methane detection near 1.65 μm [2] or acetylene detection near 1.55 μm [3]. Furthermore, in mid-infrared spectroscopy, NC-HCFs offer an additional advantage: despite low transmission of the host glass (when made out of SiO_2), light can still propagate within them due to minimal overlap between the fiber structure and the guided mode [4]. This feature enables using silica-based NC-HCFs for laser spectroscopy in the mid-infrared spectral region [5]. Several examples have been demonstrated so far with various target compounds, including formaldehyde, nitric oxide, ethane, methane, and ethylene.

During the conference I will discuss the practical aspects of gas sensing inside HCFs. Example of a HCF-based sensor is shown in Figure 1. It was designed to detect ambient methane with an interband cascade laser (ICL). Light from a laser was coupled into the HCF using an off-axis parabolic mirror. The output of the 7.5-m long HCF was placed inside a FC connector and mounted onto detector. The gas sample entered the HCF from the end-side. This sensor was characterized and a detection limit at single ppb level was achieved. Additionally, it was used for a week-long continuous monitoring of ambient methane and water vapor in atmospheric air. A diurnal cycles in methane concentrations could be observed, what proves the sensor's usability in environmental monitoring. In my talk, I will not only present details about this setup but also about other HCF-based experiments that we have performed recently, including simultaneous detection of methane and nitrous oxide at 3.3 and 4.5 µm using interband and quantum cascade lasers, and simultaneous detection of methane and oxygen using laser diodes at 761 and 1651 nm. I will also introduce novel sensing configuration that would not have been possible without hollow-core fibers: an endoscope-like gas probe that uses HCF not only as gas cell but also as a sampling tube. Advantages and technical challenges of this sensing approach will be discussed.

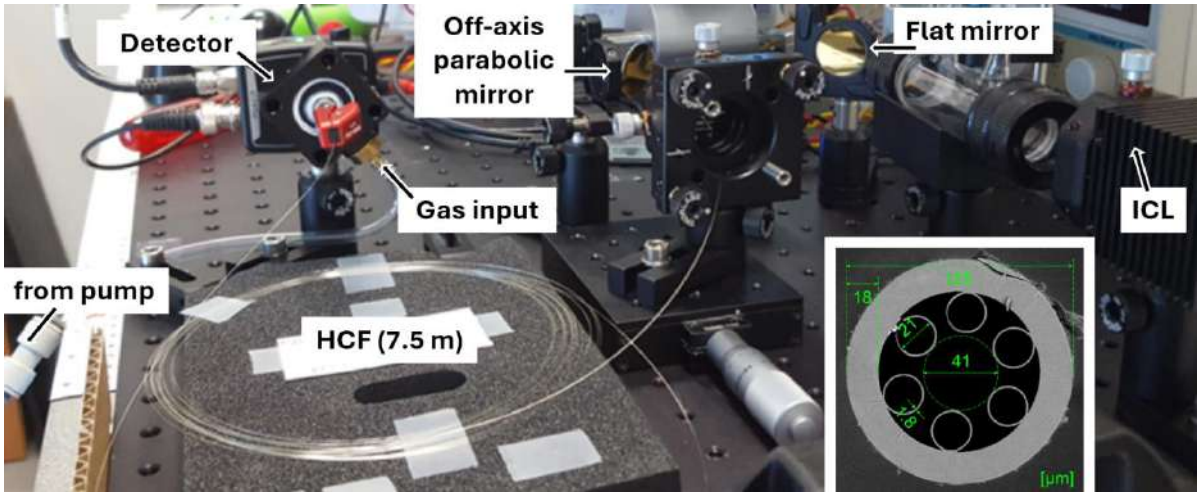

Figure 1. Example of a mid-infrared HCF-based methane sensor. Also shown is a cross-section of the HCF used in these experiments.

Acknowledgements: This work was co-financed by Ministerstwo Edukacji i Nauki, Diamentowy Grant (DI 2019 0026 49). P.G. acknowledges the Polish Ministry of Education and Science, 'Doktorat Wdrozeniowy', DWD/6/0556/2022. G.G. acknowledges Narodowe Centrum Nauki for financing his PhD program (Preludium Bis project 2019/35/O/ST7/04176).

References

1. Yu, F. and Knight, J. C., "Negative Curvature Hollow-Core Optical Fiber," IEEE J. Sel. Top. Quantum Electron. 22, 146–155, 2016.
2. Kapit, J. and Michel, A. P. M., "Dissolved gas sensing using an anti-resonant hollow core optical fiber," Appl. Opt. 60, 10354–10358 (2021).
3. Zhao, P., et al., "Mode-phase-difference photothermal spectroscopy for gas detection with an anti-resonant hollow-core optical fiber," Nat. Commun. 11, 847 (2020).
4. Fu Q. et al. "Hundred-meter-scale, kilowatt peak-power, near-diffraction-limited, mid-infrared pulse delivery via the low-loss hollow-core fiber," Opt. Lett. 47, 5301-5304 (2022)
5. Jaworski, P. "A Review of Antiresonant Hollow-Core Fiber-Assisted Spectroscopy of Gases," Sensors 21, 5640 (2021).

AES 2024, ROME - ITALY, 25 –28 JUNE 2024

Dispersion properties of highly birefringent microstructured fibers with germanium doped cores

T. Martynkien[1*], K. Tarnowski[1], K. Stefańska [1]and P. Mergo[2]

[1] *Department of Optics and Photonics, Wrocław University of Science and Technology, Wybrzeze Wyspiańskiego 27, 50-370 Wrocław, Poland*

[2] *Laboratory of Optical Fiber Technology, Maria Curie-Skłodowska University, Pl. M. Curie-Skłodowskiej 3, 20-031 Lublin, Poland*

[*]corresponding author: tadeusz.martynkien@pwr.edu.pl

Abstract: We have demonstrated both theoretically and experimentally the flexibility to tailor chromatic dispersion in highly birefringent microstructured fibers with a germanium-doped core. The presented fibers made from a single preform allow for a variety of non-linear applications, ranging from soliton generation to supercontinuum generation under all normal dispersion conditions.

We designed, manufactured and characterized serie of highly birefringent microstructured fibers with various chromatic dispersion characteristics. All fabricated fibers were drawn from single preform. The preform was made using the stack and draw technology. The fiber core fabricated with the MCVD method is moderately doped with germanium dioxide (18 mol%), while the fiber cladding was stacked from silica rods and capillaries. The capillaries were arranged in two groups located symmetrically with respect to the fiber core. In fig. 1a we show cross section of the whole fiber structure. By applying a high pressure during a fiber drawing process, we achieved lattice squeezing and consequently high birefringence. Additionally, controling the lattice pitch and size of air holes allowed us to control chromatic dispersion profiles of particular fiber. SEM images of fiber cross sections in the vicinity of the core are shown in fig. 1b-d.

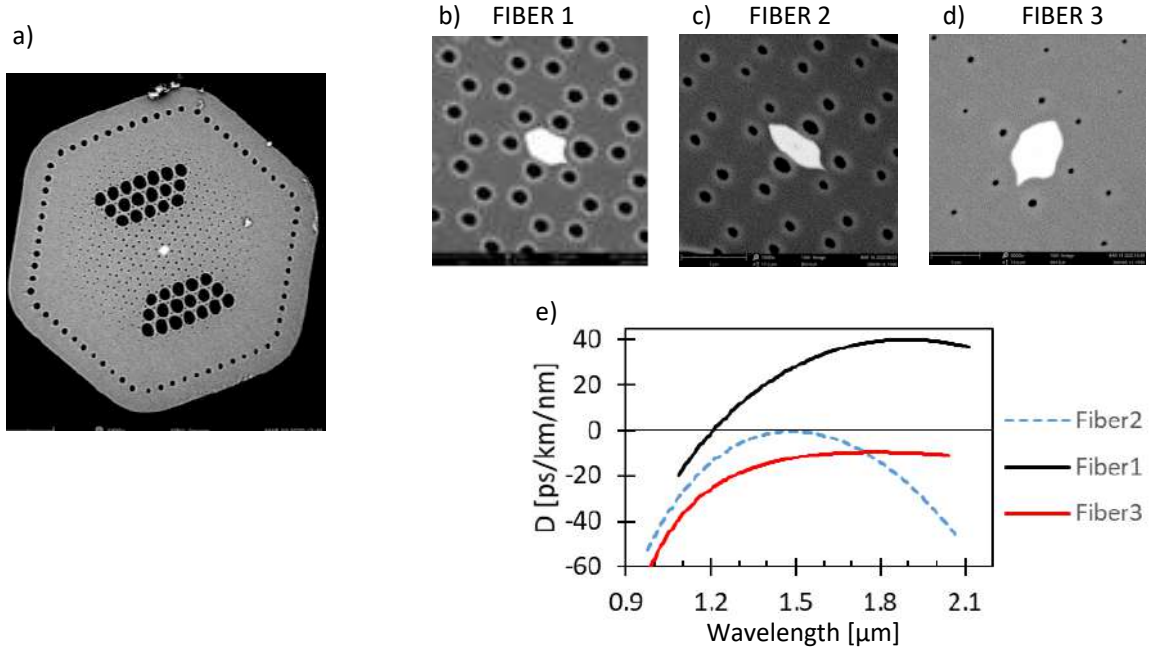

Fig. 1. SEM image of the Fiber 1 end facet (a). SEM images of fiber cross sections in the vicinity of the core: Fiber 1(b), Fiber 2 (c) and Fiber 3 (d). Experimental characteristics of chromatic dispersion vs. wavelength in analyzed fibers (e).

Using broadband interferometric measurements setup we determined phase and group modal birefringence. Modal birefringence reach 3.5×10^{-4}, 1×10^{-3} and 2×10^{-4} at 1550 nm in Fiber 1, Fiber 2 and Fiber 3, respectively. Finally, in fig. 1e we show spectral characteristics of chromatic dispersion measured using interferometric method. Fiber 1 has anomalous dispersion at 1550 nm [1] while in fiber 2 and 3 we obtained normal dispersion [2]. Remarkably, dispersion of Fiber 2 is symmetric around 1500 nm, which makes this fiber a very interesting medium for generation of all-normal dispersion supercontinuum [2, 3]. In contrast, the anomalous dispersion of Fiber 1 allow for generation of solitons and its self-frequency shift up to 2000nm, even in relatively short section of fiber [3].

To conclude, we show a method for controlling the dispersion of microstructured fibers for various nonlinear applications.

Acknowledgements

The authors acknowledge financial support from National Science Center, Poland (2018/30/E/ST7/00862).

References

1. Soboń G., Martynkien T., Tomaszewska D., et al., “All-in-fiber amplification and compression of coherent frequency-shifted solitons tunable in the 1800-2000nm range,” Photonics Res. Vol. **6**, 368–372, 2018.
2. Tarnowski K., Martynkien T., Mergo P., et al. “Polarized all-normal dispersion supercontinuum reaching 2.5 μm generated in a birefringent microstructured silica fiber,” Opt. Express Vol. **25**, 27452-27463, 2017.
3. O. Szewczyk, K. Tarnowski, A.Głuszek, et al. "All-normal dispersion supercontinuum vs frequency-shifted solitons pumped at 1560 nm as seed sources for thulium-doped fiber amplifiers," Opt. Express 29, 18122-18138 (2021).

AES 2024, ROME - ITALY, 25 –28 JUNE 2024

Pedestal-free structured-core thulium-doped fibers for applications in eye-safer fiber lasers

P. Peterka[1*], I. Kašík[1], A. Filipkowski[2], M. Kamrádek[1], D. Pysz[2], M. Franczyk[2], J. Aubrecht[1], M. Grábner[1], B. Švejkarová[1], and P. Honzátko[1]

[1]Institute of Photonics and Electronics of the Czech Academy of Sciences, Chaberská 1014/57, 182 00 Prague, Czechia
[2] Lukasiewicz Research Network, Institute of Microelectronics and Photonics, Al. Lotnikow 32/46, 02-668 Warsaw, Poland
[*]corresponding author: peterka@ufe.cz

Abstract: Review of structured-core fibers for fiber laser is given with emphasis on the proof of concept of pedestal-free thulium-doped fiber. Recent measurements and physical model of temperature dependent thulium cross sections are summarized and effects of such temperature dependence on thulium fiber laser operation are discussed.

Thulium-doped fiber lasers operating in the spectral range at around 2 μm are attractive in particular thanks to the fact that the radiation in this spectral range is absorbed by the vitreous part of the eye and therefore they are eye-safer than the more matured ytterbium fiber lasers emitting around 1 μm [1]. Although efficiency of thulium fiber lasers is approaching that of their ytterbium counterparts, the record output power of thulium fiber lasers is still orders of magnitude below its potential, and technological breakthroughs are being sought to overcome current limitations. New fiber designs, e.g., using a structured active fiber core and other new ways to mitigate thermal and temperature effects may allow for further increases in output power. In this review, we describe our proof-of-concept experiment with a thulium-doped silicon fiber without a pedestal with a large nanostructured core [2], where the initial preforms of the active medium were produced by the modified chemical vapor deposition (MCVD) and nanoparticle doping methods [3]. Pedestal free fiber design is key for easy splicing of the active fibers, mitigation of cladding mode excitation that may significantly reduce overall laser efficiency and threat reliability of the laser due to risk of splice damage [1]. Furthermore, the measurement of temperature-dependent thulium cross sections [4] will be reviewed, as well as the physical model of temperature dependent thulium cross section spectra developed by C. Jauregui and M. Grabner and described in the same paper [4]. Application of these cross-spectra to predict thulium fiber laser operation using recently derived closed-form expressions [5] for the laser threshold and tilt efficiency when pumping at 790 nm by a two-for-one process is shown.

The authors acknowledge financial support from the Czech Science Foundation, contract No. 23-05701S, and the research was co-funded by European Union and the state budget of the Czech Republic under the project LasApp CZ.02.01.01/00/22_008/0004573, and by Narodowe Centrum Nauki (OPUS LAP 020/39/I/ST7/02143).

References

1. Michalska, M., Honzatko, P., Grzes, P., Kamradek, P., Podrazky, O., Kasik, I., and Swiderski, J. “Thulium-doped 1940- and 2034-nm fiber amplifiers: Towards highly efficient, high-power all-fiber laser systems,” IEEE J. Lightwave Technol. (2023), Vol. 42, No. 1, 339-346, 2024
2. Peterka, P., Aubrecht, J., Pysz, D., Franczyk, M., Schreiber, O., Kamrádek, M, Kasik, I. and Buczyński, R., “Development of pedestal-free large mode area fibers with Tm doped silica nanostructured core,” Opt. Express, Vol. 31,

43004–43016, 2023.

3. Kamradek, M., Kasik, I., Aubrecht, J., Mrazek, J., Podrazky, O., Cajzl, J., Varak, P., Kubecek, V, Peterka, P., and Honzatko, P., “Nanoparticle and solution doping for efficient holmium fiber lasers,” IEEE Photonics J., Vol. 11, 7103610, 2019.
4. Švejkarová(Jiříčková), B., Grábner, M., Jauregui, C., Aubrecht, J., Schreiber, O., Peterka, P., “Temperature-dependent cross section spectra for thulium-doped fiber lasers,” Opt. Lett., Vol. 48, 811–814, 2023.
5. Grábner, M., Švejkarová, B., Aubrecht, J., and Peterka, P., “Analytical model of thulium-doped fiber laser pumped by two-for-one process,” IEEE J. Lightwave Technol., in print

AES 2024, ROME - ITALY, 25 –28 JUNE 2024

Linear and nonlinear optics in hollow-core photonic crystal fibres

F. Tani[1,2]

[1] Max Planck Institute for the Science of Light, Staudtstr. 2, 91058 Erlangen, Germany

[2] CNRS, UMR 8523—PhLAM—Physique des Lasers Atomes et Molécules, F-59000, Lille, France

[*]corresponding author: francesco.tani@mpl.mpg.de

Abstract: In the first part, I will present our recent results on the development of soliton-based sources of ultrashort pulses with tunable wavelengths across broad spectral ranges. I will then discuss twisted hollow-core anti-resonant fibres, our latest numerical and experimental findings, and a specific design to enhance the topological properties.

4D optical fibers thermally drawn from shape-memory polymers

C. Strutynski,* F. Désévédavy, G. Gadret, C.-H. Brachais, B. Kibler and F. Smektala.

Laboratoire Interdisciplinaire Carnot de Bourgogne (ICB), UMR CNRS 6303, Université de Bourgogne, 21078 Dijon, France

*corresponding author: clement.strutynski@u-bourgogne.fr

Abstract: In this work, we demonstrate the elaboration of shape-memory optical fibers from the thermal stretching of additively manufactured preforms. Application of light-guiding multicomponent fiber architectures that are able to switch from temporary configurations back to user-defined programmed shapes are described.

In recent years, both the variety and complexity of fiber profiles manufactured by the thermal drawing process have greatly diversified while the intricacy level of the tasks they are assigned has considerably widened [1,2]. Fibers are no longer passive objects, on the contrary, they can now combine a multitude of optical, electrical, and mechanical, functionalities providing them the ability to sense and react to their surroundings [3]. Fiber-based devices can even dynamically adapt to their environment and are able to perform three-dimensional motion by means of various strategies [4–6]. However, although a single fiber can nowadays gather a multitude of different materials (glasses, metals, polymers, semiconductors, etc.), exploiting shape-memory (SM) materials for thermal stretching has never been reported to date. In this work, we take advantage of the highly scalable preform-to-fiber drawing process to produce tens of meters of continuous polymer-based optical fibers with shape-memory abilities. The fabrication methodology is presented and the performance of light-guiding fibers possessing the ability to perform shape recovery cycles from different curvatures are discussed.

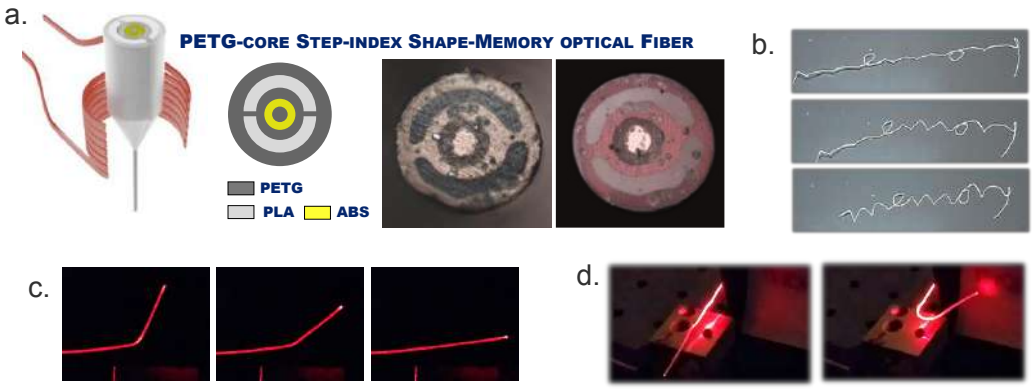

Fig. 1. (a) 2D diagram and pictures of the cross-sectional profile of a shape-memory optical fiber. (b) Shape-memory fiber transitioning from a temporary configuration to its programmed shape spelling "memory" in cursive. (c) Pictures of a light-guiding SM-fiber recovering its original straight shape when heated. (d) Pictures of a shape-memory optical fiber delivering light around an obstacle.

The preforms are additively manufactured from standard commercially-available thermoplastics. In particular, the elongated objects integrate semi-crystalline polylactic acid (PLA) domains which are responsible for the shape-memory effect. PLA is a semi-crystalline polymer, and is therefore not suitable for fiber drawing, because the process requires a material that gradually softens upon heating. Indeed, semi-crystalline polymers, unlike amorphous thermoplastics, generally remain solid until they rapidly transform into a low-viscosity liquid when reaching temperatures above their melting point T_m. To overcome this limitation, semi-crystalline materials have to be associated, in most cases, with amorphous claddings (glasses or polymers) to be successfully integrated into elongated structures. Polyethylene terephthalate glycol (PETG) is used here as the amorphous cladding to control the flow of molten PLA during the thermal elongation process. Description of a fiber fabricated using the proposed

methodology is given in **Fig. 1a**. It is built from a main PETG frame possessing (i) two lateral slots in which PLA parts are inserted and (ii) a central hole filled with an ABS tube (acting as the optical cladding) and a PETG cane (acting as the optical core of fiber).

As first experiments, we evaluate the shape-memory performances of the fabricated fiber, i.e. its ability to retain and recover a particular shape. PLA is responsible here for the shape-memory effect and the fiber can be programmed into a chosen shape using the following procedure: (i) the fiber is molded on a template object that determines the final shape, (ii) the assembly is heated above the melting temperature of PLA (here 1 min at 190 °C) to reprogram the semi-crystalline material and (iii) the fiber is rapidly cooled down to room temperature and subsequently released from the template object. After that, if the fiber sample is deformed, it will be able to recover its programmed shape when heated up. **Fig. 1b** shows pictures (from top to bottom) of a deformed fiber which recovers its programmed shape (spelling "memory" in cursive) when heated on a hot plate at ≈90 °C.

Going further, we now assess the ability of our fiber to transmit light while performing shape-changing operations. The transmission of the shape-memory waveguide in the visible range at 635 nm is then monitored throughout a series of straightening/bending cycles. In practice, straight as drawn samples are selected and bent at room temperature to form a 90° angle. After that, they are heated up using a heating block to recover a rectilinear shape. At the same time, a measurement of the output power is performed when the fibers are in a straight or curved configuration. This operation is repeated up to 20 times. The sample performs well and is able to maintain, in the rectilinear configuration, 90 % of transmission after 18 cycles. After that, the transmitted power decreases drastically due to fatigue-related damage induced to the light-guiding core. In the bent configuration, the fiber preserves a good transmission of 50-70 % also up to the 18th test iteration.

As a final experiment, an SM-PETG fiber is tested to transport a 635-nm laser beam toward a target object placed behind an obstacle (herein a black screen). The shape-memory fiber is heated to recover its programmed shape and is able to deliver the optical signal at a ≈170° angle from its original direction. The experimental operation is depicted in **Fig. 1d**. To minimize the bending losses, a curve with a 2.5-mm-bending radius is programmed to the sample. We confirm that shape-memory fibers can be successfully employed here to circumvent obstacles and illuminate hard-to-reach targets, which opens the way to new light delivery strategies in challenging and exiguous environments.

Other fiber geometries (fibers with an H-shaped PLA inclusion or featuring a larger polystyrene core, shape-memory fibered sleeves that can be combined with commercial fibers, etc.) or programmed shapes (coils, U-shapes, hooks, etc.) were produced and will be the subject of further discussions.

This research was funded by from French program "Investments for the Future" operated by the National Research Agency (ISITE-BFC, 4DMeta project, contract ANR-15-IDEX-03; and EIPHI Graduate School, SMILE project, contract ANR-17-EURE-0002). The authors also acknowledge support from the French ANR (through the TRAFIC project, contract ANR-18-CE08-0016-03), from CNRS Institute of Physics (Emergence 2017, 3D-printed optical fibers), and from European Regional Development Fund. This work benefited from the facilities of the SMARTLIGHT platform funded by the French ANR (EQUIPEX+ contract "ANR-21-ESRE-0040") and the Région Bourgogne Franche-Comté.

References

1. G. Loke, T. Khudiyev, B. Wang, S. Fu, S. Payra, Y. Shaoul, J. Fung, I. Chatziveroglou, P.-W. Chou, I. Chinn, W. Yan, A. Gitelson-Kahn, J. Joannopoulos, and Y. Fink, "Digital electronics in fibres enable fabric-based machine-learning inference," Nat. Commun. **12**(1), 3317 (2021).
2. Y. Shen, Z. Wang, Z. Wang, J. Wang, X. Yang, X. Zheng, H. Chen, K. Li, L. Wei, and T. Zhang, "Thermally drawn multifunctional fibers: Toward the next generation of information technology," InfoMat **4**(7), (2022).
3. A. F. Abouraddy, M. Bayindir, G. Benoit, S. D. Hart, K. Kuriki, N. Orf, O. Shapira, F. Sorin, B. Temelkuran, and Y. Fink, "Towards multimaterial multifunctional fibres that see, hear, sense and communicate," Nat. Mater. **6**(5), 336–347 (2007).
4. Y. He, H. Liang, M. Chen, L. Jiang, Z. Zhang, X. Heng, L. Yang, Y. Hao, J. Gan, and Z. Yang, "Optical Fiber Waveguiding Soft Photoactuators Exhibiting Giant Reversible Shape Change," Adv. Opt. Mater. **9**(21), 2101132 (2021).
5. J. Cheng, L. Zhang, K. Zhao, Y. Wang, X. Cao, S. Zhang, and W. Niu, "Flexible Multifunctional Photonic Crystal Fibers with Shape Memory Capability for Optical Waveguides and Electrical Sensors," Ind. Eng. Chem. Res. **60**(23), 8442–8450 (2021).
6. A. Leber, C. Dong, S. Laperrousaz, H. Banerjee, M. E. M. K. Abdelaziz, N. Bartolomei, B. Schyrr, B. Temelkuran, and F. Sorin, "Highly Integrated Multi-Material Fibers for Soft Robotics," Adv. Sci. 2204016 (2022).

AES 2024, ROME - ITALY, 25 –28 JUNE 2024

X-ray-based techniques for the characterization of specialty optical fibers

M. Ferraro[1,2], M. C. Crocco[1,2], R. Filosa[1,2], R. C. Barberi[1,2], R. G. Agostino[1,2]and V. Formoso[1,2,*]

[1]STAR Research Infrastructure, University of Calabria, Via Tito Flavio, 87036 Rende (CS), Italy
[2]Department of Physics, University of Calabria, Via P. Bucci, 87069 Rende, Italy
[*]corresponding author: vincenzo.formoso@unical.it

Abstract: We report on the characterization of soft glass fibers and polymer optical fibers via X-ray microtomography and small-angle X-ray scattering polymer optical fibers, respectively.

X-ray-based techniques such as computed microtomography (μCT) and small-angle X-ray scattering (SAXS) have been recently proposed as novel techniques for the characterization of optical fibers. Compared to the most conventional characterization methods, such as optical techniques or energy-dispersed X-ray spectroscopy, μCT and SAXS provide several advantages. For instance, being based on the absorption of X-rays, μCT does not require an in-vacuum environment to work, and it is virtually unaffected by fiber coating or bending [1,2]. Whereas SAXS allows for capturing material features at the nanoscale, e.g., it has been shown that SAXS permits to obtain information about the spatial variation of density and chain interaction of poly-methyl methacrylate (PMMA) fibers [3] and their phase transition to a glass state [4].

As far as μCT is concerned, analyses have mostly been performed on silica fibers. In particular, in a recent work, we showed that the X-ray absorption contrast of the dopants of standard multimode silica fibers can be used for retrieving their refractive index profile [2]. Whereas, Sandoghchi et al. reported the μCT analysis of photonic crystal fibers, by exploiting the X-ray absorption contrast between glass and air [1]. Moreover, the potential of μCT has been fully exploited in [5], where the analysis of the tomographic images allowed us to spot the presence of laser-induced damages in a silica fiber.

Recently, we reported on the applicability of μCT techniques to specialty optical fibers. In particular, we focused on soft glass fibers: we applied μCT to fluoride glass step-index fibers and nanostructured graded-index fibers [6]. These soft glass fibers turn out to be particularly suitable for μCT analyses because their materials are made of high atomic number elements, which provide a higher contrast in μCT images in comparison to silica-based fibers. Indeed, the μCT intensity is related to the material density that is affected by the doping concentration, i.e., to the atomic numbers of its atomic elements. It is for this reason that the μCT intensity along the fiber cross-section takes the shape of the refractive index at optical frequencies. Hence, μCT provides an indirect way to trace the profile of the refractive index of the fiber. In this regard, one of the most important results consists of the possibility of determining the convexity factor of parabolic graded-index fibers [2].

Finally, we are currently working on SAXS-based characterization of non-commercial state-of-the-art polymer optical fibers. Some results will be reported in the presentation.

We acknowledge financial support from Ministero dell’Istruzione, dell’Universita e della Ricerca (R18SPB8227).

References

1. Sandoghchi, S. R., et al. "X-ray tomography for structural analysis of microstructured and multimaterial optical fibers and preforms." Optics Express 22.21 (2014): 26181-26192.
2. Ferraro, Mario, et al. "X-ray computed μ-tomography for the characterization of optical fibers." Optical Materials Express 12.11 (2022): 4210-4222.
3. Beckers, Markus, et al. "Novel melt-spun polymer-optical Poly (methyl methacrylate) fibers studied by small-angle X-ray scattering." Polymers 9.2 (2017): 60.
4. Lee, Sang-In, et al. "Small-Angle X-ray Scattering Analysis on the Estimation of Interaction Parameter of Poly (n-butyl acrylate)-b-poly (methyl methacrylate)." Polymers 14.24 (2022): 5567.
5. Ferraro, Mario, et al. "Multiphoton ionization of standard optical fibers." Photonics Research 10.6 (2022): 1394-1400.
6. Crocco, Maria C., et al. "Soft glass optical fiber characterization with X-ray computed microtomography." Optical Materials Express 14.1 (2024): 70-81.

Superconducting and high-frequency neuromorphic devices

AES 2024, ROME - ITALY, 25 –28 JUNE 2024

Bifurcation Phenomena in a Circuit with a Three-Level Quantum Memristor

Finlay J Potter*, Alexandre Zagoskin, Sergey Saveliev, and Alexander G Balanov

Department of Physics, Loughborough University, Loughborough, LE11 3TU, United Kingdom

*corresponding author: f.potter@lboro.ac.uk

Abstract: We study how a model for an anharmonic three-level quantum particle, with dephasing and dissipation, can be considered as part of an artificial neuron circuit. We demonstrate that this undergoes externally controllable bifurcations to generate rich non-stationary behaviour including Andronov-Hopf, Neimark-Sacker, and torus period-doubling bifurcations.

AES 2024, ROME - ITALY, 25 –28 JUNE 2024

Superconducting systems for quantum and neuromorphic AI and reservoir computing

Sergey Saveliev

Department of Physics, School of Science, Loughborough University, UK
S.Saveliev@lboro.ac.uk

Abstract: Natural layered superconductors represent an optimal material for realising high-frequency and quantum neuromorphic systems. Within this discussion, I will delve into alternative approaches for using time-series data in training of potential AI superconducting layered systems. Additionally, I will scrutinize diverse strategies for inputting data into the mesoscopic devices of layered superconductors.

As evidenced by prior studies [1, 2], the set of coupled Josephson equations treated within the quantum regime facilitates quantum tunnelling, thereby enabling the system for versatile application in quantum wave-based reservoir computing.

Moreover, the diverse types of waves capable of propagating within layered superconductors, including surface waves [3, 4] and various nonlinear waves [5, 6], presents a unique opportunity to realise high-frequency reservoirs, whether classical or quantum in nature. The implementation of wave-based reservoir computing can harness the principles of wave information processing, recently applied in interpreting physiological and psychophysical experimental data for the monkey MT cortex [7]. A somewhat analogous methodology involving complex magnetic and acoustic wave interactions has been employed for on-chip reservoir computing [8].

References

1. Savel'ev, S., Rakhmanov, A.L., and Nori F., "Quantum terahertz electrodynamics and macroscopic quantum tunneling in layered superconductors," Physical review letters, Vol. 98, 077002, 2007.
2. Savel'ev, S., Sboychakov, A.O., Rakhmanov, A.L., and Nori, F., "Nonlocal macroscopic quantum tunneling and quantum terahertz electrodynamics in layered superconductors: Theory and simulations," Physical Review B, Vol. 77, 014509, 2008.
3. Savel'ev, S., Yampol'skii, V., and Nori, F., "Surface Josephson plasma waves in layered superconductors," Physical review letters, Vol. 95, 187002 (2005).
4. Yampol'skii, V.A., Gulevich, D.R., Savel'ev, S., and Nori, F., "Surface plasma waves across the layers of intrinsic Josephson junctions," Physical Review B, Vol. 78, 054502, 2008.
5. Savel'ev, S., Yampol'skii, V.A., Rakhmanov, A.L., and Nori, F., "Layered superconductors as nonlinear waveguides for terahertz waves," Physical Review B, Vol. 75, 184503, 2007.
6. Savel'ev, S., Rakhmanov, A.L., Yampol'skii, V.A., and Nori, F., "Analogues of nonlinear optics using terahertz Josephson plasma waves in layered superconductors," Nature Physics Vol. 2, 521, 2006.
7. Gepshtein, S., Pawar, A.S., Kwon, S., Savel'ev, S., Albright, T.D., "Spatially distributed computation in cortical circuits," Science Advances Vol. 8, abl5865, 2022.
8. Yaremkevich, D.D., Scherbakov, A.V., De Clerk, L., Kukhtaruk, S.M., Nadzeyka, A., Campion, R., Rushforth, A.W., Savel'ev, S., Balanov, A.G., Bayer, M., "On-chip phonon-magnon reservoir for neuromorphic computing," Nature Communications 14, 8296 (2023).

AES 2024, ROME - ITALY, 25 –28 JUNE 2024

Study of aspect ratio effect on radiation characteristics of rectangular shape of high-temperature superconductor Bi2212 terahertz wave emitters

T. Kashiwagi[1,2*], R. Kikuchi[1], S. Nakagawa[1], S. Yamada[1], Y. Enomoto[1], Y. Yamauchi[1], Y. Kuzumi[1], K. Maeshima[1], H. Minami[1,2]

[1]Graduate School of Pure & Applied Sciences, University of Tsukuba, 1-1-1 Tennodai, Tsukuba, Ibaraki 305-8573, Japan
[2]Division of Materials Science, Faculty of Pure & Applied Sciences, University of Tsukuba, 1-1-1, Tennodai, Tsukuba, Ibaraki 305-8573, Japan
[*]corresponding author: kashiwagi@ims.tsukuba.ac.jp

Abstract: To gain high performance THz-wave emitting devices made of single crystal of high temperature superconductor $Bi_2Sr_2CaCu_2O_{8+\delta}$, we studied the emission characteristics of rectangular crystal chips of the same area with different aspect ratios of width and length (w/L). The selectivity of the excitation modes will be discussed.

Electromagnetic waves in terahertz frequency range (THz-wave) have a great potential for fundamental and applied research fields in material sciences because vibration modes of molecules, polymers, and proteins exist in the frequencies of THz region. High performance THz-wave emitters, detectors and the related devices have been attracted for the most of applications such as non-destructive inspections, security checking, identification of chemical substances, and cancer detection[1,2].

THz-waves emitters based on the ac Josephson effect have been developed using a single crystal of high-T_c superconductor $Bi_2Sr_2CaCu_2O_{8+\delta}$ (abbreviated as Bi2212)[3]. Single crystals of Bi2212 consist of insulating Bi_2O_2 layers and superconducting CuO_2 layers stacking alternately along the crystallographic c-axis and these stacks are known as intrinsic Josephson junctions (IJJs)[4]. THz-waves can be obtained by processing Bi2212 single crystals into mesa structures and applying dc bias voltages across the IJJs[1]. The main device characteristics to date are summarized in the several review papers[5-8].

According to the previous studies, the device emission characteristics, such as emission power and frequency, are affected by size and shape of the mesa structures. A detailed understanding of the size and shape effects on the emission characteristics is an important subject to realize high-power emitters because it would be related to the impedance matching between the device structure and free space. Currently, we are developing the device characteristics using crystal chips with a sandwich structure[9]. It is well established that the self-heating of the emitter-chip due to application of bias voltages can be reduced by using the sandwich structure. In addition, we have developed fabrication processes of the crystal ships[10]. These recent technical developments have enabled us to study the device characteristics more flexibly. To obtain further understanding of the size effect, we have studied the emission characteristics of rectangular shape of crystal chips with different aspect ratios of width and length (w/L). In addition, to compare emission characteristics more precisely, the chips were made from the same crystal fragment and designed to have the same area and thickness. Here, we will discuss the emission characteristics of these samples.

Bi2212 single crystals were grown using TSFZ-method. The crystals were cut into square pieces of ~ mm^2. Then, they were annealed at 650°C for 20 hours under 0.2% O_2 gas flow to adjust the excess oxygen content of the crystals. To fabricate Bi2212 crystal chips, a wet etching method was used, which was established in our

group[10]. These chips were assembled as a THz-wave emitter using the sandwich structure[9]. To prepare rectangular crystal chips of the same area with different aspect ratios w/L, we designed a photoresist mask containing rectangles with the dimensions of 80×400 μm^2, 120×267 μm^2, and 179×179 μm^2. We selected the areas because the dimensions of 80×400 μm^2 is a typical size in our previous studies[11]. As a result, the prepared samples with three different w/L-ratios show emission of THz-waves, but no systematic characteristics were obtained for emission intensities, while a certain trend was obtained for the emission frequencies. According to the previous studies[1,11], the emission frequency characteristics of a typical rectangular mesa structure with the dimensions of 80×400 μm^2 (w/L = 0.2) can be understood by $TM_{1,0}$-mode which corresponds to a half wavelength of electric field mode along the width of the mesa structure. The observed data here indicates that the samples with w/L-ratio close to 1 trend to generate the higher excitation mode along the width and length of the crystal chip. A similar trend has been reported from several samples[12-14], for which the value of w/L ratio is higher than 0.2. The behavior of mode selectivity of higher excitation modes depending on the w/L ratio suggests that there is some characteristic length scale to determine the excitation modes in the crystal chips. In addition, the flexibility of the mode selection would be helpful to design an emitter which emits a desired frequency. These details will be reported at the meeting.

Acknowledgements:
This study was supported by the Japan Society for the Promotion of Science Grant-in-Aid for Scientific Research(B) No. JP20H02590 and No. JP23H01819.

References

1. S. S. Dhillon, *et al.*, J. Physics D: Applied Physics **50**, 043001 (2017).
2. K. Okada *et al.*, J. Phys. Photon **2**, 044008 (2020).
3. L. Ozyuzer *et al.*, Science **318**, 1291 (2007).
4. R. Kleiner, F. Steinmeyer, G. Kunkel, and P. Müller, Phys. Rev. Lett. **68**, 2394 (1992).
5. U. Welp, K. Kadowaki, and R. Kleiner, Nat. Photon. **7**, 702 (2013).
6. I. Kakeya, and H. Wang, Supercond. Sci. Technol. **29**, 073001 (2016).
7. R. Kleiner and H.B. Wang, J. Appl. Phys. **126**, 171101 (2019).
8. K. Delfanazari *et al.*, Proc. IEEE **108**, 721 (2020).
9. T. Kashiwagi *et al.*, Supercondl Sci. Technol. **30**, 074008 (2017).
10. T. Imai *et al.*, Jpn. J. Appl. Phys. **60**, 126501 (2021).
11. T. Kashiwagi *et al.*, Jpn. J. Appl. Phys. **51**, 010113 (2012).
12. M. Tsujimoto *et al*., Opt. Express **24**, 4591 (2016).
13. H. Sun *et al*., Appl. Sci. **13**, 3469 (2023).
14. K. J. Kihlstrom *et al*., Phys. Rev. Applied **19**, 034055(2023).

AES 2024, ROME - ITALY, 25 –28 JUNE 2024

Josephson transmission lines employing granular aluminum

A. V. Ustinov

Institute of Physics, Karlsruhe Institute of Technology, 76131 Karlsruhe, Germany

ustinov@kit.edu

Abstract: The dynamics of fluxons in long Josephson junctions is a well-known example of soliton physics and allows for studying highly nonlinear relativistic electrodynamics on a microscopic scale. We experimentally demonstrate slowing down relativistic fluxons in Josephson junctions whose bulk superconducting electrodes are replaced by thin films of a high kinetic inductance superconductor. Here, the amount of magnetic flux carried by each supercurrent vortex is significantly smaller than the magnetic flux quantum. Our data show that the Swihart velocity is reduced by about one order of magnitude compared to conventional long Josephson junctions. At the same time, the characteristic impedance is increased by an order of magnitude, which makes these junctions suitable for a variety of applications in superconducting electronics.

Josephson transmission lines (JTLs) with propagating fluxons are employed in superconducting digital circuits, mm-wave oscillators and recently proposed neuromorphic devices. Such fluxons are supercurrent vortices that can be accelerated by bias current up to the Swihart velocity, which is the characteristic velocity of electromagnetic waves in the junction. In experiments with conventional JTLs made of niobium or aluminum, the typical Swihart velocity is about few percent of the light velocity in vacuum, while the junction's characteristic impedance is typically less than a few ohms. This very low characteristic impedance of remained the major obstacle limiting the applications of JTLs in superconducting electronics. In our work, we overcome the above constraints by at least one order of magnitude via replacing the bulk electrodes of a JTL with a high kinetic inductance superconductor formed by a granular aluminum film [1]. We quantitatively evaluate the impact of kinetic inductance on the Swihart velocity, Josephson length, and junction impedance. We demonstrate a reduction of the Swihart velocity by one order of magnitude compared to the conventional JTLs. Correspondingly, we estimate the characteristic impedance of our JTLs to be in the range of tens of ohms, thus opening the way towards matching these JTLs to the standard 50-ohm microwave cables and circuits. This makes Josephson transmission lines formed by high kinetic inductance superconductors very promising for a variety of applications in superconducting electronics.

References

1. M. Wildermuth, L. Powalla, J.N. Voss, J. Schön, A. Schneider, M.V. Fistul, H. Rotzinger, and A.V. Ustinov, Appl. Phys. Lett. 120, 112601 (2022).

AES 2024, ROME - ITALY, 25 –28 JUNE 2024

Frequency modulated terahertz radiation from Josephson plasma emitters of a cuprate superconductor

I. Kakeya[1,*]

[1]Department of Electronic Science and Engineering, Kyoto University, Nishikyo, Kyoto 615-8510, Japan

[*] Corresponding author: kakeya@kuee.kyoto-u.ac.jp

Abstract: Communication using terahertz (~10^{12} Hz) electromagnetic waves is critical for developing 6th-generation wireless network infrastructures. Conflictions between stable radiation and the modulation frequency of terahertz sources impede the superposing of transmitting signals on carrier waves. The Josephson junctions included in a cuprate superconductor radiate terahertz waves[1] with frequencies proportional to the bias voltages[2,3]. Thus, the modulation of the bias voltage leads to the modulation of the Josephson plasma emission (JPE) frequency. This study aims to demonstrate the generation of frequency-modulated (FM) terahertz continuous waves from Josephson junctions. We achieved to demonstrate sinusoidal signal up to 4.5 GHz superimposed on sub-terahertz carrier waves in two JPE devices. One device radiates at 840–890 GHz with the maximum FM bandwidth of 40 GHz[4] and the other radiates at 400-500 GHz with high- and low bias regions. The results verify that the instantaneous JPE frequency follows the gigahertz-modulated bias voltage. The on-chip FM terahertz generation shows a sharp contrast to the mode-lock frequency comb constructed by highly sophisticated optics on a bench. A further increase of the modulation amplitude facilitates up- or down-frequency conversion over more than one octave. The obtained FM bandwidth exhibited an improvement of two orders of magnitude in the demodulation signal-to-noise ratio compared to the amplitude-modulated signal. The demonstrated FM-JPE stimulates further research on terahertz communication technology and metrology using superconducting devices.

References

1. Ozyuzer, L. *et al.* Emission of coherent THz radiation from superconductors. *Science* **318**, 1291 (2007).
2. Tsujimoto, M. *et al.* Broadly Tunable Subterahertz Emission from Internal Branches of the Current-Voltage Characteristics of Superconducting $Bi_2Sr_2CaCu_2O_{8+\delta}$Single Crystals. *Phys Rev Lett* **108**, 107006 (2012).
3. Kakeya, I. & Wang, H. Terahertz-wave emission from Bi2212 intrinsic Josephson junctions: a review on recent progress. *Supercond Sci Technol* **29**, 073001 (2016).
4. Miyamoto, M., Kobayashi, R., Kuwano, G., Tsujimoto, M. & Kakeya, I. Wide-band frequency modulation of a terahertz intrinsic Josephson junction emitter of a cuprate superconductor. *Nat Photonics* **18**, 267 (2024).

AES 2024, ROME - ITALY, 25 –28 JUNE 2024

Artificial Neuron Circuit with a Two-Level Quantum Memristor

Finlay Potter, Alexandre Zagoskin, Sergey Saveliev, and Alexander G Balanov*

Department of Physics, Loughborough University, Loughborough, LE11 3TU, United Kingdom
*corresponding author: a.balanov@lboro.ac.uk

Abstract: Our research explores a simulated neural circuit incorporating a quantum memristive switcher, considering relaxation and dephasing effects. Charge transfer within the quantum component occurs through charge tunnelling, similarly to classical diffusive memristors. We demonstrate how this mechanism induces hysteresis in the quantum device's current-voltage characteristics. Moreover, within artificial neural circuits, the quantum switcher can autonomously produce current oscillations. Our analysis shows that such oscillations occur only under moderate relaxation rates in a quantum environment, absent in purely coherent or highly decoherent scenarios. We determine the conditions initiating self-oscillations and their dependence on circuit parameters.

AES 2024, ROME - ITALY, 25 –28 JUNE 2024

Superconductor plasmonic nanoantenna array metasurfaces

K. Delfanazari

James Watt School of Engineering, University of Glasgow, G12 8UU, Glasgow, UK
*corresponding author: kaveh.delfanazari@glasgow.ac.uk

Abstract: The optical information processing at the nanometer scale may be realised by tailoring and manipulating local optical electric fields in a subwavelength domain. Here, we perform numerical modelling and experimental studies to exploit the optical properties of nanoantenna array metasurfaces patterned and fabricated at the surface of superconductive plasmonic materials.

We report on the numerical and experimental demonstration of novel chip-integrated tunable optical modulators operating at visible to near-infrared telecommunication bands. Our integrated photonic devices are based on plasmonic nano-antenna and nano-circuit metasurface arrays fabricated on the facet of superconductor thin metallic films. We engineer the photoresponse of our nano-antenna based modulator devices and observe optical modulation properties with a modulation depth MD ~ 60% at λ =27162nm,2and2a2maximum2extinction2A(λ)2=212−2R(λ)2~ 95% at λ = 650 nm, at room temperature. Moreover, with a similar photoresponse engineering technique, we observe a maximum extinction A(λ) ~ 88% at λ = 1380 nm in our near-infrared nano-circuit array-based modulators. Our optical modulators are polarization sensitive, and their photoresponse can be controlled by altering the geometrical parameters of their subwavelength elements and unit cells. Our ultracompact modulators, with their tunable and controllable photoresponse, empower new types of optical devices for applications in emerging technologies.

References

1. K Delfanazari, et al, 2022 Photonics & Electromagnetics Research Symposium (PIERS) https://ieeexplore.ieee.org/document/9792866 (2023).
2. K Delfanazari, et al, arXiv:2107.09939.
3. K Delfanazari, et al, arXiv:2106.11961.

New trends in nanophotonics

AES 2024, ROME - ITALY, 25 –28 JUNE 2024

Applications on demand with engineered composites

D. A. Pawlak[1,2], P. Piotrowski[1,2], M. Tomczyk[1], K. Sadecka[1], K. Bandopadhay[1], N. Aghad[1], K. Markus[1], A. Abbas[1], S. Saha[1], A. Materna[1], A. Bellardini[3], C. Sibilia[3]

[1]ENSEMBLE3 Centre of Excellence, Warsaw, Poland
[2]Chemistry Dept., University of Warsaw, Poland
[3]Sapienza Univ. of Rome, Italy
[*]corresponding author: dorota.anna.pawlak@ensemble3.eu

Abstract: New composite materials and their properties will be shown including various potential applications. The studied materials belong to two types of composites: (i) eutectic composites where two or more crystalline phases can be combined to enable particular functionality, (ii) glass composites where various nanoparticles can be embedded in glass matrices.

AES 2024, ROME - ITALY, 25 –28 JUNE 2024

Limits and opportunities for nonlinear nanophotonics

Alejandro Rodriguez*

Princeton University, USA
*arod@princeton.edu

Abstract: The ability to tailor light--matter interactions by structuring materials is crucial to a wide range of disciplines, e.g., spectroscopy and quantum communication. Advances in nanofabrication make it possible to investigate optical devices at the fundamental limits of achievable performance --- limited only by available material response and attainable feature sizes. In this talk, we review recent advances and applications of large-scale optimization techniques to nonlinear processes, including limitations on the ability of structuring to control spontaneous emission, second harmonic generation, and Raman scattering in resonant media.

Recent Advances in Nanophotonics and Metamaterials

AES 2024, ROME - ITALY, 25 –28 JUNE 2024

Noise-resilient exceptional-point sensors enabled by oscillation quenching phenomena

A. Suntharalingam[1], L. Fernandez-Alcazar[2], R. Kononchuk[1] and T. Kottos[1,*]

[1]Wave Transport in Complex Systems Lab, Department of Physics, Wesleyan University, Middletown, CT-06459, USA
[2]Institute for Modeling and Innovative Technology, IMIT (CONICET-UNNE), Corrientes, Argentina
[*]corresponding author: tkottos@wesleyan.edu

Abstract: We develop a self-oscillating nonlinear platform that supports transitions between two distinct neuromorphic functionalities – one having a spatially symmetric steady-state, and the other with an asymmetric steady-state – and displays nonlinear exceptional point degeneracies that can be employed for noise-resilient sensing.

We develop a self-oscillating nonlinear platform based on two coupled nonlinear RLC circuits that supports transitions between two distinct neuromorphic functionalities – one having a spatially symmetric steady-state, and the other with an asymmetric steady-state – as the capacitive coupling between these two RLC tanks varies. At the transition point the system displays nonlinear exceptional point degeneracy (NLEPDs). The latter is employed for noise-resilient sensing. The experimental data confirm the theoretical predictions and show that the system demonstrates two-orders signal-to-noise enhancement of perturbation measurements (associated with the coupling variations) near NLEPDs. Our results resolve a long-standing debate on the efficacy of EPD-sensing in active systems above self-oscillating threshold.

Acknowledgements - Partial funding support from MPS Simons Collaboration via grant No. 733698 and from NSF-CMMI-1925543. A.S. and T.K. also acknowledges partial support from grant NSF ECCS 2148318, which is supported in part by funds from OUSD R&E, NIST, and industry partners as specified in the Resilient & Intelligent NextG Systems (RINGS) program.

References

1. Suntharalingam, A., Fernandez-Alcazar, L., Kononchuk, R. and Kottos, T., “Noise resilient exceptional-point voltmeters enabled by oscillation quenching phenomena,” Nature Communications, Vol. 14, 5515, 2023.

AES 2024, ROME - ITALY, 25 –28 JUNE 2024

Large-area photonic emitters with full spatial control of intensity, phase and polarization compatible with batch fabrication by optical lithography.

V. A. Aksyuk[1*], C. Ropp[1,2], A. Azarov[1,3], D. Maurya[1,2], A Yulaev[1,2], and D. Westly[1]

[1]Physical Measurement Laboratory, National Institute of Standards and Technology, Gaithersburg, Maryland 20899, USA
[2]Department of Chemistry and Biochemistry, University of Maryland, College Park, MD 20742, USA
[2]Thesis Research, La Jolla, CA 92037, USA
[*]corresponding author: vladimir.aksyuk@nist.gov

Abstract: A modulated-waveguide photonic metamaterial grating emits millimeter-scale optical beams with arbitrary spatially-varying polarization, intensity and phase. Experiments at blue and near infrared wavelengths illustrate broad continuous dynamic range of emission intensity in a device with large minimum feature sizes, achieved via the continuous translation symmetry breaking approach.

Photonic integrated circuits (PICs) enable economical batch fabrication of complex photonic systems. Additional functionality can be enabled by accurate coupling of PICs directly to spatially-extended photonic modes in free space, such as wide collimated Gaussian beams [1]. Arbitrary spatial control over emitted intensity, wavefront and polarization state is desired. Symmetry breaking in planar waveguiding metamaterials is a powerful and intuitive way to design such emitters, which has been realized at 1550 nm via breaking of a discrete translation symmetry [2] in metamaterials consisting of arrays of pillars or holes. However, such dense 2D arrays of small features require high fabrication accuracy, making it difficult to scale them for the variety of potential applications operating in the visible range.

We have recently reported [3] a fish-bone grating design emitting well-shaped, millimeter-scale, collimated beams at a 461 nm and 780 nm wavelength directly from a PIC surface. We start with a metamaterial consisting of a dense array of lines with a continuous translation symmetry in the direction of slab mode propagation. We break this translation symmetry by modulating the line walls, allowing optical emission (Fig. 1). Starting with a transverse-electric (TE) slab mode, a mirror-symmetric harmonic wall modulation, i.e. varying the individual waveguide width in a “fish-bone” pattern (Fig. 1a,b), produces a linear, TE, s-polarized emitted wave (Fig. 1c-f and Fig. 2). Modulation strength varies to obtain the desired emission profile such as fully emitting all power into a Gaussian beam (Fig. 1c,d). Crucially, weak modulation necessary for emitting broad, millimeter-scale beams can be implemented in structures while maintaining ≈100 nm lines and spaces even for devices operating in the blue, allowing these devices to be foundry fabricated by 193 nm photolithography (Fig. 1e,f).

Continuous translation symmetry breaking retains not only the intensity and phase, but the full polarization control capability of its discrete counterpart [2], while having much larger minimum features and spaces. 3D finite element numerical analysis shows that modulating the walls in an anti-symmetric, “wiggle” fashion results in TM (p-polarized) free-space emission, while the TE (s-wave) emission remains forbidden by symmetry. By superimposing both modulations with varying relative phase shift, circular, 45-degree linear, and arbitrary elliptical polarizations can be emitted. Notably, by varying the modulation spatially across the device, arbitrary spatial phase, intensity, and polarization profiles can be obtained.

In summary, continuous translational symmetry breaking metamaterials enable large-area planar photonic beam emitters from blue to infrared, and allow generating arbitrary spatial profiles of polarization, intensity, and phase with devices compatible with foundry fabrication by photolithography.

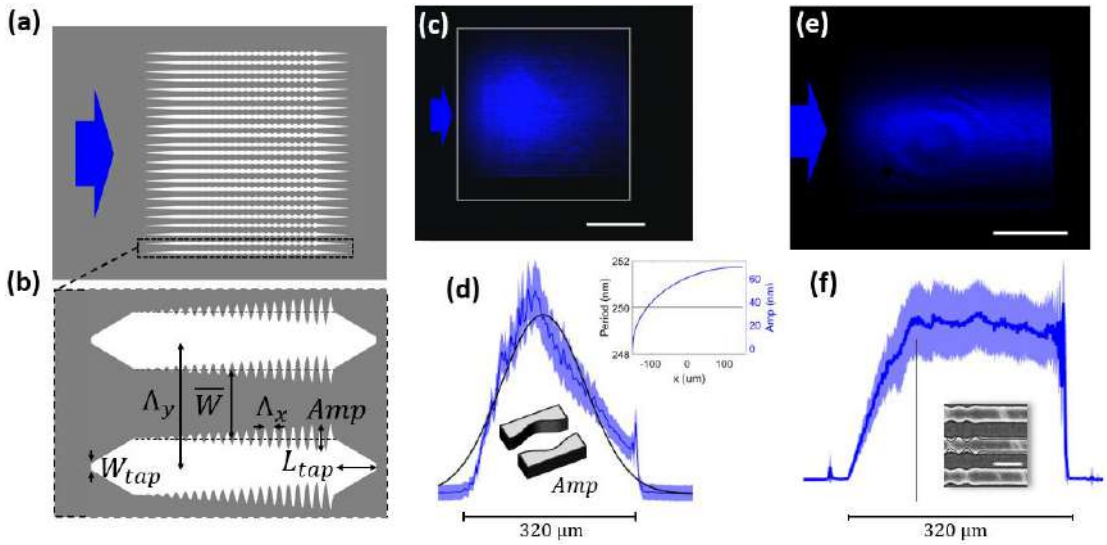

Figure 1. (a) Fish-bone grating design with slab-mode light. (b) Individual metamaterial elements. (c) 461 nm light emitted from a fish-bone grating. (d) Beam profile with Gaussian fit; Insets display unit cell and apodization details. (e,f) Beam profiles for a foundry-fabricated device patterned photolithographically.

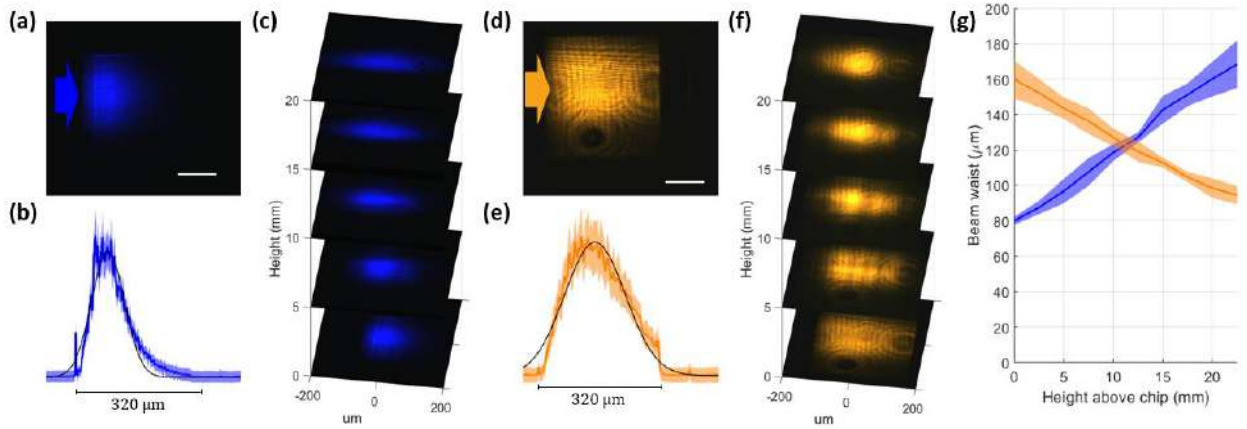

Figure 2. Beam profiles from a fish-bone grating with 90 nm minimum features. (a) Top-down view of 461 nm emission. (b) Measured beam profile with Gaussian fit. (c) Beam cross-sections vs. distance. (d) Top-down view of 780 nm emission. (e) Measured beam profile with Gaussian fit. (f) Beam cross-sections vs. distance. (g) Fitted beam waist in x direction vs. distance for 461 nm (blue, increasing) and 780 nm (orange, decreasing), with measurement uncertainties.

References

1. S. Kim, D. A. Westly, B. J. Roxworthy, Q. Li, A. Yulaev, K. Srinivasan, and V. A. Aksyuk, "Photonic waveguide to free-space Gaussian beam extreme mode converter," Light Sci Appl 7, 72 (2018).
2. Huang, Heqing, Adam C. Overvig, Yuan Xu, Stephanie C. Malek, Cheng-Chia Tsai, Andrea Alù, and Nanfang Yu. "Leaky-wave metasurfaces for integrated photonics." Nature nanotechnology (2023): 1-9.
3. Ropp, Chad, Dhriti Maurya, Alexander Yulaev, Daron Westly, Gregory Simelgor, and Vladimir Aksyuk. "Scalable and Robust Beam Shaping Using Apodized Fish-bone Grating Couplers." Optics Express, in press (2023).

Metamaterials: A Review from the Perspectives of the Effective Properties and Applications

Tatjana Gric[1,2], Vladimir Mityushev[3], Edik U. Rafailov[4]

[1]Department of Electronic Systems, Vilnius Gediminas Technical University, Vilnius, Lithuania
[2]Semiconductor Physics Institute, Center for Physical Sciences and Technology, Vilnius, Lithuania
[3]Cracow University of Technology, Cracow, Poland
[4]Aston Institute of Photonic Technologies, Aston University, Birmingham B4 7ET, UK
*corresponding author, E-mail: tatjana.gric@vilniustech.lt

Abstract

The focus of metamaterials and functional material development strategies is on the structures of the matter itself, which has resulted in the ubiquitous manipulation of light—and, more broadly, electromagnetic waves—to produce unusual and distinctive electromagnetic properties. The exact size, geometry, shape, orientation, and arrangement of the nanostructures in metamaterials are all known. These arrangements are influencing electromagnetic light waves to produce new characteristics that are hard or impossible to produce using natural materials. In order to provide a strong foundation for future research on this fascinating and quickly developing subject, this review goes into great detail about these metamaterials from the viewpoints of the effective medium theory.

1. Introduction

The Greek term "meta" means "beyond" and is where the word originated. "Metamaterials" are materials that have unique qualities not seen in naturally existing materials. These are the materials that derive their characteristics from their composition rather than the material that makes them up. V. G. Veselago made the first and most significant contribution to this field in 1968 when he stated that materials possessing both negative permittivity and negative permeability are theoretically feasible [1]. John Pendry discovered a workable method in 1999 for creating left-handed metamaterials (LHM) that defied the accepted right-hand rule [2]. He suggested creating a Thin-Wire (TW) structure with periodic arrangements to illustrate the negative effective permittivity value [3]. It was demonstrated that the structure's plasma frequency is lower than the microwave regime wave. This structure can provide an effective negative permittivity at microwave frequencies because of its low plasma frequency. Additionally, it was shown that an array of split-ring resonators might be used to create negative magnetic permeability. Then, in 2000, Smith conducted microwave tests to evaluate the unusual features of a novel LHM that exhibits simultaneously negative permittivity and permeability [4]. For the first time, Shelby et al. used copper strips and repeated unit cells of split ring resonators (SRR) in a metamaterial to demonstrate negative refraction experimentally [5-6]. Wu et al. suggested three architectures for SRRs: the symmetrical ring, the omega structure, and the S structure [7]. To fully realize the promise of metamaterials in a variety of domains, numerous researchers have worked on them. This paper examines metamaterials from the standpoint of their functional characteristics.

2. Effective medium approximation

2.1. Nanostructured metamaterial

In this instance, we'll be looking at a heterostructure that is made up of stacked sheets that are divided by dielectric layers, as seen schematically in Figure 1.

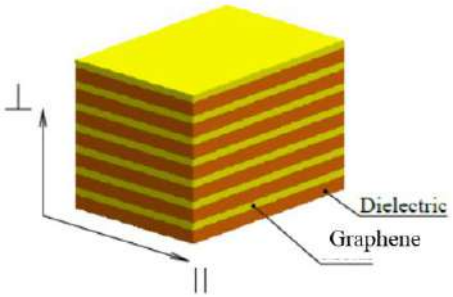

Figure 1: Anisotropic multilayer composite schematic. The plane parallel to the metamaterial interface is defined as the parallel direction, and the perpendicular direction as being parallel to the normal vector from the metamaterial surface.

We use the effective-medium approach [8] to characterize the optical response of such a system, which is appropriate if the wavelength of the radiation under consideration is significantly bigger than the thickness of any layer. Its foundation is the structure parameters' average. Therefore, we continue to discuss the effective homogeneous media for the semi-infinite periodic structure in this study. The following are the effective permittivities [9]:

$$\varepsilon_{\parallel} = \frac{\varepsilon_m d_m + \varepsilon_d d_d}{d_m + d_d} \quad (1)$$

$$\varepsilon_{\perp} = \frac{\varepsilon_m \varepsilon_d (d_m + d_d)}{\varepsilon_m d_d + \varepsilon_d d_m}, \quad (2)$$

2.2. Nanowire metamaterial

Fig. 2 displays the suggested geometry for the nanowire composites. A host material with a permittivity of ε_d is embedded with nanowires having ε_m of permittivity.

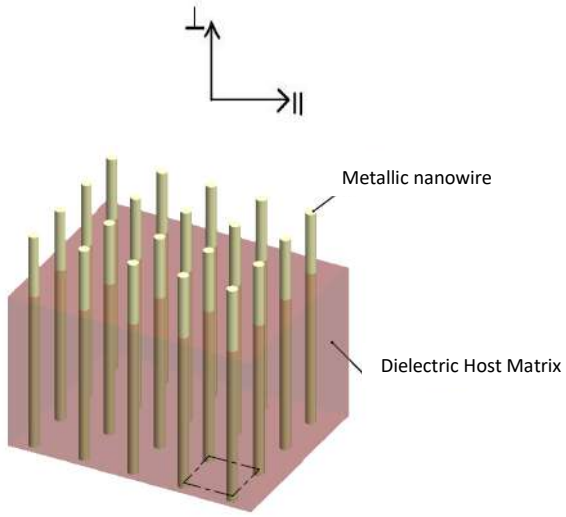

Figure 2: The uniaxial birefringent medium (a); medium unit cell (b)

We calculate the effective permittivities of the nanowire medium using the following formula based on an effective medium approximation:

$$\varepsilon_{\perp} = \varepsilon_d \left[\frac{\varepsilon_m(1+\rho)+\varepsilon_d(1-\rho)}{\varepsilon_m(1-\rho)+\varepsilon_d(1+\rho)}\right] \quad (3)$$

$$\varepsilon_{\parallel} = \varepsilon_m\rho + \varepsilon_d(1-\rho) \quad (4)$$

Here, ρ is the filling fraction ratio which is defined as:

$$\rho = \frac{nanowirearea}{unitcellarea} \quad (5)$$

2.3. Spiral nanowire metamaterial

Here, we concentrate on a two-dimensional wire whose surface is adorned with N spiral-shaped grooves that are filled with a refractive index-n_g dielectric substance [10]. As illustrated in Fig. 3, the resulting inner and outer radii are r and R, respectively, and represent the bottom and opening of the grooves. The grooves around the wire perimeter have widths of a and periods of d. As can be seen in Fig. 3, the spiral is constructed so that the intersection angle along the spiral length between the radial direction and the tangent to each spiral arm is the same. With a spiral angle of θ, these spirals are referred to as logarithmic spirals and can be parametrized as

$$x(t) = re^{t/\cos\theta}\cos t \quad (6)$$

$$y(t) = re^{t/\cos\theta}\sin t \quad (7)$$

In the limit $a < d \ll \lambda$, a metamaterial approximation, in which the textured PEC is treated a homogeneous effective medium, can be applied. The effective permittivity and permeability in the area between the inner and outer radii in this homogeneous metamaterial image take on a diagonal, spatially independent tensor form. The component of the permittivity normal to the spiral arms (z-direction) is given by $\varepsilon_n = n_g^2 d/a$, while the parallel components diverge. Inside the spiral grooves, the permeability components are adjusted such that the electromagnetic radiation travels at the speed of light. The following effective permittivity and permeability tensors for TM waves expressed in cylindrical coordinates are obtained by this procedure:

$$\bar{\bar{\varepsilon}}^{-1} = \frac{a}{2n_g^2 d}\begin{bmatrix} 1-\cos 2\theta & -\sin 2\theta \\ -\sin 2\theta & 1+\cos 2\theta \end{bmatrix} \quad (8)$$

$$\mu_z^{-1} = \frac{d}{a} \quad (9)$$

where the permittivity tensor is restricted to the xy-plane.

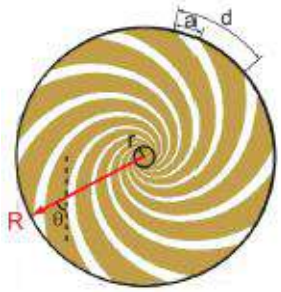

Figure 3: Localized spoof surface plasmons in a 2D subwavelength PEC wire corrugated with spiral grooves. Cross-section of the corrugated PEC wire with the inner and outer radii r and R, periodicity d, groove width a, and the spiral angle θ.

By substituting effective permittivity in different direction from Eq. (8) in Eqs. (3), (4) and by assuming a perfect rectangular structure we arrive at the effective permittivities of the spiral nanowire metamaterial as follows:

$$\varepsilon_{\perp}^{SM} = -\varepsilon_d^M \frac{\varepsilon_d^M\left(\rho^M-1\right)+\frac{ad\varepsilon_m^M\sin(2\theta)(\rho+1)}{2}}{\varepsilon_d^M\left(\rho^M+1\right)+\frac{ad\varepsilon_m^M\sin(2\theta)(\rho-1)}{2}} \quad (10)$$

$$\varepsilon_{\|}^{SM} = -\varepsilon_d^M \left(\rho^M - 1\right) - \frac{ad\varepsilon_m^M \rho^M \left(\cos(2\theta)+1\right)}{2} \quad (11)$$

2.4. Disordered tissue like metamaterials

The cell shape and intracellular structure shape must be assessed using the effective medium approximation in order to ascertain the biological tissue's effective permittivity. The Debye model, which explains various compositions well, is a standard theory to describe optical properties of each type of cell. Furthermore, it is a commonly used method for researching the dielectric characteristics of biological tissues in the frequency domain and is based on the empirical formula [11]. The effective permittivity of a mixture system is typically investigated using a model of binary mixes due to its importance in comprehending intermolecular interactions. Permittivity models based on binary mixtures are widely recognized. As an example, the Bottcher-Bordewijk model [12], Maxwell-Garnett formula [13], Bruggeman formula [14], and Hanai formula [15] do not take the frequency domain and inclusion location into account. This model, for instance [16]

$$\frac{3\varepsilon_1}{2\varepsilon+\varepsilon_1} f_1 + \frac{3\varepsilon_2}{2\varepsilon+\varepsilon_2} f_2 = 1 \quad (12)$$

can2be2used2together2with2Skipetrov's2formula2[17] as a preliminary formula for the effective permittivity $\varepsilon = \varepsilon_{\text{eff}}$. It should be mentioned that this formula is used to perform the approximate calculations of the effective properties of biological tissues. Here ε_1 denotes the permittivity of the neuron cells, ε_2 of the cancerous cells, f_1 and f_2 are the volume fractions of each cell type accordingly. Cell structure is of a random nature with some predictable average properties. We will use the exact and approximate analytical formulas for ε_{eff} by means of the structural sums [18, 19] which are calculated by the sets a and ε. Here, a = $\{a_k: k = 1,2,...,N\}$ denotes the centers of inclusions, N a number of inclusions in Representative Volume Elements (RVE), and $\varepsilon = \{\varepsilon_m: m = 1,2,...,M\}$ the permittivity of m-th component, $f = \{f_m: m = 1,2,...,M\}$ their concentrations. We will extend the theory [20-22] to complex value permittivity in order to derive analytical formula $\varepsilon_{\text{eff}} = \varepsilon(a, \varepsilon, f)$ for multiple-component medium. In general case ε_{eff} stands for the complex value tensor. We have already demonstrated theoretical analysis on several typical models of effective permittivity in metamaterials and explore the acceptability of the models in mouse and human biotissues. The effective permittivity will be calculated using the Skipetrov formula and the dependences of the effective permittivity will be calculated by frequency for different cases.

3. Application of the tissue like metamaterials approach to investigate mouse brain biopsies

The studies aimed at determining the tissue's health made use of the mouse brain tissue samples shown in Fig. 4 [23]. It is important to note that 100 samples were taken into consideration. We only showcase four of them here. Standard eosin and haematoxylin dyes were used to stain histological sections [24].

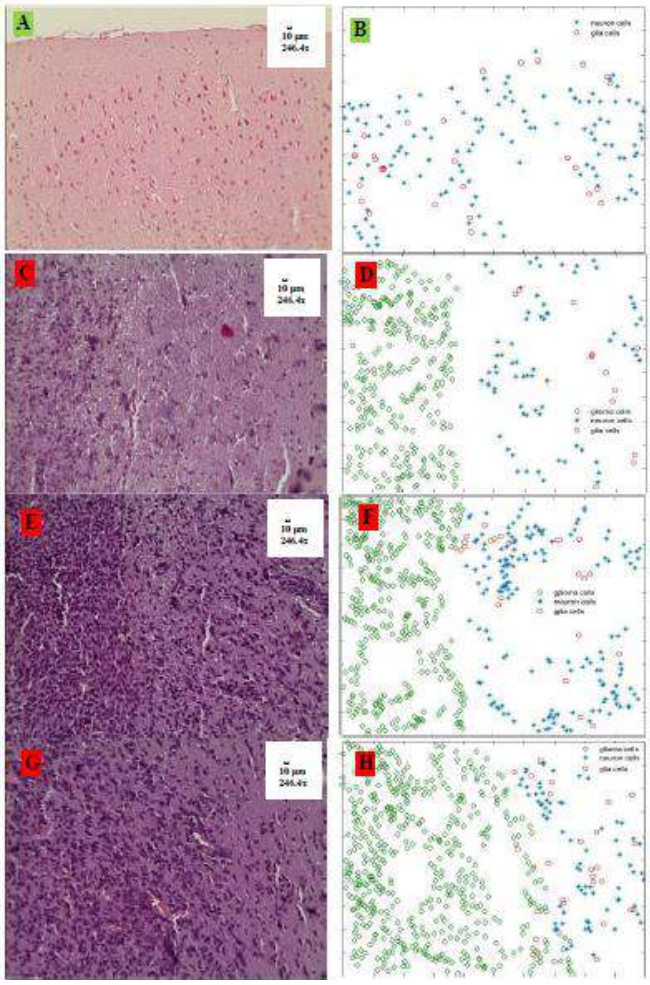

Figure 4: Pictures of brain biopsies from mice that were malignant and non-cancerous (A, B – 39M, C, D – 138M, E, F – 153M, G, H – 154M). Neuron cells are indicated with asterisks, glia cells with circles, and lymphoma cells with hexagons. The tissue samples are displayed in Figures A, C, E, and G. The digital pictures in Figures B, D, F, and H were created using the "Digitizeit" software (www.digitizeit.de/).

Analyzing biological tissue from the standpoint of the effective medium approximation is necessary to determine its health [25]. If the geometry of the medium under consideration is well-defined, the aforementioned formalism can be applied. Furthermore, the Debye and Cole-Cole models should be used to characterize the optical characteristics of each type of cell [26]. By doing this, the complex dielectric spectrum in $\varepsilon(\omega)$ space is obtained for all cell types.

By doing this, the effective permittivity's frequency dependences for various scenarios (variations in the volume fraction f, permittivities of the constituent parts (cells)) have been found. The important finding is that if the total number of glioma cells in the sample is larger than 5%, the effective permittivity might behave in an extraordinary manner as indicated by the peak of the effective permittivity curve in a specific scenario at the frequency range (0-10 THz) (Fig. 5).

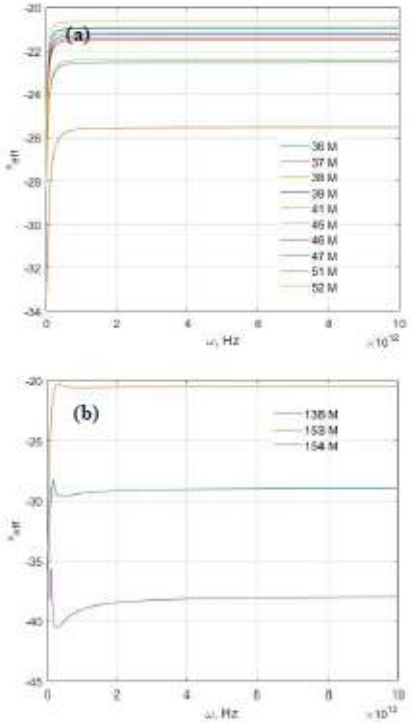

Figure 5: Effective permittivities' frequency-dependent dependencies for both healthy (a) and unhealthy (b) samples.

Effective permittivity values are negative, as Fig. 5(a) illustrates. The tissue sample under examination, which has a high degree of similarity to the metamaterial, is not exhibiting any unusual behavior. The description of the healthy tissue sample is represented by the first characteristic. It is important to note that the metamaterial (Fig. 5(b), 153 M) representing biological tissue exhibits unusual behavior since the sample's glioma cell count exceeds a predetermined threshold of 5%. Because of the remarkable behavior of the effective permittivity curves—that is, the presence of a specific peak at a frequency of approximately 0.1 THz—we may deduce that the tissue is unhealthy. As a result, when the number of unhealthy specimens in the sample exceeds a predetermined threshold, unusual behavior occurs. The sample with 154 M has a strong amplitude peak. The extremely malignant tissue zones are seen in the former feature. In conclusion, the information shown in Fig. 5(b) can be used to determine the cancer stage. The late-stage malignancy is indicated by a larger amplitude of ε_{eff}. The term "stage" in this context describes the degree of cancer and is dependent on various criteria, including the size and spread of the tumor. Knowing the cancer's stage allows for the suggestion of a course of treatment and the determination of the prognosis.

Continuing with the foregoing description of the remarkable regime shift, brain tissue biopsies can now be used to assess pathological, healthy, and intermediate "blocks" (Fig. 6). The 138M, 153M, and 154M sample pictures were rendered as blocks of various colors using this nomenclature (Fig. 6 B, D, F, H). It is important to note that metamaterial exhibits remarkable behavior in the intermediate situation, with significantly affected zones showing dramatically negative effective permittivity εeff,2 which is characterized by leaps at 0.1 THz frequency.

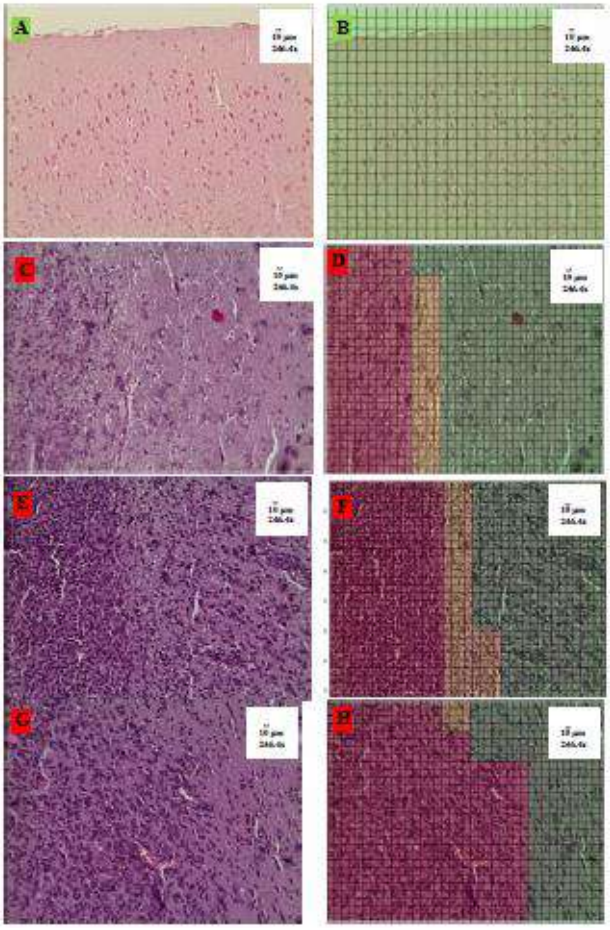

Figure 6: Pictures of brain tissue biopsies from mice, both cancerous and non-cancerous (A, B – 39M, C, D – 138M, E, F – 153M, G, H – 154M). It is shown how the tissue samples are divided into the constituent parts of the various situations. Figures A, C, E, and G show the tissue pictures; Figures B, D, F, and H show the analyzed images.

4. Conclusions

We have seen rapid growth in the field of optical metamaterials, and it will continuously advance. Although the underlying mechanism has been demonstrated in several studies highlighted in this review, further fundamental studies are needed to deal with the highly disordered metamaterial structures. In particular, it is of particular importance to take into account shape of the inclusions and their distribution. Last, but not least, since many biological tissues could be interpreted as the highly disordered anisotropic metamaterial medium, we believe that bio-inspired and bio-compatible chiral devices wilh performance that is superior to existing technologies are greatly needed. This in turn will significantly advance developments in biochemistry, biophotonics and other interdisciplinary areas.

References

[1] V. G. Veselago, The electrodynamics of substances with2simultaneously2negative2values2of2ε,2and2μ,2*Sov. Phys. Usp.* 47: 509–514, 1968.

[2] J. P. Pendry, A. J. Holden, D. J. Robbins, W. J. Stewart, Magnetism from Conductors, and Enhanced Non-linear Phenomena, *IEEE. Trans. Microwave Theory Technol.* 47: 2075, 1999.

[3] J. B. Pendry, A. J. Holden, D. J. Robbins and W.J. Stewart, Low Frequency Plasmons for Thin-Wire Structure, *J. Phys. Condens. Matter.* 10: 4785 – 4809, 1998.

[4] D. R. Smith, W. J. Padila, D. C. Vier, S. C. Nemat-Nasser, S. Schultz, Composite Medium with Simultaneously Negative Permeability and Permittivity, *Phys. Rev. Lett.* 84, 4184, 2000.

[5] J. B. Pendry, Negative refraction, *Contemporary Physics* 45: 191-202, 2004.

[6] D. R. Smith, J. B. Pendry, M. C. K. Wiltshire, Metamaterials and Negative Refractive Index**,** *Science* 305: 788-92, 2004.

[7] B. I. Wu, W. Wang, J. Pacheco, X. Chen, T. Grzegorczyk, and J. A. Kong, A study of using Metamaterial as antenna substrates to enhance gain, *Progress in Electromagnetic Research* 51: 295-328, 2005.

[8] X.2 Zhang,2 Y.2 Wu,2 „Effective2 medium2 theory2 for2 anisotropic2metamaterials,“ *Sci Rep.* 5: 7892, 2015.

[9] V. M. Agranovich and V. E. Kravtsov, Notes on crystal optics of superlattices, *Solid State Commun.* 55(1): 85–90, 1985.

[10] T. Ioannidis, T. Gric & E. Rafailov Tunable polaritons of spiral nanowire metamaterials, *Waves in Random and Complex Media*, 32(1): 381-389, 2022.

[11] P. Zakharov, F. Dewarrat, A. Caduff, and M. S. Talary, The effect of blood content on the optical and dielectric skin properties, *Physiological Measurement* 32(1): 131–149, 2011.

[12] T. H. Tjia, P. Bordewijk, and C. J. F. B¨ottcher, On the notion of dielectric friction in the theory of dielectric relaxation, *Advances in Molecular Relaxation Processes* 6(1): 19–28, 1974.

[13] J. C. Maxwell-Garnett, Colours in Metal Glasses and in Metallic Films, *Philosophical Transactions of the Royal Society A Mathematical Physical & Engineering Sciences* 203: 385–420, 1904.

[14] M. Bruggerman, W. Kalkner, A. Campus, and A. Smedberg, Electrochemical effects at the conductor/dielectric interface-a description of the mechanism, *IEEE International Conference on Solid Dielectrics* 1: 383–386, 2004.

[15] T. Hanai, A2remark2on2the2“Theory2of2the2dielectric2 dispersion2due2to2the2interfacial2polarization”,2*Colloid Polymer Science* 175(1): 61-62, 1961.

[16] M. Bruggerman, W. Kalkner, A. Campus, and A. Smedberg, Electrochemical effects at the conductor/dielectric interface-a description of the mechanism, *IEEE International Conference on Solid Dielectrics* 1: 383–386, 2004..

[17] S. E. Skipetrov, Effective dielectric function of a random medium, *Physical Review B-Condensed Matter and Materials Physics* 60(18): 12705–12709, 1999.

[18] S. Gluzman, V. Mityushev, W. Nawalaniec, Computational Analysis of Structured Media, Academic Press, Elsevier, Amsterdam, 2018.

[19] R. McPhedran, S. Gluzman, V. Mityushev, N. Rylko (eds.), 2D and Quasi-2D Composite and Nanocomposite Materials, Properties and Photonic Applications, Elsevier, Amsterdam etc. 2020

[20] S. Gluzman, V. Mityushev, W. Nawalaniec, Computational Analysis of Structured Media, Academic Press, Elsevier, Amsterdam, 2018..

[21] P. Drygas, S. Gluzman, V. Mityushev, W. Nawalaniec, Applied Analysis of Composite Media. Analytical and Computational Results for Materials Scientists and Engineers, Elsevier, 2020

[22] R. McPhedran, S. Gluzman, V. Mityushev, N. Rylko (eds.), 2D and Quasi-2D Composite and Nanocomposite Materials, Properties and Photonic Applications, Elsevier, Amsterdam etc. 2020.

[23] T. Gric, S. G. Sokolovski, N. Navolokin, O. Semyachkina-Glushkovskaya, and E. U. Rafailov, Metamaterial formalism approach for advancing the recognition of glioma areas in brain tissue biopsies, *Opt. Mater. Express* 10: 1607-1615, 2020.

[24] N. A. Navolokin, D. A. Mudrak, A. B. Bucharskaya, O. V. Matveeva, S. A. Tychina, N. V. Polukonova, G. N. Maslyakova, Effect of flavonoid-containing extracts on the growth of transplanted sarcoma 45, peripheral blood and bone marrow condition after oral and intramuscular administration in rats, *Russian Open Medical Journal* 6(3): 304, 2017.

[25] O. Kidwai, S. V. Zhukovsky, and J. E. Sipe, Effective-medium approach to planar multilayer hyperbolic metamaterials: Strengths and limitations, *Phys. Rev. A* 85: 053842, 2012.

[26] P. Zakharov, F. Dewarrat, A. Caduff, and M. S. Talary, The effect of blood content on the optical and dielectric skin properties, *Physiological Measurement* 32(1): 131–149, 2011.

AES 2024, ROME - ITALY, 25 –28 JUNE 2024

Soliton formation in an exciton-polariton condensate at a bound state in the continuum

I. Septembre[1], I. Fudjo[1], V. Develay[2], T. Guillet[2], S. Bouchoule[3], J. Zuniga-Perez[4,5], G. Malpuech[1], and D. Solnyshkov[1,6*]

[1]Université Clermont Auvergne, Clermont Auvergne INP, CNRS, Institut Pascal, Clermont-Ferrand, France
[2]Laboratoire Charles Coulomb, Université de Montpellier, CNRS, Montpellier, France
[3]Centre de Nanosciences et de Nanotechnologies, CNRS, Université Paris-Saclay, France
[4]UCA, CRHEA-CNRS, Rue Bernard Gregory, Valbonne, France
[5]MajuLab, International Research Laboratory IRL 3654, Singapore, Singapore
[6]Institut Universitaire de France (IUF), Paris, France
[*]corresponding author: dmitry.solnyshkov@uca.fr

Abstract: Here, we design a GaN/TiO_2 structure hosting a polaritonic BIC with a low condensation threshold. We analyze in detail how the repulsive interaction between exciton-polaritons affects the condensate lifetime. We study the dynamics of the condensation process in a BIC state and optimize the conditions.

Bound states in the continuum (BIC) present in photonic crystal slabs are photonic modes which are not coupled to the far field in spite of being inside the light cone [1]. Recently, BICs have been implemented in systems with strong coupling of excitons and photons. Polaritonic BICs have allowed the observation of polariton condensation with a reduced threshold [2]. However, the role played by the polariton-polariton interactions, which are one of the most interesting features of these quasiparticles, has not been analyzed for the BICs so far.

In this work, we first propose a design of a realistic BIC-based polariton laser in a GaN/TiO_2 polaritonic crystal slab, solving the Maxwell's equations with a finite-element method. We then focus on polariton-specific features, in particular, on the role played by interactions. In the conservative limit, we determine the shape of the polariton condensate due to the interactions, with and without a reservoir potential. This allows finding the average particle lifetime due to the distribution of the condensate in the reciprocal space. We then use the computed lifetimes to simulate the polariton condensation using Boltzmann equations. We find that the advantage of having a BIC is strongly reduced, if not cancelled, when the interaction with an excitonic reservoir reduces too strongly the condensate extension in real space, explaining recent experimental results [3]. We find that the formation of a soliton provides an intrinsic limitation to the lifetime enhancement by the BIC. At large pumping density, the formation of a soliton leads to the saturation of the condensate density growth rate versus pumping, which scales as $P^{1/3}$ instead of being linear. Finally, we model the polariton condensation process, solving numerically the generalized Gross-Pitaevskii equation, which allows us to take into account self-consistently the lifetime profile and the inter-particle interactions.

This research was supported by the ANR Labex GaNext (ANR-11-LABX-0014), the ANR program "Investissements d'Avenir" through the IDEX-ISITE initiative 16-IDEX-0001 (CAP 20-25), the ANR project "NEWAVE" (ANR-21-CE24-0019) and the European Union's Horizon 2020 program, through a FET Open research and innovation action under the grant agreement No. 964770 (TopoLight).

References

1. Hsu, C. W., Zhen, B., Stone, A. D., Joannopoulos, J. D. and Soljacic, M., "Bound states in the continuum," Nat. Rev. Mat., Vol. 1, 1-13, 2016.
2. Ardizzone, V. et al, "Polariton Bose-Einstein condensate from a bound state in the continuum," Nature, Vol. 605, 447-452, 2022.
3. Riminucci, F. et al, "Nanostructured GaAs/(Al,Ga)As Waveguide for Low-Density Polariton Condensation from a Bound State in the Continuum," Phys. Rev. Applied, Vol. 18, 024039, 2022.

Imaging chirality of optical fields near nano-/micro-structured materials

H. Okamoto[1*], J. Yamanishi[1*]

[1]Institute for Molecular Science, National Institutes of Natural Sciences, Japan
[*]corresponding author: aho@ims.ac.jp, yamanishi@ims.ac.jp

Abstract: We demonstrate here micro- and nano-scopic imaging of chiral optical fields with high-accuracy far-field CD microscopy, near-field polarimetry microscopy, and chiro-photoinduced force microscopy, mainly on plasmonic materials.

Chirality is a broad concept that characterizes structures in wide hierarchy of materials and systems. It is of fundamental importance to investigate geometrical structures of chirooptical responses in nanomaterials, to design chiral features and functions of the nanomaterials. We developed novel optical activity imaging methods with a few of optical measurement methods, which allow us to visualize local structures of optical activity in nanomaterials. The methods were applied to observe and control chiral plasmonic fields for two-dimensional gold nanostructures.

In the diffraction-limited far-field circular dichroism (CD) imaging, we developed a novel circular polarization modulation method that allows achieving high-accuracy CD detection even in observation of non-uniform anisotropic samples. This method has been utilized for CD imaging of plasmonic materials, chiral microcrystals, etc. As an example, Figure 1(a) shows a far-field CD microscopic image of a chiral 4-fold symmetry 2-dimensional pinwheel-shaped gold nanostructure array.[1] The CD signal is inverted when the handedness of the nanostructure is inverted. The CD signal was found to be not uniform and oscillate spatially in the single unit cell.

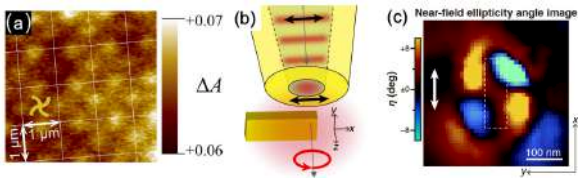

Figure 1. (a) Far-field CD image (@ 700 nm) of a pinwheel-shaped gold nanostructure array.[1] (b) Schematic of near-field polarimetry for measuring the polarization of optical fields. (c) Near-field ellipticity image (@ 800 nm) of a gold nanorod.[2]

For chiro-optical imaging beyond the diffraction limit, we developed a near-field polarimetry microscope using aperture-type optical fiber probe and a chiro-photoinduced force microscope. In the former one, the sample is illuminated with a linearly polarized optical near-field through the probe (Figure 1(b)), and the forward scattered field in the far-field is analyzed for its ellipticity (η, corresponding to CD) and polarization rotation (θ). Figure 1(c) shows a near-field ellipticity image of a gold nanorectangle.[2] In this image, the ellipticity of the scattered optical field from the sample upon near-field linearly polarized excitation parallel to the long axis of the rectangle was mapped as a function of the position of the excitation. The results suggest that strongly twisted plasmonic local fields are generated in the vicinities of metal nanostructures.

In the chiro-photoinduced force microscope, the local chiro-optical effect is detected through optical force measurements with an atomic force microscope. Atomic force microscopy is based on detection of forces between the probe tip and the matter to be observed. This principle can be applicable to optical forces due to interaction between dipoles on the probe and on the sample, induced by irradiation of light. By detecting difference between the force under left- and right-handed circularly polarized illumination with the photoinduced force microscopy, we can expect to visualize the chiral optical fields on the sample under irradiation of light. We developed an

experimental system for nanoscopic observation of chiro-optical force and imaging of chiral optical fields on the samples, based on photo-induced force microscope. We adopted gold coated AFM tip as the probe to detect interaction with the sample induced by irradiation of the system by circularly polarized light. Heterodyne frequency modulation technique was utilized to eliminate the photothermal effects of the tip apex and cantilever by the light. The photoinduced force images under illumination of left- and right-circularly polarized light were recorded, and the chiro-optical image was obtained as the difference between the two. As the test sample, we fabricated left- and right-handed gold gammadion structure arrays by electron-beam lithography method. The result of chiro-optical image of the sample is demonstrated in Figure 2. We succeeded in visualizing nanoscale chiral optical fields in the vicinity of the nanostructures. It is seen that the local chiro-optical effect is prominent at the corners of each gammadion.[3]

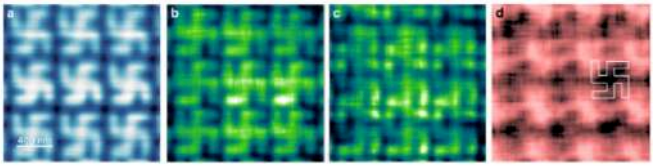

Figure 2. (From left to right) AFM image, photoinduced force images under right- and left-circularly polarized light at 785 nm, and the differential image between the two photoinduced force images, for right-handed gold gammadion array structure. The unit cell size is 540 nm.[3]

The technique provides a new method to investigate chiral optical near-fields and paves the way for revealing the physical phenomena of nanoscale chiro-optical effects and technological development based on that.

The authors thank Drs. H.-Y. Ahn, S. Hashiyada, and T. Narushima for their contributions. This work was supported by Grants-in-Aid for Scientific Research (KAKENHI Nos. JP22225002, JP15H02161, JP15K13683, JP15J01261, JP16H06505, JP17H07330, JP21H04641, JP21K18884, and JP22H05135).

References

1. T. Narushima, H. Okamoto, “Circular Dichroism Microscopy Free from Commingling Linear Dichroism via Discretely Modulated Circular Polarization,” Sci. Rep. Vol. 6, 35731, 2016.
2. S. Hashiyada, T. Narushima, H. Okamoto, “Imaging Chirality of Optical Fields near Achiral Metal Nanostructures Excited with Linearly Polarized Light,” ACS Photon. Vol. 5, 1486–1492, 2018.
3. J. Yamanishi, H.-Y. Ahn, H. Okamoto, “Nanoscopic Observation of Chiro-Optical Force,” Nano Lett. Vol. 23, 9347–9352, 2023.

Visualization of photonic band structures of topological and non-Hermitian photonic crystals

Yuto Moritake[1*], Taiki Yoda[1,2], and Masaya Notomi[1,2]

[1]Department of Physics, Tokyo Institute of Technology, Japan
[2]NTT Basic Research Laboratories, NTT Corporation, Japan
[*]corresponding author: moritake@phys.titech.ac.jp

Abstract: Topological and non-Hermitian photonics realize novel photonic phenomena. Momentum space spectroscopy is commonly used to experimentally measure band structures, Q-factors, and topological properties. The paper presents recent our demonstration, including deterministic BIC, dynamic topological phase transitions, nano-scale visualization of topological plasmonic crystals, and observation of chiral exceptional points.

Topological and non-Hermitian photonics is the research field where topological and non-Hermitian systems are investigated using photonic structures. Especially, photonic crystal is one of the ideal platforms for topological and non-Hermitian photonics due to its rich physical properties and designability. To investigate them experimentally, the researchers often use momentum space spectroscopy, which can directly measure the photonic band structures [1]. The momentum space spectroscopy can measure not only band structure but also Q-factors and topological properties from the signal linewidth and polarization information, which makes this method useful for topological and non-Hermitian photonics. In this paper, we introduce our resent results about visualization of photonic band structures in topological and non-Hermitian photonic crystals. We introduce four types of photonic crystals. The first one is observation of "deterministic" bound states in the continuum (BICs) in symmetry perturbed photonic crystals (Fig. 1(a)) [2,3]. The second one is dynamic topological phase transition using topological photonic crystals with patterned GST (phase change material) films (Fig. 1(b)) [4]. The third one is nano-scale visualization of topological band and edge states in metallic photonic crystals (plasmonic crystals) [5]. The last one is observation of chiral exceptional points in non-Hermitian photonic crystal with graphene loading (Fig. 1(c)) [6]. Our home-made measurement system can provide high-quality band images, enabling us to determine Q-factors with high accuracy and to observe bands in non-Hermite systems with large losses. Thanks to these features, we can directly observe topological and non-Hermitian properties.

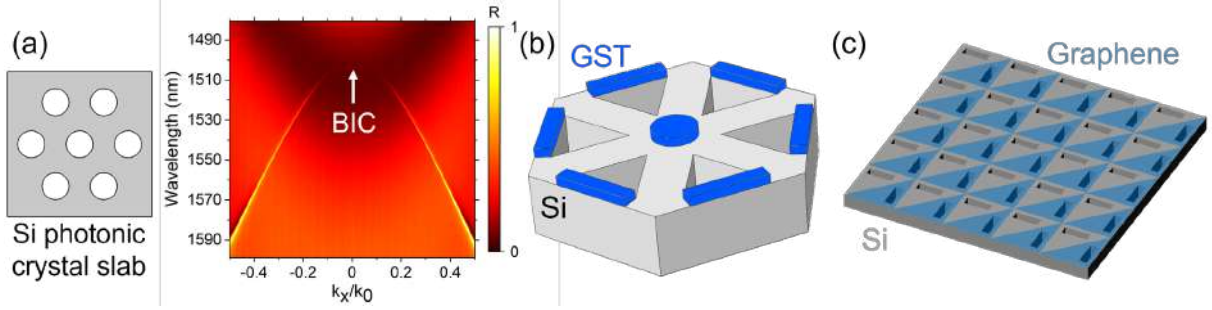

Fig.1 (a) observation of BIC in Si photonic crystal using home-made momentum plane spectroscopy. Schematics of (b) GST loaded topological photonic crystal and (c) graphene loaded non-Hermitian photonic crystals.

Acknowledgement
This work was supported by KAKENHI JP20H05641 and JP21K14551.

References

1. Zhang, Y et al., “Momentum-space imaging spectroscopy for the study of nanophotonic materials,” Science Bulletin, Vol. 66. No. 8, 824. 2021.
2. Yoda, T. et al., “Generation and Annihilation of Topologically Protected Bound States in the Continuum and Circularly Polarized States by Symmetry Breaking,” Phys. Rev. Lett., Vol. 125, 053902, 2020.
3. Yoda T. et al., “Experimental observation of bound states in the continuum generated by spatial symmetry breaking,” CLEO2021.
4. Uemura, T. et al., “Experimental demonstration of reconfigurable photonic topological phase transition with phase-change materials,” CLEO2023.
5. Saito, H. et al., “Valley-Polarized Plasmonic Edge Mode Visualized in the Near-Infrared Spectral Range,” Nano Lett., Vol. 21, 6556, 2021.
6. Suzuki, S. et al., “Non-Hermitian Chirality and Topological Properties of Graphene-loaded Photonic Crystals,” CLEO2023.

AES 2024, ROME - ITALY, 25 –28 JUNE 2024

Dielectric cylindrical and ring resonators: hot spots and photonic resonances

K. A. Bronnikov[1*], M. F. Limonov[1], and N. S. Solodovchenko[1]

[1] ITMO University, St. Petersburg, Russia
[*]corresponding author: kirill.bronnikov@metalab.ifmo.ru

Abstract: The results of theoretical and experimental study of photonic resonances upon the transition from a cylinder to a ring dielectric resonator are presented. The transition is accompanied by the appearance of a hot spot in the hole only for azimuthal harmonics with $m = 1$, which follows from Mie theory.

Dielectric cylindrical and ring resonators are widely used as elements of modern photonic devices. Common designs exploit the regime of whispering gallery modes at high frequencies, when the size of the resonator is sufficiently larger than the wavelength. Recently, their optical properties in the lower frequency region have been actively studied, which resulted in the observation of interesting effects, such as (quasi-) bound states in the continuum [1, 2]. The existence of high-quality modes in the low-frequency part of the spectrum enables the creation of near- and subwavelength resonators, and suggests dielectric cylinders and rings as basic elements of compact all-dielectric photonic devices. Despite the apparent similarity between these two types of structures, it is known that the scattering spectra of a ring resonator is fundamentally different from that of a cylinder [3]. Thus, the question arises: when a coaxial hole is introduced into the cylinder, at what geometrical parameters (the radius of the hole) the cylinder becomes the ring in terms of its optical properties, and what indicates this transition? Here, we perform a detailed study on the transformation of photonics properties of the resonator upon the transition between two objects with different topology: a cylinder and a ring. The results of theoretical and experimental study of photonic resonances accompanied by the appearance of an electric hot spot are presented.

The cylinder-to-ring transition occurs with the creation of a coaxial hole in the cylinder. Using the three-layer Mie theory [4] it can be shown that immediately after the formation of the hole an electric hot spot appears inside it. This effect takes place only for cylinder eigenmodes with azimuthal number $m = 1$, since these modes have a maximum electric field in the center of the hole (Fig. 1c). Other modes with $m \neq 1$ do not form hot spots, since they have a zero electric field in the center of the air hole (Fig. 1b, d, e). Fig. 1a shows the calculated electric field amplitude in the center of the resonator depending on the ratio of the inner and outer radii of the ring R_{in}/R_{out}. As can be seen, when the radius of the hole increases the field amplitude of the hot spot corresponding to the $m = 1$ mode drops, while the electric field of other azimuthal harmonics ($m = 0, 2, 3$ as an example) stay zero at the center. In this regard, the hot spot can be considered as an indicator of the transition from a cylinder to a ring.

Considering scattering spectra of the resonators, we observe the transformation of resonances of the cylinder with somewhat uniform distribution along the spectrum into separate groups of resonances – so-called “ring gallery modes” [3] – in the scattering spectrum of the ring. Each of these groups begins with a broad Fabry-Perot-like mode, followed by an equidistant set of longitudinal modes with increasing azimuthal number m. Performed numerical calculation of the scattering cross-section spectra demonstrates good agreement with the experimentally measured spectra (Fig. 1f).

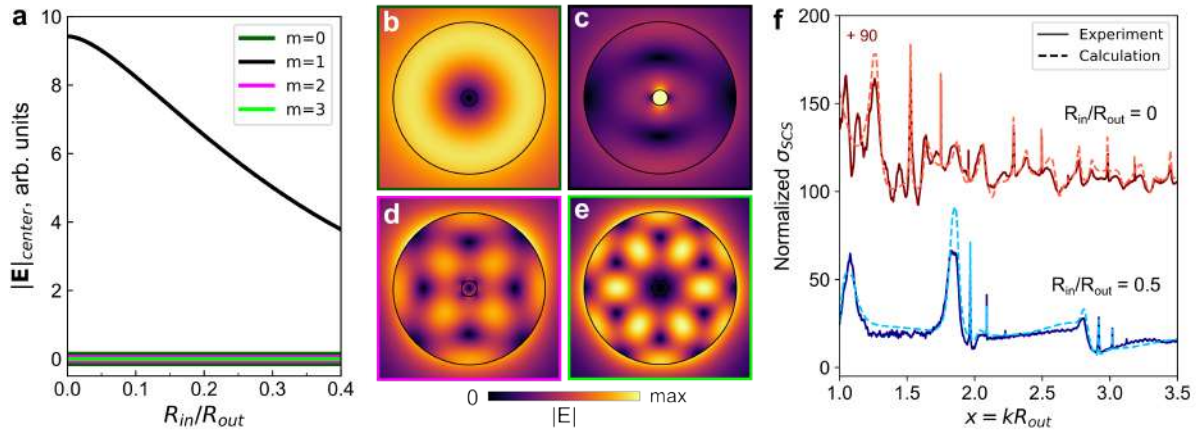

Figure 1. (a) Electric field amplitude in the center of an infinite ring resonator with $\varepsilon = 43$ depending on the size of the hole (R_{in}/R_{out} parameter) for several azimuthal modes ($m = 0$–3) calculated using the three-layer Mie theory. (b-e) Calculated electric field distributions for the same ring at $R_{in}/R_{out} = 0.1$ for the modes with (b) $m = 0$, (c) $m = 1$, (d) $m = 2$, (e) $m = 3$. (f) Experimental and calculated scattering cross-section spectra of the cylinder ($R_{in}/R_{out} = 0$) and ring ($R_{in}/R_{out} = 0.5$) resonators with $\varepsilon = 43$ and height-to-radius ratio $h/R_{out} = 0.12$.

This work was financially supported by the Russian Science Foundation grant (project No 23-12-00114).

References

1. Bogdanov, A. A., et al., “Bound states in the continuum and Fano resonances in the strong mode coupling regime”, Advanced Photonics, Vol. 1, No. 1, 016001, 2019.
2. Sedeh, H. B. and Litchinitser, N. M., “Singular optics empowered by engineered optical materials”, Nanophotonics, Vol. 12, No. 14, 2687–2716, 2023.
3. Solodovchenko, N. S., et al., “Cascades of Fano resonances in light scattering by dielectric particles”, Materials Today, Vol. 60, 69–78, 2022.
4. Huang, Y., et al., “Optimization of photonic nanojets generated by multilayer microcylinders with a genetic algorithm”, Opt. Express, Vol. 27, No. 2, 1310–1325, 2019.

Algorithm-driven Design of Metasurfaces for Multi-dimensional Light Manipulation

Wei Ma[1*] and Bo Xiong[1]

[1] College of Information Science and Electronic Engineering, Zhejiang University, Hangzhou, 310027, China.
[*]corresponding author: ma_wei@zju.edu.cn

Abstract: We present an algorithm-driven strategy to automatically design metasurfaces for multi-dimensional light manipulation. Our metasurface design pipeline comprises iterative optimization steps, integrating gradient-based optimization or heuristic algorithms enhanced by machine learning models. This approach has been experimentally validated using multi-channel holograms, focusing lenses, and guided light control.

Recently, with the aid of intelligent algorithms, the nanophotonic community has witnessed tremendous development in the design, measurement and application of nanophotonic devices and systems. The core impetus is the prevalence of inverse design methods, which convert a design problem into an optimization problem, and solve it with various algorithms automatically 1.

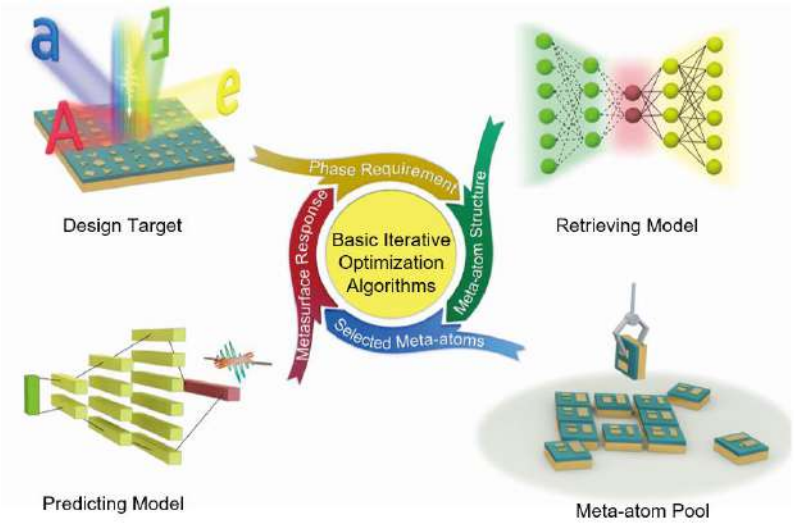

Figure 1 General end-to-end design pipeline for metasurface enhanced by machine learning

In this talk, we conceptually propose and experimentally demonstrate an end-to-end design pipeline with embedded statistical machine learning models for automatic design of metasurfaces. Instead of a two-step design routine including designing each meta-atom through a parameter sweep and then arrange them periodically, we resort to statistical machine learning as the bridge that directly links the structural parameters of each single meta-atom and the target metasurface performance. The machine learning model is composed of several probabilistic inverse retrieving models and a deterministic predicting model, which accurately capture and faithfully reproduce the statistical features of the high-dimensional joint distribution of meta-atom structures and their optical responses. Consequently, instead of artificially decoupling the complex optical response into independent sub-targets, a system-level multi-object optimization can be implemented to fully exploit the design space to push the design capacity to its physical limit. Under this design scheme, we experimentally demonstrated several design examples of metasurfaces including multi-channel holograms[2],

wavelength-multiplexed light focusing[3], guided-wavefront manipulation[4], and ultra-compact fully etched grating coupler.[5]

References

1. Yihao Xu, Bo Xiong, Wei Ma*, Yongmin Liu*, "Software-defined nanophotonic devices and systems empowered by machine learning", Progress in Quantum Electronics, Vol. 89, 100469, 2023.
2. Wei Ma*, Yihao Xu, Bo Xiong, Lin Deng, Ruwen Peng*, Mu Wang, and Yongmin Liu*, "Pushing the Limits of Functionality-multiplexing Capability in Metasurface Design based on Statistical Machine Learning", Advanced Materials, Vol. 34, No. 16, 2110022, 2022.
3. Bo Xiong, Yihao Xu, Wenwen Li, Wei Ma,* Tao Chu,* and Yongmin Liu*, "Deep Learning Design for Multiwavelength Infrared Image Sensors Based on Dielectric Freeform Metasurface", Advanced Optical Materials, online, (2024). https://doi.org/10.1002/adom.202302200
4. Wei Ma*, Maojing Hou, Ruiqi Luo, Bo Xiong, Nan Liu, Guandong Liu, and Tao Chu, "Topologically-optimized on-chip metamaterials for ultra-short-range light focusing and mode-size conversion", Nanophotonics, Vol. 12, No. 6, 1189-1197, 2023.
5. Qiao Wang, Ruiqi Luo, Nan Liu, Maojing Hou, Bo Xiong, Guandong Liu, and Wei Ma*, "Single-step-etched ultra-compact metamaterial grating coupler enabled by a hierarchical inverse design approach", SCIENCE CHINA Physics, Mechanics & Astronomy, Vol. 67, No. 2, 224211, 2024.

AES 2024, ROME - ITALY, 25 –28 JUNE 2024

Perfect absorption and thermal radiation control of MIM metasurfaces

Y. Nishijima[1,2,3,4,*], T. Kawaida[1], M. Tanaka[1], K. Sekiya[1]

1. *Department of Electrical and Computer Engineering, Graduate School of Engineering,*
2. *Yokohama National University, 79-5 Tokiwadai, Hodogaya-ku*
3. *Institute of Advanced SciencesYokohama National University, 79-5 Tokiwadai, Hodogaya-ku*
4. *Institute for Multidisciplinary Sciences Yokohama National University, 79-5 Tokiwadai, Hodogaya-ku*
5. *PRESTO, JST*

**nishijima-yoshiaki-sp@ynu.ac.jp*

Abstract: We have realized the thermal radiation control of MIM metasurface using the concept of metalens. The reflection phase was obtained FDTD simulation and fabricated the metasurface by electron beam lithography. The focal spot of thermal radiation can be seen with desired focal point.

1. Introduction

The absorption metasurface, consisting of Metal – Insulator – Metal nanostructures (MIM), has a unique optical property. The bottom metal film layer prohibits light transmission; The incident light is strongly localized in the insulator layer and absorbed by the MIM metasurface. At the same time, due to Kirchhoff's law of thermal radiation, which indicates the equivalence of absorption and emission efficiency, the absorption metasurface became the thermal radiation metasurface. We have developed MIM metasurfaces as mid-infrared light sources and other sensing applications [1-7]. Due to these optical properties, MIM metasurface is focused as the mid-infrared light source for infrared optical sensors. However, the thermal radiation pattern for far-field from the conventional radiative metasurface is spread out over approximately 120 degrees. This will lose the amount of light that is taken into the detectors. To resolve this problem, we tried to realize the thermal radiation control without a lens and the other optical components, based on the metalen technology.

2. Experiments

2-1. FDTD simulations for design of metasurface

The design of the metasurface was optimized using FDTD (Finite differential time domain) simulation with commercial software (Ansys Lumerical FDTD solver). The components of MIM structures were set with gold-SiO2-gold nanodisk; all permittivity was set to Palik's data. The thickness of the gold film was 200 nm, SiO2 was 150 nm, and a gold nanodisk thickness was 50 nm. In addition, The radius of the gold nanodisk was adjusted from 0.5 μm to 1.3 μm, and the period of the simulation region was set to 3 μm with periodic boundary conditions. The phase of optical reflection at the desired wavelength was monitored with a power monitor, which was put above the plane wave light source. There is no way to calculate thermal radiation directly using the FDTD method. Therefore, in this study, we have designed a total metasurface based on the phase of reflection light.

2-2. Fabrication of metasurface

Metasurface fabrication using electron beam lithography was performed as described elsewhere in more detail based on a previous report. In short, 5 nm Cr and 200 nm Au were thermal deposited on a silicon substrate first. After depositing 5 nm Cr, a set of samples with SiO2 layers from 100 nm to 500 nm (with a 100 nm step)

were deposited by electron-beam (EB) evaporation. After, an electron beam lithography (EBL) resist was spin-coated, and EBL exposure was performed to define the top-layer metallic nanostructures. After development, Cr 5 nm and various metals were deposited, and lift-off followed.

2-3. Experimental setup for thermal radiation pattern

Micro spectroscopy was used for spectral characterization of meta-surface MIM structures, which had a footprint with a 300 mm cross-section. A Fourier transform infrared (FT-IR) spectrometer and a microscope unit (FTIR-6000 and IRT-1000, JASCCO) were used to measure the reflection spectra in the mid-infrared region. Film of Au of 350 nm thickness was used for the reflection reference, with 98% reflectance in the entire mid-infrared area. Thermal radiation was measured using the FTIR system. Compact FTIR (ARCOptix) was connected to collimation mirrors and reflection objective lenses. The sample was set on the piezo heater and in the x, y, and z tri-axial stages.

3. Results and discussions

The metasurface was fabricated with the uniform disk, f = 5 mm, f = 7.5 mm, and f = 10 mm setting with a 5 mm total disk area. From the reflection spectra, absorption peaks have appeared around 5 mm. The uniform metasurface was set to minimize the reflection at 5 mm. Due to the different sizes of disks, the focusing metasurface has lower absorption compared to the uniform disk metasurface. The thermal radiation results show apparently focusing features in the designed focal length except for the uniform wavelength.

4. Conclusions

We first reported controlling the thermal radiation of the MIM metasurface using the metalens concept. The FDTD simulation results successfully controlled the focal spot. This means that the reflection phase should have a high correlation with that of the phase of thermal radiation. The performance of the metasurface is not completely optimized, but the directional control radiation should be applied to the mid-infrared sensors, energy harvesting, radiation cooling, and so on.

5. Acknowledgement

YN is grateful for partial support from the Japan Society for the Promotion of Science (JSPS), Grants-in-Aid for Scientific Research, and JSPS Bilateral Joint Research Projects between Japan and Lithuania. This work was partially supported by PRESTO, Japan Science and Technology Agency (JST) (JPMJPR22B6).

6. References

[1] Y. Nishijima, A. Balčytis, S. Naganuma, G. Seniutinas, S. Juodkazis, “Kirchhoff’s metasurfaces towards efficient photo-thermal energy conversion,” *Scientific reports*, **9**, 8284, 2019

[2] N. To, S. Juodkazis, Y. Nishijima, “Detailed Experiment-Theory Comparison of Mid-Infrared Metasurface Perfect Absorbers,” *Micromachines*, **11**, 409, 2020

[3] Y. Nishijima, S. Morimoto, A. Balcytis, T. Hashizume, R. Matsubara, A. Kubono, N. To, R. Meguya, J. Morikawa, S. Juodkazis, “Coupling of molecular vibration and metasurface modes for efficient mid-infrared emission,” *Journal of Materials Chemistry C*, **10**, 451-462, 2022.

[4] Y. Nishijima, N. To, A. Balcytis, and S. Juodkazis, “Absorption and scattering in perfect thermal radiation absorber-emitter metasurfaces,” *Optics Express*, **30**, 4058-4070, 2022.

[5] Y. Nisijima, S. Judkazis, “The tunable coupling between metasurface and molecular vibration towards the platform of spectral analysis”, *Bulletin of the Chemical Society of Japan*, **95**, 1318–1324, 2022.

[6] Y. Nishijima, S. Kimura, Y. Takeshima, and S. Jodkazis, “Metasurfaces as energy valves for sustainable energy management,” *Micromachines*, **13**, 1769, 2022

[7] Y. Nishijima, S. Judkazis, “Control of vibration-metasurface coupling at mid-infrared spectral window for inorganic thermal emitters”, *Bulletin of the Chemical Society of Japan,* **95**, 1411–1418, 2022.

The summary should describe the approach and the article's major contributions, emphasizing the importance and significance of the results with proper cited reference to be listed in the reference section at the end of the article. The paper length should not exceed 2 pages. Equations, figures, tables and references should follow a sequential numerical scheme in order to ensure a logical development of subject matter.

For equations,

$$\nabla \times \bar{E}\left(\bar{r},t\right) = -\frac{\partial \bar{B}\left(\bar{r},t\right)}{\partial t} \tag{1}$$

Figures and Tables: Give each figure and table a separate concise caption. It begins with Figure or Table, followed by the appropriate Arabic numeral and period. The maximum width of figure or table may not exceed 17 cm. Make symbols, line thickness, and lettering in proper scale in relation to the overall figure size.

Acknowledgements, if any, including all funding information, should be gathered into a brief statement at the end.

References

1. Lastname, F. M. “Title of the journal paper,” Journal Title Abbreviation, Vol. 34, No. 10, 1064–1076, 1986.
2. Lastname, F. M. and F. M. Lastname, “Title of the journal paper,” Journal Title Abbreviation, Vol. 34, No. 10, 1064–1076, 1986.
3. Lastname, F. M., F. M. Lastname and F. M. Lastname, “Title of the journal paper,” Journal Title Abbreviation, Vol. 34, No. 10, 1064–1076, 1986.

Inverse Design for wavelength and polarization multiplexing in optical metasurfaces

Bo Xiong[1*], and Wei. Ma[1]

[1]Zhejiang University, China
[*]corresponding author: bo.xiong@zju.edu.cn

Abstract: By introducing the engineered noise to the precise solution of Jones matrix elements, we break the fundamental limit of polarization multiplexing capacity of metasurfaces. We experimentally demonstrate up to 11 independent holographic images using a single metasurface illuminated by different polarizations.

Near-infrared multi-spectral and multi-polarization imaging technology enhances target detection and recognition by distinguishing the spectral characteristics of various targets. However, traditional imaging systems heavily rely on complex optical filter designs that are often bulky and mechanically unstable, posing significant challenges for miniaturization and integration challenging. In this talk, we firstly designed a freeform dielectric metasurface with the wavelength-multiplexing focusing effect based on a deep learning model, which can separate the mixed near-infrared light into distinct wavelengths. To effectively modulate the complex amplitude of the transmitted light at three distinct near-infrared wavelengths (1150, 1350, and 1550 nm), high-index silicon freeform nanostructures supporting rich resonant modes were proposed. An inverse design model based on deep learning was utilized to generate individual freeform nanostructures pixel by pixel, satisfying the complex amplitude requirement for a multiplexed metalens design. Finally, a metasurface was employed to realize near-infrared multispectral imaging, which allowed for the distinct detection and decoding of images at the three target wavelengths. Moreover, we also designed a polarization multiplexing metasurfaces based on genetic algorithm, in which noise engineering has been introduced to break the polarization multiplexing capacity of metasurfaces that roots from the dimension constraints of the Jones matrix. Illuminated by the incidence with different linear polarization states, the metasurface can generate up to 11 independent holographic images at the corresponding channels. To the best of our knowledge, it is the highest capacity reported for polarization multiplexing. The proposed technology has a wide range of applications in clinical medicine, biological tissue imaging, and deep-space exploration.

References

1. **B Xiong**, Y Xu, W Li, W Ma*, T Chu*, Y Liu* "Deep Learning Design for Multiwavelength Infrared Image Sensors Based on Dielectric Freeform Metasurface", **Advanced Optical Materials** 2302200 (2024)
2. **B. Xiong**, Y. Liu, Y. H. Xu, L. Deng, C. W. Chen, J. N. Wang, R. W. Peng*, Y. Lai, Y. M. Liu*, and M. Wang*, "Breaking the limitation of polarization multiplexing in optical metasurfaces with engineered noise," **Science**, Vol. 379, No. 6629, 294-299 (2023).
3. **B. Xiong**, Y. H. Xu, J. N. Wang, L. Li, L. Deng, F. Cheng, R. W. Peng*, M. Wang* and Y. M. Liu*, "Realizing colorful holographic mimicry by metasurfaces", **Advanced Materials** 33(21), 2005864 (2021).

AES 2024, ROME - ITALY, 25 –28 JUNE 2024

Plasmonic/Excitonic hybrid systems for nanoscale thermometry

L. Ramò[1], V. Venturino[1], E. Peci[1], E. Spotorno[1], M. Magnozzi[1], M. C. Giordano[1], D. Convertino[2], G. Orlandini[2], C. Coletti[2], M. Canepa[1], F. Bisio[3*]

[1]Dipartimento di Fisica, Università degli Studi di Genova, Via Dodecaneso 33, 16146 Genova (Italy)
[2]Center for Nanotechnology Innovation @NEST, Istituto Italiano di Tecnologia, Piazza San Silvestro 12, I-56127 Pisa, Italy
[3]CNR-SPIN, C.so Perrone 24, 16152 Genova (I)
[*]corresponding author: francesco.bisio@spin.cnr.it

Abstract: We report the fabrication and validation of an experimental system that exploits plasmonic Au nanoparticles to generate heat on a nanometric lateral scale, and measures the local temperature increase in the surroundings of these nanoparticles by means of carefully placed monolayers of transition metal dichalcogenide (TMDC).

Heat is commonly defined as the energy that is transferred from one body to another as the result of a difference in temperature. Whereas on the macroscopic scale heat-propagation phenomena are governed by bulk materials' properties and ruled by the Fourier equation, when the characteristic size of the systems under scrutiny shrinks, finite-size effects start to become relevant.

Heat transmission at the nanoscale presents a fascinating arena for scientific inquiry and technological innovation. At this diminutive scale, materials behave uniquely, often defying classical thermodynamic principles and demanding novel approaches to understand and manipulate heat transfer. One of the key phenomena at play is the ballistic transport of heat carriers, where phonons and electrons propagate across nanomaterials with minimal scattering. This ballistic transport contributes to remarkably high thermal conductivities observed in some nanomaterials, defying conventional limitations. The interplay between quantum confinement and surface effects profoundly influences heat transmission at the nanoscale. Surface effects play a pivotal role in nanoscale heat transmission, dictating thermal boundary conductance and phonon scattering rates. As the volume-to-surface ratio escalates in nanostructures, interfacial interactions become increasingly dominant, mediating heat transfer between disparate materials.

Understanding and harnessing heat transmission at the nanoscale hold immense technological promise across diverse fields, including nanoelectronics, thermoelectric energy conversion, and thermal management of nanoscale devices. To this end, it is of paramount importance to develop systems and strategies to create heat on a nanometric scale, and to measure the ensuing temperature distribution with atomic-scale accuracy. In this contribution, we report the fabrication and validation of a nanosystem designed to generate heat on the few-nm lateral scale and measure the achieved temperature variation with atomic-scale precision. The system exploits the thermoplasmonics effect in Au nanoparticles for heat generation, and the temperature-dependent optical response of monolayer TMDC to measure the temperature less than 1 nm away from the particle surface.

The device consists of an array of plasmonic nanodisks (NDs) fabricated on a glass substrate. The NDs are arranged on a square lattice, and have a diameter of 100 nm, gap of 200 nm and a thickness of 15 nm. They exhibit a localized surface plasmon resonance (LSPR) at λ=780 nm photon wavelength (1.5 eV). On the Au NDs, we transferred a WS_2 monolayer flake encapsulated in hBN monolayers. The optical absorbance of the hybrid system is reported in Figure 1. There, we can see the LSPR peak at 1.5 eV, accompanied by the A, B and C excitons of WS_2 at increasingly higher energy.

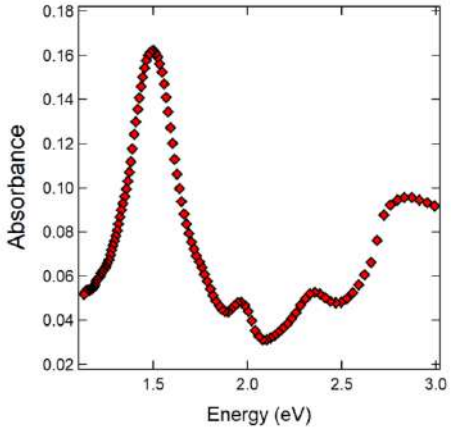

Figure 1: absorbance spectrum of the hybrid WS_2/NDs systems.

The system could be excited by two co-focused laser beams: the former, a low-fluence beam with λ=532 excited the photoluminescence (PL) from WS_2, while the latter was tuned with the LSPR of the Au NDs.

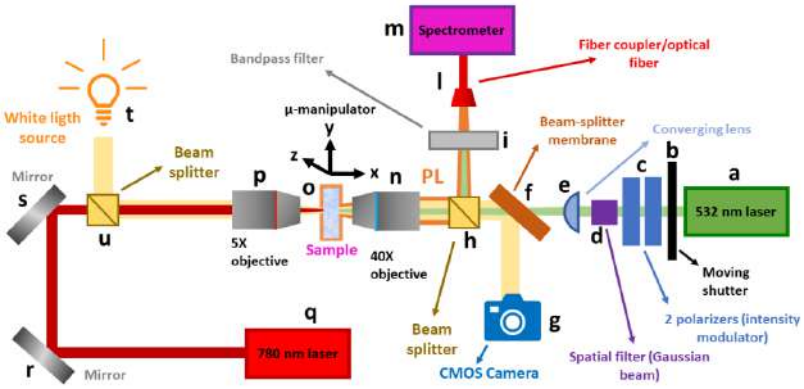

Figure 2: schematic representation of the experimental setup for nanoscale thermometry.

Comparing the PL spectra with/without the LSPR excitation, a clear redshift by 10 meV could be observed, corresponding to a temperature variation of the WS_2 of approximately 35K induced by the thermoplasmonics heating of the Au NDs. The hybrid plasmonic/excitonic system represents therefore a viable approach to measure the local temperature variation in nanosystems.

References

1. Ramò L. *et al.* "Thermal Scanning-Probe Lithography for Broad-Band On-Demand Plasmonic Nanostructures on Transparent Substrates" ACS Appl. Nano Mater. 6, 19, 18623–18631, 2023.

AES 2024, ROME - ITALY, 25 –28 JUNE 2024

Integrated Photonics for Quantum Information Processing and Artificial Neural Networks

Imtiaz Alamgir[1], Luigi Di Lauro[1], Stefania Sciara[1], Abdul Rahim Aadhi[1], Celine Mazoukh[1], Hao Yu[1,2] Bennet Fischer[1], Nicolas Perron[1], Nicola Montaut[1], Mario Chemnitz[1], Brent E. Little[3], Sai T. Chu[4], David J. Moss[5], Zhiming Wang[2] and Roberto Morandotti[1*]

[1]Institut national de la recherche scientifique (INRS-EMT), Varennes J3X 1P7, Canada
[2]Institute of Fundamental and Frontier Sciences, University of Electronic Science and Technology of China, China
[3]QXP Technology, Inc, China
[4]City University of Hong Kong, China
[5]Optical Sciences Centre, Swinburne University of Technology, Australia
*corresponding author: Roberto.Morandotti@inrs.ca

Abstract: Integrated photonics advances emerging quantum information processing and artificial neural network technologies. This work employs on-chip, reconfigurable devices for highly efficient, intelligent, and secure classical and quantum information processing. We demonstrate simultaneous operations with high speed, low power consumption, and small footprints, paving the way for next generation telecommunication solutions.

Artificial intelligence and quantum information science provide innovative tools for advanced signal processing toward emerging smart technologies in the fields of, e.g., communication and optical computing [1, 2]. For instance, software/electronic-based artificial neural networks have been used to optimize telecom data transmission [3]. Yet, current implementations are inefficient to process real-time signals due to high latency and low processing speeds. Similarly, quantum signal processing has been pivotal to implement quantum communication in fiber networks to guarantee unbreakable data security [4]. However, fiber-based quantum communication suffers from limited distances and low transmission speeds, due to photons scattering and losses.

We develop integrated, reconfigurable all-optical neural networks (ONNs) to process and recover nonlinearly distorted telecom signals at ultrafast speeds. In parallel, we use on-chip photonics for the generation and processing of complex entangled photon states toward high-speed quantum key distribution (QKD). These implementations are realized by utilizing a single all-integrated photonic platform, which comprises a nonlinear source (spiral waveguide or microring resonator) [5] and an on-chip programmable interferometry system [6].

Our proposed ONNs feature a recurrent network topology [1], where the encoded information density is enhanced via the use of a microcomb [3] and manipulated by means of wavelength division multiplexing techniques. We apply our ONNs for nonlinear channel equalization to regenerate the temporal waveform of the transmitted signal, which undergoes dispersive and nonlinear impairments due to propagation in the fiber channel. In general, this complex task demands the implementation of rigorous digital signal processing e.g., digital back propagation, requiring extensive computational power and a detailed understanding of the transmission system. Our objective is to develop highly versatile and easily integrable ONN platforms that are capable of processing telecom signals at ultra-high speeds and with reduced latency. Preliminary results suggest that our tunable ONN devices can process and accurately reconstruct nonlinearly distorted telecom waveforms, achieving processing speeds exceeding GHz/s with nanosecond-level latency.

The spiral waveguide and the cascade of on-chip interferometers can also be exploited for the generation of high-dimensional (qudit) time-entangled photon states at telecom wavelengths. The interferometers generate

pulse burst that subsequently induce spontaneous four-wave mixing and thus generate time-entangled photon pairs in the spiral waveguide. The programmable interferometers, combined with external fiber-based GHz speed phase modulation, are used for quantum state processing i.e., for quantum interference and quantum state tomography measurements, as well as telecom-compatible secure QKD. The use of entangled photons provides robustness against eavesdropping attacks, as they allow the exchange of a device-independent secret key. The use of qudits guarantees an increase in the secret key rate, noise resilience, and information capacity. From preliminary tests, we estimate a record high secret key rate of several hundred kbit/s and a quantum bit error rate below 12%. These results show the high robustness of the cryptography key generated via our photonic qudits against eavesdropping attacks.

Our platform provides compact and CMOS compatible solutions that enable significant scaling of information through time or frequency multiplexing, establishing it as a highly suitable candidate for signal processing applications. Moreover, the high nonlinearity and low heat dissipation profiles of our devices, will position our research in line with the needs for energy efficiency required by next-generation ONN, while also boosting quantum state processing, and the security of quantum optical signals in fiber telecom networks.

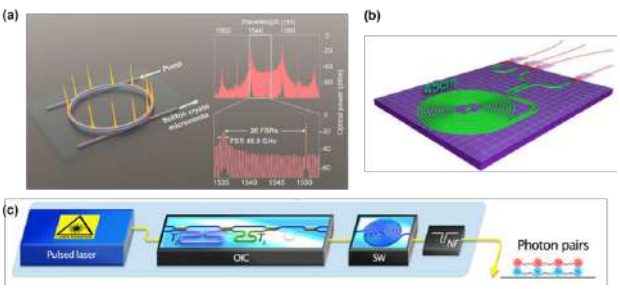

Fig. 1. (a) Schematic representation of an integrated microring resonator employed to generate a soliton crystals comb at C-band. Adapted from [7]. (b) Schematic representation of a spiral waveguide. Adapted from [5]. (c) Schematic representation of the scheme used for photon state generation. OIC: on-chip interferometer cascade; T1, T2: transmission ratios of the interferometers; SW: spiral waveguide; NF: notch filter.

References

1. Shastri, B.J., Tait, A.N., Ferreira de Lima, T., Pernice, W.H.P., Bhaskaran, H., Wright, C.D., Prucnal, P.R., “Photonics for artificial intelligence and neuromorphic computing”, Nature Photonics, Vol. 15, 102-114, 2021.
2. Flamini, F., Spagnolo, N., Sciarrino, F., “Photonic quantum information processing: a review”, Reports on Progress in Physics, Vol. 2, No. 1, 016001, 1-32, 2019.
3. Xu, X., Tan, M., Corcoran, B., Wu, J., Boes, A., Nguyen, T.G., Chu, S.T., Little, B.E., Hicks, D.G., Morandotti, R., Mitchell, A., Moss, D.J., “11 TOPS photonic convolutional accelarator for optical neural networks”, Nature, Vol. 589, 44-51, 2021.
4. Wen, W., Chen, Z., Lu, L., Yan, W., Xue, W., Zhang, P., Lu, Y., Zhu, S., Ma, X., “Realizing an entanglement-based multiuser quantum network with integrated photonics”, Physical Review Applied, Vol. 18, No. 2, 024059, 1-4, 2022.
5. Moss, D.J., Morandotti, R., Gaeta, A.L., and Lipson, M., “New CMOS-compatible platforms based on silicon nitride and Hydex for nonlinear optics”, Nature Photonics, Vol. 7, 597-607, 2013.
6. Wetzel, B., Kues, M., Roztocki, P., Reimer, C., Godin, P.L., Rowley, M., Little, B.E., Chu, S.T., Viktorov, E., Moss, D., Pasquazii, A., Peccianti, M., and Morandotti, R., “Customizing supercontinuum generation via on-chip adaptive temporal pulse-splitting”, Nature Communications, Vol. 9, No. 4884, 1-10, 2018.
7. Xu, X., Tan, M., Corcoran, B., Wu, J., Nguyen, T.G., Boes, A., Chu, S.T., Little, B.E., Morandotti, R., Mitchell, A., Hicks, D.G., and Moss, D.J., “Photonic perceptron based on a Kerr microcomb for high-speed, scalable, optical neural networks”, Laser & Photonics Reviews, Vol. 14, No. 2000070, 1-10, 2020.

AES 2024, ROME - ITALY, 25 –28 JUNE 2024

Anisotropic polaritons in van der Waals layered crystals

Andrea Mancini[1*], Nicola Melchioni[1], Giacomo Venturi[1], Stefano Chiodini and Antonio Ambrosio[1]

[1] Centre for Nano Science and Technology, Fondazione Istituto Italiano di Tecnologia, Via Rubattino 81, Milan 20134, Italy
[*]corresponding author: andrea.mancini@iit.it

Abstract: Hyperbolic polaritons, stemming from the hybridization of light and excitations in highly anisotropic materials, exhibit intriguing properties such as directional propagations and negative refraction. Strongly confined polaritons in van der Waals crystals have recently attracted considerable attention for novel applications in energy-efficient photonics, nanoscale routing of light, and vibrational sensing.

Hyperbolic materials, characterized by extreme anisotropy in their optical properties, have been explored thanks to their unique light-propagation properties with unbounded wavevectors isofrequency contours. Their unique property of having permittivities with opposite signs along different directions enabled the demonstration of negative refraction[1] and hyperlensing[2] in artificial metamaterials. However, these systems can work only in the effective medium approximation and are as such confined to low wavevector applications due to the limits imposed by nanofabrication resolution.

Recently, natural van der Waals (vdW) exhibiting natural hyperbolicity in the mid-infrared have been investigated for nanophotonic applications. The high structural anisotropy of vdW results in the presence of optical phonons with strongly different energies, which lead to the presence of frequency regions where the permittivity assumes positive and negative values along distinct crystal directions. At these frequencies, light strongly couples with optical phonons, leading to the formation of mixed light-matter states called phonon polaritons (PhP). Out-of plane PhPs hyperbolicity was first reported in hBN flakes[3,4], followed by the discovery of in-plane hyperbolic PhPs in MoO_3 thin films[5,6]. Since then, lower symmetric crystals led to the observation of shear[7] and ghost polaritons[8], enhancing the possibilities of nanoscale light control below the diffraction limit.

While PhPs are highly attractive for their low-losses, they are inherently confined to the far and mid-infrared part of the spectrum because of the characteristic energy of optical phonon. Here we consider the possibility of lowering the operational frequency of hyperbolic polaritons by employing novel vdW crystals.

References

1. High, Alexander A., et al. "Visible-frequency hyperbolic metasurface." Nature, 522.7555, 192-196, 2015.
2. Liu, Zhaowei, et al. "Far-field optical hyperlens magnifying sub-diffraction-limited objects." Science, 315.5819, 1686-1686, 2007.
3. Dai, Siyuan, et al. "Tunable phonon polaritons in atomically thin van der Waals crystals of boron nitride." Science, 343.6175, 1125-1129, 2014.
4. Ambrosio, Antonio, et al. "Selective excitation and imaging of ultraslow phonon polaritons in thin hexagonal boron nitride crystals." Light: Sci. Appl., 7.1, 27, 2018.
5. Ma, Weiliang, et al. "In-plane anisotropic and ultra-low-loss polaritons in a natural van der Waals crystal." Nature, 562.7728, 557-562, 2018.
6. Zheng, Zebo, et al. "A mid-infrared biaxial hyperbolic van der Waals crystal." Sci. Adv. 5.5, eaav8690, 2019.

7. Passler, Nikolai C., et al. "Hyperbolic shear polaritons in low-symmetry crystals." Nature, 602.7898, 595-600, 2022.
8. Ma, Weiliang, et al. "Ghost hyperbolic surface polaritons in bulk anisotropic crystals." Nature, 596.7872, 362-366, 2021.

Acknowledgements

The authors acknowledge funding from ERC grants “METAmorphoses”, grant agreement no. 817794 and Fondazione Cariplo, grant no 2019–3923.

Integrated Phased Array Antenna Using Phase Change Materials

Rahuldas Kutteeri [1], Martino De Carlo [1], Francesco De Leonardis [1], Richard A. Soref [2], and Vittorio M. N. Passaro [1*]

[1] Photonics Research Group, Department of Electrical and Information Engineering, Politecnico di Bari, Italy

[2] University of Massachusetts, Boston, USA
[*]vittorio.passaro@poliba.it

Abstract

Tunable true time delay is achieved by manipulating Bragg grating resonators (BGRs) with phase change materials, thereby realizing programmable on/off reflectors. By programming these reflectors placed at specific positions, a time delay in optical signals is induced, enabling ∼1550 nm beam steering in microwave phased array antennas (MPAAs).

Index terms- Bragg grating resonators, Phase Changing Materials, True time delay, Microwave Photonics.

1. Introduction

Microwave beam shaping and steering find widespread use, particularly in telecommunication, defense, security etc. Beam steering adjusts for relative displacement between transmitter and receiver, turning a secure advantage over wireless radio networks due to the narrowness of the microwave beam. However, current systems for generating and steering narrow beams are bulky, costly, and mainly ground-based, limiting their applications. The aim is to reduce their size, weight, and power consumption. Photonic integrated circuits (PICs) using microwave phased array antenna (MPAA) technology provide a promising solution, generating narrow beams with wide steering angles and fast tuning speeds. Operating in the infrared range, PICs are ideal for example for communication and sensing. Manipulating the phase and/or amplitude of coherent emitters within optical phased array enables precise control over the electromagnetic field near the emitters. PICs integrate various photonic functionalities onto a single substrate, facilitating the integration of large numbers of parallel components essential for microwave photonics. Micro and nanofabrication techniques ensure robust, reproducible platforms with electro-optical control, enabling high bandwidths and precise electromagnetic path length control, crucial for minimizing errors.

The most straightforward approach for integrating beam shaping and steering in two dimensions involves utilizing a 2D array of coherent emitters, enabling control over output phase and possibly the power for each emitter. Initial efforts were focused on one-dimensional (1D) arrays fabricated in indium phosphide [1] and silicon photonic technology [2], with non-uniform emitter spacing utilized to suppress unwanted side lobes. To achieve 2D beam steering, a stack of 1D silicon PICs was proposed [3], and subarrays with varying emitter spacing were suggested to suppress side lobes. Another approach is to expand the inherent 1D array of emitters in planar edge-emitting PICs into a 2D array using a photonic lantern [4]. High-contrast silicon photonics, leveraging vertical grating couplers, offers an elegant solution for realizing full 2D emitter arrays on PIC surfaces [5]. Sun et al. developed a 64×64 array comprising 4096 emitters, enabling active beam shaping and steering through the addition of thermo-optic phase tuners [6]. Abediasl et al. further advanced this approach by presenting a silicon photonic PIC with active amplitude and phase control of an 8×8 array, facilitating full arbitrary dynamic beam shaping [7]. Several intriguing applications of these 2D silicon photonic optical phased arrays have been identified and explored [8]. One-dimensional beam steering and two-dimensional beam steering are achieved later [9]. Substantial research efforts have been devoted to achieving beam steering through the utilization of true time delay (TTD) methods. While earlier studies predominantly focused on employing phase shifters to achieve TTD, this approach resulted in a phenomenon termed "beam squinting" [10].

Our study investigates an alternative method derived from previous research, utilizing Phase Change Materials (PCMs) as a generally effective approach for achieving precise TTD. Specifically, the electromagnetic path selection, crucial for attaining the desired outcomes, is facilitated by incorporating PCMs within Bragg Grating Reflectors (BGRs), so inducing significant shift of the Bragg wavelength along the wavelength axis when the material phase of the PCM is changed. The architecture employed in this study starts from a previous work [11], with a notable modification: the integration of a layer of PCM instead of a thermo-optic (TO) heater. The advantages of using PCMs rather than TO heaters on a SIO (Silicon on Insulator) platform, primarily rely on the possibility of realizing a non-volatile beam-steering device. Moreover, the high refractive index change induced by the phase change in PCMs, ensures the possibility of using simple BGRs rather than WBGRs used in [11], thus making more accurate the match between design and fabrication.

Our primary objective was to streamline the design of the TTD controller. Notably, our chip facilitates both transmission and reception functionalities. All BGRs utilized in our design are identical and initially aligned at a common resonance wavelength (λ_{BA} ∼1468 nm), in amorphous condition.

The structure of this paper is as follows: Section 2 presents the working principle followed by an exploration of specific PCM-based SOI BGRs. In Section 3, we present some numerical results, offering a comprehensive analysis of the TTD system through parametric simulations to assess the delay line characteristics. Furthermore, we evaluate the performance of the beamformer system. Lastly, the discussion and conclusions are summarized in Sections 4 and 5, respectively.

2. Basic concept

In the microwave phased array antenna (MPAA), multiple radiating elements are arranged in a configuration with parallel rows, in which each row realizes a delay line.
Our focus in this application centers on different delay lines, each having an array housing of 7 PCM-based integrated BGRs, separated by SOI waveguides in between them, as depicted in Fig. 1. This study is based on the utilization of Sb_2S_3 (Antimony trisulfide) as PCM to enable precise time delay control, with a specific emphasis on integrating PCM into Bragg grating resonators (BGRs), as depicted in Fig. 2. Indeed, Sb_2S_3 well fits as a compelling material for on-chip programmable photonic devices, due to its low intrinsic losses in both amorphous and crystalline states around a wavelength of 1550 nm, ensuring minimal signal attenuation.

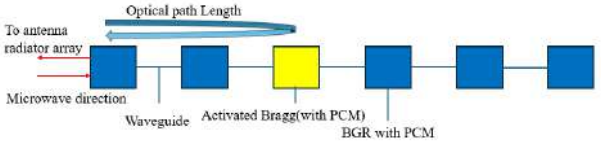

Figure 1. Delay line containing a cascade of BGRs connected by waveguide sections. The yellow box shows the activated BGR (crystalline phase).

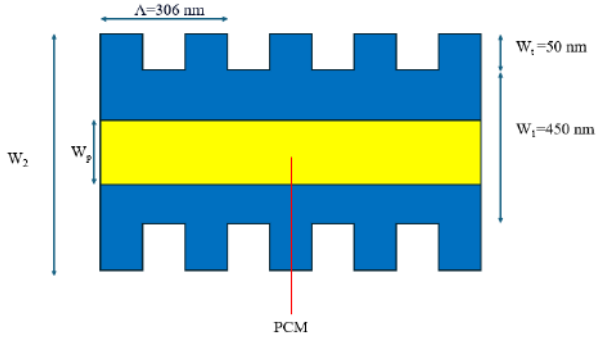

Figure 2. Top view of Silicon on insulator strip waveguide showing the geometry of one PCM coated Bragg-grating resonator

Secondly, the refractive index contrast (Δn) between crystalline and amorphous phases of ~0.60 allows for high on-chip compactness, crucial for including more delay lines with more reflectors in the same area. Moreover, Sb_2S_3 enables reversible optical switching making it suitable for dynamic phase control [12]. The activation (transitioning from amorphous to crystalline state of PCM) of a specific BGR within the array will shift its resonance wavelength from λ_{BA} (~1468 nm) to λ_{BC} (~1550 nm) inducing a reflection at the operating wavelength (1550 nm) that determines the optical path length (Figure 1), thus changing the microwave delay. So, when the phase of the PCM changes from amorphous to crystalline, the device acts as an turned-on reflector in a certain range of wavelengths around 1550 nm. This effectively enables the creation of a microwave phase array by employing multiple delay lines and selectively activating reflectors along each line.
The BGR in Fig. 2 is designed by alternating two cross-sections with widths of 450 nm (W_1) and 550 nm (W_2), with the same height (H) of 220 nm. A period (Λ) of the Bragg grating, set at 306 nm, is designed to ensure the resonant Bragg wavelength in its crystalline phase at 1550 nm. Additionally, the height of the PCM matches that of the Silicon in the BGR (220 nm), while selecting a width (W_p) of 150 nm. Our simulations employ a comprehensive mixed full-vectorial mathematical model based on Finite Element Method (FEM), Coupled Mode Theory (CMT), and Transfer Matrix approaches.

3. Numerical Results

PCM exhibits a significant refractive index contrast between its crystalline and amorphous states (3.308 and 2.712, respectively) [12]. According to Bragg resonance condition $\lambda_B=2n_{eff}\Lambda$ where λ_B (~1550 nm) is the Bragg wavelength, n_{eff} is the effective index and Λ is the grating period, by integrating PCM into Bragg resonators a large index contrast in the average effective refractive index of the Bragg resonator is induced (being ~0.60 the index contrast from crystalline to amorphous phase), resulting in a remarkable shift in the reflection/transmission spectrum of BGRs, as shown in Fig. 3. A strong Bragg wavelength shift from ~1468 nm to ~1550 (Figure 3) nm can be observed when changing the phase of the PCM from amorphous to crystalline.

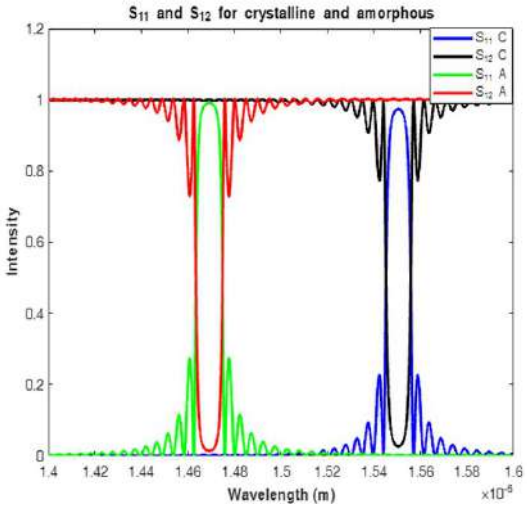

Figure 3. Reflection and Transmission spectral response of PCM coated Bragg resonator. S_{11} & S_{12} are referred as reflection and transmission in crystalline or amorphous state, respectively.

This significant Bragg wavelength shift demonstrates the effectiveness and significance of incorporating PCM into the Bragg grating resonators. The high Bragg wavelength shift makes it possible to use less critical BGRs, rather than WBGRs [11].

Subsequently, we have investigated a series of 7-BGRs delay lines (figure 4). The length of the waveguides between neighbor BGRs along the same delay line is non-uniformly chosen based on trigonometric analysis and beam steering requirements [11]. This relation allows for non-uniform spacing along the delay line to achieve the desired beamforming characteristics. If d_{min} = 370.4 µm is the distance between the center of first and second BGR along the delay line, chosen according to Eq. 1, and c is the free space light speed, being Θ_{min} the minimum steering angle (8°) and f_{max} the maximum frequency of the modulating microwave signal to be transmitted, we can select a set of angles (Θ_i) ranging from 8° ($\Theta_{min} = \Theta_1$), 16°, 24°, 32°, 40°, to 48° through:

$$d_{min} = \frac{c}{4 f_{max} n_{eff}} \sin \Theta_{min} \qquad (1)$$

$$d_{i,NL} = NL \cdot d_{min} \frac{\tan \Theta_i}{\tan \Theta_{min}} \qquad (2)$$

In Fig. 4, S is the vertical distance between two delay lines and is selected as 1.25 cm for X band (8÷12 GHz) calculated according to the equation 3, where λ(min) is the minimum microwave band wavelength.

$$S = 0.5 \times \lambda(min) \qquad (3)$$

$d_{i,NL}$ (µm)	Steering Angle (degree)
370.4	8
755.8	16
1200	24
1600	32
2200	40
2900	48

Table 1. $d_{i,NL}$ values and corresponding steering angles for NL=1.

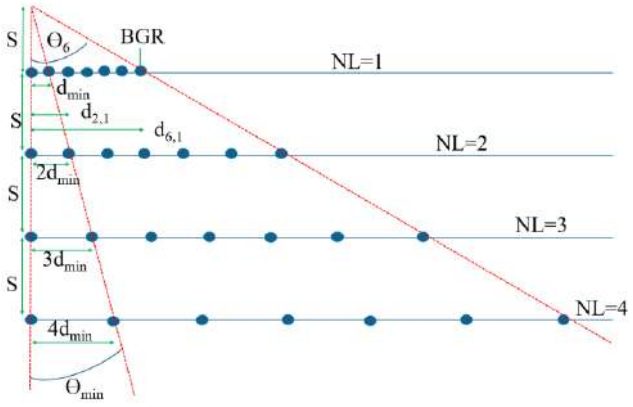

Figure 4. Array of delay lines with corresponding steering angles.

By using this equation, separation between BGRs is obtained to have desired steering angles (Table 1). The number of delay lines influences the narrowness of the output microwave beam. With the use of calculated separation between center of one BGR from another (Eq. 2), system can achieve the beam steering performance by controlling the phase shifts. The group delay of the delay line has been calculated as dϕ/dω, where ϕ represents the total phase of the signal reflected by the delay line, and ω denotes the angular frequency.

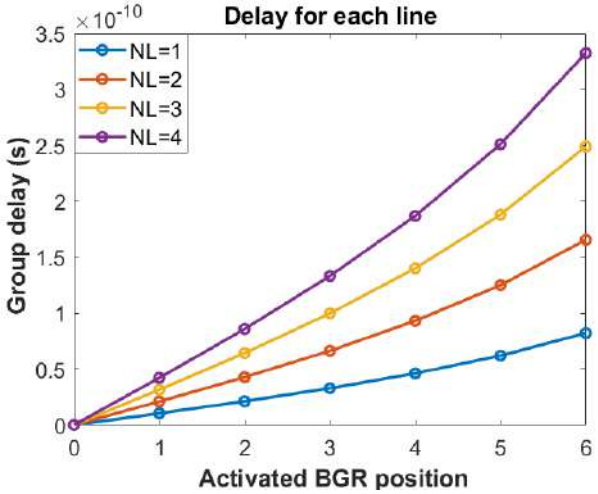

Figure 5. Group delay induced when each BGR is activated for different delay lines (NL).

Figure 5 shows that different time delay is induced when each BGR is activated on for different delay line. Maximum induced time delay obtained (last BGR activated) for each line is 82.37 ps, 165.7 ps, 249.1 ps, 332.5 ps, respectively.

4. Discussion

Time delay increases with the activated BGR along a delay line, clearly indicating the path difference induced delay. The separation between the first and the second BGR on each line is chosen as an integer multiple of d_{min} of the first delay line. By incorporating several delay line along with the programmable on/off BGRs, beam steering can be achieved for the desired angle. Performance evaluation metrics, such as group delay induced by activating specific BGRs and the calculated delay times for different configurations, provide valuable insights into the effectiveness of the PCM-BGR integration for achieving tunable true time delay. The results demonstrate the feasibility of digital programming for beamforming in microwave phased array antennas, showcasing the potential for dynamic phase control and efficient modulation of light phase and amplitude. Furthermore, broader implications of integrating phase-change materials with BGRs are focused, highlighting the advancements in achieving tunable true time delay and beam steering functionalities in integrated phased array antennas. This study's findings open up new possibilities for enhancing the performance and flexibility of communication systems

through the innovative integration of PCM with photonic devices, paving the way for the development of advanced integrated photonic devices.

5. Conclusions

This work points out the significance of incorporating Phase Change Materials along with Bragg Grating Resonators to obtain tunable true time delay in integrated phase array antennas. By utilizing the refractive index contrast between material phases, a programmable on/off reflector is simulated for beam steering at 1550 nm. This innovation offers a more advanced phase array antenna performance and thereby various research opportunities in communication applications.

Acknowledgements

This work was partially supported by the European Union under the Italian National Recovery and Resilience Plan (NRRP) of NextGenerationEU, partnership on "Telecommunications of the Future" (PE00000001 - program "RESTART").

References

[1] Flamand G, De Mesel K, Moerman I, Dhoedt B, Hunziker W, Kalmar A, Baets R, Van Daele P, Leeb W. "InP-based PIC for an optical phased-array antenna at 1.06 μm". IEEE Photonics Technol Lett. 12, 876–8, 2000.

[2] Kwong D, Hosseini A, Zhang Y, Chen RT. "1×12 Unequally spaced waveguide array for actively tuned optical phased array on a silicon nanomembrane". Appl Phys Lett 99, 051104, 2011.

[3] Hosseini A, Kwong D, Zhang Y, Chandorkar SA, Crnogorac F, Carlson A, Fallah B, Bank S, Tutuc E, Rogers J, Pease RFW, Chen RT. "On the fabrication of three-dimensional silicon-on-insulator based optical phased array for agile and large angle laser beam steering systems". J Vac Sci Technol B. 28, C601–C607, 2010.

[4] Thomson RR, Birks TA, Leon-Saval SG, Kar AK, Bland-Hawthorn J. "Ultrafast laser inscription of an integrated photonic lantern". Opt Express. 19, 5698–5705, 2011.

[5] Mekis A, Gloeckner S, Masini G, Narasimha A, Pinguet T, Sahni S, De Dobbelaere P. "A grating-coupler-enabled CMOS photonics platform". IEEE J Sel Topics Quantum Electron. 17, 597–608, 2011.

[6] Sun J, Timurdogan E, Yaacobi A, Hosseini ES, Watts MR. "Large-scale nanophotonic phased array". Nature 493, 195–199, 2013.

[7] Abediasl H, Hashemi H. "Monolithic optical phased-array transceiver in a standard SOI CMOS process". Opt Express. 23, 6509–6519, 2015.

[8] Aflatouni F, Abiri B, Rekhi A, Hajimiri A. "Nanophotonic projection system". Opt Express. 23, 21012–21022, 2015.

[9] Heck M. J. R. Highly integrated optical phased arrays: photonic integrated circuits for optical beam shaping and beam steering" Nanophotonics 6, 93-107, 2017.

[10] H. Subbaraman, M. Y. Chen, and R. T. Chen, "Photonic crystal fiber based true-time-delay beamformer for multiple RF beam transmission and reception of an X-band phased-array antenna" J. Lightwave Technol. 26, 2803–2809, 2008.

[11] Soref, R. A., De Leonardis, F., and Passaro, V. M. N. "Integrated On-Chip Bragg Time-Delay system for Thermo-Optical control of a microwave antenna," J. Lightwave Technol. 36, 5849–5856, 2018.

[12] Song, C., Gao, Y., Wang, G., Chen, Y., Xu, P., Gu, C., Shi, Y., & Shen, X. "Compact nonvolatile 2×2 photonic switch based on two-mode interference". Opt Express, 30, 30430, 2022.

Liquid Crystal Thin Films for Low-Cost Large-Area Diffractive Optical Gratings with Excellent Efficiency

K. Neyts[1*], M. Stebryte[2], F. Van Acker[2], S. Liu[2], X. Ke[1], and I. Nys[2]

[1]SKLADT, the Hong Kong University of Science and Technology, Hong Kong
[2]LCP group, LCP Department, Ghent University, Belgium
[*]corresponding author: eeneyts@ust.hk

Abstract: Liquid crystals are soft materials which self-organize in 3D structures that may have a photonic band gap that in the visible range. Variable boundary conditions at the surfaces that enclose the liquid crystal layer can encode a geometric phase, leading to diffractive optical elements with very high efficiency.

Liquid crystals (LC) are well known for their ability to modify the polarization of light in electronic displays. However, LCs are also used to fabricate thin film diffractive optical elements with remarkable properties. Compared to photorefractive materials the variation in refractive index is much higher (typically 0.2 instead of 0.01), which leads to a much wider photonic band gap. Compared to metamaterials, the variation in refractive index is more smooth, which leads to much higher diffraction efficiencies.

The fabrication of LC diffractive gratings is based the illumination of a thin layer of photosensitive material with linearly polarized blue or UV light [1]. The polarization of the illumination determines the average alignment of the LC's long molecular axis, called the director. By using interference illumination, the director orientation at the surface can vary rapidly over the area and periodic structures with period as low as 200 nm have been demonstrated. Different types of LC material can be used. For nematic LC the lowest energy state is obtained when the director orientation is homogeneous. Rapid variations of the director require a lot of elastic energy (Figure 1a) and this sets a lower boundary for the period in the grating [2]. Chiral LC is a soft material which self-organizes in a helical structure with pitch determined by the chemical composition of the LC mixture. In this case very short periods may be obtained [3-7], as illustrated in Figure 1b. Finally blue phase (BP) LC has a more complex 3D arrangement of double twist cylinders in a cubic lattice. In this case the period is in the order of 200 – 300 nm [8].

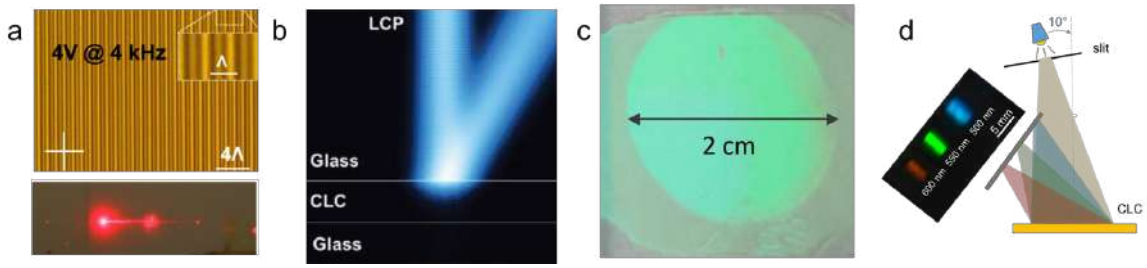

Figure 1: a) linear grating with high diffraction efficiency, from [9]; b) numerical simulation of diffracted circularly polarized light on a chiral LC grating, from [4]; c) 2 cm diffractive grating with lens functionality [10]; d) setup for a single component diffractive grating, from [10].

The LC diffractive gratings operating in transmission or reflection are based on the geometric phase, which is usually smooth, continuous, but at the same time have complex features to encode optical functionalities such

as lensing. A high efficiency is obtained for circularly polarized light. In transmission, the handedness of the circular polarization is reversed if the LC layer behaves as a half wave plate, and the azimuthal orientation of the director determines the geometric phase. In reflection, the handedness of the circular polarization remains the same and the geometric phase is again determined by the orientation of the director at the surface. Reflective gratings can achieve high efficiency (>90% in the first diffraction order) even for high diffraction angles (>45^{o} in a glass substrate). A single component spectrometer demonstrates how lensing and diffraction can be combined in LC reflective diffractive components, as illustrated in Figures 1c and 1d [10].

The 3D material structure, anisotropic properties and optical simulation of nematic and chiral LC will be discussed and applications will be presented.

References

1. Chigrinov, V.G.; Kozenkov, V.M.; Kwok, H.S., Photoalignment of Liquid Crystalline Materials: Physics and Applications; John Wiley & Sons: Chichester, UK, 2008; pp. 1–231.
2. Chulwoo Oh and Michael J. Escuti, Achromatic diffraction from polarization gratings with high efficiency, Opt. Lett. 33, 2287-2289 (2008).
3. Lee Yun-Han, Kun Yin, Shin-Tson Wu, Reflective polarization volume gratings for high efficiency waveguide-coupling augmented reality displays, Opt. Express 25 (22) (Oct 2017) 27008–27014.
4. Nys, I., Migle Stebryte, Yera Ye. Ussembayev, Jeroen Beeckman, Kristiaan Neyts, Tilted chiral liquid crystal gratings for efficient large-angle diffraction, Adv. Opt. Mater. 7 (22) (2019) 1901364.
5. Stebryte, M. , Inge Nys, Yera Ye. Ussembayev, Jeroen Beeckman, Kristiaan Neyts, Large angle forward diffraction by chiral liquid crystal gratings with inclined helical axis, Crystals 10 (9) (2020).
6. Zhang, S. et al., Twisting Structures in Liquid Crystal Polarization Gratings and Lenses. Crystals 2021, 11, 243.
7. Van Acker, Frederik, Bo-han Lin, Chun-ta Wang, Kristiaan Neyts, Jeroen Beeckman, Defect modes generated in a stack of spin coated chiral liquid crystal layers, Crystals, accepted
8. Liu, Sunqian, et al. “Two-Step Photoalignment with High Resolution for the Alignment of Blue Phase Liquid Crystal.” ADVANCED OPTICAL MATERIALS, vol. 10, no. 17, 2022.
9. Nys, I., S. Liu, Y.-N. Huang, O. Strzeżysz, P. Kula, K. Neyts, Geometric Phase Flat Optical Gratings with High Diffraction Angle Based on Dual-Frequency Nematic Liquid Crystal. Adv. Optical Mater. 2023, 11, 2300972.
10. Stebryte, M., Inge Nys, Jeroen Beeckman, Kristiaan Neyts, Chiral liquid crystal based holographic reflective lens for spectral detection (2022) OPTICS EXPRESS. 30(24). p.42829-42839.

AES 2024, ROME - ITALY, 25 –28 JUNE 2024

Redox-tunable conducting polymer plasmonics and metasurfaces

Magnus Jonsson[1]

[1] Organic Photonics and Nanooptics Group, Laboratory of Organic Electronics, Linköping University, Sweden

*corresponding author: magnus.jonsson@liu.se

Abstract: Conducting polymers can function as redox-tunable plasmonic materials, opening for chemically and electrically controlled nanooptics and metasurfaces.[1-3] I will present the background to this emerging area of nanooptics and discuss recent results, including based on straining conducting polymers to induce redox-tunable hyperbolic properties.[4]

References:

1. Conductive polymer nanoantennas for dynamic organic plasmonics
   S. Chen, E. S. H. Kang, M. S. Chaharsoughi, V. Stanishev, P. Kühne, H. Sun, C. Wang, M. Fahlman, S. Fabiano, V. Darakchieva and M. P. Jonsson
   Nature Nanotechnology 2020, 15, 35-40
2. Electrical Tuning of Plasmonic Conducting Polymer Nanoantennas
   A. Karki, G. Cincotti, S. Chen, C. Wang, V. Stanishev, V. Darakchieva, M. Fahlman and M. P. Jonsson
   Advanced Materials 2022, 34, 13, 2107172
3. Doped Semiconducting Polymer Nanoantennas for Tunable Organic Plasmonics
   A. Karki, Y. Yamashita, S. Chen, T. Kurosawa, J. Takeya, V. Stanishev, V. Darakchieva, S. Watanabe and M. P. Jonsson
   Communications Materials 2022, 3, 48
4. Tuneable anisotropic plasmonics with shape-symmetric conducting polymer nanoantennas
   Y. Duan, A. Rahmanudin, S. Chen, N. Kim, M. Mohammadi, K. Tybrandt and M. P. Jonsson
   Advanced Materials 2023, 35, 51, 2303949

AES 2024, ROME - ITALY, 25 –28 JUNE 2024

Precision Unleashed: Coherence-Moderated Sensing for Simultaneous Accuracy and High Bandwidth

J. Dickmann[1,2,3*]

[1]Technical University of Braunschweig, Institute for Semiconductor Technology, Hans-Sommer-Str. 66, 38106 Braunschweig, Germany
[2]LENA (Laboratory for Emerging Nanometrology), Langer Kamp 6a/b, 38106 Braunschweig, Germany
[3]CAVITY technologies UG (haftungsbeschränkt), Wilhelmsgarten 3, 38100 Braunschweig, Germany
[*]corresponding author: j.dickmann@tu-braunschweig.de

Abstract: I present an interferometric approach to length measurement in which interferometer visibility and mid-fringe detection are combined. Numerical simulations and experimental results demonstrate the effectiveness of the proposed method.

In sensing and metrology, reconciling accuracy, measurement range, and speed poses a challenge. Interferometric sensors, renowned for high precision, often compromise range due to periodicity. This contribution introduces a concept leveraging the limited coherence of the measuring laser, offering both ultra-high accuracy and an extensive measurement range. This breakthrough has implications for precision manufacturing [1], biomedical sensing [2], and structural health monitoring [3]. We detail the experimental implementation and showcase measurement results, affirming the efficacy of this approach.

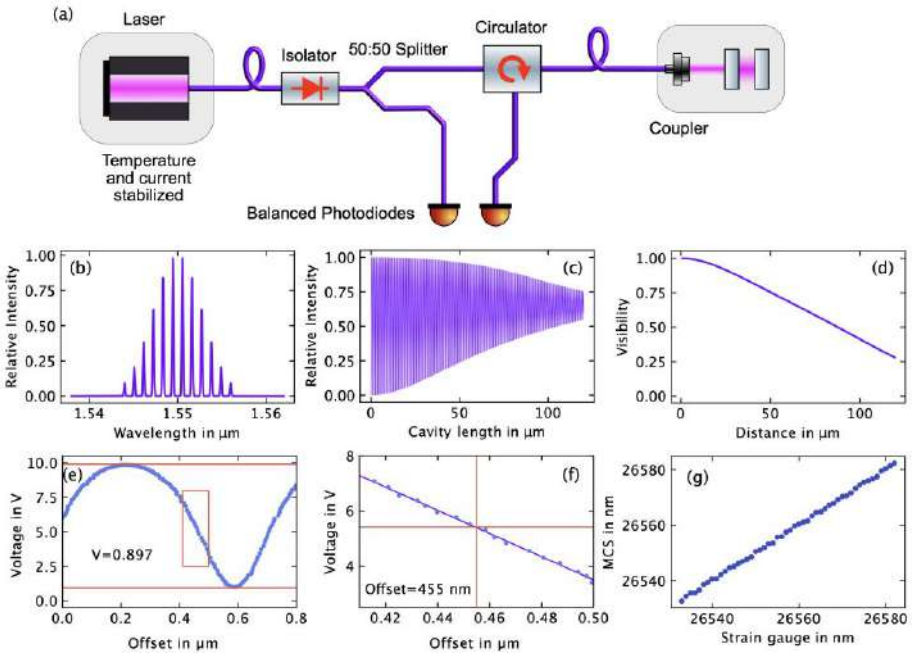

Figure 1: (a) Schematic of the coherence-moderated sensing scheme. (b) Typical emission spectrum of a Fabry-Pérot laser diode. (c) Calculated reflection signal of the measurement cavity. (d) Calculated visibility versus length of the measurement cavity. (e) Real-time measurement signal, recorded by scanning the measurement cavity. (f) Detail of (e). (g) Results of the displacement-step experiment for the determination of measurement accuracy.

The experimental setup for the length measurement, illustrated in Fig. 1 (a), employs a Fabry-Pérot laser diode (Thorlabs FPL1009S) with moderate coherence. The laser output is directed into a cavity comprising two parallel silicon mirrors with a refractive index of n = 3.4757 at a wavelength of λ = 1.55 μm [4], creating a metastable resonator with a finesse of 2.65 [5]. The interference signal, generated by the laser lines (Fig. 1 (b)), diminishes with cavity length (Fig. 1 (c)), and its reflection is measured using the circulator in Fig. 1(a). Visibility (V) is computed from the raw signal using the formula [6]:

$$V = \frac{I_j^{\max} - I_j^{\min}}{I_j^{\max}}, \tag{1}$$

where $I_j^{\max}$ and $I_j^{\min}$ represent the intensity of the maximum and minimum of the j-th fringe. Fig. 1 (d) displays the visibility obtained via a peak-finding algorithm. Utilizing a ring piezo (Thorlabs PA44M3KW, resonant frequency 150 kHz), the cavity length is detuned by 0.8 μm for each measurement, ensuring the capture of an entire fringe (Fig. 1(e)). The decreasing visibility serves as an absolute length measure, and by calculating the exact position of the mid-fringe for the measured visibility (here V = 0.897), the starting point of the measurement is determined. Real-time linear regression (Fig. 1(f)) establishes the offset, subtracted from the calculated mid-fringe position to achieve the accurate cavity length. The method was tested in a displacement-step experiment (Fig. 1(g)), demonstrating an accuracy of better than one nm for a measurement range of 120 μm.

The developed coherence-moderated sensing system can be used for photonic-integrated measurement of temperature, acceleration, pressure and all other measured variables that can be traced back to the change in length of an optical cavity.

Acknowledgements: Funded by the Deutsche Forschungsgemeinschaft (DFG, German Research Foundation) under Germany's Excellence Strategy—EXC-2123 QuantumFrontiers—390837967 and by European Association of National Metrology Institutes. This project (20FUN08 NEXTLASERS) has received funding from the EMPIR programme co-financed by the Participating States and from the European Union's Horizon 2020 research and innovation programme.

References

1. Yang, S. and Zhang, G., "A review of interferometry for geometric measurement," Meas. Sci. Technol., Vol. 29, 102001, 2018.
2. Kavcic, A., et al., "Deep tissue localization and sensing using optical microcavity probes," Nat. Commun., Vol. 13, 1269, 2022.
3. Kosowska, M., et al., "Low-coherence photonic method of electrochemical process monitoring," Sci. Reports, Vol. 11, 12600, 2021.
4. Li, H., "Refractive index of silicon and germanium and its wavelength and temperature derivatives," J. Phys. Chem. Ref. Data, Vol. 9, 561-658, 1980.
5. Ismail, N., et al., "Fabry-pérot resonator: spectral line shapes, generic and related airy distributions, linewidths, finesses, and performance at low or frequency-dependent reflectivity," Opt. express, Vol. 24, 16366-16389, 2016.
6. Dickmann, J., et al., "Moderate-coherence sensing with optical cavities: ultra-high accuracy meets ultra-high measurement bandwidth and range," Commun. Eng., Vol. 3, No. 1, 17, 2024.

AES 2024, ROME - ITALY, 25 –28 JUNE 2024

Hybridized Silicon Metasurface with Two-Dimensional Nanomaterials for Perfect Absorption

Junichi Takahara[1,2*]

[1]Graduate School of Engineering, Osaka University, Japan
[2] Photonics Center, Graduate School of Engineering, Osaka University, Japan
[*]corresponding author: takahara@ap.eng.osaka-u.ac.jp

Abstract: We study hybridized silicon metasurface with atomically-thin two-dimensional nanomaterials to enhance the absorption. We design Mie resonators based on degenerate critical coupling principle and demonstrate the enhancement of absorptivity of exciton mode at visible range in transition-metal dichalcogenide (WS_2) as well as perfect absorption of graphene at 1550nm.

Hybridized metasurfaces with two-dimensional (2D) nanomaterials such as graphene and transition-metal dichalcogenide (TMDC) have been investigated intensively and they can be applied to next-generation optoelectronic devices in the future [1]. The high mobility and transparency of monolayer graphene, combined with its flexibility and environmental stability, are suitable for ultrafast photonic devices. In contrast to graphene, most TMDC such as tungsten sulfide (WS_2) have a direct-band gap and exciton modes with large binding energy, which are suitable for efficient emission/modulation devices. However, for instance the absorptivity of Dirac electrons in graphene is only 2.3% for any wavelength. Such weak interaction between light and those atomically-thin 2D materials prevents to realize actual photonic devices. In order to overcome the above limitation, we have proposed hybridized system (see Fig. 1) of silicon metasurface with 2D nanomaterials based on the principle of degenerate critical coupling (DCC) [2,3].

In this talk, I will talk about hybridized silicon metasurface with graphene as well as WS_2 to enhance the absorption significantly. First, I will review our studies about an embedded silicon (Si) perfect absorber (PA) in the visible region by radiative loss control based on DCC. I will demonstrate the absorption enhancement by 15.5 times in monolayer WS_2 formed on Si metasurface by DCC of electric dipole (ED) and magnetic dipole (MD) modes. Then, I will talk about PA at 1.55μm by monolayer graphene formed on hollow cuboidal Si metasurface which supports toroidal electric dipoles (TED). We will present how to realize the hybridized metasurface to transfer monolayer graphene/hBN onto the Mie resonators.

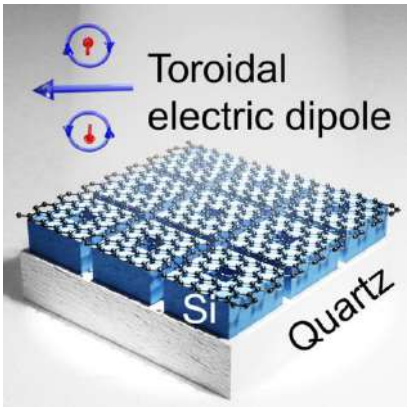

Fig. 1 Hybridized hollow cuboidal Si metasurface with graphene [3].

References

1. C.W. Qiu, T. Zhang, G. Hu, and Y. Kivshar, “Quo Vadis, Metasurfaces?”, Nano Lett. Vol. 21, 5461-5474, 2021.
2. R. Xu and J. Takahara, “Radiative loss control of an embedded silicon perfect absorber in the visible region,” Opt. Lett., Vol. 46, No. 4, 805–808, 2021.
3. R. Xu, J. Fujikata, and J. Takahara, “Graphene perfect absorber based on degenerate critical coupling of toroidal mode,” Opt. Lett., Vol. 48, No. 6, 1490-1493, 2023.

AES 2024, ROME - ITALY, 25 –28 JUNE 2024

Transparent Materials with Low Radiative Cooling Efficiency

Kotaro Kajikawa*

Tokyo Institute of Technology, Japan
*corresponding author: kajikawa@ee.e.titech.ac.jp

Abstract: Radiative cooling (RC) materials have been extensively studied, but transparent materials without RC performance have yet to be studied. Most transparent materials have a certain high RC performance, but there are cases where it is better to have no RC. An example is the freezing of car windshields in winter. Our research group studied transparent materials having low RC performance. As a result, we found that metamaterials of silver nanowire-dispersed polymers have such properties.

Radiative cooling (RC) materials have been extensively studied because they can cool objects without electricity [1]. On the other hand, transparent materials without RC performance have not been studied. Most transparent materials have a certain RC performance, but there are cases where it is better to have no RC. An example is the freezing of car windshields in winter. At midnight, the windshield is sometimes covered with a cloth to prevent a freeze. Our research group studied transparent materials having low RC performance.

We have investigated transparent "non-radiative materials (non-RC)" materials. The materials investigated are glass plates coated with ITO (Indium Tin Oxide), DMD (dielectric/metal/dielectric: AZO(Aluminum-doped Zinc Oxide)/Ag/AZO), and AgNWs (silver nanowires) dispersed in a polymer matrix. They are transparent in the visible region and highly reflective in the mid-infrared region.

The RC measurements were performed in both in-house and in-field setups. The temperature reduction, defined as $\Delta T = T_{amb} - T_{samp}$, was measured in both cases, where T_{amb} and T_{samp} are the ambient and the sample temperatures, respectively.

The temperature reduction measured in the field was negligible for ITO and DMD, whereas that for a glass plate was 1.5 K. The reduction for AgNW dispersed in a polymer matrix was 0.3 K, which is lower than that of a glass plate. These results show that they can be used as non-RC materials.

References

1. Raman, A. P., Anoma, M. A., Zhu, L., Rephaeli, E., and Fan, S., “Passive radiative cooling below ambient air temperature under direct sunlight”, Nature, Vol. 515, 540-544, 2014.

AES 2024, ROME - ITALY, 25 –28 JUNE 2024

Mid-infrared dielectric antennas on epsilon-near-zero material for sensing

Paolo Biagioni[1*], Francesco Rusconi[1], Pierre Felhen[2], Fernando Gonzalez-Posada[3], Laurent Cerutti[3], Giovanni Pellegrini[4], Marco Finazzi[1], Thierry Taliercio[3]

[1]Dipartimento di Fisica, Politecnico di Milano, Milano, 20133 Italy
[2]NSE3 (CNRS UMR3208) Institut franco-allemand Saint-Louis, France
[3]IES, Univ Montpellier, UMR CNRS 5214, Montpellier, France
[4]Dipartimento di Fisica, Università di Pavia, Pavia, Italy
[*]corresponding author: paolo.biagioni@polimi.it

Abstract: We introduce a sensing platform based on mid-infrared dielectric antennas engineered on a heavily doped semiconductor acting as an epsilon-near-zero material, which is employed to improve the conditions for efficient light confinement and sharp localized resonances in dielectric antenna resonators. We benchmark the system with surface-enhanced infrared absorption experiments.

Nanoantennas play a major role in light manipulation at the nanoscale, thanks to the highly confined and enhanced electromagnetic fields associated with localized and collective resonances [1]. The traditional materials of choice for nanoantennas are noble metals, however, there are intrinsic limitations associated to their use. In fact, plasmonic resonances suffer from ohmic losses, affecting the quality factor and the lifespan of the antenna itself. Moreover, magnetic resonances supported by metallic plasmonic antennas are weak, which is detrimental for specific applications such as those requiring enhanced optical chirality [2, 3].

In the last years, dielectric nanoantennas have been proposed as an alternative to plasmonics. While there are many demonstrations for dielectric nanoantennas working in the visible and near-infrared spectral range [3-6], their extension to the mid infrared (MIR) is not yet fully established. In particular, the epitaxial growth of crystalline semiconductor materials, which are the preferred choices for high-quality dielectric antennas working in the MIR, typically relies on a similar semiconductor substrate, with a refractive index close to the one of the antenna. This environment configuration hinders the establishment of strong resonances for dielectric antennas in the MIR.

In this work, as a solution to this problem, we employ an InAs layer as the substrate [7]. By properly varying the doping of the InAs layer during the layer growth, we obtain a material showing a zero crossing of the real part of the permittivity, the so-called epsilon-near-zero (ENZ) condition [8], that can be tuned over a broad wavelength range in the MIR. We fabricate an array of dielectric nanoantennas on top of the ENZ substrate exploiting an undoped InAs layer by standard e-beam lithography (Figure 1a). By spectrally overlapping the localized and lattice resonance frequencies of the antenna array with the ENZ frequency of the substrate, we observe a pronounced resonance (Figure 1b). Numerical electromagnetic simulations also demonstrate that the associated field enhancements are expected to reach values similar to the ideal situation of the same antennas in vacuum.

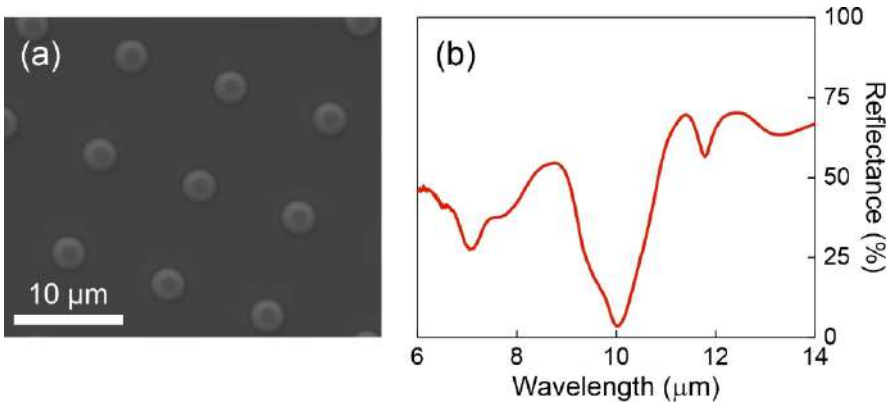

Figure 1 Scanning electron microscope top view of the InAs nanoantennas (panel a) and the spectral response of the array (panel b), highlighting the occurrence of the designed resonance around 10 µm wavelength.

To assess the perspectives for molecular sensing in the fingerprint region, we also perform surface-enhanced infrared absorption experiments by coating the antenna array with a layer of perfluorooctyltrimethoxysilane (PFTMS) molecules. Comparison of the spectra acquired with and without the molecular layer clearly highlight the coupling between the localized dielectric resonances and the vibrational absorption lines of the molecules. The demonstration of an efficient dielectric platform working in the MIR opens therefore new possibilities in surface-enhanced spectroscopy, biosensing, and chiroptical analysis.

References

1. Biagioni, P., J.-S. Huang and B. Hecht, "Nanoantennas for visible and infrared radiation", Rep. Prog. Phys., Vol. 75, No. 2, 024402, 2012.
2. García-Etxarri, A. and J. Dionne, "Surface-enhanced circular dichroism spectroscopy mediated by nonchiral nanoantennas", Phys. Rev. B, Vol. 87,235409, 2013.
3. García-Guirado, J., M. Svedendahl, J. Puigdollers and R. Quidant, "Enhanced Chiral Sensing with Dielectric Nanoresonators", Nano Lett., Vol. 20, No. 1, 585-591, 2020.
4. Albella, P., R.A. de la Osa, F. Moreno and S.A. Maier, "Electric and Magnetic Field Enhancement with Ultralow Heat Radiation Dielectric Nanoantennas: Considerations for Surface-Enhanced Spectroscopies", ACS Photonics, Vol. 1, No. 6, 524-529, 2014.
5. Kuznetsov, A.I., A.E. Miroshnichenko, M.L. Brongersma, Y.S. Kivshar and B. Luk'yanchuk, "Optically resonant dielectric nanostructures", Science, Vol. 354, No. 6314, 2472, 2016.
6. Zilli, A., D. Rocco, M. Finazzi. A. Di Francescantonio, L. Duò, C. Gigli, G. Marino, G. Leo, C. De Angelis and M. Celebrano, "Frequency Tripling via Sum-Frequency Generation at the Nanoscale", ACS Photonics, Vol. 8, No. 4, 1175-1182, 2021.
7. Bahro, B.F., F. Gonzalez-Posada, M.-J. Milla-Rodrigo, M. Bomers, L. Cerutti and T. Taliercio, "All-semiconductor plasmonic gratings for biosensing applications in the mid-infrared spectral range", Opt. Exp., Vol. 24, No. 14,16175-16190, 2016.
8. Kim. J, A. Dutta, G.V. Naik, A.J. Giles, F.J.Bezares, C.T. Ellis, J.G. Tischler, A.M.Mahmoud, H. Caglayan, O.J. Glembocki, A.V. Kildishev, A. Boltasseva and N. Engheta, "Role of epsilon-near-zero substrates in the optical response of plasmonic antennas", Optica, Vol. 3, No. 3, 339-346, 2016.

Crystallization of Induce Optical Vortex by Bessel Beams

Sahil Sahoo and Yuri Gorodetski*
Electrical and Electronic Engineering department,
Ariel University, 407000, Ariel, Israel
* corresponding author: yurig@ariel.ac.il

Abstract

The process of optical vortex formation through interference patterns culminates in the creation of an optical vortex lattice. Our study illustrates the gradual emergence of optical vortices and their crystallization within the array, resulting in the formation of an optical vortex lattice. This phenomenon is exemplified through the implementation of a Bessel beams array on the plasmonic metasurface.

1 Introduction

Optically driven vortex lattices have opened up new and interesting applications in optics. These lattices have a pivotal function in the construction of the pseudo vortex structures in the ultra-cold atomic Bose-einstein condensates gas.[1] Furthermore, they are important in the creation process of photonic crystal fabrication.[2] The generation of these lattices is achieved through beam interference. Researchers have propelled the field forward by employing multi-beam interference techniques. This involves utilizing circularly polarized illumination through the metasurfaces with orthogonal nano-slit pairs, combined with spiral segments, contributing to the generation of optical vortex lattice fields.[3] These fields result from the combination of geometric and dynamic phases, creating intricate lattice patterns.[2,3]

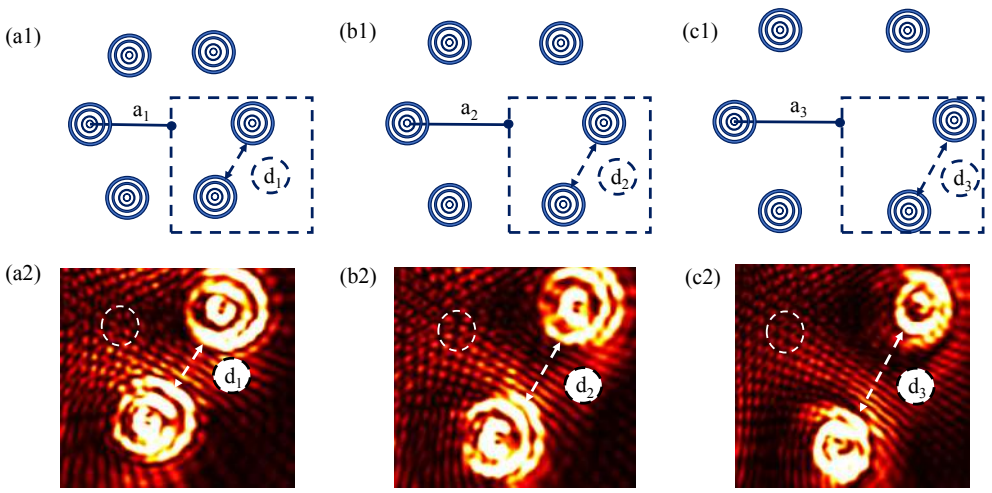

Figure 1: In Figures (a1), (b1), and (c1), we depict the hexagonal arrangement of Bessel beams with hexagonal radii of $8\lambda_{spp}$, $9\lambda_{spp}$, and $11\lambda_{spp}$ respectively. Consequently, the separation distance between the Bessel beams increases, as indicated by $d_1 < d_2 < d_3$. In Figures (a2), (b2), and (c2), we illustrate the evolution of vortices for different array sizes. As the distance changes, these vortices eventually converge towards the center to form a crystalline structure of vortex lattice.

Advanced techniques, including spin-based plasmonic effects with different geometries, further enhance the formation of optical lattice structures by directing plasmonic waves towards the centre of the geometry, enabling superposition and intricate pattern creation.[4] Plasmonic waves arise from the interaction of an electromagnetic (EM) wave with a metallic subwavelength structure. This interaction entails coupling EM waves with confined electronic oscillations which are known as surface plasmon polaritons (SPPs). The near-field intensity distribution of SPPs is influenced by the polarization state of the incident beam. By designing a plasmonic cavity with a polarization-dependent geometric phase, a plasmonic vortex Bessel beam can be produced.[5] We have demonstrated how the core region of a hexagonal array of Bessel beams at each corner may exhibit intricate interference patterns caused by plasmonic waves. The emergence of an optical vortex lattice is governed by the intrinsic topological characteristics of this configuration and the modifications made to the hexagonal array size. The interference of plasmonic waves leads to the formation of vortices, and as the array size increases, these vortices appear to merge successively, ultimately forming the complete lattice of vortices as shown in Figure 1. The gradual formation of the vortex lattice mirrors offering an intriguing analogy to crystallization process. While researchers have studied vortices crystallization in the rotation of atomic-molecular Bose-Einstein by thermal quenching,[6,7] there is still a knowledge gap concerning the formation of vortex crystals through plasmonic wave interference, which we are studying by gradually increasing the array size. The sequential addition of vortices suggests that the vortex formation occurs during interference, however, it appears that changing the array size causes the initially generated vortices to move toward more stable energy state. Eventually, the energy reaches a point of maximum stability, culminating in the formation of a vortex crystal. Moreover, the vortex lattice demonstrates remarkable topological stability, it appears to be able to preserve its structure regardless of disturbances such as the blocking of a single Bessel beam from the array. This shows the lattice exhibits remarkable topological stability, making it resilient to the disturbance.

References

[1] J. R. Abo-Shaeer, C. Raman, J. M. Vogels, and W. Ketterle, "Observation of vortex lattices in bose-einstein condensates," *Science*, vol. 292, no. 5516, pp. 476–479, 2001.

[2] R. Zhang, Y. Zhang, L. Ma, X. Zeng, X. Li, Z. Zhan, X. Ren, C. He, C. Liu, and C. Cheng, "Nanoscale optical lattices of arbitrary orders manipulated by plasmonic metasurfaces combining geometrical and dynamic phases," *Nanoscale*, vol. 11, pp. 14024–14031, 2019.

[3] H. Gao, Y. Li, L. Chen, J. Jin, M. Pu, X. Li, P. Gao, C. Wang, X. Luo, and M. Hong, "Quasi-talbot effect of orbital angular momentum beams for generation of optical vortex arrays by multiplexing metasurface design," *Nanoscale*, vol. 10, pp. 666–671, 2018.

[4] S. Tsesses, R. Dahan, K. Wang, T. Bucher, K. Cohen, O. Reinhardt, G. Bartal, and I. Kaminer, "Tunable photon-induced spatial modulation of free electrons," *Nature Materials*, vol. 22, p. 345–352, Jan. 2023.

[5] Y. Gorodetski, A. Niv, V. Kleiner, and E. Hasman, "Observation of the spin-based plasmonic effect in nanoscale structures," *Phys. Rev. Lett.*, vol. 101, p. 043903, Jul 2008.

[6] S.-W. Su, C.-H. Hsueh, I.-K. Liu, T.-L. Horng, Y.-C. Tsai, S.-C. Gou, and W. M. Liu, "Spontaneous crystallization of skyrmions and fractional vortices in fast-rotating and rapidly quenched spin-1 bose-einstein condensates," *Phys. Rev. A*, vol. 84, p. 023601, Aug 2011.

[7] C.-F. Liu, H. Fan, S.-C. Gou, and W.-M. Liu, "Crystallized and amorphous vortices in rotating atomic-molecular bose-einstein condensates," *Scientific reports*, vol. 4, p. 4224, 02 2014.

AES 2024, ROME - ITALY, 25 –28 JUNE 2024

Tunable Bound States in the Continuum in Magneto-Optic and Graphene Metasurfaces

J. L. Pura,[1] J. R. Deop-Ruano,[2] D. R. Abujetas,[3] A. Manjavacas,[2] V. Giannini,[1] A. García-Martín,[4] J. A. Sánchez-Gil[1,*]

[1]Instituto de Estructura de la Materia (IEM), CSIC, Madrid, Spain
[2]Instituto de Óptica (IO), CSIC, Madrid, Spain
[3]Universidad de Castilla La Mancha, Toledo, Spain
[4]Instituto de Micro y Nanotecnología (IMN), CSIC, Tres Cantos, Spain
[*]corresponding author: *j.sanchez@csic.es*

Abstract: Bound states in the continuum (BICs) emerging in planar particle arrays (metasurfaces) have attracted much interest lately in photonics. In this work, magnetic and electric means to actively manipulate two kinds of symmetry-protected BICs are presented on the basis of either magneto-optic or graphene meta-atoms.

Bound states in the continuum (BICs) have attracted much interest lately in photonics for their (theoretically) infinite Q factor. These states lie in the radiation continuum, but counterintuitively cannot couple to any radiation channel[1]. A common approach is to exploit metasurfaces, planar arrays in the non-diffractive regime, which limit the outgoing channels to only the specular ones, which can in turn be suppressed by tuning the parameters of the system in various manners, leading to symmetry-protected[2] or accidental BICs[3]. Nonetheless, whereas tunable metasurfaces based on a variety of mechanisms have been proposed, the active tunability of symmetry-protected BICs remains largely unexplored, mostly due to the strong dependence on geometrical constraints. In this regard, magnetically or electrically controllable metasurfaces might be suitable platforms for active manipulation of BICs, based on either MO or graphene meta-atoms. These structures can manipulate electromagnetic waves with high efficiency and flexibility, enabling a wide range of potential applications in areas such as sensing, imaging, and communications[4,5].

In this work, we propose two kinds of metasurfaces to actively control the transition between BICs and quasi-BICs, breaking the corresponding protecting symmetries by MO or electrical manipulation. One is based on all-dielectric, single meta-atom metasurfaces with magneto-optical activity[7], supporting a symmetry-protected BIC stemming from a vertical-dipole resonance (as shown for e.g. Bi:YIG nanodisks): upon applying a magnetic field parallel to the metasurface and perpendicular to the plane of incidence, we show that the MO activity induced terms in the meta-atom polarizabilities equivalent to tilting the vertical dipole resonances, thus allowing for tuning and switching the BIC[7].

The second one is based on graphene metasurfaces, artificially engineered sheets of graphene disposed in periodic arrays of subwavelength-scale[8]. In particular, we propose a configuration consisting of a square array of graphene microdisk dimers, which supports bound states in the continuum (BICs) in the IR for both TE and TM polarizations[9], arising at the Γ-point due to the π-rotation symmetry of the array. In order to break the symmetry of the array to obtain quasi-BICs, typically done by (passively) changing the geometry of the unit cell, we propose here to induce different Fermi levels with an external voltage to the graphene microdisks in each dimer, otherwise identical in shape. The Fermi level directly affects graphene conductivity, and hence its polarizability,

making them asymmetric as far as the π-rotation symmetry of the polarizabilities is concerned.

In summary, we propose two (magnetic and electric controllable) means to break the BIC symmetry in a controlled manner for two different metasurfaces supporting symmetry-protected BICs in the visible and IR domains with the following unit cells, respectively: single magneto-optic nanodisks and graphene microdisk dimers.

We acknowledge the financial support from the grants BICPLAN6G (TED2021-131417B-I00), LIGHTCOMPAS (PID2022-137569NB-C41 and PID2022-137569NB-C42), and TEM-FLU PID2019-109502GA-I00 funded by MCIU/AEI/10.13039/501100011033, "ERDF A way of making Europe", and European Union NextGenerationEU/PRTR. We also acknowledge the financial support from a Margarita Salas contract CONVREC-2021-23 (University of Valladolid and European Union NextGenerationEU), a predoctoral fellowship from the MCIN/AEI assigned to Grant No. PID2019-109502GA-I00 and a 2022 Leonardo Grant for Researchers in Physics, BBVA Foundation.

References

1. C. W. Hsu, B. Zhen, A. D. Stone, D. D. Joannopoulos, and M. Solijacic, "Bound states in the continuum," Nature Review Materials, Vol. 1, 16048, 2016.
2. D. R. Abujetas, N. van Hoof, S. Huurne, J. Gómez-Rivas, and J. A. Sánchez-Gil, "Spectral and temporal evidence of robust photonic bound states in the continuum on terahertz metasurfaces," Optica, Vol. 6, 996, 2019.
3. D. R. Abujetas, J. Olmos-Trigo, J. A. Sánchez-Gil, "Tailoring Accidental Double Bound States in the Continuum in All-Dielectric Metasurfaces," Adv. Opt. Mat., Vol. 10, 2200301, 2022.
4. B. Yu, L. Huang, X. Li, and Y. Wang, ''Magnetically controllable metasurface and its application,'' Front. Optoelectron., vol. 4, pp. 154−169, 2021.
5. T. Guo and C. Argyropoulos, "Recent advances in terahertz photonic technologies based on graphene and their applications", Adv. Photonics Res., Vol. 2, 2000168, 2021.
6. D. R. Abujetas, Nuno de Sousa, A. García-Martín, J. M. Llorens, J. A . Sánchez-Gil, "Active angular tuning and switching of Brewster quasi bound states in the continuum in magneto-optic metasurfaces", Nanophotonics, Vol. 10, 4223, 2021.
7. D. R. Abujetas, Nuno de Sousa, A. García-Martín, J. M. Llorens, J. A . Sánchez-Gil, "Active angular tuning and switching of Brewster quasi bound states in the continuum in magneto-optic metasurfaces", Nanophotonics, Vol. 10, 4223, 2021.
8. J. R. Deop-Ruano, S. Sanders, A. Alabastri, W. J. M. Kort-Kamp, D. A. R. Dalvit, and A. Manjavacas, "Optical Response of Periodic Arrays of Graphene Nanodisks", Phys. Rev. Applied, Vol. 18, 044071, 2022.
9. J. L. Pura, J. R. Deop-Ruano, D. R. Abujetas, A. Manjavacas, V. Giannini, J. A. Sánchez-Gil, "Tunable bound states in the continuum in active metasurfaces of graphene disk dimers," Nanophotonics, Vol. 12, 4453, 2023.

AES 2024, ROME - ITALY, 25 –28 JUNE 2024

Magnetic control of electrically uncharged magneto-optical particles

M. I. Marqués[1*], S. Edelstein[2], P.A.Serena [2,] B. Castillo López de Larrinzar [3]and A. García-Martín[3]

[1]Departamento de Física de Materiales, IFIMAC and Instituto de Física de Materiales Nicolás Cabrera" Universidad Autónoma de Madrid, 28049 Madrid, Spain
[2]Instituto de Ciencia de Materiales de Madrid (ICMM-CSIC), Campus de Cantoblanco, 28049 Madrid, Spain
[3]Instituto de Micro y Nanotecnología IMN-CNM, CSIC,CEI UAM+CSIC, Isaac Newton 8, Tres Cantos, 28760 Madrid, Spain
[*]corresponding author: manuel.marques@uam.es

Abstract: In this work we present a method to perform magnetic control of electrically uncharged particles based on magneto-optical materials illuminated by a spinning monochromatic light field. We analyze the behavior of these particles under different isotropic optical configurations, and we calculate the value of the induced magnetic charge.

Constant magnetic fields are known to interact with electrically charged particles inducing Lorentz forces that point in a direction perpendicular to the field. However, if the particle is electrically discharged, it is impossible to induce a force using a constant magnetic field. An exotic option is to mimic a magnetic charge on a neutral particle. This false magnetic monopole will interact with the magnetic field just as an electric charge would do with an electric field through the Coulomb interaction. Attempts to generate this magnetic charge have mainly relied on quasiparticles generated using condensed matter spin ice networks [1-3]. In this work we present another option based on neutral magneto-optical particles illuminated by a spinning monochromatic light field [4]. We will analyze the behavior of these particles under different fluctuating isotropic optical configurations [5,6], and we will calculate the value of the induced magnetic charge. We will prove that this is a purely non-reciprocal effect as the reciprocal equivalent (a chiral dipole) despite presenting a dichroic response, does not experience any force when illuminated by the spinning field. The magnetic charge induced by impinging radiation on the magneto-optical dipole is found to depend linearly on the helicity of the field. In addition, this artificial monopole experiences a dichroic permanent optical torque and does not interact with an external electric field.

We acknowledge financial support from the Spanish Ministry of Science and Innovation (MCIN), AEI and FEDER (UE) through projects PID2022-137569NB-C43, PID2022-137569NB-C41 and TED2021-131417B-I00 and the María de Maeztu (CEX2018-000805-M) Program for Centers of Excellence.

References

1. S. T. Bramwell, S. R. Giblin, S. Calder, R. Aldus, D. Prabhakaran, and T. Fennell, Measurement of the charge and current of magnetic monopoles in spin ice, Nature 461, 956 (2009).
2. S. J. Blundell, Monopoles, magnetricity, and the stray field from spin ice, Phys. Rev. Lett. 108, 147601 (2012).
3. C. Castelnovo, R. Moessner, and S. L. Sondhi, Magnetic monopoles in spin ice, Nature 451, 42 (2008).

4. S. Edelstein, R. M. Abraham-Ekeroth, P. A. Serena, J. J.Saenz, A. Garcia-Martin, and M. I. Marques, Magnetooptical stern-gerlach forces and nonreciprocal torques on small particles, Phys. Rev. Res. 1, 013005 (2019).
5. J. Luis-Hita, M. I. Marques, R. Delgado-Buscalioni, N. de Sousa, L. S. Froufe-Perez, F. Scheold, and J. J.Saenz, Light induced inverse-square law interactions between nanoparticles: “mock gravity" at the nanoscale, Phys. Rev. Lett. 123, 143201 (2019).
6. J. Luis-Hita, J. J. Saenz, and M. I. Marques, Active motion induced by random electromagnetic fields, ACS Photonics 9, 1008 (2022).

AES 2024, ROME - ITALY, 25 –28 JUNE 2024

Pushing the Limit of Multiplexing Capacity in Optical Metasurfaces

Yongmin Liu[1,2,*]

[1]Department of Mechanical and Industrial Engineering, Northeastern University, Boston, Massachusetts, USA
[2]Department of Electrical and Computer Engineering, Northeastern University, Boston, Massachusetts, USA
[*]corresponding author: y.liu@northeastern.edu

Abstract: We apply both physics-guided and data-driven approaches to push the limit of multiplexing capacity in optical metasurfaces. As a result, a single metasurface can generate distinct functions, such as holograms and focusing lenses, by varying the wavelength and polarization of the incident light.

Over the past decade, we have witnessed tremendous progress and success of optical metasurfaces. By tailoring the geometry of the building blocks of metasurfaces and engineering their spatial distribution, we can control the amplitude, polarization state, phase and trajectory of light in an almost arbitrary manner.[1-2] For practical applications such as high-capacity optical display, information encryption, and data storage, it is crucial to encode distinct functionalities into a single meta-device and increase the information channels. In this talk, I will present our recent works that aim to push the multiplexing limit in optical metasurfaces through both physics-guided and data-driven approaches. In the first part of my talk, I will show that we can break the fundamental limit of polarization multiplexing capacity of metasurfaces by introducing the engineered noise to the precise solution of Jones matrix elements.[3] We experimentally demonstrate up to 11 independent holographic images using a single metasurface illuminated by visible light with different polarizations. To the best of our knowledge, it is the highest capacity reported for polarization multiplexing. Combining our noise engineering method with the position multiplexing scheme, we design and demonstrate another metasurface that can generate 36 distinct images, forming a holographic keyboard pattern. In the second part of my talk, I will show that machine learning enables us to accelerate the development of complex metasurfaces (and other photonic structures) with high efficiency, accuracy and fidelity.[4-5] The developed machine learning models, after training, can evaluate the optical responses of metasurfaces and inversely design them in less than seconds. We propose to embed machine learning models in both gradient-based and nongradient optimization loops for the automatic implementation of multifunctional metasurfaces.[6] Fundamentally different from the traditional two-step approach that separates phase retrieval and meta-atom structural design, the proposed end-to-end framework facilitates full exploitation of the prescribed design space and pushes the multifunctional design capacity to its physical limit. With a single-layer structure that can be readily fabricated, metasurface focusing lenses and holograms are experimentally demonstrated in the near-infrared region. They show up to eight controllable responses subjected to different combinations of working frequencies and linear polarization states.

Acknowledgements: The work was supported by the National Science Foundation under grants 2202268 and ECCS-1916839.

References

1. Yu, N.; Genevet, P.; Kats, M. A.; Aieta, F.; Tetienne, J.-P.; Capasso, F.; Gaburro, Z., Light propagation with phase discontinuities: generalized laws of reflection and refraction. *Science* **2011,** *334* (6054), 333-337.
2. Kildishev, A. V.; Boltasseva, A.; Shalaev, V. M., Planar Photonics with Metasurfaces. *Science* **2013,** *339* (6125),

1232009.
3. Xiong, B.; Liu, Y.; Xu, Y.; Deng, L.; Chen, C.-W.; Wang, J.-N.; Peng, R.; Lai, Y.; Liu, Y.; Wang, M., Breaking the limitation of polarization multiplexing in optical metasurfaces with engineered noise. *Science* **2023,** *379* (6629), 294-299.
4. Ma, W.; Liu, Z.; Kudyshev, Z. A.; Boltasseva, A.; Cai, W.; Liu, Y., Deep learning for the design of photonic structures. *Nature Photonics* **2021,** *15*, 77-90.
5. Xu, Y.; Xiong, B.; Ma, W.; Liu, Y., Software-defined nanophotonic devices and systems empowered by machine learning. *Progress in Quantum Electronics* **2023**, 100469.
6. Ma, W.; Xu, Y.; Xiong, B.; Deng, L.; Peng, R. W.; Wang, M.; Liu, Y., Pushing the limits of functionality‐multiplexing capability in metasurface design based on statistical machine learning. *Advanced Materials* **2022,** *34* (16), 2110022.

AES 2024, ROME - ITALY, 25 –28 JUNE 2024

Tailoring the emission and the photodynamics of quantum emitters with simple and optimized high-index dielectric nanostructures

Mélodie Humbert[1,2], R. Hernandez[1,2], Peter R. Wiecha[3], Jonas Muller[3], Etienne Palleau[2], Frank Fournel[4], Vincent Larrey[4], Aurélie Lecestre[3], Guilhem Larrieu[3], Christian Girard[1], Vincent Paillard[1], Laurence Ressier[2], and Aurélien Cuche[1,*]

[1]CEMES-CNRS, Université de Toulouse, CNRS, UPS, Toulouse, France
[2]LPCNO, Université de Toulouse, CNRS, INSA, UPS, 135 Avenue de Rangueil, 31077 Toulouse, France
[3]LAAS-CNRS, Université de Toulouse, CNRS, INP, Toulouse, France
[4]Université Grenoble Alpes, CNRS, CEA-Leti Minatec, Grenoble, France
*corresponding author, E-mail: aurelien.cuche@cemes.fr

Abstract: Through experimental and theoretical methods, we demonstrate the controllable photodynamics of quantum emitters (NV colored centers in nanodiamonds) precisely positioned near silicon dimer nanoantennas using AFM nanoxerography. Then, by designing specific geometries with an evolutionary optimization algorithm, we explore enhancing the directional emission of these quantum sources numerically.

Introduction

Improving the brightness and efficiency of single photon sources by the mean of optically resonant nanostructures is a major stake for the development of efficient nanodevices for quantum communications.

For a couple of decades, these resonant nanostructures have mainly been made of noble metal that sustain strong localized resonances (LSPR) that can be used to manipulate, concentrate or redirect visible light. Such properties have led to numerous actual or potential applications in integrated optics, sensors, nonlinear optics, field-enhanced spectroscopies, or photovoltaics. Recently, an alternative emerged with high refractive index dielectric nanostructures, which offer the same range of applications as plasmonics by manipulating Mie optical resonances instead of LSPR [1].

These resonances can be efficiently tuned by modifying the size, shape, and material of those nanostructures (e.g. silicon, n ~ 4) [2]. Furthermore, high index dielectric nanostructures offer several key advantages when compared to their metallic counterparts: absorption losses are far weaker for wavelengths longer than the direct band gap, access to semiconductor (CMOS) technology for nanostructure fabrication, and presence of intrinsic strong magnetic and electric resonances, providing an unique opportunity to spatially separate and redistribute the energy of the magnetic and electric parts of the electromagnetic field in the near field, otherwise inextricably connected in the far field [3].

Discussion

We discuss here the effect of simple high index dielectric nanoantennas on the spontaneous emission of model quantum emitters. First, we accurately positioned arrays of nanodiamonds hosting NV colored centers in the gap

of silicon dimer nanoantennas, using atomic force microscopy (AFM – [4]) nanoxerography [5]. The NV center is an ideal model system exhibiting single photon emission properties at room temperature, which is well adapted for proof of concept experiments in quantum nano-optics. Since the emission rate of the emitters, and therefore the local density of photonic states (LDOS), are modified by the nanostructure, we show by the mean of time-resolved photoluminescence acquisitions that the photodynamics of these emitters can be enhanced by the coupling to the nanoantenna down to the single photon emission regime [5]. Our experimental results are in good agreement with multipolar analysis and numerical simulations based on the Green Dyadic Method - GDM.

Next, to go a step further, we numerically investigate controlling the directional emission of quantum dipolar sources using complex Si antennas. These antennas, composed of specific numbers of building blocks, are optimized via an Evolutionary Algorithm (EA). The resulting geometries enable precise tailoring of emission direction, enhancing light intensity within defined solid angles. Our numerical experiments demonstrate the effectiveness of these EA-optimized antennas.

Acknowledgements

This work was supported by Programme Investissements d'Avenir under the program ANR-11-IDEX-0002-02, reference ANR-10-LABX-0037-NEXT, by the HiLight ANR project ANR-19-CE24-0026, by LAAS-CNRS micro and nanotechnologies platform member of the French Renatech network, by the CNRS and INSA (M.H. PhD grant), by the Région Midi-Pyrénées via the Institute for Quantum technologies in Occitanie (IQO), and by the computing facility center CALMIP of the University of Toulouse under grants P12167 and P1107.

References

1. Kallel, H., Arbouet, A., Benassayag, G., Chehaidar, A., Poti, A., Salem, B., Baron, T., Paillard, V., "Tunable enhancement of light absorption and scattering in Si1xGex nanowires", Phys. Rev. B 12, 085318, 2012.
2. Wiecha, P.R., Cuche, A., Arbouet, A., Girard, C., Colas des Francs, G., Lecestre, A., Larrieu, G., Fournel, F., Larrey, V., Baron, T., Paillard, V., "Strongly directional scattering from dielectric nanowires", ACS Photonics 4, 2036, 2017.
3. Wiecha, P.R., Majorel, C., Girard, C., Arbouet, A., Masenelli, B., Boisron, O., Lecestre, A., Larrieu, G., Paillard, V., Cuche, A., "Enhancement of electric and magnetic dipole transition of rare-earth-doped thin films tailored by high-index dielectric nanostructures", Appl. Opt. 58, 1682, 2019.
4. Humbert, M., Hallez, Y., Larrey, V., Fournel, F., Palleau, E., Paillard, V., Cuche, A., Ressier, L., "Versatile, rapid and robust nanopositioning of single-photon emitters by AFM-nanoxerography", Nanotechnology 33, 215301, 2022.
5. Humbert, M., Hernandez, R., Mallet, N., Larrieu, G., Larrey, V., Fournel, F., Guérin, F., Palleau, E., Paillard, V., Cuche, A., Ressier, L., "Large-scale controlled coupling of single-photon emitters to high index dielectric nanoantennas using AFM nanoxerography", Nanoscale 15, 599, 2023.

AES 2024, ROME - ITALY, 25 –28 JUNE 2024

Cylindrical vector beams for control of light emission of quantum emitters coupled to silicon nanoantennas

M. Montagnac[1], J-M. Poumirol[1], A. Cuche[1], Y. Brûlé[2], G. Colas des Francs[2], J. Müller[3], G. Larrieu[3], V. Larrey[4], F. Fournel[4], O. Boisron[5], B Masenelli[5], G. Agez[1] and V. Paillard[1*]

[1] CEMES-CNRS, Université de Toulouse, Toulouse, France.
[2]ICB, Université de Bourgogne, CNRS, Dijon, France
[3]LAAS-CNRS, Université de Toulouse, Toulouse, France
[4]CEA-LETI, Université Grenoble-Alpes, Grenoble, France
[5]Université de Lyon, Université Lyon 1, CNRS UMR 5510, ILM, Villeurbanne, France.

[*]corresponding author: vincent.paillard@cemes.fr

Abstract: Controlling the light emission of quantum emitters coupled to optically resonant nanostructures is essential for the development of efficient nanosources of light and for enhanced spectroscopies [1]. The photoluminescence (PL) intensity of a quantum emitter at a position **r** around a nanoantenna is given the following equation [2]:

$$I(\mathbf{r}, \omega_{exc}, \omega_{em}) = P_{exc}(\mathbf{r}, \omega_{exc}) \times \phi_{em}(\mathbf{r}, \omega_{em}) \times C_{coll}(\mathbf{r}, \omega_{em}) \quad (1)$$

where $P_{exc}(\mathbf{r},\omega_{exc})$ is the excitation rate proportional to the pump at the excitation angular frequency, $\phi_{em}(\mathbf{r},\omega_{em})$ is the quantum yield related to the photon local density of states (LDOS) at the emission angular frequency, and $C_{coll}(\mathbf{r},\omega_{em})$ is the collection efficiency. Most works have been devoted to LDOS engineering for emission rate control [3] and/or to dipole positioning for emission directivity control [4]. In contrary, the pump influence has been rarely considered experimentally.

We investigate in the nonsaturated regime the influence of focused cylindrical vector beams on the PL of a europium ion-doped thin film deposited on silicon nanorings, used as nanoantennas. We demonstrate that the shape and polarization of the excitation beam can be used to manipulate light emission of quantum emitters, as azimuthally or radially polarized cylindrical vector beam offers to spatially separate the electric and magnetic fields, in addition to the effect of the silicon nanorings resonant at the excitation wavelength [5-6]. Thus, radial and azimuthal polarized beams exciting ring-shape nanoantennas allow engineering the near field hot spots, hence the silicon nanoring Raman signal and the local Eu^{3+} PL enhancement.

The experimental results of PL and Raman mappings are in very good agreement with FDTD numerical simulations giving the electric near field either in the Si ring (to describe the Raman signal) or in the luminescent thin film (to describe the PL behavior). An interesting result is to obtain as function of the polarization and the nanoring size either a ring-like shape or a centered spot for the enhanced PL signal (see figure 1). We also evidence that beyond near-field effects, the PL signal at the emission wavelength is function of the nanoring size, hence-LDOS dependent. More complex nanoantenna structures could be designed to optimize the three parameters controlling the PL intensity as given by equation 1.

We acknowledge partial funding from ANR (project HiLight ANR 19-CE24-0020-01), University of Toulouse supercomputing facility (CALMIP projects P12167 and P19042), and LAAS nanotechnology platform (member of RENATECH network).

References

1. Bidault, S., Mivelle, M., and Bonod, N. “Dielectric nanoantennas to manipulate solid-state light emission,” J. Appl. Phys. **126**, 094104 (2019).
2. Koenderink, A. F. “Single photon nanoantennas,” ACS Photon. **4**, 722 (2017).
3. Brûlé, Y., *et. al,* “Magnetic and electric Purcell factor control through geometry optimization of high index dielectric nanostructures,” Opt. Express **30**, 20360 (2022).
4. Hernandez R., *et al.* “Directional silicon nanoantennas for quantum emitter control designed by evolutionary optimization”, J. Opt. Soc. Am. B **41**, 108 (2024)
5. Montagnac, M., *et al*. “Engineered near- and far-field optical response of dielectric nanostructures using focused cylindrical vector beams,” J. Appl. Phys. **131**, 133101 (2022).
6. Montagnac, M., *et al*. “Control of light emission of quantum emitters coupled to silicon nanoantenna using cylindrical vector beams,” Light: Sci. & Appl. **12**, 239 (2023).

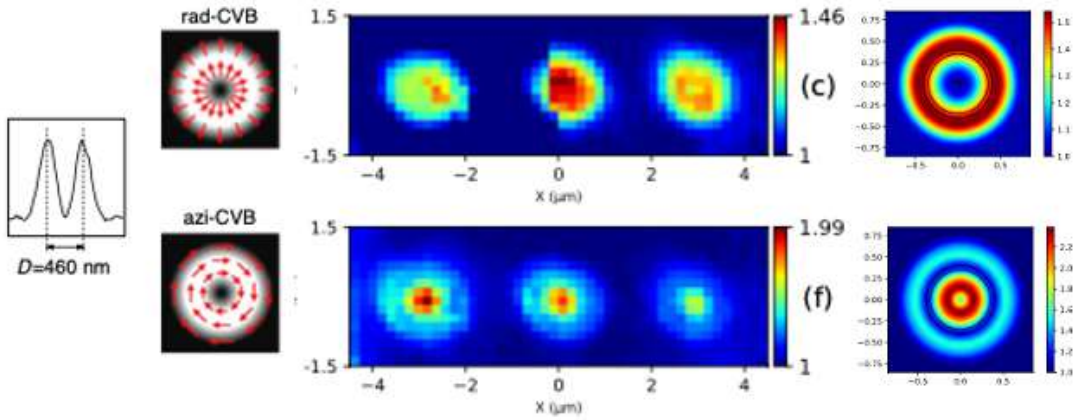

Figure 1: PL mapping of Eu3+-doped thin film on Si nanorings (radius from 500, 450, 400 nm from left to right, width of 50 nm, height of 90 nm). The polarization is either radial (upper row) or azimuthal (lower row). The right column corresponds to FDTD simulations for each polarization of the electric near field in the luminescent thin film (nanoring radius of 400 nm)

AES 2024, ROME - ITALY, 25 –28 JUNE 2024

Enhancing Electric and Magnetic Light-Matter Interactions with Plasmonic Nanoantennas

Sébastien Bidault
Institut Langevin, ESPCI Paris, Université PSL, CNRS, France
sebastien.bidault@espci.fr

Abstract: Using DNA nanotechnology and scanning probe microscopy, we demonstrate that a strong coupling regime can be reached between quantum emitters and a gold nanoantenna at room temperature, but also that the magnetic component of light-matter interactions can be manipulated for lanthanide ions in the near-field of a plasmonic cavity.

Light-matter interactions in condensed media at room-temperature are fundamentally limited by electron-phonon coupling. In order to render the exceptional optical properties of single quantum systems (such as indistinguishable single-photon emission and nonlinearities) accessible without the need for cryogenic environments, it is essential to enhance and optimize their interaction cross-sections with light. Plasmonic antennas have shown amazing promise towards this goal thanks to their ability to enhance optical fields by several orders of magnitude in deeply sub-wavelength volumes.

To this end, we exploit DNA molecules to create plasmonic resonators with a control over both their nanoscale dimensions and their chemical environment. Using this strategy, we were able to reach a strong-coupling regime between a gold nanodimer and 5 organic molecules [1]. We propose the DNA-based assembly of dimers of plasmonic nanocubes in order to provide reproducible single-molecule strong coupling [2] and to make the coherent interaction of light with single quantum emitters feasible at room temperature.

Plasmonic nanoantennas also have the ability to manipulate independently the electric and magnetic components of light in order to interact with electric or magnetic transitions in solid-state emitters such as lanthanide ions. Using an aluminum nanoantenna milled at the end of a scanning-probe tip, we can control both stimulated excitation and spontaneous emission processes, mediated by either electric or magnetic transition dipoles [3]. By tuning the relative distance between a Eu^{3+}-doped nanoparticle and the nanoantenna, we can map the distributions of electric and magnetic fields as well as the electric and magnetic local densities of optical states with subwavelength resolution [4], demonstrating the versatility of plasmonic antennas in manipulating and enhancing light-matter interactions at the nanoscale.

References

1. Heintz, J., N. Markešević, E. Y. Gayet, N. Bonod, and S. Bidault, “Few-Molecule Strong Coupling with Dimers of Plasmonic Nanoparticles Assembled on DNA,” ACS Nano 15, 1473, 2021.
2. Heintz, J., F. Legittimo, and S. Bidault, “Dimers of Plasmonic Nanocubes to Reach Single-Molecule Strong Coupling with High Emission Yields,” Journal Title Abbreviation, J. Phys. Chem. Lett. 13, 11996, 2022
3. Reynier, B., E. Charron, O. Markovic, X. Yang, B. Gallas, A. Ferrier, S. Bidault and M. Mivelle, “Full control of electric and magnetic light-matter interactions through a nanomirror on a near-field tip”, Optica 10, 841, 2023.
4. Reynier, B., E. Charron, O. Markovic, B. Gallas, A. Ferrier, S. Bidault and M. Mivelle, “Nanoscale Control over Magnetic Light-Matter Interactions”, arXiv:2402.00666, 2024.

AES 2024, ROME - ITALY, 25 –28 JUNE 2024

Moderate-refractive-index nanoantennas for QD fluorescence enhancement

R. Ramos[1], A.I. Barreda[1], and B. García-Cámara[1,*]

[1]Group of Displays and Photonic Applications, Carlos III University of Madrid, Spain

[*]corresponding author: braulio.garcia@uc3m.es

Abstract: Single-photon sources are promising devices due to its importance in applications such as quantum devices. Improvements on the excitation and emission efficiencies are required. In this work, we design resonant nanostructures based on both plasmonic and moderate-refractive-index materials to manage photons at the excitation and emission wavelengths of CdSe/ZnS quantum dots.

The growing demand of nanoscale light-emitting diodes (nano-LEDs) requires a strong enhancement of the photoluminescence properties of quantum emitters, e.g. quantum dots, as well as the design of strategies to manage and direct the emitted photons into the desired direction [1,2]. While fluorescence enhancement can be achieved by increasing the pump intensity in the surroundings of the quantum emitter, the guiding of the emitted photons into the collection system requires larger efforts [3,4]. In this way, the use of resonant nanoantennas is widely spread in the last years for these tasks. Plasmonic nanoparticles [5] and also plasmonic nanoparticles on-mirror [6] has a large capability of tightly confine the light field and providing large Purcell factors. In contrast, plasmonic materials suffer from ohmic losses. On the other hand, high-refractive index dielectric nanoparticles (HRID NPs) have been probed as remarkable structures without inherent losses in the visible range and with the ability of shaping the scattering patterns [7]. However, their fluorescence enhancement capability is still far from that of plasmonic methods. For this reason, hybrid methods are currently explored, combining the high confinement of the plasmonic structures and the directionality capabilities of dielectric ones [8]. Additionally, in the last years, a new kind of resonant nanoparticles with promising properties has been proposed. There are called moderate-refractive-index nanoparticles, and they can support similar Mie resonances of HRID NPs offering a new opportunity [9, 10].

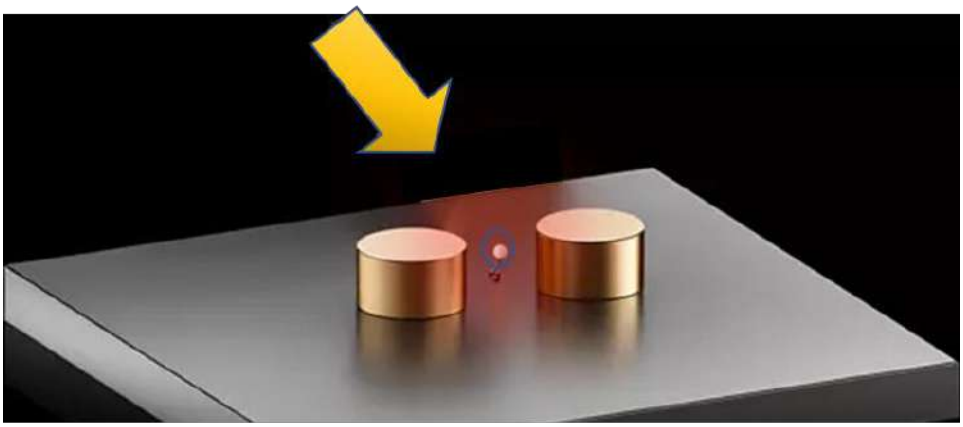

Figure 1. Scheme of the proposed structure where nanoparticles are arranged as dimers combining made of different materials

In this sense, in this work, we explore the ability of enhancing the fluorescence of quantum dots by means of hybrid dimers of nanostructures combining both metallic and moderate-refractive index nanoparticles, as shown in Figure 1, with the aim of finding a novel design that can provide large confinements such as plasmonic nanoparticles and directionality capabilities like high-refractive-index dielectric nanoaparticles.

Acknowledgements. This work was funded by the Spanish Research Agency (AEI) through the project No. PID2022-137857NA-I00. A.B. thanks MICINN for the Ramon y Cajal Fellowship (grant No. RYC2021-030880-I). R.R thanks also the Spanish Research Agency (AEI) for his predoctoral grant.

References

1. Koenderink, F. A.,"Single-photon nanoantennas," ACS Photonics, Vol. 4, 710– 722, 2017.
2. Romeira, B., J. Borme, H. Fonseca, J. Gaspar and J.B. Nieder, "Efficient light extraction in subwavelength GaAs/AlGaAs nanopillars for nanoscale light-emitting devices," Opt. Express, Vol. 28, No. 22, 32302-32315, 2020.
3. Wu, T, M. Gurioli, and P. Lalanne, "Nanoscale Light Confinement: the Q's and V's," ACS Photonics, Vol. 8, No. 6, 1522–1538, 2021.
4. Song, Y., R. Liu, Z. Wang, H. Xu, Y. Ma, F. Fan, O. Voznyy and J. Du, "Enhanced emission directivity from asymmetrically strained colloidal quantum dots," Science Adv., Vol. 8, No. 8, eabl8219, 2022.
5. Song, B. Z.Jiang, Z. Liu, Y.Wang, et al. "Probing the Mechanisms of Strong Fluorescence Enhancement in Plasmonic Nanogaps with Sub-nanometer Precision", ACS Nano, Vol. 14, No. 11, 14769-14778, 2020.
6. Baumberg, J. J., J. Aizpurua, M.H. Mikkelsen and D.R.Smith, " Extreme nanophotonics from ultrathin metallic gaps," Nat. Materials 2019, Vol. 18, 668– 678 2019.
7. Barreda, A. S. Hell, M.A. Weissflog, A. Minovich, T. Pertsch and I. Staude, "Metal, dielectric and hybrid nanoantennas for enhancing the emission of single quantum dots: A comparative study," J. Quant. Spectros. Rad. Trans, Vol. 276, 107900, 2021.
8. Dmitriev, P.A, E. Lassalle, L, Ding et al. "Hybrid dielectric-plasmonic nanoantenna with multiresonances for subwavelength photon sources," ACS Photonics, Vol. 10, 582–594, 2023.
9. Kim, S., S. Lepeshov, A. Krasnok and A. Alu, "Beyond Bounds on Light Scattering with Complex Frequency Excitations" Phys. Rev. Lett., Vol. 129, 203601, 2022.
10. Wu, Y., R. Sun, S. Zhang and S. Wu, "Synthesis of Dielectric Nanospheres with Moderate-Refractive-Index and Applications in Photon Manipulating," Eur. J. Inorg. Chem. Vol. 26, e202200665, 2023.

AES 2024, ROME - ITALY, 25 –28 JUNE 2024

Gain-controlled nonlinearity and interactions in wave-based neuromorphic photonic systems

Giulia Marcucci[1], Luana Olivieri[2] and Juan Sebastian Totero Gongora[2,*]
[1]School of Physics and Astronomy, University of Glasgow, United Kingdom
[2]Emergent Photonics Research Centre, Dept. of Physics, Loughborough University, United Kingdom
[*]Corresponding author: j.totero-gongora@lboro.ac.uk

Abstract: In this presentation, we analyse the optimal learning conditions for a gain-controlled, nonlinear wave reservoir computing system based on erbium-doped multimode fibres.

Physical reservoir computing involves harnessing the dynamics of a physical system, such as an optical or electronic device, to perform computational tasks [1]. The system denoted as the reservoir, processes input signals through its dynamic response, and the desired output is obtained by linearly combining the reservoir's response with appropriate readout mechanisms. This approach exploits the rich dynamics of complex physical systems to solve various tasks efficiently, ranging from signal processing to regression, classification, and sensing.

Nonlinear waves in multimode systems are rapidly emerging as a compelling substrate for optical reservoir computing. Unlike standard neuromorphic photonic systems, where artificial neurons are mapped one-to-one to interconnected photonic devices, wave-based photonic reservoirs encode and process information entirely in the optical domain, enabling significant parallelism within single optical components [2]. The computational capabilities of wave-based reservoirs rely on the interplay between optical nonlinearity (e.g., cubic nonlinearities in optical fibres or nonlinear crystals) and complex wave interactions (e.g., in linear scattering media) [3–6]. Recent results suggest wave-based reservoirs must exceed a specific degree of nonlinearity or configurational disorder to achieve an effective learning [3]. The primary rationale is that the role of the reservoir is to project the input data into a high-dimensional space of nonlinear features expressed in a physical system in the observable degrees of freedom of the state of the system [7]. However, nonlinearity and disorder are generally fixed by the geometric and material properties of the photonic device, and a detailed analysis of the critical thresholds in nonlinearity and complexity required to perform computations is still critically missing.

In this context, light-matter interactions in gain media provide an ideal platform to investigate the mutual interplay between complexity and nonlinearity [8]. Gain media, such as erbium-doped fibres or semiconductor amplifiers, can induce nonlinear optical effects due to the saturation of their amplification processes [9]. As the intensity of the optical signal increases, the gain medium's response becomes nonlinear, leading to phenomena such as gain saturation, four-wave mixing and mode-locking. Additionally, nonlinear effects in gain media can facilitate mode coupling, where different modes of the optical signal interact and exchange energy, enabling the manipulation and transformation of the signal within the medium.

This presentation will discuss our recent theoretical results on a gain-controlled, nonlinear wave reservoir based on erbium-doped multimode fibres (ED-MMF) [10]. In our approach, reservoir computing is implemented by shaping the wavefront of the pump and probe beams in the fibre [11]. Thanks to the nonlinear interactions between signal and pump modes within the gain medium, we show how the ED-MMF implements a tuneable

nonlinear transformation of the input field, where the degree of nonlinear coupling between different fibre modes can be controlled through easily accessible global parameters of the system, such as pump and signal power. The ability to dynamically tune the degree of nonlinearity in our system enables us to identify the best operating conditions for our reservoir by investigating the numerical and information-theoretical properties of the measurement matrix for different degrees of nonlinear coupling.

This work was supported by the UK Engineering and Physical Sciences Research Council (EPSRC, Grant number EP/W028344/1) and The Leverhulme Trust (Leverhulme Early Career Fellowship ECF-2023-315).

References

1. G. Tanaka, T. Yamane, J. B. Héroux, R. Nakane, N. Kanazawa, S. Takeda, H. Numata, D. Nakano, and A. Hirose, "Recent advances in physical reservoir computing: A review," Neural Netw. **115**, 100–123 (2019).
2. B. J. Shastri, A. N. Tait, T. Ferreira de Lima, W. H. P. Pernice, H. Bhaskaran, C. D. Wright, and P. R. Prucnal, "Photonics for artificial intelligence and neuromorphic computing," Nat. Photonics **15**(2), 102–114 (2021).
3. G. Marcucci, D. Pierangeli, and C. Conti, "Theory of Neuromorphic Computing by Waves: Machine Learning by Rogue Waves, Dispersive Shocks, and Solitons," Phys. Rev. Lett. **125**(9), 093901 (2020).
4. U. Teğin, M. Yıldırım, İ. Oğuz, C. Moser, and D. Psaltis, "Scalable optical learning operator," Nat. Comput. Sci. **1**(8), 542–549 (2021).
5. D. Pierangeli, D. Pierangeli, D. Pierangeli, G. Marcucci, C. Conti, C. Conti, and C. Conti, "Photonic extreme learning machine by free-space optical propagation," Photonics Res. **9**(8), 1446–1454 (2021).
6. S. Gigan, "Imaging and computing with disorder," Nat. Phys. **18**(9), 980–985 (2022).
7. M. Dale, J. Dewhirst, S. O'Keefe, A. Sebald, S. Stepney, and M. A. Trefzer, "The Role of Structure and Complexity on Reservoir Computing Quality," in *Unconventional Computation and Natural Computation*, I. McQuillan and S. Seki, eds. (Springer International Publishing, 2019), **11493**, pp. 52–64.
8. J. S. Totero Gongora, A. E. Miroshnichenko, Y. S. Kivshar, and A. Fratalocchi, "Anapole nanolasers for mode-locking and ultrafast pulse generation," Nat. Commun. **8**, 15535 (2017).
9. M. Rowley, P.-H. Hanzard, A. Cutrona, H. Bao, S. T. Chu, B. E. Little, R. Morandotti, D. J. Moss, G.-L. Oppo, J. S. Totero Gongora, M. Peccianti, and A. Pasquazi, "Self-emergence of robust solitons in a microcavity," Nature **608**(7922), 303–309 (2022).
10. G. Marcucci, L. Olivieri, and J. S. Totero Gongora, "Optimal learning in reservoir computing systems based on gain-controlled multimode fibres," under review (2024).
11. R. Florentin, V. Kermene, J. Benoist, A. Desfarges-Berthelemot, D. Pagnoux, A. Barthélémy, and J.-P. Huignard, "Shaping the light amplified in a multimode fiber," Light Sci. Appl. **6**(2), e16208 (2017).

AES 2024, ROME - ITALY, 25 –28 JUNE 2024

Photonic Neuromorphic Computing

F. Brückerhoff-Plückelmann[1,2], J. Dijkstra[2], I. Bente[1], and W. Pernice[1,2*]

[1] Physical Institute, University of Münster; Münster, 48149, Germany
[2]Kirchhoff-Institute for Physics, University of Heidelberg; Heidelberg, 69120, Germany
[*]corresponding author: wolfram.pernice@kip.uni-heidelberg.de

Abstract: Photonics enables multiple degrees of freedom for parallel data processing and unique circuit designs. We discuss computation schemes based on the incoherent superposition of optical pulses and show different applications. Exemplary, we present a prototype fabricated in the Silicon on Insulator platform for optical convolution processing.

The development of deep neural networks for image recognition and natural language processing led to a significant demand for computational power. For example, state-of-the-art models like GPT-3 from OpenAI consist of 175 billion parameters and take about 1.3 GWh to train [1]. Neuromorphic computing architectures aim to improve data processing by emulating the working principles of biological brains. In particular, parallel in-memory computing enables large throughput with minimal power dissipation. Photonic data processing allows for multiple degrees of freedom, especially wavelength division multiplexing, for parallel computing and memory addressing.

First, we demonstrate a photonic hardware accelerator for matrix-vector multiplications (MVMs) which lie at the heart of artificial neural networks. We deploy a solely power-based encoding scheme and avoid phase sensitivity by choosing a sufficient wavelength detuning between the various optical pulses propagating through the circuit. We perform the MVMs with a photonic crossbar array that effectively implements a tunable beamsplitter network. Here we encode the input vectors in the power of optical pulses of different wavelengths which simultaneously propagate through a tunable beamsplitter network. The matrix weights are encoded into attenuators setting the coupling. In this way, the attenuators serve as memory and computation units simultaneously. Finally, we measure the optical power at the outputs of the crossbar array to obtain the results of the MVM, effectively reducing the computation to a transmission measurement [2,3].

Figure 1A shows a photonic crossbar array integrated in the Silicon on Insulator platform. We couple the optical carrier signals via a fiber array to the chip and deploy electro-absorption modulators (EAMs) to encode the input vectors on the carriers. For the MVM, a 9x3 crossbar array implements a beam splitter network, weighting and overlapping the input pulses. For weighting, we again use EAMs. At the output, integrated photodetectors measure the power in the components. All electronic components are bonded to a PCB connected to DACs and ADCs controlled by a single FPGA.

Convolution processing is a natural choice for photonic computing, due to the comparable small matrix sizes and large amount of data. We load a Sobel filter for edge detection into the crossbar array and pixel-wise modulate the input image of the Münster castle, Figure 1B, to the input EAMs. Figure 1C shows measured optical power at the output of the crossbar, clearly highlighting the edges. At the expense of switching speed and switching power, non-volatile memory can be used within the crossbar instead of the EAMs, for example, the phase change material Germanium-Antimony-Telluride (GST). In this way, no static power supply is required to hold the state of the memory [2].

Going one step further, also non-linearities can be integrated into the circuit to emulate a full artificial neural network. By using the switching properties of GST as a non-linearity and making use of wavelength multiplexing for addressing, also large-scale optical neural networks can be realized [4].

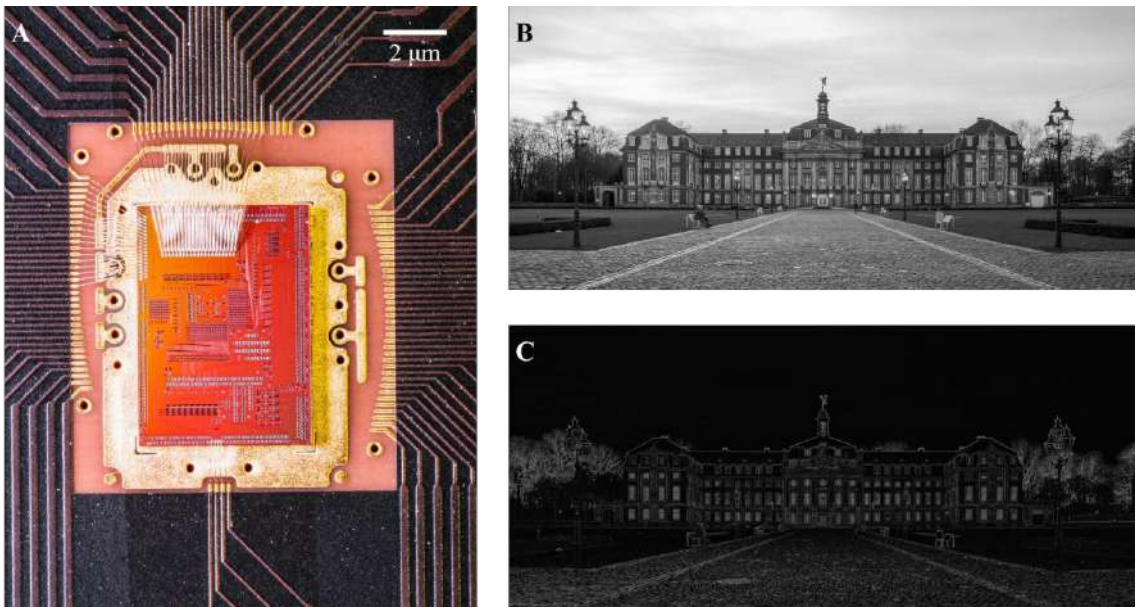

Figure 1 Incoherent Photonic Matrix Processor for Convolution Processing. A, We fabricate the chip on the Silicon on Insulator platform. We couple the optical carrier signals via directional couplers to the crossbar array, consisting of electro-absorption modulators for input and weight encoding and photodetectors to measure the output vector. We glue and bond the chip to a printed circuit board. **B,** We deploy multiple high-voltage DACs to load the kernel values in the crossbar array and use high-speed DACs of an FPGA to send the input image to the photonic processor. **C,** We obtain the result of the convolution by measuring the optical power at the photodetectors. In this case, we loaded a Sobel filter for edge detection into the crossbar array.

References

1. Patterson, D., Gonzalez, J., Le, Q., et al. “Carbon Emissions and Large Neural Network Training,” arXiv, 2021.
2. Feldmann, J., Youngblood, N., Karpov, M., et al. “Parallel convolutional processing using an integrated photonic tensor core,” Nature, Vol. 589, 52–58, 2021.
3. Brückerhoff-Plückelmann, F., Feldmann, J., Gehring, H., et al. "Broadband photonic tensor core with integrated ultra-low crosstalk wavelength multiplexers," Nanophotonics, vol. 11, no. 17, 4063-4072, 2022.
4. Brückerhoff-Plückelmann, F., Bente, I., Becker, M., et al. “Event-driven adaptive optical neural network,” Sci. Adv., Vol. 9, eadi9127, 2023.

AES 2024, ROME - ITALY, 25 –28 JUNE 2024

Wafer-scale structural coloration using gray-scale lithographic nanofabrication

Wen-Di Li[1*], Z. F. Gan[1], C. W. Liang[1], Z. Sun[1], and S. B. Huang[1]

[1]The University of Hong Kong, Hong Kong, China
[*]corresponding author: liwd@hku.hk

Abstract: Gray-scale lithographic nanofabrication techniques, including gray-scale interference lithography using patterned secondary exposure, gray-scale etching and thin-film deposition using ultrafine metal masks, etc. are introduced to generate structural coloration over wafer-scale area.

Colors play crucial roles in daily lives for the ability to carry information. Most commonly, colors are generated from pigments by absorbing light of certain wavelengths. Recently structural colors using nanoscale building blocks to physically manipulate visible electromagnetic waves, have been increasingly investigated due to the higher resolution, saturation, and durability than pigment-based colors. However most published structural color works using two-dimensional (2D) nanostructures can only be fabricated on small areas of millimeter scale or less because they need to use electron beam lithography (EBL), which is an expensive and time-consuming tool for high-resolution patterning of spatially varying structures. Recently we have proposed a high-throughput and wafer-scale nanopatterning method of interference lithography and grayscale-patterned secondary exposure (IL-GPSE) that could spatially modulate nanostructure feature sizes on large scale while maintaining sufficiently high resolution[1]. Here, we employ the IL-GPSE method in the fabrication of wafer-scale structural color paintings that improves the patterning efficiency by orders of magnitude when compared with EBL, implying great potential applications of structural color metasurfaces such as biomedical sensing[2], anti-counterfeiting, and information encryption[3].

Figure 1a schematically demonstrates the fabrication of dimension-varying 2D nanostructures achieved by IL-GPSE, composed of a high-contrast IL for fabricating large-area periodic nanostructures and a secondary exposure for locally tailoring structural dimensions. Figure 1b shows the centimeter-scale photoresist pattern fabricated by IL-GPSE, displaying various colors while Figure 1c shows the corresponding SEM images of different feature sizes. Figure 2 demonstrates that IL-GPSE allows large-area structural color paintings using a specially designed secondary exposure intensity distribution, such as bio-inspired butterfly patterns and renowned artwork replications.

We are also working on the development of modulating the thickness or height of coloration structures spatially with designed profiles through gray-scale etching and gray-scale thin film deposition. By combining a set of versatile gray-scale

dimension modulation techniques that spatially vary the structural dimensions on both vertical and lateral directions, innovative large-area structural coloration can be realized.

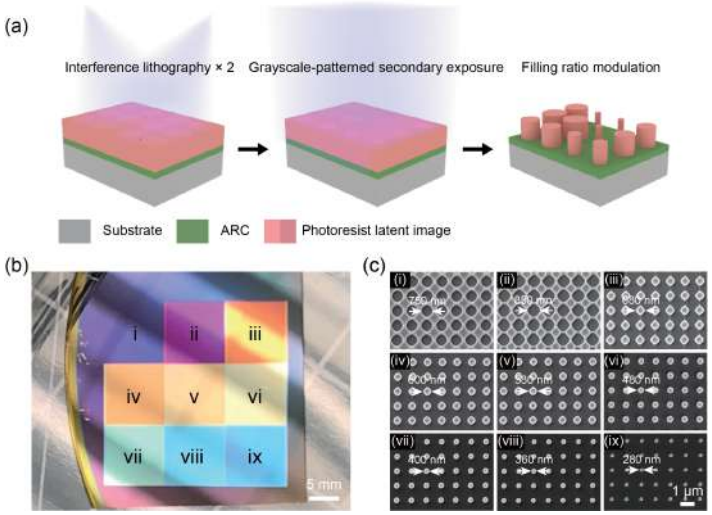

Figure 1 (a) Schematic of spatial modulation of filling ratio for 2D nanostructures using IL-GPSE. (b) The fabricated centimeter-scale structural coloration using different secondary exposure doses, displaying various colors. (c) SEM images of different regions in (b), showing nanostructures with different feature sizes modulated by IL-GPSE.

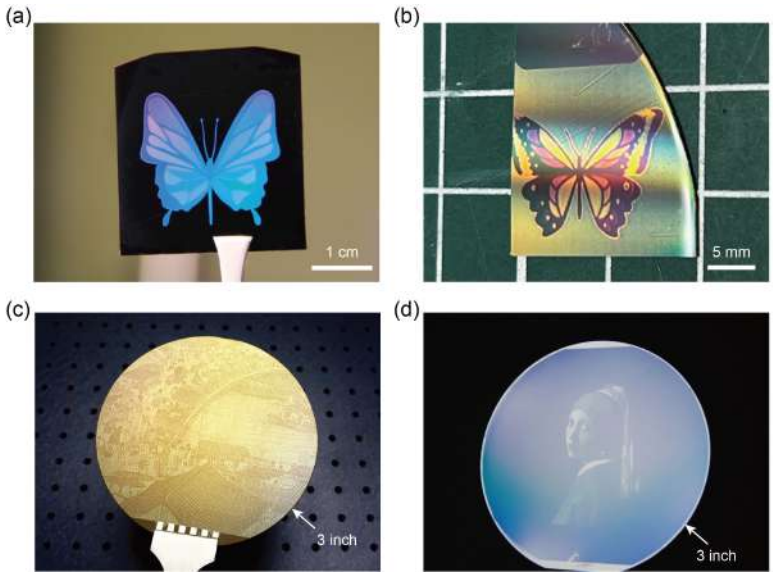

Figure 2 Structural color paintings based on IL-GPSE nanopatterning method. (a, b) Centimeter-scale bio-inspired structural color matasurface showing butterfly patterns. (c, d) Wasfer-scale structural color paintings of *Along the River During the Qingming Festival* and *Girl with a Pearl Earring*.

Low-index nonlinear optics

W. Jaffray[1], S. Stengel[1], A. Boltasseva[2], V. M. Shalaev[2], A. Di Falco[3], and M. Ferrera[1*]

[1]Heriot-Watt University, Institute of Photonics and Quantum Sciences, SUPA, Edinburgh EH14 4AS, UK
[2] Purdue University, School of Electrical and Computer Engineering, West Lafayette, Indiana 47907, USA
[3]University of St. Andrews, School of Physics and Astronomy, Fife, KY16 9SS, UK
[*]Corresponding author: *m.ferrera@hw.ac.uk*

Abstract: Transparent conducting oxides have transitioned from industrial use to a focus for photonic research. This overview covers historical findings, highlights our latest accomplishments, and explores future directions in nonlinear integrated photonics and light acceleration within time-varying media.

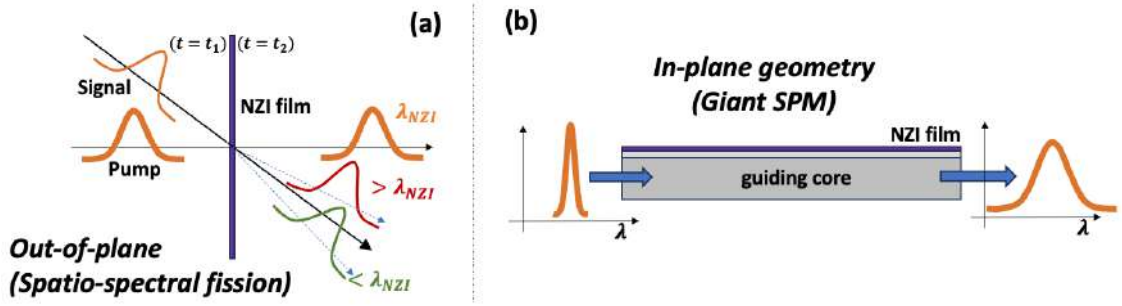

Figure 1 - *Extreme nonlinearities in TCO-based systems. a) Spatio-spectral fission at a spatio-temporal interface. b) Giant nonlinear self-phase modulation of a pulse propagating along a silicon nanowire coupled to an NZI thin film.*

In recent years, the optics and photonics communities have reinvigorated their interest in transparent conducting oxides (TCOs), materials long used in making transparent electrodes for photovoltaic and communication technologies [1]. This revitalized interest in TCOs is driven by two primary factors. Firstly, TCOs offer a promising substitute for noble metals in the development of ultra-compact plasmonic devices, thanks to their metallic properties, low optical absorption, and versatility in fabrication [2]. Secondly, within the near infrared spectral region, these materials exhibit remarkably high optical nonlinearities near their crossover point, where the real part of the dielectric permittivity changes sign. In addition to this, due to their hybrid nature as wide-bandgap materials with the Fermi level in the conduction band, both interband and intraband ultra-fast nonlinearities are enabled [3].

This unique blend of properties has opened a rich field of nonlinear physics that is still being unraveled. Additionally, TCOs' role as epsilon-near-zero (ENZ) materials across a wide near-infrared spectrum, including the entire telecom bandwidth, has led to the demonstration of novel electromagnetic phenomena such as supercoupling, wavefront freezing, and photon doping [4]. A standout feature of TCOs in the ENZ domain is their ability to achieve an extremely low real refractive index, facilitating a slow-light effect that significantly boosts their nonlinear optical properties and lays the groundwork for the emerging field of near-zero-index photonics [5-6].

The rapid advancement in the study of nonlinear optics within conductive oxides is marked by a remarkable list of groundbreaking experiments showcasing unprecedented effects such as unitary index change, ultra-fast and bandwidth-large nonlinear frequency shift, efficient ultra-low-power frequency conversion, etc. [7-10]. All these research achievements define a new era for TCO-based photonics, from their origins as industrial materials for transparent electrodes to their role in pioneering low-loss plasmonics and now, opening new avenues in integrated nonlinear optics.

Figure 1 is a schematic of the most recent research efforts developed in our labs, which include the first full spatio-spectral fission of an ultra-fast optical pulse (Fig.1-a) and the creation of a new set of nonlinear interconnects particularly suitable for the design of optical neural networks (Fig.1-b) [11].

Low-index bulk materials, fundamentally represented by TCOs operating in a generous NIR spectral window, are still producing a remarkable set of ground-breaking research results which are expected to disrupt several fields including all-optical photonics, quantum optics, and machine learning assisted optical computing [12].

References

1. W. Jaffray, et al., “Transparent conducting oxides: from plasmonics integrated photonics” Adv. Opt. Phot. 14 (2), 148-208 (2022)
2. N Kinsey, et al., “Near-zero-index materials for photonics” Nat. Rev. Mater. 4 (12), 742-760 (2019)
3. M. Clerici, et al. “Controlling hybrid nonlinearities in conducting oxides via two-colour excitation” Nat. Commun. 8 (1), 1-7 (2017)
4. I. Liberal, N Engheta “Near-zero refractive index photonics” Nat. Photonics 11 (3), 149-158 (2017)
5. J.B. Khurgin, et al. “Adiabatic frequency shifting in epsilon-near-zero materials: the role of group velocity” Optica 7 (3), 226-231 (2020)
6. W. Jaffray, et al., “Nonlinear Loss Engineering in Near‐Zero‐Index Bulk Materials” Adv. Opt. Mater. 12 (1), 2301232 (2023)
7. O. Reshef, et al. “Beyond the perturbative description of nonlinear response of low-index materials” Opt. Lett. 42, 16, 3225-3228 (2017)
8. W. Jaffray, et al. “Near-zero-index ultra-fast pulse characterization” Nature Commun. 13 (1), 1-8 (2022)
9. M. Z. Alam, et al., “Large optical nonlinearity of nanoantennas coupled to an epsilon-near-zero material” Nature Photonics 12 (2), 79-83 (2018)
10. E. G. Carnemolla, et al., “Visible photon generation via four-wave mixing in near-infrared near-zero-index thin films” Optics Letters 46 (21), 5433-5436 (2021)
11. W. Jaffray, et al. “Engineering Waveguide Nonlinear Effective Length via Low Index Thin Films” https://arxiv.org/abs/2310.17597 (2024)
12. I. Liberal, A. Alù, N. Engheta “Zero-index metamaterials for classical and quantum light” Appl. Phys. Lett. 120, 260401 (2022)

AES 2024, ROME - ITALY, 25 –28 JUNE 2024

THz metamaterial-based devices and ultrafast modulators

S. Tzortzakis[1,2]

[1]Institute of Electronic Structure and Laser, Foundation for Research and Technology Hellas, 71110 Heraklion
[2]Materials Science and Technology Department, University of Crete, 71003 Heraklion, Greece
[*]corresponding author: stzortz@iesl.forth.gr

Abstract: 2D and 3D metamaterial-based devices are shown to control passively and actively the properties of broadband THz radiation. Broadband polarization control and ultrafast self-induced amplitude modulation are demonstrated.

Terahertz (THz) radiation is becoming more and more attractive for numerous applications, from sensing and security to wireless telecommunications. Passive optical devices like polarizers and filters, as well as ultrafast amplitude modulators become a necessity to support the development of the applications. THz metamaterials have emerged as a polyvalent platform for developing both passive and active devices.

Here we discuss our progress in developing 3-dimensioal (3D) chiral metamaterials that present strong broadband optical activity without ellipticity [1]. The design of the 3D chiral metamaterials consists of pairs of U-shaped resonators that are ”twisted” vertically and present a large and ultra-broadband pure optical activity in the low THz regime. The 3D chiral metamaterial structure was fabricated though Direct Laser Writing by Multiphoton Polymerization, followed by selective metallization through electroless plating with silver, and characterized through THz time-domain spectroscopy.

We also discuss the development of ultrafast THz modulators based on cavities with graphene as the active medium [2]. A thin film graphene-based THz perfect absorbing device whose absorption and phase characteristics can be modulated through THz self-actions in the sub-picosecond time scale. The device consists of a single-layer graphene placed on an ionic liquid substrate, back-plated by a metallic back-reflector, with the graphene doping level mediated through electrostatic gating. We experimentally record an absorption modulation of more than 3 orders of magnitude from the initial perfect absorption state, when the device is illuminated with THz field strengths in the range of 102 to 654 kV/cm.

In parallel to the above, we will be discussing also novel laser additive manufacturing techniques we have been developing for accelerating the engineering throughput of 2D and more importantly 3D metamaterial devices. Holographic beam shaping [4] and parallel beam processing enable faster fabrication times and larger volume samples.

Acknowledgements: This work has been partially funded by the Hellenic Foundation for Research and Innovation (H.F.R.I.) under the “2nd Call for H.F.R.I. Research Projects to support Faculty members and Researchers” (Project Number: 4542).

References

1. I. Katsantonis, M. Manousidaki, A. D. Koulouklidis, C. Daskalaki, I. Spanos, C. Kerantzopoulos, A. C. Tasolamprou, C.

M. Soukoulis, E. N. Economou, S. Tzortzakis, M. Farsari, M. Kafesaki, Strong and Broadband Pure Optical Activity in 3D Printed THz Chiral Metamaterials. Adv. Optical Mater. **11**, 2300238 (2023)

2. A. D. Koulouklidis, A. C. Tasolamprou, S. Doukas, E. Kyriakou, M. S. Ergoktas, C. Daskalaki, E. N. Economou, C. Kocabas, E. Lidorikis, M. Kafesaki, and S. Tzortzakis, "Ultrafast Terahertz Self-Induced Absorption and Phase Modulation on a Graphene-Based Thin Film Absorber," ACS Photonics **9**, 3075-3082 (2022)
3. M. Manousidaki, D. G. Papazoglou, M. Farsari, and S. Tzortzakis, "3D holographic light shaping for advanced multiphoton polymerization," Optics Letters **45**, 85 (2020)

AES 2024, ROME - ITALY, 25 –28 JUNE 2024

Electrochemically-tunable and light-emitting metasurfaces

V. E. Ferry[1*]

[1]University of Minnesota, USA
[*]corresponding author: veferry@umn.edu

Abstract: This talk will discuss two strategies for new, tunable metasurfaces. The first part of the talk will discuss the use of electrolyte gating to control the optical properties of materials, focusing on $La_{1-x}Sr_xCoO_{3-d}$ (LSCO) as an exemplary case. The second part will discuss large-area fabrication methods for multilayer, flexible devices.

Alternative materials for metasurfaces enable new properties and lay the foundation for advanced applications. Phase-change materials that change optical properties in response to an applied stimulus, such as voltage, are highly attractive for the development of tunable and switchable metamaterials. The first part of this talk will focus on new electrochemical materials that exhibit significant modulation in optical response under applied voltage.

$Sr_xCoO_{3-\delta}$ (SCO) has attracted considerable attention recently as a voltage-tunable materials system. $La_{1-x}Sr_xCoO_{3-\delta}$ (LSCO) offers similar advantages, but with additional advantages in stability. As deposited, LSCO has a perovskite structure. We focus here on ion-gated systems. Application of a positive gate voltage facilitates the formation and migration of oxygen vacancies. This is accompanied by substantial change in magnetic, electrical, thermal, and optical properties.

We fabricate electric double layer transistors consisting of thin-films of LSCO and an ion gel. We use spectroscopic ellipsometry to map the complex refractive index across the phase diagram of LSCO before and after gating. At $x < 0.18$, as-grown LSCO has a perovskite crystal structure and high refractive index. Upon application of a gate voltage, the LSCO films change to another lower-index, lower-loss insulating perovskite state with $\Delta n > 0.6$. At $x > 0.18$, as-grown LSCO has a perovskite structure and is a lossy metal. Application of the gate voltage transforms LSCO to an oxygen-vacancy-ordered brownmillerite crystal structure with high-index ($n > 2.5$) and low-loss. LSCO is therefore an interesting platform material for switchable metasurface applications, and can be used in either optical applications that require on-off switching (at $x > 0.18$) or resonance modulation (at $x < 0.18$).

The second part of the talk will show an example metasurface, comprised of patterned plasmonic and light-emitting semiconductor nanostructures, where tuning the refractive index of the substrate switches the polarization state of the luminescence from the semiconductor array. We will discuss two fabrication routes to creating these patterned semiconductor nanocrystal structures, one based on direct-write electron-beam lithography, and the other using a novel roll-to-roll compatible printing method.

Acknowledgements. The work on LSCO was supported primarily by the National Science Foundation through the University of Minnesota MRSEC under Award Number DMR-2011401. Parts of this work were performed in the Characterization Facility at the University of Minnesota, which receives partial support from NSF through the MRSEC program. Portions of this work were also conducted in the Minnesota Nano Center, which is supported by NSF through the National Nano Coordinated Infrastructure (NNCI) under Award Number

ECCS-2025124. The work on nanocrystal patterning was supported by the National Science Foundation under Award 2102835.

References

1. Chakraborty, R. D. , W. Postligione, S. Ghosh, K. A. Mkhoyan, C. Leighton, and V. E. Ferry, “Optical properties of electrochemically gated $La_{1-x}Sr_xCoO_{3-\delta}$ as a topotactic phase change material,” Adv. Opt. Mater., Vol. 11, No. 16, 2300098, 2023.
2. Ramamurthy, M., P. Pachidis, B. M. Cote, and V. E. Ferry, “Circularly polarized photoluminescence from nanostructured arrays of light emitters,” ACS Appl. Nano Mater., Vol. 1, No. 1, 491 - 499, 2023.
3. Donie, Y. J., M. Ramamurthy, R. D. Chakraborty, L. F. Francis, C. D. Frisbie, and V. E. Ferry, “Roll-to-roll compatible topochemical wetting control for metamaterial printing,” Adv. Opt. Mater., in press, 2024.

AES 2024, ROME - ITALY, 25 –28 JUNE 2024

Dispersion tuning of spoof surface plasmon polaritons by MEMS-integrated metasurfaces

L. Franke[1], S. Klingel[1], and M. Rahm[1,*]

[1]Department of Electrical and Computer Engineering and Research Center OPTIMAS, Erwin-Schroedinger-Strasse, RPTU Kaiserslautern-Landau, 67663 Kaiserslautern, Germany

[*]corresponding author: marco.rahm@rptu.de

Abstract: Compact plasmonic networks for high-frequency on-chip communication shrink electromagnetic waves to subwavelength scales. Metasurfaces handle spoof surface plasmon polaritons (SSPPs) at microwave and terahertz frequencies, but real-time reconfigurability is challenging. We developed a tunable SSPP low-pass filter that effectively blocks SSPP transmission upon activation at a frequency of 106 GHz.

The development of plasmonic networks and their miniaturization is critical for advancing on-chip communication at higher frequencies. While numerous designs exist for metallic metasurface pathways that guide and statically manipulate confined spoof surface plasmon polaritons (SSPPs) at lower frequencies, achieving real-time reconfigurability remains a formidable challenge. Current practical approaches predominantly involve the incorporation of graphene monolayers onto metasurfaces [1,2].

In this study, we introduce a dynamically tunable metasurface for SSPP waveguides, utilizing a fishbone structure with electrostatically deflectable microbridges. Voltage application between the metasurface and a ground electrode on the substrate's backside allows for modulation of the upper cutoff frequency for the SPPs, which implies an effective shift in the dispersion curve towards higher wavenumbers. By leveraging the advancements in micro-electromechanical systems, scalable implementations at frequencies beyond the proposed range of 80 GHz to 120 GHz are feasible.

Figure 1(a) shows the simulation model of the fishbone SSPP metasurface. The tapered region avoids reflection of the SSPPs, when they enter the waveguide from the excitation region and are collected at the exit, respectively. The filter section marks the untapered territory. Figure 1(b) displays the calculated electric field of a snapshot of the propagating SSPP 50 µm away from the surface. The SSPP frequency is 106 GHz. In this plot, the microbridges are undeflected and the filter is open, such that the SSPP can pass the filter almost without attenuation. In the case shown in Fig. 1(c), the microbridges are deflected and the dispersion curve of the metasurface is shifted that the SSPPs cannot pass the low pass filter and are scattered out, absorbed and reflected.

The fishbones are comprised of a 320 µm long static metallic section on a 50 µm thick silicon substrate and a 390 µm long metallic microbridge section on a flexible SiO2 beam over a 30 µm deep gap in the substrate. Upon electric field actuation, the metallized microbridges are pulled towards the ground electrode. Figure 2 displays a SEM image of the microbridges.

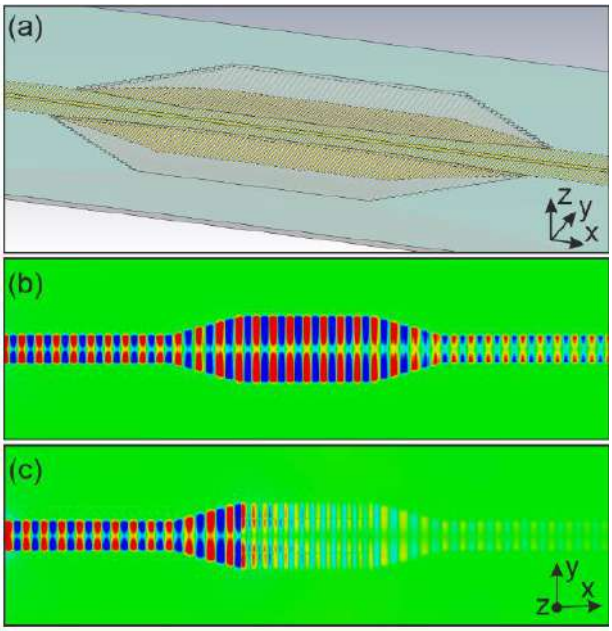

Fig. 1: (a) Simulation model of the fishbone SSPP metasurface with taper region and filter section, (b) Calculated electric field of the SSPP at 106 GHz for undeflected microbridges (open filter) and (c) for deflected microbridges (closed filter).

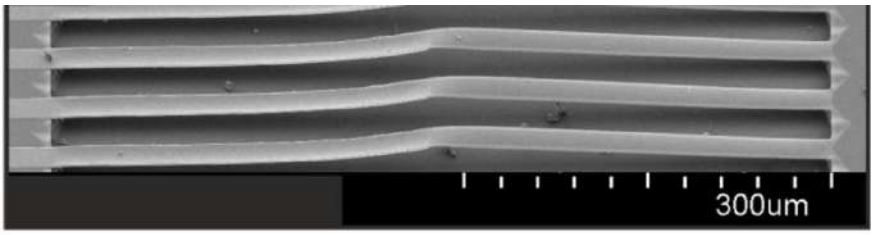

Fig. 2: SEM image of the microbridges, consisting of a static and a flexible part, the latter of which is pulled down towards the substrate upon application of an electric bias field.

The authors acknowledge the financial support of the project by the German Research Foundation (project number 458851938, GZ RA 1903/6-1).

References

1. A. -Q. Zhang,W. B. Lu, Z. -G. Liu, B.Wu and H. Chen, ”Flexible and Dynamically Tunable Attenuator Based on Spoof Surface Plasmon Polaritons Waveguide Loaded With Graphene,” IEEE Transactions on Antennas and Propagation, vol. 67, no. 8, pp. 5582-5589 (2019).
2. Feng, M., Zhang, B., Ling, H., Zhang, Z., Wang, Y., Wang, Y., Zhang, X., Hua, P., Wang, Q., Song, A. and Zhang, Y., ”Active metal–graphene hybrid terahertz surface plasmon polaritons. Nanophotonics,” vol. 11, no. 14, pp. 3331-3338 (2022).

AES 2024, ROME - ITALY, 25 –28 JUNE 2024

Elastic Wave Focusing and Optomechanical Coupling in a Nano-Opto-Electro-Mechanical Device

A. Gueddida[1], L. Carpentier[1], G. Lévêque[1], Y. Pennec[1], and B. Djafari-Rouhani[1*]

[1]IEMN, UMR CNRS 8520, University of Lille, 59652 Villeneuve d'Ascq, France

[*]corresponding author: bahram.djafari-rouhani@univ-lille.fr

Abstract: We study theoretically an optomechanic cavity inside a phoxonic nanobeam. The acoustic cavity mode is excited by an IDT structure in front of the nanobeam. Our results concern the design of a metasurface to focus the acoustic wave into the nanobeam and the search of high frequency (10 GHz) cavity phonons.

Our Nano-opto-electromechanical device consists of an optomechanical (OM) cavity inside a phoxonic nanobeam connected to two sets of inter-digitated transducers (IDT) at its input and output for the purpose of acoustic wave excitation and detection. The optical modes in the OM cavity is excited by an external optical waveguide terminated by a Bragg mirror made of tapered holes. A scheme of the device is presented in Figure 1(a).

The phoxonic cavity consists[1] of a periodic array of holes and stubs that exhibit simultaneously acoustic bandgap in the GHz range and optical bandgap in the telecom range of 1550 nm. We have demonstrated various cavities[1,2] supporting both acoustic modes in the range of 2-4 GHz, optical modes of high-quality factors and a sufficiently strong OM coupling rate g of the order of MHz. Also, we investigated the possibility of exciting the phononic cavity modes by means of a set of IDT in front of the nanobeam[3].

In this work, we focus on two new directions, namely (i) the design of a metasurface to focus the elastic wave generated by the IDTs towards the entrance of the nanobeam, and (ii) the search of high frequency acoustic cavities working in the range of 6-10 GHz.

The metasurface consists of an array of sub-wavelength resonant pillars exhibiting a gradient phase response that results from the variation in their geometrical parameters. To realize the focusing functionality, the phase response should span a range of 2π which can be achieved by the superposition of two different resonances of the pillars such as a compressional and a bending mode. This feature was demonstrated both theoretically[4] and experimentally[5] by changing the heights of the pillars. Later, we proposed to obtain a similar functionality by using elliptical pillars[6,7] with a constant height but a gradient in their ellipticity, which is much more suitable for the microfabrication technologies. In this work, we adapted this concept to incident flexural waves (f=4 GHz) on a silicon plate of thickness 220 nm. We have demonstrated that the proposed metasurface allows to focus the incident flexural waves into a focal spot with an intensity six times that of the incident wave with a full width at half maximum (FWHM) of the focal spot equal to $0.39\times\lambda$ (Figure 1(b)).

Another objective is the design of OM cavities that support phonon localized modes in the range of 10 GHz while the optical cavity modes keep a high-quality factor and allows a strong OM coupling rate. In some of our previous works[1,2], we proposed tapered cavities where the sizes of the holes and stubs in the center of the cavity were increased (resp. decreased) with respect to the phoxonic crystal parameters in order to decrease (resp. increase) the cavity phonon frequency in the range of 2-4 GHz. In contrast, to go to 10 GHz frequencies, we adopted here an opposite solution, namely putting a long length stub at the center and relying on its high frequency second order breathing mode to compresses the holes and create the conditions for strong OM coupling. Different tapered cavities are under investigation and some promising solutions are expected. One example is presented in Figure 1(c) where we show the acoustic and

optical fields of the cavity with a coupling rate of g=5 MHz.

In parallel, we are exploring the possibility of using simultaneous localized acoustic and optical modes at the interface between two topologically different phoxonic crystals. The principle is based on the analogy with the Su-Schrieffer-Heeger (SSH) model by making a pairing of the pillars and constructing a unit cell with two sub-units. Both photonic and phononic topological interface modes have been obtained by this approach.

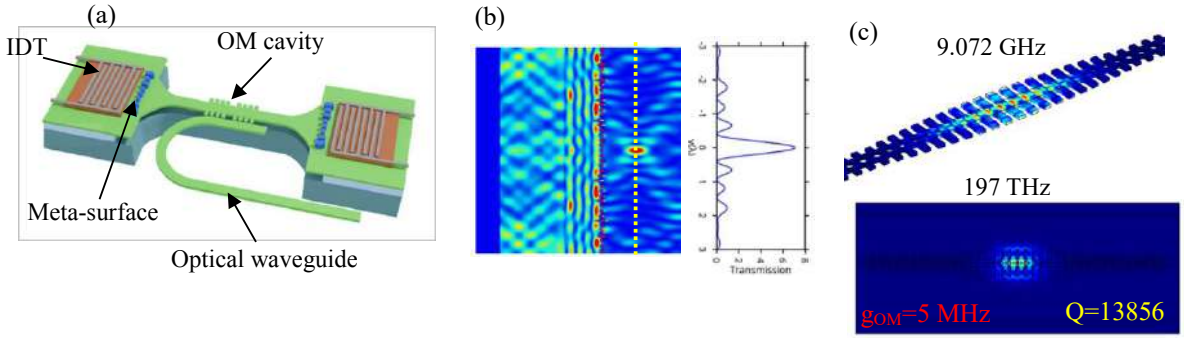

Figure 1 : Schematic view of the opto-electromechanical device. (b) Elastic wave focusing effect of the metasurface. The blue curve represents the transverse intensity evaluated along the yellow line crossing the focal spot. (c) An example of phononic and photonic cavity modes providing high OM coupling rate g_{OM}.

Acknowledgements. This work is part of the project MAGNIFIC of the European Union's Horizon Europe research and innovation program under grant agreement No 101091968 and the CHIST-ERA Call 2021 under the grant agreement No CHIST-ERA-20-NOEMS-003.

References

1. Djafari Rouhani, B. et al, "Phoxonic crystals and cavity optomechanics", Comptes Rendus Physique 17, 555, 2016.
2. Gueddida, A. et al, "Coupling of integrated waveguide and optomechanic cavity for microwave phonon excitation in Si nanobeams", Photonics. 7, 67, 2020.
3. Korovin, A. et al, "Conversion between surface acoustic waves and guided modes of a quasi-periodic structured nanobeam", J. Phys. D : Applied Physics. 52, 32LT01, 2019.
4. Jin, Y. et al, "Elastic metasurfaces for deep and robust subwavelength focusing and imaging", Phys. Rev. Appl. 15, 024005, 2021.
5. Wang, W. et al "Experimental realization of a pillared metasurface for flexural wave focusing", APL Materials 9, 051125 2021.
6. Djafari Rouhani, B. et al, "Elastic metasurface made of elliptic shape pillars for acoustic wave focusing", Proceedings of 2022 IEEE International Ultrasonics Symposium.
7. Carpentier, L. et al, "Elliptic pillars based metasurface for elastic waves focusing in a plate", Submitted to APL Materials.

AES 2024, ROME - ITALY, 25 –28 JUNE 2024

Energy transfer mechanisms in nanophotonic systems for pulsed photocatalysis

A. Alabastri[1,*]

[1]Department of Electrical and Computer Engineering, Rice University, United States
[2]Author Affiliation, Country
[*]corresponding author: alabastri@rice.edu

Abstract: Upon pulsed illumination, plasmon decay generates a spatially dependent, out-of-equilibrium hot carrier population, enhancing light-matter interaction in the ultrafast regime. This process, crucial for photothermal catalysis, allows for the analysis of hot electrons, thermalized electrons, and lattice effects in driving chemical reactions, offering insights into the mechanisms underpinning photocatalytic efficiency.

I will discuss how electromagnetic radiation can be concentrated in nanoscale structures and the role the inhomogeneous absorption pattern plays in differently shaped nanostructures. Simulation results on hot and thermalized electron injection from conductive nanostructures into adsorbates will be presented. Such injection represents an additional channel through which electromagnetic energy can leave an illuminated nanoparticle, in addition to scattered radiation and heat dissipation to the environment. The energy 'lost' to adsorbates is associated with chemical reactions, and its evaluation allows for the comparison of hot electrons, thermalized electrons, and lattice effects in photothermal catalysis.

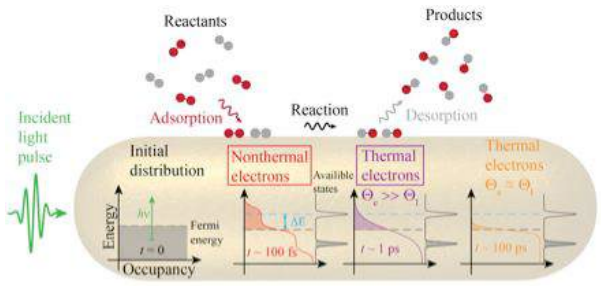

Hot electrons, thermalized electrons and lattice vibrations can contribute to chemical reactions, exchanging energy with reactants adsorbed at the nanoparticle surface.

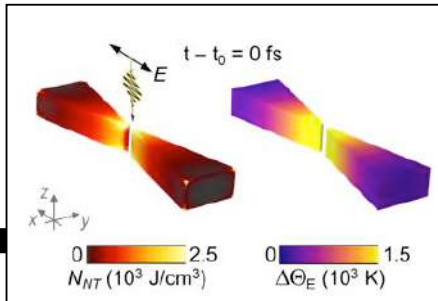

Upon illumination, metallic nanostructures display an inhomogeneous hot and thermalized electron distribution.

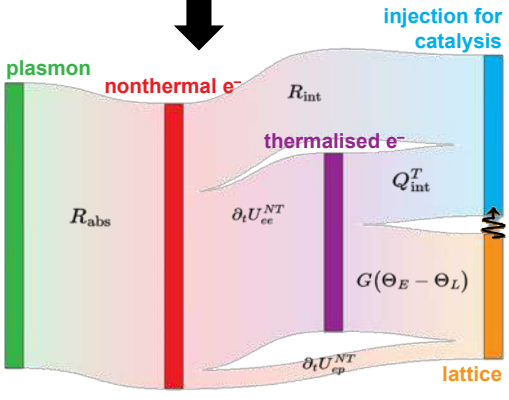

Upon pulsed excitation, the excited plasmons decay and along the energy relaxation pathways, part of the energy can be exchanged with molecules for catalysis before energy is lost to the environment.

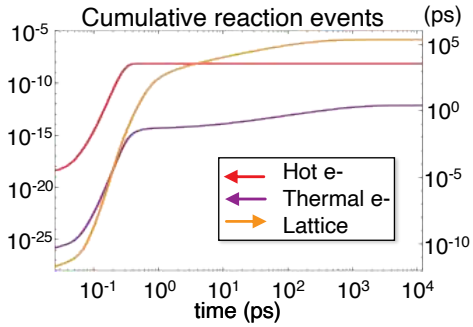

By computing the energy utilized for catalytic effects, through a Generalized Extended 2-Temperature model it is possible to evaluate the cumulative chemical reaction events overt time associated with different catalytic mechanisms.

References

1. A. Schirato, M. Maiuri, A. Toma, S. Fugattini, R. Proietti Zaccaria, P. Laporta, P. Nordlander, G. Cerullo, A. Alabastri* and G. Della Valle*, "Transient optical symmetry breaking for ultrafast broadband dichroism in plasmonic metasurfaces", Nat. Phot., 14, 723-727, 2020
2. A. Schirato, A. Mazzanti, R. Proietti Zaccaria, P. Nordlander, A. Alabastri* and G. Della Valle*, "All-Optically Reconfigurable Plasmonic Metagrating for Ultrafast Diffraction Management", Nano Lett., 21, 3, 1345-1351, 2021
3. J. Cunha, A. Alabastri, R. Proietti Zaccaria, "Heat and Temperature Localization via Fabry–Pérot Resonances at the Tip of a Nanofocusing Cone", Adv. Opt. Mat., 10, 18, 2200746, 2022
4. A. Schirato, G. Crotti, R. Proietti Zaccaria, A. Alabastri, G. Della Valle, "Hot carrier spatio-temporal inhomogeneities in ultrafast nanophotonics", New J. of Phys., 24, 045001, 2022
5. L. Yuan, Y. Zhao, A. Toma, V. Aglieri, B. Gerislioglu, Y. Yuan, M. Lou, A. Ogundare, A. Alabastri*, P. Nordlander*, and N. J. Halas*, "A Quasi-Bound States in the Continuum Dielectric Metasurface-Based Antenna–Reactor Photocatalyst", Nano Lett., 24, 1, 172-179 (2024)
6. K. Sanders, A. Schirato, R. Proietti Zaccaria, G. Della Valle, P. Nordlander and A. Alabastri, "Quantifying ultrafast energy transfer from plasmonic hot carriers for pulsed photocatalysis on nanostructures", submitted

AES 2024, ROME - ITALY, 25 –28 JUNE 2024

Nanophotonic paths to enhance the open circuit voltage in perovskite and organic photovoltaic cells

Francisco Bernal Texca[1], Martina D'andrea[1], Jordi Martorell [1,2,*]

[1]Author Affiliation, Country ICFO-The Institute of Photonic Sciences, The Barcelona Institute of Science and Technology, 08860 Castelldefels, Barcelona, Spain.

[2]Departament de Física, Universitat Politécnica de Catalunya, 08860 Castelldefels, Barcelona, Spain.

[*]corresponding author: jordi.martorell@icfo.eu

Abstract: A nanophotonic structuration of perovskite and organic solar cell architectures is considered to enhance the open-circuit voltage. Numerical and experimental results to limit Boltzmann losses and set the path to take the limit efficiency from planar single junction cells from 33% to 43% will be presented.

Light management strategies to enhance the performance of solar cells predominantly target an increase in short-circuit current density via a more effective sunlight absorption. On the contrary, optical approaches to limit open-circuit voltage (V_{oc}) losses are seldom explored. In the current work we take a radical shift for enhancing the efficiency of perovskite and organic solar cells by focusing on targeting an increase in the V_{oc} by considering the incorporation of a nanophotonic structuration designed to serve as angular restrictor for the emission photons.

We will present different nanophotonic structures which primary objective is to mitigate losses associated with bimolecular radiative recombination, specifically Boltzmann losses, without the reliance on sunlight concentration. This approach aims to preserve the advantages inherent from a planar configuration in solar cells. We will discuss numerical and experimental results where light emission and quasi-Fermi level splitting is modified by the incorporation of different nanophotonic structures. We will also discuss how the nanophotonic structuration can control the V_{oc} to open paths for surpassing the planar geometry single junction solar cell power conversion efficiency limit and push it from 33% to levels close to 43%.

AES 2024, ROME - ITALY, 25 –28 JUNE 2024

Infrared radiation from sub-λ antennas and high mobility graphene devices

L. Abou-Hamdan[1,2], A. Schmitt[3], S. Rossetti[1,2], R. Bretel[3], S. Bidault[1], V. Krachmalnicoff[1], J.-P. Hugonin[4], C. Voisin[3], R. Haidar[2], P. Bouchon[2], J.-J. Greffet[4], E. Baudin[3,5], Y. De Wilde[1*]

[1]Institut Langevin, ESPCI Paris, Université PSL, CNRS, F-75005 Paris, France
[2]DOTA, ONERA, Université Paris-Saclay, F-91123 Palaiseau, France
[3]Laboratoire de Physique de l'Ecole Normale Supérieure, ENS, Université PSL, CNRS, Sorbonne Université, Université Paris-Cité, F-75005 Paris, France
[4]Laboratoire Charles Fabry, IOGS, Université Paris-Saclay, F-91123 Palaiseau, France
[5]Institut Universitaire de France, France
[*]yannick.dewilde@espci.fr

Abstract: We demonstrate the use of thermal fluctuations to explore the electromagnetic resonances of dimers of infrared metal-insulator-metal antennas and single dielectric resonators. Next, we investigate the radiation from graphene transistors encapsulated in boron nitride and find infrared electroluminescence signatures concomitant with efficient energy transfer via hyperbolic phonon polaritons.

Thermal fluctuations can be used to excite the electromagnetic resonances of materials and microstructures. We have used this method combined with infrared spatial modulation spectroscopy (IR-SMS) to explore the resonances of sub-wavelength infrared antennas. After the development of the IR-SMS method to study thermally excited single metal-insulator-metal (MIM) antennas [1], we have used the same approach to study MIM-antenna dimers [2]. Measurements of their far-field thermal radiation spectrum show that the dimers behave as two independent MIM antennas as long as they are separated by 500 nm or more, but that hybrid modes appear when the gap separation between the MIM antennas is 100 nm. Figure 1 shows in particular that the simultaneous thermal excitation of two hybrid modes results in a splitting of the resonance peak observed in a dimer made of two MIM antennas with size 2 µm and 2.5 µm, respectively. Dielectric microspheres are also attractive to tailor the thermal radiation spectrum. For single SiO2 microspheres, we evidence the excitation of

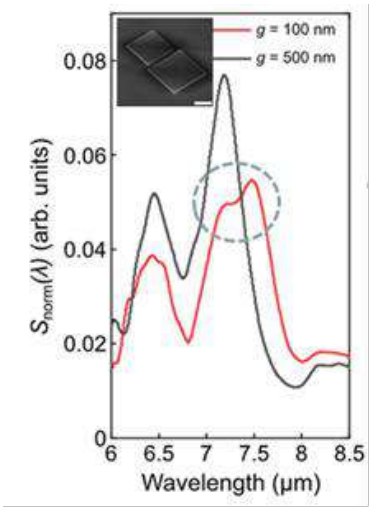

Figure 1: Infrared thermal radiation spectra of a dimer of MIM antennas of lateral width 2 µm and 2.5 µm (inset) separated by a gap g of 100 nm and 500 nm.

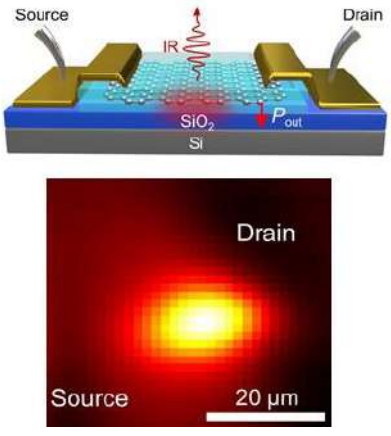

Figure 2: Far-field image (bottom) of the infrared radiation produced by a graphene/hBN transistor (top) under high bias voltage.

both surface phonon-polariton (SPhP) modes and geometrical Mie modes [3].

Next, we have investigated the radiation produced by transistors made of a high mobility graphene layer encapsulated between two layers of hexagonal boron nitride (hBN) with a thickness of a few tens of nanometers. In this geometry, it had been predicted through electrical transport studies that the device would probably become electroluminescent under a sufficiently large bias voltage [4]. As figure 2 shows, we indeed recently observed the occurrence of an infrared emission associated to an interband electronic current that settles beyond the Zener-Klein threshold. This particular electroluminescent emission, directly observed here for the first time, is concomitant with the opening of an efficient heat transfer mechanism in which electrons in graphene radiatively recombine with the hyperbolic phonon-polariton modes of hBN, producing an efficient heat sink towards the substrate [5].

The research leading to these results has received partial funding from the European Union Horizon 2020 research & innovation program under grant agreement No.881603 "Graphene Core 3", and from the French ANR-21-CE24-0025-01 "ELuSeM". This work has received support from program “Investissements d’Avenir” launched by the French Government. The authors also thank the following people for their contribution: M. Tharrault, D. Mele, A. Pierret, M. Rosticher, T. Taniguchi, K. Watanabe, C. Maestre, C. Journet, B. Toury, V. Garnier, P. Steyer, J. H. Edgar, E. Janzen, JM. Berroir, G. Fève, G. Ménard, B. Plaçais, C. Voisin, E. Bailly, B. Vest, and N. Bardou.

References

1. Li, C., et al., " Near-Field and Far-Field Thermal Emission of an Individual Patch Nanoantenna ", Phys. Rev. Lett. 121, 243901, 2018.
2. Abou-Hamdan, L., et al., " Hybrid modes in a single thermally excited asymmetric dimer antenna ", Opt. Lett. 46, 981, 2021.
3. Abou-Hamdan, L., et al., " Transition from Phononic to Geometrical Mie Modes Measured in Single Subwavelength Polar Dielectric Spheres", ACS Photonics 9, 2295 (2022).
4. Yang, W., et al., " A graphene Zener–Klein transistor cooled by a hyperbolic substrate", Nature Nanotech. 13, 47, 2018.
5. Abou-Hamdan, L., Schmitt, A., et al., "Direct observation and control of near-field radiative energy transfer in a natural hyperbolic material ", arXiv:2310.08351.

AES 2024, ROME - ITALY, 25 –28 JUNE 2024

Nanoresonators and Metasurfaces for Enhanced Infrared/Terahertz Light-Matter Interaction

L. Razzari

Institut National de la Recherche Scientifique, Centre Énergie Matériaux Télécommunications (INRS-EMT), 1650 Blvd. Lionel-Boulet, Varennes, Québec, J3X 1P7, Canada
*corresponding author: luca.razzari@inrs.ca

Abstract: I will summarize our main findings on how structured surfaces can enhance radiation-matter interaction. This includes our studies on terahertz spectroscopy of low-dimensional materials and on infrared nonlinear processes in dielectric metasurfaces.

This presentation will review some of our main findings on how nanoresonators and metasurfaces can boost the interaction of infrared/terahertz radiation with different types of materials. I will report on how metallic nanoantennas can enhance terahertz spectroscopy of low-dimensional systems. I will also show that such resonators can enable phonon strong coupling at the nanoscale. I will end by presenting nonlinear optical experiments on dielectric metasurfaces in the infrared spectral region, showing that surface engineering can artificially alter wavelength conversion processes such as third harmonic generation.

AES 2024, ROME - ITALY, 25 –28 JUNE 2024

Towards a full quantum photonics platform

Christophe Couteau[1*], Roy Konnoth Ancel[1], Surena Fatemi[1,2], Christoph Becher[2] Régis Deturche[1], and Sylvain Blaize[1]

[1]Laboratory Light, nanomaterials and nanotechnologies – L2n, Université de Technologie de Troyes & CNRS UMR 7076, 10000 Troyes, France
[2] Fachrichtung Physik, Universität des Saarlandes, 66123 Saarbrücken, Germany
[*]corresponding author: userid@institution.edu

Abstract: The past decade has witnessed remarkable progress in photonic material platforms, opening up numerous new possibilities for on-chip quantum applications. Advances in material growth, defect passivation methods, and microfabrication technologies have led to a significant reduction in waveguide propagation loss, paving the way for the emergence of various material systems. These advancements have fueled the development of photonic integrated circuits capable of manipulating photonic quantum states, thus driving the field of integrated quantum photonics forward. Integrated quantum photonics offers a promising avenue for the miniaturisation and scalability of optical quantum circuits. In this context, we describe a new platform based on glass that we want to employ for quantum photonics applications [1,2].

The integration of nano-emitters onto optical circuits poses a formidable challenge in nano-photonics [3]. Merging the optical properties of nano-emitters with the integration and scalability advantages of integrated optics remains a significant hurdle. Additionally, there is a pressing need within the scientific community for integrated optical systems capable of manipulating light-matter interactions at the nanoscale. In this study, our objective is to establish a novel platform centered on an integrated device capable of operating across both the visible and telecommunication bands, while exhibiting high compatibility with standard optical fiber coupling. Our proposed platform entails a hybrid structure comprising a high-refractive-index layer in contact with the top surface of an ion-exchanged glass waveguide (IEW). This hybrid configuration serves as an efficient light coupler for both nano-emitter excitation and collection. Drawing from previous advancements by the L2n at the UTT [4,5], our innovative approaches aim to optimize coupling strategies and minimize attenuation. We commence by presenting an on-chip single photon source fully characterized using a silver ion exchange waveguide with minimal photon attenuation operating within the visible spectrum. To achieve this, we explore the hybridization of nano-emitters with our low-loss photonic platform, focusing on refining coupling techniques and reducing attenuation. The advancement of technologies facilitating low-loss coupling to fiber networks and compatibility with microfabrication techniques has greatly supported these efforts. Moreover, we explore the integration of optical functionalities onto circuits, including polarizers, beamsplitters, filters, and rotators. Figure 1 illustrates a schematic of a fully pigtailed device dedicated to an on-chip single photon source based on an IEW augmented with a thin TiO2 layer deposited on its surface.

The emitted photons undergo coupling with the hybrid modes of the photonic structure, gradually transitioning into hybrid photonic backward and forward modes of the IEW. These modes are detectable from both ends of the optical pigtailed fibers. The nano-emitter interacts with the tightly confined electric

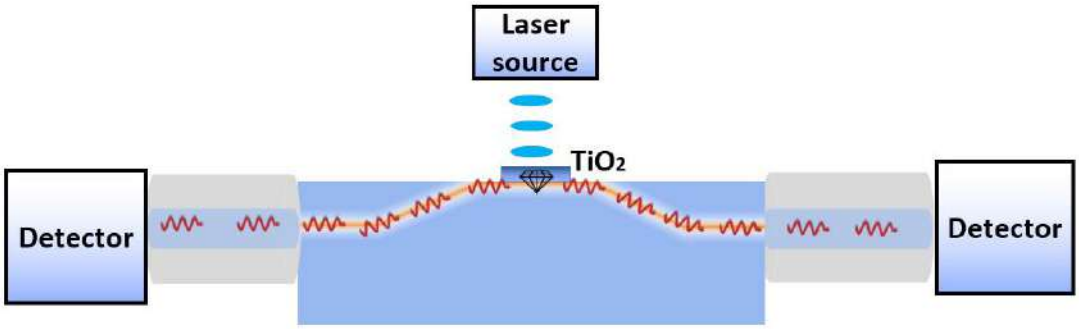

Figure 1: schematic of an integrated single-photon source on an ion-exchange waveguide with a TiO_2 layer for better coupling.

field, resulting in increased emission rates that enhance coupling efficiency and the Purcell factor. In systems featuring effective coupling of hybrid photonic modes, a significant proportion of emitted photons can be efficiently captured by optical fibers. Developing a design capable of efficient performance at both excitation and emission wavelengths presents a significant challenge. Additionally, we will introduce novel devices tailored for ion-exchanged waveguides operating at 1550 nm, including splitters, polarizers, and polarization rotators, and explore the integration of single photon detectors.

Acknowledgements: the authors would like to thank the Graduate School (École Universitaire de Recherche) "NANO-PHOT", contract ANR-18-EURE-0013, they acknowledge the use of the nano'mat platform from the CNRS Renatech network and funding from the FEDER, the Grand Est Region and the Aube Department. This work received support from French National Agency for Research-ANR of the OQULUS project under the France 2030 initiative, contract ANR-23-PETQ-0013. The authors are thankful of the European project DigiQ.

References

1. Christophe Couteau, Stefanie Barz, Thomas Durt, Thomas Gerrits, Jan Huwer, Robert Prevedel, John Rarity, Andrew Shields, and Gregor Weihs. Applications of single photons in quantum metrology, biology and the foundations of quantum physics, Nature Physics Reviews 5, 354 (2023).
2. Christophe Couteau, Stefanie Barz, Thomas Durt, Thomas Gerrits, Jan Huwer, Robert Prevedel, John Rarity, Andrew Shields, and Gregor Weihs. Applications of single photons to quantum communication and computing, Nature Physics Reviews 5, 326 (2023).
3. M. Nahra, D. Alshamaa, R. Deturche, V. Davydov, L. Kulikova, V. Agafonov, and C. Couteau. Single germanium vacancy centers in nanodiamonds with bulk-like spectral stability, AVS Quantum Sci. 3, 012001 (2021).
4. Xiaolun Xu, Aurélie Broussier, Tiziana Ritacco, Mackrine Nahra, Fabien Goeffray, Ali Issa, Safi Jradi, Renaud Bachelot, Christophe Couteau, Sylvain Blaize. Towards the Integration of Nanoemitters by Direct Laser Writing on Optical Glass Waveguides, Photonics Research, 8, 1541 (2020).
5. Giuseppe Emanuele Lio, Josslyn Beltran Madrigal, Xiaolun Xu, Ying Peng, Stefano Pierini, Christophe Couteau, Safi Jradi, Renaud Bachelot, Roberto Caputo, Sylvain Blaize. Integration of Nanoemitters onto Photonic Structures by Guided Evanescent-Wave Nano-Photopolymerization, J. Phys. Chem. C 123, 23 (2019).

AES 2024, ROME - ITALY, 25 –28 JUNE 2024

Nanophotonics on the Tip of a Fiber: Membrane-on-Fiber Technology

A. Fiore[1,*], A.L. Hendriks[1], L. Picelli[1], M.S. Cano-Velázquez[1], D. Rabelink[1], P. Dreverman[1], M. Dolci[1], P.J. van Veldhoven[1], P. Zijlstra[1], E. Verhagen[1,2]

[1] Eindhoven University of Technology, Eindhoven, The Netherlands

[2] Center for Nanophotonics, AMOLF, Amsterdam, The Netherlands
[*]corresponding author: a.fiore@tue.nl

Abstract: By transferring nanopatterned membranes on the tip of optical fibers, we combine the power of nanophotonics with the flexibility of fiber sensing. Using this Membrane-on-Fiber technology, we report a variety of fiber-tip sensors of physical and biochemical parameters

Lab-on-fiber technologies enable the definition of optimized structures inside, around or on top of a fiber tip [1,2]. Among the several approaches to fabricate these structures, wafer-scale fabrication and transfer to the fiber tip has been proposed as a potentially scalable method, leveraging the flexibility, resolution and high yield of semiconductor manufacturing processes [3-8]. Recently, our group demonstrated a transfer method which relies on defining a suspended semiconductor membrane, which is then transferred to the fiber facet by inserting the fiber through a hole etched in the backside of the wafer [9], see Fig. 1. When the fiber tip is correctly cleaved and clean, the transfer process has a high yield. After transfer the fiber tip can be dipped in different liquids, cleaned and dried numerous times without removal of the membrane, due to the strong van der Waals force between the membrane and the silica fiber facet [9].

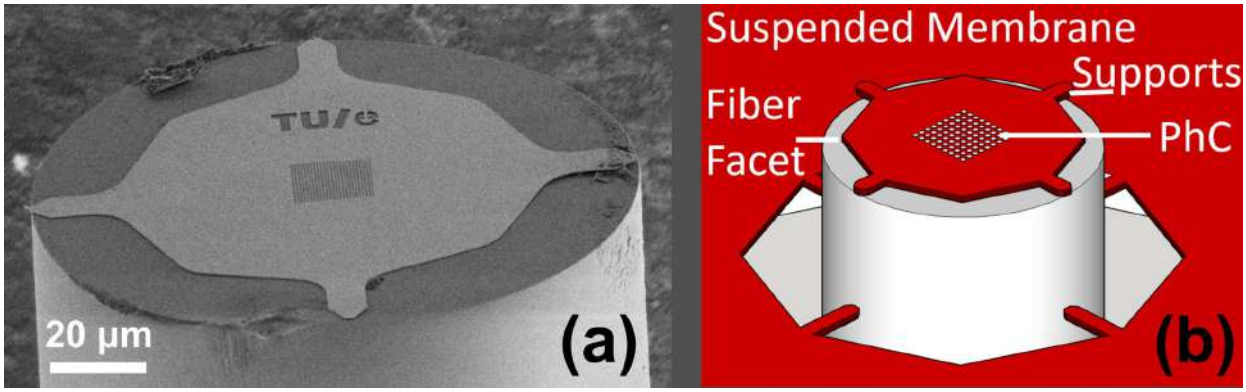

Fig. 1: (a) Scanning-electron-microscope image of a transferred photonic crystal; (b) Schematics of the membrane transfer process

A key advantage of this method is the flexibility, as it allows the transfer of any photonic structure patterned on a thin semiconductor membrane (in our case: InP). As sensor structure, we have employed guided-mode resonances in photonic crystals (PhCs) in order to create a spectral feature in reflection and used them to sense physical parameters in the environment of the fiber-tip. We optimized the PhC design in order to achieve a reflectance spectrum displaying a polarization-independent Lorentzian-like lineshape. Using commercial fiber

sensor interrogators, we achieve an imprecision of about 1 pm in the wavelength measurement [10] . When the PhC is used as temperature or refractive index sensor, this translates into imprecisions of ~20 mK and ~10^{-5} RIU, respectively. Using these structures, a fiber-tip bioassay for the sensing of antibodies at the sub-nM level has been demonstrated.

We also demonstrated more complex sensing functionalities on the fiber tip. By embedding a p-i-n junction within the membrane, we can produce a photocurrent by nonresonant optical pumping, and measure the voltage across the junction through the electro-optic effect (in this case a polarized resonance was used). This allows generating and measuring electrical signals, and enables a novel electronic-photonic sensing modality, where the sensing is electrical and the readout is optical. We used this approach to demonstrate cryogenic temperature sensing in a temperature regime where the optical response to temperature is negligible [11]. We also demonstrated the fiber-tip transfer of optomechanical structures, opening a route towards high-performance, yet practical optomechanical sensors of displacement, mass and vacuum pressure with extremely small footprint and simple packaging.

Finally, we have investigated fiber-tip nanophotonic cavities combining wavelength-scale optical confinement and efficient fiber coupling. Using advanced design methods for optimizing the far-field emission of the cavity, cavities featuring mode volume $<(\lambda/n)^3$, quality factor Q>3'000 and a spectral modulation >20% in reflection were obtained. Leveraging the strong field confinement in these structures, we have demonstrated the detection of single nanoparticles with diameters down to 50 nm, directly from the fiber tip [12].

This research was funded by the Netherlands Organization for Scientific Research (NWO) through projects No. 18477 and 024.002.033. It is part of the research program of NWO.

References

[1] A. Ricciardi et al., "Lab-on-fiber technology: a new vision for chemical and biological sensing", Analyst 140, 8068 (2015)

[2] M. Pisco and A. Cusano, "Lab-on-Fiber Technology: A Roadmap toward Multifunctional Plug and Play Platforms", Sensors 20, 4705 (2020)

[3] E.J. Smythe et al., "A Technique to Transfer Metallic Nanoscale Patterns to Small and Non-Planar Surfaces", ACS Nano 3, 59 (2009)

[4] S. Scheerlinck et al., "Metal Grating Patterning on Fiber Facets by UV-Based Nano Imprint and Transfer Lithography Using Optical Alignment", IEEE J. Lightwave Technol. 27, 1415 (2009)

[5] D.J. Lipomi et al., "Patterning the Tips of Optical Fibers with Metallic Nanostructures Using Nanoskiving", Nano Lett. 11, 632 (2011)

[6] I.W. Jung et al., "Highly Sensitive Monolithic Silicon Photonic Crystal Fiber Tip Sensor for Simultaneous Measurement of Refractive Index and Temperature", IEEE J. Lightwave Technol. 29, 1367 (2011)

[7] G. Shambat et al., "Optical fiber tips functionalized with semiconductor photonic crystal cavities", Appl. Phys. Lett. 99, 191102 (2011)

[8] B. Wang et al., "Photonic crystal cavity on optical fiber facet for refractive index sensing", Opt. Lett. 37, 833 (2012)

[9] L. Picelli et al., "Scalable wafer-to-fiber transfer method for lab-on-fiber sensing", Appl. Phys. Lett. 117, 151101 (2020)

[10] M.S. Cano-Velázquez et al., "Temperature-Compensated Solution Concentration Measurements Using Photonic Crystal Fiber-Tip Sensors", Sensors 23, 7703 (2023)

[11] L. Picelli et al., "Hybrid electronic-photonic sensors on a fiber tip", Nature Nanotechnology, 18, 1162 (2023)

[12] A.L. Hendriks et al., "Detecting Single Nanoparticles using Fiber-Tip Nanophotonics", Optica, to be published

AES 2024, ROME - ITALY, 25 –28 JUNE 2024

Recent Advances in the Research of Graphene-based 2D Heterostructures for THz Plasmonic Device Applications

T. Otsuji[1]

[1]RIEC: Research Institute of Electrical Communication, Tohoku University, Japan

*corresponding author: otsuji@riec.tohoku.ac.jp

Abstract: This paper reviews recent advances in the research of graphene-based 2D heterostructures for terahertz plasmonic device applications.

To realize the next-generation ultra-high-speed, ultra-broadband 6G/7G THz wireless communication systems, the development of room-temperature, intense, and ultrafast laser transistors as well as highly sensitive, fast-response detectors operating in a wide sub-terahertz (THz) to THz range are the mandatory conditions [1]. However, THz electromagnetic waves are still unexplored frequency rsources bridging radio and light waves.

Carrier-injection pumping of GL can enable negative-dynamic conductivity in the THz range, leading to new types of THz lasers [2] but suffering from weak quantum efficiency below the 2.3% limit. Metasurface structures promoting the instability of graphene Dirac plasmons (GDPs) [3] are promising for obtaining giant THz gain and coherent THz oscillation. There are several different mechanisms for the GDP instability [4,5]. We have theoretically discovered a new type of the GDP instability mediated by ballistic injection of GDFs and strong Coulomb drag effect of the GDPs [6-8]. Our original asymmetric dual-grating gate (ADGG) GFET structure is suited to promote various types of the GDP instabilities as well as fast, sensitive THz detection [9,10]. The emergence of the black-phosphorus (b-P), black-Arsenic (b-As), and the compounds of these materials (b-As_xP_{1-x}), in which the energy gap ΔG varies from 0.15 to 1.2 eV depending on the number of the atomic sheets and the carrier transport holds a strong in-plane anisotropy, opens new prospects for the creation of the THz sources [11,12] and detectors [13,14].

The author thanks V. Ryzhii, A. Statou, C. Tang, K. Tamura, T. Suemitsu, H. Fukidome, M. Ryzhii, V. Mitin, and M.S. Shur for their contributions. The devices were fabricated at the Nano-Spin facility, RIEC, Tohoku Univ. This work was supported by JSPS KAKENHI 21H04546, Japan, and NICT-B5G #JPJ012368C01301, Japan.

References

1. Sengupta, K. et al. Nat. Electron., Vol. 1, 622-635, 2018.
2. Yadav, D. et al. Nanophotonics, Vol. 7, 741-752, 2018.
3. Boubanga-Tombet, S. et al. Phys. Rev. X, Vol. 10, 031004, 2020.
4. Otsuji, T. et al. Nanophotonics, Vol. 11, 1677-1696, 2022.
5. Ryzhii, V. et al. Appl. Phys. Lett., Vol. 116, 140501, 2020.
6. Ryzhii, V. et al. Phys. Rev. Appl., Vol. 16, 014001, 2021.
7. Ryzhii, V. et al. Phys. Rev. Appl., Vol. 16, 064054, 2021.
8. Ryzhii, M. et al. Appl. Phys. Lett., Vol. 120, 111102, 2022.
9. Delgado-Notario, J.A. et al. Nanophoton., Vol. 11, 519-529, 2022.
10. Tamura, K. et al. APL Photonics, Vol. 7, 16101, 2022.
11. Ryzhii, V. et al. Phys. Rev. B, Vol. 100, 115436, 2019.
12. Ryzhii, V. et al. Opt. Exp., Vol. 28, 24136, 2020.
13. Ryzhii, V. et al. Phys. Rev. Appl., Vol. 19, 064033, 2023.
14. Ryzhii, V. et al. Sci. Rep., Vol. 13, 9665, 2023.

AES 2024, ROME - ITALY, 25 –28 JUNE 2024

Light-modulated van der Waals Force Microscopy

Benfeng Bai*

Department of Precision Instrument, Tsinghua University, Beijing 100084, China
*corresponding author: baibenfeng@tsinghua.edu.cn

Abstract: A novel scanning probe technique, named light-modulated van der Waals force microscopy (LvFM), is developed by detecting the dynamic tip-sample van der Waals force. It can realize compositional imaging of nanomaterials (especially 2D materials) with an ultra-high spatial resolution of ~10 nm far below the optical diffraction limit under ambient conditions.

Since the invention of atomic force microscope (AFM) in 1986, it works on manipulating the absolute magnitude of van der Waals (vdW) force between AFM probe tip and specimen, by which spatial resolution of 1000 times better than the optical diffraction limit has been achieved. This kind of tip-sample force is, however, less sensitive to the alternation of atom species than to tip-sample separations, resulting in the difficulty of compositional identification, even under multi-modal strategies and other AFM variations.

Here, we report a phenomenon of light enhancement of dynamic tip-sample vdW force and the enhancement factor is found specific to materials. The force difference prior and after light illumination, instead of the tip-sample force itself, is employed for discriminating heterogeneous phases of materials. Based on this new principle, we propose a new technique, called the light-modulated van der Waal force microscopy (LvFM),[1] which can realize not only the functionality of AFM but also the capability of compositional characterization of materials. As proof-of-principle experiments, the LvFM has been successfully applied to discriminate the heterogeneous crystalline phase regions (2H phase and 1T' phase) of a $MoTe_2$ film and the compositional distribution of a h-BN and WS_2 heterostructure, which demonstrate not only an ultra-high compositional resolution represented by 20 dB enhancement factor and 150 times of the detection limit, but also a sub-10 nm lateral spatial resolution much smaller than the tip size of 20 nm. The simplicity of the opto-thermal mechanism, minuteness of excitation light power and wide availability of boosting lasers at various wavelengths imply broad applications of LvFM on nanomaterial characterization, which fills in the gap of compositional imaging and nanodefect characterization of various nanomaterials especially low-dimensional materials. It may have wide and important applications in the research and development of nanomaterials, especially for next-generation semiconductor industry.

We acknowledge the support by the National Natural Science Foundation of China (62175121 and 61960206003).

References

1. Y.-X. Han, B. Bai, J.-Y. Zhang, *et al*., “Light-enhanced van der Waals force microscopy,” arXiv, 2310:12518, 2023.

AES 2024, ROME - ITALY, 25 –28 JUNE 2024

Near-field heat transfer in many-body systems: application to thermal management and energy harvesting

P. Ben-Abdallah*

Laboratoire Charles Fabry, UMR 8501, Institut d'Optique, CNRS, Université Paris-Saclay, 2 Avenue Augustin Fresnel, 91127 Palaiseau Cedex

*corresponding author: pba@institutoptique.fr

Abstract: In this talk I will discuss some peculiarities of many-body systems to control the near-field radiative heat exchanges and to harvest near-field energy using pyroelectric conversion systems.

In the first part of this presentation I will introduce the theoretical framework [1,2] to deal with radiative heat exchanges in many-body systems composed of multiple thermal emitters.

Then I will discuss how these systems can be used to control the radiative heat exchanges at subwavelength scale using a local tuning of temperatures or by applying external actuations. In particular I will introduced a thermal analog of transistor [3], a three terminal system based on phase change materials, which can be used to switch, modulate, and even amplify heat flux through exchange of thermal photons opening the door to thermal logic gates [4]. Also I will introduce a radiative Hall effect [5] in systems made of small magneto-optical objects under the action of an external magnetic field. In a similar way to classical Hall effect, I will show that this effect which consists in the appearance of a heat flux in the direction transversal to a primary temperature gradient, can be used to locally control heat flux.

In the last part of my presentation I will explore the possibility to harvest the near-field energy confined close to a solid using graphene-based many-body pyroelectric converters [6] made with an active layer encapsulated between two graphene field-effect transistors deposited on the source and on the cold sink. I will describe the operating mode of these converters and I will show that the net power density generated by these devices can surpass the current production capacity of current near-field thermophotovoltaic converters by several orders of magnitude with low grade heat sources (T < 500K) and small temperature differences (ΔT~100K).

References

1. Biehs S. A. et al. , "Near-field radiative heat transfer in many-body systems," Rev. Mod. Phys., Vol. 93, 025009, 2021.
2. Ben-Abdallah P., Biehs S.-A. and Joulain K., "Many-body radiative heat transfer theory," Phys. Rev. Lett., Vol. 107, 114301, 2011.
3. Ben-Abdallah P. and Biehs S.-A., "Near-field thermal transistor", Phys. Rev. Lett., Vol. 112, 044301, 2014.
4. Kubytskyi V., Biehs S.-A. and Ben-Abdallah P., "Radiative bistability and thermal memory", Phys. Rev. Lett., Vol. 113, 074301, 2014.
5. Ben-Abdallah P., "Photon thermal Hall effect", Phys. Rev. Lett., Vol.116, 084301, 2016.
6. Latella I. and Ben-Abdallah P., "Graphene-based autonomous pyrolectric system for near-field energy conversion," Sci. Rep., Vol. 11, 19489, 2021.

AES 2024, ROME - ITALY, 25 –28 JUNE 2024

Electron–Plasmon Interactions in Nanoplasmonics: Fundamentals and Applications

P. André D. Gonçalves[1*], F. Javier García de Abajo[1,2],

[1] ICFO – The Institute of Photonic Sciences, Av. Carl Friedrich Gauss, 3, 08860 Castelldefels (Barcelona), Spain
[2] ICREA – Catalan Institution for Research and Advanced Studies, Passeig Lluís Companys 23 08010 Barcelona, Spain
[*]corresponding author: andre.goncalves@icfo.eu

Abstract: We exploit the interaction between free electrons and surface plasmons to unveil quantum nonlocal effects in nanoplasmonics and retrieve the quantum surface response of metals. In addition, we show that electron–plasmon interactions can be leveraged to resolve the ultrafast dynamics of plasmons imprinted on the photoemission spectrum from nanostructures.

Capitalizing on the ability of free electrons to produce deeply subwavelength near-fields that carry wave vector components commensurable with those governing the quantum-mechanical response of metals, we demonstrate their ability to probe quantum nonlocal effects imprinted on the optical response of metallic nanostructures [1]. In particular, we discuss how electron energy-loss spectroscopy (EELS) and cathodoluminescence (CL) can be used to infer quantum surface response functions (namely, the Feibelman *d*-parameters) that encapsulate those quantum effects [1]. Our proposed scheme provides a promising route for measuring the quantum surface response of metals using state-of-the-art electron-beam spectroscopies.

In the second part, we harness the potential of photoelectron spectroscopies to probe quasiparticle dynamics and investigate signatures multi-plasmon effects in the photoemission spectrum from plasmonic nanostructures (including metallic nanoparticles and graphene nanoislands) [2]. Such effects, driven by electron–plasmon interactions, lead to the emergence of sidebands separated from the main core-level peak by quanta of the plasmon energy. Our work extends previous theories which have thus far been limited to semi-infinite planar systems and offers an additional scheme to study multi-plasmon excitations in nanoplasmonics. We further predict the appearance of energy-gain satellites (whereby quanta of the plasmon energy are transferred to the outgoing photoelectron) in optically pumped (preceding the photoemission event) nanostructures [2].

Our work opens new avenues for utilizing electron–plasmon interactions to explore quantum nonlocal effects in nanoplasmonics and to resolve ultrafast dynamics of nanoscale optical fields in nanostructures.

References

1. Gonçalves, P. A. D. and García de Abajo, F. J., “Interrogating quantum nonlocal effects in nanoplasmonics through electron-beam spectroscopy”, Nano Lett. **23**, 4242–4249 (2023).
2. Gonçalves, P. A. D. and García de Abajo, F. J., “Multi-plasmon effects and plasmon satellites in photoemission from nanostructures”, Nanoscale **15**, 11852–11859 (2023).

AES 2024, ROME - ITALY, 25 –28 JUNE 2024

Two-photon plasmon induced polymerization for the deterministic integration of single photon sources

Abdelrahman Abdelaal, Ali Issa, Dandan Ge, Aurélie Broussier, Christophe Couteau, Sylvain Blaize, Renaud Bachelot, Safi Jradi*

Laboratory Light, nanomaterials & nanotechnologies - L2n, UTT & CNRS UMR 7076, Troyes, France
*corresponding author: safi.jradi@utt.fr

Abstract: In this work, we report on the use of a hybrid and functionalized photopolymers to selectively integrate nano-emitters on specific preselected sites of plasmonic nano-antennas and optical waveguides by plasmon induced two-photon polymerization at the nanoscale.

The integration of nano-emitters into plasmonic and photonic devices in a spatially control manner and with nanometer precision has become a great challenge. In this work, we use the plasmon induced photopolymerization combined with surface functionalization to selectively integrate nano-emitters into plasmonic and photonic waveguides. For this, two approaches were developed. The first one consists of using a photosensitive formulation containing quantum dots (QDs) where acrylic monomers are grafted on blue, green and red emitting QDs [1] before using it to integrate the nano-emitters by 2-photon polymerization (TPP) in the near field of a single gold nano-cube [2]. The second approach uses functionalized photopolymers making it possible to attach negatively charged nanoparticles right at the preselected polymerized sites [3-4]. Since the resulting active medium is a spatial memory of specific plasmonic modes, it is anisotropic, making the hybrid nanosources sensitive to light polarization [5]. The ability to adjust their statistical average lifetime by controlling the volume of the nanopolymer is demonstrated on semiconductor colloidal quantum dots. Trapping and immobilizing single photon emission from a single QD was demonstrated and confirmed through g(2) autocorrelation measurements. These 2 approaches have been investigated to integrated single photons sources in a deterministic manner into photonic integrated circuits.

References

[1] A. Issa, et al., ACS Applied Materials & Interfaces 15 (21), 25819-25830, 2023.
[2] D Ge, et al., Nature Communications 11 (1), 3414, 2020.
[3] A. Issa, et al., ACS Applied Materials & Interfaces 13 (35), 41846-41856, 2021.
[4] A. Abdelaal, et al, Langmuir 39 (13), 4583-4588, 2023.
[5] D. Ge, et al., Photonics research 10 (7), 1552-1566, 2022.

AES 2024, ROME - ITALY, 25 –28 JUNE 2024

Enhanced Light-Matter Interactions by engineered metal nanoantennas: Applications in advanced Biosensing

M.G.Manera[1*], A. Colombelli[1], D. Lospinoso[1], R. Rella[1]

[1]CNR-IMM Lecce, Italy

[*]corresponding author: mariagrazia.manera@cnr.it

Abstract: Design, fabrication, and characterization of engineered plasmonic nanostructures is here presented for the realization of sensitive and innovative biosensing transducers. Main attention will be dedicated to the last results in plasmon-enhanced magneto-optic effects.

Plasmonics is a rapidly advancing field that combines photonics, electronics, and nanotechnology. Plasmons excitations, namely the collective motion of conduction electrons in metals, is used to couple light with nano-objects and generate new optical effects at the nanoscale. Current research in this field is constantly oriented to propose innovative plasmonic systems with novel functionalities and improved performance.

The presentation will be an overview of my research group recent activity in this field. It is focused on the design, fabrication, and characterization of engineered plasmonic nanostructures. The goal is to investigate light-matter interactions below the diffraction limit of light for the realization of sensitive, efficient, and specific transducers able to monitor chemical and biosensing events at their interface with environment.

The research group uses cost-effective micro and nanofabrication techniques to create long and short-range periodic arrangements of metal nanostructures on planar and flexible substrates.

The realized plasmonic nanostructures works as antennas amplifying the incoming and scattered radiation. This is accompanied by a dramatic localization and enhancement of the electric field associated with light at optical frequencies. Our interest is developing metal nanoantennas with enhanced functionalities, investigating their near and far field optical properties for understanding the electromagnetic processes involved at the nanoscale.

Light localization at nanoscale volumes, compatible with biomolecule dimensions, is exploited for transducing molecular surface binding events into far-field optical signals. In this frame, metal nanoantennas are properly engineered to efficiently probe the local refractive index variations upon the biomolecular surface binding events yielding high refractometric sensitivities. This enables label-free real-time analysis of biomolecular interactions by optical spectroscopy.

In addition to biosensing, the field enhancement associated with metal nanoantennas is investigated for its potential in enhancing emissive phenomena such as Raman and fluorescence spectroscopies. By optimizing surface plasmon properties, detection limits of investigated analytes can be pushed up to a single molecular level, ensuring both sensitivity and specificity.

To achieve new functionalities, the combination of nanoscale electromagnetic (EM) fields with other material properties are illustrated. In particular, the potential offered by magnetophotonics to manipulate light below the diffraction limit by an external agent, i.e., a magnetic field, is demonstrated.

In this frame, effects of plasmon modes excitation on the Magneto-Optic (MO) activity on metal nanoantennas will be presented. A sizable MO activity in bare noble metal nanostructures upon modulation with

a low-intensity magnetic field is numerically and experimentally demonstrated. When interrogated as refractive index sensing transducers, they resulted in an MO signal achieving a resolution one order of magnitude higher than the traditional plasmonic sensing platforms.

This original way to control light-driven phenomena using magnetism is demonstrated to allow fine engineering of the distribution of local field on the transducers surfaces that, together with strong confinement of EM energy over small volumes, can ensure high sensing abilities at the single-molecule level.

Overall, the research group's work contributes to the advancement of knowledge in plasmonics and its applications in nanophotonics, metamaterials, and biosensing.

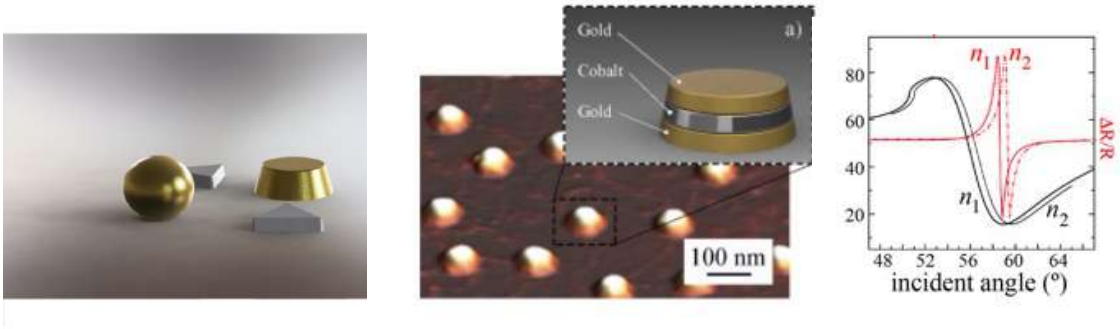

Figure1: Representative image of plasmonic nanostructures for investigation of their optical and MO properties and related transducing signals used for monitor refractive index changes at the metal-dielectric interface.

References

1. Colombelli, A., Lospinoso, D., Rella, R., Manera M.G., "Tunable Nanoplasmonic Transducers: Performance Analysis and Potential Application," chemosensors, Vol. 11, No. 2, 109, 2023.
2. Colombelli, A., Lospinoso, D., Rella, R., Manera M.G., "Shape Modulation of Plasmonic Nanostructures by Unconventional Lithographic Technique," Nanomaterials, Vol. 12, 547, 2022.
3. Lastname, F. M., F. M. Lastname and F. M. Lastname, "Magnetophotonics for sensing and magnetometry toward industrial applications," Journal of Applied Physics, Vol. 130, No. 23, 230901, 2021.
4. Manera M.G., Colombelli, A., Taurino, A., Garcia Martin, A., Rella, R., "Magneto-Optical properties of noble-metal nanostructures: functional nanomaterials for bio sensing," Scientific reports, 12640, 2018.

AES 2024, ROME - ITALY, 25 –28 JUNE 2024

Sustainable photocatalysis with scalable plasmonic metasurfaces

Alberto Naldoni[1,2]

[1]*Department of Chemistry and NIS Centre, University of Turin, Turin 10125, Italy*

[2]*Czech Advanced Technology and Research Institute, Regional Centre of Advanced Technologies and Materials Department, Palacký University Olomouc, Šlechtitelů 27, Olomouc 78371, Czech Republic*

alberto.naldoni@unito.it

Abstract. I will present recent results on the use of plasmonic metasurfaces in sustainable chemical reactions such as carbon dioxide reduction, hydrogen production, fuel cell operation. The complex relationship between optical resonances and chemical reactivity will be critically discussed being key to distinguish the reaction mechanism and to enhance their photochemical performance.

Plasmonic metasurfaces produce various non-linear effects that can dramatically increase the rate of photocatalytic reactions. In this talk, I will present recent results on the fabrication of scalable multimetallic metasurfaces and their activity and selectivity in sustainable chemical reactions such as carbon dioxide reduction, hydrogen production, fuel cell operation. The complex relationship between optical resonances and chemical reactivity will be critically discussed being key to distinguish the reaction mechanism and to enhance their photochemical performance.

AES 2024, ROME - ITALY, 25 –28 JUNE 2024

Micro-thermo-mechanical devices for THz detection

B. Bertoni[1], L. Vicarelli[1], S. Zanotto[2], S. Roddaro[1], A. Tredicucci[1,*] and A. Pitanti[1,2]

[1]Dipartimento di Fisica, Università di Pisa, Largo B. Pontecorvo 3, Pisa, Italy
[2]NEST Laboratory, CNR Istituto Nanoscienze, Piazza San Silvestro 12, Pisa, Italy
[*]Corresponding author: alessandro.tredicucci@unipi.it

Abstract: Thermomechanical microbolometers are a promising technology for THz detection. To control their absorption, we embed 2D layers/metamaterials, while transduction is performed either through optical probing of the mechanical resonance, or through magnetic flux modulation by an inductive element. The latter allows parallel read-out of large arrays of different mechanical frequencies.

AES 2024, ROME - ITALY, 25 –28 JUNE 2024

Achieving Non-Local Optical Response in Planar Metamaterials

V. A Fedotov

Center for Photonic Science and Engineering, Skolkovo Institute of Science and Technology, 121205, Moscow, Russia
*corresponding author: v.fedotov@skoltech.ru

Abstract: We present a recently discovered planar metamaterial, which supports strong collective excitation not found in metasurfaces. The supported non-local mode is virtually dispersionless yet ensures high sensitivity of the metamaterial response to incidence angle and enables non-resonant giant angular Goos-Hänchen shift (up to 1.5°) in specular transmission and reflection.

Over the last decade the concept of artificially engineered media has revolutionized the field of optics, pushed the boundaries of microfabrication and stimulated the development of novel characterization techniques. Recent demonstrations of anomalous reflection and refraction of light by metasurfaces opened another exciting chapter in optical engineering [1]. Non-local metasurfaces are an emerging sub-class of metasurfaces supporting collective resonant excitations of metamolecules [2, 3]. The non-locality of their response is underpinned by diffractive coupling between metamolecules and, therefore, on a fundamental level, such metasurfaces operate as diffractive optical devices that differ very little from trivial photonic crystal slabs, resonant waveguide gratings or sophisticated diffraction gratings. Unlike metasurfaces, planar metamaterials do not re-shuffle light into various diffraction orders but modify the characteristics of specular transmission and reflection instead, which effectively renders them as very thin slabs of some exotic materials. While such a regime of operation of artificial photonic media remains more desirable for applications in wavefront manipulation, optical imaging, image processing, spatial filtering and emission control, the engineering of non-local response in planar metamaterials is challenging due to the lack of mechanisms enabling long-range coupling among metamolecules. In this talk we are going to present and discuss a recently discovered planar metamaterial operating in he visible part of the spectrum, which can support strong collective excitations of its metamolecules not found in metasurfaces. One of the distinct features of the supported non-local mode is that it's virtually dispersionless yet ensures high sensitivity of the metamaterial response to the angle of incidence. The latter enables the engineering of non-resonant giant angular Goos-Hänchen shift (up to 1.5°) in specular transmission and reflection, thus, making the application of the effect for steering and manipulation of light beams a practical proposition.

References

1. N. Yu and F. Capasso, "Flat optics with designer metasurfaces," Nat. Mater., Vol. 13, 139−150, 2014.
2. A. Overvig and A. Alù, "Diffractive Nonlocal Metasurfaces," Laser Photon. Rev., Vol. 16, 2100633, 2022.
3. K. Shastri and F. Monticone, "Nonlocal flat optics," Nat. Photon., Vol. 17, 36–47, 2023.

AES 2024, ROME - ITALY, 25 –28 JUNE 2024

Efficient nonlinearities in metasurfaces enabled by bound states in the continuum

H. Harutyunyan[1*]

[1]Dpartment of Physics, Emory University, Atlanta, GA 30322, USA

[*]corresponding author: hharuty@emory.edu

Abstract: We present a novel approach to designing high-quality bound states in the continuum (BIC) in dielectric metasurfaces using magnetic dipole resonances coupled to a mirror, enabling strong light–matter interaction without the need for asymmetric geometry or polarization dependence. This simplifies fabrication and enhances practical applications, demonstrated by a record-breaking third harmonic generation efficiency. Additionally, we showcase superior modulation characteristics with a pulsewidth-limited switching time of 100 fs and a remarkably low energy consumption, facilitated by the narrow photonic resonance of our metasurface. Our findings offer significant potential for optical sensing, quantum photonics, and nonlinear devices.

AES 2024, ROME - ITALY, 25 –28 JUNE 2024

Chip-scale Nanophotonic Technologies and Applications

Yeshaiahu (Shaya) Fainman

Department of Electrical and Computer Engineering, University of California Dan Diego, La Jolla, California 92093, USA
yfainman@ucsd.edu

Abstract: Dense photonic integration requires miniaturization of materials, devices, circuits and systems, including passive components (e.g., engineered composite metamaterials, filters, etc.), active components (e.g., modulators and nonlinear wave mixers) and integrated circuits (Fourier transform spectrometer, programmable phase modulator of free space modes, linear algebra processors, etc.).

The integration of photonic systems requires miniaturization of the optical components, similar to the effort that has led to the extensive miniaturization in electronics. For applications involving a photonics layer between different components on the same chip, the photonic components must be comparable in size to the electronic components, and minimally interfere with each other when densely packed. By taking advantage of advances in lithographic tools it is possible to arrange deeply subwavelength features in a patterned material composition to act as a metamaterial with space variant polarizability. These nanofabrication capabilities enabled us to move forward from diffractive optical elements to artificially engineered composite dielectrics with space variant polarizability on deeply subwavelength scale [1-5] to construct polarization selective structures and various functional metasurface devices. This concept was also extended to resonant inhomogeneous materials and devices on a chip using a single step E-beam lithography to define resonant nanophotonic geometried such as photonic crystal quantum wires [6, 7], coupled quantum wires [8, 9], and realization of all optical pulse compressor on a chip [10]. With the intend of moving from passive to active artificially engineered metamaterials, we explored engineering of nonlinear optical metasurfaces [11-13] and nonlinear silicon rich silicon nitride [14-16] as well as using these engineered optical nonlinearities to realize an ultrafast, 1GHz frame rate spatial light modulator [17].

Miniaturized integrated spectrometers will have unprecedented impact on applications ranging from unmanned aerial vehicles to mobile phones, and silicon photonics promises to deliver compact, cost-effective devices. Mirroring its ubiquitous free-space counterpart, a silicon photonics-based Fourier transform spectrometer (Si-FTS) can bring broadband operation and fine resolution to the chip scale. Here we will present the modeling and experimental demonstration of a thermally tuned Si-FTS accounting for dispersion, thermo-optic non-linearity, and thermal expansion. We show how these effects modify the relation between the spectrum and interferogram of a light source and we develop a quantitative correction procedure through calibration with a tunable laser. Providing design flexibility and robustness, the Si-FTS is poised to become a fundamental building block for on-chip spectroscopy [18]. Moreover, taking advantage of nanofabrication we will discuss on-chip spectrometers using stratified waveguide filters and machine learning [19].

Moving forward, we will discuss chip-scale integrated circuit/system that will allow to realize linear algebra accelerator with superior performance in speed, energy consumption and size compared to its electronic counterpart. Such system can be manufactured using monolithic CMOS compatible manufacturing and impact such applications as deep learning and artificial intelligence [20] as well as 6G and beyond wireless MIMO systems [21].

Acknowledgements

This work was supported by the Defense Advanced Research Projects Agency (DARPA) DSO's NAC and NLM Programs, the National Science Foundation (NSF) grants NSF ECCS-2023730 and NSF ECCS-2217453, the Army Research Office (ARO), the Ofice of Naval Research (ONR), the San Diego Nanotechnology Infrastructure (SDNI) supported by the NSF National Nanotechnology Coordinated Infrastructure (grant ECCS-2025752), and the ASML/Cymer Corporation. We also thank SDNI and all of UCSD's nano3 cleanroom staff and Dr Maribel Montero for their assistance with samples fabrication.

References

1. M. Born and E. Wolf, Principles of Optics (Pergamon, 1999).
2. O. Wiener, Abh. Sachs. Ges. Acad. Wiss., Math.-Phys. Kl, No. 6, 32, 1912
3. Richter, P. C. Sun, F. Xu and Y. Fainman, Appl. Opt., 34, 2421, 1995
4. F. Xu, R. Tyan, P. C. Sun, C. Cheng, A. Scherer and Y. Fainman, Opt. Lett., 20, 2457, 1995
5. R. Tyan, P. C. Sun, A. Scherer and Y. Fainman, Opt. Lett., 21, 761, 1996
6. HC. Kim, K. Ikeda, and Y. Fainman, J. of Lightwave Technology, 25, 5, 1147-1151, 2007
7. HC. Kim, K. Ikeda, and Y. Fainman, Opt. Lett., 32, 5, 539-541, 2007
8. K. Ikeda, M. Nezhad, Y. Fainman, Appl. Phys. Lett., 92, 20, 201111, 2008
9. D.T.H. Tan, K. Ikeda and Y. Fainman, Appl. Phys. Lett., Vol. 95, 141109-11, 2009
10. D.T. H. Tan, P. C. Sun,Y. Fainman, Nature Communications, Vol. 1, 1-6, 2010
11. H. Lin, M. Yang, R. Sharma, M. W. Puckett, S. Montoya, C. D. Wurm, F. Vallini, E. E. Fullerton, and Y. Fainman, Applied Physics Letters 110, 113103 (2017)
12. H. Lin, F. Vallini, M. Yang, R. Sharma, M. W. Puckett, S. Montoya, C. D. Wurm, E. E. Fullerton & Y. Fainman, Scientific Reports v. 7, 9983 (2017)
13. H. H. Lin, R. Sharma, A. Friedman, B. M. Cromey, F. Vallini, M. W. Puckett, K. Kieu, Y. Fainman, APL PHOTONICS, 4, 3: 036101, 2019
14. K. Ikeda, R.E. Saperstein, N. Alic, and Y. Fainman, Optics Express, 16, 12987-12994, 2008
15. M. W. Puckett, R. Sharma, H. Lin, M. Yang, F. Vallini, and Y. Fainman, Opt. Express, 24, 16923-16933, 2016
16. A. Friedman, H. Nejadriahi, R. Sharma, Y. Fainman, Opt. Lett., 46, 17, 4236-4239, 2021
17. A. Smolyaninov, A. El Amili, F. Vallini, S. Pappert, Y. Fainman, Nature Photonics, Feb. 11 2019
18. M. Souza, A. Grieco, N. Frateschi, Y. Fainman, NATURE COMMUNICATIONS 9, 665, 2018
19. A. Li, Y. Fainman, Nature Communications, 12, Article number: 2704, 2021
20. TC Hsueh, Y Fainman, B Lin, arXiv preprint arXiv:2402.08192, 2023
21. TC Hsueh, Y Fainman, B Lin, arXiv preprint arXiv:2402.08192, 2024.

AES 2024, ROME - ITALY, 25 –28 JUNE 2024

Backward terahertz-wave parametric oscillation and its innovation

H. Minamide[1]

[1]RIKEN center for Advanced Photonics, RIKEN, Japan

[*]corresponding author: minamide@riken.jp

Abstract: A high-brightness sub-terahertz-wave parametric oscillation with a peak power of 200 W has been successfully demonstrated, which is based on an originally design of slant-stripe-type periodically-poled lithium niobate. It has an ultra-wide frequency tunability of several hundred GHz and can be widely used for nondestructive testing applications.

Sub-terahertz (sub-THz) frequencies, below 1 THz, have seen remarkable development in next-generation (6G) wireless communications. On the other hand, an alternative attraction of sub-THz waves is their high material penetration, which makes them suitable for non-destructive testing applications. With the maturity of modern society, various new materials and structures have been invented and developed. In the production field, novel and conventional materials are efficiently utilized and provided to us as useful products. As social responsibility to product makers, quality inspection of manufactured and ready-made products is extremely important in a social environment that demands safety and security. In such manner, the demand for inspection objects is expanding in accordance with the times. Since nondestructive testing has solved many problems using conventional technologies such as X-rays and ultrasonic waves, the evolving development of materials and the inspection environment have created a demand for multimodal measurement and the introduction of new technologies.

Backward optical parametric oscillator is a promising light-source and provides true applications. The OPO was theoretically proposed in 1966 [1]. The wavelength conversion under a particular condition generates counter-propagating waves inside a nonlinear crystal and it provides self-feedback effect without any cavity. The simple scheme offers compactness, stability, and lightweight.

Especially, backward OPO in THz frequency region attracts much attention because THz-wave source for general use has been expected for a long time due to many applications of nondestructive inspection. And wide tunability provides a high accuracy for a depth resolution in an optical coherence tomography. However, the difficulty to realize the bright source is brought by the momentum mismatch under forward light and counter-propagating THz wave.

Recently, we have demonstrated high conversion efficiency from near-infrared to terahertz waves in Mg-doped lithium niobate [2-4]. This result demonstrates the true potential of lithium niobate in terahertz-wave generation, which we have investigated in detail. In particular, with the miniaturization of terahertz wave sources as one of our goals, we have broadened the focus of our research from our success with bulk lithium niobate crystals to quasi-phase-matched crystals.

Consequently, we discovered backward terahertz-wave parametric oscillation [5] by designing and fabricating a unique periodically-poled lithium niobate crystal, which oscillates simply by irradiating pump beam. Under this unique quasi-collinear phase matching condition, THz-wave oscillation occurs in the direction opposite to the direction of propagation of the pump beam. It was also discovered that a cascade conversion process can be manifested, in which the Stokes radiation down-converted from the pump beam is further

converted downward. This is a promising approach to achieve photon conversion efficiency that exceeds the Manley-Lowe relation in the first-order conversion and aims at high power output. Furthermore, CW injection seeding to the first-order Stokes beam from an external source is expected to reduce the oscillation threshold, and in practice, it was demonstrated that the oscillation threshold can be reduced by 63% and the quantum conversion efficiency can be improved by 47% [6]. Tuned from these various results, the peak intensity of the maximum terahertz wave output reached approximately 200 W at 0.3 THz. This output is an unparalleled achievement for a palm-sized light source with gyrotron-class output power. Very recent research has investigated the frequency tunability provided by quasi-collinear phase matching, which can be extended to a maximum oscillation frequency of 0.9 THz [7]. The frequency tunability range is from about 0.3 THz to 0.9 THz, a vast tuning range that is difficult to achieve with other technologies.

Acknowledgements

This work was supported in part by Innovative Science and Technology Initiative for Security Grant Number JPJ004596, ATLA, Japan. The authors would like to thank Prof. H. Ito of RIKEN/Tohoku University and Prof. M. Kumano of Tohoku University for fruitful discussions.

References

1. S. E. Harris, "Proposed Backward Wave Oscillation in Infrared - (Parametric Oscillation Birefringence Internal Feedback Nonlinear Optics T)," (in English), Appl. Phys. Lett., vol. 9, no. 3, pp. 114-&, 1966.
2. S. Hayashi, K. Nawata, T. Taira, J. Shikata, K. Kawase, and H. Minamide, "Ultrabright continuously tunable terahertz-wave generation at room temperature," (in English), Sci Rep-Uk, vol. 4, p. 05045, Jun 5 2014.
3. H. Minamide, S. i. Hayashi, K. Nawata, T. Taira, J.-i. Shikata, and K. Kawase, "Kilowatt-peak Terahertz-wave Generation and Sub-femtojoule Terahertz-wave Pulse Detection Based on Nonlinear Optical Wavelength-conversion at Room Temperature," Journal of Infrared, Millimeter, and Terahertz Waves, vol. 35, no. 1, pp. 25-37, 2014.
4. K. Nawata et al., "Effective Terahertz Wave Parametric Generation Depending on the Pump Pulse Width Using a LiNbO3 Crystal," IEEE T. THz Sci. Techn., vol. 7, no. 5, pp. 617-620, 2017.
5. K. Nawata, Y. Tokizane, Y. Takida, and H. Minamide, "Tunable Backward Terahertz-wave Parametric Oscillation," Sci. Rep., vol. 9, no. 1, p. 726, 2019.
6. Y. Takida, K. Nawata, and H. Minamide, "Injection-seeded backward terahertz-wave parametric oscillator," APL Photonics, vol. 5, no. 6, p. 061301, 2020.
7. J. E. Muldera, K. Nawata, Y. Takida, D. Yadav, and H. Minamide, "Tunable backward terahertz-wave parametric oscillator centered at a high frequency of 0.87 THz with injection seeding," Opt. Express, vol. 31, no. 15, pp. 23966-23973, 2023.

AES 2024, ROME - ITALY, 25 –28 JUNE 2024

Nonlinear generation of optical beams with orbital angular momentum on $\chi^{(2)}$ dielectric films and metasurfaces

L. Coudrat[1], D. De Ceglia[2,3], R. Tanos[4], J.-M. Gérard[4], C. De Angelis[2,3], A. Degiron[1], and G. Leo[1,4*]

[1] MPQ, Université Paris Cité and CNRS, France
[2] CNIT and DIE, University of Brescia, Italy
[3] INO, CNR, Italy
[4] Université Grenoble Alpes, CEA, INP, IRIG, PHELIQS, France
[5] Institut Universitaire de France (IUF)

[*]corresponding author: giuseppe.leo@u-paris.fr

Abstract: We report on the generation of second-harmonic vortices with either a uniform film or an optical metasurface, fabricated in a hybrid AlGaAs-on-sapphire platform. In the former case we demonstrate spin-to-orbital angular momentum transfer, while in the latter we generate orbital angular momentum with arbitrary topological charge via a nonlinear meta-hologram.

AES 2024, ROME - ITALY, 25 –28 JUNE 2024

Metasurfaces in Laser Cooling and Trapping of Neutral Atoms Towards Quantum Information Processing & Quantum Sensing

Thu H. H. Le[1*], R. Takei[1], S. Kagami[2], A. Takamizawa[3], Y. Kurashima[1]

[1]Department of Electronics and Manufacturing, The National Institute of Advanced Science and Technology (AIST), Japan
[2]NEC-AIST Quantum Technology Cooperative Research Laboratory, Japan
[3]Research Institute for Physical Measurement, The National Institute of Advanced Science and Technology (AIST), Japan
[*]corresponding author: thu.le@aist.go.jp

Abstract: This study reports a novel scheme of using flat optics composed of geometric phase metasurfaces to prepare arrays of individual cold atoms trapped in the optical tweezers. This method exploits the capabilities of metastructures in controlling the phase, amplitude and polarization states of light at sub-wavelength resolution to generate specific wavefronts necessary for magneto-optical trapping (MOT) and dipole optical trapping (ODT) of alkali-metal atoms. This work highlights the potential of metasurfaces in integrating laser cooling and trapping within a compact apparatus, and the engineering of large scale many-body systems for quantum information processing, quantum simulations, and precision measurements.

Arrays of individual cold neutral atoms have recently emerged as promising platforms for a variety of applications including quantum metrology, quantum computing, and quantum networking[1]. Notably, their long coherence times, scalable architecture, and reconfigurable nature have facilitated the essential primitives required for high-fidelity quantum information processing[2]. In addition to fundamental studies on the physics of quantum systems involving cold atoms, significant efforts are underway to develop robust techniques to prepare array of atoms within a compact system. This is particularly crucial for effectively transferring cutting-edge quantum sciences into practical applications. However, the major challenge lies in the bulky optical elements employed in conventional magneto optical trapping (MOT) and dipole optical trapping (ODT) apparatus, which not only restrict the miniaturization but also hinder the scalability and fidelity of trapping individual atoms.

In this study, we propose and validate a novel scheme of using metasurfaces to ultimately manipulate the wavefront of light for cooling the alkali-metal atoms via MOT and assembling them into a periodic array via ODT. Metasurfaces are composed of nanofins structures of high-index dielectric materials which act as half waveplates, and the spatial rotation of each nanofin by an angle α allows us to imprint the geometric phase at sub-wavelength resolution, as depicted in Fig. 1(a). This type of metastructure, known as geometric phase or Pancharatnam-Berry (PB) phase metastructure, facilitates the precise and independent manipulation of optical amplitude, phase, and polarization, enabling the generation of arbitrary wavefronts.

In cooling of alkali-metal atoms via MOT, the metasurface is designed to diffract the incident circularly polarized laser beam into five beams, each with precise intensity and circular polarization states. By using a mirror and a quarter-waveplate to reflect the transmitted beam, all beams converge at the center of a quadrupole magnetic field, generating the necessary restoring forces to meet the MOT condition. This configuration has enabled the successful cooling of alkali-metal atoms using one single laser beam.

Atom ensembles, cooled by MOT, are then arranged into the desired array by employing the dipole optical trapping based on optical tweezer principle. In this process, it is essential to generate optical tweezers array with sufficiently high trapping potentials, while ensuring the geometric configurations, and intensity uniformity in each traps. The major approach is using liquid crystal-based spatial light modulators (SLMs) and a high numerical

aperture (*NA*) objective lens[1]. However, this method has several drawbacks, including insufficient focusing and limitations in both the scale and geometry of the generated trap arrays. In this study, we present a metasurface hologram which is capable of simultaneously generating and focusing light into holographic spots array with high trapping potentials.

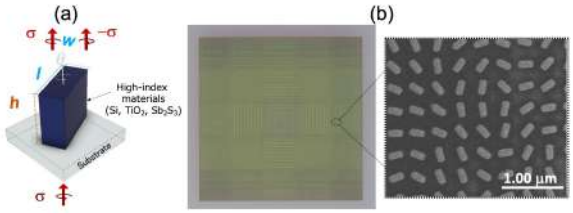

Fig. 1. (a) Unit structure of Pancharatnam-Berry (PB) phase metasurface, (b) the microscopic and SEM images of the fabricated hologram.

The phase-only hologram corresponding to the target image of a focusing spots array is calculated by the modified iterative Fourier-transform algorithm (IFTA). The metasurface hologram, comprised of silicon nanofin structures, is fabricated using electron beam lithography, followed by the etching of silicon using inductively coupled plasma reactive ion. Fig. 1(b) shows the microscopic and scanning electron microscopic (SEM) images of the fabricated hologram. The sample was then mounted on a motorized XYZ stage of an inverted microscope, with the metasurface facing downward. The sample was irradiated with a collimated and circularly polarized laser beam. The reconstructed holographic image, observed through a 50× objective lens (NA=0.95) on the transmission side, reveals the successful creation of the designed 20×20 focusing spot array, as shown in Fig. 2. The reconstructed array exhibits notably low noise and high precision, which can be attributed to the recording phase information in pixel sizes significantly smaller (less than 1/20) than those in conventional methods. It its also noteworthy that high transmission efficiency is achieved due to the suppression of undesired diffraction orders.

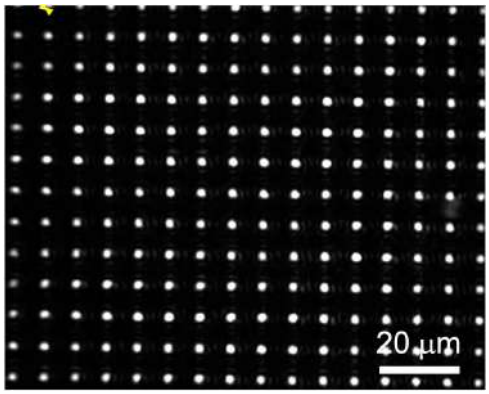

Fig. 2 The reconstructed holographic image of the designed 20×20 spots array

In summary, we have demonstrated and verified the performance of metasurfaces in magneto-optical trapping and dipole optical trapping of alkali-metal atoms. The cooling and trapping of atoms with metasurfaces, without the need for extra optical components, demonstrates exceptional precision in positioning, high optical efficiency, and scalability potential. These characteristics highlights the potential of metasurfaces in realization of compact and lower-power quantum systems, with diverse applications in quantum metrology, quantum information processing, and atomic physics.

Acknowledgements:

This study was partially supported by PRESTO (JPMJPR235C) from The Japan Science and Technology Agency. The authors gratefully acknowledge Nano-processing Facilities (AIST-NPF) and the Open Facilities of National Institute of Materials Science (NIMS), Japan for the support in nanofabrication processes.

References

1. Kaufman, A. M., et al. “Quantum science with optical tweezer arrays of ultracold atoms and molecules”, *Nat. Phys.* **17**, 1324-1333, 2021.
2. Ludkin, M. D., et al. “Logical quantum processor based on reconfigurable atom arrays”, *Nature* **626**, 58-65, 2024.

AES 2024, ROME - ITALY, 25 –28 JUNE 2024

Enabling new life science tools through visible integrated nanophotonics

P. Van Dorpe[1,2]

[1]imec, Kapeldreef 75, 3001 Leuven, Belgium
[2]KU Leuven, Dept. of Physics and Astronomy, Celestijnenlaan 200D, 3001 Leuven
[*]corresponding author: pvandorp@imec.be

Abstract: The building blocks and circuits of integrated nanophotonics allow for a deep miniaturization and/or parallelization of optical functionality. Life science applications often require visible wavelengths. For that purpose, silicon nitride nanophotonics offers an ideal platform.
We will review our recent applications of the platform in molecular sensing, cytometry, optogenetics, and microscopy.

Silicon nitride nanophotonics offers a platform that is ideally suited for visible-light bio applications. Allowing to integrate complex optical functionality on a small footprint, including on-chip routing and manipulation of free-space radiation.

We will review our recent applications of the platform in high-throughput molecular sensing [1], cytometry, optogenetics [2,3], and microscopy [4].

References

1. Neutens P. et al, J. Biophotonics 2024, 17(1), e202300279
2. Mahanty et al, News and Views, Nature electronics 6, 939 (2023)
3. Neutens P. et al, 2023 International Electron Devices Meeting (IEDM), San Francisco, CA, USA, 2023, pp. 1-4,

AES 2024, ROME - ITALY, 25 –28 JUNE 2024

Strong termination dependence of quasi-BIC's lifetime and frequency in plasmonic double-nets

Cédric Schumacher[1], Bilel Abdennadher[1], Ullrich Steiner[1], and Matthias Saba[1*]

[1]Adolphe Merkle Institute, University of Fribourg, Chemin des Verdiers 4, 1700 Fribourg, Switzerland
[*]corresponding author: matthias.saba@unifr.ch

Abstract: Plasmonic double-nets (PDNs) – or interlaced wire media – support broadband, single-mode longitudinal dispersion that gives rise to *quasi-BIC* resonances with extreme lifetime in PDN slabs. We show why the quasi-BIC resonance frequency and quality factor strongly depend on the slab termination, providing critical insight towards the application of PDNs.

AES 2024, ROME - ITALY, 25 –28 JUNE 2024

Spin and lattice dynamics of FePt nanoparticles at fundamental time and lengthscales

H. A. Dürr[1]

[1]Department of Physics and Astronomy, Uppsala University, Box 516, 75120 Uppsala, Sweden
hermann.durr@physics.uu.se

Abstract: Nanoscale light-matter interaction in magnetic materials is a topic of intense research in view of potential applications in high-density magnetic recording. I will provide an overview of recent advances in probing and understanding the magnetization and lattice dynamics of FePt nanoparticles of ~10 nm size following ultrafast laser excitation.

AES 2024, ROME - ITALY, 25 –28 JUNE 2024

Optical Spin Waves

V. Karakhanyan[1], R. Salut[1], M. A. Suarez[1], N. Martin[1], and T. Grosjean[1*]

[1]Optics department, FEMTO-ST Institute UMR 6174, University of Franche-Comté, CNRS, France
[*]corresponding author: thierry.grosjean@univ-fcomte.fr

Abstract: The precession of the magnetic moments in magnetic materials, forming spin waves, has many applications in magnetism and spintronics. We show that an optical analog of spin waves (OSW) can be generated in arrays of plasmonic nanohelices.

The concept of chirality is ubiquitous, impacting fields from biology and medicine to physics and materials science [1,2]. In optics, chiral effects is usually linked to helical waves carrying angular momentum. Recent research has explored the concept of photonic skyrmions by analogy to skyrmions in magnetic material [3,4]. Similarly, we investigate the possibility of generating a photonic counterpart to the spin waves propagating in ferromagnets.

Utilizing gold-coated carbon helices, we demonstrate that near-field coupling between adjacent homochiral helices results in optical waves with intrinsic angular momentum tied to the nanostructures' handedness. These waves propagate independently of the helix direction and are reflected at interfaces between enantiomeric nanohelices, forming heterochiral arrays. Such a property mirrors the reflection of spin waves between two magnetic materials of opposite magnetization (i.e., of oppostite precession handedness). We fabricated chains of helical nanoantennas and observed energy transport indicative of optical spin waves. The ability of these waves to be guided and reflected within the nanoantenna arrays highlights their potential for integrated photonic applications. The experimental results confirm our theoretical predictions [5].

The ability of OSW to be guided in a chain of subwavelength chiral structures and to be reflected at the interface between enantiomeric elements holds promise for angular momentum transfer and manipulation in compact integrated platforms. Spin-optical functionalities may arise from the combination of diverse operations on OSW including waveguiding, focusing, interference, steering and modulation, within metamaterials and metasurfaces possibly merging positive and negative refractive indices.

This work is funded by the French Agency of Research, the Region "Bourgogne Franche-Comté", the EIPHI Graduate School, the French RENATECH network.

References

1. A. Salam, J. Mol. Evol., vol. 33, pp. 105–113, 1991.
2. W. H Brooks et al. Curr. Top. Med. Chem., vol. 11, no. 7, pp. 760–770, 2011
3. S. Tsesses et al. Science, vol. 361, no. 6406, pp. 993–996, 2018.
4. L. Du et al. Nat. Phys., vol. 15, no. 7, pp. 650–654, 2019.
5. V. Karakhanyan et al. 2023.

AES 2024, ROME - ITALY, 25 –28 JUNE 2024

System bath approach in nonlinear optical thermodynamics

K. G. Makris[1,2*], G. Pyrialakos[3] and D. N. Christodoulides[3]

[1]*ITCP-Physics Department, University of Crete, Heraklion, 71003, Greece*

[2]*Institute of Electronic Structure and Laser (IESL) FORTH, Heraklion, 71110, Greece*

[3]*Ming Hsieh Department of Electrical and Computer Engineering, University of Southern California, Los Angeles, California 90089, USA*

[*]corresponding author: makris@physics.uoc.gr

Abstract: In the framework of the new direction of nonlinear optics, that of optical thermodynamics, we provide an equilibrium statistical mechanics approach of weakly nonlinear systems. Moreover, by employing a system-bath approach we formulate a non-equilibrium statistical mechanics approach, based on Langevin, Fokker-Planck type of equations for the modal amplitudes.

The study of nonlinear highly multimoded optical systems has attracted a lot of interest lately [1]. Predicting the complex nonlinear response of such systems especially when hundreds or thousands modes, is a challenging task, and thus a theory that explains and successfully predicts such a complex behavior is still missing. Towards this direction, quite recently however, a self-consistent theoretical framework has emerged, what we call *"Optical Thermodynamics"* [2–7]. In particular, optical thermodynamic theory is capable of describing such complex phenomena by means of thermodynamics of the system's supermodes. A complete set of thermodynamical variables was determined and thus was able to describe and accurately predict the equilibrium behavior of the multimoded system. The equation of state, the entropy and the Rayleigh-Jeans modal occupancies distribution was derived axiomatically either on thermodynamical grounds [2–4] or equivalently on statistical mechanical foundations [5-7]. Such an approach is universal since it can be applied to any weakly nonlinear optical multimode system of finite number of supermodes that involves a finite number of conserved quantities.

The first part of the talk is devoted to the understanding of the role of equilibrium fluctuations and the second part to develop a non-equilibrium description of the system. In order to achieve our first goal we are going to rely on the grand canonical formalism [5] and directly calculate the relevant fluctuations based on the grand partition function expression. For non-equilibrium, we develop a Langevin type of approach and Fokker-Planck type of formalism for the modal projection coefficients and derive effective stochastic or probability density equations that govern every supermode. Our analytical expressions are compared with direct numerical results of system-bath simulations, in all cases, and the agreement is excellent. Our results universally apply to any other weakly nonlinear highly multimoded bosonic lattice.

Acknowledgements: This project was funded by the European Research Council (ERC- Consolidator) under the grant agreement No. 101045135 (Beyond Anderson).

References

1. L. G. Wright, D. N. Christodoulides, and F. W. Wise, Nat.Phot. **9**, 306 (2015).
2. F. O.Wu, A. U. Hassan, and D. N. Christodoulides, Nat.Phot. **13**, 776 (2019).
3. M. Parto, F. O. Wu, P. S. Jung, K. G. Makris, and D. N. Christodoulides, Opt.Lett. **44**, 3936 (2019).
4. F. O. Wu, P. S. Jung, M. Parto, M. Khajavikhan, and D. N. Christodoulides, Comm.Phys. **3**, 1 (2020).
5. K. G. Makris, Fan. O. Wu, P. S. Jung, and D.N. Christodoulides, Opt.Lett. **45**, 1651 (2020).
6. F. O. Wu, Q. Zhong, H. Ren, P. S. Jung, K. G. Makris, and D. N. Christodoulides, Phys.Rev.Lett.**128**, 123901 (2022).
7. G. G. Pyrialakos, F. O. Wu, P. S. Jung, H. Ren, K. G. Makris, Z. H. Musslimani, M. Khajavikhan, T. Kottos, and D. Christodoulides, Phys. Rev. Res. **6**, 013072 (2024).

Photonic filter in the 300 GHz band with SiN microresonator frequency comb

Takasumi Tanabe[1*], Koya Tanikawa[1], Manto Imamura[1], Ayaka Yomoda[1], Satoki Kawanishi[1], and Shun Fujii[2]

[1]Department of Electronics and Electrical Engineering, Faculty of Science and Technology, Keio University, Japan
[2]Department of Physics, Faculty of Science and Technology, Keio University, Japan
[*]corresponding author: takasumi@elec.keio.ac.jp

Abstract: This study introduces a soliton-comb-based photonic filter targeting the 300 GHz band, employing a uni-traveling-carrier photodiode for enhanced terahertz frequency operation. Theoretical and experimental analyses demonstrate its superior stopband suppression, offering significant advancements in high-speed wireless communications through the novel integration of optical and electrical domains.

In the fast-paced world of wireless communications, the demand for wider bandwidths and increased data rates has led to the exploration of the terahertz (THz) frequency band, focusing on the 300 GHz band. Recent advances in microresonator frequency combs have paved the way for generating high-repetition optical pulses at 300 GHz. This breakthrough is crucial for producing 300 GHz signals through the use of uni-traveling-carrier photodiodes (UTC-PDs) to convert optical signals into microwaves, notable for their significantly lower noise compared to those generated through traditional radio-frequency signal multiplexing [1].

With these advancements, we delve into developing and applying soliton combs in photonic filters for high-frequency radio waves. Soliton combs, created by microresonators, are in a mode-locked state that yields highly repetitive pulse trains. We use the soliton microcombs not only to generate 300 GHz waves but also to enable highly sophisticated filtering operations.

The experimental setup for soliton comb generation involves a silicon nitride ring resonator with a free spectral range (FSR) of 299.5 GHz. The power kick method, controlled by an acousto-optic modulator, initiates soliton comb generation. The stability of the comb is maintained using the Pound-Drever-Hall method.

The UTC-PD plays a crucial role in converting the optical signals from the soliton comb into microwave signals. Unlike conventional photodiodes, the UTC-PD can operate at high frequencies and detect the beat signals of two adjacent longitudinal modes from the soliton comb. This conversion is vital for generating microwave signals with low noise at the 300 GHz band [1].

The frequency response for a typical finite impulse response using a soliton comb is described by [2],

$$H(\omega) \propto \sum_{n=0}^{N-1} p(n) e^{-j\omega nT}, \tag{1}$$

where ω is the angular frequency, n is the mode number of the comb, N is the number of comb lines, $p(n)$ is the power of the comb lines corresponding to the impulse response, and T is the delay between taps. As illustrated in Fig. 1(a), introducing variable delays modifies the transfer function according to Eq. (1). This change is visually represented in Fig. 1(b) corresponding to the shapes of the comb lines $p(n)$ as depicted in Figs. 1(d). Furthermore, the utilization of a UTC-PD for detecting adjacent modes separated by 300 GHz alters the frequency response as,

$$H_c(\omega) = \sum_{n=0}^{N-2} \sqrt{p(n)p(n+1)} e^{-j\omega nT} + \sum_{n=1}^{N-1} \sqrt{p(n)p(n-1)} e^{-j\omega nT}. \tag{2}$$

This adaptation results in a distinct frequency response profile tailored for precise filtering applications within the 300 GHz domain. The system's amplitude response is showcased in Figs. 1(c), illustrating significant distinctions between responses derived from Eq. (1). Notably, Fig. 1(b) and 1(c) highlight the response when the comb's power follows the profile displayed in Fig. 1(d), with a comb count of ten. Adjusting the delay T to match the filter's FSR reciprocal (100 ps) elucidates the stark contrasts in amplitude responses between Eqs. (1) and (4) mainly showcase the enhanced suppression ratio in the filter's rejection zone.

Finally, we show some experimental results of 300 GHz photonic filter operation in Fig. 2. The experimental filter matches well with the theoretical design in all cases.

In conclusion, we successfully demonstrate photonic filters operating in the 300 GHz band using a soliton comb combined with a delay line. We confirm the terahertz-band photonic filter operations by incorporating a UTC-PD. The advancements are expected to contribute significantly to next-generation high-speed wireless communications, highlighting the soliton comb's role in high-frequency applications.

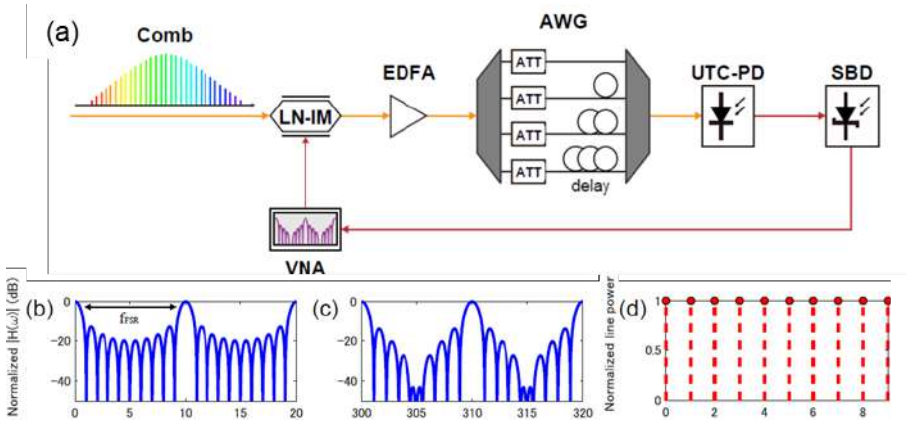

Fig. 1: (a) Experimental setup. Delays are applied to the generated soliton microcombs and then injected into the UTC-PD. It allows 300 GHz photonic filter operation. (b) Filter operation at baseband frequency. (c) Photonic filter operation at 300 GHz frequency. (d) Microcomb used to achieve the filters in (b) and (c).

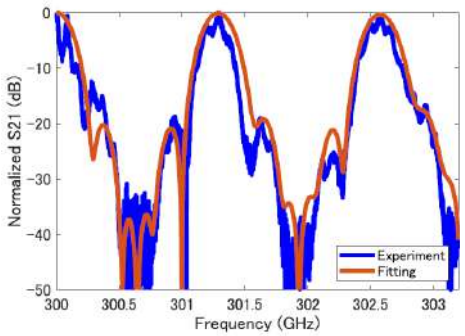

Fig. 2 Experimental demonstration of the 300 GHz filtering.

References

1. T. Tetsumoto, *et al.*, "Optically referenced 300 GHz millimetre-wave oscillator," Nat. Photonics **15**, 516 (2021).
2. J. Hu, *et al.*, "Reconfigurable radiofrequency filters based on versatile soliton microcombs," Nat. Commun. **11**, 4377 (2020).

Part of this work was supported by the Strategic Information and Communications R&D Promotion Programme (SCOPE) (#JP225003008) from the Ministry of Internal Affairs and Communications.

AES 2024, ROME - ITALY, 25 –28 JUNE 2024

A Finite Difference Numerical Package for Multiphysics Simulations of Nanophotonic Systems

M. Tamagnone[1*], H. Gupta[1,2], T. Contino[1,2], M. A. Yaqub[1,2], and M. W. Ashraf[l]

[1]Istituto Italiano di Tecnologia, via Morego 30, 16163 Genova, Italy
[2]Dipartimento di Chimica e Chimica Industriale, Università degli Studi di Genova, Genova, Italy
[*] michele.tamagnone@iit.it

Abstract: We present a new numerical finite difference numerical package capable of handling periodic driven or eigenvalue linear problems in an arbitrary number of dimensions and with user-defined physical laws (e.g. Maxwell's or Schrodinger's equations). We then illustrate the applications to experimental nanophotonic devices and highly confined polaritons in 2D materials.

This project has received funding from the European Research Council (ERC) under the European Union's Horizon 2020 research and innovation programme (Grant agreement No. 948250).

AES 2024, ROME - ITALY, 25 –28 JUNE 2024

Hybrid low loss integrated photonics: from chipscale frequency combs, frequency agile lasers, erbium amplifiers to cryogenic quantum interconnects

Tobias J. Kippenberg*
Swiss Federal Institute of Technology, Lausanne (EPFL)
*corresponding author: tobias.kippenberg@epfl.ch

Abstract:
Recent advances in attaining ultra low loss highly confining silicon nitride waveguides with loss in the dB-meter range, and their heterogeneous integration with MEMS and Lithium Niobate have opened up novel applications that benefit not only from scalable manufacturing, compact form factor and low power, but crucially have now reached a point where the performance is on par and even exceeding that of legacy optical systems. I will describe a range of novel advances, including photonic integrated circuit based frequency agile lasers with fiber laser phase noise, parametric traveling wave amplifiers, Erbium amplifiers on chip, as well as soliton frequency combs, with applications from coherent communications, LiDAR to cryogenic quantum interconnects.

Functional UV metalenses

Thomas F Krauss[1], Augusto Martins[1,2,3], Roxanne Guenette[3], Kezheng Li[1] and Emiliano R Martins[2]

[1] School of Physics, Engineering and Technology, University of York, York, YO10 5DD, UK
[2] São Carlos School of Engineering, Department of Electrical and Computer Engineering, University of São Paulo, São Paulo 13566-590, Brazil
[3] Department of Physics, University of Manchester, Manchester, M13 9PL, UK.

Abstract. The ability of metalenses to impose arbitrary phase profiles onto an optical wavefront continues to inspire new applications. Here, we explore the extension of the metalens paradigm into the UV and demonstrate two important applications, namely fluorescence detection at 350nm and VUV (<200nm wavelength) operation for particle physics applications.

Introduction. The advantages of metalenses to enable miniaturized optical systems are well established, especially in the visible and infrared wavelength regimes. A key issue is the choice of material, where high refractive index is key [1] for realising full control over the wavefront, such ultrawide field of view [2] and polarisation multiplexing [3], where we have been able to use silicon down to the green wavelength range. The ultraviolet (UV) presents a final frontier, because high index materials with tolerable loss are not available, and feature size scales as the wavelength, so realizing a large size metalenses with a high numerical aperture (NA) in the UV is a major challenge. Here, we describe two recent advances that address these challenges.

1. Fluorescence collection at 350 nm wavelength. The collection of fluorescent light poses two challenges, namely a) a high numerical aperture (NA), because the collection efficiency of a lens scales as NA^2, and b) a reasonable size, because a practical fluorometer has size restrictions, where practical constraints demand that the emitting source is a certain distance away from the lens. There have only been very few demonstrations of metalenses in the UV, all of which have been smaller than 1 mm in diameter, and therefore do not meet the second criterion. Instead, we introduce a novel type of single-layer, thin-film hybrid metalens that features an NA of 0.9 and a diameter of 6.2 mm. This hybrid metalens combines elements of a Fresnel lens on the inside with a binary grating on the outside; using a binary grating on the outside prevents the well-known shadowing effect of Fresnel lenses at high NA while allowing large area operation. As a result, we are able to show the corresponding combination of high NA and large area and demonstrate the efficient detection of tryptophan-like fluorescence (TLF) [4]. TLF is a well-studied proxy for water contamination with faecal coliforms. The WHO limit for contamination of drinking water corresponds to concentrations of 1 ppb or better, which we are able to demonstrate with our metalens fluorometer.

2. Focussing in the VUV (< 200nm wavelength). Going to even shorter wavelength, we have recently also explored operation in the vacuum ultraviolet (VUV), which has barely been considered because of the many technical difficulties, despite numerous scientific and technological opportunities. Creating metaoptic elements at this short wavelength is challenging due to the scarcity of transparent materials and the small sizes of the required nanostructures. By using UV-grade silica, we are able to present the first VUV (175 nm) metalens with high (>50%) transmission [5]. The fact that silica has a relatively low refractive index ($n \approx 1.54$ at 200 nm) makes the metalens design even more challenging, but we have developed a design and a corresponding fabrication process that affords successful operation even at this short wavelength. In particular, we show that the Nyquist requirement for subwavelength structures can be traded off against the feasibility of the fabrication process. As a result, we achieve a step-change in diffraction efficiency for wavelengths shorter than 300 nm. Our large numerical aperture (NA = 0.5) metalens shows an average diffraction efficiency of $(53.3 \pm 1.4)\%$, which opens up new avenues for compact flat optic systems operating in the VUV range.

3. Conclusion. We show that the metalens paradigm has great promise even in the technologically challenging UV wavelenth range by demonstrating an efficient fluorometer with high collection efficiency at 350 nm and a VUV metalens with high transparency at 175 nm.

4. References

[1] H. Liang, A. Martins, B-H. V. Borges, J. Zhou, E. R. Martins, J. Li & T. F. Krauss "High performance metalenses: numerical aperture, aberrations, chromaticity, and trade-offs" Optica 6, pp. 1461-1470 (2019).
[2] A Martins, K Li, J Li, H Liang, D Conteduca, BHV Borges, TF Krauss & E.R. Martins, "On metalenses with arbitrarily wide field of view", ACS Photonics 7 (8), 2073-2079 (2020)
[3] A. Martins, K. Li, G. S. Arruda, D. Conteduca, H. Liang, J. Li, B-H. V. Borges, T. F. Krauss, E. R. Martins, "Correction of Aberrations via Polarization in Single Layer Metalenses", Adv Opt Mat 10, 2102555 (2022)
[4] K. Li, A. Martins, S. Bohora, A. Dhakal, E. R. Martins & Thomas F. Krauss, "Hybrid Metalens for Miniaturised Ultraviolet Fluorescence Detection", Advanced Optical Materials 11, 2300852 (2023).
[5] A. Martins, T. Contreras, C. Stanford, M. Tuzi, J. M. Albo, C. O. Escobar, A. Para, A. Kish, J-S. Park, T. F. Krauss & R. Guenette, "High efficiency glass-based VUV metasurfaces", arXiv preprint arXiv:2401.11315 (2024)

AES 2024, ROME - ITALY, 25 –28 JUNE 2024

Programmable Nanophotonics with Phase-Change Materials: Towards Multilevel Tunability and Low-Loss devices

F. Bentata[1,2], C. Laprais[1], N. Baboux[1], P. Genevet[3], S. Monfray[2], G. Saint-Girons[1], X. Letartre[1], L. Berguiga[1], and S. Cueff[1]

[1]CNRS, Ecole Centrale de Lyon, INSA Lyon, Universite Claude Bernard Lyon 1, CPE Lyon, INL, UMR5270, 69130 Ecully, France
[2]STMicroelectronics, 850 Rue Jean Monnet, Crolles, 38920, France
[3]Université Côte d'Azur, CNRS, CRHEA, 06560 Valbonne, France
[*]corresponding author: sébastien.cueff@ec-lyon.fr

Abstract: We experimentally demonstrate phase-change materials (PCM) based programmable nanophotonic devices. Specifically, we propose and demonstrate approaches leveraging intermediate states of tunability in various PCM such as VO_2, GST and the emerging low-loss PCM Sb_2S_3.

Phase change materials (PCMs) are currently revolutionizing nanophotonics by providing ways to tune and reconfigure optical functionalities without any moving parts. Building on this phenomenon, the last decade has witnessed many exciting reports of novel devices exploiting PCMs such as for example beam-steering, tunable light emission, reflection and absorption, programmable metasurfaces and reconfigurable neural networks [1-3]. A large majority of the first studies were using standard PCMs such as GeSbTe as simple binary on-off switches, in which the ON state is the amorphous phase and the OFF state the fully crystalline phase. However, PCMs present another degree of freedom for tunability: the possibility to encode multilevel non-volatile states via partial crystallization. Furthermore, recently a new class of low-loss PCMs emerged (e.g. Sb_2S_3 and Sb_2Se_3), with negligible optical absorption in the near-infrared [4,5].
In this talk, we will present recent results on the physics and properties of PCMs and on original methods to program PCMs into various multilevel states of crystallization. We will then present nanophotonic devices leveraging this multilevel programming and conclude on the perspectives for this technology.

We acknowledge fundings from the French National Research Agency (ANR) under the project MetaOnDemand (ANR-20-CE24-0013).

References

1. E. Mikheeva, et al. "Space and time modulations of light with metasurfaces: recent progress and future prospects." in ACS photonics 9 (2022).
2. S. Cueff et al. "VO_2 nanophotonics." APL Photonics 5.11 (2020).
3. B. J. Shastri, et al. "Photonics for artificial intelligence and neuromorphic computing." Nature Photonics 15, 102 (2021).
4. W. Dong et al. "Wide bandgap phase change material tuned visible photonics." Advanced Functional Materials 29 1806181 (2019)
5. M. Delaney, et al. "A new family of ultralow loss reversible phase-change materials for photonic integrated circuits: Sb_2S_3 and Sb_2Se_3." Advanced Functional Materials 30, 2002447 (2020)

AES 2024, ROME - ITALY, 25 –28 JUNE 2024

Disorder as a degree of freedom for photonic nanomaterials

Rémi Carminati[1,2] **and Romain Pierrat**[1]

[1]Institut Langevin, ESPCI Paris, PSL University, CNRS, France
[2]Institut d'Optique Graduate School, Paris-Saclay University, France
[*]remi.carminati@espci.psl.eu

Abstract: Engineering the degree of partial order in scattering materials offers the possibility to design and fabricate novel metamaterials for photonics. We will discuss the basic principles of light interaction with correlated disordered materials, and present a few illustrative examples.

Disordered materials structured on scales ranging from tens of nanometers to micrometers scatter light, which is at first sight a disadvantage for applications in photonics. However, scattering is also an effective way of modulating light-matter interaction.

We will show that the ability to control the level of disorder offers a powerful degree of freedom to tune the level of absorption [1] or to create structural coloration or transparency [2,3], to cite only a few examples. Engineering the degree of partial order allows one to design and fabricate (nano)materials halfway between amorphous systems and photonic crystals [4], that have emerged as a new class of metamaterials.

Another interesting feature is that strongly scattering non-linear materials (powders) can exhibit an efficient response, for example in terms of generation of harmonics. We will analyze the mechanism for preserving the efficiency in the case of second harmonic generation [5].

[1] F. Bigourdan, R. Pierrat, R. Carminati, Opt. Express 27 (2019) 8666
[2] O. Leseur, R. Pierrat, R. Carminati, Optica 3 (2016) 763
[3] C. Salameh et al. , PNAS 117 (2020) 11947
[4] K. Vynck, R. Pierrat, R. Carminati, L.S. Froufe-Pérez, F. Scheffold, R. Sapienza, S. Vignolini, J.J Sáenz, Rev. Mod. Phys 95, 045003 (2023)
[5] R. Samanta, R. Pierrat, R. Carminati, S. Mujumdar, Phys. Rev. Applied 18 (2022) 054047 ; Phys. Rev. A 108, 053501 (2023)

AES 2024, ROME - ITALY, 25 –28 JUNE 2024

Compact terahertz harmonic generation in the Reststrahlenband in nanophotonic graphene resonators

Miriam Serena Vitiello

[1] *NEST, CNR - Istituto Nanoscienze and Scuola Normale Superiore, Piazza San Silvestro 12, 56127, Pisa, Italy*

*miriam.vitiello@sns.it

Abstract: Harmonic generation is a result of a strong non-linear interaction between light and matter. It is a key technology for optics, as it allows the conversion of optical signals to higher frequencies. Here, we demonstrate third harmonic generation at 9.63 THz by optically pumping single-layer graphene, coupled to a circular split ring resonator (CSRR) array, with a 3.21 THz frequency quantum cascade laser (QCL).

Topological phenomena and OAM manipulation in photonic graphene

Zhigang Chen
The MOE Key Laboratory of Weak-Light Nonlinear Photonics, TEDA Applied Physics Institute and School of Physics, Nankai University, Tianjin, China
zgchen@nankai.edu.cn

Graphene has attracted immense attention due to its fundamental interest and highly exploited applications. Apart from carbon-based monolayer graphene materials, various synthetic honeycomb lattices (HCLs) have been employed as artificial graphene for electrons, atoms and photons. In particular, photonic graphene - an HCL of evanescently coupled waveguide arrays, has been proposed and demonstrated as an ideal platform for investigation of unconventional edge states and pseudospin angular momentum, among other intriguing phenomena. In this talk, I will present a few examples of our recent demonstrations on topological control and manipulation of OAM modes in photonic graphene-like structures, including topological singularity mapping that leads to stair-wise generation of OAM beams and topological protection of OAM transport.

AES 2024, ROME - ITALY, 25 –28 JUNE 2024

Plasmon-Driven Photografting of Molecularly Imprinted Polymers onto Metal Nanostructures for Enhanced SERS Sensor Performance

A. Khitous[1,2], C. Molinaro[1,2], K. Haupt[1,2], S. Gree[1,2] and O. Soppera[1,2]*
[1]Université de Haute-Alsace, CNRS, IS2M UMR 7361, F-68100 Mulhouse, France
[2]Université de Strasbourg, France
3Université de Technologie de Compiègne, France
*corresponding author: olivier.soppera@uha.fr

Abstract: This paper introduces a rapid and versatile method to coat gold nanoparticles (AuNPs) with molecularly imprinted polymers (MIPs) via near-field radical photopolymerization. The resulting AuNPs@MIPs hybrid nanoparticles exhibit exceptional sensitivity and specificity for surface-enhanced Raman spectroscopy (SERS) and localized surface plasmon resonance (LSPR) analyses.

AES 2024, ROME - ITALY, 25 –28 JUNE 2024

Advances in optically-tunable metasurfaces

D.A. Pidgaiko[1,2,*] and I. Staude[1,2]

[1]Institute of Solid State Physics, Friedrich Schiller University Jena, 07743 Jena, Germany
[2]Institute of Applied Physics, Abbe Center of Photonics, Friedrich Schiller University Jena, 07745 Jena, Germany
[*]corresponding author: dmitrii.pidgaiko@uni-jena.de

Abstract: Here we present our advances with all-optical tunable metasurfaces with different approaches. Tunable metasurfaces, using organic photoswitches or liquid crystals, enable spatially variant optical responses. Additionally, a cascaded meta-optical system achieves ultrafast, all-optical switching for diverse wavefront manipulations, promising advancements in various applications.

Nanophotonic is one of the paramount areas in modern research - the advances in novel optical materials and devices capable of manipulating light at the nanoscale anticipate overcoming the fundamental limits of electronic devices in information processing performance. Metasurfaces and two-dimensional photonic structures play a major role because they can be fabricated with highly developed planar fabrication techniques and exhibit high interaction efficiency with light. Metasurfaces have proved to be superior tools for the amplitude, phase, polarization, and spatial distribution of light manipulation, holography, beam steering in both linear and nonlinear regimes, optical harmonics generation etc. For the vast majority of demonstrations, metasurfaces are designed for a specific optical effect and cannot be manipulated after fabrication. In order to broaden the application range of nanoscale flat optics the realization of tunable metasurfaces by external stimuli is required.

In our research, we propose a few concepts of all-optical tunability. The first approach is based on the combination of metasurfaces with organic photoswitches [1]. Such polymers provide the ideal means to facilitate optical tuning as they can rapidly transition between two isomers upon stimulation with light and are recoverable either optically or thermally in the dark. We report on the use of two different photoswitch-containing polymers, polyspiropyran and polyazobenzene, for metasurface resonance tuning. Either photoswitch can be used independently and when coated on a metasurface, can induce spatially-resolved red- or blue-shifts, respectively, in the metasurface resonance. However, the disparate wavelength tuning of the two photoswitches means they can also be used in combination; to add advanced functionality to metasurface resonance tuning and potential applications in logic processing or optical neural networks [2].

An additional benefit of light as a stimulus is that it can be used in combination with other stimuli. By carefully designing dual-responsive copolymers, we demonstrate that light can be used in combination with other stimuli such as temperature [3] or electric potential.

The second approach utilizes integration of metasurfaces into tunable-polymer-assisted liquid crystal (LC) cells [4,5]. The in-plane orientation of the LC molecules follows the alignment direction of the tunable polymer AtA-2, which is coated onto the metasurface and upper cell window and can be switched with linearly polarized light [4]. Using a digital mirror device one can change the AtA-2 orientation locally, thus creating spatially variant alignment conditions for the LC. We integrate a silicon metasurface featuring various Mie-type resonances into an inhomogeneously aligned LC. The spatially-resolved transmittance of the LC-integrated metasurface reveals a spectral shift of the resonances in the exposed region. It can be explained by the local in-plane reorientation of the LC molecules, causing a local change in the refractive index along the direction of polarization of the incident light. It is possible to change the alignment of the LC multiple times by repeated light

exposure of varying polarization. Our results demonstrate that metasurfaces embedded into inhomogeneously aligned LCs allow for the controlled and reconfigurable implementation of spatially variant optical response functions. Possible applications include reconfigurable images, holograms, gratings and Fresnel zone plates.

Finally, we introduce a cascaded meta-optical system consisting of a monolayer TMD, a quarter-wave plate, and a silicon metasurface designed for ultrafast all-optical switching of complex wavefronts. Two linearly polarized (perpendicular to each other) femtosecond pulses excite the second harmonic in the TMD monolayer. The polarization of the second harmonic signal is determined by the time delay between the pulses. Spatially resolved pump-probe experiments demonstrate second harmonic beam deflection, Gaussian-to-Vortex beam switching and topological charge switching at femtosecond-time scales. Importantly, given the capability of polarization-selective metasurfaces to imprint also more complex spatial phase profiles, our approach has the potential to enable switching between any two wavefronts with nearly arbitrary intensity profiles and pulse-duration limited dynamics. Our results can thus enable new technological developments in the fields of highspeed communications, remote sensing, ultrafast optics, and holographic techniques.

References

1. Walden, Sarah L., et al. "Two-Color Spatially Resolved Tuning of Polymer-Coated Metasurfaces." ACS nano (2024).
2. Becker, Marlon, et al. "Adaptive Photochemical Nonlinearities for Optical Neural Networks." Advanced Intelligent Systems 5.12 (2023): 2300229.Zou, C., et al. _Adv. Opt. Mater._ **11**, 2202187 (2022).
3. Zou, Chengjun, et al. "Electrically tunable transparent displays for visible light based on dielectric metasurfaces." Acs Photonics 6.6 (2019): 1533-1540.
4. Izdebskaya, Yana V., et al. "Multifunctional metasurface tuning by liquid crystals in three dimensions." Nano Letters 23.21 (2023): 9825-9831.Sinelnik, Artem, et al. "Ultrafast all-optical second harmonic wavefront shaping." Nature Communications 15.1 (2024): 2507.
5. Klimmer, Sebastian, et al. "All-optical polarization and amplitude modulation of second-harmonic generation in atomically thin semiconductors." Nature Photonics 15.11 (2021): 837-842.

AES 2024, ROME - ITALY, 25 –28 JUNE 2024

Linear Frequency Generation in Time-Varying Dispersive Interfaces

C. Rizza[1*], M. A. Vincenti[2], A. Contestabile[1], G. Castaldi[3], V. Galdi[3], and M. Scalora[4]

[1] University of L'Aquila, Department of Physical and Chemical Sciences, I-67100 L'Aquila, Italy
[2] Department of Information Engineering, University of Brescia, I-25123 Brescia, Italy
[3]University of Sannio, Department of Engineering, Fields & Waves Lab, Benevento, I-82100, Italy
[4]Aviation and Missile Center, U.S. Army CCDC, Redstone Arsenal, Alabama 35898-5000, USA
[*]corresponding author: carlo.rizza@univaq.it

Abstract: We suggest a new scheme for linear frequency generation in a time-varying dispersive metasurface. The effect is activated by a temporal boundary (i.e., an abrupt change in the metasurface electromagnetic parameters) enabling the excitation of the system's natural frequencies. Remarkably, the temporal boundary allows the direct far-field excitation of surface-wave modes without additional spatial structuring or prolonged temporal modulations.

Time-varying metasurfaces are compact devices and can be used to generate new frequencies without resorting to the conventional nonlinear effects. As a leading example, a time-varying thin film [1], with a prolonged time-periodic modulation of an impedance surface, generates new frequencies and provides an unconventional approach to obtain the direct far-field excitation of surface-wave modes without the need for additional spatial structures. Here, we investigate a time-varying, dispersive interface that features Lorentzian dispersion, whose parameters are modulated in time. This structure exhibits an unusual linear frequency generation at the resonance, and, more importantly, enables coupling between propagating and evanescent waves, without the need for periodic or extended temporal modulations. These effects are activated by a temporal boundary effect, i.e., a sudden step-like change in the interface's constitutive properties. Specifically, we consider a time-varying, dispersive dielectric layer of thickness L (with L<<λ, and λ denoting a characteristic wavelength) sandwiched between two homogeneous, stationary and nondispersive half-spaces, with relative permittivity $\boldsymbol{\varepsilon}_{\mathrm{L}}$ and $\boldsymbol{\varepsilon}_{\mathrm{R}}$. We investigate TE modes of the kind $\mathrm{Re}\left[E\left(z,t\right)e^{ik_x x}\right]\hat{\mathbf{e}}_y$, where k_x is the conserved transverse wavenumber, $\hat{\mathbf{e}}_\alpha$ is an α-directed unit vector. The metasurface lies at the plane z=0 and the interaction with the metasurface can be described in terms of sheet transition conditions, i.e., $\Delta E = 0,\ \Delta H = \frac{dP(t)}{dt}$,with $\Delta G = G\left(z=0^+,t\right) - G\left(z=0^-,t\right)$ (*G=E,H*) and *P(t)* the y-component of the surface polarization. Note that any field component *G* is of the form $\mathrm{Re}\left[G\left(z,t\right)e^{ik_x x}\right]$. The dynamics of the surface polarization is given by $\frac{d^2P}{dt^2} + \gamma P + \omega_0^2 P = \varepsilon_0 L \omega_p^2(t) E(0,t)$ (ε_0 is the vacuum permittivity), ω_0 and γ are the resonance frequency and damping parameter, respectively (constant over time), whereas ω_p is the time-varying plasma frequency. In the scenario where the system shows a temporal boundary, i.e., the plasma frequency has a sudden switch, we derive analytical solutions (see further details in [2]). In the stationary scenario (constant plasma frequency), the

metasurface can support discrete bound modes that propagate along x and exhibit evanescent decay along z. These bound modes generally cannot be directly excited by a propagating wave impinging from either side. Conversely, as demonstrated in the following example, the temporal boundary activates the natural resonance modes supported by the metasurface when interacting with an incident wave packet. These resonances can manifest as either radiative or bound modes, which can couple with a propagating incident field that is significantly detuned from the resonance. As a relevant example, we consider a scenario where a wave packet impinges at oblique incidence on the time-varying interface. Specifically, we assume that the incident field is at a reference plane z=-L_1=- 35 c/ω_0, with t_0=53/$\boldsymbol{\omega}_0$, $\sigma = 4/\omega_0$, $\omega_1 = 2.5\omega_0$, and $k_x = 1.44\omega_0/c$. Moreover, we set $\omega_p^2 = \omega_0^2 A(t)$, where $A(t) = A_1 + (A_2 - A_1)U(t)$ [*U(t)* is the standard unit step function] with A_2=1.2, A_1=1, and L=0.16c/ω_0, $\varepsilon_L = 2, \varepsilon_R = 1$. Results are reported in Fig.1. The reflection (Fig.1 b) and transmission (Fig.1 c) spectra exhibit sharp peaks at the resonant modes. For the chosen parameters, the resonant modes are bound since their eigenfrequencies lie within the evanescent spectral range (highlighted with green shading in Fig.1). Therefore, the excitation of the natural resonance modes induced by the temporal boundary enables the coupling of a propagating wave packet with bound modes (surface waves), without the need for any spatial subwavelength structuring or extended time-periodic modulations.

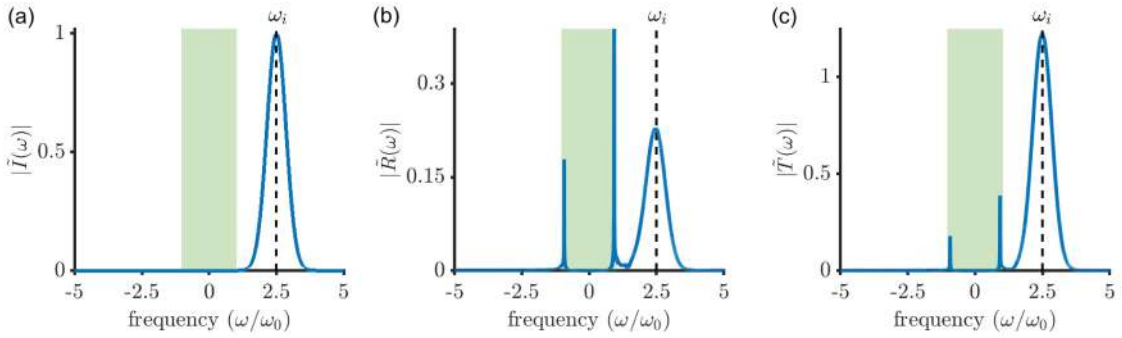

Fig.1 (a), (b), (c) Normalized spectra of the incident, reflected, and transmitted wave packets, respectively, where the dashed vertical lines indicate the carrier frequency of the incident field. All spectra are normalized with respect to the peak value of incident one.

Acknowledgements: Research was supported by PRIN-2022 PNRR initiative (GAMING project, CUP E53D23014870001) and by University of L'Aquila (PAT-BOOSTER-GAMING, CUP C18H23000780002). This work has also been funded by the European Union - NextGenerationEU under the Italian Ministry of University and Research (MUR) National Innovation Ecosystem grant ECS00000041 - VITALITY - CUP E13C22001060006.

References

1. Galiffi E. and Wang Y.-T., Lim Z. , Pendry J. B., Alù A. and Huidobro P. A., Phys. Rev. Lett., Vol. 125, , No. 12, 127403, 2020
2. Rizza C., Vincenti M.A., Contestabile A., Castaldi G., Galdi V., and Scalora M., "*Harnessing the natural resonances of time-varying dispersive interfaces*" submitted to PRL, 2024.

AES 2024, ROME - ITALY, 25 –28 JUNE 2024

Quantum metric and non-Hermitian Berry curvature in a plasmonic lattice

Javier Cuerda

Department of Applied Physics, Aalto University School of Science, Aalto FI-00076, Finland
javier.cuerda@aalto.fi

Abstract: We experimentally observe the quantum geometric tensor, namely the quantum metric and the Berry curvature, for a square lattice of radiatively coupled plasmonic nanoparticles. While the quantum metric emerges from the interplay of polarization and the mode structure, the origin of the Berry curvature is due to the system losses.

References

1. Cuerda, J., J. M. Taskinen, N. Källman, L. Grabitz, and P. Törmä, “Observation of Quantum metric and non-Hermitian Berry curvature in a plasmonic lattice”, arXiv:2305.13174 (accepted in Phys. Rev. Research), 2024.
2. Cuerda, J., J. M. Taskinen, N. Källman, L. Grabitz, and P. Törmä, “Pseudospin-orbit coupling and non-Hermitian effects in the Quantum Geometric Tensor of a plasmonic lattice”, arXiv:2305.13244 (accepted in Phys. Rev. B), 2024.

AES 2024, ROME - ITALY, 25 –28 JUNE 2024

Layered Metal-Dielectric-Metal Nanocavities with Vanishing Permittivity: Resonance Coupling and Strong Light-Matter Interaction

Aniket Patra [1,2], V. Caligiuri [2,3], Bruno Zappone [3], Antonio De Luca [2,3], and Roman Krahne [1]

[1] Optoelectronics Research Line, Istituto Italiano di Tecnologia, via Morego 30, 16163 Genova, Italy
[2] Dipartimento di Fisica, Università della Calabria, via P. Bucci 33b, 87036 Rende (CS), Italy
[3] CNR-Nanotec, via P. Bucci 33c, 87036 Rende, Italy
[*]corresponding author: roman.krahne@iit.it

Abstract: Layered Metal-Dielectric-Metal nanocavities sustain resonances with vanishing permittivity that modes can be tuned by the thickness of the dielectric. Multiple resonances can be engineered by including higher harmonics, and by stacks of interacting cavities. Integrating such cavity systems with light emitters enables emission enhancement, directional control, and strong light-matter interaction.

Layered Metal-Dielectric-Metal (MDM) structures provide a highly versatile platform for light manipulation. With a dielectric layer thickness in the range of the excitation wavelength, this system acts as a photonic cavity with resonances that have vanishing dielectric permittivity. The layered structure can be seen as a homogenized metamaterial that sustains Epsilon-Near-Zero (ENZ) modes. Interestingly, the similarity of the Helmholtz to the Schrödinger equation enables to apply the formalisms of quantum mechanics to analyze the ENZ modes. With this view the ENZ resonances can be understood as resonant tunneling of photons through the metamaterial. [1,2,3] This quantum analogy can be extended to strongly coupled cavity systems that feature bonding and anti-bonding modes, and which for large number of cavities form ENZ bands that can be described by the Kronig-Penney model.[4] In the double-cavity system one can tune the splitting of the two low-energy cavity modes to tune the wavelength of the cavity resonances to the emission and absorption bands of emitting dyes, for example layers of perovskite nanocrystals, which can be used to enhance their radiative rate.[5] The MDM cavity platform allows to fabricate superabsorbers, optical resonators for light emission enhancement and directional control,[6] and can provide switching elements in ultrafast signal processing. [7] Therefore, MDM cavities constitute highly versatile ultrathin optical metamaterial with tunable resonances in the visible range, with the practical advantage that they can be implemented on large areas by cost-efficient thermal deposition methods.

In coupled cavity systems involving layered MDM resonators the resonance matching can be designed by the thickness of the dielectric layer in the MDM stack. Here we present two very different approaches for obtaining coupled resonators. On one hand, we combine MDM cavities with Guided-Mode-Resonators (GMR) by fabricating the GMR onto the top metal layer of the MDM cavity.[8] Such highly anisotropic double cavity system allows for polarization control on the resonance splitting, and the color filter behavior of the MDM enables a side selective response. On the other hand, we investigate MDM systems where the dielectric layer is doped with light emitting molecules. We observe strong light-matter coupling with a Rabi splitting exceeding 100 meV, and find that the polaritons inherit the ENZ properties of the MDM cavity system. Furthermore, present an elegant method to vary the thickness of the dielectric layer in the MDM system (that corresponds to the length of the cavity) in situ by using a surface-forces apparatus (SFA).[9] This approach allows to map the anticrossing of the modes in a double cavity system in a single experiment. Applying the SFA to the dye-doped

MDM system allows to detect the strong coupling of multiple cavity harmonics with the dye emission in a single, rapid, and continuous sweep of cavity thickness. Furthermore, the complementarity of the ellipsometric spectroscopy study of the dye-doped MDM experiment with the SFA experiment allows to investigate the impact of the in-plane and out-of-plane wave vector on the Rabi splitting. [10]

In conclusion, MDM nanocavities provide a versatile platform for the design of coupled resonator systems and light control. Introducing light emitters in the dielectric layers results in polaritonic resonances with ENZ properties, which introduce the features of vanishing dielectric permittivity to strong light-matter interaction

References

1. Caligiuri, V., Palei, M., Biffi, G., Artyukhin, S., Krahne, R. "A Semi-Classical View on Epsilon-near-Zero Resonant Tunneling Modes in Metal/Insulator/Metal Nanocavities", *Nano Lett.* **2019,** 19, 3151-3160.
2. Caligiuri, V., Palei, M., Biffi, G., Krahne, R. "Hybridization of Epsilon-near-Zero Modes Via Resonant Tunneling in Layered Metal-Insulator Double Nanocavities", *Nanophoton.* **2019**.
3. Zappone, B., Caligiuri, V., Patra, A., Krahne, R., De Luca, A. Understanding and Controlling Mode Hybridization in Multicavity Optical Resonators Using Quantum Theory and the Surface Forces Apparatus, *ACS Photon.* **2021**.
4. Caligiuri, V., Biffi, G., Patra, A., Pothuraju, R. D., De Luca, A., Krahne, R. "One-Dimensional Epsilon-near-Zero Crystals", *Adv. Photon.Res.* **2021,** 2, 2100053.
5. Caligiuri, V., Palei, M., Imran, M., Manna, L., Krahne, R. "Planar Double-Epsilon-near-Zero Cavities for Spontaneous Emission and Purcell Effect Enhancement", *ACS Photon.***2018,** 5, 2287-2294.
6. Caligiuri, V., Biffi, G., Palei, M., Martín-García, B., Pothuraju, R. D., Bretonnière, Y., Krahne, R. "Angle and Polarization Selective Spontaneous Emission in Dye-Doped Metal/Insulator/Metal Nanocavities", *Adv. Opt. Mater.* **2020,** 8.
7. Kuttruff, J., Garoli, D., Allerbeck, J., Krahne, R., De Luca, A., Brida, D., Caligiuri, V., Maccaferri, N. "Ultrafast All-Optical Switching Enabled by Epsilon-near-Zero-Tailored Absorption in Metal-Insulator Nanocavities", *Commun.s Phys.* **2020,** 3.
8. Patra, A., Pothuraju, R. D., De, D., Caligiuri, V., Vijaya, R., De Luca, A., Krahne, R. "Design and Polarization Control of the Modal Splitting in Hybrid Anisotropic Nanocavities", *Adv. Opt. Mater.* **2023,** n/a, 2202876.
9. Zappone, B., Caligiuri, V., Patra, A., Krahne, R., De Luca, A. "Understanding and Controlling Mode Hybridization in Multicavity Optical Resonators Using Quantum Theory and the Surface Forces Apparatus", *ACS Photon.* **2021,** 8, 3517-3525.
10. Patra, A., Caligiuri, V., Zappone, B., Krahne, R., De Luca, A. "In-Plane and out-of-Plane Investigation of Resonant Tunneling Polaritons in Metal–Dielectric–Metal Cavities", *Nano Lett.* **2023,** 23, 1489-1495.

Advanced Techniques for Computational Electromagnetics, by Maha Ben Rhouma

AES 2024, ROME - ITALY, 25 –28 JUNE 2024

An efficient method for calculating resonant modes in biperiodic photonic structures

N. Zhang[1*] **and Y. Y. Lu**[1]

[1]Department of Mathematics, City University of Hong Kong, Hong Kong, China
*corresponding author: nzhang234-c@my.cityu.edu.hk

Abstract: A new method is proposed for calculating resonant modes in biperiodic structures. We avoid using PMLs and reduce the Maxwell's equations to a small nonlinear eigenvalue problem that is solved by contour integral method. Numerical examples show that our method is efficient with respect to memory usage and CPU time.

We consider a non-magnetic structure that is bounded in z by $|z| < d$, sandwiched between two homogeneous media, and periodic in x and y with period L. A resonant mode has a real Bloch wavevector $[\alpha, \beta, 0]^\mathsf{T}$ and a complex angular frequency ω [1]. In a unit cell $\Omega = S \times \mathbb{R}$, where $S = (0, L) \times (0, L)$, it satisfies an outgoing radiation condition in z and the frequency-domain Maxwell's equations

$$\nabla \times \mathbf{E} = \mathrm{i}\frac{\omega}{c}\mathbf{H}, \quad \nabla \times \mathbf{H} = -\mathrm{i}\frac{\omega}{c}\varepsilon\mathbf{E}, \tag{1}$$

where ε is the dielectric function, c is the speed of light in vacuum, $\mathbf{E}$ is the electric field, and $\mathbf{H}$ is a scaled magnetic field.

For some $D > d$, the planes $\Gamma_\pm = S \times \{z = \pm D\}$ divide the unit cell Ω into three subdomains Ω_+, Ω_- and Ω_D with the z-intervals $(D, +\infty)$, $(-\infty, -D)$ and $(-D, D)$, respectively. The tangential electromagnetic fields at $\Gamma_\pm$ can be related by exterior and interior transverse impedance (TI) operators derived from the Maxwell's equations in $\Omega_\pm$ and Ω_D, respectively. Since the fields are smooth at $\Gamma_\pm$, we can approximate them by a small number of Fourier terms:

$$\mathbf{H}_T^\pm \approx \sum_{m,n=-M}^{M} \mathbf{H}_{T,mn}^\pm F_{mn}(x, y), \ \mathbf{E}_T^\pm \approx \sum_{m,n=-M}^{M} \mathbf{E}_{T,mn}^\pm F_{mn}(x, y) \tag{2}$$

where $F_{mn}(x, y) = \exp\left[\mathrm{i}(\alpha x + \beta y) + \mathrm{i}2\pi(mx + ny)/L\right]$, $\mathbf{H}_T = [H_x, H_y, 0]^\mathsf{T}$, $\mathbf{E}_T = [E_x, E_y, 0]^\mathsf{T}$, and M is a small positive integer. The TI operators are then approximated by matrices $\mathbf{T}_{\text{ext}}$ and $\mathbf{T}_{\text{int}}$. Consequently, a resonant mode can be approximated by solving the following nonlinear eigenvalue problem:

$$\mathbf{T}(\omega)\mathbf{h} = 0, \ \mathbf{T} = \mathbf{T}_{\text{ext}} - \mathbf{T}_{\text{int}}. \tag{3}$$

where the vector $\mathbf{h}$ represents the Fourier coefficients of tangential magnetic fields.

The matrix $\mathbf{T}_{\text{ext}}$ can be written in an analytical form since the fields in $\Omega_\pm$ have Rayleigh expansions. However, for a generic structure, the fields in Ω_D do not have an explicit form, and thus, the matrix $\mathbf{T}_{\text{int}}$ does not have an analytical expression. In this paper, we use a finite element method (FEM) to approximate the matrix $\mathbf{T}_{\text{int}}$. It can be shown that $\mathbf{T}_{\text{int}} = -\mathbf{C}\mathbf{K}^{-1}\mathbf{B}$, where $\mathbf{K}$ is the stiffness matrix, $\mathbf{B}$ and $\mathbf{C}$ correspond to Fourier transform coefficients of finite element basis functions. The matrix $\mathbf{T}_{\text{int}}$ is the Schur complement of a sparse argument

matrix $\hat{\mathbf{K}} = [\mathbf{K}\ \mathbf{B}; \mathbf{C}\ \mathbf{O}]$, and it can be calculated by a partial factorization method implemented in existing packages including MUMPS [2] and PARDISO [3]. Such a method is fast and memory-efficient compared with LU factorization and forward and backward iterations.

In order to verify the efficiency of our method, we calculate resonant modes in a PhC slab which is a uniform slab (surrounded by air) with a square lattice of elliptic air holes. The thickness of the PhC slab is $2d = 0.5L$. The lengths of semimajor and semiminor axes of the elliptic air holes are $0.3L$ and $0.2L$, respectively, and the angle between the major axis and the x axis is $\pi/6$. The dielectric constant of the slab is 4.0804 (silicon nitride). We consider resonant modes with $\alpha L/2\pi = -0.13$ with $\beta L/2\pi = 0.18$. We adopt the first kind lowest-order Nédélec element to approximate the interior TI matrix $\mathbf{T}_{\text{int}}$ at $D = 0.3L$. We use the contour integral method with $N_q = 21$ quadrature points to calculate resonant modes inside a circle in the complex ω plane with the center at $\omega_0 L/c = 4.3$ and radius $\rho L = 0.05$. Numerical example shows that there exists only one resonant mode inside the circle. We emphasize that the method does not provide spurious solutions. Tables 1 shows the normalized frequency for

Table 1: The normalized resonant wavenumber $\omega L/c$ with $N_q = 21$.

h/L	$M = 6$	$M = 5$	$M = 4$
5.00E−2	4.34590−i2.30610E−3	4.34590−i2.30601E−3	4.34591−i2.30590E−3
2.50E−2	4.34922−i2.24245E−3	4.34922−i2.24239E−3	4.34922−i2.24236E−3
1.25E−2	4.35007−i2.22697E−3	4.35008−i2.22691E−3	4.35008−i2.22688E−3
6.25E−3	4.35029−i2.22337E−3	4.35029−i2.22332E−3	4.35029−i2.22328E−3

different M and mesh size h. It can be seen that the convergence in M is much faster than that in h. Therefore, we only need relatively small TI matrices to retain the accuracy even though h is very small. Moreover, at a fixed h, we have chosen a large value $N_q = 21$ to solve problem (3) with very high accuracy (twelve digits). In fact, considering the error of domain discretization, a small N_q is enough to obtain a result with relatively high accuracy. For example, for $M = 6$ and h =2.50E−2, we can obtain $\omega L/c$ =4.34922−i2.24245E−3 with $N_q = 11$.

For our method, the cost of contour integral method is much smaller than that of the building the matrix $\mathbf{T}_{\text{int}}$. Since we adopt a fast and memory-efficient method to calculate the matrix $\mathbf{T}_{\text{int}}$, numerical results show that our method is indeed efficient with respect to CPU time and memory usage compared with a similar FEM with PMLs. For example, when h =2.50E−2, $N_q = 21$ and $M = 6$, the CPU time is 7 min by our method. Moreover, with $N_q = 11$, the CPU time of our method is only 4 min. However, for the same mesh size h, the CPU time is 44 min by a similar FEM with PMLs. In addition, the peak memory required by our method is 12 GB. For a similar FEM with PMLs, the peak memory required is 64 GB.

References

1. Fan, S. and Joannopoulos, J. D, "Analysis of guided resonances in photonic crystal slabs," Phys. Rev. B, Vol. 65, No. 23, 235112, 2002.
2. Lin, H.-C., Wang, Z., and Hsu, C. W., "Fast multi-source nanophotonic simulations using augmented partial factorization," Nat. Comput. Sci., Vol. 2, No. 12, 815–822, 2022.
3. Petra, C. G., Schenk, O., Lubin, M., and Gärtner, K., "An augmented incomplete factorization approach for computing the Schur complement in stochastic optimization," SIAM J. Sci. Comput., Vol. 36, No. 2, C139–C162, 2014.

Simulating photoemission performance of a nanostructured photocathode with a coupled finite difference time domain – Monte Carlo technique

M. Popov[1], I. Valuev[1], and S. Belousov[1*]

[1]Hipercone Ltd, Israel
[*]corresponding author: belousov@hipercone.com

Abstract: We simulate the photoemission process in nanostructured thin film bialkali antimonide photocathodes on metallic substrates. Utilizing 3D finite difference time domain simulation of the optical excitation, fully coupled with a 3D Monte Carlo simulation of electron generation, transport and emission, we obtain quantum efficiency and emittance of the photocathode.

High-performance photocathodes have a great potential for x-ray free eletron lasers, advanced light sources and other applications [1]. Quantum efficiency (QE) together with emittance are key perfomance figures of merit for photocathodes, characterizing their electron emission capability and directionality. Relatively low band gap bialkali antimonide (e.g. K_2CsSb) photocathodes are readily driven by visible light, however their performance does not exceed 10% [2]. It has been demonstrated theoretically, that subwavelength manipulation of the excitation optical field with surface plasmon polaritons (SPPs) by adding 1D periodical nanostructure on the photocathode substrate has potential for boosting photocathode performance [3].

In this Contribution, we present a technique for 3D simulation the photoemission response of photocathodes, comprised from thin film bialkali antimonide coating layer on top of a nanostructured silver surface with a 2D periodicity. We calculate the broadband optical excitation with the finite difference time domain (FDTD) method. Using our high-performance software tool HiFDTD, featuring space-temporal blocking for the mesh update, enables accurate 3D representation of strong optical field gradients intrinsic to the metallic-based nanostructure [4]. The obtained 3D distribution of optical fields is used as an input for simulating electron generation, transport, and emission with an in-house 3D Monte Carlo solver, which implements three-step Spicer model of the photoemission process [5].

By using the developed technique, we demonstrate how tailoring the geometrical parameters of the nanostructure to provide a strong coupling of the excitation light to the SPPs modes, leads to the performance boost of the nanostructured photocathodes. We show that using fully 2D periodically nanostructured metallic substrate enables the increase of the QE irrespective of the impinging light polarization, and demonstrate the superiority of the 2D periodicity design as compared to the 1D periodicity and planar designs.

References

1. J. Schaber, R. Xiang, and N. Gaponik, “Review of photocathodes for electron beam sources in particle accelerators,” Journal of Materials Chemistry C, Vol. 11, 3162–3179 (2023).
2. M. A. H. Schmeißer, S. Mistry, H. Kirschner, S. Schubert, A. Jankowiak, T. Kamps, and J. Kühn, “Towards the operation of Cs-K-Sb photocathodes in superconducting rf photoinjectors,” Phys. Rev. Accel. Beams, Vol. 21, 113401 (2018).
3. Z. Jiang, Q. Gu, and X. Li, “Monte Carlo simulations of electron photoemission from plasmon-enhanced bialkali

photocathode", Physical Review Accelerators and Beams, Vol. 24, 033402 (2021).

4. S. Belousov, S. Khilkov, V. Levchenko, A. Perepelkina, and I.Valuev, "Hipercone FDTD: vectorized highly scalable full-wave electromagnetic solver". In International Applied Computational Electromagnetics Society Symposium (ACES) - IEEE, March, 2018. pp. 1-2
5. K. L. Jensen, E. J. Montgomery, "Photoemission Theory and the Development of High Performance Photocathodes", Journal of Computational and Theoretical Nanoscience, Vol.6, 1754–1769 (2009).

AES 2024, ROME - ITALY, 25 –28 JUNE 2024

Controlling thermal state in many-body systems

P. Ben-Abdallah*

Laboratoire Charles Fabry, UMR 8501, Institut d'Optique, CNRS, Université Paris-Saclay, 2 Avenue Augustin Fresnel, 91127 Palaiseau Cedex

*corresponding author: pba@institutoptique.fr

Abstract: We introduce new methods to actively control thermal states in many-body systems. We also explore the adiabatic evolution of thermal states in non-reciprocal systems, highlighting the emergence of a Berry phase that can either speed up or slow down the relaxation process, in contrast to the dynamical phase.

The thermalization process in many-body systems is intricately influenced by the collective interactions among sub-systems and their surroundings. This presentation will introduce novel approaches to actively manipulate thermal states [1] in arbitrary non-reciprocal systems close to their equilibrium state. Specifically methods for guiding a portion of the system follow a predeterminted trajectory during relaxation as for insulating specific elements from the rest of the system, will be discussed. Additionally, the presentation will outline the prerequisites for a system to converge towards a minimal temperature with minimal energy expenditure or time.

In the latter part of the presentation, emphasis will be placed on the adiabatic evolution of thermal states in non-reciprocal many-body systems coupled to their environment and subject to periodic drivings [2]. Within such systems, it will be demonstrated that, alongside the dynamical phase a Berry phase may also emerge influencing the relaxation dynamics. Unlike the dynamical phase which invariably drives the system towards equilibrium, the geometric phase may either accelerate or decelerate the relaxation process.

References

1. Ben-Abdallah P. and Rodriguez A. W. , "Controlling local thermal states in classical many-body systems," Phys. Rev. Lett., Vol. 129, 260602, 2022.
2. Biehs S.-A. and Ben-Abdallah P.,, "Heat transfer mediated by the Berry phase in nonreciprocal many-body systems," Phys. Rev. B, Vol. 106, 235412, 2022.

AES 2024, ROME - ITALY, 25 –28 JUNE 2024

Excitation engineering-based fault diagnosis of phased antenna arrays

Uday K Khankhoje[1], Prajosh K P[1], Sreekar Sai Ranganathan[1], and Francesco Ferranti[2]

[1]Department of Electrical Engineering, Indian Institute of Technology Madras, Chennai, India
[2]Department of Applied Physics and Photonics, Vrije Universiteit Brussel and Flanders Make, Belgium

Abstract: In this talk, recent results in the area of fault diagnosis of phased array antenna arrays will be discussed. These results are based on the use of a single fixed measurement location and the optimization of the excitations of the antenna elements of the array based on compressed sensing concepts. This is different from many approaches in the literature where measurements are taken at varying locations in space for example with a moving probe.

Phased antenna arrays are at the heart of modern wireless communication systems. They offer various functionalities as beam forming and servicing multiple users purely by electronic control. Their proper functioning is necessary to meet the required standards of performance. The elements in the phased array antennas are susceptible to damage that can severely degrade the radiation pattern and related performances. Therefore, it is essential to have simple and efficient techniques to assess the health of these systems in a way that minimizes their downtime. In this talk, we highlight recent advances in the area of fault diagnosis of phased array antenna arrays [1-4]. In [1-4], a single fixed receiver collects the fields being radiated by an array with excitations optimized to reduce the mutual coherence of the sensing matrix, which directly led to a reduction in the needed number of measurements to detect the location and number of faults [1]. Mutual coupling effects are taken into account in [2], multi-carrier precoding systems are investigated in [3], and a reference-free fault diagnosis is proposed in [4]. Multiple pertinent numerical results will validate these techniques.

References

1. K. P. Prajosh, U. K. Khankhoje, and F. Ferranti, “Element excitation optimization for phased array fault diagnosis,” Journal of Electromagnetic Waves and Applications, vol. 35, no. 1, pp. 39–50, Jan. 2021.
2. K. Prajosh, S. S. Ranganathan, F. Ferranti, and U. K. Khankhoje, “Efficient mutual-coupling aware fault diagnosis of phased array antennas using optimized excitations,” IEEE Antennas and Wireless Propagation Letters, vol. 21, no. 9, pp. 1906–1910, June 2022.
3. S. S. Ranganathan, K. P. Prajosh, U. K. Khankhoje, and F. Ferranti, “Spotting faults over the spectrum: Fast and online antenna array fault diagnosis for multi-carrier precoding systems,” IEEE Transactions on Wireless Communications, vol. 22, no. 10, pp. 7025-7037, Oct. 2023.
4. K. P. Prajosh, F. Ferranti, U. K. Khankhoje, “Reference-free fault diagnosis and corrected field prediction in a planar antenna array,” IEEE Antennas and Wireless Propagation Letters, vol. 23, no. 2, pp. 743-747, Feb. 2024.

A FEM-IE and FEM-FEM domain decomposition approach to solve non-matching multi-scale domains

J. Mologni, and K.Zhao[2]

[1]Ansys Inc, USA
*corresponding author: juliano.mologni@ansys.com

Abstract: The presented approach decomposes the original model into an unlimited number of FEM and optionally IE domains. The meshes on the interface can be non-matching, enabling the simulation of multi-scale problems such as an IC on a package on a PCB or an antenna on a platform.

One of the biggest challenges of complex multi-scale problems when using a numerical technique such as FEM (Finite Element Method) or IE (Integral Equation) is the mesh generation due to the difference on the physical size of the geometries involved on such the models. As an example, meshing and solving a section of an IC (Integrated Circuit) in isolation should be straightforward, however, meshing an entire assembly such as an IC, plus a package and a PCB (Print Circuit Board) is very challenging due to the orders of magnitude difference on the physical dimensions involved (nm to cm). Similar challenges are observed on applications such as antennas, which are usually a few cm long, on platforms, which are usually several meters long.

In this paper we present an approach based on domain decomposition method that decomposes the original problem into numerous FEM and optionally BEM domains. The domains communicate through Robin transmission condition enforced on the interface between the domains. The meshes on the interfaces are non-matching (non-conformal), hence the domains can be modularly treated and independently meshed, overcoming the challenge of meshing multi-scale problems. The resulting system is a fully coupled matrix.

FEBI (Finite Element Boundary Integral) is a technique that starts by partitioning the original problem domain Ω into two non-overlapping subdomains Ω1 and Ω2, as shown in Figure 1 [1].

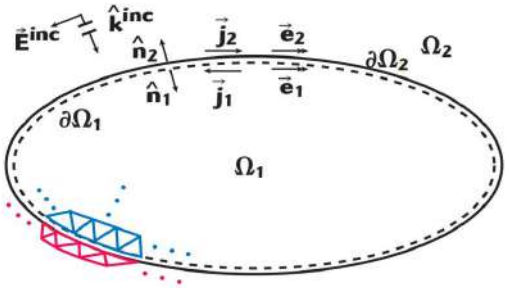

Fig. 1. Domain decomposition of the full model into FEM and IE domains

The interface between Ω1 and Ω2 is denoted as ∂Ω1 in the FEM domain and ∂Ω2 in the IE domain. This distinction is required because the present formulation allows non conformal coupling between two domains. This means that the mesh, the basis function and basis order, the matrix assembling and solution process can be treated independently for each domain. A multi-scale application using this technique is shown in figure 2,

where the dielectric loaded horn antenna is solved with FEM and the parabolic dish, and the shell of the conducting feed is solved with IE. Note the smooth continuation of the fields on the surface of the conducting feed on the interface between the FEM and IE domains.

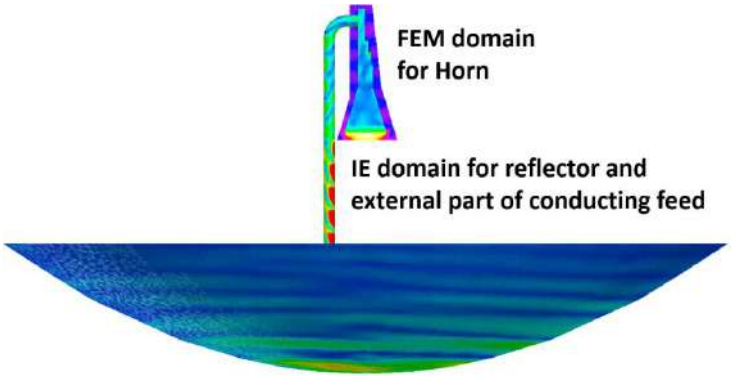

Fig. 2. Electric field on a horn antenna plus conducting feed and parabolic dish solved with FEBI

A similar approach can be used on FEM-FEM domains. Figure 3 shows a Package on PCB FEM system where the Package is meshed independently from the PCB and the native domains, but they are solved in a fully couple system matrix without compromising the accuracy.

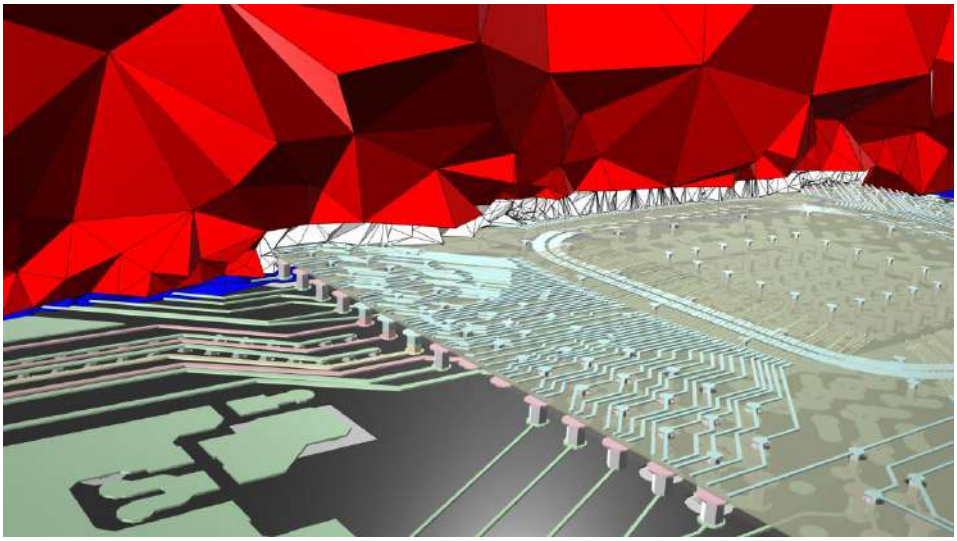

Fig. 3. Tetrahedra FEM mesh on a PCB (blue elements), bondwire package (white elements) and native (white elements) domains.

By employing this techniques, complex multi-scale systems can be meshed and solved by partitioning the model into subdomains that can be meshed independently but solved in a fully coupled manner.

References

1. J. Silvestro, K. Zhao and A. Sligar, "Hybrid Finite element: boundary integral technique for efficient Simulation of radiation and Scattering," Microwave Journal, Jan.2011, pp. 74-80

AES 2024, ROME - ITALY, 25 –28 JUNE 2024

New generation of photonic simulation with hardware accelerated FDTD and automatic differentiation.

Zongfu Yu
University of Wisconsin, Madison, WI USA
Flexcompute Inc, Watertown, MA USA

Abstract: Future research and development will increasingly rely on computer simulation technology. In the field of optics and photonics, a new generation of hardware and software technology is making electromagnetic simulation more powerful than ever. Three application examples will be discussed, including the training of photonic neuromorphic computing media, validation of the Nobel Prize-winning theory of Anderson localization, and optimization of radiative cooling coatings. These powerful simulations are enabled by three technologies, including 1. Fast Compute: Hardware-accelerated finite-difference time-domain (FDTD) simulation; 2. Fast Gradient: Automatic differentiation for gradient-based optimization. 3. Fast Resource: Elastic computing provided by the cloud.

References

Yamilov, A., Skipetrov, S. E., Hughes, T. W., Minkov, M., Yu, Z., & Cao, H. (2023). Anderson localization of electromagnetic waves in three dimensions. *Nature Physics*, 1-6.

Hughes, T. W., Minkov, M., Liu, V., Yu, Z., & Fan, S. (2021). A perspective on the pathway toward full wave simulation of large area metalenses. *Applied Physics Letters*, *119*(15).

AES 2024, ROME - ITALY, 25 –28 JUNE 2024

The optimal dielectric near-field antenna

O. D. Miller[1*]

[1]Dept of Applied Physics and Energy Sciences Institute, Yale University, New Haven, CT, USA
[*]corresponding author: owen.miller@yale.edu

Abstract: What is the maximum Purcell enhancement of a dielectric antenna? For minimum feature size d, we propose a surprising scaling law 1/d^r, with exponent r <= 2 strongly dependent on material permittivity. Conventional bowties approach these limits. A novel three-material, dual-polarizability design outperforms the two-material bound, offering orders-of-magnitude improvements.

AES 2024, ROME - ITALY, 25 –28 JUNE 2024

Ubiquitous Analog Reservoir Computing: Modelling, Optimising, and Controlling Dynamics-Driven Hardware AI

G. Marcucci[1*]

[1]School of Physics & Astronomy, University of Glasgow, Glasgow G12 8QQ, United Kingdom.
[*]corresponding author: giulia.marcucci@glasgow.ac.uk

Abstract: This study explores the modelling, optimisation, and control of Analog Reservoir Computing (ARC) systems to advance energy-efficient hardware AI. Utilising complex wave propagation within diverse physical domains – nonlinear, random, and multimodal photonics, hydrodynamics, visual brain-computer interfaces, and quantum optics – this research aims to establish innovative ARC frameworks.

Neuromorphic computing (NMC) is a prominent field within the expanding community of scientists dedicated to developing analog and unconventional computers. Its primary objective is to create machines based on brain-like algorithms, enabling them to possess the unique problem-solving capabilities observed in the human brain.

Achieving this goal requires integrating state-of-the-art software architectures and innovative hardware paradigms, which continually interact and advance. Complex systems, which exist in a delicate balance between order and chaos, have proven to be highly suitable for implementing NMC hardware. Such systems demonstrate superior learning capabilities compared to excessively rigid or overly chaotic ones.

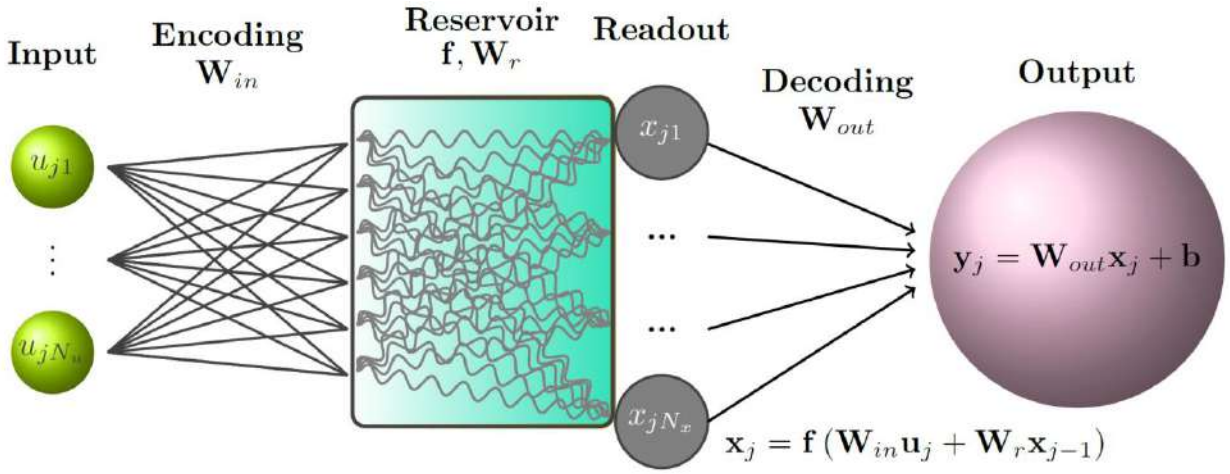

Figure 1. Pictorial representation of a wave-based echo state network architecture.

In the realm of NMC, the line between software and hardware development blurs. From an algorithmic standpoint, the two most significant architectures in NMC are spiking neural networks~(SNNs) and reservoir computing~(RC). SNNs are artificial neural networks~(ANNs) that rely on time-dependent synapses, where neurons transmit information only when they surpass the activation potential threshold. On the other hand, RC represents a specific type of recurrent neural network~(RNN) in which training occurs solely at the readout stage. Figure 1 describes an echo state network~(ESN), a widespread RC paradigm, including a vanilla formulation of its equations.

Analog RC (ARC) represents the in-hardware implementation of modifications of the ANN sketched in Fig. 1, where encoding, reservoir, and decoding are actual physical systems. In this presentation, I will briefly overview my recent developments in ARC and discuss future directions for optimising its learning performance. Specifically, I will report on the differences and similarities of ARC systems exploiting:

- Visual BCIs (encoding via frequency multiplexing, reservoir through steady-state visual evoked potentials, decoding via EEG) [1];
- Quantum optics (encoding using linearly polarised Fock states, reservoir through BosonSampling, decoding via photon-number-resolving detector) [2];
- Multimode fibers (encoding via spatial light modulator (SLM), reservoir with gain-controlled multimode fibers, decoding via CCD camera) [3];
- Nonlinear optics (encoding with SLM, reservoir via self-focusing Kerr effect, decoding via CCD camera) [4];
- Free-space optical propagation (encoding via SLM, reservoir with random phase mask, decoding via CCD camera) [5];
- Nonlinear acoustics (encoding via low-amplitude waves, reservoir through solitary wave collision in shallow water, decoding via imaging in the collision region) [6];

My first key contribution to ARC emphasises the significance of complexity in the holistic encoding-reservoir-decoding system [4]. This work demonstrates that learning in a nonlinear RC design occurs beyond a specific nonlinearity threshold, which strongly depends on the chosen encoding strategy. Following this route, I will detail strategies to optimise information encoding in ARC using evolutionary algorithms [7], and control reservoir nonlinearity by spatial modulation of the gain profile in a multimode fiber [3].

References

1. G. Wang, *et al*., "Human-Centred Physical Neuromorphics with Visual Brain-Computer Interfaces", *under review* (2024).
2. S. Nerenberg, *et al*., "Photon Number-Resolving Quantum Reservoir Computing", ArXiv:2402.06339, (2024).
3. G. Marcucci, *et al*., "Optimal learning in reservoir computing systems based on gain-controlled multimode fibres", *under review* (2024).
4. G. Marcucci, *et al*., "Theory of neuromorphic computing by waves: machine learning by rogue waves, dispersive shocks, and solitons", *Phys. Rev. Lett.* **125**, 093910 (2020).
5. D. Pierangeli, *et al*., "Photonic extreme learning machine by free-space optical propagation", *Photon. Res.* **9**, 1446 (2021).
6. G. Marcucci, *et al*., "A New Paradigm of Reservoir Computing Exploiting Hydrodynamics", *Phys. Fluids* **35**, 071703 (2023).
7. A. Pierro, *et al*., "Optimization of a Hydrodynamic Computational Reservoir through Evolution", *Proc. GECCO* **2023**, 202 (2023).

Novel Machine-learning Techniques for Inverse Design and Knowledge Discovery in Electromagnetics

Mohammadreza Zandehshahvar, Mahmoodreza Marzban, Mohammad H. Javai, and Ali Adibi
School of Electrical and Computer Engineering
Georgia Institute of Technology
Atlanta, GA 30332-0250
Phone: (404) 385-2738
Fax: (404) 894-4641
Email: adibi@ece.gatech.edu

Short Abstract:
This talk is focused on new machine-learning-based techniques for solving large-scale electromagnetic problems in reduced-dimensionality design and response spaces. The dimensionality reduction of the response space is performed using manifold learning. The dimensionality of the design space is highly reduced by combining manifold learning with a new approach using the spatial bases to represent the geometrical design parameters. The resulting appraoch enables solving large-scale electromagnetic problems far more efficiently than brute-force computations. It is shown that by considerably simplifying the input-output relation, this appraoch can enable inverse design of electromagnetic structures while providing priceless information about the physics of wave-matter interaction in these structures. Result of application of this technique to practical metaphotonic structures involving the design, fabrication, and characterization tasks will also be presented.

Biography

Ali Adibi is the director of Bio and Environmental Sensing Technologies (BEST) and a professor and Joseph M. Pettit chair in the School of Electrical and Computer Engineering, Georgia Institute of Technology. His research group has pioneered several structures in the field of integrated nanophotonics for both information processing and sensing. He is the author of more than 220 journal papers and 520 conference papers. He is the editor-in-chief of the Journal of Nanophotonics, and the nanophotonic program track chair of the Photonics West meeting. He is the recipient of several awards including Presidential Early Career Award for Scientists and Engineers, Packard Fellowship, NSF CAREER Award, and the SPIE Technology Achievement Award. He is also a fellow of OSA, SPIE, and AAAS.

AES 2024, ROME - ITALY, 25 –28 JUNE 2024

Inevitable radiation decay of surface plasmon at any metal-dielectric interface

A. Krokhin[1*], K. Rocapricone[2], A.Bozhko[1], G. Nazarikov[3], and V. Drachev[4]

[1]University of North Texas, USA
[2]Oak Ridge National Laboratory, USA
[3]Eindhoven University of Technology, The Netherlands
[4]Skolkovo Institute of Science and Technology, Russia
[*]corresponding author: arkady@unt.edu

Abstract: A radiative decay of surface plasmon due to existence of a few-nanometer-thick epsilon-near-zero (ENZ) transition layer between metal and dielectric is predicted, calculated, and experimentally demonstrated. The transition layer is formed by spill-out electrons and surface roughness. Radiative losses may exceed Joule losses, thus strongly reducing surface plasmon propagation length.

Surface plasmon at metal-dielectric interface is considered to be a genuine surface mode. The fields of surface plasmon decay exponentially away from a sharp boundary, where dielectric function suffers a discontinuity jump from negative value in metal to positive value in dielectric. In real structure this nonanalytic behavior is smoothed out by a narrow transition layer. Within this layer the dielectric function takes the values much less than in the metal or dielectric, i.e., the transition occurs through epsilon-near-zero (ENZ) layer. The transition layer may be formed by spill-out electrons, which leave metal due to quantum fluctuations. At atomically flat surface the spill-out electrons form a cloud of a few angstroms width. More extended transition layer separates two rough surfaces. Depending on their quality, the transition layer may reach dozens of nanometers width. The narrow transition layer does not affect electrodynamics boundary conditions. In particular, the Fresnel formulas remain true [1].

However, strongly localized field of surface plasmon turns out to be very sensitive to presence of ENZ layer that leads to several essential effects [2,3]. The most important is the additional channel of decay of surface plasmon due to radiation. The ENZ layer "opens" a window through which the energy radiates into dielectric, i.e., in real situation surface plasmon is not a surface mode. This can be seen from the analysis of the wave equation for the *p*-polarized wave with $H_y = H(z)\exp(ikx - \omega t)$,

$$\frac{d}{dz}\left(\frac{1}{\varepsilon(z)}\frac{dH}{dz}\right) + \left(\frac{\omega^2}{c^2} - \frac{k^2}{\varepsilon(z)}\right)H(z) = 0, \qquad (1)$$

The logarithmic singularity of the solution to this equation near the point $z = z_0$ where $\varepsilon(z)$ vanishes is discussed in Ref. [1]. Function $\varepsilon(z)$ is a smooth function with asymptotical values $\varepsilon(\omega) < 0$ at $z \to -\infty$ (metal), $\varepsilon_d > 0, z \to \infty$ (dielectric), and a narrow transition layer of width δ. Direct perturbation theory over a small parameter $k\delta \ll 1$ is not applicable to Eq. (1) because of singularity at $z = z_0$. We overcome this difficulty by rewriting Eq. (1) in Fourier representation

$$\frac{\omega^2}{c^2}h(p) = \int_{-\infty}^{\infty}(k^2 + pp')\eta(p - p')h(p')dp', \;\; h(p) = \frac{1}{2\pi}\int_{-\infty}^{\infty} e^{-ipz}\varepsilon(z)dz. \qquad (2)$$

For a sharp boundary the thickness of the transition layer $\delta = 0$, the kernel $\eta(p - p')$ is Hermitian and the eigenvalue problem (2) gives the well-known spectrum for surface plasmon $\omega_0^2 = k^2c^2\left(\varepsilon_d^{-1} - |\varepsilon(\omega)^{-1}\right)$ and exponential decay of $H(z)$ at $\pm\infty$. The Hermiticity of the kernel is lost if there is a point z_0 on the pass of integration over z in Eq. Bypassing the pole gives an imaginary contribution to $h(p)$ even if $\varepsilon(z)$ is real,

$$\eta(p) = \frac{1}{2\pi}\int_{-\infty}^{\infty} \frac{e^{-ipz}}{\varepsilon(z)} dz - 2\pi i \operatorname*{Res}_{z=z_0} \frac{e^{-ipz}}{\varepsilon(z)}, \quad (4)$$

where the Cauchy principal value of integral is assumed. The second term in (4) breaks the hermiticity of the kernel resulting in the complex eigenvalues $\omega(k) = \omega_0(k) + \omega'(k) - i\omega''(k)$. The imaginary correction to the eigenfrequency means that the surface plasmon loses energy even if the metal is lossless. To compare the contribution of radiation and dissipative losses for surface plasmon propagating along a silver-vacuum interface, the propagation lengths $L = \mathrm{Im}\, k/2$ due to Joule and radiative losses are plotted in Fig. 1. Even for very narrow transition layer $\delta = 0.5$ Å the radiative losses exceed the Joule losses in silver at room temperature.

In the experiment the angular shift $\Delta\theta$ of the minimum in the reflected light under strong dc field applied normal to the interface was measured. The field **E** changes the electron distribution in the transition layer, thus

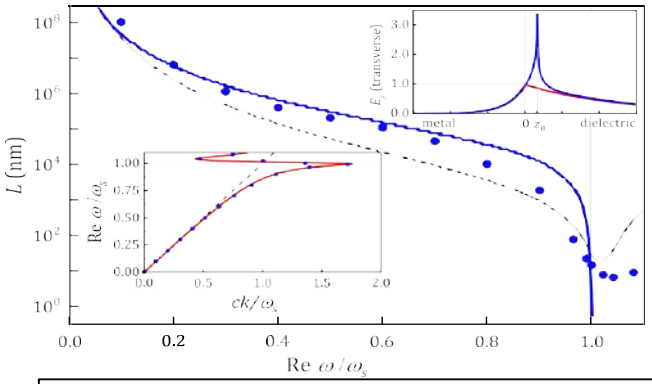

Figure 1. The decay length L of surface plasmon at silver-vacuum interface due to Joule (black) and radiative (blue) losses. Left inset: Dispersion relation for the model of a sharp boundary ($\delta = 0$, red) and for a transition layer (δ = 0.5 Å, blue dots). Right inset: Enhancement of the electric field near the ENZ point (blue) as compared to the structure without the transition layer.

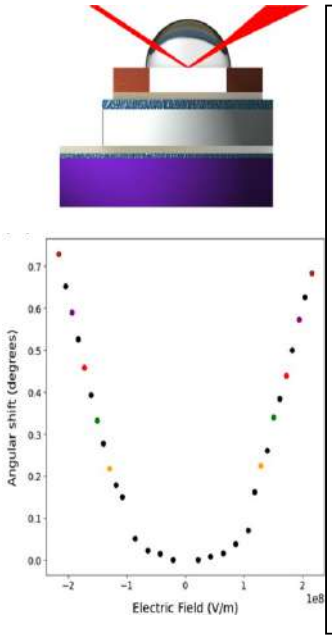

Figure 2. Set up of the experiment in Otto configuration. The graph shows the shift $\Delta\theta$ under the dc field **E** directed up or down along the normal to the interface. The shift is positive for both directions of **E** that corresponds to the red shift in the resonance.

affecting the thickness δ of the transition layer. The angular shift $\Delta\theta$ is due to the δ-dependent correction $\omega'(k)$ to the plasmonic dispersion. The measured shift $\Delta\theta$ in Fig. 2 confirms the presence of the transition layer and its influence on the dispersion of surface plasmon.

This work is supported by the US AFOSR grant FA9550-23-1–0630.

References

1. Landau, L.D, E. M. Lifshitz, and L. P. Pitaevskii, "Electrodynamics of Continuous Media," 2nd ed., (Pergamon, New York, 1984).
2. Akimov, Yu. A. and H. S. Chu, "Plasmon coupling effect on propagation of surface plasmon polaritons at a continuous metal/dielectric interface," Phys. Rev. B, Vol. 83, 165412, 2011.
3. Roccapriore, K., A. Bozhko, G. Nazarikov, V. Drachev and A. Krokhin, "Surface plasmon at a metal-dielectric interface with an epsilon-near-zero transition layer," Phys.Rev. B, Vol. 103, L161404, 2021.

Connecting antenna and diffraction theory with the radiation of Fisher information in scattering experiments

J. Hüpfl[1,*], F. Russo[1], L. M. Rachbauer[1], D. Bouchet[2], J. Lu[3], U. Kuhl[3], and S. Rotter[1]

[1] *Institute for Theoretical Physics, Vienna University of Technology (TU Wien), 1040, Vienna, Austria.*
[2] *LIPhy, Université Grenoble Alpes, CNRS, Grenoble, 38402, Auvergne-Rhône-Alpes, France.*
[3] *Institut de Physique de Nice (INPHYNI), Université Côte d'Azur, CNRS, 06108, Alpes-Maritimes, France.*
[*] *Corresponding author: jakob.huepfl@tuwien.ac.at*

Abstract: Electromagnetic waves are used over a wide range of disciplines to precisely estimate a target's properties. We explore how these waves interact with matter to gather Fisher information from an object of interest and transmit it to the far-field. By identifying information sources, we build a connection to antenna theory.

Electromagnetic waves not only serve to transmit information between a sender and receiver, but can also be employed to extract information on a system's parameters. This paradigm is widely used in areas ranging from radar technology [1] to gravitational wave detection [2]. An important quantity in this context is the Fisher Information (FI), which measures how much information a signal contains on a system parameter θ (e.g. the position or orientation of a target). This can be employed to optimize measurement setups [3] in order to estimate θ as precisely as possible. In our recent work [4], we showed that similar to the energy of electromagnetic waves, the FI is a local quantity assigned to the waves, which flows throughout the system, similar to an energy flux. More specifically, we consider a general system as illustrated in Fig. 1 **a**, where a dielectric target scatterer (grey cuboid), located inside a disorder (orange cylinders) is illuminated by an incident field (red incoming arrows). The energy now propagates throughout the system in accordance with the Poynting theorem

$$\nabla \cdot \boldsymbol{S}^P = \frac{1}{2}\Re[\boldsymbol{j}^* \cdot \boldsymbol{E}_\omega]\,, \tag{1}$$

where $\boldsymbol{E}_\omega$ is the electric field amplitude and $\boldsymbol{S}^P = \frac{1}{2}\Re(\boldsymbol{E}_\omega^* \times \boldsymbol{H}_\omega)$ the Poynting vector quantifying the flux of energy. This energy flux is created and annihilated by electric currents $\boldsymbol{j}$, while staying conserved otherwise. Without any currents or absorption channels, the outgoing energy will thus be equivalent to the incoming one. In analogy to this picture, we can show that in the case of shot noise limited measurements it is possible to

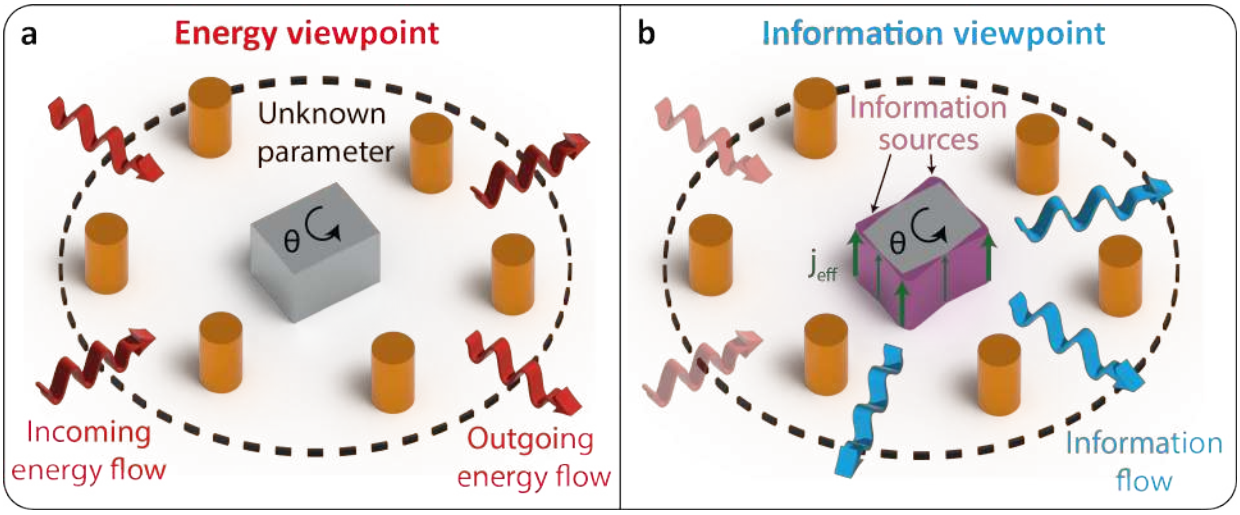

Figure 1: **Illustration of precision measurements in complex systems. a**, In the energy viewpoint, a scattering region containing cylindrical and rectangular scatterers is illuminated by coherent light providing an incoming flow of energy (red incoming arrows). A parameter θ (here the angular orientation of the rectangular scatterer) is estimated from the outgoing energy flow (red outgoing arrows). **b**, In the alternative information viewpoint presented here, Fisher information on a specific parameter θ is created in those areas that are sensitive to changes in θ (purple areas), by effective surface currents $\boldsymbol{j}_{\text{eff}}$ (green arrows). The information flows associated with these information sources are indicated by the blue outgoing arrows.

formulate the problem in an information picture (Fig. 1 **b**), where in direct comparison to the Poynting theorem the FI follows a continuity equation

$$\nabla \cdot \boldsymbol{S}^{\mathrm{FI}} = \frac{1}{2}\Re[\boldsymbol{j}^{*}_{\mathrm{eff}} \cdot \partial_\theta \boldsymbol{E}_\omega]\,. \tag{2}$$

The Fisher Information flows out of the system as a FI flux $\boldsymbol{S}^{\mathrm{FI}} = \frac{2}{\hbar\omega}\Re(\partial_\theta \boldsymbol{E}^{*}_\omega \times \partial_\theta \boldsymbol{H}_\omega)$ (blue arrows), while getting generated by effective current densities $\boldsymbol{j}_{\mathrm{eff}}$ (green arrows). In the case of static isotropic dielectrics with the permittivity function $\epsilon(\boldsymbol{r})$, these currents are given by $\boldsymbol{j}_{\mathrm{eff}} = -4\mathrm{i}\hbar^{-1}(\partial_\theta \epsilon)\boldsymbol{E}_\omega$. This highlights that the effective currents are located at parts of the dielectric that are sensitive to changes in θ (corners of the cuboid) and which interact with the incident field. To highlight in which way these information sources determine the patterns of radiation to the far-field, consider the example of a cube located in free space, illuminated by a plane wave propagating in positive z direction as depicted in Fig. 2 **a**. If we want to estimate the cube's position along the z direction, then the effective currents $\boldsymbol{j}_{\mathrm{eff}}$ (green arrows) are located at the front and back side of the cube (purple areas). The corresponding radiation pattern of FI (Fig. 2 **b**) shows that most of the information is back reflected along the negative z direction (larger amplitudes and darker color indicate stronger FI radiation along the spherical angle), while smaller Fraunhofer diffraction lobes are also present (inset). Importantly, the effective current density generating FI on each side of the cube shows a close resemblance to the effective electric current density that (based on the surface equivalence principle) is commonly used for the calculations of the energy radiation pattern of aperture antennas. This observation now allows us to explain the FI radiation pattern by connecting it to the energy radiation pattern of two such rectangular aperture antennas. These insights could prove especially useful in the field of levitated optomechanics, where considerable interest is focused on controlling the spatial radiation of information of particles of various shapes to reduce measurement noise [5].

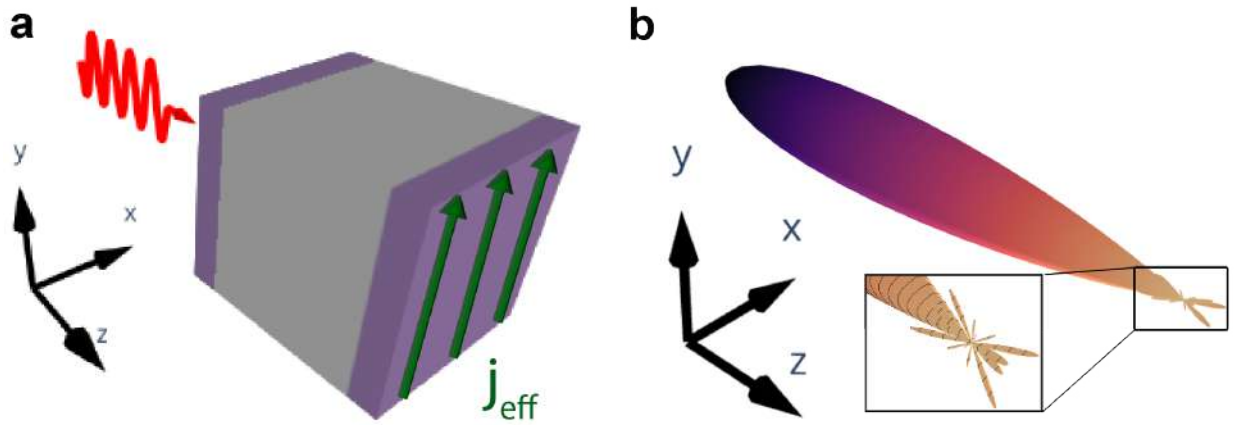

Figure 2: **FI radiation patterns.** **a**, A weakly scattering cube with sidelength $L = 1.4\lambda$ is illuminated by a plane wave (red line) propagating along the positive z direction to estimate the cube's position along the z direction. The effective currents $\boldsymbol{j}_{\mathrm{eff}}$ (green arrows) are located at the front and backside indicated by purple. **b**, Corresponding angular FI radiation patterns, where larger amplitudes and darker colors indicate stronger radiation in a specific direction. The radiation patterns show strong similarities to the interference of Fraunhofer diffraction patterns emanating from two rectangular aperture antennas.

References

[1] Alberto Moreira et al. "A tutorial on synthetic aperture radar". In: *IEEE Geoscience and Remote Sensing Magazine* 1.1 (2013), pp. 6–43. DOI: 10.1109/MGRS.2013.2248301.

[2] Benjamin P Abbott et al. "Observation of gravitational waves from a binary black hole merger". In: *Physical Review Letters* 116.6 (2016), p. 061102. DOI: 10.1103/PhysRevLett.116.061102.

[3] Fan Liu et al. "Cramér-Rao bound optimization for joint radar-communication beamforming". In: *IEEE Transactions on Signal Processing* 70 (2021), pp. 240–253.

[4] Jakob Hüpfl et al. *Continuity Equation for the Flow of Fisher Information in Wave Scattering*. 2023. arXiv: 2309.00010.

[5] Patrick Maurer, Carlos Gonzalez-Ballestero, and Oriol Romero-Isart. "Quantum theory of light interaction with a Lorenz-Mie particle: Optical detection and three-dimensional ground-state cooling". In: *Phys. Rev. A* 108 (3 Sept. 2023), p. 033714. DOI: 10.1103/PhysRevA.108.033714.

Chiral waveguides and exceptional points

A. De Corte[1], M. Besbes[2], H. Benisty[2], S.F. Koufidis[3], M.W. McCall[3], and B. Maes[1*]

[1] University of Mons, Micro- and Nanophotonic Materials Group, Research Institute for Materials Science and Engineering, University of Mons, 20 Place du Parc, B-7000 Mons, Belgium
[2] Laboratoire Charles Fabry, Institut d'Optique Graduate School, CNRS, Université Paris Saclay, 2 Av. Augustin Fresnel, 91127 Palaiseau Cedex, France
[3] Imperial College of Science, Technology and Medicine, Blackett Laboratory, Department of Physics, Prince Consort Road, London SW7 2AZ, United Kingdom
[*]corresponding author: bjorn.maes@umons.ac.be

Abstract: In chiral waveguides with gain and loss, we report coupling between TE and TM modes leading to interesting dispersion patterns of avoided crossings and symmetry-broken zones. Additionally, even without gain and loss, we obtain backward modes via exceptional points in waveguides with a large chirality.

Photonic devices respecting parity-time (PT) symmetry have produced many interesting phenomena in recent years [1]. In waveguides e.g., under a certain gain-loss threshold, the modes are propagating, whereas above that threshold, called the exceptional point (EP), one mode is amplified and the other decays. This creates a mode dispersion with two characteristic 'forks', for the real and imaginary part, respectively, on each side of the EP (dashed lines in Fig. 1c). In addition, chiral materials are extensively studied due to their different response to left-handed and right-handed circularly polarized light [2]. We utilize material chirality with coupled waveguides to create novel guiding behaviors, first in coupled waveguides with balanced gain and loss separated by a chiral material (Fig. 1a), then by coupling a waveguide with large chirality to an achiral waveguide (Fig. 2a). We simulate these structures with the finite element method using the SimPhotonics software, a Matlab toolbox developed at the Laboratoire Charles Fabry.

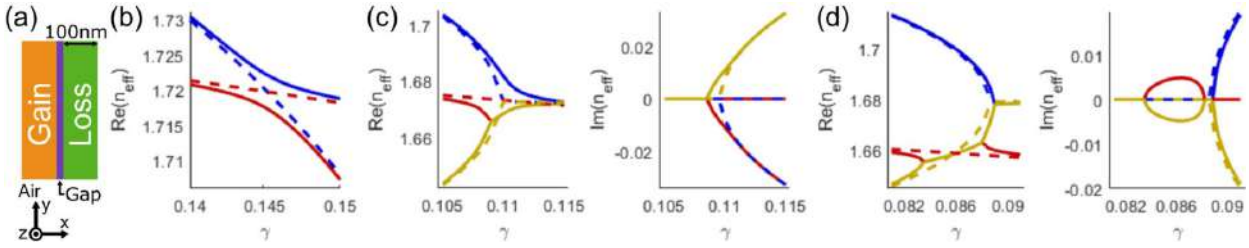

Figure 1: (a) PT-symmetric waveguides with a chiral gap. Dispersion for gap: (b) 12nm, (c) 32nm (d) 44nm. Dashed and solid lines refer to achiral and chiral gaps, respectively.

Two rectangular PT-symmetric waveguides are considered, one with gain and the other with loss (Fig. 1a), separated by a gap made of achiral or chiral material (purple in Fig. 1a) [3]. The mode dispersion is plotted by varying the gain-loss parameter γ. We focus our analysis on three modes: two modes of a TE-polarized PT fork and one mode of a TM fork. The introduction of chirality in the gap enables coupling between TE and TM modes when their dispersions cross (degeneracy). When the gap is narrow (<20nm) and achiral, a crossing occurs between the TM and TE mode (red and blue dashed lines in Fig. 1b). In contrast, an anti-crossing appears when chirality is introduced in the gap (solid lines in Fig. 1b). For medium-sized gaps (around 30nm), the TM mode crosses the EP for an achiral gap, where 2 TE modes coalesce (dashed lines in Fig. 1c). All three modes then interact under the effect of chirality, giving rise to a hybrid dispersion (solid lines in Fig. 1c). The anti-crossing width reaches values

close to a homogeneous chiral medium, despite the narrowness of the gap. For a larger gap (>40nm), the TM mode crosses the lower TE mode (red and gold dashed lines in Fig. 1d). Interestingly, their chiral interaction leads to the appearance of a PT-broken zone, followed by a `symmetry recovery' zone (solid lines in Fig. 1d).

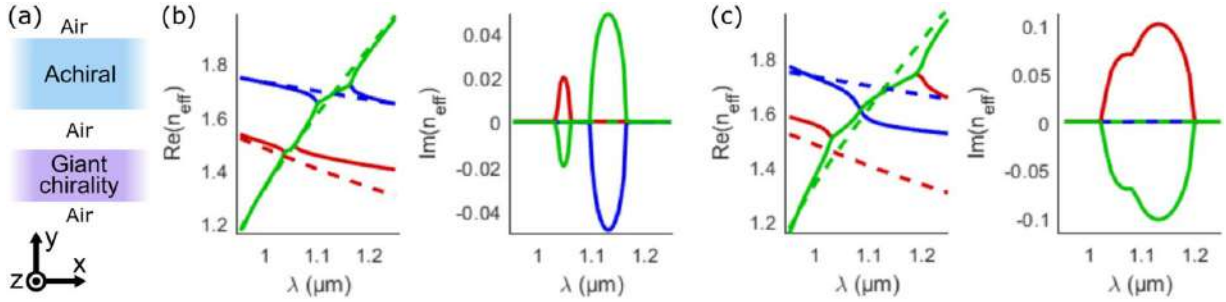

Figure 2: (a) Coupled chiral and achiral waveguides. Dispersion for gap of: (b) 200nm, (c) 100nm.

Exceptional points were recently achieved without gain or loss by coupling forward- and backward-propagating modes [4]. Furthermore, giant chirality can access negative refractive states, and thus backward mode propagation, without the necessity of simultaneous negative permittivity and permeability [5]. We combine these two approaches by examining the coupling between a slab with giant chirality and a thicker achiral waveguide (Fig. 2a). Their dispersion as a function of wavelength highlights important interactions. The modes of the achiral waveguide (red and blue dashed lines in Fig. 1b,c) are forward, while the chiral waveguide presents a backward mode (green dashed line). Figure 1b shows the dispersion for a 200nm air gap (solid lines). The interaction of forward and backward modes creates a PT-like 'broken zone' around each chiral-achiral crossing. When the gap is sufficiently small (e.g., 100nm, solid lines in Fig. 1c), the two zones merge to create one broken zone. Interestingly, the forward mode (blue) that crosses this large PT-broken zone gradually evolves from the higher order achiral mode (shorter λ) to the lower-order achiral mode (longer λ), by hybridizing with the broken modes during the transition.

Overall, chirality induces a rich variety of dispersion patterns with non-Hermitian features. On the one hand, with balanced gain and loss, chirality couples polarizations to create anti-crossings and broken zones. On the other hand, when a large-chirality backward mode interacts with a forward mode, an exceptional point appears in a device, intriguingly, without gain and loss.

A. De Corte is a FRIA grant holder of the Fund for Scientific Research F.R.S.-FNRS.

References

1. Feng, L., R. El-Ganainy and L. Ge, "Non-Hermitian photonics based on parity-time symmetry," Nat. Photonics, Vol. 11, 752, 2017.
2. M. Hentschel et al, "Chiral plasmonics," Sci. Adv., Vol. 3, No. 5, e1602735, 2017.
3. A. De Corte, M. Besbes, H. Benisty, B. Maes, "Chiral materials to control exceptional points in parity-time symmetric waveguides, " Phys. Rev. A, accepted.
4. T. Mealy and F. Capolino, "Exceptional points of degeneracy with indirect band gap induced by mixing forward and backward propagating waves," Phys. Rev. A, Vol. 107, 012214, 2023.
5. J. B. Pendry, "A chiral route to negative refraction," Science, Vol. 306, No. 5700, 1353, 2004.

AES 2024, ROME – ITALY, 25-28 JUNE 2024

Concepts for oblique semi-guided waves: integrated optics with negative effective permittivity

M. Hammer*, L. Ebers, H. Farheen, S. Alhaddad, A. Hildebrandt, and J. Förstner

Theoretical Electrical Engineering, Paderborn University, Paderborn, Germany
* manfred.hammer@uni-paderborn.de

Abstract: Scattering losses are fully suppressed, if guided waves in a high-contrast dielectric slab encounter an elongated obstacle at a sufficiently large oblique angle. We review the underlying arguments and a series of device concepts, including a step transition, high-contrast gratings, and the evanescent excitation of OAM fiber modes.

Semi-guided waves

Dielectric optical slab waveguides are mostly associated with the standard scalar 2-D TE and TM modes. Taking into account the lateral dimension as well, obvious 3-D solutions for guided waves can be constructed from these, either with an in-plane dependence of infinite plane harmonic waves, or as superpositions of these, in the form of in-plane localized wave bundles, e.g. as beams of Gaussian shape. Things become interesting, if one considers the incidence of these "semi-guided waves" on an elongated discontinuity in the slab, at some not too small angle, and if this happens in a slab of sufficient refractive index contrast [1].

2-D integrated photonics with negative effective permittivity

Irrespective of the shape and size of the obstacle, a variant of Snell's law applies, separately for each pairing of incoming and outgoing modes. Power transfer to specific waves is allowed or forbidden, depending on the angle of incidence, and on the effective indices of the fields involved. Critical angles of incidence can be identified, beyond which any power transfer to non-guided waves is suppressed. Then the input power is carried away from the discontinuity exclusively by semi-guided waves.

The problem is governed by vectorial equations on a 2-D cross sectional domain, that are formally identical to the equations for the eigenmodes of 3-D channel waveguides. Here, these need to be solved as an inhomogeneous scattering problem, with the incoming semi-guided wave as a right-hand-side, and subject to transparent boundary conditions. An effective permittivity takes the place of the physical relative permittivity. Depending on the effective index and angle of the incoming wave, that effective permittivity can become locally negative, causing the suppression of propagating nonguided outgoing fields.

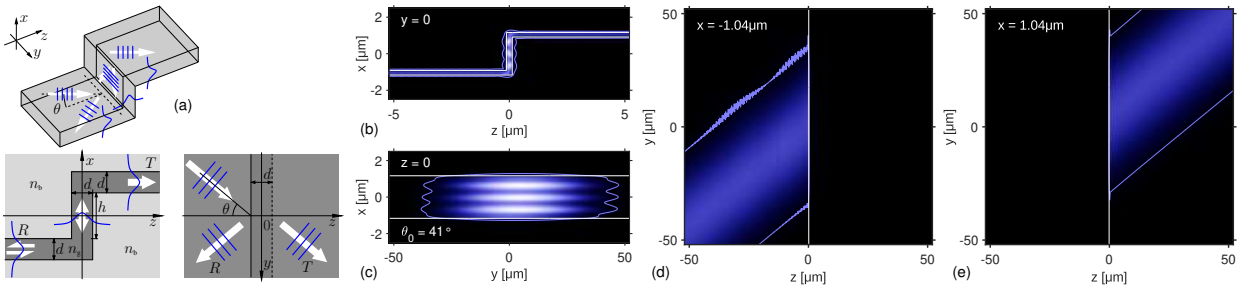

Figure 1: Oblique incidence of a semi-guided Gaussian beam (TE) at a step structure (a), electromagnetic energy density (b)–(e) for a bundle of 45 μm width and angle of incidence $\theta = 41°$. Parameters: $h = 1.83\,\mu$m, $d = 0.25\,\mu$m, $n_g = 3.4$, $n_b = 1.45$, wavelength $\lambda = 1.55\,\mu$m; reflectances and transmittances: $R_{TE} = 0.02$, $R_{TM} < 0.01$, $T_{TE} = 0.96$, $T_{TM} = 0.02$. (Figure adapted from Ref. [2])

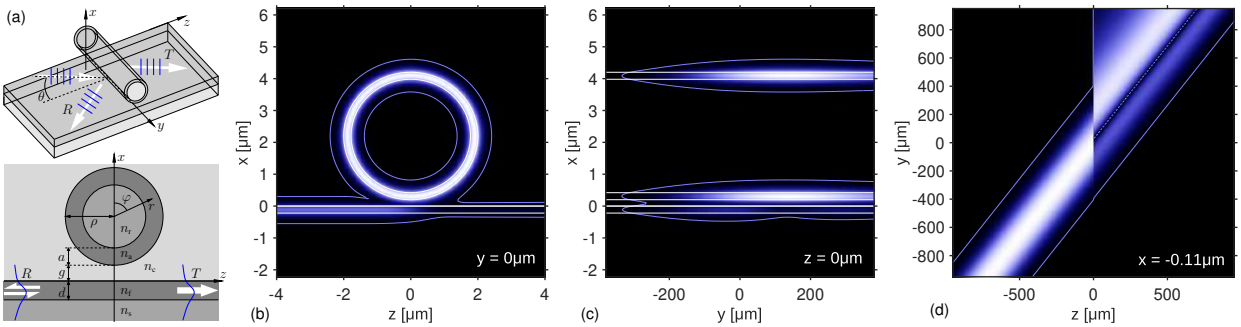

Figure 2: Evanescent excitation of a coated fiber (a) by a TE-polarized wave bundle of width $224\,\mu$m *at angle of incidence* $\theta = 52.85°$ *and wavelength* $1.55\,\mu$m*, absolute electric field (b)–(d). Parameters:* $n_s = 1.45$, $n_f = 3.45$, $n_c = 1.0$, $n_r = 1.45$, $n_a = 3.45$; $d = 0.22\,\mu$m, $\rho = 2\,\mu$m, $a = 0.22\,\mu$m, $g = 0.2\,\mu$m*. At maximum, the orbital angular momentum (OAM) mode of angular order* 13 *of the fiber carries about* 80% *of the input power. (Figure adapted from Ref. [3])*

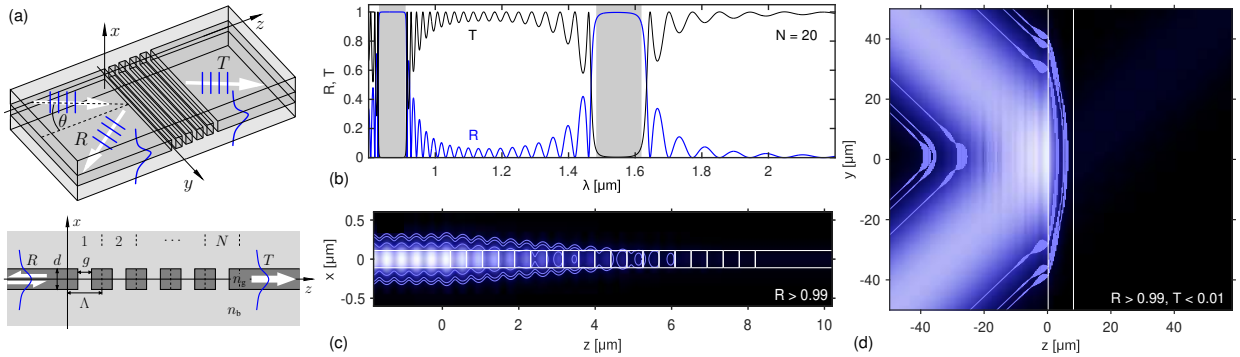

Figure 3: A high-contrast slab waveguide grating, schematic (a), and cross-section view (b). Results for $N = 20$ *periods, for parameters* $n_b = 1.45$, $n_g = 3.45$, $d = 0.22\,\mu$m, $\Lambda = 420\,$nm, $g = 10\,$nm*, for incoming semi-guided TE waves at angle* $\theta = 45°$*: Reflectance* R *and transmittance* T *versus wavelength* λ *(c), energy density for plane wave excitation (d), and for excitation by a beam of width* $35\,\mu$m *(e), at wavelength* $1.55\,\mu$m*. (Figure adapted from Ref. [4])*

Numerical examples

Figs. 1–3 show some example configurations, for typical parameters from silicon photonics. All fields approximate solutions of the Maxwell equations in the frequency domain, in full 3D. Due to the constancy of the structures along one in-plane axis (y, cf. Figs. 1(a)–3(a)), these can be assembled conveniently [2, 3] by analytically superimposing 2-D solutions [5] for some range of angles of incidence. Out-of-plane scattering losses are absent in all cases.

Acknowledgements

Financial support from the German Research Foundation (Deutsche Forschungsgemeinschaft DFG, projects HA 7314/1-1, GRK 1464, and 231447078–TRR 142/3-2022, subprojects C05, B06 and C11), and from the Ministry of Culture and Science of the state of North Rhine-Westphalia (project PhoQC) is gratefully acknowledged.

References

[1] M. Hammer, L. Ebers, A. Hildebrandt, S. Alhaddad, and J. Förstner. In *2018 IEEE 17th International Conference on Mathematical Methods in Electromagnetic Theory (MMET)*, pages 9–15, 2018.

[2] M. Hammer, A. Hildebrandt, and J. Förstner. *Journal of Lightwave Technology*, 34(3):997–1005, 2016.

[3] M. Hammer, L. Ebers, and J. Förstner. *Journal of the Optical Society of America B*, 38(5):1717–1728, 2021.

[4] M. Hammer, H. Farheen, and J. Förstner. *Journal of the Optical Society of America B*, 40(4):862–873, 2023.

[5] M. Hammer. *Optics Communications*, 338:447–456, 2015.

AES 2024, ROME - ITALY, 25 –28 JUNE 2024

Variational approaches for light bullets characterization in nonlinear optics

P. Parra-Rivas*, Y. Sun, and S. Wabnitz

[1] Dipartimento di Ingegneria dell'Informazione, Elettronica e Telecomunicazioni, Sapienza Universitá di Roma, via Eudossiana 18, 00184 Rome, Italy
*corresponding author: pedro.parra-rivas@uniroma1.it

Abstract: We show how variational approaches based on Ritz and Kantarovitch optimization techniques are fundamental for investigating and characterizing the formation and dynamics of spatiotemporal solitons, also known as light bullets, in nonlinear optical waveguides. In this work, we focus on soliton stabilization when considering simultaneously quadratic and quartic chromatic dispersion effects.

Solitons arise in a plethora of different natural contexts, including hydrodynamics, plasma and condensed matter physics, biology, and nonlinear optics, to cite a few [1]. In nonlinear optics, these particle-like objects may emerge in nonlinear media due to a double balance between dispersive or diffractive effects and light confinement in either time or space, leading to temporal or spatial solitons, respectively [2]. Light confinement may be related to the nonlinear dependence of the refractive index with the light intensity (optical Kerr effect), which yields to spatial self-(de)focusing and temporal self-phase modulation (SPM). The previous spatial and temporal effects can be coupled and occur simultaneously, such that dispersion and diffraction counteract Kerr nonlinearity at once, leading to light confinement in space-time, and therefore to the formation of coherent spatiotemporal solitons, also known as *light bullets* (LBs) [3]. In bulk Kerr media these states may undergo different types of instabilities, such as wave collapse, which can make them unstable and even destroy them [2,3].

By applying variational approaches based on the Ritz and Kantarovitch optimization methods and performing full 3D numerical simulations in the generalized 3D+1 nonlinear Schrödinger equation, it has been possible to characterize how the influence of parabolic 2D potentials, representing graded refractive index (i.e., GRIN) of the material, may improve the stability of bullets, arresting wave collapse partially [4, 5]. However, a full stabilization of these multidimensional states requires other stabilization mechanisms.

In this work, we demonstrate how the combination of quadratic and quartic chromatic dispersion improves considerably the stability of LBs. Besides, the quartic dispersion introduces a new controllable parameter which facilitates the manipulation of these states improving their versatility for potential technological applications. To show this, we compute, applying a Kantarovitch optimization approach, LB approximate solutions. These computations allow us to determine the stability of such states by applying the Vakhitov-Kolokolov and Lyapunov criteria [2]. These approximate solutions then serve as initial conditions for accurate numerical simulations which provide a full characterization of the dynamics of the system.

This work unveils the connection between our LBs and those appearing in two different parameter limits: (i) the pure quartic LBs predicted theoretically in GRIN Kerr nonlinear media with anomalous quadratic dispersion [6], and (ii) those emerging in bulk media in the absence of the GRIN structure when the quartic dispersion coefficient is negative [7]. In this last case, we provide analytical approximations of LBs, something that was so

far absent.

We are currently studying the effects that other types of nonlinear contributions, such as quintic self-defocusing nonlinearities may have on the extension of the LB existence region. Preliminary results show that these elements have positive effects on the LBs stabilization and lead to LBs bistability. These findings are key to understanding the formation of LBs in passive multimode cavities where the spatiotemporal dynamics are much more complex [8].

This work was supported by the Marie Sklodowska-Curie Actions (101064614,101023717), AddSapiexcellence grant (Sapienza University).

References

[1] T. Dauxois, P. Michel, "*Physics of Solitons"*, Cambridge University Press (2006).
[2] Y. S. Kivshar, and G. P. Agrawal, "*Optical solitons: From fibers to photonic crysta*l", Academic Press (2003).
[3] Y. Silberberg, "*Collapse of optical pulses"*, Opt. Lett. **15**, 1282-1284 (1990).
[4] S.-S., Yu, *et al.*, *Spatio-temporal solitary pulses in graded-index materials with Kerr nonlinearity*, Op. Comm., **119**, 167–170, (1995).
[5] P. Parra-Rivas, Y. Sun, and S. Wabnitz, *(Invited) Spatiotemporal soliton stability in multimode fibers: A Hamiltonian approach*, Optik, **287**, 171079 (2023).
[6] P. Parra-Rivas, *et al., Pure quartic three-dimensional spatiotemporal Kerr solitons in graded-index media,* Physical Review A (in press) (2024).
[7] G. Fibich and B. Ilan, *Optical light bullets in a pure Kerr medium*, Opt. Lett. **29**, 887 (2004).
[8] Y. Sun, *et al.,* "*Robust three-dimensional high-order solitons and breathers in driven dissipative systems: a Kerr cavity realization*", Physical Review Letters, **131**, 137201 (2023).

The windowed Fourier series with a complex-plane path deformation as an efficient discretization for spatial spectral integral equations.

R. J. Dilz[1*]

[1]Eindhoven University of Technology, The Netherlands
[*]corresponding author: r.dilz@tue.nl

Abstract: We propose using an error-function-windowed Fourier series representing electromagnetic fields for integral equations of finitely sized scatterers. Using a previously developed complex-plane path-deformation, we represent the electromagnetic fields accurately in the spectral domain and quickly transform between spectral and spatial domain. This inifinitely differentiable basis leads to quick numerical convergence.

Domain integral equations lead to large, dense system matrices for which it is near impossible to solve the resulting matrix equation. Integral equations for finitely sized scattering problems in homogeneous backgrounds can be sped up by employing Fourier transforms that diagonalize (parts of) the system matrix. This leads to an efficient matrix vector product with which scattering problems can be solved iteratively. For discrete spatial basis functions, like a voxel grid, Discrete Fourier Transforms (DFTs) can be employed such as in the Conjugate Gradient Fast Fourier Transform (CGFFT) method [1]. More continuous basis functions can be used as well, and thoses bases can be sped up with FFTs as well. Examples of such basis functions are a Fourier series basis for periodic problems [2], or spatial spectral methods like Gabor frames [3] and Hermite interpolation [4] for aperiodic problems. In principle, such higher order basis function do allow for more accuracy at equal system size. Spatial spectral methods require the spectral-domain Green function, with its poles and branchcuts, to be accurately represented. Complex-plane deformations as proposed in [3] and [4] can be used for this.

The current challenge with Gabor frames and Hermite interpolation is that some mathematical operations are hard to efficiently carry out. Although Fourier transforms are almost trivial in Gabor frames, and straightforward when using Hermite interpolation, the operation of multiplication is much more time-consuming, especially in higher dimensions. To some extent this has limited the speed of spatial spectral methods. Better speeds are reached through approximations to the Gabor frame in [5], but it is challenging to track the effect of these approximations.

In this summary we introduce the windowed Fourier series, which combines a fast FFT-based Fourier transformation with a fast pointwise multiplication operation. Together with the trivial addition and innerproduct operations, these operations form the essentials with which domain integral equations can be solved iteratively.

To discretize spatial range $[-r_x, r_x]$ with N basis functions, we have a sampling interval $\Delta_x = r_x/2N$. In this approach, the basis functions are defined by

$$b_n(x) = \text{sinc}((x - n\Delta_x)(1 - e_k/2)r_k) \exp\left(-\frac{(x - n\Delta_x)^2 t_k^2}{4}\right), \tag{1}$$

with corresponding testing functions

$$t_n(x) = \delta(x - n\Delta_x). \tag{2}$$

Here we define $r_k = \pi/\Delta_x$ the spectral range that is discretized of which only a fraction e_x is usable, because the window function with transition length t_k cuts it off. Using this r_k, a similar basis can be constructed for the spectral domain by substituting $x- > k$ and vice versa everywhere. We use the same $e_k = e_x$, and $t_k = t_x r_k/r_x$ in both domains.

Due to the discrete translation symmetry in the basis functions, Fourier transforms can be computed efficiently. Fourier transforms of functions $f(x)$, represented in this basis through $f(x) \approx \sum_n f_n b_n(x)$, can be computed by

$$\hat{f}_n = \text{FFT}\left[f_{n'}\right]_n \frac{1}{2}\left\{-\text{erf}\left(\frac{n\Delta_k - (1 + e_k/2)r_k}{t_k}\right) + \text{erf}\left(\frac{n\Delta_k + (1 - e_k/2)r_k}{t_k}\right)\right\}. \tag{3}$$

This is computed quickly through a Fast Fourier Transform (FFT) and the multiplication with a pre-computed window function which is the part of Eq. (3) containing the error-functions. This is illustrated in Fig. 1 Multiplication of functions is simply done in an element-wise fashion: $f_i = g_i h_i$. Note that there is a similarity between the computational steps within this method and the FFT-enhanced approximation to Gabor frame-based discretization as published in [5]. However, the proposed method circumvents many of the approximations that were made in [5], by directly defining a windowfunction. Additionally, the implementation is much simpler, since an implementation of a Gabor frame is not required anymore.

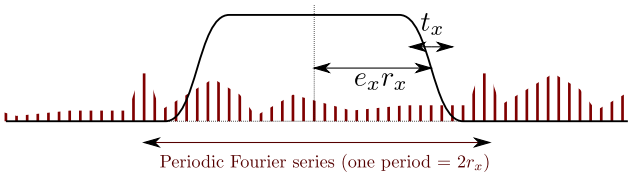

Figure 1: The relation between the window function and the samples for the FFT.

In this way, a spatial spectral discretization is defined that satisfies the requirements for solving finitely sized scattering problems. An interesting characteristic of the windowing approach is that the windowing effectively multiplies some of the values in Eq. (3) with zero, discarding some information. This can be seen as a way of oversampling, since there are more samples then there is information. Similarly, for Gabor frames, the Balian Low theorem dictates that it is necessary to have oversampling as well [6, 7], in order to arrive at an efficient sampling in finite regions of both spatial and spectral domains.

To show the effectiveness of this spatial spectral discretization, we compare it with a spatial spectral discretization based on Hermite interpolation as published in [4]. We compute the scattering of a scalarly polarized 2D scattering problem of a circular cilinder (radius 11, $\varepsilon_r = 1.5$) embedded in vacuum. Simulation parameters were set to $N = 105$, $\Delta_x = 0.5$, $e_x = 0.5$, and $t_x = 1.64$ for the windowed Fourier series, and for the Hermite discretization we took 2 derivatives into account, took a sampling distance $\Delta_x = 0.7$ with 75 sampling points, leading to 225 sampling points per direction. For both discretizations, we employed the same spectral domain path deformation path shifted by a distance $0.13j$ into the complex plane, and using an 8-term Taylor series to approximate the result on the complex-plane path.

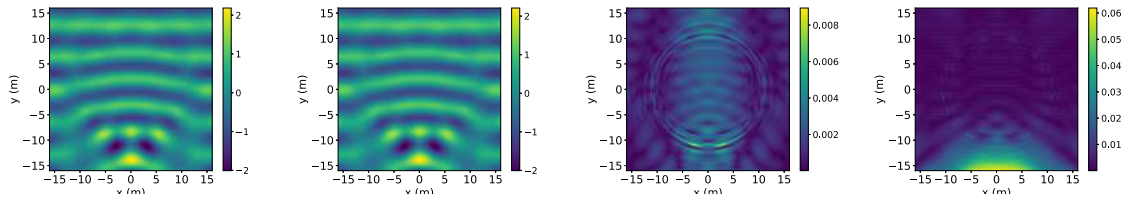

Figure 2: From left to right; First: Real part of z-component of electric field around scatterer for the windowed Fourier series. Second shows the same for the Hermite interpolation-based simulation. Third shows the error with respect to an analytical reference for the windowed Fourier series, while the fourth shows the same for the Hermite interpolation.

The results are shown in Figure 2. The simulation based on the windowed Fourier series took 2.7s, whereas the simulation based on the Hermite interpolation took 23.6s. The relative average L^2 errors (as computed on the domain $[-16, 16]^2$), were 0.0017 and 0.012 for the windowed Fourier series and the Hermite interpolation, respectively.

In conclusion, we introduced the the Windowed Fourier series, which reached more accurate results in less computation time and with less unknowns for a typical simulation case of scattering from a dielectric cilinder.

References

[1] P. Zwamborn and P. M. van den Berg, "The three-dimensional weak form of the conjugate gradient FFT method for solving scattering problems," *IEEE Trans. Microwave Theory Tech*, vol. 40, no. 9, pp. 1757–1766, Sep 1992.

[2] L. Li, *4. Mathematical Reflections on the Fourier Modal Method in Grating Theory*. SIAM, 2001, pp. 111–139. [Online]. Available: https://epubs.siam.org/doi/abs/10.1137/1.9780898717594.ch4

[3] R. J. Dilz and M. C. van Beurden, "An efficient complex spectral path formulation for simulating the 2D TE scattering problem in a layered medium using Gabor frames," *Journal of Computational Physics*, vol. 345, pp. 528–542, 2017.

[4] ——, "A Hermite-interpolation discretization for the spatial spectral integral equation method in multilayered media," *Progress In Electromagnetics Research B*, vol. 80, pp. 37–57, 2018.

[5] ——, "Fast operations for a Gabor-frame based integral equation with equidistant sampling," *IEEE Antennas and wireless propagation letters*, Accepted on October 4th.

[6] R. Balian, "Un principe d'incertitude fort en theorie du signal ou en mecanique quantique," *Comptes Rendus de l'Académie des Sciences. Série II. Mécanique, Physique, Chimie, Sciences de la Terre et de l'Univers*, 1981.

[7] G. Battle, "Heisenberg proof of the Balian-Low theorem," *Letters in Mathematical Physics*, vol. 15, pp. 175–177, 1988.

AES 2024, ROME - ITALY, 25 –28 JUNE 2024

Time domain topology optimization for dispersive nanophotonics inverse design

J. Gedeon[1,2,3,*], E. Hassan[4,5], and A. Calà Lesina[1,2,3]

[1] Hannover Centre for Optical Technologies, Leibniz University Hannover, 30167 Hannover, Germany

[2] Institute for Transport and Automation Technology, Faculty of Mechanical Engineering, 30823 Garbsen, Germany

[3] Cluster of Excellence PhoenixD, Leibniz University Hannover, 30167 Hannover, Germany

[4] Department of Applied Physics and Electronics, Umeå University, SE-901 87 Umeå, Sweden

[5] Department of Electronics and Electrical Communications, Menoufia University, Menouf 32952, Egypt

[*]corresponding author: johannes.gedeon@hot.uni-hannover.de

Abstract: We propose a parallel topology optimization method in the time-domain for the inverse design of linear optical materials with arbitrary dispersion and anisotropy. The technique is demonstrated for 3D free-form nanophotonic structures with broadband performance.

Topology optimization (TopOpt) has emerged as a powerful and widely used approach for designing optical structures with desired functionalities, gaining significant traction in the photonics engineering field over the past decade [1]. Traditionally, topology optimization techniques are performed in the frequency domain to achieve high efficiency within a single or narrow frequency range [2]. However, frequency domain methods are computationally less efficient when dealing with highly dispersive materials or when aiming for broadband optimization, and they also face scalability issues when applied to large scale systems.

To address these challenges, we introduce a novel method to perform topology optimization for linear optical materials with arbitrary dispersion and anisotropy aiming at broadband performance. In our optimization algorithm, we develop a universal adjoint scheme based on the time-dependent Maxwell's equations and the Complex-conjugate Pole-residue Pair (CCPR) model. By integrating the CCPR model using auxiliary equations within the Finite-Difference Time-Domain (FDTD) method, our approach can accurately represent any material by adjusting the model's coefficients to match their complex dielectric permittivity function. For gradient-based optimization, we apply the adjoint method, allowing for efficient broadband response analysis of dispersive structures in a single simulation, along with gradient data for numerous design variables with just one more simulation run. Our method has been incorporated into a scalable, parallelized in-house FDTD code with TopOpt implementation. As a demonstration, we focused on optimizing dispersive nanostructures for field confinement in nanocavities. Optical nanocavities are crucial for a wide range of optical applications such as quantum information [3], spectroscopy [4], semiconductor photon-electron interaction enhancement [5], and energy harvesting [6]. More details about our study of time domain topology optimization of arbitrary dispersive materials for broadband 3D nanophotonics inverse design can be found in our recent publication [7], and more results will be presented at the International Conference on Antennas and Electromagnetic Systems 2024.

Our method enables the tackling of diverse inverse design problems for broadband performance involving high material dispersion, such as broadband absorbers with plasmonic metals, nano-structured thin films for solar cell efficiency maximization, or broadband anti-reflective coatings using dielectrics. Moreover, the time domain formulation is particularly advantageous for exploring time-dependent objectives.

Acknowledgements

We acknowledge the computing time granted by the Resource Allocation Board and provided on the supercomputer Lise and Emmy at NHR@ZIB and NHR@Göttingen as part of the NHR infrastructure (calculations were conducted with computing resources under the project nip00059). We acknowledge the central computing cluster operated by Leibniz University IT Services (LUIS), which is funded by the Deutsche Forschungsgemeinschaft (DFG, German Research Foundation), project number INST 187/742-1 FUGG. This research was supported by the Deutsche Forschungsgemeinschaft (DFG, German Research Foundation) under Germany's Excellence Strategy within the Cluster of Excellence PhoenixD (EXC 2122, Project ID 390833453), and under the Project CA 2763/2-1 (Project ID 527470210). A.C.L. acknowledges the German Federal Ministry of Education and Research (BMBF) under the Tenure-Track Program.

References

1. Molesky, S., Z. Lin, A.Y. Piggott, W. Jin, J. Vuckovic, and A.W. Rodriguez, "Inverse design in nanophotonics," Nature Photonics, Vol. 12, No. 11, 659–670, 2018.
2. Hammond, A.M., A. Oskooi, M. Chen, Z. Lin, S.G. Johnson, and S.E. Ralph, "High-performance hybrid time/frequency-domain topology optimization for large-scale photonics inverse design," Opt. Express, Vol. 30, No. 3, 4467–4491, 2022.
3. Sugimoto, H. and M. Fujii, "Broadband Dielectric–Metal Hybrid Nanoantenna: Silicon Nanoparticle on a Mirror," ACS Photonics, Vol. 5, No. 5, 1986–1993, 2018.
4. Taminiau, T.H., F.D. Stefani, F.B. Segerink, and N.F. van Hulst, "Optical antennas direct single-molecule emission. Nature Photonics," Vol. 2, No. 4, 234-237, 2008.
5. Albrechtsen, M., B.V. Lahijani, R. E. Christiansen, V.T.H. Nguyen, L.N. Casses, S. E. Hansen, N. Stenger, O. Sigmund, H. Jansen, J. Mork, and S. Stobbe, "Nanometer-scale photon confinement in topology-optimized dielectric cavities," Nature Communications, Vol. 13, No. 1, 2022.
6. Duarte, F., J.P.N. Torres, A. Baptista, and R.A.M. Lameirinhas, "Optical Nanoantennas for Photovoltaic Applications," Nanomaterials," Vol. 11, No. 2, 422, 2021
7. Gedeon J., E. Hassan, and A. Calà Lesina, "Time-domain topology optimization of arbitrary dispersive materials for broadband 3d nanophotonics inverse design," ACS Photonics, Vol. 10, 2023.

AES 2024, ROME - ITALY, 25 –28 JUNE 2024

Optimal design of sub-relativistic dielectric particle accelerators

R. Palmeri[1,2*], G. S. Mauro[3], G. Torrisi[3], N. Salerno[4] and G. Sorbello[3,4]
[1]DIIES, University Mediterranea of Reggio Calabria, Italy
[2]Institute for the Electromagnetic Sensing of the Environment, National Council of Research (IREA-CNR), Italy
[3]Laboratori Nazionali del Sud - Istituto Nazionale di Fisica Nucleare, Italy
[4]Department of Electric, Electronics, and Computer Engineering, University of Catania, Italy
[*]corresponding author: roberta.palmeri@unirc.it

Abstract: A simple and effective approach is proposed for the optimal design of sub-relativistic particle accelerators. It relies on a physics-based procedure guarantying the particle-wave synchronicity in an optimally tapered slot waveguide without introducing any approximation on the accelerating field. The final design performance is compared with a previous design based on a constant accelerating field approximation.

The dielectric laser accelerators (DLA) [1] are a novel class of linear accelerators deserving great interest because of the possibility they offer in gathering high accelerating gradient (several hundred of MV/m) with very compact structures. The design of this kind of devices by adopting standard full-wave procedures could represent a bottleneck due to the high number of parameters to be optimized; on the other hand, inverse design [2] based procedures are starting to be investigated.

In this respect, the proposed approach serves as an intermediate solution between a fully automated inverse design and an exhaustive parametric optimization. In fact, it relies on a physics-based procedure that allows to keep the particle-wave synchronicity along the accelerating structures. The envisaged structure is a non-uniform slot waveguide whose tapering and total extension are properly derived to preserve the synchronicity based on the input power and the desired energy gain [3].

The authors first introduced a physics-based procedure in [4], leveraging solely on a calibration curve relating the effective index and the rib's width of the slot waveguide, under the approximation of a constant accelerating field along the accelerating channel. The method allowed to determine the optimal tapering capable of ensuring synchronicity for a given particle velocity and a viable laser power. However, the constant field approximation, valid for short waveguides, showed its limit for longer waveguides where a large increase of the field within the gap occurs due to the smaller and smaller rib's width.

In order to tackle such a situation, we propose herein an improved physics-based approach by considering an additional calibration curve relating the field intensity to the rib's width. This allows to perfectly predict and match the particle velocity with the phase velocity along the accelerating structure and hence gather higher gain in longer structures.

In Fig. 1 it is reported a comparison of the energy gradient obtained with the previous approach based on the constant field (E_0) approximation [red curves] and with the improved one taking into account the actual field variation along the channel [blue curves]. Notably, the analytical derivations are compared with full-wave simulations of the optimized tapered structures and a perfect agreement can be observed in both cases.

More results concerning operative frequencies, employed materials and input powers will be shown at the conference.

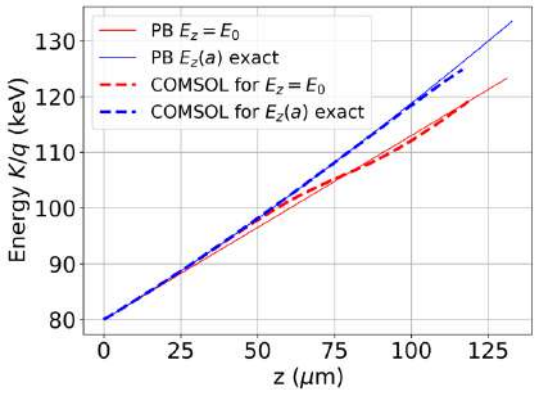

Fig. 1. Comparison between acceleration profile and output energy achievable with the physics-based (PB) approach in case of constant accelerating field approximation (continuous red curves) and exact field (continuous blue curve), and corresponding full-wave simulations with COMSOL Multiphysics (dashed curves).

Acknowledgment

The authors acknowledge financial support from the National Ministry of University and Research as part of the PRIN 2022 projects DOSE (2022MANFK5) and IDEAS (202293B5X), and from INFN V National Committee through the MICRON grant.

References

1. England, R. J., et al., "Dielectric laser accelerators," RMP, Vol. 86, No. 4, 1337, 2014.
2. Palmeri, R. and T. Isernia, "Inverse design of EBG waveguides through scattering matrices," EPJ Appl. Metamater., Vol. 7, 10, 2020.
3. Zhao, Z., et al. "Design of a tapered slot waveguide dielectric laser accelerator for sub-relativistic electrons," Opt. Express, Vol. 26, 22801–22815, 2018.
4. Palmeri, R., et al., "Optimization of sub-relativistic co-propagating accelerating structures," Opt. Express, 31, 38891-38909, 2023.

AES 2024, ROME - ITALY, 25 –28 JUNE 2024

Long-range super-Planckian heat transfer between nano-emitters in a resonant cavity

K. Asheichyk[1], P. Ben-Abdallah[2], M. Krüger[3], and R. Messina[2*]

[1]Department of Theoretical Physics and Astrophysics, Belarusian State University, 5 Babruiskaya Street, 220006 Minsk, Belarus
[2]Laboratoire Charles Fabry, UMR 8501, Institut d'Optique, CNRS, Université Paris-Saclay, 2 Avenue Augustin Fresnel, 91127 Palaiseau Cedex, France
[3]Institute for Theoretical Physics, Georg-August-Universität Göttingen, 37073 Göttingen, Germany
[*]corresponding author: riccardo.messina@institutoptique.fr

Abstract: We study radiative heat transfer between two nano-emitters placed inside different types of closed cavities by means of a fluctuational-electrodynamics approach. We highlight a very sharp dependence of this transfer on cavity width and connect this to the matching between the material-induced resonance and the resonant modes of the cavity.

Two bodies kept at different temperatures and separated by vacuum exchange heat radiatively via the transfer of thermal photons. While this energy flux is limited at far separation distances by Stefan-Boltzmann's law, the pioneering works of Rytov [1] and Polder and Van Hove [2] showed that this limit can be overcome in the so-called near field, i.e., when the separation distance is small compared to the thermal wavelength (around 10 microns at ambient temperature). This amplification can be remarkable for materials supporting resonant modes of the electromagnetic field [3] (in particular polar materials supporting phonon-polaritonic resonances in the infrared region of the spectrum).

The possibility to transport this energy from a thermal source at distances larger than its thermal wavelength remains today a challenging problem which could find broad applications in a variety of the fields (e.g., thermal management and information transfer). With this respect, a remarkable attention has been paid during the past decade to the study of heat transport between two closely separated emitters or within a larger set of emitters, the main goal being to manipulate and tailor the radiative heat exchanges at the nanoscale. Some of these works have focused on the transfer between emitters in the proximity of a substrate or a cylindrical waveguide, showing how the two nano-emitters can couple through the surface resonance existing at the interface between this external body and vacuum and how this additional channel contributes to the transfer by amplifying or inhibiting it. More specifically, some works have considered the impact of confinement on the heat transfer between two nanoparticles, by placing them inside a planar cavity, revealing interesting effects [4–8]. However, they do not address at all the role played by the cavity width in the exchanged flux and especially how the presence of the cavity can make the heat transport strongly super-Planckian (far above the blackbody limit) at large separation distance between the emitters.

In this work we study the near-field radiative heat transfer between two nano-emitters placed inside a cavity (both planar and cylindrical) and highlight the crucial role played by the cavity width. More specifically, we unveil the major interplay between cavity resonant modes, whose frequencies are purely governed by the cavity width and material, and resonances existing at the interface between each nano-emitter and vacuum, giving the leading contribution to near-field radiative heat transfer in vacuum. We show that this interplay and the matching

of these resonances is at the origin of a very sharp dependence of heat transfer on cavity width, allowing for order-of-magnitude variations, as well as transitions from amplification to inhibition with respect to transfer in vacuum, with variations of the cavity width in the micron range. We also show that the characteristic distance at which the effect takes place depends on the geometry, providing a simple tool to choose the most convenient geometry depending on the desired distance. Our results pave the way to easier strategies to export and tune near-field super-Planckian radiative heat flux to distances larger than the thermal wavelength.

P.B.-A. and R.M. acknowledge financial support from Labex Nanosaclay, Grant No. ANR-10-LABX-0035 (Flagship project MaCaCQu). K.A. is supported by the Deutsche Forschungsgemeinschaft (DFG, German Research Foundation) through the Walter Benjamin fellowship (Project No. 453458207).

References

1. Rytov, S. M., "Theory of Electrical Fluctuations and Thermal Radiation" (Academy of Sciences Press of USSR, Moscow, 1953).
2. Polder, D. and van Hove, M., "Theory of Radiative Heat Transfer between Closely Spaced Bodies", Phys. Rev. B **4**, 10 (1971).
3. Joulain, K., Mulet, J.-P., Marquier, F., Carminati, R. and Greffet, J.-J., "Surface electromagnetic waves thermally excited: Radiative heat transfer, coherence properties and Casimir forces revisited in the near field", Surf. Sci. Rep. **57**, 59 (2005).
4. Sääskilahti, K., Oksanen, J. and Tulkki, J., "Quantum Langevin equation approach to electromagnetic energy transfer between dielectric bodies in an inhomogeneous environment", Phys. Rev. B **89**, 134301 (2014).
5. Asheichyk, K. and Krüger, M., "Heat radiation and transfer in confinement", Phys. Rev. B **98**, 195401 (2018).
6. Zhang, Y., Dong, J., Tang, G. and Yi, H.-L., "Many-particle radiative heat transfer in a nonreciprocal graphene plasmonic cavity", Phys. Rev. B **103**, 195433 (2021).
7. Chen, J., Wang, B. X. and Zhao, C. Y., "Near-field radiative heat transport between nanoparticles inside a cavity configuration", Int. J. Heat Mass Transf. **196**, 123213 (2022).
8. Zhang, Y.-J., Zhang, Y., Yang, S.-H. and Yi, H.-L., "Strain-induced control of radiative heat transfer between nanoparticles in a plasmonic cavity", Int. J. Heat Mass Transf. **202**, 123677 (2023).

AES 2024, ROME - ITALY, 25 –28 JUNE 2024

Observation of multipole-type excitations through nanoscale spatial structure of light: from mesoscopic systems to single molecules

H. Ishihara

Department of Materials Engineering Science, Osaka University, Japan
*corresponding author: ishi@mp.es.osaka-u.ac.jp

Abstract: Interaction between multipole-type excitations and light with nanoscale spatial structures gives rise to a variety of physical and chemical functions. This presentation delves into optical response theories addressing nanoscale spatial structures of light and experimental observations of multipole-type excitations across materials ranging from mesoscopic systems to single molecules.

Multipole-type excitations are typically not induced by light under the conditions where the long wavelength approximation (LWA) holds. However, they play crucial roles in various physical and chemical processes, such as multi-photon processes and chemical reactions. Hence, investigating their distinct properties manifested in interactions with light is imperative. When light possesses nanoscale spatial structures, violating the LWA, multipole-type of excitations can be achieved even in one-photon processes. In such scenarios, nonlocal response becomes pivotal, necessitating a theoretical framework that addresses it to predict phenomena and analyze experimental results.

Nonlocal response is significant in two extreme situations. One is the case where the wavefunctions of excited states are coherently extended over long ranges in high-quality samples. We theoretically predicted wave-wave coupling between multipole excitons and light waves, exhibiting significant nonlinearity and ultra-fast radiative decay. This was exemplified by system-size-selective enhancement of nonlinear response in GaAs thin layers [1], and experimental demonstrations of 100 fs radiative decay in CuCl thin films [2]. Moreover, radiative decays of 10 fs were observed for ZnO thin layers [3]. Spatial correlation between light waves and excitonic waves plays a crucial role in their coupling, leading to giant coupling phenomena, thereby enabling functions such as large nonlinearity and ultra-fast optical responses on a 10 fs timescale. Recently, such theoretical predictions have been extended to plasmon polaritons [4] and magnon polaritons [5].

Another case arises from the localized surface plasmon resonance (LSPR), which induces remarkably localized and enhanced electric fields. The electric field oscillating at the incident light frequency exhibits spatial variation even within single molecules, thereby activating multipole-type excitations. Theoretical demonstrations have been conducted for molecules, including single-walled carbon nanotubes (SWCNTs) in metallic nanogaps [6][7], and experimental validation of optical forbidden transitions has been achieved for a single nanogap with SWCNTs using resonance Raman scattering techniques [8].

Recently, we have explored the possibility of observing spatial maps of multipole-type excitations using photoinduced force microscopy (PiFM), wherein spatial patterns reflecting multipole polarizations have been theoretically demonstrated [9]. Furthermore, spatial patterns representing multipole-type polarizations within single pentacene molecules, arising from interactions with neighboring molecules and the substrate, have been successfully observed using state-of-the-art PiFM techniques [10].

Multipole-type excitations observed in the aforementioned works exhibit peculiar functions, such as large nonlinearity and exceptionally fast radiative decay, owing to giant coupling with light. Exploring their potentials for applications paves the way for developing functional devices. Furthermore, in cases studied using LSPR, the targeted molecules are transparent at light frequencies corresponding to activated transitions, veiling their potentials. However, considering their crucial roles in physical and chemical processes, such as multi-photon processes and chemical reactions, insights gained from studying peculiar properties of multipole-type excitations hold significance for future technological advancements based on nanomaterials.

References

1. H. Ishihara, et al., ***Phys. Rev. Lett***. **89** 017402 (2002).
2. M. Ichimiya, et al., ***Phys. Rev. Lett***. **103** 257401 (2009).
3. T. Kinoshita, et al., ***Phys. Rev. Lett***. **122** 157401 (2019).
4. T. Yokoyama, et al., ***Phys. Rev***. B**105** 165408 (2022)
5. K. Kato, T. Yokoyama, H. Ishihara, ***Phys. Rev. Appl***. **19** 034035 (2023)
6. T. Iida, Y. Aiba, H. Ishihara, ***Appl. Phys. Lett***. **98** 053108 (2011)
7. S. Uryu, H. Ajiki, H. Ishihara, ***Phys. Rev. Lett***. **110**, 257401 (2013)
8. M. Takase, et al., ***Nat. Photon***. **7** 550 (2013)
9. H. Yamane, et al., ***Opt. Exp.*** **31**, 3415 (2023)
10. T. Yamamoto, et al., ***ACS Nano*** **18**, 1724 (2024)

All-dielectric epsilon-near-zero Bragg-wall microcavities with tailored coupling efficiency and figure of merit

M. J. Huttunen*, A. Panahpour, J. Kelavuori
Photonics Laboratory, Physics Unit, Tampere University, FI-33014 Tampere, Finland
*Corresponding author: mikko.huttunen@tuni.fi

Abstract: All-dielectric microcavities based on Bragg reflection waveguides (BRWs) operating near their cutoff frequencies are introduced as high figure of merit epsilon-near-zero (ENZ) structures. The structures exhibit ultra-low losses and facilitate coupling of light inside the ENZ media.

Nonlinear optical effects play a pivotal role in photonics, particularly in advancing optical computing, communication, sensing, and metrology. However, nonlinear processes are intrinsically very weak resulting in high pump power requirements that are challenging to meet particularly in the context of modern integrated photonics. Despite challenges, recent research has shown promising avenues for enhancing nonlinear phenomena, such as Kerr effect, four-wave mixing and harmonic generation, through epsilon-near-zero (ENZ) media [1]. However, conventional ENZ materials and structures often suffer from high losses or low figures of merit (FOMs), defined as the ratio of real to imaginary parts of the permittivity [2], restricting their use in real applications.

Here, we introduce planar Bragg reflection waveguides (BRWs) [3] operating near their cutoff frequencies as all-dielectric ENZ microcavities, exhibiting very high FOM values (Fig. 1a) [4]. By exploiting the impedance mismatch between the ENZ waveguide and the surrounding medium, ENZ resonant modes are established through reflectance from the cavity side walls (Fig. 1b). By BRW design, i.e. adjusting the number of Bragg reflector layers and lateral dimensions of the microcavity, we tailor the real and imaginary parts of the effective index of refraction of the ENZ mode, as well as adjust the quality factors (Q-factors) and Purcell factors (PFs) of the ENZ media. Thus, we can adjust the Q-factor from low values for potential applications in rather fast nonlinear effects to very high values for PF enhancement, low threshold lasing or highly sensitive detectors.

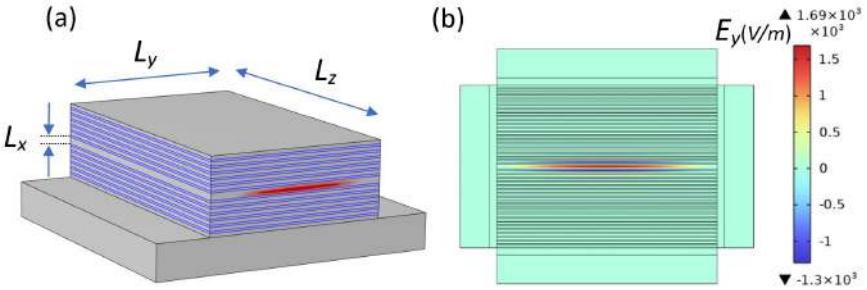

Fig. 1: (a) Schematic view of a BRW with finite lateral sizes and (b) its transverse cross-section view, showing the y-component of electric field, corresponding to an ENZ mode of the waveguide, computed by 2D mode-analysis COMSOL simulation.

We derive scaling relations for the Q-factor and Purcell factor F_P in such structures as:

$$Q \approx \frac{1}{2\epsilon''} \frac{\partial[\omega\epsilon'(\omega)]}{\partial\omega} \approx \frac{1}{2n\kappa} \quad \text{and} \quad F_P \approx \frac{3n_{core}}{\pi^2}\frac{n}{\kappa}$$

in terms of angular frequency (ω), real and imaginary parts of effective permittivity (ε', ε'') and effective refractive index (n, κ) of the BRW. Looking at the above relations one clearly sees how reduction of the imaginary part of the effective refractive index κ is crucial for increasing the achievable values of Q and F_P.

In BRWs, negligible material and modal losses combined with strong dispersion near the cutoff frequency (Fig. 2c and 2d) result in remarkably high Q-factors (~10^6) and Purcell enhancement factors (~10^3). The dispersion is very similar to the case of lossless perfect electric conductor waveguides (Fig. 2a) and quite different from plasmonic waveguides near cutoff wavelength as shown in Fig. 2b, that exhibit marked material/ohmic losses.

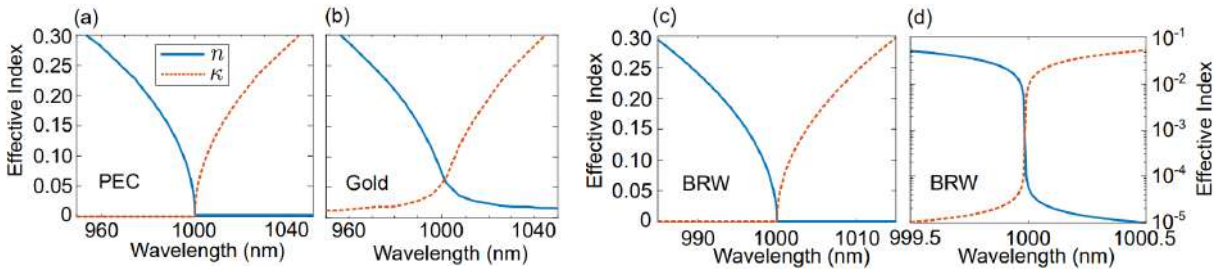

Fig. 2: Dispersion curves of (a) a PEC waveguide, (b) a gold-wall waveguide and (c) a BRW around the cutoff wavelength of 1000 nm. The transverse dimensions of the PEC and gold wall waveguides are the same. (d) A magnified view of the BRW dispersion curve near the cutoff wavelength, shown in logarithmic scale.

In overall, due to significant potential for Purcell factor enhancement, these structures hold promise for boosting optical gain and enabling low-threshold lasing in diverse laser systems. In addition, exploiting other ENZ features in BRW microcavities, such as spatial coherency of the cavity ENZ modes suggests potential application of such structures in development of single-mode high-power semiconductor lasers with improved beam quality. We believe our work lays the groundwork for realizing high-performance, all-dielectric ENZ microcavities with broad applications in nonlinear optics and laser technology.

References

1. Reshef, O., De Leon, I., Alam, M.Z. and Boyd, R.W., “Nonlinear optical effects in epsilon-near-zero media”. Nature Reviews Materials, Vol. 4, No. 8, 535-551, 2019.
2. Javani, M.H. and Stockman, M.I., “Real and imaginary properties of epsilon-near-zero materials”. Physical review letters, Vol. 117, No. 10, 107404, 2016.
3. Yeh, P. and Yariv, A., “Bragg reflection waveguides”, Optics Communications, Vol, 19, No. 3, 427-430, 1976.
4. Panahpour A., Kelavuori J., and Huttunen, M. J. "Strong Purcell Effect in All-Dielectric Epsilon-Near-Zero Microcavities" arXiv preprint arXiv:2402.09718, 2024.

AES 2024, ROME - ITALY, 25 –28 JUNE 2024

Perfect absorption with electric and magnetic lattice resonances

L. Cerdán[1,2], J. R. Deop-Ruano[2], J. J. Alvarez-Serrano[2], and A. Manjavacas[2]

[1]Instituto de Química-Física Blas Cabrera (IQF-CSIC), Consejo Superior de Investigaciones Científicas, Spain
[2]Instituto de Óptica (IO-CSIC), Consejo Superior de Investigaciones Científicas, Spain
*corresponding author: l.cerdan@csic.es

Abstract: We present a strategy to overcome the limitation impeding 2D periodic arrays sustaining lattice resonances to absorb more than half of the incident power. We exploit a couple dipole model to design arrays of metallo-dielectric nanoparticles supporting independent electric and magnetic lattice resonances that, once spectrally overlapped, afford perfect absorption.

When metallic nanostructures are arranged in a periodic array, their localized plasmons can interact coherently to generate collective, strong, and spectrally narrow electromagnetic modes known as lattice resonances (LRs) [1]. However, 2D arrays supporting LRs in which only electric or magnetic dipoles are involved can absorb at most half of the incident power [2]. One approach to obtaining perfect absorption consists in spectrally overlapping the LR with a localized mode of the individual constituents of the array with different parity, in what is regarded as a generalized Kerker effect [3]. However, the overlapping wavelength cannot be easily modified, since the spectral position of the localized mode can only be changed by modifying the polarizability of the nanostructures, which, in turn, modifies the properties of the LR. Here, we report a novel approach to attain perfect absorption based on the spectral overlap of two different LRs [4]. Our approach relies on the use of a bipartite rectangular array with a unit cell composed of both metallic and dielectric nanostructures. Their proper arrangement leads to the emergence of independent dipolar electric and magnetic LRs, which we denote as ED-LR and MD-LR, respectively. We exploit the semi-analytic nature of a coupled dipole model (CDM) to find beforehand the optimal nanostructure disposition and to assess and dissect the optical response of the system.

As depicted in Fig. 1a, we consider a bipartite periodic rectangular array with periods a_x = 654 nm and a_y = 649 nm. The unit cell contains a nanoparticle (NP) of gold, with diameter D_1 = 98 nm, located in the origin (x_1=0, y_1=0), and a NP of silicon, with diameter D_2 = 140 nm, placed at the center of the unit cell (x_1=a_x/2, y_1=a_y/2). We use gold and silicon NPs because the metallic nature of the former results in a strong electric dipole resonance, which can be the source of ED-LRs, whereas the high-refractive-index dielectric nature of silicon produces both electric and magnetic dipole resonances, potentially leading to both ED- and MD-LRs. The array is located in the *xy*-plane, surrounded by vacuum, and excited at normal incidence by an electromagnetic plane wave polarized along the *x*-axis. Given that the sizes of the NPs are significantly smaller than both the periods and excitation wavelength λ, we can describe its optical response using the well-established CDM [5]. In it, the optical properties of the LR can be determined from the analysis of the following eigenvalue problem [5]:

$$\begin{pmatrix} \boldsymbol{p_i} \\ \boldsymbol{m_i} \end{pmatrix} = \sum_{j=1}^{2} \begin{pmatrix} \alpha_i^{EE}\mathbb{I}_{3\times3} & 0 \\ 0 & \alpha_i^{MM}\mathbb{I}_{3\times3} \end{pmatrix} \begin{pmatrix} \mathcal{G}_{ij}^{EE} & \mathcal{G}_{ij}^{EM} \\ \mathcal{G}_{ij}^{ME} & \mathcal{G}_{ij}^{MM} \end{pmatrix} \begin{pmatrix} \boldsymbol{p_j} \\ \boldsymbol{m_j} \end{pmatrix}, \quad (1)$$

with $\boldsymbol{p_i}$ and $\boldsymbol{m_i}$ being the electric and magnetic dipoles induced in the *i*-th particle of the unit cell, α_i the corresponding polarizability, and $\mathcal{G}_{ij}$ the different components of the lattice sum (i.e., Fourier transform of the dipole–dipole interaction tensor). This quantity contains all the information regarding the interaction between the elements of the array. In particular, $\mathcal{G}_{21}^{EM}$ describes the electric-magnetic (EM) coupling between the two

monopartite arrays. Since we aim to independently tune the ED-LR and MD-LR, we must locate the two NPs so that these terms vanish. This is accomplished by placing one NP at the origin of the unit cell and the other one at its center (Fig. 1b). In addition, for this configuration, $\mathcal{G}_{21}^{EE}$ is maximized in absolute terms. Thus, the bipartite array should support a single ED-LR resulting from the hybridization of the ED-LRs supported by the two monopartite arrays, and a single MD-LR, solely supported by the silicon monopartite array. Furthermore, under this configuration, the spectral position of the MD-LR and ED-LR should be governed by a_x and a_y, respectively. Thus, by properly choosing a_x and a_y, the two LRs can be made to overlap. All these predictions are confirmed in Fig. 1c-d, where we show that, with our array geometrical parameters, we can attain a LR with perfect absorption and a quality factor Q = 2.4×10^3. Furthermore, the electric and magnetic dipoles contribute each with half the absorption (Fig. 1c). Finally, each monopartite array absorbs nearly half the incident light, with the silicon one absorbing marginally stronger, as it contributes to both the ED- and MD-LRs (Fig. 1d). Our results provide clear, yet general, guidelines for the rational design of complex 2D arrays capable of sustaining LRs with perfect absorption, thus leveraging its potential for applications requiring an efficient absorption of light.

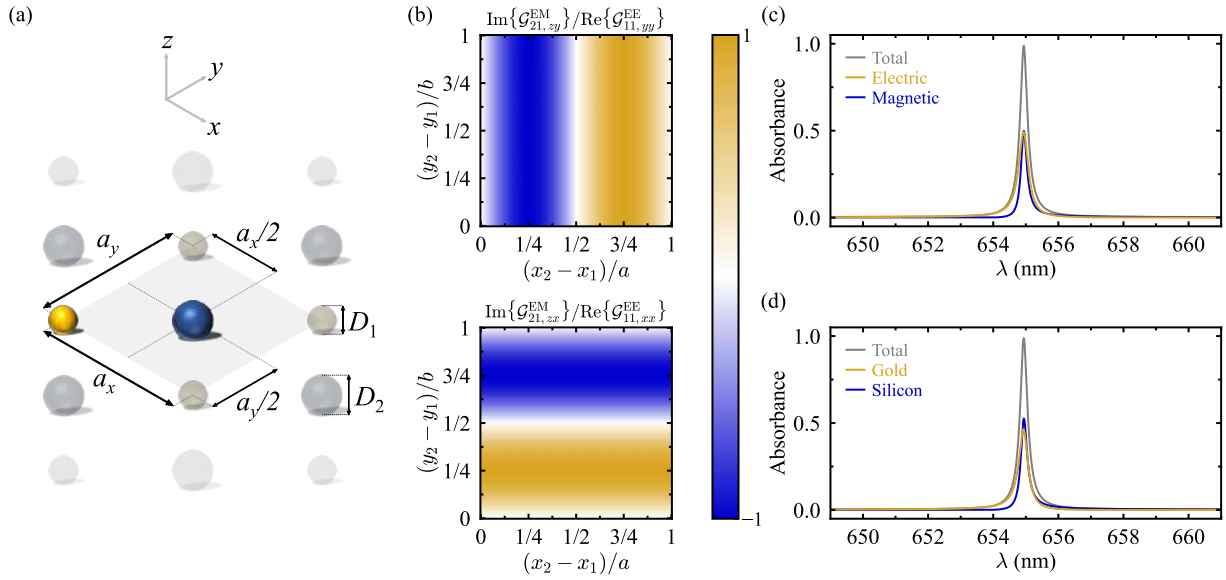

Figure 1: a) Schematics of a bipartite rectangular 2D array built from gold and silicon nanospheres. b) Relevant Electric-Magnetic (EM) coupling terms of the lattice sum $\mathcal{G}_{21}$, as a function of the relative position of particle 2 with respect to particle 1. c-d) Absorbance spectra for the bipartite array, along with the explicit contributions of electric and magnetic dipoles (c), and the contributions of the gold and the silicon nanoparticles (d).

References

1. V.G. Kravets, A.V. Kabashin, W.L. Barnes, A.N. Grigorenko, “Plasmonic Surface Lattice Resonances: A Review of Properties and Applications”, Chem. Rev. 118, 912–5951, 2018.
2. R. Alaee, M. Albooyeh, C. Rockstuhl, “Theory of Metasurface Based Perfect Absorbers” J. Phys., 50, 503002, 2017.
3. V. E. Babicheva, A. B. Evlyukhin, “Resonant Lattice Kerker Effect in Metasurfaces with Electric and Magnetic Optical Responses”, Laser Photon. Rev., 11, 1700132, 2017.
4. L. Cerdán, J. R. Deop-Ruano, J. J. Alvarez-Serrano, and A. Manjavacas, “Perfect Absorption with Independent Electric and Magnetic Lattice Resonances in Metallo-Dielectric Arrays” Adv. Opt. Mater. 2302737, 2024.
5. S. Baur, S. Sanders, A. Manjavacas, “Hybridization of Lattice Resonances” ACS Nano 12, 1618-1629, 2018.

AES 2024, ROME - ITALY, 25 –28 JUNE 2024

Implementing Inhomogeneous Broadening in Time Domain Photonic Simulations

L. J. Prokopeva[1*] and A. V. Kildishev[1*]

[1]Elmore Family School of Electrical and Computer Engineering and Birck Nanotechnology Center,
Purdue University, 1205 W State St, West Lafayette, IN 47907, USA
[*]corresponding authors: lprokop@purdue.edu, kildishev@purdue.edu

Abstract: We present new causal generalizations of the classic Lorentz/Sellmeier/Drude/Debye dispersion models that include inhomogeneous broadening with a given probability density function. Conceptual implementations in an FDTD solver based on MiniMax Optimized Semi-analytical Approximation (MiMOSA) are demonstrated with Gaussian statistics and can be extended to other distributions.

The field of *time-domain* (TD) computational electromagnetics kicked off in the mid-60s with the publication of Yee's second-order explicit numerical finite-difference scheme on a staggered grid. Later, starting from the early 90s, the problem of introducing basic dispersion models into TD solvers with preserved stability, causality, and convergence order was addressed based on the discretization of auxiliary differential equations (ADE) or recursive numerical schemes for the convolution integral (RC). Up to this day, only basic dispersion mechanisms – the Lorentz (including modification with nonzero phase), Sellmeier, Debye, and Drude models – are available for *time domain* simulations.

These dispersion laws usually cover most of the RF design problems. However, in photonic applications, with a higher frequency range comes a significant diversity of light-matter interactions, and the idealized Lorentz/Debye/Drude models derived in the assumption of *homogeneous* broadening with Lorentzian lineshape $1/(1+x^2)$ fail to provide sufficient accuracy. Over the years, multiple generalizations with non-Lorentzian lineshape were suggested for optical materials characterization, where different empirical parameters were introduced in the frequency domain (FD) to compensate for experimental deviations from the classical TD models. Examples include the Cole-Cole, Cole-Davidson, Havriliak-Negami, Cody-Lorentz, Tauc-Lorentz, Kim, generalized Drude, critical points models, etc. Even though these models became handy in the FD-based ellipsometry fitting, e.g., for amorphous and phase-change materials, the retrieved dispersion cannot be consequently employed in the TD Maxwell solvers due to a lack of TD implementation algorithms. Some of the generalized models have a purely empirical FD-based nature, are not causal, and even lack a physically meaningful explanation.

In this work, we present a systematic approach to introduce inhomogeneous broadening in the classic dispersion models in a physically consistent causal manner. We also developed numerical implementation of these models in the time domain solvers based on the MiMOSA method (MiniMax Optimized Semi-analytical Approximation) [1].

In the suggested new models, we assume that the statistical deviations in the material are defined with a probability density function $G(x)$ and a variance parameter σ. The Lorentz model with inhomogeneous broadening (iL) reads

$$\chi_{\mathrm{iL}}(\omega) = \frac{1}{\sigma}\int_{\mathbb{R}} \frac{ax}{x^2 - (\omega + \imath\Gamma)^2} G\left(\frac{x-\Omega}{\sigma}\right)\mathrm{d}x\,, \tag{1}$$

where χ is the relative susceptibility as a function of frequency ω; a, Ω, and Γ are classic Lorentz amplitude, oscillation frequency, and (homogeneous) broadening parameters, respectively; σ is the inhomogeneous broadening. The Drude model with inhomogeneous broadening (iD) is given with a frequency-dependent conductivity function as

$$\sigma_{\mathrm{iD}}(\omega) = \frac{1}{\sigma}\int_{\mathbb{R}} \frac{\sigma_0 \Gamma}{\Gamma - \imath x} G\left(\frac{x-\omega}{\sigma}\right) \mathrm{d}x\,, \tag{2}$$

where additionally to the inhomogeneous broadening parameter σ, we have classic Drude parameters: σ_0 is the DC conductivity, and Γ is the homogeneous broadening.

Finally, the inhomogeneously broadened Debye model (iDe) is identical to the corresponding Drude (iD) model,

$$\chi_{\mathrm{iDe}}(\omega) = \int_{\mathbb{R}} \frac{\Delta\varepsilon \Gamma}{\Gamma - \imath x} G\left(\frac{x-\omega}{\sigma}\right) \mathrm{d}x\,, \tag{3}$$

where Δε and 1/Γ are the permittivity jump and the Debye relaxation time, respectively.

Note that when $\sigma \to 0^+$, the PDF converges into the delta function, and three models degenerate to their classic versions. If the distribution is Gaussian, $G(x) = \frac{1}{2\pi}\mathrm{e}^{-x^2/2}$ (in accordance with the classical Boltzmann statistics of the carriers and the Doppler shift), then Eqs. (1-3) give Gauss-Lorentz, Gauss-Debye, and Gauss-Drude models, and the solution of the integrals can be written in the Faddeeva functions (or plasma dispersion function).

The numerical tests were performed for Gaussian distribution on experimental data with conventional Yee's FDTD solver and confirmed second-order convergence of all inhomogeneously broadened numerical models.

Acknowledgment

This work is supported by the USA ONR Award N00014-20-S-B001, and the USA AFOSR Award FA9550-21-1-0299.

References

1. Prokopeva, L.P., Peana S., and Kildishev A.V., "Gaussian dispersion analysis in the time domain: efficient conversion with Padé approximants," Comput. Phys. Commun., Vol. 279, 108413, 2022.

AES 2024, ROME - ITALY, 25 –28 JUNE 2024

2D Quantitative Inverse Scattering via Suitable Reformulations as an Effective Way to Reduce Non-linearity

Martina T. Bevacqua and Tommaso Isernia

Università degli Studi Mediterranea di Reggio Calabria, Reggio Calabria, Italy

[*]*corresponding author*: martina.bevacqua@unirc.it

Abstract: In this contribution, attention is devoted to possibility of reducing the non-linearity of inverse scattering problem by means of effective and smart reformulations of the basic equations, in particular the Lippmann–Schwinger one. Some reformulations proposed in literature are reviewed and discussed under a unitary perspective.

The inverse scattering problem [1] is a significant topic in electromagnetics due to the huge number of applications (biomedical imaging, nondestructive testing, subsurface imaging, and so on). Moreover, the problem is theoretically relevant because of its nonlinearity and ill-posedness, and its solution represents a very difficult task.

The nonlinearity arises from mutual and self-interactions amongst the different parts of the scatterer or different scatters and is the cause of local minima of the relevant cost function to be minimized. The local minima are ‘false solutions’ of the problem and completely different from the ground truth. The more the problem departs from a linear one, the greater the risk of being trapped into a false solution.

As a countermeasure to non-linearity, both linearized and qualitative methods [1] seem to allow a very easy implementation and require a limited amount of computer memory and computational time, even though they suffer from several limitations induced by the adopted approximated model and the reduction of the achievable information. On the other hand, when the problem is faced by means of quantitative fully non-linear methods, if appropriate a priori information is available, they can be equipped with a good starting guess, regularization schemes, or constraints in order to avoid false solutions.

Alternatively, a possibility to reduce as much as possible the *degree of non-linearity* of inverse scattering problems [2] is that of reformulating the basic equations and thus introducing new effective scattering models. For instance, in the case of 2D lossy media, it has been shown that, by taking advantage of the features of the Green's function, a convenient reformulation of the integral equations can reduce the degree of non-linearity and hence the occurrence of false solutions [3]. In the same line of reasoning and motivated by the contraction integral equation in tackling forward problems with strong conductivities, in [4] a family of new integral equations is proposed. Finally, recently in [5],[6] the Y0 model, based on a convenient decomposition of the pertaining Green’s function, is introduced.

In this contribution, the rationale underlying *smart reformulations of the scattering equations* will be discussed. Moreover, we will compare and provide a unitary perspective for the above different contributions. Finally, new effective possibilities and hybridizations between the above models and possible extensions to the 3D problem will be discussed and introduced.

References

1. X. Chen, Computational Methods for Electromagnetic Inverse Scattering. Wiley, 2018.
2. O. M. Bucci, N. Cardace, L. Crocco, and T. Isernia, "Degree of nonlinearity and a new solution procedure in scalar two-dimensional inverse scattering problems," J. Opt. Soc. Am. A, vol. 18, pp. 1832-1843, 2001.
3. M. D'Urso, T. Isernia and A. F. Morabito, "On the Solution of 2-D Inverse Scattering Problems via Source-Type Integral Equations," in IEEE Transactions on Geoscience and Remote Sensing, vol. 48, no. 3, pp. 1186-1198, March 2010.
4. Y. Zhong, M. Lambert, D. Lesselier and X. Chen, "A New Integral Equation Method to Solve Highly Nonlinear Inverse Scattering Problems," in IEEE Transactions on Antennas and Propagation, vol. 64, no. 5, pp. 1788-1799, May 2016.
5. M. T. Bevacqua and T. Isernia, “An Effective Rewriting of the Inverse Scattering Equations via Green’s Function Decomposition," in IEEE Transactions on Antennas and Propagation vol. 69, no. 8, pp. 4883-4893, Aug. 2021.
6. M. T. Bevacqua and T. Isernia, “Quantitative Non-Linear Inverse Scattering: A Wealth of Possibilities Through Smart Rewritings of the Basic Equations,” in IEEE Open Journal of Antennas and Propagation, vol. 2, pp. 335-348, 2021.

AES 2024, ROME - ITALY, 25 –28 JUNE 2024

Computational Electromagnetics in Atomic Scale: First-Principles Approach

T. Takeuchi[1], M. Uemoto[2], and K. Yabana[3,*]

[1]Metamaterials Laboratory, RIKEN Cluster for Pioneering Research, Japan
[2]Department of Electrical and Electric Engineering, Kobe University, Japan
[3]Center for Computational Sciences, University of Tsukuba, Japan
[*]corresponding author: yabana@nucl.ph.tsukuba.ac.jp

Abstract: We develop a computational electromagnetics method that describes light propagation in atomic scale coupling first-principles electron dynamics calculation and Maxwell equations for light propagation. We apply the method for various nonlinear and/or nonlocal optical phenomena where quantum electronic motion is significant, including plasmonic and semiconductor meta-surfaces.

As the size of nanoparticles decreases in meta-surfaces, quantum effects become more pronounced in their optical response. Most commonly seen is the effect of surface spill-out of electrons, and as the distance between nanoparticles decreases, the effect of tunneling currents flowing between nanoparticles appears. As the intensity of the pulsed light increases, nonlinear light-matter interaction becomes significant. High order harmonic generations from dielectric meta-surfaces have been attracting interest. To describe the optical response of meta-surfaces with such quantum and/or nonlinear effects, it is important to develop a method that simultaneously describes the quantum dynamics of electrons and the propagation of light. We have been developing a theoretical and computational method for the interaction of optical pulses with various materials based on the time-dependent density functional theory (TDDFT), either within the jellium approximation, which replaces the detailed atomic structure with smooth positive background charge, or by an ab initio calculation. Coupling Maxwell equations with electronic motion described by TDDFT, nonlinear and/or nonlocal light propagation of pulsed light can be described. The method has been implemented in an open-source software SALMON, developed by the authors' group [1]

To connect electron dynamics described by TDDFT and light propagation by Maxwell equations, we make use of a course-graining approximation. We explain it for two distinct cases: For nanoparticles whose size is less

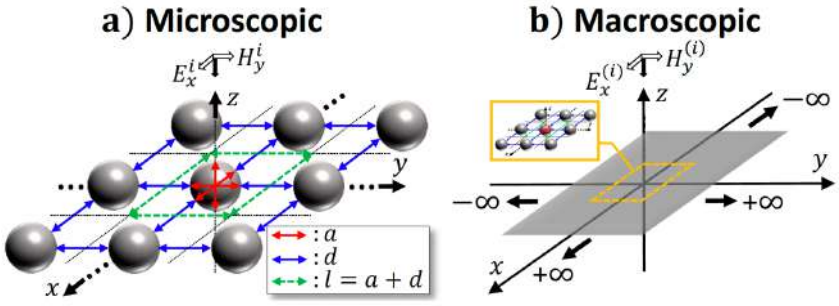

Fig. 1: Schematic description of computational method for small nanoparticles. (a) In microscopic scale, we solve time-dependent Kohn-Sham equation with periodic boundary condition. (b) In macroscopic scale, meta-surface is treated as uniform thin layer with two-dimensional current density.

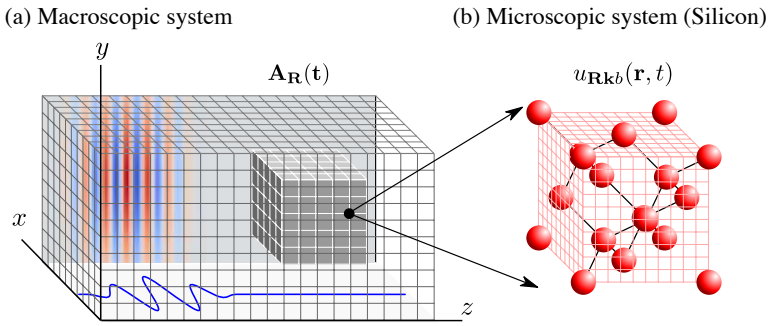

Fig. 2: Schematic description of computational method for large nanoparticles. (a) In macroscopic scale, Maxwell equation is solved in course-grid. (b) In microscopic scale, electronic motion is described assuming electronic motion in an infinite system under a spatially-uniform, time-dependent electric field.

than a few nano-meters, we can describe electronic motion by solving time-dependent Kohn-Sham (TDKS) equation, the basic equation of TDDFT, for the nanoparticle in real time and real space. To connect with macroscopic Maxwell equation, we make a course-graining approximation that produces 2D current. (See Fig. 1)

For nanoparticles whose size is comparable to the wavelength of light (a few hundred nano-meters), it is impossible to solve the TDKS equation for electrons in the nanoparticle. Instead, we make use of a course-graining approximation for the nanoparticle: The nanoparticle is considered to be composed of a number of small cubes and electronic motion in the cubes is described by the TDKS equation for an infinitely periodic system under a spatially-uniform electric field (See Fig. 2). In this method, although we cannot take into account the surface effects, nonlinear light-matter interaction can be fully taken into account.

We have been applying both methods for various phenomena. The former method has been applied to investigate quantum effects in plasmonic meta-surfaces. Effects of quantum tunneling and electron spill-out have been reported in the linear [2] and nonlinear [3,4] responses. The latter method has been applied to investigate light propagation under extremely nonlinear conditions such as high harmonic generations in thin films [5] and nonlinear light propagation in semiconductor meta-surface [6].

References

1. L M. Noda et.al, “SALMON: Scalable Ab-initio Light-Matter simulator for Optics and Nanoscience”, Comp. Phys. Comm. **235**, 356 (2019); https://salmon-tddft.jp.
2. T. Takeuchi and K. Yabana, “Operation of Quantum Plasmonic Metasurfaces Using Electron Transport through Subnanometer Gaps”, ACS Photonics 6, 2517 (2019).
3. T. Takeuchi and K. Yabana, “Extremely large third-order optical effects caused by electron transport in quantum plasmonic metasurfaces with subnanometer gaps”, Sci. Reports 10, 21270 (2020).
4. T. Takeuchi and K. Yabana, “Electron spill-out effect on third-order optical nonlinearity of metallic nanostructure”, Phys. Rev. A106, 063517 (2022).
5. S. Yamada, T. Otobe, D. Freeman, A. Kheifets, and K. Yabana, “Propagation effects in high-harmonic generation from dielectric thin films”, Phys. Rev. B107, 035132 (2023).
6. K. Kihara, G. Matsuura, S. Yamada, and M. Uemoto, “First-principles simulation of nonlinear optical properties of nanostructured semiconductors”, Proc. 34th Symp. Of Association for Condensed Matter Photophysics.

AES 2024, ROME - ITALY, 25 –28 JUNE 2024

Calculating free-electron nonlinearities in nonclassical plasmonic heavily doped semiconductor systems

H. Hu[1] and C. Ciracì[*]

[1] Istituto Italiano di Tecnologia, Center for Biomolecular Nanotechnologies, 73010 Arnesano, Italy
[*]corresponding author: Huatian.hu@iit.it

Abstract: Free-electron dynamics have a substantial contribution to the optical nonlinearity in heavily doped semiconductor systems. We applied both frequency- and time-domain approaches based on the finite-element method to explore a significant third-harmonic generation and optical Kerr bistability.

Understanding the nonlinear light-matter interaction at the nanoscale has been a long-standing fundamental target since it guides the design rule for minimized and integrated nonlinear photonic devices. Achieving a strong and ultrafast nonlinear optical response is essential for various fields such as optical information processing and artificial intelligence training. Yet, efficiently manipulating light with light is still challenging, leading to an urgent demand of exploring new physics for higher nonlinear interactions.

Free electrons in plasmonic structures can provide extra degrees of freedom in modulating nonlinearities in the system when the spatial nonlocality is considered. The hydrodynamic model reveals that the third-order nonlinearity due to the free electrons could even be orders of magnitude higher than that of the conventional bulk susceptibility when the equilibrium density is low. [1] To reveal the hydrodynamic contribution of the optical nonlinearity in Drude material, we calculated the third-harmonic generation coefficients by numerically solving the hydrodynamic equations coupled with the Maxwell equation and compared them with the experiments. A Thomas-Fermi level approximation is considered for quantum pressure. Linear and nonlinear responses of each field harmonic are solved individually with undepleted pump approximation. The results prove the existence and domination of the nonlinearity from the free-electron dynamics as a surface contribution over the conventional bulk susceptibility.

Kerr nonlinearity is a third-order process that supports fascinating phenomena such as optical bistability and self-focusing. A high optical Kerr nonlinearity at the nanoscale is a crucial element in ultrafast optical neuromorphic computation devices as it can enable all-optical nonlinear activation functions.[2] Employing a time-domain simulation within a finite-element framework, we could apply a beam-envelope approach to efficiently and self-consistently solve electromagnetic wave equation and hydrodynamic formalism with Kerr nonlinear contributions. With such a beam-envelope approach, a time step as large as 300 times of period of light could be reached for a convergent result. The solution of the nonlinear sources from the previous time step was used for computing the field at the current step for computational stabilization. We show that heavily doped semiconductor structures can provide giant free-electron Kerr nonlinearities supported by the longitudinal bulk plasmon mode. This high nonlinearity originates from the multibody properties of the free electron gas as the electron-electron interaction can be naturally taken into account in the hydrodynamic theory when proper kinetic energy functionals are considered.

The authors acknowledge funding from the European Union’s Horizon Europe Research and Innovation Program (Grant Agreement No. 101046329).

References

1. F. De Luca, et.al, Phys. Rev. B, 103, 115305 (2021)
2. J. Niu, et.al, Advanced Optical Materials, 11, 2300223 (2023).

AES 2024, ROME - ITALY, 25 –28 JUNE 2024

Metasurfaces with Angular Invariant Scattering

K. Achouri[1*]

[1]Swiss Federal Institute of Technology in Lausanne (EPFL), Switzerland
[*]corresponding author: karim.achouri@epfl.ch

Abstract: We demonstrate that, under specific conditions, the response of a metasurface may become invariant with respect to the angle of wave propagation. This effect is due to relationships between electric and magnetic responses reminiscent of the Kerker conditions. These conditions were obtained using a zero-thickness metasurface modeling technique and are supported by numerical verifications.

A metasurface is typically made of a periodic arrangement of scattering particles engineered to produce desired optical transformations. Intuitively, we generally expect that the scattering particles composing a metasurface individually exhibit angular varying responses, unless, of course, the particles are symmetric within the plane of incidence, e.g., if the particle is a sphere. But even if the metasurface is made of an array of spheres, we still expect its scattering response to depend upon the angle of incidence, as the coupling between the particles is typically angle-dependent.
However, analyzing the scattering response of a metasurface in terms of effective material parameters reveals that, under certain conditions, the reflection and transmission coefficients may become angular invariant. Indeed, using the generalized sheet transition conditions (GSTC) [1]

$$\hat{\mathbf{z}} \times (\mathbf{H}^+ - \mathbf{H}^-) = j\omega \mathbf{P}_\parallel - \hat{\mathbf{z}} \times \Delta_\parallel M_z,$$
$$\hat{\mathbf{z}} \times (\mathbf{E}^+ - \mathbf{E}^-) = -j\omega \mu \mathbf{M}_\parallel - \hat{\mathbf{z}} \times \Delta_\parallel P_z/\epsilon,$$

along with the bianisotropic constitutive relations given by

$$\mathbf{P} = \epsilon \bar{\bar{\chi}}_{\mathrm{ee}} \cdot \mathbf{E} + \bar{\bar{\chi}}_{\mathrm{em}} \cdot \mathbf{H}/c_0,$$
$$\mathbf{M} = \bar{\bar{\chi}}_{\mathrm{mm}} \cdot \mathbf{H} + \bar{\bar{\chi}}_{\mathrm{me}} \cdot \mathbf{E}/\eta_0,$$

it is trivial to express the metasurface scattering parameters in terms of its effective susceptibility tensors, $\bar{\bar{\chi}}$, and investigate its angular scattering properties [1,2].

For illustration, let us consider the case of a TM-polarized plane wave obliquely impinging on a dielectric metasurface in the xz-plane. Using the above equations, and considering a typical metasurface harboring both electric and magnetic responses, we readily find the two following condition: (1) $\chi_{\mathrm{mm}}^{yy} = \chi_{\mathrm{ee}}^{xx}$ and $\chi_{\mathrm{ee}}^{zz} = -\chi_{\mathrm{ee}}^{xx}$, and (2) $\chi_{\mathrm{mm}}^{yy} = -4/(\chi_{\mathrm{ee}}^{xx} k^2)$ and $\chi_{\mathrm{ee}}^{zz} = 0$. They both lead to the angular scattering response given by

$$F(\theta) = \frac{2j + \chi_{\mathrm{ee}}^{xx} k_z}{2j - \chi_{\mathrm{ee}}^{xx} k_z},$$

where $F(\theta)$ corresponds to a transmission/reflection coefficient in the case of condition (1)/(2). Cleary, this function corresponds to an angularly invariant amplitude since $|F(\theta)|^2 = 1$ but still exhibits an angularly dependent phase. Two examples of possible structures corresponding to such responses are shown in Fig. 1.

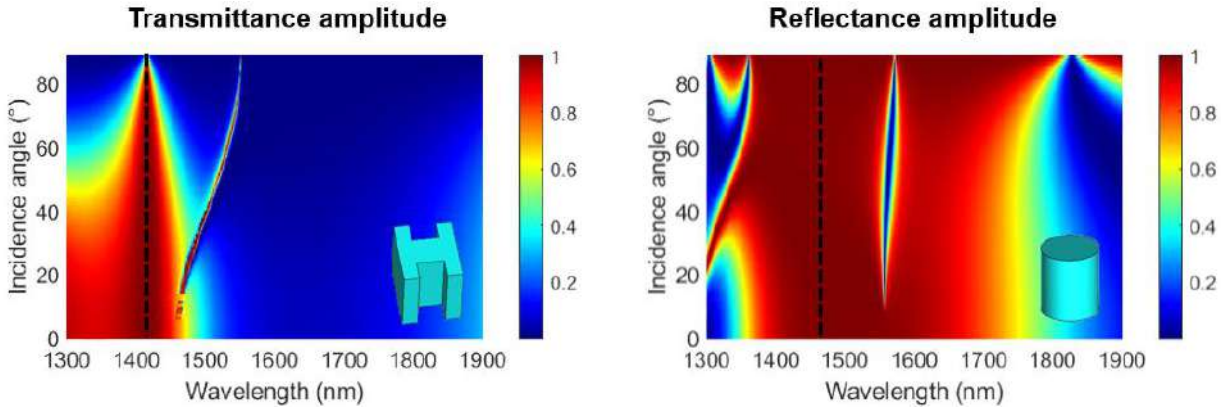

Figure 1. Dielectric metasurfaces exhibiting angular invariant full transmittance (left) or full reflectance (right) indicated by the dashed lines. The insets show the metasurfaces scattering particle.

Next, we consider the case of a purely bianisotropic metasurface for which $\chi_{\mathrm{mm}}^{yy} = \chi_{\mathrm{ee}}^{xx} = 0$ and $\chi_{\mathrm{em}}^{xy} = -\chi_{\mathrm{me}}^{yx}$ leading to the reflection and transmission coefficients

$$T(\theta) = \frac{4 + \left(\chi_{\mathrm{em}}^{xy} k\right)^2}{4 - \left(\chi_{\mathrm{em}}^{xy} k\right)^2} \quad \text{and} \quad R(\theta) = \pm \frac{4j\chi_{\mathrm{em}}^{xy} k}{4 - \left(\chi_{\mathrm{em}}^{xy} k\right)^2},$$

where the $\pm$ sign refer to propagation in the $\pm z$-directions. This time both amplitude and phase of the scattering parameters are angularly invariant. An example of such a metasurface is shown in Fig. 2.

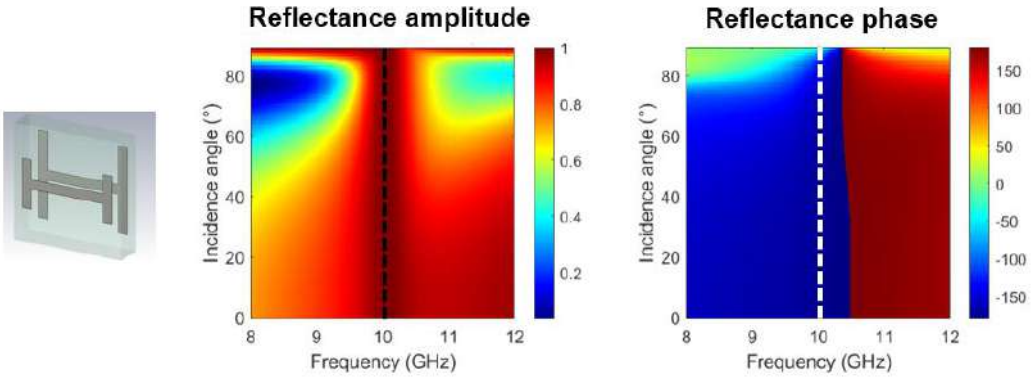

Figure 2. Bianisotropic metasurface with angular invariant full reflectance and (almost) constant phase indicated by the dashed lines. The metasurface unit cell is shown in the left image.

At the conference, we will show more details about the modeling procedure and demonstrate that the simulated structures do indeed correspond to the aforementioned conditions. We shall also discuss other cases of invariant angular scattering responses, which may find applications in optical transformations requiring angular invariance.

References

1. K. Achouri and C. Caloz, Electromagnetic metasurfaces: theory and applications. Hoboken, NJ: Wiley-IEEE Press, 2021.
2. K. Achouri and O. J. F. Martin, “Angular Scattering Properties of Metasurfaces,” IEEE Trans. Antennas Propagat., vol. 68, no. 1, pp. 432–442, Jan. 2020

Green's functions for electromagnetism on a lattice

B. P. de Hon[1]

[1]Eindhoven University of Technology, The Netherlands
*corresponding author: b.p.d.hon@tue.nl

Abstract: Electromagnetic lattice Green's functions on a Yee mesh can be computed via the vector potential 1-form that satisfies a scalar *no-neighbours*, seventh-order, eighteenth-degree, discrete-time recurrence scheme. Boundary conditions are no longer required, and the scheme allows for very large lattice distances.

1. Introduction

There is a natural connection between differential k-forms and discrete k-forms that follow the rules of discrete exterior calculus (DEC). Chen and Chew[1] have explored this connection for electromagnetism on simplicial meshes. In their work, the Hodge star operators encode the local medium properties and geometry to map primal cochains to dual cochains.

I am interested in the much simpler problem involving a regular cubic grid (a cubic lattice) embedded in Euclidean space with uniform medium properties. In this case DEC automatically leads to a dual cubic lattice, and Maxwell's equations become the Yee scheme [2], also known as finite difference time domain (FDTD). However, instead of handling the electromagnetic k-forms, I propose to work with the vector potential 1-form and the scalar potential 0-form. The vector potential satisfies the scalar lattice wave equation for which co-workers and I have developed a no-neighbours recurrence scheme. The purpose of this paper is to extend that work and compute electromagnetic lattice Green's functions from the vector potential.

2. Electromagnetic fields and potentials as differential forms

Let us consider Euclidean 3D space ($n = 3$) with uniform permittivity ε, permeability μ, and wave speed c with $c^{-2} = \varepsilon\mu$. The absence of magnetic charge implies that the magnetic flux 2-form is closed, i.e., $dB = 0$, where d denotes the exterior derivative. Hence, we may express B in terms of a vector potential 1-form A via $B = dA$. From the law of Farady-Henry we infer that we may express the electric field 1-form in term of A and the scalar potential 0-form ϕ according to

$$E = -\frac{\partial}{\partial t}A - d\phi. \tag{1}$$

Finally, we adopt the Lorenz gauge, which together with the law of Ampère-Maxwell leads to

$$-c^{-2}\frac{\partial}{\partial t}\phi = \star d \star A \quad \Rightarrow \quad \mathsf{F}A + c^{-2}\frac{\partial^2}{\partial t^2}A = \mu \star J, \tag{2}$$

in which $\star$ is the Hodge star that maps k-forms to $n-k$-forms, and

$$F = (-1)^{kn+1}\left(\star d \star d + (-1)^n d \star d \star\right) \tag{3}$$

denotes the Hodge (or de Rham) Laplacian operating on k-forms, and producing k-forms.

Let us assume that $\mu \star J$ is a unit-amplitude impulsive z-directed (vertical) dipole located along a vertical edge of a cubic grid. The corresponding vector potential is the lattice Green's function (LGF) that will also be directed along vertical edges of the grid (which correspond to the horizontal faces of the dual grid). In Figure 1, I have sketched a Yee cell (green), the dual Yee cell (orange), and the Laplace-de Rham operator F acting on A, and its constituents $\star d \star dA$ (vertical edges) and $-d \star d \star A$ (horizontal faces).

3. A no-neighbours recurrence scheme for the lattice Green's function

FDTD for the electromagnetic fields is an explicit recurrence scheme, in which the electric or magnetic field value at a node at the current discrete instant in time only depends on the magnetic or electric field values at the neighbouring points at the previous instant in time. In an unbounded domain this can only be achieved exactly if one lets the computational domain grow with every time step. Alternatively, one could use boundary conditions that mimick the unbounded surroundings, such

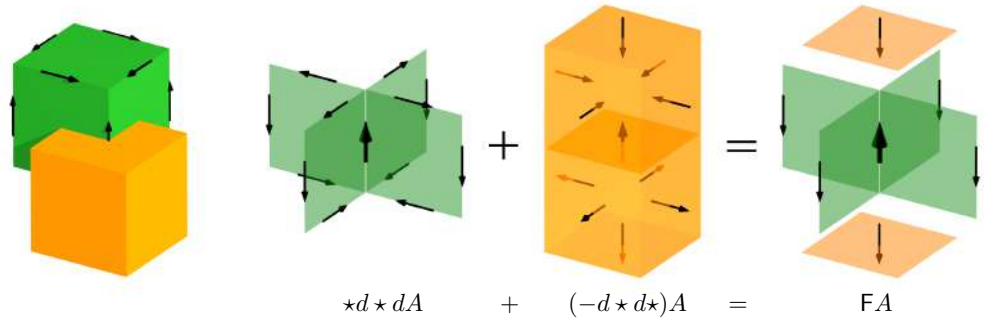

Figure 1: Left: the Yee cell (green) with the 1-form A (electric vector potential) defined on its edges, and the dual Yee cell (orange). Right: the Laplace-de Rham operator F acting on A, and its constituents $\star d \star dA$ (left middle), and $-d \star d \star A$ (right middle).

as perfectly matched layers. Fortunately, there is an alternative, viz., a fast, *no-neighbours*, seventh-order, eighteenth-degree, discrete-time recurrence scheme for the lattice Green's function (LGF) [3]. I have used this scheme in combination with (1) and the Lorenz gauge in (2) to compute the electric- and magnetic-field LGF components, and the fields that results through convolution with a sufficiently smooth pulse (a 1536-point Ricker wavelet). Figure 2 shows the dominant cartesian components of the electric-field LGF (the x-component is very small) at a very far lattice point $(2982, 197019, 200001)$.

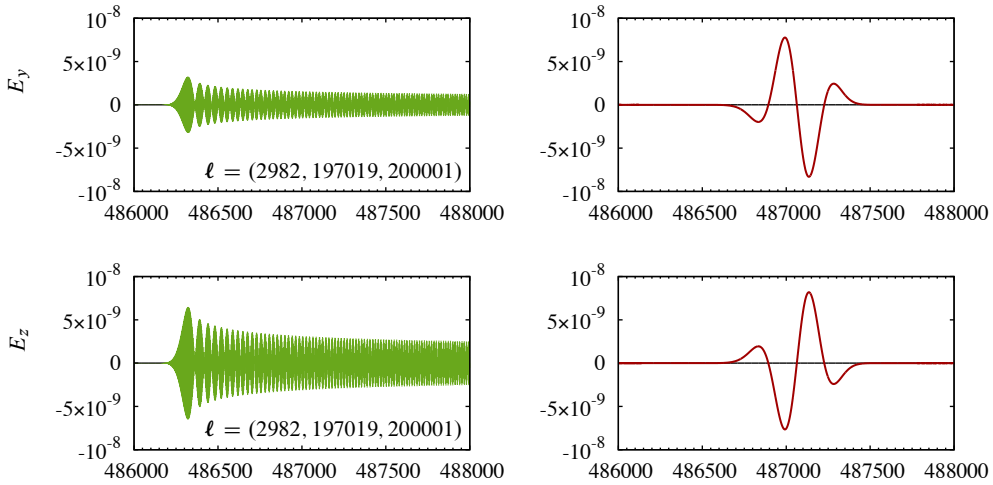

Figure 2: The two dominant electric-field lattice Green's function cartesian components at the lattice point $(2982, 197019, 200001)$, and the results after convolution with a smooth pulse.

References

[1] S. C. Chen and W. C. Chew, "Electromagnetic theory with discrete exterior calculus," *Progress In Electromagnetics Research*, vol. 159, pp. 59–78, 2017.

[2] K. Yee, "Numerical solution of initial boundary value problems involving Maxwell's equations in isotropic media," *IEEE Trans. Antennas Propag.*, vol. 14, no. 3, pp. 302–307, 1966.

[3] B. P. de Hon, S. J. Floris, and J. M. Arnold, "No-neighbours recurrence schemes for space-time green's functions on a 3D simple cubic lattice," *Journal of Physics A: Mathematical and Theoretical*, vol. 51, no. 8, p. 085201, 2018.

AES 2024, ROME - ITALY, 25 –28 JUNE 2024

Efficient FEM simulation of resonance modes of VCSELs

L. Kuen[1,2*], M. Hammerschmidt[1], P.-I. Schneider[1], L. Zschiedrich[1], and S. Burger[1,2]

[1] Zuse Institute Berlin, Germany
[2] JCMwave GmbH, Germany
[*]corresponding author: kuen@zib.de

Abstract: We present convergence investigations for VCSELs with rotational symmetry and of full 3D geometries. The aim is to obtain parameters for the numerical setup, that allow for accurate and efficient simulations. These parameters can then be used to reliably find the fundamental mode, which is e.g. required for optimization.

Vertical-cavity surface-emitting lasers (VCSEL) are widely used light sources in optics, e.g. for communications and sensing. The simulation of these structures plays an important role in the design process [1,2]. Quantities of interest are in principle the wavelength, the field distribution, and the Q-factor of the fundamental resonance mode. However, quantities such as the far-field or the amount of radiation in the beam direction may also be of interest. Depending on the structure of the VCSEL, different models can be simulated, where the easiest is a 1D and the most complex is a full 3D setup. A sketch of a VCSEL is shown in Fig. 1(a) and a part of the corresponding densely populated spectrum close to the fundamental resonance mode is given in Fig. 1(b). In case, that the VCSEL is cylindrical symmetric, this is used to reduce computational effort by representing the azimuthal direction via Fourier coefficients [3]. However, there exists also designs for special applications, for example, to control the polarization, e.g. with the help of a line grating, which breaks the cylindrical symmetry [4,5], thus a 3D simulation is necessary.

We perform simulations using the finite element method (FEM), embedded in the solver JCMsuite to solve time-harmonic Maxwell's equations in the frequency domain [6,7]. Here, the eigenmodes are computed using the Arnoldi method [8]. The solver allows for adaptive h- and p-refinement, this allows for fast and accurate simulations. Numerical models of VCSELs with rotational symmetry and full 3D structures are investigated [9]. Convergence studies regarding mesh resolution and FEM degree are performed. This results in parameters for accurate and fast simulations. Furthermore, the detection of the fundamental resonance is investigated. The reliable calculation of the fundamental mode is essential, e.g. for further optimization.

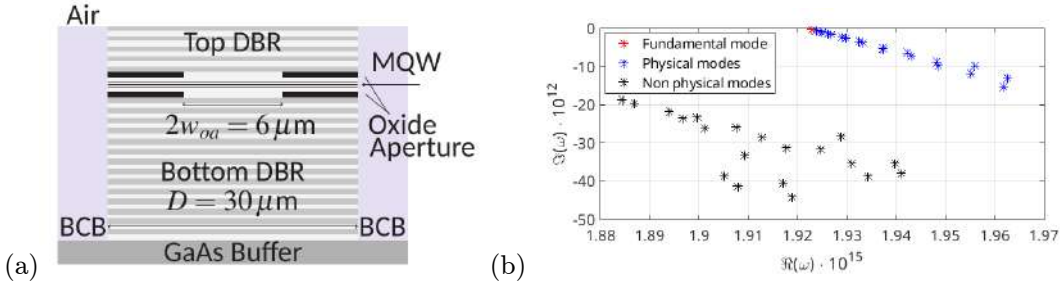

Figure 1: (a) Sketch of a cross section of a VCSEL (not to scale). (b) Spectrum of the eigenvalues in the region of the fundamental resonance.

Acknowledgements: This project is co-financed by the European Regional Development Fund (EFRD, application no. 10184206, QD-Sense). This project (20FUN05 SEQUME) has received funding from the EMPIR programme co-financed by the Participating States and from the European Union's Horizon 2020 research and innovation programme.

References

1. N. Ledentsov, V. Shchukin, N. Ledentsov, J.-R. Kropp, S. Burger, and F. Schmidt, "Direct Evidence of the Leaky Emission in Oxide-Confined Vertical Cavity Lasers," IEEE J. Quant. Electron., Vol. 52, No. 3, 1-7, 2016.
2. L. Kuen, F. Betz, F. Binkowski, P.-I. Schneider, M. Hammerschmidt, N. Heermeier, S. Rodt, S. Reitzenstein, and S. Burger, " Applying a Riesz-projection-based contour integral eigenvalue solver to compute resonance modes of a VCSEL," Proc. SPIE, Vol. 12575, 125750J, 2023.
3. P.-I. Schneider, N. Srocka, S. Rodt, L. Zschiedrich, S. Reitzenstein, and S. Burger, "Numerical optimization of the extraction efficiency of a quantum-dot based single-photon emitter into a single-mode fiber," Opt. Express, Vol. 26, No. 7, 8479-8492, 2018.
4. M. Gebski, J. A. Lott, and T. Czyszanowski, "Electrically injected VCSEL with a composite DBR and MHCG reflector," Opt. Express, Vol. 27, No. 5, 7139, 2019.
5. P. Debernardi, J. M. Ostermann, M. Feneberg, C. Jalics and R. Michalzik, "Reliable polarization control of VCSELs through monolithically integrated surface gratings: a comparative theoretical and experimental study," IEEE J. Sel. Top. Quantum Electron., Vol. 11, No. 1, 107-116, 2005.
6. JCMwave GmbH, "JCMsuite." https://jcmwave.com/.
7. J. Pomplun, S. Burger, L. Zschiedrich, and F. Schmidt, "Adaptive finite element method for simulation of optical nano structures," Phys. Status Solidi B, Vol. 244, No. 10, 3419-3434, 2007.
8. Y. Saad, "Numerical methods for large eigenvalue problems, Revised Edition," SIAM, 2011.
9. M. Rozova, J. Pomplun, L. Zschiedrich, F. Schmidt, S. Burger, "3D finite element simulation of optical modes in VCSELs, " Proc. SPIE, Vol. 8255, 82550K, 2012.

AES 2024, ROME - ITALY, 25 –28 JUNE 2024

Efficient simulation and design of large-scale metasurfaces

D. Huynh[1*], J. Niegemann[2], H. H. M. Cheng[3], T. Leportier[2], F. Duque-Gomez[2], S.-S. Kim[4], and A. Reid[2]

[1]Ansys Germany GmbH, Germany
[2]Ansys Canada Ltd., Canada
[3]Ansys Japan K.K., Japan
[4]Ansys UK Limited, United Kingdom
[*]corresponding author: dan-nha.huynh@ansys.com

Abstract: Optical metasurfaces, made of nano-scale elements that manipulate light locally, present an exciting technology for customizing optical responses. They have garnered significant attention, particularly in the realm of augmented and virtual reality. Here, we present our recent progress in efficiently simulating and optimizing mm-sized and cm-sized metasurfaces.

Due to substantial advancements in the research and fabrication of optical metasurfaces, there has been a surge of interest from academia and industry [1]. One of their key properties is to facilitate the manipulation of the optical response at the nanoscale by carefully arranging and adjusting their smallest building blocks, the meta-atoms. Notably, they enable the creation of metalenses, which are smaller and more lightweight than their diffractive counterparts [2]. This is especially useful in the context of improving commercially available heavy and bulky augmented and virtual reality (AR/VR) headsets [3]. However, the design of such metasurfaces is challenging due to the vast parameter space arising from millions of meta-atoms per surface. Moreover, there is a need to translate the microscopic near-field response to macroscopic far-field propagation.

In this presentation, we show how to overcome those challenges by combining different solvers. First, we build a database of individual meta-atom responses based on their design parameters and different excitations. To this end, we employ the local periodic approximation (LPA) and compute the individual response using rigorous coupled wave analysis (RCWA). We then assemble the meta-atoms to form a metasurface with a desired far-field outcome. For metasurfaces spanning up to a few millimeters, we can use a GPU-accelerated finite difference time-domain (FDTD) method in combination with a near-to-far-field transformation to obtain reference results. For even larger sizes, we use a hybrid approach based on raytracing, balancing performance and accuracy. As an illustrative example, we showcase our complete workflow with the design of a metalens-based eye-tracking system for AR/VR applications.

References

1. Pan, M., Y. Fu, M. Zheng et al., “Dielectric metalens for miniaturized imaging systems: progress and challenges”, Light Sci Appl 11, No. 195, 2022.
2. Engelberg, J. and U. Levy, “The advantages of metalenses over diffractive lenses”, Nat Commun 11, No. 1991, 2020.
3. Cheng, H. H. M. et al., "Optimization and tolerance for an exit pupil expander with 2D grating as out-coupler", Proc. SPIE 12449, Optical Architectures for Displays and Sensing in Augmented, Virtual, and Mixed Reality (AR, VR, MR) IV, Vol. 124490X, 2023.

AES 2024, ROME - ITALY, 25 –28 JUNE 2024

A few recent developments in nanophotonic scintillators

Charles Roques-Carmes[1]

[1] E.L. Ginzton Laboratory, 348 Via Pueblo, Stanford University, CA 94305, USA
[*]corresponding author: chrc@stanford.edu

Abstract: Scintillation is a form of spontaneous emission in materials excited by x-rays or other high energy particles. In this talk, I will review recent developments in the design of nanophotonic scintillators and materials to enhance and control scintillation.

Recent developments at the intersection of nanophotonics and scintillator materials development have led to the conceptualization and demonstration of so-called "nanophotonic scintillators [1-4]." Nanophotonic scintillators consist of scintillator materials integrated into nanophotonic structures, patterned at the scale of their optical emission wavelength. Nanophotonic scintillators are a promising platform to control and enhance spontaneous light emission in scintillators.

Mechanisms of light control and generation enhancement with nanophotonic scintillators include (1) angular light emission control and outcoupling enhancements with surface-patterned scintillators [1,2]; and (2) enhancement of the rate of spontaneous emission by volumetric patterning, leveraging the Purcell effect [3,4]. Each of these methods entail the development of dedicated nanofabrication methods to realize wavelength-scale patterns into scintillator materials.

In this talk, I will review some recent theoretical and experimental developments in nanophotonic scintillators. I will first present a general theoretical framework to model scintillation in arbitrary nanophotonic structures, which also lends itself to shape optimization of nanophotonic structures for enhanced scintillation. Then, I will review some recent experimental demonstrations in surface-patterned photonic crystal scintillators and multilayer scintillators. Based on this framework and recent theoretical proposals, I will also present other nanophotonic scintillator designs for enhanced spatial resolution and efficiency, as well as their applications to scintillation-based x-ray imaging.

References

1. C. Roques-Carmes, N. Rivera, A. Ghorashi, S. E. Kooi, Y. Yang, Z. Lin, J. Beroz, A. Massuda, J. Sloan, N. Romeo, Y. Yu, J. D. Joannopoulos, I. Kaminer, S. G. Johnson, M. Soljacic, "A framework for scintillation in nanophotonics," Science, 375, 837 (2022).
2. A. Knapitsch, P. Lecoq, "Review on photonic crystal coatings for scintillators," International Journal of Modern Physics A 29, 1430070 (2015).
3. Y. Kurman, A. Shultzman, O. Segal, A. Pick, I. Kaminer, Photonic-Crystal Scintillators: Molding the Flow of Light to Enhance X-Ray and γ-Ray Detection. Physical Review Letters 125, 040801 (2020).
4. Y. Kurman, N. Lahav, R. Schuetz, A. Shultzman, C. Roques-Carmes, A. Lifshits, S. Zaken, T. Lenkiewicz, R. Strassberg, O. Be'er, Y. Bekenstein, and Ido Kaminer, Purcell-enhanced X-ray scintillation, arXiv preprint, arXiv:2302.01300 (2023)

AES 2024, ROME - ITALY, 25 –28 JUNE 2024

Extreme Dielectric Confinement of Light
Inverse Design, Experimental Realization, Applications.
Going Beyond the Second Dimension

Rasmus E. Christiansen*[1,3], Jesper Mørk[2,3], Ole Sigmund[1,3]

[1]DTU Construct, Department of Civil and Mechanical Engineering, Technical University of Denmark, Denmark

[2]DTU Electro, Department of Electrical and Photonics Engineering, Technical University of Denmark, Denmark

[3]NanoPhoton—Center for Nanophotonics, Technical University of Denmark, Denmark

*corresponding author: raelch@dtu.dk

The talk discusses the use of topology optimization as a nanophotonic inverse design tool [1,2,3] to tailor dielectric structures for extreme spatial confinement of light; tailoring and realizing said structures for different material platforms and applications, discussing among others experimental evidence of sub-diffraction limited single-emitter mode-volumes [4,5]. The talk explores the potential for realizing stronger spatial confinement by allowing design-freedom beyond the second dimension with potentially remarkable findings.

It is well known that light-matter interaction strength scales with both the spatial confinement (mode volume) and temporal confinement (quality factor) of the photonic mode supported by the environment in which the interaction takes place [6]. Realizing a strong interaction through tight spatial confinement in (near)lossless materials, dielectrics, may pave the way for a wide range of applications exploiting single emitters at the nanoscale. Applications such as realizing nano-scale LEDs, few-photon detectors, single-emitter-based nano-scale lasers, achieving non-linear optics using single photons and interfacing photonics and electronics at the nanoscale.

References

1. Bendsøe M. P., Kikuchi N. "Generating optimal topologies in structural design using a homogenization method", Computer Methods in Applied Mechanical Engineering Vol 71, 197–224, 1988.
2. Christiansen R. E. and Sigmund O., "Inverse design in photonics by topology optimization: tutorial", Journal of the Optical Society of America B, Vol. 38 No 2, 496-509, 2021.
3. Jensen J. S. and Sigmund O. "Topology optimization for nano-photonics," Laser & Photonics Reviews, Vol 5, No 2, 308-321, 2011.
4. Albrechsen M., Lahijani B. V., Christiansen R. E, Nguyen V. T. H., Casses L. N., Hansen S. E., Stenger N., Sigmund O., Jansen H., Mørk J. and Stobbe S., "Nanometer-scale photon confinement in topology-optimized dielectric cavities," Nature Communications, Vol 13, 6281, 2022.
5. Xiong M., Christiansen R. E., Schröder F., Yu Y., Casses L. N., Semenova E., Yvind K., Stenger N., Sigmund O. and Mørk J., "Experimental realization of deep sub-wavelength confinement of light in a topology-optimized InP nanocavity," Optical Materials Express, Vol. 14 No. 2, 397-406, 2024.
6. Purcell E. M., "Spontaneous emission probabilities at radio frequencies," Phys. Rev. Vol. 69, 681, 1946.

AES 2024, ROME - ITALY, 25 –28 JUNE 2024

Fast and Efficient Design-by-Optimization of Complex Microwave Devices Using Novel FEM Techniques

Michał Baranowski [(1)], Adam Lamecki[(1,2)], Lukasz Balewski[(2)] and Michal Mrozowski[(1,2)],

(1)WETI, Gdansk University of Technology, Poland,

(2) EM Invent Ltd., Gdansk, Poland http://www.eminvent.com

*corresponding author: m.mrozowski@ieee.org

Abstract: This paper presents novel techniques for fast and efficient FEM-based optimization of microwave devices of arbitrary shape. These techniques include model order reduction, zero-pole optimization, and mesh deformation. They overcome the challenges of computational cost and geometry representation, and enable a complete design-by-optimization closure of a microwave product development.

Microwave systems are essential for various applications such as communication, radar, imaging, and sensing. The design of these systems involves modeling and optimizing devices with complex geometries that operate at high frequencies. However, this is a challenging task that requires accurate and efficient computational tools.

Traditional electronic design automation tools (EDA) are not suitable for this task, as they are based on circuit models that cannot capture the full-wave behavior of microwave devices. Therefore, designers need to use software simulators that solve Maxwell's equations numerically, which describe the electromagnetic fields and waves in the devices.

One of the most powerful and versatile techniques for solving Maxwell's equations is the finite element method (FEM). FEM is widely used in commercial software for simulating passive RF and microwave circuits and antennas. FEM can handle arbitrary geometries, material properties, and boundary conditions, and can provide accurate solutions in the frequency or time domain.

However, FEM has a major drawback: it is computationally expensive. A single analysis can take a long time, especially for large and complex devices. This makes it impractical to run complex optimization tasks based on full-wave solutions, which are often needed to improve the performance and reduce the size of the devices. As a result, the design-by-optimization approach, which can expedite product development, cannot be easily applied using FEM.

Another challenge for FEM-based design is the limitation of geometry representation. Most commercial software can only handle geometries that are described by Boolean operations on geometric primitives, such as cylinders, spheres, and polygons. This restricts the design space and prevents designers from performing free-form shape optimization, which can achieve superior performance and size reduction. This is especially relevant for the emerging fabrication technology of additive manufacturing (or 3D printing), which can produce very complex shapes that are not possible with conventional manufacturing methods.

Fortunately, recent advances in computational electromagnetics have shown that novel techniques can overcome these challenges and enable fast and efficient FEM-based optimization and a complete design-by-optimization closure of a microwave product development [1-3]. These techniques include model order reduction (MOR), zero-pole optimization, and mesh deformation. MOR is a technique that reduces the

complexity of the FEM model by extracting a low-order equivalent circuit that preserves the input-output behavior of the original model. This allows for fast frequency sweeps and sensitivity analysis, which are essential for optimization. Zero-pole optimization is a technique that optimizes the FEM model directly in the frequency domain by adjusting the locations of the zeros and poles of the transfer function. This allows for fast optimization convergence, even for poor initial designs. Mesh deformation is a technique that modifies the FEM mesh to accommodate the changes in the geometry during the optimization process. This avoids the need to remesh the device, which can be time-consuming and introduce errors.

To use these techniques, a FEM code has to be specifically designed for optimization tasks, especially those involving free-form deformation of solids and fast parametric sweeps. By using these new techniques, the design cycle of complex microwave devices of arbitrary shape can be significantly shortened, such that a complete cycle can be done within hours or even minutes, relying entirely on a numerical solution of Maxwell's equations using FEM.

During the conference, we will discuss the key elements needed for successful application of speedy design-by-optimization of microwave components of high complexity and complex shapes. We will present examples of designs involving tens of variables completed in less than an hour. We will also show examples of microwave filters for satellite communication with unprecedented performance achieved due to unconventional shapes. The versatility, efficiency, and accuracy of the developed techniques will be demonstrated by providing the detailed runtime data, animated figures showing optimization progress, and finally the results of measurements of selected microwave components designed using the state-of-the-art computational techniques described above.at the end.

Acknowledgment This work was supported by the Polish National Science Centre,
under Agreements Centre under grants no UMO-2019/33/B/ST7/00889 and 2020/39/O/ST7/02897

References

1. Balewski L, Fotyga G, Mrozowski M, Mul M, Sypek P, Szypulski D, Lamecki A. Step on it bringing fullwave finite-element microwave filter design up to speed. IEEE Microwave Magazine. 2020 Feb 5;21(3):34-49.
2. Lamecki A. A mesh deformation technique based on solid mechanics for parametric analysis of high-frequency devices with 3-D FEM. IEEE Transactions on Microwave Theory and Techniques. 2016 Sep 21;64(11):3400-8
3. Baranowski M, Balewski Ł, Lamecki A, Mrozowski M, Galdeano J. The design of cavity resonators and microwave filters applying shape deformation techniques. IEEE Transactions on Microwave Theory and Techniques. 2023 Jan 31.]

AES 2024, ROME - ITALY, 25 –28 JUNE 2024

Fluctuational electrodynamics effects in graphene-based nanosystems

Mauro Antezza[1,2]

[1]Laboratoire Charles Coulomb (L2C), UMR 5221 CNRS-University of Montpellier, F-34095 Montpellier, France
[2]Institut Universitaire de France, Ministère de l'Enseignement Supérieur et de la Recherche, 1 rue Descartes, F-75231, Paris, France
[*]corresponding author: mauro.antezza@umontpellier.fr

Abstract: We discuss graphene effects on two main fluctuational electrodynamics: Casimir effect and radiative heat transfer.

We will start discussing the different available models of graphene conductivity and their relations [1]. After, we will discuss the effect of graphene through its conductivity and shape on two paradigmatic fluctuation induced phenomena in periodic nanostructured graphene-based nano-systems: the Casimir forces [2] and the radiative heat transfer [3].

References

1. Pablo Rodriguez-Lopez, and Mauro Antezza "Graphene conductivity: Kubo model versus QFT-based model", arXiv:2403.02279 (2024)

2. Youssef Jeyar, Minggang Luo, Kevin Austry, Brahim Guizal, Yi Zheng, H. B. Chan, and Mauro Antezza, "Tunable nonadditivity in the Casimir-Lifshitz force between graphene gratings", Phys. Rev. A 108, 062811 (2023)

3. Minggang Luo, Youssef Jeyar, Brahim Guizal, Junming Zhao, and Mauro Antezza "Effect of the graphene grating coating on near-field radiative heat transfer" Appl. Phys. Lett. 123, 253902 (2023)

AES 2024, ROME - ITALY, 25 –28 JUNE 2024

Wave propagation in four-dimensional media: effective media in space and time and cascaded frequency conversion

V. Pacheco-Peña[1*], and N. Engheta[2]

[1]School of Mathematics, Statistics and Physics, Newcastle University, Newcastle Upon Tyne, NE1 7RU, United Kingdom
[2]Department of Electrical and Systems Engineering, University of Pennsylvania, PA 19104, USA.
[*]victor.pacheco-pena@newcastle.ac.uk engheta@seas.upenn.edu

Abstract: We will discuss how effective medium concepts can be translated from space to the time domain and further extended to space and time via space-time interfaces. Cascaded dielectric slab waveguides with induced time interfaces of their cladding will also be discussed along with their potential for cascaded frequency conversion.

In addition to controlling light-matter interactions in three-dimensional (3D) space[1–3], there is a growing interest in exploring wave propagation in space-time media (i.e., four-dimensions, 4D, as time is added into the mix)[4]. An example of time modulation is time interfaces where the electromagnetic properties of the medium where the wave propagates is rapidly changed in time from one value to a different one. Interestingly, time interfaces (time/temporal boundaries) were first studied in the last century, demonstrating frequency conversion and conservation of momentum[5,6]. Applications of time interfaces include, among others, inverse prism and temporal aiming[7,8], meta-atoms[9], temporal equivalent of the Brewster angle[10], stopping and amplifying waves[11,12], time gratings[13], filters and computing[14,15], generalization of the Snell's law in 4D[16], as well as the first experimental demonstrations from water waves to the optical regime[17–19].

In this presentation, we will discuss some of our recent efforts in the field by implementing rapid changes of the relative permittivity of the medium where a wave propagates to induce time interfaces. In a recent work, we have shown how concepts known in the frequency domain such as effective medium theory can find the equivalent in the time domain when the permittivity of the medium is rapidly changed in time from ε_{r1} to ε_{r2} at a time $t = t_0$, and then periodically modulated between ε_{r1} and ε_{r2} for $t > t_0$. Such temporally periodic modulation of $\varepsilon(t)$ can then be modelled as an equivalent temporal medium with a permittivity following a single step function in time, where ε is rapidly changed from ε_{r1} to ε_{reff} (effective value)[20]. Here, we further exploit such effective medium concept in the time domain to show how it can be extended to 4D where certain subwavelength regions in space are periodically modulated in time while other subwavelength regions are kept constant. In this way, a space-time effective medium theory can be obtained[21]. Additionally, we will discuss wave propagation in all dielectric slab waveguides where the cladding is changed in time from ε_{r1} to ε_{r2} while the permittivity of the core is kept constant. Cascaded space-time dielectric waveguides will also be presented using both straight waveguides and ring resonators[22]. Their potential for cascaded frequency conversion will be discussed in detail during the conference.

Acknowledgements: V.P.-P. would like to thank the support of the Leverhulme Trust under the Leverhulme Trust Research Project Grant scheme (RPG-2020-316 and RPG-2023-024). N. E. acknowledges partial support from the Simons Foundation/Collaboration on Symmetry-Driven Extreme Wave Phenomena (grant 733684). V. P.-P. has applied a CC BY public copyright license to any Author Accepted Manuscript (AAM) version arising from this submission.

References

1. Riley, J. A., Healy, N. & Pacheco-Peña, V. Plasmonic meniscus lenses. *Sci. Rep.* **12**, 894 (2022).
2. Zentgraf, T., Liu, Y., Mikkelsen, M. H., Valentine, J. & Zhang, X. Plasmonic Luneburg and Eaton lenses. *Nat. Nanotechnol.* **6**, 151–5 (2011).
3. Legaria, S., Teniente, J., Kuznetsov, S., Pacheco-Peña, V. & Beruete, M. Highly Efficient Focusing of Terahertz Waves with an Ultrathin Superoscillatory Metalens: Experimental Demonstration. *Adv. Photonics Res.* **2**, 2000165 (2021).
4. Pacheco-Peña, V., M. Solís, D. & Engheta, N. Time-varying electromagnetic media: opinion. *Opt. Mater. Express* **12**, 3829 (2022).
5. Morgenthaler, F. Velocity Modulation of Electromagnetic Waves. *IEEE Trans. Microw. Theory Tech.* **6**, 167–172 (1958).
6. Fante, R. Transmission of electromagnetic waves into time-varying media. *IEEE Trans. Antennas Propag.* **19**, 417–424 (1971).
7. Akbarzadeh, A., Chamanara, N. & Caloz, C. Inverse prism based on temporal discontinuity and spatial dispersion. *Opt. Lett.* **43**, 3297 (2018).
8. Pacheco-Peña, V. & Engheta, N. Temporal aiming. *Light Sci. Appl.* **9**, 1–12 (2020).
9. Pacheco-Peña, V. & Engheta, N. Spatiotemporal Isotropic-to-Anisotropic Meta-Atoms. *New J. Phys.* **23**, 095006 (2021).
10. Pacheco-Peña, V. & Engheta, N. Temporal equivalent of the Brewster angle. *Phys. Rev. B* **104**, 214308 (2021).
11. Pacheco-Peña, V., Kiasat, Y., Solís, D. M., Edwards, B. & Engheta, N. Holding and amplifying electromagnetic waves with temporal non-Foster metastructures. *arxiv 2304.03861* (2023). doi:10.48550/arXiv.2304.03861
12. Wang, X., Mirmoosa, M. S. & Tretyakov, S. A. Controlling surface waves with temporal discontinuities of metasurfaces. *Nanophotonics* **12**, 2813–2822 (2023).
13. Galiffi, E. *et al.* Wood Anomalies and Surface-Wave Excitation with a Time Grating. *Phys. Rev. Lett.* **125**, 127403 (2020).
14. Castaldi, G., Pacheco-Peña, V., Moccia, M., Engheta, N. & Galdi, V. Exploiting space-time duality in the synthesis of impedance transformers via temporal metamaterials. *Nanophotonics* **10**, 3687–3699 (2021).
15. Castaldi, G., Rizza, C., Engheta, N. & Galdi, V. Multiple actions of time-resolved short-pulsed metamaterials. *Appl. Phys. Lett.* **122**, (2023).
16. Pacheco-Peña, V., Fink, M. & Engheta, N. Temporal chirp, temporal lensing and temporal routing via space-time interfaces. *ArXiv 2311:10855* 1–11 (2023).
17. Bacot, V., Labousse, M., Eddi, A., Fink, M. & Fort, E. Time reversal and holography with spacetime transformations. *Nat. Phys.* **12**, 972–977 (2016).
18. Moussa, H. *et al.* Observation of temporal reflection and broadband frequency translation at photonic time interfaces. *Nat. Phys.* **19**, 863–868 (2023).
19. Lustig, E. *et al.* Time-refraction optics with single cycle modulation. *Nanophotonics* **12**, 2221–2230 (2023).
20. Pacheco-Peña, V. & Engheta, N. Effective medium concept in temporal metamaterials. *Nanophotonics* **9**, 379–391 (2020).
21. Pacheco-Peña, V. & Engheta, N. Merging Effective Medium Concepts of Spatial and Temporal Media: Opening new avenues for manipulating wave-matter interaction in 4D. *IEEE Antennas Propag. Mag.* **65**, 39–49 (2023).
22. Pacheco-Peña, V. & Engheta, N. Spatiotemporal cascading of dielectric waveguides. *arXiv:2312.12233* (2023).

AES 2024, ROME - ITALY, 25 –28 JUNE 2024

Plasmonic Mid Infrared Photothermal Microscopy

Sahil Sharma[1,2], Joby Joseph[1], Qammer H Abbasi[2], Hasan T Abbas[2*],

[1]Department of Physics, Indian Institute of Technology Delhi, Hauz Khas, New Delhi, 110 016, India[2]

James Watt School of Engineering University of Glasgow, Glasgow G12 8QQ
[*]Corresponding author: Hasan.Abbas@glasgow.ac.uk

Abstract: Here we introduce a novel mid-infrared photothermal microscopy technique employing surface plasmon resonance to boost sensitivity. Pulsed infrared lasers induce molecular vibrational absorption in cells, causing localized temperature shifts and refractive index alterations. This method allows for high-resolution infrared spectroscopy within living cells, revolutionizing cellular imaging, and advancing biomedical research with unprecedented precision and detail.

Mid-infrared photothermal microscopy [1] represents a significant leap in imaging technology, seamlessly merging the structural insights of mid-infrared spectroscopy with the exceptional spatial resolution capabilities of fluorescence microscopy. By enabling label-free, high-resolution imaging of cellular dynamics and chemical composition, this technique plays a vital role in diverse fields such as biomedical research, drug development, materials science, and environmental monitoring. Its ability to unveil both sample constituents and their precise spatial distribution within biological samples unlocks new dimensions of analysis and discovery, propelling scientific advancements and innovation forward.

In this technique, a sample that is composed of certain molecular functional groups such as alkane, alkene, carbonyl, etc. is illuminated with a specific mid-infrared wavelength (depending on bond strength, bond length, and the masses of the atoms involved) inducing absorption and localized temperature changes (photothermal effect) [2] that alter the refractive index. Subsequently, a probe laser with a wavelength in the visible region is used to detect and analyze these refractive index changes. A visible light laser provides better resolution due to its shorter wavelength, allowing for finer detail and increased sensitivity in detecting small changes in the refractive index or other optical properties of the sample, compared to mid-infrared light sources. However, the current technique suffers from weak dependence of the scattering on the temperature. It means that it is not sensitive enough to the change in temperature due to absorption. This leads to poor contrast images.

Here, we introduce a mid-infrared photothermal microscopy technique enhanced by surface plasmon resonance (SPR), significantly improving sensitivity. SPR [3] arises from the collective oscillation of free electrons on a metal surface when illuminated by polarized monochromatic light, such as laser light, under specific conditions.

When the refractive index of the dielectric medium adjacent to the metal film changes in an SPR system, it affects the resonance condition, leading to observable changes in SPR signals. These observable changes are extremely sensitive that is they can detect 0.01% change in the refractive index.

The refractive index change is related to temperature change which can be obtained from the SPR signal through [3],

$$\Delta T = \frac{\partial T}{\partial \theta}\,\Delta\theta = \frac{1}{\frac{\partial n}{\partial T}} \cdot \frac{1}{\frac{\partial \theta}{\partial n}} \cdot \Delta\theta \qquad (1)$$

Here θ is the SPR resonant angle and $\partial n/\partial T$ is the temperature coefficient of refractive index, and $\partial\theta/\partial n$ is the SPR sensitivity. While (1) allows us to quantify the relationship between temperature change and the SPR signal, it does not inherently provide information about the spatial profile of the heating. However, by measuring the SPR signal at different locations across the sample, it is possible to infer the spatial distribution of temperature changes. Also, because the surface plasmon waves are evanescent in nature, chemical information close to the surface can be recorded which gives more specificity to this technique and axial resolution which we cannot get in conventional mid-infrared photothermal microscopy.

Figure 1 shows a simulation of SPR at gold-water interface with fixed resonance angle. If the refractive index of the dielectric (water) is changed, significant decrease in SPR signal is observed. Hence proving the sensitivity of the SPR signal.

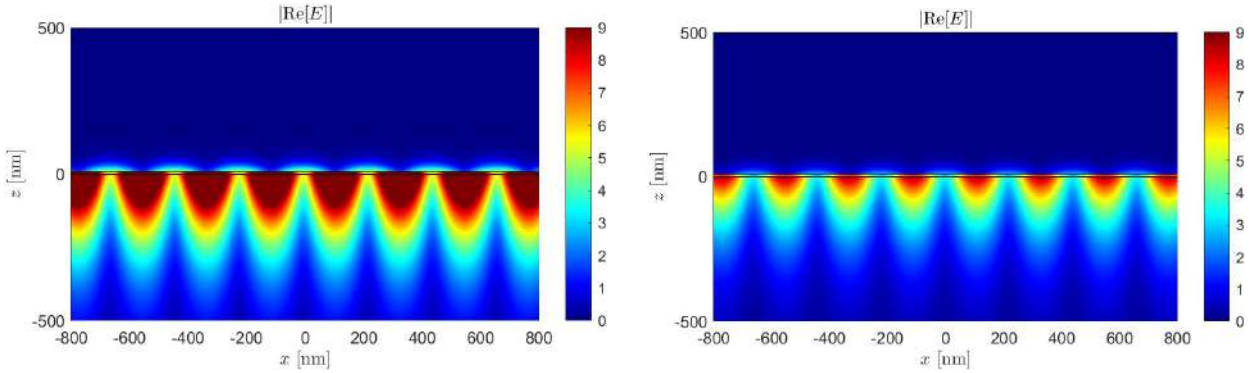

(a) (b)

Figure 1 : (a) represents the surface plasmon resonance signal at gold water interference with refractive index of 1.33 (b) represents surface plasmon resonance by changing the refractive index from 1.33 to 1.34 but keeping the resonance angle same as (a).

In conclusion, our technique combining mid-infrared photothermal microscopy with surface plasmon resonance offers exceptional sensitivity and resolution for cellular imaging and temperature profiling. Leveraging SPR signals, it provides insights into spatial temperature changes, promising significant advancements in biomedical and scientific research.

References:

1. Yeran Bai, "Ultrafast chemical imaging by widefield photothermal sensing of infrared absorption." Sci. Adv., Vol. 34, No. 10, pp. 1064–1076, 1986.

2. S Adhikari, "Photothermal Microscopy: Imaging the Optical Absorption of Single Nanoparticles and Single Molecules." ACS Nano, Vol. 34, No. 10, pp. 1064–1076, 1986.

3. Chen, Z. Shan, X., Guan, Y., Wang, S., Zhu, J.-J., & Tao, N. "Imaging Local Heating and Thermal Diffusion of Nanomaterials with Plasmonic Thermal Microscopy." ACS Nano, Vol. 34, No. 10, pp. 1064–1076, 1986.

AES 2024, ROME - ITALY, 25 –28 JUNE 2024

Existence of accidental bound states in the continuum in periodically perturbed slabs

Amgad Abdrabou[1], **Wangtao Lu**[2], **and Ya Yan Lu**[3,*]

[1]Elmore Family School of Electrical and Computer Engineering, Purdue University, West Lafayette, USA
[2]School of Mathematical Sciences, Zhejiang University, Hangzhou, China
[3]Department of Mathematics, City University of Hong Kong, Hong Kong, China
*corresponding author: mayylu@cityu.edu.hk

Abstract: Bound states in the continuum (BICs) have many applications in photonics, but their existence is only proved for a few simple cases. In this paper, we identify a precise mathematical condition under which certain accidental BICs exist in periodically perturbed slabs and provide a rigorous proof for their existence.

A bound state in the continuum (BIC) is an eigenmode of a wave system that decays in open directions, but for the same frequency and wavevector, there are propagating waves to or from infinity in the same directions [1]. In recent years, BICs have found many applications in photonics. The existence of BICs is attributed to a number of physical mechanisms [1]. The BICs having a symmetry mismatch with the radiating waves are the so-called symmetry-protected BICs, and their existence can be proved rigorously. BICs can also appear due to destructive interference, as Friedrich and Wintgen showed for a system of three 1D Schrödinger equations [2]. In photonic systems, some BICs seem to appear due to the destructive interference of two resonant modes, and they are referred to as Friedrich-Wintgen BICs. In other cases, BICs are found by tuning one or more parameters such that all radiation channels are accidentally closed. However, there is no general theory on the existence of accidental BICs in photonic systems.

In this paper, we present a rigorous existence theory for a class of accidental BICs in a fairly general periodically perturbed slab. The structure is given by a dielectric function $\epsilon(y,z) = \epsilon_*(z) + \delta F(y,z)$, where ϵ_* describes a slab of thickness $2D$ surrounded by air [$\epsilon_*(z) > 1$ for $|z| < D$ and $\epsilon_*(z) = 1$ for $|z| > D$], F is the perturbation profile (real, periodic in y with minimum period L, even in both y and z, and $F = 0$ if $|z| > D$), and δ (real, near 0) is the amplitude of the perturbation. For the E polarization, a BIC of frequency ω in such a periodic slab can be written as $u_{\text{bic}} = \varphi(y,z)e^{i\beta z}$, where u_{bic} is the x component of the electric field, φ is periodic in y with period L and tends to 0 as $z \to \pm\infty$, $\beta \in [-\pi/L, \pi/L]$ is the Bloch wavenumber, ω satisfies $\omega/c > |\beta|$, and c is the speed of light in vacuum. For the same polarization, the uniform slab has guided modes (even or odd in z) below the lightline. A guided mode of the slab is given by $u_{\text{slab}} = \phi(z)e^{i\beta y}$, where ϕ is the mode profile (a real function of z) and β is the propagation constant. The mode exists only below the lightline for frequency ω_0 given by a dispersion relation $\omega_0 = \hat{\omega}_{\text{slab}}(\beta) < c|\beta|$. Since we are considering periodic perturbations of the slab, the slab mode is written as $u_{\text{slab}} = [\phi(z)e^{i2p\pi y/L}]e^{i\beta_0 y}$, where $|\beta_0| \le \pi/L$ and $\beta = \beta_0 + 2p\pi/L$ for an integer p. The dispersion relation can be written as $\omega_0 = \omega_{\text{slab}}(\beta_0; p)$ for $|\beta_0| \le \pi/L$. If $\omega_0/c > |\beta_0|$, we can formulate a 1D scattering problem for the slab by specifying plane incident waves with wavevector $(\beta_0, \pm\gamma_0)$ from $z = \mp\infty$, where $\gamma_0 = \sqrt{(\omega_0/c)^2 - \beta_0^2}$. The solution of this scattering problem can be written as $u_{\text{sca}} = \psi(z)e^{i\beta y}$. We can choose the amplitudes of the incident waves, such that ψ is real and has the same even/odd parity in z as ϕ.

The accidental BICs are associated with one slab mode and depends on the perturbation profile F. Our result can be stated as follows: *If a slab mode* $\{\phi, \beta_0, p, \omega_0\}$*, the scattering solution* $\{\psi, \beta_0, \omega_0\}$*, and profile* F *satisfy*

$$\int_\Omega F(y,z)\phi(z)\psi(z)\cos\left(\frac{2p\pi y}{L}\right) d\mathbf{r} = 0 \tag{1}$$

where $\Omega = \{(y,z) : |y| < L/2, -\infty < z < \infty\}$*, and* $|\beta_0| < \omega_0/c < 2\pi/L - |\beta_0|$*, then for any sufficiently small* δ*, there is a BIC* $\{\varphi, \omega, \beta\}$ *in the perturbed slab with frequency* ω *near* ω_0 *and Bloch wavenumber* β *near* β_0*.*

Equation (1) is a real scalar equation, and it can be used to find one real parameter. For a given F, we can use Eq. (1) to solve β_0. Notice that p is usually fixed, but ϕ, ψ and ω_0 all depend on β_0. Alternatively, we can fix β_0, p, ϕ and ψ, introduce a parameter a in F, and use Eq. (1) to solve a. In other words, we can design a perturbation profile F, so that the BIC is near (β_0, ω_0) in the β-ω plane. We emphasize that the existence of a BIC is guaranteed for all real δ near 0, and the BIC depends on δ continuously. As $\delta \to 0$, the BIC tends to the slab mode u_{slab}. This fact is related to the symmetry of the perturbation profile and the robustness of BICs in 2D periodic structures with reflection symmetries in both y and z [3]. In fact, the robustness theory implies that the BIC will continue its existence when $|\delta|$ is increased until (β, ω) moves out the domain of one radiation channel. For a nonzero δ near 0, the perturbed slab supports a band of resonant modes given by a dispersion relation $\omega = \omega_{\text{res}}(\beta)$, where β is real and ω is complex [4]. The real part of $\omega_{\text{res}}(\beta)$ is close to $\omega_{\text{slab}}(\beta; p)$. Our theory implies that there is always a β near β_0, such that the imaginary part of $\omega_{\text{res}}(\beta)$ is zero.

As an example, we consider a slab with $\epsilon_*(z) = 11.56$ for $|z| < D = L/2$ and a perturbation corresponding to a periodic array of circular cylinders with radius a and a slightly different dielectric constant. In the yz plane, the cross sections of the cylinders are circular disks located on the y axis. We have $F(y,z) = -1$ if (y,z) is inside a circular disk and $F = 0$ otherwise. For fixed $\beta_0 = 0.15(2\pi)/L$, there is a slab mode with $p = -1$ and $\omega_0 \approx 0.35723(2\pi c/L)$. Solving Eq. (1), we get $a \approx 0.4102L$. Our theory ensures the existence of a BIC in the perturbed slab near (β_0, ω_0) for any δ near 0. For $\delta = 0.1$, the dielectric constant of the circular cylinders is 11.46, and we found a BIC with $\beta \approx 0.15133(2\pi/L)$ and $\omega \approx 0.3586(2\pi c/L)$.

References

1. C. W. Hsu, B. Zhen, A. D. Stone, J. D. Joannopoulos, and M. Soljačić, Bound states in the continuum, *Nat. Rev. Mater.* Vol. 1, 16048, 2016.
2. H. Friedrich and D. Wintgen, Interfering resonances and bound states in the continuum, *Phys. Rev. A*, Vol. 32, 3231–3242, 1985.
3. L. Yuan and Y. Y. Lu, Bound states in the continuum on periodic structures: perturbation theory and robustness, *Optics Letters*, Vol. 42, 4490–4493, 2017.
4. A. Abdrabou and Y. Y. Lu, Indirect link between resonant and guided modes on uniform and periodic slabs, *Phys. Rev. A*, Vol. 99, 063818, 2019.

AES 2024, ROME - ITALY, 25 –28 JUNE 2024

The dawn of global optimization in photonics and electromagnetics ?

P. Bennet[1], A. Khaireh-Walieh[2], D. Langevin[1], O. Teytaud[3], P. Wiecha[2] and A. Moreau[1*]

[1]Université Clermont Auvergne, Clermont Auvergne INP, CNRS, Institut Pascal, F-63000 Clermont-Ferrand, France
[2]LAAS, Université de Toulouse, CNRS, Toulouse, France
[3] Meta AI Research Paris, Paris, France
[*]corresponding author: antoine.moreau@uca.fr

Abstract: Optimization is notoriously difficult for wave problems, because of the large number of resonances in even the simplest structures. However, thanks to Moore's law and progress in rigorous benchmarking of global algorithms, it becomes possible to rely on such an approach to provide innovative designs.

Global optimization relies on meta-heuristics, versatile algorithms often inspired by nature like genetic algorithms, to provide solutions to many problems, from parameter retrieval (finding the parameters for a model that best reproduce the experimental data) and optimization (assessing the potential of a structure for a given purpose) to more complex inverse design problems. The latter problems are usually characterized by a large number of parameters that can be modified (geometrical or material parameters), the idea being that putting as few constraints as possible on an optimization may yield interesting novel results.

Meta-heuristics, when electromagnetic waves are considered, can prove particularly costly as they rely on full simulations to estimate how efficient a solution is. In addition, there has been a massive amount of new algorithms in the last 20 years, making it difficult to identify which algorithms are the most relevant[1]. Old school genetic algorithms are for instance completely inefficient in comparison with most modern algorithms and their use should probably be banned – yet they continue to be presented as usable in photonics. Finally, the community is deterred from using meta-heuristics because they are non deterministic, and prove tricky to tune effectively. On top of that, recent advances in inverse design based on the adjoint method (and thus local methods close to steepest descent algorithms) also produced convincing results[2] and moved many researchers away from a rather costly and difficult approach[3].

For photonics problem, steepest descent and the like are also struggling to reliably provide efficient solutions to inverse design problems, given the very large number of local minima characterizing wave problems[4]. On the contrary, some global optimization algorithms are able to provide efficient structures which can even be understood from a physical point of view[5,6,7]. A rigorous statistical analysis of the way these algorithms function allows to assess the quality of the solutions that are provided. If such a methodology is applied to an optimization problem, for a relevant complexity domain, global optimization increasingly seems to be a suitable choice. While the computational cost may remain high, meta-heuristics are often easy to parallelize so that they can run in a reasonable amount of time. Algorithms like Differential Evolution are particularly easy to code and deploy. We expect such basic optimization tools to become widely used in a near future – whether for increasing

the performances of already existing designs, retrieve more reliably parameters or even generate original structures using an inverse design approach.

References

1. Sörensen, K. (2015). Metaheuristics—the metaphor exposed. *International Transactions in Operational Research*, *22*(1), 3-18.
2. Su, L., Vercruysse, D., Skarda, J., Sapra, N. V., Petykiewicz, J. A., & Vučković, J. (2020). Nanophotonic inverse design with SPINS: Software architecture and practical considerations. *Applied Physics Reviews*, *7*(1).
3. Sigmund, O. (2011). On the usefulness of non-gradient approaches in topology optimization. *Structural and Multidisciplinary Optimization*, *43*, 589-596.
4. Bennet, P., Langevin, D., Essoual, C., Khaireh-Walieh, A., Teytaud, O., Wiecha, P., & Moreau, A. (2024). Illustrated tutorial on global optimization in nanophotonics. *JOSA B*, *41*(2), A126-A145.
5. Barry, M. A., Berthier, V., Wilts, B. D., Cambourieux, M. C., Bennet, P., Pollès, R., ... & Moreau, A. (2020). Evolutionary algorithms converge towards evolved biological photonic structures. *Scientific reports*, *10*(1), 12024.
6. Bennet, P., Juillet, P., Ibrahim, S., Berthier, V., Barry, M. A., Réveret, F., ... & Moreau, A. (2021). Analysis and fabrication of antireflective coating for photovoltaics based on a photonic-crystal concept and generated by evolutionary optimization. *Physical Review B*, *103*(12), 125135.
7. Teytaud, O., Bennet, P., & Moreau, A. (2022). Discrete global optimization algorithms for the inverse design of silicon photonics devices. *Photonics and Nanostructures-Fundamentals and Applications*, *52*, 101072.

AES 2024, ROME - ITALY, 25 –28 JUNE 2024

Probing Terahertz pulses with nonclassical radiation

D. Adamou[1], L. Hirsh[1], T. Shields[1], S. Yoon[1], A. C. Dada[2], J. M. R. Weaver[1], D. Faccio[2], L. Caspani[3], M. Peccianti[4], and M. Clerici[1,5,*]

[1]James Watt School of Engineering, University of Glasgow, Glasgow G12 8QQ, UK
[2]School of Physics and Astronomy, University of Glasgow, Glasgow G12 8QQ, UK
[3]Institute of Photonics, Department of Physics, University of Strathclyde, Glasgow G1 1RD, UK
[4]Emergent Photonics Research Centre, Department of Physics, Loughborough University, Loughborough LE11 3TU, UK
[5]Dipartimento di Scienza e Alta Tecnologia, Università degli Studi dell'Insubria, Via Valleggio 11, 22100, Como, Italy
[*]corresponding author: matteo.clerici@uninsubria.it

Abstract: We report on our initial efforts to increase the sensitivity of Terahertz time-resolved sensing using quantum metrology, specifically through squeezed states, exploring discrete and continuous variable methods.

Terahertz time-domains spectroscopy (TDS) relies on the time-resolved measurement of the electric field of a carrier-envelope phase stable far-infrared radiation performed employing short (<1 ps) optical probe pulses. The electric field is transformed into polarization rotation information thanks to the electro-optical effect in a suitably chosen nonlinear crystal.

This measurement approach can achieve transform-limited sensitivities, which are limited by the probe shot noise. Quantum mechanics can, therefore, be harnessed to increase the sensitivity [1], rendering THz-TDS an interesting system for investigating the potential application of well-known quantum metrology approaches.

For instance, leveraging NOON states for optimal phase estimation could enhance THz spectroscopy. In our experiment, we employed weak squeezed vacuum states as probes in THz electro-optic sampling, with single-photon detectors capturing the signals. The ability to observe a THz signal in this condition is a first step towards employing NOON states in THz-TDS and allowed us to define the operational regimes where such a discrete value approach might be relevant [2].

More recently, we have tested continuous variable approaches that are more likely to deliver actual benefits for the THz-TDS in standard operating conditions. We will report on the development of a twin-beam source able to produce ultrashort pulses required for THz-TDS with a ~3dB noise reduction below the standard quantum limit at >500 nW average power pulses. We will discuss our results and design choices for the employed solutions and present our view on this interesting endeavour.

The authors acknowledge support from UKRI (Fellowship "In-Tempo" EP/S001573/1), Innovate UK 10001572 (TS/W002558/1, HiQuED), Innovate UK 10075401 (TS/Y005910/1, BQS), and from the Defence Science and Technology Laboratory (DSTL, DSTLX-1000144632).

References

1. Virally. S. et al., "Enhanced electro-optic sampling with quantum probes", *Phys. Rev. Lett.* **127,** 270504 (2021).
2. Shields. T. et al., "Electro-Optical Sampling of Single-Cycle THz Fields with Single-Photon Detectors", *Sensors* **22,** 9432 (2022).

Hybrid Simulation Techniques Combining Finite Difference and Fourier expansions for Nanophotonic Devices

M. Besbes, C. Sauvan and H. Benisty

Université Paris-Saclay, Institut d'Optique Graduate School, CNRS, Laboratoire Charles Fabry
2 Av. Augustin Fresnel, 91127 Palaiseau Cedex, France

Abstract: The finite difference method is combined with classical horizontal Fourier expansions to provide a quick simulation of nanophotonic devices under illumination, avoiding eigenmode calculations. Thanks to a careful implementation and proper vertical slicing choices, a large reduction of computational time is obtained, compatible with subsequent tools such as reduced models.

The Fourier Modal Method (FMM), also known as Rigorous Coupled-Wave Analysis (RCWA), is a powerful rigorous computational technique that is nowadays extensively employed in the simulation and analysis of nanophotonic devices [1-4]. A non-exhaustive list includes photonic-crystal slabs, metamaterials, plasmonic or dielectric metasurfaces, nanostructured photovoltaic cells…. It belongs to the class of differential methods, which requires the resolution of coupled differential equations. In the case of light propagation along the z direction, the formulation of Maxwell's equations in Fourier space along x and y leads to

$$\frac{dE}{dz} = A(z)H \quad \text{and} \quad \frac{dH}{dz} = B(z)E, \tag{1}$$

where $A(z)$ and $B(z)$ are matrices containing the Fourier coefficients of the permittivity, the permeability, and their inverse and E (resp. H) is a vector formed with the Fourier coefficients of the transverse components of the electric (resp. magnetic) field. The differential equations in Eq. (1) can be solved numerically (e.g., with Runge-Kutta techniques, shooting method); the method is then known as the differential method [5]. When the permittivity is invariant along z, Eq. (1) can be solved rigorously by computing the eigenvalues and eigenvectors of the matrix product AxB . This is the basic principle of the FMM [1]. The latter is also often employed in the general case of a z-dependent permittivity distribution by using a staircase approximation that slices the structure in several z-invariant layers. The electromagnetic fields in each layer can then be connected with each other with the S-matrix approach [6].

While FMM offers numerous advantages for simulating nanophotonic devices, it also comes with some limitations, particularly for large-scale structures or pseudo-randomly geometries. As the period of the structure increases in the (x,y) plane, the computational demands of FMM simulations escalate accordingly. Indeed, due to the resolution of an eigenvalue problem, the necessity to solve for a greater number of Fourier terms results in excessively long simulation times, rendering it impractical for real-time or high-throughput analysis.

To address these challenges and reduce CPU time, one viable solution is to turn back to the differential method. We propose a numerically efficient implementation of the differential method based on a centered finite difference (FD) scheme to solve the differential equations (1) without performing eigenmode calculations. We show that, for nanophotonic structures with subwavelength thicknesses, the FD discretization points along z can be limited to a small number without loss of accuracy. Therefore, even in the case of a z-invariant structure, the gain in CPU time compared to FMM is larger than one order of magnitude for large numbers of Fourier terms. The proposed method also demonstrates high efficiency in computing the spatial distribution of the electromagnetic field along the z axis, significantly reducing CPU time requirements.

To illustrate our approach, we consider a 2D plasmonic metasurface for biosensing applications (Figure 1.). We conduct a comparative analysis on CPU time calculation and accuracy between the FMM and our Fourier-FD method. Two parameters are discussed: the number of Fourier terms m and the number of subdivisions N for the FD scheme.

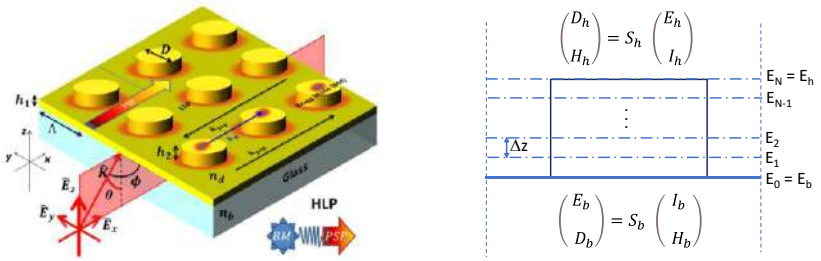

Figure 1. Overview of the studied plasmonic metasurface (gold on a glass substrate) (left) and its discretization along z for Finite Difference computation (right).

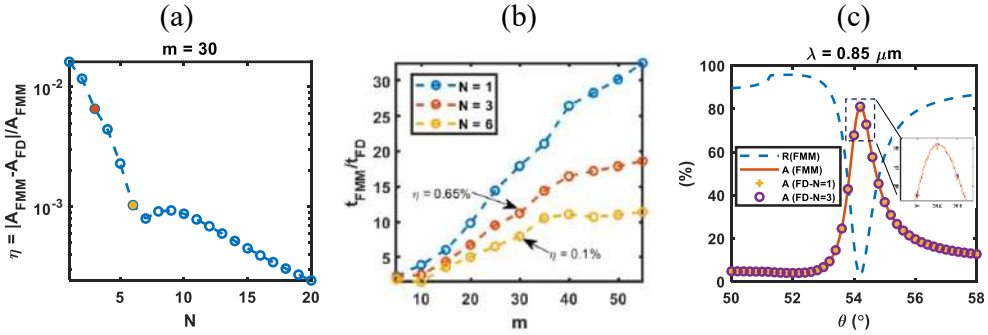

Figure 2. (a) Relative error η on the absorption in the metasurface in Fig. 1 for $m = 30$ and $\theta = 54°$. (b) Gain in CPU time for $N = 1$, 3 and 6 subdivisions. (c) Comparison between absorption spectrum calculated with FMM and Fourier-FD method for $N = 1$ and 3.

The gain in CPU time is significant for the large numbers of Fourier terms although it appears to stabilize at the highest m (at $m \sim 35$ for $N = 6$). Obviously, the precision with the FD method is better when the number of subdivisions is larger. The relative error (Figure 2a) falls below 10^{-2} as soon as $N > 2$. The FD step Δz for this regime is then close to $\frac{\lambda}{15|n|}$ or smaller. The presented approach is particularly suitable for modeling thin gratings, conical nanoparticles, and large-scale metamaterials. Reduced model approaches as well as domain decomposition techniques are also easily adapted with the Fourier-FD method.

References

[1] See for instance L. Li, "New formulation of the Fourier modal method for crossed surface-relief gratings", J. Opt. Soc. Am. A 14, 2758 (1997) and references therein.
[2] V. Liu and S. Fan, ""S^4: A free electromagnetic solver for layered periodic structures", Comp. Phys. Com. 183, 2233 (2012).
[3] J.-P. Hugonin and P. Lalanne, "Reticolo software for grating analysis", arXiv:2101.00901.
[4] https://github.com/SimPhotonicsFMM/Sources
[5] M. Nevière, E. Popov, "Light Propagation in Periodic Media, Differential Theory and Design", Marcel Deker Inc, 2003
[6] N. Chateau and J.-P. Hugonin, "Algorithm for the rigorous coupled-wave analysis of grating diffraction", J. Opt. Soc. Am. A 11, 1321 (1994)

AES 2024, ROME - ITALY, 25 –28 JUNE 2024

Advanced optical metasurface design for imaging and sensing

Tian Gu

[1]Materials Research Laboratory, Massachusetts Institute of Technology, Cambridge, Massachusetts, USA

[*]corresponding author: gutian@mit.edu

Abstract: Flat optical systems based on metasurfaces herald a new era of dynamic control over light propagation, processing, and interaction with matter, offering improved performance and introducing novel capabilities. However, these advancements come with their own set of challenges, markedly distinct from those faced by traditional optical systems. In particular, the complexity of meta-optics is escalating rapidly, driven by the large number of nano-scale optical structures operating in macro-scale system/environments and the pursuit of multiple functional goals. This complexity thereby necessitates a holistic approach to the design and engineering framework of materials, devices, and systems that spans multiple scales and physics domains, alongside the development of computationally efficient design strategies. In my talk, I will explore both the opportunities and obstacles associated with employing optical metasurfaces for a wide range of applications. Capitalizing on advanced design techniques, device architectures and materials, we demonstrate metasurface-based optical components and systems with high performance, ultra-compactness and new functions across various uses.

AES 2024, ROME - ITALY, 25 –28 JUNE 2024

Programmable Photonic Processor for Chaotic Signal Recovery in the Presence of Atmospheric Turbulence

H. Huang[1], S. Zaminga[1], A. Martinez[2], F. Morichetti[2], A. Meloni[2], and F. Grillot[1,3*]
[1] LTCI Télécom Paris, Institut Polytechnique de Paris, Palaiseau, 91120, France
[2] Dipartimento di Elettronica, Informazione e Bioingegneria, Politecnico di Milano, Milano, 20133, Italy
[3] Center for High Technology Materials, University of New-Mexico, Albuquerque, NM 87106, USA
[*]Corresponding author: grillot@telecom-paris.fr

Abstract: We demonstrate the decisive functionality of a silicon photonic mesh as a programmable photonic processor to implement a signal compensation algorithm to recover optical chaos signals after propagation through atmospheric turbulence. This breakthrough is of great potential in optical signal processing applications, like free-space optical chaos communication in impaired environments.

Transmission through chaos represents an innovative approach in the field of optical communications where chaotic signals are utilized to carry information [1]. Unlike traditional methods of signal modulation, chaos transmission leverages the unpredictable and nonlinear properties of chaotic dynamical systems. In this context, a chaotic signal is generated by a transmitter and used to modulate the data to be transmitted. The receiver, synchronized with the transmitter, can then retrieve the original data. This approach has recently been employed in coherent optical systems and free-space mid-infrared communications [2][3]. However, the practical implementation of such a system can be complex as the security key of the transmission channel relies on maintaining chaos synchronization between the transmitter (TX) and the receiver (RX). In this work, we examine for the first time the utility of a programmable photonic processor for correcting chaotic signals disturbed by atmospheric turbulence. The processor consists of a mesh of electrically tunable Mach-Zehnder interferometers integrated on silicon wafer [4]. The chaotic carrier is generated by a distributed feedback laser diode operating at 1.55 microns. By using a spatial light modulator, we emulate the impact of atmospheric turbulence on the wavefront. Our study reveals numerous alterations of the chaotic carrier depending on the transmission distance and the amplitude of turbulence. When the programmable photonic processor is activated, efficient recovery of the chaotic carrier is observed. The signal compensation algorithm associated with the photonic processor thus allows the restoration of optical signal power even in the presence of strong turbulence, which constitutes a very promising advancement for the development of secure optical communications in free space.

The generation of the chaotic carrier is achieved by applying external optical feedback to the laser. The laser is biased at 13 mA and its operating temperature is maintained at 20°C. An optical attenuator is used to control the power of the feedback returned to the laser cavity. The turbulence is emulated by generating various phase masks replicated by a spatial light modulator. During propagation, emulated atmospheric turbulence affects the optical beam with a random phase and amplitude modulation, resulting in scintillation and wandering. In order to realistically reproduce conditions encountered in different environments, both the transmission distance and the turbulence parameter are taken into account [5]. When the photonics processor is not activated, chaos properties are deteriorated beyond recognition. Fig. 1a depicts the frequency spectrum at the TX side in blue, and the frequency spectra at the RX side in green and red. When turbulence mitigation is performed (in green), the output power is efficiently recovered, contrarily to what is observed when the photonic processor optimization is not accomplished (in red). The critical role played by the photonic processor is further corroborated by the 2D

cross-correlation diagrams obtained before (Fig. 1b) and after (Fig. 1c) turbulence effects compensation. The intensity of the receiver is represented on the x-axis, that of the transmitter on the y-axis. A straight line with 45°-positive slope is an indicator of efficient correlation and good synchronization in chaos communication applications. This result proves the effectiveness of the photonic processor in enhancing the performance of optical signal transmission under challenging weather conditions. This enables innovative free-space secure communication techniques, including chaos LIDAR and chaos-based cryptography.

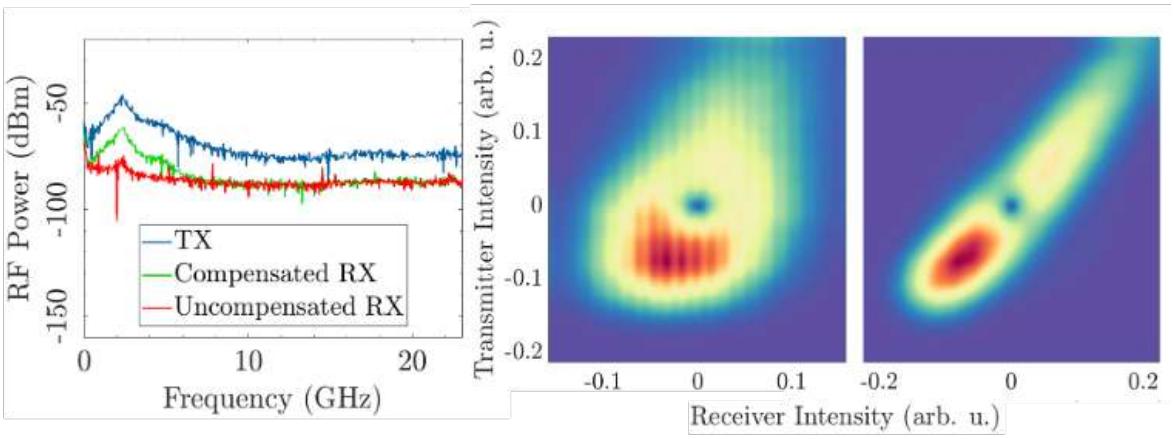

Fig. 1. a) Frequency spectra of transmitter (blue) and receiver (green, red). Green and red lines are respectively obtained with and without turbulence mitigation. b-c) 2D Correlation diagram for the intensity of the transmitter (y-axis) and the receiver (x-axis).

In conclusion, this work demonstrates that a chaotic carrier of an optical signal at 1.55 microns is significantly degraded in the presence of atmospheric turbulence. However, the compensation algorithm associated with the photonic processor restores the optical signal power even in the presence of strong turbulence, thus representing an advancement for the development of secure optical communications in free space in the near-infrared range.

Authors acknowledge the Direction Générale de l'Armement (DGA), the Optopirat project supported by the French National Research Agency (ANR) and the European Office for Scientific Research (AFSOR) under grant FA8655-22-1-7032.

References

1. A. Uchida, "Optical communication with chaotic lasers: applications of nonlinear dynamics and synchronization", John Wiley & Sons, 2012.
2. Y. Xie et al., "100 Gb/s coherent chaotic optical communication over 800 km fiber transmission via advanced digital signal processing", Advanced Photonics, Vol. 3, No. 1, 016003, 2024.
3. O. Spitz et al., "Private communication with quantum cascade laser photonic chaos", Nature Communications, Vol. 12, No. 3327, 1-8, 2021.
4. S. M. SeyedinNavadeh et al., "Determining the optimal communication channels of arbitrary optical systems using integrated photonic processors", Nature Photonics, Vol. 18, 149-155, 2024.
5. L. C. Andrews et. al., "Laser Beam Propagation through Random Media", 2nd ed. Bellingham: SPIE Press, 2005.

AES 2024, ROME - ITALY, 25 –28 JUNE 2024

Analog computing with nonlinear flat optics

C. De Angelis

CNR-INO and University of Brescia, Dept. of Information Engineering, Via Branze 38, 25123, Brescia, Italy
costantino.deangelis@unibs.it

Abstract: Digital signal processing has revolutionized many fields of science and engineering, but it still shows critical limits; a long-sought solution is optical analog computing. We demonstrate here that nonlinear phenomena combined with engineered nonlocality in flat optics can be leveraged to synthesize Volterra kernels able to outperform linear devices.

REFERENCES

[1] Hail, C.U., Foley, M., Sokhoyan, R. et al., "High quality factor metasurfaces for two-dimensional wavefront manipulation" Nat Commun 14, 8476 (2023).
[2] Overvig, A. and Alù, A., "Diffractive nonlocal metasurfaces," Laser Photonics Rev. 16, 2100633 (2022).
[3] Kwon, H., Sounas, D., Cordaro, A., Polman, A. and Alù, A. "Nonlocal Metasurfaces for Optical Signal Processing," Phys. Rev. Lett., 121, 173004 (2018).
[4] de Ceglia, D., Alù, A., Neshev, D. N. and De Angelis, C., "Analog image processing with nonlinear nonlocal flat optics," Opt. Mater. Express 14, 92 (2024).

AES 2024, ROME - ITALY, 25 –28 JUNE 2024

Multi-channel optics: thickness bound, efficiency bound, and designs that reach them

Chia Wei Hsu[1*]

[1]Ming Hsieh Department of Electrical and Computer Engineering, University of Southern California, Los Angeles, California 90089, United States
[*]corresponding author: cwhsu@usc.edu

Abstract: We show that once the functionality of a multi-channel optical system is specified, one can determine its minimal thickness and maximal transmission efficiency by analyzing its target transmission matrix. By integrating these bounds into the design process, we come up with inverse-designed high-numerical-aperture wide-field-of-view metalenses with record-breaking efficiencies.

Multi-channel devices can realize diverse functions, and computational inverse design has unlocked many potentials. Here, we show that it is possible to predict the required device footprint before doing the design, as well as predicting the optimal device dimensions and using them to reach the highest possible performance.

The device thickness correlates with how much a localized input spreads when it reaches the output side. We show that given a device's target function, one can write down the target transmission matrix (without having to know the structure of the device), determine the lateral spreading, and predict the minimal device thickness [1].

A multi-channel device with perfect transmission efficiency is characterized by a unitary transmission matrix. The degree of unitarity is correlated with the transmission efficiency. We show that from the given target function of the device, we can put a rigorous bound on the channel-averaged transmission efficiency by analyzing the singular values of the target transmission matrix [2].

Beyond setting bounds, we also introduce a more active way to use theoretical bounds, identifying previously unknown system parameters that maximize the efficiency bound itself. Combining this strategy with inverse design, we came up with high-numerical-aperture wide-field-of-view metalens designs reaching the "maximized bound" and greatly exceeding current efficiency records [3].

References

1. Li, S. and C. W. Hsu, "Thickness bound for nonlocal wide-field-of-view metalenses," Light: Science & Applications, Vol. 11, 338, 2022.
2. Li, S. and C. W. Hsu, "Transmission efficiency limit for nonlocal metalenses," Laser Photonics Rev., Vol. 17, 2300201, 2023.
3. Li, S., H.-C. Lin and C. W. Hsu, "High-efficiency high-numerical-aperture metalens designed by maximizing the efficiency limit," Optica, Vol. 11, 454–459, 2024.

AES 2024, ROME - ITALY, 25 –28 JUNE 2024

From machine learning for design to fabrication of nanophotonic structures

Francesco Ferranti[1]

[1]Department of Applied Physics and Photonics, Vrije Universiteit Brussel and Flanders Make, Belgium

Abstract: In this talk, machine learning techniques for nanophotonics design will be presented where concepts like response features, adaptive frequency sampling, and feasible design space are discussed. Also, metasurfaces for imaging, communication, and bioimaging applications fabricated by two-photon polymerization and e-beam lithography, will be illustrated for multiple applications.

Photonics, a multidisciplinary field that encompasses the study and manipulation of light, has witnessed profound transformations thanks to machine learning (ML) techniques. ML models, as deep neural networks, can be used to accelerate the design flow in nanophotonics. However, a large number of data samples can be needed to train and validate deep neural networks and therefore the potential speed-up in a design flow offered by these models can be drastically reduced. It is important to note that data samples are often collected from electromagnetic simulations, which can result computationally expensive. Some methods that can be used to achieve high modeling accuracy without requiring a high amount of data samples will be presented. For example, the concept of response features, adaptive frequency sampling, and feasible design space will be discussed. ML models can be compact, interpretable, and built in a low-data scenario [1,2]. Also, some metasurface-based examples for imaging, communication, and bioimaging applications based on diverse nanofabrication technologies, such as two-photon polymerization [3] and e-beam lithography [4], will be illustrated. In [3], two-photon polymerization-based metalenses with high numerical aperture and for optical fiber applications are proposed. In [4], metalenses for optical aberration correction in combination with gradient index lenses in microendoscopy are proposed. Multiple techniques and results will be illustrated in the talk.

References

1. F. Ferranti, ”Feature-based machine learning for the efficient design of nanophotonic structures,” Photonics and Nanostructures - Fundamentals and Applications, vol 52, Dec. 2022.
2. F. Ferranti, "Feature-Based Inverse Modeling of Nanophotonic Devices," 2023 Photonics & Electromagnetics Research Symposium (PIERS), Prague, Czech Republic, July 2023.
3. K. Vanmol, A. A. Abdul Nazar, H. Thienpont, F. Ferranti, J. Van Erps, “Fabrication of multilevel metalenses using multiphoton lithography: from design to evaluation”, vol. 32, no. 6, pp. 10190-10203, Feb. 2024
4. S. Thomas, J. G. George, F. Ferranti, S. Bhattacharya, “Metaoptics for aberration correction in microendoscopy”, Optics Express, vol. 32, no. 6, pp. 9686-9698, Feb. 2024.

AES 2024, ROME - ITALY, 25 –28 JUNE 2024

Design and simulation of phase-gradient metasurfaces for antenna applications

A. Monti[1], S. Vellucci[2], M. Longhi[2], M. Barbuto[2], M. Karamirad[1], D. Ramaccia[1], L. Stefanini[1], A. Toscano[1], and F. Bilotti[1]

[1] ROMA TRE University, Rome, Italy; e-mail: alessio.monti@uniroma3.it
[2] NICCOLÒ CUSANO University, Rome, Italy
*corresponding author: alessio.monti@uniroma3.it

Abstract: In this work, we explore the novel functionalities enabled by transmissive phase-gradient metasurfaces in antenna systems, such as scan-range enhancement and radiation shaping. Several examples for both individual antennas and phased arrays are provided to confirm the versatility of phase-gradient metasurfaces for next-generation wireless systems.

In the ever-evolving landscape of wireless communication systems, the quest for compact, efficient, and versatile antennas remains a cornerstone. Traditional antenna designs have shown several limitations, particularly in achieving desired beam steering, focusing, and shaping capabilities without compromising on size or performance. However, recent developments in metamaterials and metasurfaces have fostered a revolution in antenna engineering, offering unprecedented control over electromagnetic wave manipulation [1].

Among the different innovations, phase-gradient metasurfaces have emerged as a promising solution to introduce novel functionalities in pre-existing antenna systems. Phase-gradient metasurfaces, in fact, can impart spatially varying phase shifts on incident electromagnetic waves allowing precise control over wavefront propagation and shaping within compact and lightweight platforms [2]-[5].

In this contribution, we review some of our recent research efforts about the modelling and design of phase-gradient metasurfaces, especially in view of their application in antenna systems. We will focus on two relevant scenarios, shown in Fig. 1. In the first case, a properly designed phase-gradient metasurface (*i.e.*, meta-dome) is used to increase the scan-range of a phased array without compromising its broadside gain [6]. This effect, which is not possible using conventional planar phase-gradient designs [7], has been obtained by exploiting the shape of the metasurface as an additional design tool able boosting its non-local response [8]. As it can be appreciated in Fig. 1(a), in fact, the designed meta-dome does not affect the field radiated by the phased array in broadside direction, while being able to effectively steer the beam for oblique incidence. We will also discuss how such a similar effect can be achieved even with regular planar structures, by increasing the complexity of the meta-atoms and their intrinsically weak spatial dispersion [9].

As a second example, shown in Fig. 1(b), we consider the design of a reconfigurable cylindrical coat for wire antennas [10]. The coat, consisting of strip-based meta-atoms loaded with varactor diodes, is able to locally correct the phase-fronts radiated by the dipole. Consequently, the coat can be used for beamforming purposes, being able to convert the original omnidirectional diagram into a single- or multi-beam one.

During the talk, a specific attention will be dedicated to the modelling and simulation methods of both static and reconfigurable phase-gradient metasurfaces, and an effective multi-step design procedure will be discussed and validated.

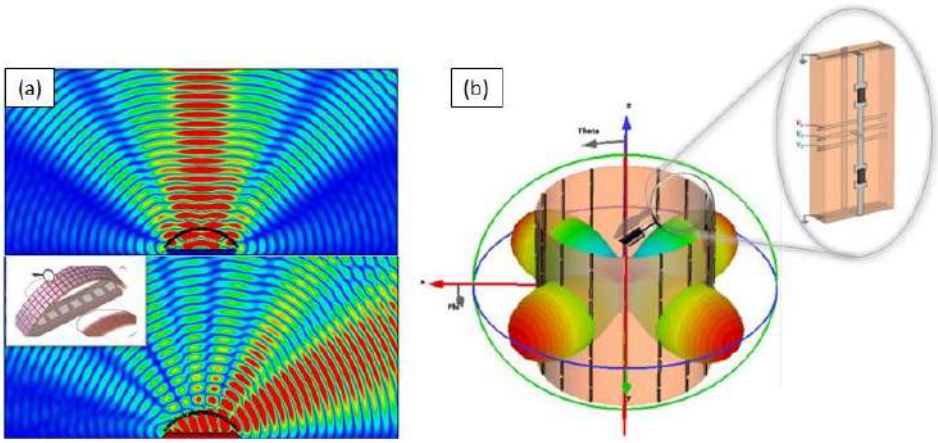

Fig. 1: (a) Quadratic-gradient metasurface with curved shape (meta-dome) able to increase the scan-range of a phased array with limited insertion loss; (b) Wire antenna covered with a cylindrical reconfigurable phase-gradient metasurface exhibiting a tunable radiation pattern.

This work has been developed in the frame of the activities of the projects MANTLES and MEETAPP, funded by the Italian Ministry of University and Research under the PRIN 2017 and 2022 programs (protocol number 2017BHFZKH and 2022ZZ8APA, respectively).

References

1. S.A. Tretyakov, "Metasurfaces for general transformations of electromagnetic fields," Philos. Trans. Royal Soc. A, vol. 373, 20140362, 2015.
2. C. Pfeiffer and A. Grbic, “Cascaded metasurfaces for complete phase and polarization control,” Appl. Phys. Lett., vol. 102, 231116, 2013.
3. J.P.S. Wong, A. Epstein, and G.V. Eleftheriades, “Reflectionless wide angle refracting metasurfaces,” IEEE Antennas Wireless Propag. Lett., vol. 15, pp. 1293–1296, 2016.
4. M. Barbuto et al., "Metasurfaces 3.0: a New Paradigm for Enabling Smart Electromagnetic Environments," IEEE Trans. Antennas Propag., vol. 70, no. 10, pp. 8883-8897, Oct. 2022.
5. A. Monti, A. Alù, A. Toscano, and F. Bilotti, “Design of high-Q passband filters implemented through multipolar all-dielectric metasurfaces,” IEEE Trans. Antennas Propag, 68, pp. 5142-5147, 2020.
6. A. Monti et al., “Quadratic-Gradient Metasurface-Dome for Wide-Angle Beam Steering Phased Array with Reduced Gain-Loss at Broadside," IEEE Trans. Antennas Propag, vol. 71, pp. 2022-2027, 2023.
7. G.A. Egorov, and G.V. Eleftheriades, "Near-Field Angular Scan Enhancement of Antenna Arrays Using Metasurfaces," IEEE Trans. Antennas Propag., vol. 71, pp. 2350-2362, 2023.
8. A. Monti et al., “Non-planar Phase-Gradient Metasurfaces for Spatially-Dispersive Beam-Steering Devices,” Proceedings of Metamaterials 2022, doi: 10.1109/Metamaterials54993.2022.9920942.
9. A. Monti, A. Alù, A. Toscano, and F. Bilotti, "Design and Applications of Spatially-Dispersive Phase-Gradient Metasurfaces," Proceedings of the 17th European Conference on Antennas and Propagation, 2023, doi: 10.23919/EuCAP57121.2023.10133796.
10. S. Vellucci et al., "Phase-Gradient Huygens Metasurface Coatings for Dynamic Beamforming in Linear Antennas," IEEE Trans. Antennas Propag., Vol. 71, pp. 7752-7765, 2023.

Antenna theory and design

AES 2024, ROME - ITALY, 25 –28 JUNE 2024

Design of an Antipodal Vivaldi Antenna with upper shell

S. Rudys[1,2], O. Suvorova[1*]

[1] Faculty of Physics, Vilnius University, Vilnius, Lithuania

[2] Antanas Gustaitis' Aviation Insitute, Vilnius Gediminas Technical University, Vilnius, Lithuania

[*]corresponding author: olga.suvorova@ff.vu.lt

Abstract: In the paper we introduce a design of antipodal Vivaldi antenna (AVA), which is covered by dielectric protective shell. To understand the features of proposed antenna we performed extensive simulations in Ansys HFSS2022. The aim of our current work is to construct the prototype of low profile, lightweight, low cost antenna, which at the same time can produce the highest possible gain in the range 4-6 GHz. We started with compact AVA, well described in literature [1,2]. A step-by-step optimization procedure has been employed to obtain the best geometry of antenna. Since our prototype expected to be used as a part of radar or communication systems, we decided to use covering made from reinforced polystyrene (permittivity 2.5-2.7, dielectric loss tangent 0.002) in order to protect antenna from harsh weather conditions. This covering was placed in certain short distance around antenna. Simulated antenna achieved a maximum gain approximately 16 dB between operation frequency 4.5-6 GHz. Our nearest future work targeted to fabrication of proposed antenna, and to validation its performance.

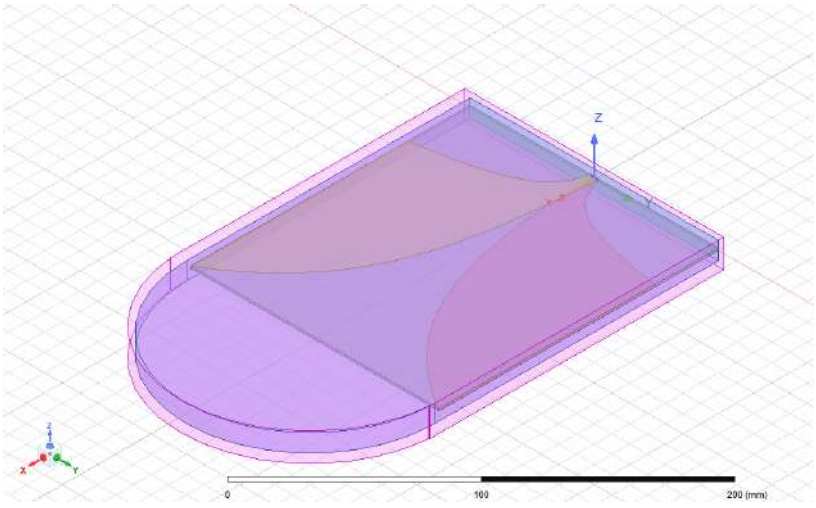

Figure 1. Geometry of proposed AVA. Protective shell is denoted by light purple color.

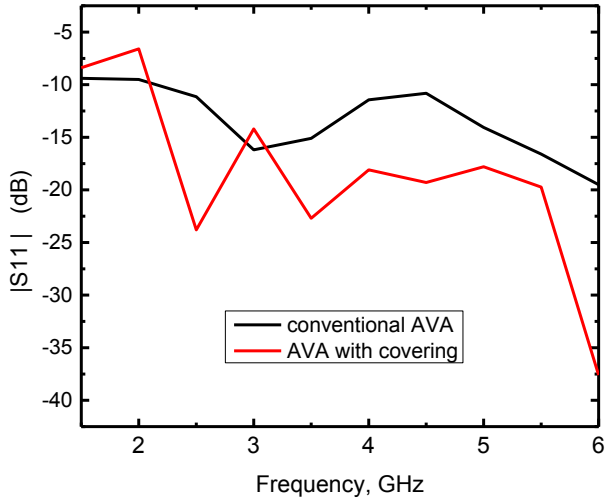

Figure 2. The influence of shell (covering) on simulated return loss of AVA. Both AVAs have the same geometry

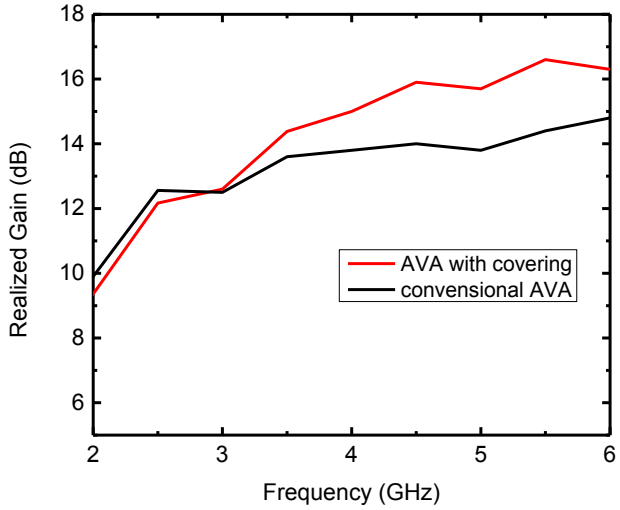

Figure 3. The influence of shell (covering) on simulated gain of AVA. Both AVAs have the same geometry

References

1. Moosazadeh M., Kharkovsky S.; Case J.T., Samali B., "Miniaturized UWB Antipodal Vivaldi Antenna and Its Application for Detection of Void Inside Concrete Specimens", IEEE Antennas and Wireless Propagation Letters, Vol. 16, 1317 – 1320, 2016.
2. Jolani F., Dadashzadeh G., Naser-Moghadasi M., Dadgarpour A.," Design and Optimization of Compact Balanced Antipodal Antenna", Progress in Electromagnetics Research C, Vol. 9, 183–192, 2009.

Effective wearable camouflaged UHF antenna

S. Rudys[1,2], **J. Banys**[1]

[1] Institute of Applied Electrodynamics and Telecommunications, Vilnius University, Sauletekio al. 3, Vilnius, Lithuania
[2]Antanas -Gustaitis' Aviation Institute, Vilnius Tech, Sauletekio al. 11, Vilnius 10223, Lithuania
*corresponding author: rudys@elmika.com

Abstract: Cavity-backed slot wearable antenna is developed for applications in 400 MHz frequency band. Exclusive properties of an antenna are low thickness (5mm) and low electromagnetic energy absorbing by human body in comparison with conventional hand-held radio antenna.

The Most significant problem of wearable antennas is low efficiency due to absorbing of electromagnetic radiation by human body [1]. To reduce absorbing, the cavity-backed slot antennas are widely used in high UHF band. The thickness of these antennas is comparable to quarter wavelength [2]. The aim of this contribution is to develop wearable and invisible, placed under the clothes antenna in 70 cm band. Therefore, the thickness of an antenna in the order of tens of centimeters or even centimeters is not acceptable.

Another important aspect is high loses (10-20 dB) of conventional hand-held radio antennas when radio device is placed on the belt or even near the head of operator. These losses are caused by absorbing electromagnetic radiation by the human body. Some screening surface can be helpful. The approach of cavity-backed slot antennas can provide screening effect and unidirectional radiation. The bigger is ground plane of cavity-backed slot antenna, the lower is radiation to human body. Dimensions of the wearable antenna are limited by dimensions of human body and were chosen 230x300 mm. It is a tradeoff between screening and convenience of using. One of possible arrangements of an antenna on the human and structure of an antenna are presented in figure 1.

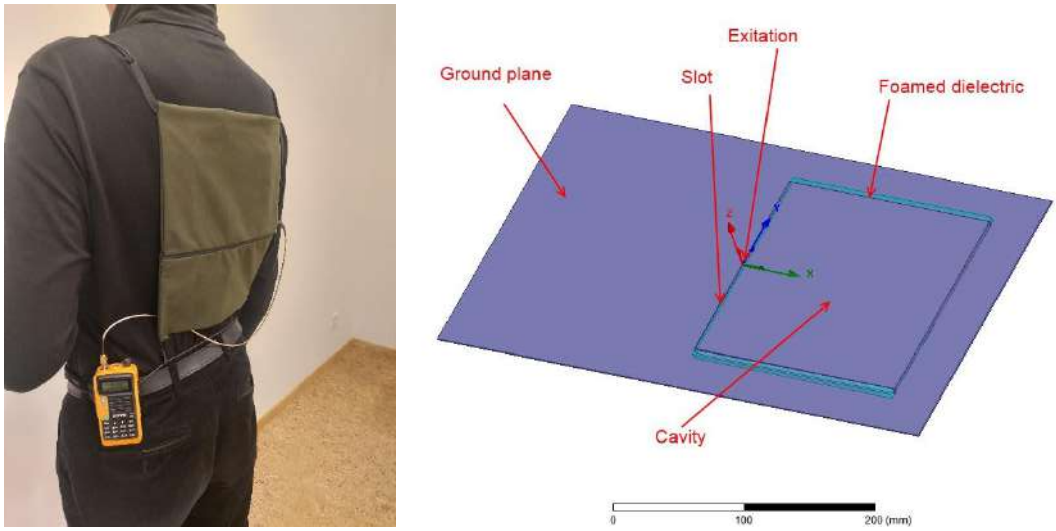

Figure 1. The view of antenna when mounted on the human on the left and structure of an antenna on the right.

Low thickness of the cavity leads to high reactance. To reduce the reactive part of impedance and to make its real part close to 50 Ohms, slot is pi shaped. To keep a cavity rigid and flexible enough, the cavity is formed on

the foamed dielectric plate. Despite electrically the antenna is cavity-backed slot antenna, but mechanically, cavity is in front of ground plane. Excitation is connected to the center of the slot via quarter wave 150 Ohm cable/transformer and LC circuit.

This antenna, arranged on the human, provides 3-20 dB higher gain than antenna of portable radio. Gain difference depends on the position of portable radio monopole antenna – less when this antenna is near the head, more when antenna is near the belt. Due to low thickness, slot antenna is narrowband. -10 dB reflection losses are in the bandwidth of 10 MHz. It is enough for practical applications. Resonance frequency can be tuned by variable capacitor.

References

1. Koulouridis, S. Body Absorbed Radiation and Design Issues for Wearable Antennas and Sensors. Wireless Mobile Communication and Healthcare. MobiHealth 2011. Lecture Notes of the Institute for Computer Sciences, Social Informatics and Telecommunications Engineering, vol 83. Springer, Berlin, Heidelberg.
2. A. Nizami, Y. Salchak, N. Albadri, M. Radwan, H. G. Espinosa and D. V. Thiel, "A Buried Cavity Backed Slot Antenna for Agriculture and Infrastructure Monitoring," 2021 IEEE Asia-Pacific Microwave Conference (APMC), Brisbane, Australia, 2021, pp. 326-328

Bi-CMOS Design of Miniature BP-NGD Circuit with RLC-Parallel Network (invited)

M. Guerin[1], S. Ngoho[2], F. Haddad[1], H. Du[3], F. Wan[3], W. Rahajandraibe[1] and B. Ravelo[3]
[1]Aix-Marseille University, CNRS, University of Toulon, IM2NP UMR7334, Marseille, France
[2]Association Française de Science des Systèmes (AFSCET), 151 Bd de l'Hôpital, Paris 75013, France
[3]NUIST, Nanjing 210044, Jiangsu, China
*Corresponding author: blaise.ravelo@yahoo.fr

Abstract: This paper looks over the Bi-CMOS design of bandpass (BP) type negative group delay (NGD) circuit. After reminding the synthesis equation of the fascinating BP-NGD passive cell, the design method is described. The study is validated by Cadence® simulation of BP-NGD proof-of-concept (PoC) circuit designed in 130-nm BiCMOS technology. Theoretical and simulation results show excellent correlation with -0.2-ns NGD amplitude around 5-GHz center frequency over 0.46-GHz NGD bandwidth. The BP-NGD PoC insertion and reflection losses are 2.53-dB and 12-dB, respectively.

1. Introduction: A fundamental NGD circuit theory was initiated by analogy with filters [1]. Innovative topologies of low-pass (LP), high-pass (HP) and bandpass (BP) type NGD functions were identified [1]. The NGD circuit is intended to microwave applications as an independent-frequency phase shifter [2-3]. To overcome the miniaturization limitation, Bi-CMOS NGD circuits were designed with LP [4-5], HP [6] and BP [2-3] NGD cells. However, because of the NGD counterintuitive effect, the fascinating circuit design method remains unfamiliar to non-specialist microwave engineers. This paper is dedicated to Bi-CMOS integrated circuit (IC) design of BP-NGD parallel RLC-network.

2. BP-NGD Topology Theory: The two-port RLC-parallel network BP-NGD cell under study is depicted by Fig. 1(a). By denoting R_0=50 Ω and $s=j2\pi f$ the Laplace variable, the passive cell S-parameters can be established by S-parameter theory. As a matter of fact, the theoretical model of the associated reflection and transmission parameters are expressed as: $S_{11}(s)=Z(s)/[2R_0+Z(s)]$ (1) and $S_{21}(s)=2R_0/[2R_0+Z(s)]$ (2) with $Z(s)= RLs/[RLCs^2+Ls+R]$ (3), respectively. This cell has a BP-NGD type behavior because its group delay (GD) is negative as $GD(f)<0$ in certain band if $f \in [f_a,f_b]$ shown in the ideal diagrams of Fig. 1(b). Ideal S_{21} of a such BP-NGD function should behave as seen in Fig. 1(c). At the NGD center frequency $f_n=1/[2\pi\sqrt{(LC)}]$ (4), the NGD amplitude is equal to:

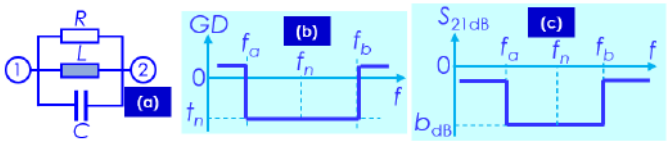

Fig. 1. BP-NGD (a) cell under study, (b) GD and (c) S_{21} ideal diagrams.

$t_n = GD(f_n) \Rightarrow t_n = -2R^2C/(2R_0+R)$ (5). It can be noticed that $t_n=GD(f_n)<0$, $S_{11}(f_n)<a<1$, and $S_{21}(f_n)=b\neq 0$.

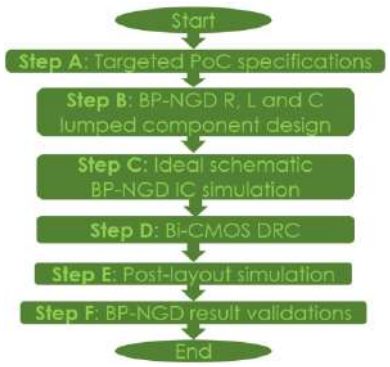

Fig. 2. Design flow of BP-NGD

The BP-NGD design formulas of constituting resistor, inductor and capacitor components in function of specifications (f_n,t_n,b=1-a) are written as: $R = 2R_0 b/(1-b)$ (6), $L = -R^2/[2\pi^2 f_n^2 t_n (2R_0+R)]$ (7), and $C = -0.5t_n(2R_0+R)/R^2$ (8), respectively. The proposed Bi-CMOS BP-NGD IC design method is indicated by the flow chart organized in 6 steps displayed by Fig. 2. After defining the BP-NGD specifications and analytical synthesis of R, L and C, Step D constitutes the Bi-CMOS design particularity with technological implementation of each component which are implemented in high Ohmic unsalicided N+poly, symmetrical high current spiral and metal-insulator-insulator

Bi-CMOS circuit. technology, respectively.

3. BP-NGD Bi-CMOS IC Design & Simulation: The BP-NGD IC PoC was designed to target the 5G 802.11a specifications. Thus, the NGD center frequency f_n=5 GHz, GD amplitude t_n=-0.2 ns and reflection coefficient $A=S_{11}(f_n)$=-12 dB were fixed as objective. After design calculations with previously proposed formulas (6), (7) and (8), we got the constituting components R=33.5 Ω, L=85.37 pH and C=11.87 pF of PoC with 0.054 mm^2 size displayed in Fig. 3(a). The corresponding PoC was simulated in both the ADS® and Cadence® environments from 4.5 GHz to 5.5 GHz. Consequently, we have the comparison S-parameters and GD plotted in Fig. 3(b) and Fig. 3(c), respectively. An excellent correlation between the calculation and simulation comparison can be seen in Figs. 3. As expected, we observe the BP-NGD intriguing behavior of GD diagram with NGD amplitude equal to -0.198 ns with NGD cut-off frequencies f_a≈4.77 GHz and f_b≈5.23 GHz. It is worth to remark that the BP-NGD function property $f_a f_b \approx f_n^2$ is verified.

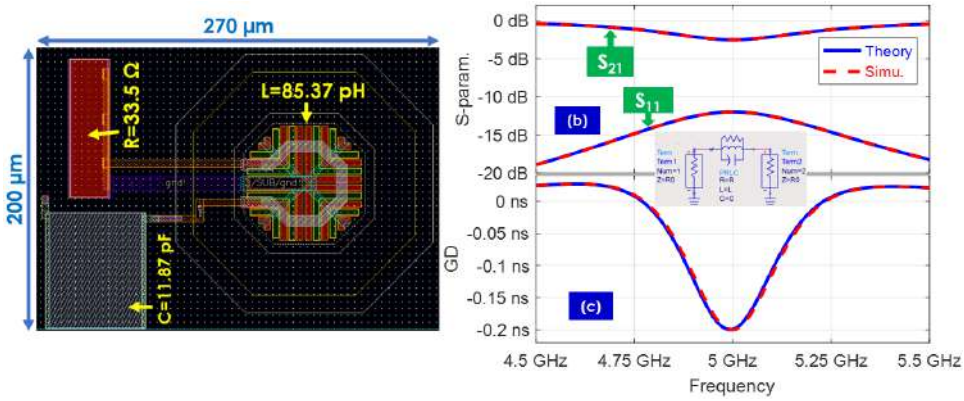

Fig. 3. BP-NGD PoC (a) Cadence® design, and theoretical and simulated (b) S-parameter and (c) GD diagrams.

4. Conclusion: A design theory of a microwave unfamiliar BP-NGD circuit operating in the 5G 802.11a frequency band is introduced. The BP-NGD model is validated by ADS® and Cadence® simulations with PoC having 5-GHz center frequency. The miniature BP-NGD will be soon used for applications in the improvement of 6G communication system against the undesirable EMC/EMI effects.

Acknowledgements: The work was supported in part by NSFC under Grants 62350610268 & 62371241 and in part by the National Key Research and Development Program of China under Grant 2022YFE0122700.

References

1. Ravelo, B., "Similitude between the NGD function and filter gain behaviours," Int. J. Circ. Theor. Appl., vol. 42, no. 10, 1016-1032, 2014.

2. Ravelo, B. et al., "Design Method of Constant Phase-Shifter Microwave Passive Integrated Circuit in 130-nm BiCMOS Technology with Bandpass-Type Negative Group Delay," IEEE Access, vol. 10, no. 1, 93084-93103, 2022.

3. Guerin, M. et al., "Bi-CMOS design of a*exp(-j*φ0) phase shifter as miniature microwave passive circuit using bandpass NGD resonant circuit," PIER B, vol. 104, 1-19, 2024.

4. Ravelo, B. et al., "130-nm BiCMOS design of low-pass negative group delay integrated RL-circuit," Int. J. Circ. Theor. Appl., vol. 50, no. 6, 1876-1889, 2022.

5. Wan, F. et al., "Design and Experimentation of Inductorless Low-Pass NGD Integrated Circuit in 180-nm CMOS Technology," IEEE Trans. CADICS, vol. 41, no. 11, 4965-4974, 2022.

6. Guerin, M. et al., "Theory and Original Design of Resistive-Inductive Network High-Pass Negative Group Delay Integrated Circuit in 130-nm CMOS Technology," IEEE Access, vol. 10, no. 1, 27147-27161, Mar. 2022.

AES 2024, ROME - ITALY, 25 –28 JUNE 2024

Unfoldable fully textile antenna using memory form technology mechanism

B.AGNUS[1], Y.HERVE[1], L.MERCIER[1,2] and S.CARRAS[3]

[1]SCIENTEAMA, 4 avenue de Cambridge 14200 France
[2] LATMOS/IPSL, UVSQ Université Paris-Saclay, Sorbonne Université, CNRS, France
[3]FILIX SAS, Rue Saint-Aventin, F-10150 Creney-prés-Troyes, France
[*]corresponding author: benoit.agnus@scienteama.com

Abstract: Scienteama Company has developed a new technologic approach for textile antenna conception. Performances of these antennae has been confirmed so far today until X band at least.

Focusing on space applications the interest of these antennae is double due to very low mass and high flexibility (close to 4 time less than a classic antenna and wrinkled to be installed in a small area) thank to the textile properties.
Very flexible structure permits to target large antenna surface regarding size of the spacecraft and unfoldable solutions for nanosatellites. Newspace trend required today new technologies for these kind of items in order to improve radiofrequency links.
Scienteama has developed several kind of antenna structure with a proprietary textile approach using textile properties and memory form wires combined directly in the textile structure.
Thank to this technology that is patented by Scienteama, several kind of antenna made with textile implementation could be equipped with deployment features:

- Parabolic antenna that could be unfolded with bio inspired method coming from flower opening.
- Dipole and monopole structure permitting long structure deployement for low frequency.
- Other structures like periodic log or spiral, patch antenna etc …

These antennas provide a new interesting vision of trading of the size, mass and performances.
Combining origami textile method and thermic based deployment of memory form structures.

Antenna structure with this technic is composed of textile assembled following a Scienteama process in order to get the best mass / size ration including the memory form property optimized in the positioning in order to get the best energy / deployment ratio using thermal increase with propagation of a current.

Power necessary for unfold the antenna is depending of the size and mass of the structure.
In earth atmosphere the air is acting as a cooling system and reduces the thermal elevation and a solution is to manage thermal gradient in the textile architecture.
In space, the vacuum configuration is helping the mechanism.

As a preliminary trial set of experience, the following table is giving some results of necessary energy used to get the deployment:

Type of antenna structure	Antenna textile surface	Electric power used for deployment (on earth)
Dipole or monopole	15cm X 0,5 cm	0,5 – 1 W
	20 cm x 4 cm	2 W
	40 cm X 4 cm	4 – 6 W
	100 cm X 2 cm	6 – 10 W
Parabolic offset	60 cm	15 – 20 W
Parabolic dish	15 cm	2 - 3 W

Table 1: Energy necessary for antenna deployment.

Under vacuum, first trails are ongoing and energy necessary is less.
Further tests will be performed in order to measure the reduction due to vacuum.

References

1. S. Carras, B. Agnus, B. Ravelo and B. Nsom, “Experimentation of an Ambient Micro-Energy Harvester Pillow”, Proc. Congrès Français de Mécanique 2019, Brest, France, 26-30 Août 2019, pp. 1-8
2. Z. Xu, B. Ravelo, B. Agnus and S. Carras “Substrate microgrid fiber effects on microstrip line,” Proc. AES 2018 symposium, round-trip marseille cruise, june 24 – july 1, 2018.
3. B. Agnus, S. Carras, B. Ravelo, "Improvement of Textile Antenna System Wireless Link Budget with Parabolic Textile Reflector", Proc. AES 2019, the 7th Advanced Electromagnetics Symposium, Lisbon, Portugal, 24-26 July 2019, pp. 1.
4. K. Elis, M. Romier, L. Feat, D. Belot, “Etude d’une antenne à pointage mécanique en bande X utilisant un guide d’onde coudé non-dépolarisant”,XXIèmes Journées Nationales Micro-ondes 14-17 mai 2019 – Caen
5. L. Mercier, B.Agnus, Y. Hervé and S .Carras “Investigation of the textile technology impact’s on the RF performances of a fully textile offset parabolic antenna design. AES 2023 Torremolinos, Spain , 5 – 8 June 2023

Array antennas, active, adaptive and reconfigurable antennas

A Variable 60 GHz Liquid Crystal Phase Shifter

Shreya S. Menon[1*], Shahin Salarian[2], Dariush Mirshekar-Syahkal[2]
[1]Department of Electronics, Cochin University of Science & Technology, Cochin, India, shreyasmenon@cusat.ac.in
[2]Institute RF Research Laboratory, School of Computer Science & Electronics Engineering,
University of Essex, Colchester, Essex, CO43SQ, UK
*corresponding author, E-mail: shreyasmenon@cusat.ac.in

Abstract

This paper presents a novel, compact phase shifter addressing array antenna spacing issues in the 60 GHz band. Its dimensions and simple architecture make it ideal for mm-wave phased array antenna designs. Simulations indicate the three-section phase shifter achieves a differential phase shift of 85°+10° and maintains transmission loss below 1 dB across the 6 GHz band (59-64 GHz). This innovation offers promising solutions for high-frequency array antenna applications.

1. Introduction

The original generous 7 GHz bandwidth available at 60 GHz band (57-64) for licensed-free wireless communication has motivated development of 60 GHz wireless networks including recently proposed 60 GHz WiFi. Beam steering capability is a requirement for such systems. It can be achieved with phased array antenna, and, for a low-cost 60 GHz system, the array is inevitably planar integrated with the system.

One suitable phase shifting element for a phased array antenna is a uniform section microstrip line on liquid crystal (LC). However, the differential phase shift resulting from a short line is very low. Hence, very long sections of uniform transmission line for a reasonable phase shift is required, which is unpractical in an array antenna environment. To moderately reduce the length, LCs with very high anisotropy as reported in [1] can be employed. To further reduce the length, other types of LC-based phase shifters like meander-line phase shifter and reflection type phase shifter have been proposed [3]-[5], but their dimensions as well as their other complexities still can give most antenna designers dilemma while implementing them in a corporate fed planar array environment.

The loaded line phase shifter is a very compact structure whose phase shift depends on the reactive loading. The working of the loaded line phase shifter with up to two sections has been presented in [6] with equations for the transmission coefficient and phase shift for a single section and double cascaded section. Adding a LC layer beneath the structure and applying a controlling voltage to it, the permittivity change and consequently the phase shift of the structure can be controlled without needing complex switches. This is essentially the work to be presented in this paper for a three-section loaded line phase shifter.

2. Structure

The three-section loaded line phase shifter on liquid crystal is shown in Fig. 1 and Fig. 2. The microstrip line shown in Fig. 2 is patterned with the specified dimensions on the bottom face of the top layer (Rogers 5880). The bottom substrate which is a LC has a thickness of h1=0.101mm, a dielectric constant of εr1=2.78 to 3.37 (depending on the bias voltage), and an average loss tangent of tanδ1=0.0263. By varying the bias voltage, the relative permittivity changes from 2.78 to 3.37. The values of the parameters of the top substrate (as shown in Fig.1) are h2=0.127mm, εr2=2.2 and tanδ2=0.0009. The dielectric thicknesses are selected small to mitigate the effect of surface waves in the 60 GHz band. As well as it is related to the thickness of the dielectrics and the shape and dimensions of the conductor pattern, the bandwidth of the structure is a function of the dielectric constants of the substrates.

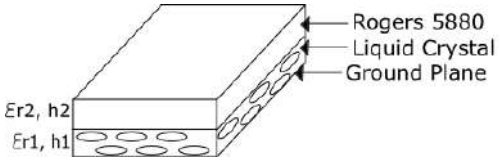

Fig. 1. Two layered substrate with liquid crystal

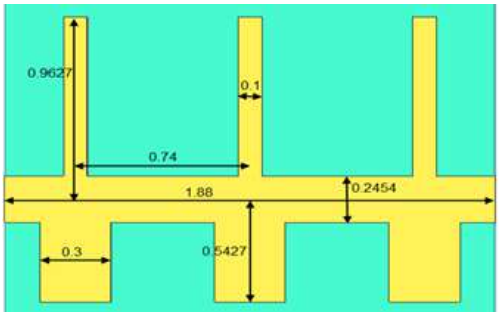

Fig. 2. *T hree-section loaded line phase shifter conductor pattern*

Therefore, the dielectric constant of the top layer has been chosen as low as it is commercially available. Considering the LC layer, its effective dielectric constant is typically around 3 and cannot be reduced further. The feed line is assumed to be 50 Ω achieved using 250 um linewidth, Fig. 2.

3. Results and Discussion

The complete structure is simulated first with εr1=2.78 and εr2=2.2, and then with εr1=3.37 and εr2=2.2; which are the two extreme cases corresponding to the lowest and highest bias voltage. Each section of the three-section loaded line phase shifter, Fig. 2, consists of a narrow microstrip stub of width 0.1 mm and length 0.9627 mm (≈ λ/8) and a relatively wide microstrip line of width 0.3 mm and length 0.5427 mm (≈λ/4). Within the band, the wide stub with small length always provides a capacitive loading, as shown in Fig. 3, and the narrow stub with longer length swings from capacitance to inductance, as shown in Fig.4. Thus, each section of the loaded line is a parallel resonant circuit and the total susceptance of it is resultant parallel admittance. The return loss and differential phase shift (phase shift difference when permittivity of liquid crystal changes due to applied voltage) of each section are evaluated using the equations reported in [6] and compared with those obtained from simulations from a commercial software package (ADS) using its Schematic (circuit solution) and Momentum (accurate EM discretization solution) facility. These results are shown in Fig. 5, Fig. 6 and Fig. 7. As can be seen in Fig 5 and Fig. 6, the discrepancy between the different methods for resonant frequencies is about 4%. Since the Momentum solutions take care of all EM interactions, the associated results are considered to be more dependable and used in the rest of analysis in this work.

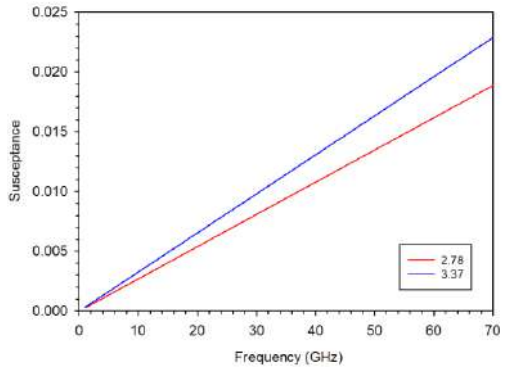

Fig. 3. Susceptance of the wide short (λ/8) section in Fig. 2 with frequency

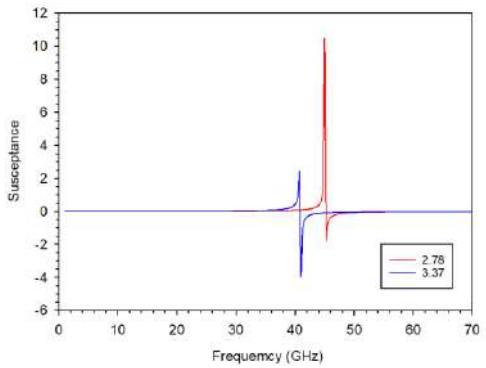

Fig. 4. Susceptance of the narrow long (λ/4) section in Fig. 2 with frequency

From Fig. 7, it is noticed that the differential phase shift is a function of frequency. The average differential phase shift over the bandwidth which is about 100 MHz at the center frequency of 57.6 GHz (which these information can be found by comparing the -10 dB return losses in Fig. 5 and Fig. 6) is about 40 degree which is satisfactory for WiFi and similar applications. For one-section, the bandwidth and the center frequency can be increased by judicious selection of the stub dimensions. However, in this paper we are concerned with three-section loaded line.

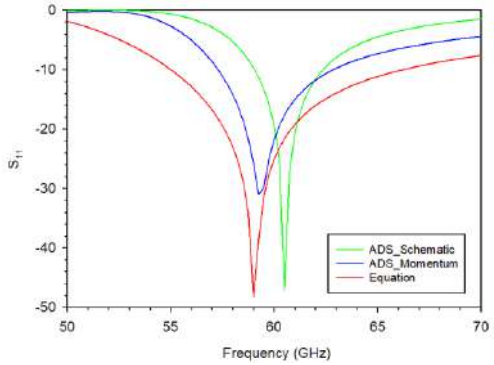

Fig. 5. Return loss of one section of loaded line phase shifter for εr1=3.37

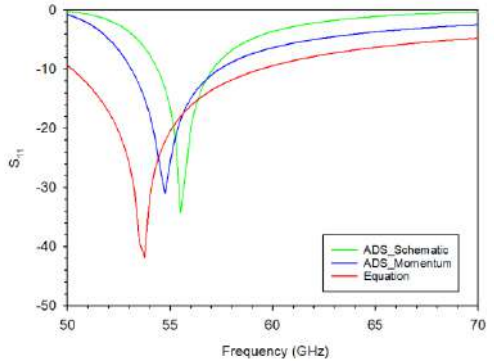

Fig. 6. Return loss of one section of loaded line phase shifter for εr1=2.78

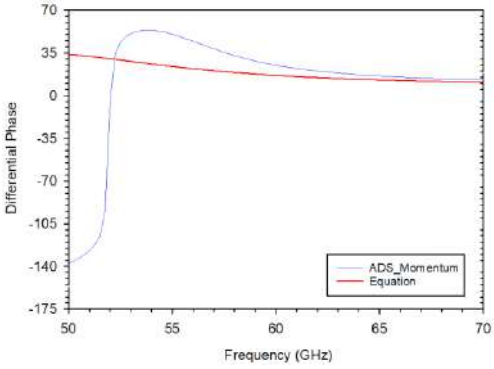

Fig. 7. Differential phase shift of one section of loaded line phase shifter

To increase the differential phase shift, three sections were cascaded to give higher differential phase shift. The return loss and differential phase shift for three-section loaded line phase shifter is formulated as

$$S_{11} = \frac{A_{21}}{A_{11}} \quad (1)$$

$$S_{21} = \frac{1}{A_{11}} \quad (2)$$

$$\Delta\phi = \tan^{-1}\left(\frac{-real(\mathrm{A}_{11,\perp})}{imag(\mathrm{A}_{11,\perp})}\right) - \tan^{-1}\left(\frac{-real(\mathrm{A}_{11,\square})}{imag(\mathrm{A}_{11,\square})}\right) \quad (3)$$

Where,

$$A_{21} = B^2 e^{-j2\theta} + j\left(\frac{B^3}{4} - Be^{-j2\theta} + \frac{B^3}{4}e^{-j2\theta} + \frac{B}{2}\right)$$

$$A_{11} = \frac{B^2}{4} + e^{j2\theta}\left(1 + \mathrm{j}\frac{B}{2}\right)^2 + \frac{B^2}{4}e^{-j2\theta}\left(1 - \mathrm{j}\frac{B}{2}\right)$$

$$+\frac{B^2}{4}\left(1 + \mathrm{j}\frac{B}{2}\right) + j\frac{B^3}{8} + j\frac{B}{2}e^{j2\theta}\left(1 + \mathrm{j}\frac{B}{2}\right)^2$$

$A_{XX,\perp} = A_{XX}$ with ε_{r1}=2.78; $A_{XX,\square} = A_{XX}$ with ε_{r1}=3.37 and B is the total susceptance of a section of loaded line phase shifter. However, as mentioned previously, results from this formulation cannot be as accurate as those produced by EM simulator like ADS, but useful if an EM simulator is not accessible.

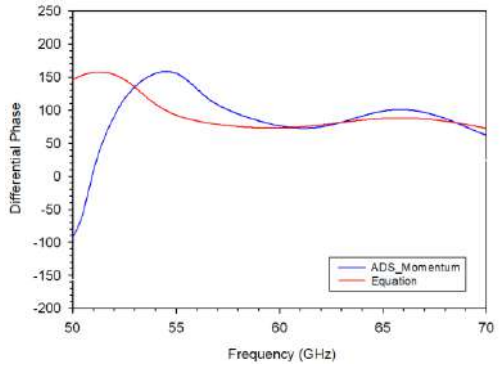

Fig. 8. Differential phase shift of proposed three-section loaded line phase shifter

In our three-section loaded line phase shifter, Fig. 1 and Fig. 2, the distance between the sections is optimized for better return loss. The return loss and differential phase shift of the final design are evaluated using (1) - (3) and compared with simulations from a commercial software package (ADS). They are shown in Fig 8. As can be seen in Fig 8, the results from the formulation and the EM simulator are in a rather good, but not close enough over some frequencies due to neglecting EM interactions in the formulation (1) - (3). The differential phase shift predicted by the EM simulator (which we consider it to be more accurate) is about 85°±5° over 59-64 GHz (ie: 6 GHz bandwidth) with a transmission loss not more than 1 dB as shown Fig. 9. This bandwidth is suitable for many applications including IoT and rapid file transfers through 60 GHz band.

4. Conclusions

A compact three-section loaded line phase shifter is proposed, modelled and simulated for 60 GHz band. Its dimension is 1.88 mm X 1.55 mm and its bandwidth is around 6 GHz. The phase shifter is based on liquid crystal providing a differential phase shift of 85° with 1 dB insertion loss. Its ease of structure and specification make it very desirable in many phased array environments.

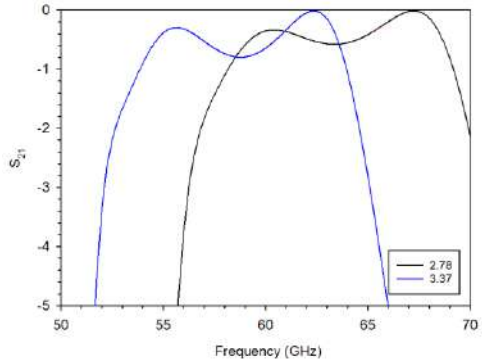

Fig. 9. Transmission loss (mag.) of the three-section loaded line phase shifter for εr1=2.78 turning into εr1=3.37

References

[1] Yu. Garbovskiy, V. Zagorodnii, P. Krivosik, J. Lovejoy, R. E. Camley, Z. Celinski, A. Glushchenko, J. Dziaduszek and R. Dąbrowski, "Liquid crystal phase shifters at millimeter wave frequencies," Journal of Applied Physics, vol. 111, Issue 5, 2012.

[2] S. Bulja and D. Mirshekar-Syahkal, "Meander line millimetre-wave liquid crystal based phase shifter," Electronics Letters , vol.46, no.11, pp.769,771, May 27 2010.

[3] S. Bulja, D. Mirshekar-Syahkal, M. Yazdanpanahi, R. James; S. E. Day, and F. A. Fernandez, "Liquid crystal based phase shifters in 60 GHz band," European Conference on Wireless Technology (EuWIT), pp.37,40, 27-28 Sept. 2010.

[4] P. Deo, D. Mirshekar-Syahkal, L. Seddon, S. E. Day and F. A. Fernandez, "60 GHz liquid crystal phased array using reflection-type phase shifter," 7th European Conference on Antennas and Propagation (EuCAP), pp.927,929, 8-12 April 2013.

[5] S. Bulja, D. Mirshekar-Syahkal, M. Yazdanpanahi, R. James, S. E. Day and F. A. Fernandez, "60 GHz Reflection Type Phase Shifter based on liquid crystal," IEEE Radio and Wireless Symposium (RWS), pp.697,699, 10-14 Jan. 2010.

[6] Robert E. Collin, Foundations for Microwave Engineering, 2nd ed., IEEE press series on electromagnetic wave theory, John Wiley Publication:New Jersey, 2001.

Review of 3D Printed Beam-Steering Dielectric Lens Antennas for Millimeter-Wave Applications

J.L. Masa-Campos[1*], M. H. Rasekhmanesh [2], A. Piroutiniya [2], J. Melendro-Jimenez [1], E. García-Marín[2], P. Sanchez-Olivares [1], A. Tamayo-Dominguez [1], J.M. Fernandez-Gonzalez [1]

[1]Centro de Investigación en Procesado de la Información y Telecomunicaciones, ETSI Telecomunicación, Universidad Politécnica de Madrid, 28040 Madrid, Spain,
[2]Group of RadioFrequency: Circuits and Systems (RFCAS), Escuela Politécnica Superior, Universidad Autónoma de Madrid, 28049 Madrid, Spain
[*]corresponding author: joseluis.masa@upm.es

Abstract: In this paper a review of implemented 3D Printed Beam-Steering Antennas based on Gradient Index Lenses is presented for millimeter-wave applications. The appropriated design of the feeder in correspondence with the lens parameters is included for an optimum aperture efficiency. Several topologies have been used to feed the lens in linear (LP) and circular (CP) polarization from 25 to 95 GHz.

Lens Antenna Topologies: Gradient Index (GRIN) [1] lens antennas (Figure 1) are an excellent choice for low-cost and easy manufacturing multi-beam antennas (MBAs), especially due to the advances in 3D printing technologies in recent years. In this kind of lenses, the phase uniformity of the electric field (E-field) at the lens aperture for an appropriate collimated radiation is achieved by means of different density of perforations though a planar dielectric structure, which creates different dielectric permitivities inside and, consequently, propagation constants. An external low directive antenna is required to properly feed the dielectric lens structure, by generating a focalized wave at the lens aperture that originates a high gain pattern.

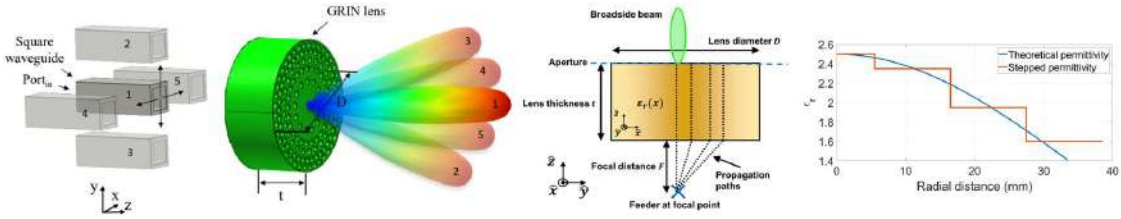

Figure 1: Geometry of a Beam-Steering Dielectric Gradient Index (GRIN) Lens Antenna

These lens antenna designs share some common aspects with reflector antennas, that possibilities the definition of a total aperture efficiency $\eta_{Total-aper}$ (1). This parameter is composed of different efficiencies related to: the tapered amplitude (η_{taper}) and the non-uniform phase (η_{phase}) of the electric field (E-field) at the lens aperture, the blocking efficiency (η_{block}) to consider the portion of the reflected signal at the lens and propagated back to the feeder, and the spillover efficiency (η_{spill}) for the portion of the radiation signal from the feeder that is not focused by the lens. This total aperture efficiency establishes the achieved antenna directivity D_0 (2) related to the lens aperture area $A_{lens-aper}$.

$$\eta_{Total-aper} = \eta_{taper} \cdot \eta_{phase} \cdot \eta_{pol} \cdot \eta_{block} \cdot \eta_{spill} \quad (1)$$

$$D_0 = \frac{4\pi}{\lambda_0^2} \cdot A_{lens-aper} \cdot \eta_{Total-aper} \quad (2)$$

By means of properly designing the lens physical parameters (especially lens diameter D and thickness t)

related with the feeder radiation pattern and its adequate placement at the lens focal distance (F), an optimum design can be achieved in terms of maximum achievable $\eta_{Total-aper}$, as in Figure 2a can be checked for several feeder radiation patters (ideally modeled as $cos^n(\theta)$). The corresponding E-field amplitude illumination at the aperture lens edge (pedestal value C) is also computed in Figure 2b.

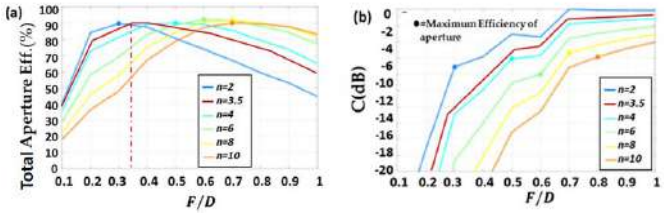

Figure 2: Optimum GRIN lens design related to F/D ratio and type of radiation patter of the feeder: a) Total aperture efficiency, b) Amplitude pedestal of the aperture E-field at lens edge.

By using this design method several prototype examples of GRIN Beam-Steering Dielectric Lens Antennas [1]-[3] are shown in Fig. 3, operating at different frequency ranges from 25 to 95 GHz. In all cases, the GRIN lenses have been manufactured by resin Stereolitography 3D printing method. A set of microstrip patches (Figure 3a) or pyramidal horn antennas (Figure 3b) have been used to feed a planar GRIN lens, while a dual mode bow-tie cavity radiating to a stepped GRIN lens (Figure 3c) or a square open waveguide illuminating an integrated GRIN lens + dielectric polarizer (Figure 3d) have been fabricated and measured with very good performance.

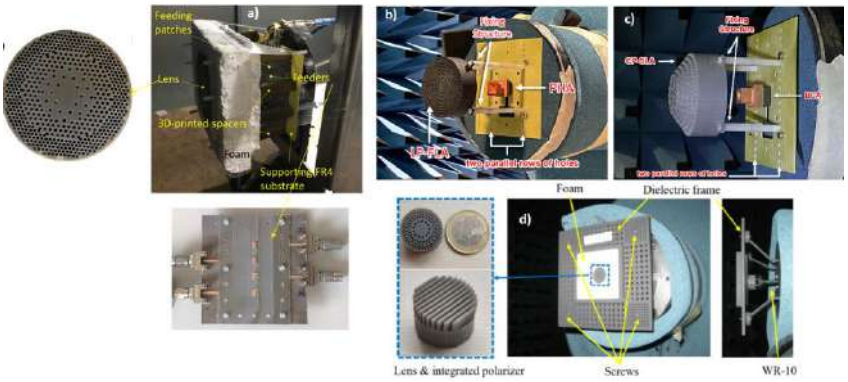

Figure 3: Prototypes of 3D Printed Beam-Steering Dielectric GRIN Lens Antennas: a) Planar lens with patch feeder (LP), b) Planar GRIN lens with pyramidal horn feeder (LP), c) Stepped lens with bow-tie cavity feeder (CP, d) Planar lens + polarizer with opened square waveguide (CP)

References

1. E. Garcia-Marin, D.S. Filipovic, J. L. Masa-Campos and P. Sanchez-Olivares. “Low‐cost lens antenna for 5G multi‐beam communication,” Microwave and Optical Technology Letters, Vol. 62, No. 5, 3611–3622, 2020.
2. A. Piroutiniya, M. H. Rasekhmanesh, J. L. Masa-Campos, J. López-Hernández, E. Garcia-Marin, A. Tamayo-Dominguez, P. Sánchez-Olivares and J A. Ruiz-Cruz, “Beam Steering 3D Printed Dielectric Lens Antennas for Millimeter-Wave and 5G Applications,” Sensors, Vol. 23, 6961-1–6961-26, 2023
3. J. Melendro-Jimenez, P. Sanchez-Olivares, A. Tamayo-Dominguez, X. Sun and J. M. Fernandez-Gonzalez, "3D Printed Directive Beam-Steering Antenna Based on Gradient Index Flat Lens With an Integrated Polarizer for Dual Circular Polarization at W-Band," IEEE Transactions on Antennas and Propagation, Vol. 71, No. 1, 1059-1064.

Funding: This work was supported by the Spanish Government under grant PID2020-116968RB C32 (DEWICOM), PID2020-112545RB-C51 (InTerSpaCE), TED2021-130650B-C21 (ANT4CLIM) and funded by MCIN/AEI/ 10.13039/501100011033 (Agencia Estatal de Investigación) and by UE (European Union) "NextGenerationEU"/ PRTR.

AES 2024, ROME - ITALY, 25 –28 JUNE 2024

A Performance Analysis of Partial LIS for 6G Systems

Mário Marques da Silva [1,3,4,5*], **Rui Dinis** [2,3,4]

[1] Universidade Autónoma de Lisboa, Portugal
[2] Faculty of Sciences and Technology, Universidade Nova, Portugal;
[3] Autonoma TechLab, Portugal
[4] Instituto de Telecomunicações, Portugal
[5] Ci2—Centro de Investigação em Cidades Inteligentes, Portugal
[*]corresponding author: mmsilva@autonoma.pt

Abstract: Large Intelligent Surfaces (LIS) emerges as a pivotal technology, acting as near-field beamformers, facilitating the new requirements of 6G. We analyze the impact of utilizing the entire LIS array versus a subset of its antennas, and we explore different receiver types, with varying complexities.

6G communications are expected to reach the requirements of a peak data rate of, at least, 1 Tbps in nomadic access (100 times higher than 5G) and 1 Gbps in a mobile environment (10 times higher than 5G), while the energy efficiency is expected to be 10 to 100 times better than 5G, with a spectral efficiency 5 to 10 times better than 5G. These requirements are expected to be achieved with LIS systems associated with terahertz bands and block transmission techniques [1]. Note that the higher the carrier frequency is, the greater the channel coherence bandwidth.

To meet these demands, 6G will employ advanced techniques such as block transmission, error correction codes, and Large Intelligence Surfaces (LIS). The LIS system, akin to a beyond-massive MIMO, boasts an even greater number of antenna elements, enabling unprecedented capacities and data rates. Interestingly, while wireless communications typically operate in the far-field beyond the Fraunhofer distance [2,3], the LIS system functions in the near-field. This near-field beamforming, distinct from traditional beamforming, allows precise directionality not only in bearing and elevation but also in distance. Consequently, it minimizes interference between users who share alignment in bearing and elevation but are located at varying distances. LIS surfaces act as near-field beamformers, facilitating exceptionally high symbol rates and enabling robust interference avoidance. In this article, we delve into the intricacies of LIS systems, specifically examining the impact of utilizing the entire LIS array versus a subset of its antennas. Our analysis centres around an LIS system coupled with Single Carrier with Frequency Domain Equalization (SC-FDE). Additionally, we explore different receiver types, each varying in complexity. Notably, when we opt for antenna elements situated closer to the user equipment—rather than the entire LIS—the computational complexity diminishes. This reduction arises from the direct relationship between computational load and the number of antennas employed. In other words, adopting a partial LIS configuration yields several advantages: (1) Energy Efficiency: by focusing on specific antenna elements, that is, partial LIS, we achieve a reduction in energy consumption that comes from the lower computational requirements; (2) Interference Mitigation: the partial LIS setup effectively curtails interference levels, resulting in performance that tends to overcome that of the complete LIS system.

We consider Monte Carlo simulations, as defined in [1]. Figure 1 shows the performance results with 4X225 LIS system, with 2 users, without LDPC codes, with and without Partial LIS. 4X225 LIS system means that 4 panels of 225 antennas each are utilized (15 antennas on each side of the panel), making a total of 900 antennas as part of the LIS. Like the previous graphic, the number of users is 2, which means that there is a reference user

and one interfering user. The “Full-LIS” corresponds to using the total 900 antennas, while the "Partial LIS One Panel” corresponds to using the panel (with 225 antennas) that is closer to each user, mitigating the interferences. As can be seen, like the results of the previous figure, results obtained with "Partial LIS One Panel” overcome the performance obtained with “Full LIS”, for the different receiver types. This happens because the number of antennas per panel is still sufficiently high (225 antennas), allowing a good gain in terms of diversity, while mitigating the interference over the interfering user due to the use of a single panel, instead of the whole LIS. In terms of receiver types, it is viewed that ZF and MMSE receivers achieve the same performance, leading to the best results. This is followed by the low complexity MRC receiver, whose performance is always between those obtained with ZF/MMSE and EGC receiver. It is worth noting that, in the case of the “Full LIS”, the performance obtained with the MRC receiver is almost superimposed of those obtained with the ZF/MMSE receivers, while in the case of the “Partial LIS One Panel” the MRC shows a small degradation compared with the ZF/MMSE. Note that the receiver types are defined in [1].

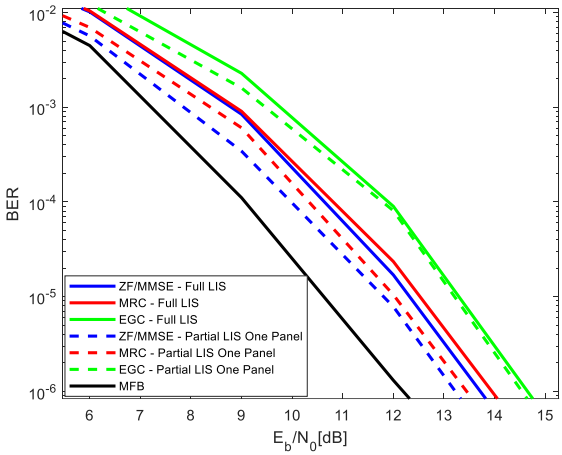

Figure 1. Performance results for 4X225 LIS System, with 2 users, without LDPC codes, with and without Partial LIS.

Acknowledgments: We acknowledge the support of FCT/MCTES, through national funds and, when applicable, co-funded EU funds under the projects UIDB/EEA/50008/2020 and 2022.03897.PTDC. We also acknowledge the support of Autonoma TechLab for providing an interesting environment in which to carry out this research.

References

1. Marques da Silva, M; Gashtasbi, A.; Dinis, R.; Pembele, G.; Correia, A.; Guerreiro, J.; “On the Performance of Partial LIS for 6G Systems”. MDPI Electronics, 2024, 13, 1035. https://doi.org/10.3390/electronics13061035
2. M. Marques da Silva, R. Dinis, G., Martins, “On the Performance of LDPC-Coded Massive MIMO Schemes with Power-Ordered NOMA Techniques”, MDPI Applied Sciences 11(18), 8684, 17 September 2021 (https://doi.org/10.3390/app11188684)
3. Marques da Silva, M.; Dinis, R.; Guerriero, J. “A Low Complexity Channel Estimation and Detection for Massive MIMO using SC-FDE”. Telecom 2020, 1, 3–17.

Millimeter/Terahertz and nano-optical antennas

THz Near-field Molecular Fingerprint Sensor for glucose detection

Hyeji Son[1], Jeong-Sik Jo[2], Hyunwoo Park[1], Jae-Won Jang[2] and Teun-Teun Kim[1*]

[1]Department of Physics, University of Ulsan, Ulsan, Korea
[2]Division of Physics and Semiconductor Science, Dongguk University, Seoul, Korea
[*]corresponding author: ttkim@ulsan.ac.kr

Abstract: In the terahertz (THz) regime, molecular fingerprint spectroscopy has become feasible, but existing fabrication methods remain costly and challenging for mass production. In this study, we propose an efficient approach with nanogap structure using AFM-based nanolithography to effectively detect target materials in the THz range.

While molecules such as sugars and polymers exist in normal modes of vibration in the terahertz (THz) region, sensitive THz spectral fingerprinting is challenging due to weak light-material interactions. Recently, limitations were overcome through direct near-field measurement using subwavelength THz resonance imaging (STRING) [1]. Previous research involved fabricating subwavelength resonators with a coaxial ring aperture using electron-beam lithography, a costly and challenging process for mass production. Furthermore, for practical applications, it is essential to design sensors that match the molecular vibrations of glucose for diagnosing diabetes. In this work, we propose a design for a nanogap square loop with a resonance frequency of 1.4 THz associated with glucose (Fig. 1a). The simulation results demonstrate strong signals that depend on the polarization direction of incident THz waves, making it suitable for molecular fingerprinting (Fig. 1b). Since analysis can be conducted with just a single metal gap structure, eliminating the need for periodic structures, the size of the sensor can be innovatively reduced. To realize this, we are utilizing AFM-based nanolithography techniques that employ physical interactions between the probe and the specimen. A resist layer is formed on the substrate, and the desired structure is created by removing the resist material using a probe, followed by etching gold (Fig. 1c). This method enables efficient nanometer-scale line patterning, ideal for near-field terahertz (THz) molecular fingerprinting, and suggests the potential for developing a non-contact diabetes sensor using THz waves, facilitated by AFM-based nanolithography and the STRING method.

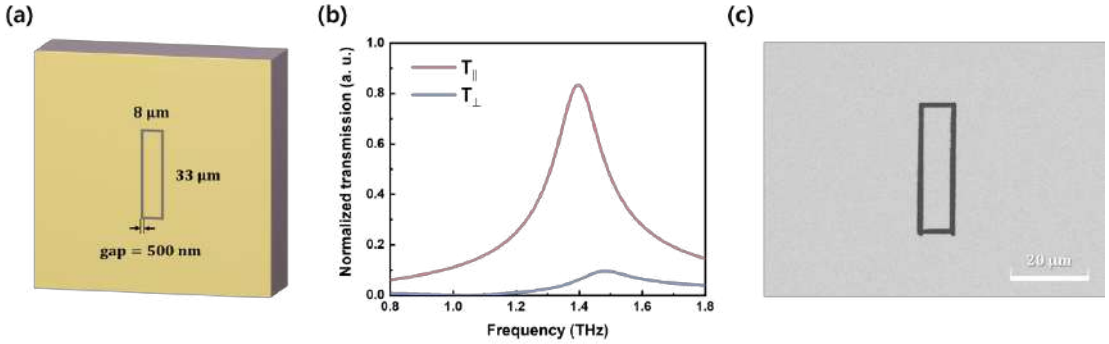

Fig. 1. (a) Schematic design of single nanogap square loop with the resonance frequency of glucose (1.4 THz). (b) Simulation results for glucose detection. (c) Microscopic image of the structure designed for glucose detection.

Acknowledgements, this work was supported by National Research Foundation of Korea (NRF) through the government of Korea (NRF-2021R1C1C100631612)

References

1. Taewoo Ha et al., “Subwavelength Terahertz Resonance Imaging (STRING) for Molecular Fingerprinting,” Nano Lett., Vol. 22, No. 24, 10200-10207, 2022.

Electromagnetically coupled on-chip antenna in CMOS technology for multi-color sensing applications

A. V. Chernyadiev[1*], D. B. But[1], K. Ikamas[2], W. Knap[1] and A. Lisauskas[2]

[1]CENTERA Laboratories, Institute of High Pressure Physics PAS, Warsaw, Poland
[2]Institute of Applied Electrodynamics and Telecommunications, Vilnius University, Vilnius, Lithuania
[*]corresponding author: acherniadev@unipress.waw.pl

Abstract: In this article, we present a design of an antenna coupled to a bright and a dark split-ring resonator atoms. The concept of coupled resonators is promising for multi-color broadband material characterization.

Introduction: On-chip antennas are a typical solution for free space RF signal transmission in the millimeter frequency range. Recently, in light of the advancements made in the field of metamaterials and nanofabrication integration of subwavelength structures in the chip [1] design becomes increasingly common, addressing issues on the way to efficient terahertz integrated circuits. Among the applications explored are beam shaping, polarizability control, filter design, spatiotemporal modulation, and signal processing. Complementary metal-oxide semiconductor (CMOS) technology provides a great platform for design of such electromagnetic structures. Its multilayered planar architecture allows researchers to explore ultra-strongly coupled meta-atoms, as a result of the vertical alignment of the structures [2].

Design: The top view of the investigated coupled structures is shown in Fig.1a. The structures are implemented in different metal layers of the backend-of-the-line of a silicon chip: antenna – top metal layer, split-ring resonator (SRR) bottom metal layer. They are separated by approximately 6.5 μm.

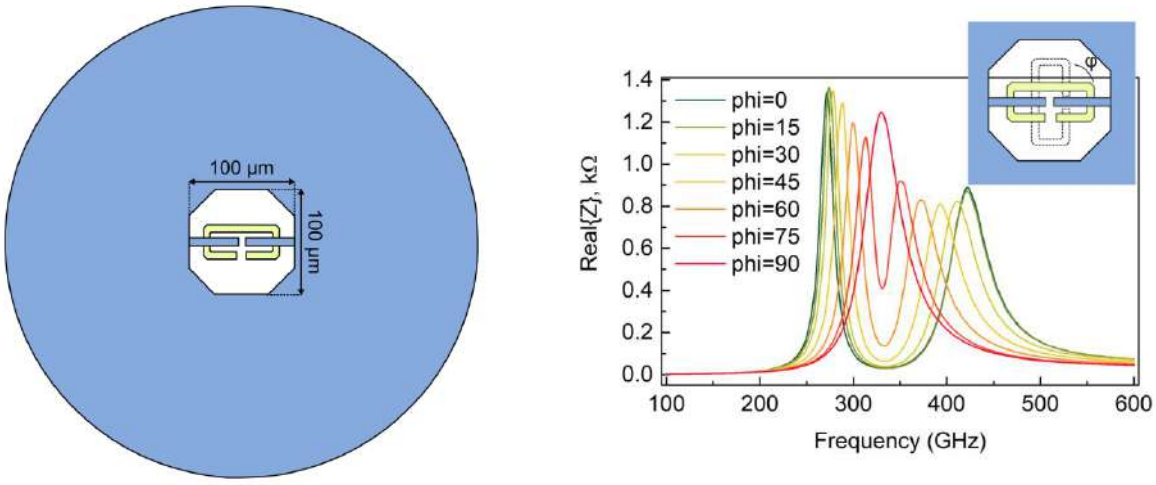

Figure 1. Electric dipole-dipole coupling between a slot-dipole antenna and a single split-ring resonator: a) schematic layout; b) coupled structures impedance spectrum evolution from the parallel alignment of the antenna and the SRR (φ = 0) to the orthogonal alignment (φ = 90) with a step of 15 degrees.

The results obtained with this design can be found in our previous works [2, 3] in which we estimate the

coupling strength, propose a simple RLC circuit-based model for their analysis and explore the near-field sensing application. In Fig.1b the results of the electric dipole-dipole interaction dependence on the geometrical orientation of the SRR with respect to the antenna are shown. The largest resonance mode splitting and therefore the strongest coupling is observed for the parallel orientation of the gaps of the antenna and the SRR (electric dipoles are aligned). As the SRR is rotated towards an orthogonal position the splitting decreases until it disappears completely when the SRR reaches the 90-degree position and cannot be excited directly by an electromagnetic wave. This result is in contrast with the one in [4], in which the splitting between two vertically oriented split-ring resonators was retained due to the magnetic dipole-dipole coupling. In our case, the antenna and the SRR have very different magnitudes of the dipole moments.

In Fig. 2 the result of the antenna coupled to a bright (possible to excite with an electromagnetic wave) and a dark (orthogonal orientation prohibiting direct excitation by external light) SRRs, which are vertically separated, is presented.

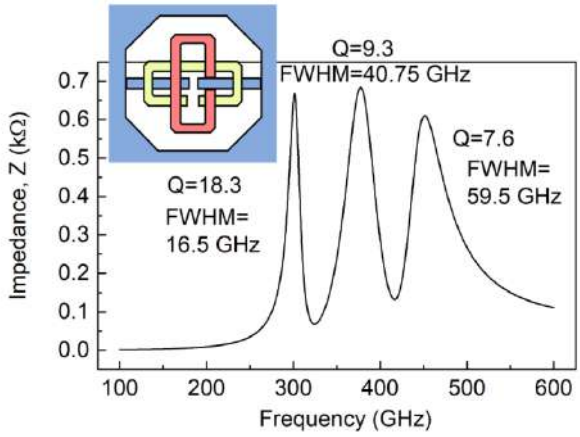

Figure 2. Impedance spectrum of the antenna coupled to a bright and a dark SRR.

Summary: CMOS technology gives researchers freedom to explore coupling phenomena and adapt them to the particular objective. Electromagnetically coupled structures can yield higher Q-factor resonances and serve as an alternative to resonance detectors integrated with patch antennas designed for different frequencies. Integrating coupled resonators with an oscillating circuit could result in reconfigurable THz sources. These advancements would pave the way toward the multi-color lab-on-chip module for various sensing applications.

References

1. Alibakhshikenari M. *et al*., "A comprehensive survey on antennas on-chip based on metamaterial, metasurface, and substrate integrated waveguide principles for millimeter-waves and terahertz integrated circuits and systems," IEEE Access, Vol. 10, 3668-3692, 2022.
2. Chernyadiev, A. V., D. B. But, Y. Ivonyak, K. Ikamas, A. Lisauskas, "A CMOS-integrated terahertz near-field sensor based on an ultra-strongly coupled meta-atom," Scientific Rep., submitted for publication.
3. Chernyadiev, A. V., D. B. But, C. Kołaciński, K. Ikamas and A. Lisauskas, "Metasurface-coupled near-field sensor implemented in 180nm CMOS," 2022 24th International Microwave and Radar Conference (MIKON), Gdansk, Poland, 1-5, 2022.
4. Liu, N., H. Liu, S. Zhu and H. Giessen, "Stereometamaterials," Nature Photon., Vol. 3, 157–162, 2009.

AES 2024, ROME - ITALY, 25 –28 JUNE 2024

Low-loss Functional Waveguide Devices Fabricated with a UV-Curable Resin Type 3D Printer, RECILS, and Metal Plating in 200–400 GHz Band

Junji Yumoto*

Institute for Photon Science and Technology, University of Tokyo, Japan
*corresponding author: yumoto@ipst.s.u-tokyo.ac.jp

Abstract: This study introduces a groundbreaking method for producing waveguide devices in the 200–400 GHz band, utilizing a novel UV-curable resin type 3D printer, RECILS, and metal plating. This method has been experimentally verified to yield low-loss waveguide devices, such as bandpass filters, bent and twisted waveguides, outperforming conventional machining techniques.

The use of electromagnetic waves in the sub-THz band (0.1–1 THz) is becoming increasingly important for future wireless communications, sensors, radio astronomy, and other applications. Research on elemental technologies and system demonstrations in the sub-THz band is advancing rapidly, contributing to the development of Beyond 5G and 6G technologies. To address the challenges of high-frequency signal transmission through cables, smaller cross-sectional metallic waveguides are employed to propagate wireless signals. As the frequency increases, the cross-sectional size of the waveguide decreases; for instance, the standardized size for the 300 GHz band is WR-3 (a cross-section of waveguides: 0.86 × 0.43 mm^2). These structures are regarded known as sub-mm scale hollow structures with high aspect ratios (smsHS) in bulk metal, are increasingly difficult to fabricate using conventional machining.

3D printers facilitate the creation of hollow structures, including those with high aspect ratios, through their layering process. Despite numerous studies on 3D printing, fabricating smsHS structures for sub-THz waveguide devices remains a significant challenge. To address this, we developed a novel UV-curable resin type 3D printer, RECILS [1], which achieves palm-sized fabrication with the desired resolution of 20–30 μm. However, the objects fabricated with RECILS hinder the confinement of electromagnetic waves. A promising solution is to coat the surface of RECILS-printed objects with metal, thus enabling wave confinement.

This paper presents a novel fabrication technique for waveguide devices in the 200–400 GHz range. Our method integrates smsHS fabrication using RECILS with metal plating on the surfaces of hollow structures and flanges, a process we refer to as RECILS WG Fabrication Technology (RECILS WGFT) [2].

Fig. 1 RECILS-printed straight waveguide for 200–400 GHz

Figure 1 depicts a waveguide printed using RECILS with standardized UG387 flanges. This straight waveguide has a cross-section of 0.86 × 0.43 mm^2 and measures 25.4 mm in length. Its hollow structure and flanges are coated with nickel (Ni) and copper (Cu). The measured insertion losses for these straight waveguides range from 0.5 to 0.8 dB per inch in the 200–400 GHz frequency band, comparable to those of bulk metal waveguides.

Bandpass filter (BPF) waveguide devices, fabricated using RECILS WGFT, incorporate five internal resonators interconnected by a cavity iris, as shown in Fig. 2(a), which presents an X-ray CT image.

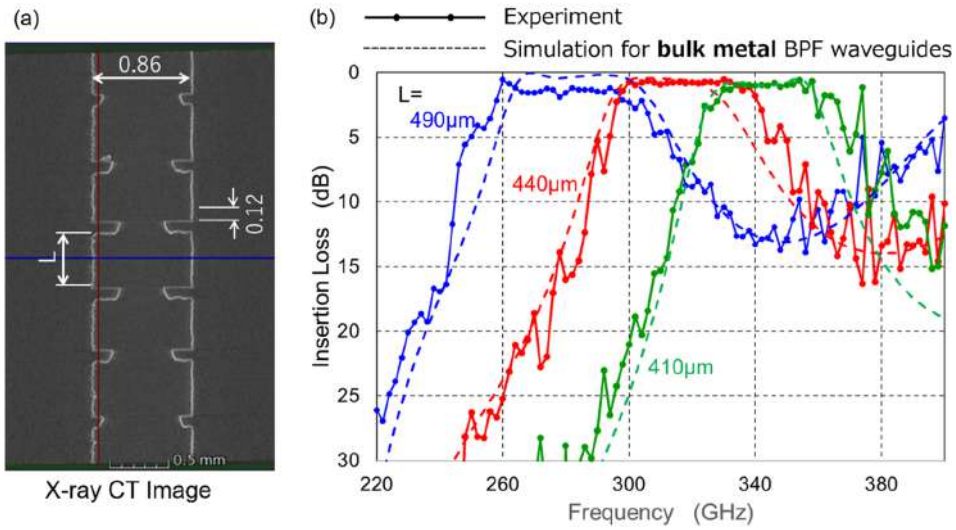

Fig. 2 (a) X-ray CT image of BPF waveguide. (b) Insertion loss of 3 BPF waveguides with L of 490 μm (blue), 440 μm (green), and 410 μm (green). Broken lines represent simulations assuming bulk metal BPF waveguides having the same structures.

Fig. 2(b) displays the performance characteristics of three BPFs with resonator lengths L of 410, 440, and 490 μm. The insertion loss in the passband and the extinction ratio were approximately 1 dB and over 30 dB, respectively.

Waveguide devices in the sub-THz band fabricated with RECILS WGFT demonstrate low-loss and lightweight properties, showing significant promise in this domain. The ability to produce twisted and bent waveguides further underscores the potential of this technology. Continued advancements are expected to usher in a new era of 3D integrated waveguide circuits in the sub-THz band.

References

1. Kentaro Soeda, Hirosuke Suzuki, Shuichi Yokobori, Kuniaki Konishi, Hiroharu Tamaru, Norikatsu Mio, Makoto Kuwata-Gonokami and Junji Yumoto, “RECILS: High Resolution and High-Speed SLA 3D Printer Using a Plane Building Platform and a Cylindrical Window”, Lasers in Manufacturing Conference 2021 Proceedings, https://wlt.de/sites/default/files/2021-10/system_technology_process_ control/Contribution_322.pdf.
2. Kentaro Soeda, Kazunori Naganuma, Yoshinori Yamaguchi, Kuniaki Konishi, Hiroharu Tamaru, Norikatsu Mio, Hiroshi Ito and Junji Yumoto, “3D-Printed Wave Guide for 220 GHz-325 GHz Band”, 47th International Conference on Infrared, Millimeter and Terahertz Waves (IRMMW-THz 2022), https://doi.org/10.1109/IRMMW-THz50927.2022.9895857.
3. Kentaro Soeda, Kazunori Naganuma, Yoshinori Yamaguchi, Kuniaki Konishi, Hiroharu Tamaru, Norikatsu Mio, Hiroshi Itoh and Junji Yumoto, “3D-Printed Wave Guide for 220 GHz-325 GHz Band”, SPIE Photonics West, Paper 12885-45, January 2024.

Real-time Spectroscopy Using Terahertz Parametric Generator and Detector

K. Murate*, S. Mine, and K. Kawase

Nagoya University, Chikusa-ku, Nagoya 464-8603, Japan
*corresponding author: murate@nuee.nagoya-u.ac.jp

Abstract: Simultaneous terahertz (THz) wave generation of up to 15 wavelengths from injection-seeded THz parametric generator (is-TPG) was achieved using Stokes beams, generated by cascade processes in a nonlinear optical crystal, as the pump and seed beams.

Our research group has been studying the injection-seeded terahertz (THz) wave parametric generator (is-TPG) with a wide dynamic range of 1–2 THz; this system has various applications including measurements through packaging materials for reagent identification[1]. Recently, we achieved real-time acquisition of fingerprint spectra of reagents using multiwavelength generation[2], pulse train generation[3], and rapid wavelength switching[4]. Moreover, simultaneous identification of reagents and high-speed imaging have been performed with this system by introducing machine learning[5]

However, multi-wavelength is-TPGs must match the number of external cavity laser diodes (ECLDs) for injection seeding with the number of THz wavelengths. Therefore, to date, these systems have been limited to about five wavelengths due to cost and control issues. In this study, instead of using a large number of ECDLs, we attempted to generate more than 10 wavelengths, which is sufficient for practical spectroscopy in the 1–2 THz regime, using a higher-order Stokes beam produced from MgO-doped $LiNbO_3$ crystals as pump and seed beams. Higher-order Stokes beams are generated at multiwavelengths due to a cascade process of parametric conversion when the $LiNbO_3$ crystal is pumped strongly[6, 7]. This eliminates the need for having the same number of seed lasers as the number of THz wavelengths and contributes significantly to system cost reduction.

The experimental setup is shown in Fig. 1. The pump was an amplified pulse beam from a microchip Nd:YAG laser (wavelength: 1064 nm; repetition rate: 20 Hz; pulse width: 575 ps; pulse energy: 60 mJ). The cascade process was efficiently initiated by injecting a pulsed seed beam together with the pump beam into two $LiNbO_3$ crystals for generating multi-wavelength Stokes beams. The pulsed seed was a Stokes beam generated from another $LiNbO_3$ crystal, which is omitted in Fig. 1. As illustrated in the upper part of Fig. 1, multiple higher-order Stokes and anti-Stokes beams were generated. These beams were guided to the crystal for THz-wave generation by a 4f optical system. Given that the beams from the two crystals must be placed in the same optical path, a half-mirror

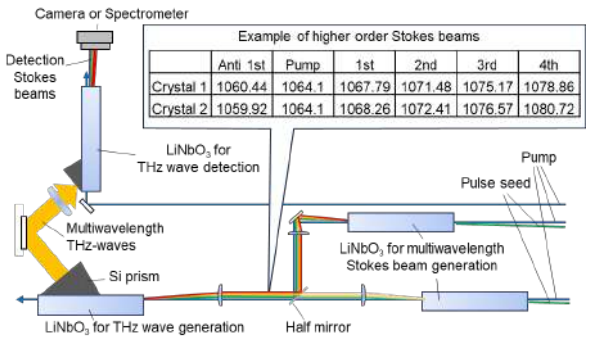

	Anti 1st	Pump	1st	2nd	3rd	4th
Crystal 1	1060.44	1064.1	1067.79	1071.48	1075.17	1078.86
Crystal 2	1059.92	1064.1	1068.26	1072.41	1076.57	1080.72

Figure 1. Experimental setup for multiwavelength THz-wave generation by optical mixing between two sets of higher order Stokes beams.

was inserted in the middle of the 4f optical system.

The generated THz-waves were up-converted to NIR detection Stokes beams by a THz parametric detector and were detected by a camera or a spectrometer. Here, THz parametric detection uses the inverse process of generation[1], in which the detection Stokes beam is generated at an angle that satisfies the non-collinear phase matching condition. Therefore, even if multiple wavelengths of THz-waves are injected at once, each wavelength is spatially separated[2].

Figures 2(a) and (b) show the results of camera and spectrometer observations of the detection Stokes beams, respectively. Fourteen wavelengths of THz-wave generation were observed in the range of 0.73–2.29 THz. These included frequencies in which first-order anti-Stokes radiation contributed to the generation, as well as frequencies that were thought to be generated by four-wave mixing of Stokes radiation inside $LiNbO_3$. Furthermore, when the spectrometer was set to a lower frequency range, 350 GHz generation was also observed, for a total of 15 wavelengths of THz-waves. The difference in intensity between the NIR camera and the spectrometer at some frequencies is thought to be due to the coupling efficiency of the spectrometer.

Finally, sample measurements were performed using this system. The results of the measurement of maltose pellets with 12-wavelength generation and with frequencies approximately aligned to the absorption line of the reagent are shown in Fig. 3. The upper panel of the figure shows the detection Stokes beams when no sample was inserted, the middle panel displays the detection Stokes beams when samples were inserted, and the lower panel is the absorption spectrum measured with THz-TDS. A decrease in the Stokes beam radiation consistent with each absorption line was observed. This measurement was realized at a laser repetition rate of 20 Hz, which means that the reagent information was obtained in real time.

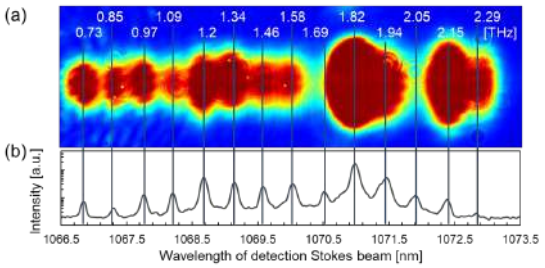

Figure 2. Simultaneous generation of 14 wavelengths of THz-waves. Up-converted detection Stokes beams measured by (a) a camera and (b) a spectrometer.

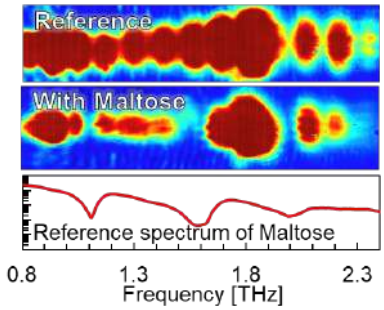

Figure.3 Real-time measurement result with maltose insertion.

Acknowledgements This work was partially supported by Japan Science and Technology Agency (JST) ASPIRE Program (JPMJAP2340) and FOREST Program (JPMJFR212J), Japan Society for the Promotion of Science KAKENHI (22J20963).

References

1. K. Murate, S. Mine, and K. Kawase, “Terahertz Parametric Generators and Detectors for Nondestructive Testing Through High-Attenuation Packaging Materials,” IEEE J. Sel. Top. Quantum Electron., vol. 29, 8500813, 2023.
2. K. Murate, S. Hayashi, and K. Kawase, "Multiwavelength terahertz-wave parametric generator for one-pulse spectroscopy," Appl. Phys. Express, vol. 10, 032401, 2017.
3. K. Murate, R. Kawaguchi, S. Hayashi, and K. Kawase, “Pulse Burst Multiwavelength Terahertz-Wave Spectroscopic Measurement Using Parametric Wavelength Conversion,” IEEE Trans. Terahertz Sci. Technol., vol. 13, 561–564, 2023.
4. S. Mine, K. Kawase, and K. Murate, “Real-time wide dynamic range spectrometer using a rapidly wavelength-switchable terahertz parametric source,” Opt. Lett., vol. 46, 2618-2621, 2021.
5. K. Murate, S. Mine, Y. Torii, H. Inoue, and K. Kawase, “Wide dynamic range and real-time reagent identification and imaging using multi-wavelength terahertz parametric generation and machine learning,” Sci. Rep., vol. 13, 12743, 2023.
6. S. Mine, K. Kawase, and K. Murate, “Cascaded Terahertz Parametric Generation Under Noncollinear Phase-Matching Condition,” J. Infrared Milli. Terahz Waves, vol. 45, 116–123, 2024.
7. R. Zhang et al., “Widely Tunable Terahertz-Wave Parametric Oscillator with a Shallow Surface Cross-pump Configuration,” J. Infrared Milli. Terahz Waves, vol. 42, pp. 851–862, 2021.

AES 2024, ROME - ITALY, 25 –28 JUNE 2024

Photonics-based millimeter- and THz wave visualization and its applications

S. Hisatake*

Gifu University, Japan
*corresponding author: hisatake.shintaro.f4@f.gifu-u.ac.jp

Abstract: We are developing a photonics-based system that measures the spatial distribution of the amplitude and phase of electric fields, visualizing fields from 100 MHz to 600 GHz. In this paper, we describe the principle and characteristics of this system and its application to antenna characterization, millimeter-wave EMC, THz imaging, etc.

Millimeter-wave (30 GHz-300 GHz) and terahertz wave (100 GHz-10 THz) frequencies are anticipated to play critical roles not only in next-generation high-capacity wireless communications but also in a variety of applications including radar and imaging. In such high-frequency domains, the spatial characteristics of the beam assume a significance not seen in the microwave band. There is a pressing need for technology capable of visualizing the spatial distribution of the amplitude and phase of the electric field with minimal perturbation to the field being tested. We are developing a technology based on photonics that visualizes the spatial distribution of the amplitude and phase of electric fields across a wide bandwidth [1, 2]. Our measurement technique employs an electro-optic (EO) probe equipped with an electro-optic crystal at the tip of an optical fiber, which, due to its lack of metal components, enables measurements with very low disturbance. The generation and detection of RF signals utilize a beat signal from two free-running lasers, which represents a second major feature of broad bandwidth [3]. In the presentation, we will describe the principle and characteristics of this system and its application to antenna characterization, millimeter-wave EMC, THz imaging, etc. Figure 1 shows examples of the applications of the visualization technique. By moving the EO probe in front of the high-gain Cassegrain antenna, the amplitude and phase distributions were visualized. Radiation patterns of the antenna can be calculated from the measured near-field distribution. Figure 1 also shows the visualization of the leaky wave of the flexible waveguide at 70 GHz.

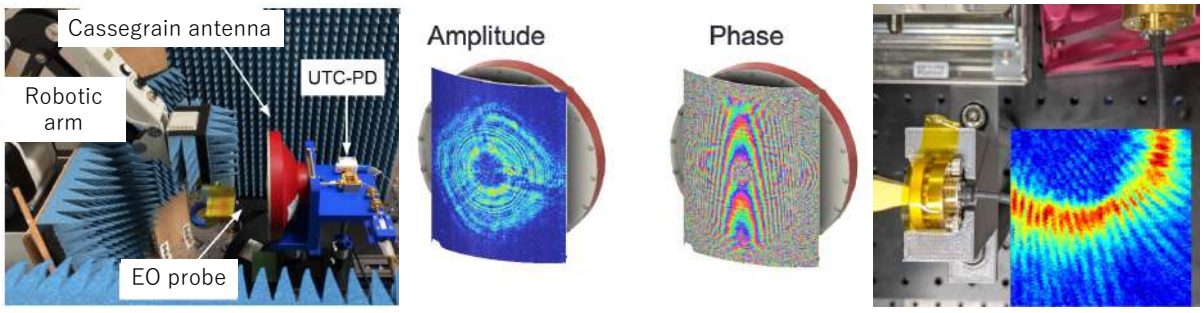

Figure 1. Applications of the visualization technique.

This work has been partly supported by Japan Science and Technology Agency (JST) as part of Adopting Sustainable Partnerships for Innovative Research Ecosystem (ASPIRE), Grant Number JPMJAP2324, commissioned research (JPJ012368C04301) by National Institute of Information and Communications Technology (NICT), Japan, and "R&D of high-speed THz communication based on radio and optical direct conversion" (JPJ000254) made with the Ministry of Internal Affairs and Communications of Japan.

References

1. S. Hisatake and T. Nagatsuma, "Nonpolarimetric technique for homodyne-type electrooptic field detection", Appl. Phys. Exp., vol. 5, no. 1, 2011.
2. S. Hisatake, H. H. N. Pham, and T. Nagatsuma, "Visualization of the spatial–temporal evolution of continuous electromagnetic waves in the terahertz range based on photonics technology," Optica 1, 365-371, 2014.
3. S. Hisatake, “Millimeter-Wave and THz-Wave Visualization,” in Handbook of Radio and Optical Networks Convergence. Springer, Singapore. https://doi.org/10.1007/978-981-33-4999-5_31-1, 2023.

AES 2024, ROME - ITALY, 25 –28 JUNE 2024

Advances in ultrafast terahertz scanning tunneling microscopy

F. A. Hegmann*

Department of Physics, University of Alberta, Edmonton, Alberta T6G 2E1, Canada
*corresponding author: hegmann@ualberta.ca

Abstract: Probing ultrafast phenomena on the nanoscale is essential to our understanding of excitation dynamics in materials. Terahertz scanning tunneling microscopy (THz-STM) is a powerful technique that can image sub-picosecond dynamics in materials at the atomic scale. This talk will discuss recent advances, current challenges, and future directions of THz-STM.

The ability to directly probe ultrafast phenomena on the nanoscale is essential to our understanding of excitation dynamics in materials and in the development of new device technologies. However, achieving this capability has been challenging and is the focus of research in many labs around the world. Terahertz scanning tunneling microscopy, or THz-STM, is a powerful new technique that enables direct imaging of sub-picosecond dynamics in materials down to the atomic scale. In this technique, picosecond-duration THz pulses are antenna-coupled to the sharp metal tip of an STM, and the resulting field enhancement at the junction produces sub-picosecond transient tunnel currents that can be used to probe ultrafast dynamics on the nanoscale [1-36].

THz-STM was first demonstrated by Cocker *et al.* [1], showing the photoexcitation dynamics in a single InAs nanodot with simultaneous 0.5 ps time resolution and 2 nm spatial resolution under ambient conditions. Operation in ultrahigh vacuum allows for THz-pulse-induced tunnel currents confined to single atoms, as reported for THz-STM of silicon surfaces [2] and single pentacene molecules [3]. THz-STM has recently been used to study metal surfaces [4], graphene nanoribbons [5], 2H-$MoTe_2$ and Bi_2Se_3 [6], C60 films [7], applying localized forces to single molecules [8], inducing luminescence in materials [9], probing the dynamics of single vacancies in WSe_2 [10], and THz wave rectification and molecular coherent oscillations [11,12]. Much work has focused on characterizing the near-field waveform [13-21], coherent control of tunnel currents [2,6,16,17,22], modeling the THz-STM signal [2,4,19], increasing bandwidth [18] and efficiency [23], increasing the THz pulse source repetition rate [23,24], studying thermal and nonthermal tunneling effects [25,26], and achieving attosecond time resolution [27,28]. There have also been several THz-STM review articles [29-36].

This talk will discuss how THz-STM works and how it can provide new insight into ultrafast nanoscale dynamics of materials and devices. Recent advances, current challenges, and future directions will also be discussed.

Funding support from NSERC, CFI, Alberta Innovates, and ATUMS is acknowledged.

References

1. T. L. Cocker, V. Jelic, M. Gupta, S. J. Molesky, J. A. J. Burgess, G. De Los Reyes, L. V. Titova, Y. Y. Tsui, M. R. Freeman, and F. A. Hegmann, Nat. Photon. 7, 620 (2013).

2. V. Jelic, *et al.*, Nat. Phys. 13, 591 (2017).

3. T. L. Cocker, *et al.*, Nature 539, 263 (2016).

4. Y. Luo, V. Jelic, *et al.*, Phys. Rev. B 102, 205417 (2020).
5. S. E. Ammerman, *et al.*, Nat. Commun. 12, 6794 (2021).
6. S. Yoshida, *et al.*, ACS Photonics 6, 1356 (2019).
7. S. Yoshida, *et al.*, ACS Photonics 8, 315 (2021).
8. D. Peller, *et al.*, Nature 585, 58 (2020).
9. K. Kimura, *et al.*, ACS Photonics 8, 982 (2021).
10. C. Roelcke, *et al.*, Nat. Photon. (2024); doi.org/10.1038/s41566-024-01390-6
11. S. Chen, *et al.*, Nano Lett. 23, 2915 (2023).
12. Y. Xia, *et al*., Phys. Rev. Lett. 132, 076903 (2024).
13. P. H. Nguyen, *et al.*, Phys. Can. 71, 157 (2015).
14. D. Peller, *et al.*, Nat. Photon. 15, 143 (2021).
15. J. Takeda and I. Katayama, Nat. Photon. 15, 70 (2021).
16. K. Yoshioka, *et al.*, Nat. Photon. 10, 762 (2016).
17. K. Yoshioka, *et al.*, Nano Lett. 18, 5198 (2018).
18. M. Müller, *et al.*, ACS Photonics 7, 2046 (2020).
19. S. E. Ammerman, *et al*., Phys. Rev. B 105, 115427 (2022).
20. H. Li, *et al.*, ACS Photonics (2024); doi.org/10.1021/acsphotonics.3c01451
21. V. Jelic, *et al*., arXiv:2310.14335 [cond-mat.mes-hall]
22. J. Allerback, *et al*., ACS Photon. 10, 3888 (2023).
23. M. Abdo, *et al*., ACS Photonics 8, 702 (2021).
24. H. Azazoglu, *et al*., Rev. Sci. Instrum. 95, 023703 (2024).
25. N. M. Sabanés, *et al*., ACS Nano 16, 14479 (2022).
26. H. Azazoglu, *et al*., Surf. Sci. 743, 122465 (2024).
27. M. Garg and K. Kern, Science 367, 411 (2020).
28. M. Garg, *et al*., Nat. Photon. 16, 196 (2022).
29. T. L. Cocker, V. Jelic, R. Hillenbrand, and F. A. Hegmann, Nat. Photon. 15, 558 (2021).
30. T. L. Cocker and F. A Hegmann, in J Lloyd-Hughes, *et al*., "The 2021 ultrafast spectroscopic probes of condensed matter roadmap", Journal of Physics: Condensed Matter 33, 353001 (2021).
31. T. Tachizaki, *et al*., APL Mater. 9, 060903 (2021).
32. R. Gutzler, *et al*., Nat. Rev. Phys. 3, 441 (2021).
33. M. Peplow, Nature 544, 408 (2017).
34. Y. Tian, *et al*., Surf. Rev. Lett. 25, 1841003 (2018).
35. M. Müller, Prog. Surf. Sci. 99, 100727 (2024).
36. I. Katayama, *et al.*, J. Appl. Phys. 133, 110903 (2023).

Analytical, Computational and numerical techniques

AES 2024, ROME - ITALY, 25 –28 JUNE 2024

Shortened Conical Horn Antennas Loaded by Lenses

***J. M. Gil[1], M. A. González[1], R. Gómez[2], J. Rubio[2], J. García[1].**

[1]Signals, Systems and Radio Communications Department, Information Processing and Telecommunication Center, Universidad Politécnica de Madrid, Spain
[2]Computers and Communications Technology Department, Universidad de Extremadura, Spain
[*]corresponding author: josemaria.gil@upm.es

Abstract: At this work we present a procedure of designing ultra-short conical horns corrected by single and double lenses for wireless communication systems. We show some compact and shortened prototypes at 60 GHz, achieving a reasonable directivity and radiation parameters as well as low return losses within a broad bandwidth.

SUMMARY

The design of small cheap compact antennas has a relevant interest in order to be included in ultra-high speed communication systems for wireless applications. The task of such antennas is to link the transceivers in the network. Conical horns antennas are some good candidates for these systems. They have a remarkable radiation performance as high directivity, low cross polar level and symmetric patterns with low return losses over a wide bandwidth. However, they are devices very long and weighed, so they are not adequate to be integrated in such systems. When we shorten or make more compact antennas the phase diagram results deteriorated at the aperture. However, the use of dielectric cores and lenses can compensate and repair the phase distribution avoiding the worsening of the performance of the antenna. On the other hand, the increase of the weight due to the lenses becomes acceptable for many.

To achieve this goal, we need a full-wave robust method, reliable and with a low computational cost in order to design competitive optimized designs. At the present work, we use a technique based on finite elements applied to bodies of revolution (BoR-FEM), by closing the problem by means of an expansion of spherical modes (SM) which surround the antenna (BoR-FEM-SM). This approach has been used for our group for many years due [1], [2].

This method explotes the axial symmetry of conical antennas demanding only bidimensional meshes what are compatible with full-wave problems presenting a very low computational cost; it is worth to noting that the more used commercial codes which cope with multi-dielectric structures do not offer this tool.

The use of additive techniques of manufacture, like 3D printing and the metallization of the external dielectric layer constitutes also an interesting option to get components at these frequencies.

Though several authors have published some studies about shortened conical horns, lens-corrected, [3], [4], [5], [6], or meta-horns [7], we add some new results to these lines of design. At [8], a preliminary work of this issue was presented.

Acknowledgements: This work was partially supported by the Ministerio de Ciencia e Innovación (MCIN/AEI/10.13039/501100011033 / FEDER, UE) under project PID2021-122856NB-C22

References

1. J. M. Gil, J. Monge, J. Rubio, and J. Zapata, “A CAD-Oriented method to analyse and design radiating structures based on bodies of revolution by using finite elements and generalized scattering matrix”, IEEE Trans. Antennas and Propagation, vol. 54, pp. 899-907, March 2006.

2. José Martínez-Fernández, José M. Gil, and Juan Zapata, Ultrawideband Optimized Profile Monopole Antenna by Means of Simulated Annealing Algorithm and the Finite Element Method, Member, IEEE Transactions on antennas and propagation, VOL. 55, NO. 6, June 2007.

3. E. L. Holzman, “A Highly Compact 60-GHz Lens.Corrected Conical Horn Antenna”, IEEE Antennas and Wireless Propagation Letters, Vol. 3, pp. 280-282, 2004.

4. M. Shaik and T. Rama, “Concave Lens Integrated Conical Horn at 60 GHz for Energy Efficient Wireless Applications”, International Conference on Advances in Computing, Communications and Informatics (ICACCI), Mysore, India, August 2013.

5. A. Rolland, M. Ettorre, M’Hamed Drissi, L. Le Coq, and R. Sauleau, “Optimization of Reduced-Size Smooth-Walled Conical Horns BoR-FDTD and Genetic Algorithm”, IEEE Trans. Antennas and Propagation, vol. 58, No. 9, pp. 3094-3100, September 2010.

6. D. Wu, Z. Feng and X. Zhuang, “A Novel Focusing Conical Horn Antenna Loaded with Dielectric”, IEEE International Wireless Symposium, Shenzen, China, April 2015.

7. D. Ramaccia, F. Scattone, F. Bilotti, and A. Toscano, Broadband Compact Horn Antennas by Using EPS-ENZ Metamaterial Lens, IEEE Transactions On Antennas And Propagation, Vol. 61, No. 6, June 2013.

8. J. M. Gil, *“*Compact Shortened V-Band Conical Dielectric Core Horns Corrected by Lenses*”,* Radio Science, Vo. 57, No. 11, November 2022.

The Impact of 5G on Human Health

Yahya Salameh Hassan Khraisat

Electrical and Electronics Engineering
(Al Balqa Applied University)
Irbid, Jordan

*corresponding author, E-mail: yahya_khr@bau.edu.jo

Abstract

With the introduction of 5G, data transmission speeds in wireless mobile technologies have dramatically risen. On the other hand, it has put society in jeopardy due to the problems that surfaced throughout its execution. This essay was written because many people believe that 5G radiation is now the primary cause of cancer. I investigated the extent to which biological tissue (DNA) is absorbed and penetrated by the 5G electromagnetic energy pattern. The vast quantity of data that can be transferred in a short amount of time throughput (data speed measured in megabits per second) and the blazingly quick transmission delay (latency) are two important characteristics of 5G technology (Fifth Generation of Telecommunication). People have been using electromagnetic fields (EMFs) for communication and broadcasting for decades. At the moment, 700 MHz or lower frequencies are used for digital television. Low-frequency (800, 900 MHz) technologies were also used by earlier (yet still in use) technologies such as 2G, 3G, 4G, and 4G+. Both high- and low-frequency signals will be used in 5G. The low band (700 MHz) and the high band (800 MHz) (3.5 GHz) are the two bands that 5G will primarily use to operate. Mm Wave bands above 6 GHz will be employed in the near future. (24 GHz, 28 GHz, and higher are some examples). Theoretical models and actual findings agree that the real maximum power of a Massive-MIMO antenna is always less than 25% of the maximum peak power.

Keywords—5G, Human Health, Impact, Ionized, Non Ionized, Specific Absorption Rate.

1. Introduction

The need for internet data access has led to a steady rise in the use of mobile wireless devices. 5th generation mobile wireless technology was developed in response to the need for more dependable and quick data access. This is accurate since, in comparison to existing mobile wireless technologies, 5G employs radio waves to carry data more swiftly. The non-ionizing portion of the electromagnetic spectrum is where 5G mobile wireless network technology is located, as depicted in figure 1 [1].

5G is being developed to increase data delivery latency, user data speeds, mobile data capacity per area, and the amount of wireless devices that can be linked. Regarding network connectivity and data transmission speed, 5G technology is more dependable and broadly applicable than existing mobile wireless technologies [2]. Although 5G provides many solutions, its widespread use has led to a number of problems that have made it perceived as a threat to human life. Concerns regarding the safety of human health are also raised by the proliferation of 5G wireless broadband technology, which has a lower radio frequency and the smallest wavelength [3]. Although several health problems have been linked to 5G, this has not been demonstrated.

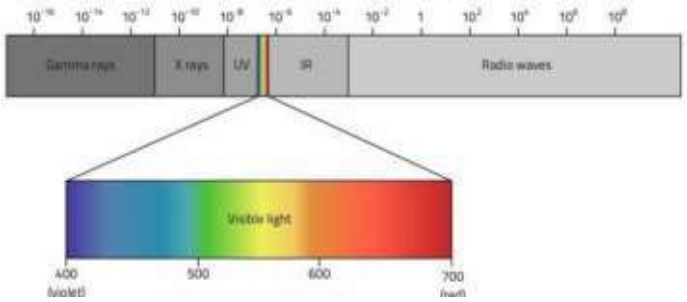

Figure 1: Electromagnetic Spectrum

Nevertheless, once rats exposed to microwave radiation began to exhibit different behaviors, the Federal Communication Commission (FCC) set exposure limits in 1990. The exposure limit was set in order to protect individuals from the dangers of short-term heating caused by radiofrequency radiation (RFR) [4].

Let's look at the radio frequency's wavelength, frequency, and position within the electromagnetic spectrum, as depicted in figure 1. Higher frequency electromagnetic radiation, or ionizing radiation, is what x-rays and gamma rays are. Nonionizing radiation (ELF) includes light ultraviolet (UV), infrared (IR), microwave (MW), radio frequency (RF), and very low frequency (VLF). The electromagnetic spectrum is seen in figure 1.

Early research indicates that MMW increases skin temperature, alters gene expression, promotes cellular proliferation and protein synthesis related to metabolic, inflammatory, and oxidative stress processes, may be harmful to the eyes, and interferes with neuromuscular dynamics. More research is necessary to fully understand and assess the impacts of MMW in particular and RF-EMF in general on health. But it seems like there is enough data to support biological consequences, apply the cautious principle, identify exposed individuals as potentially vulnerable, and modify current restrictions. A thorough understanding of the pathophysiological mechanisms

linking exposure to radiofrequency electromagnetic fields (RF-EMF) to health risk should also guide modern clinical practice, especially in light of growing epidemiological data and studies demonstrating the significant role extrinsic factors play in cancer risk, indication that no infectious diseases are spreading [5].

I.1 Objectives of this paper

The paper primary goal is to determine the effect of radiation from fifth-generation networks on human health by comparing the rate at which the human body absorbs radiation from neighboring networks to that rate. For human details, we will create a number of algorithms that will be represented in two layers of neural networks. Examination of the electromagnetic radiation that 5G technology generates. The 5G absorption rate into biological tissue will be determined by a machine learning technique built on artificial neural networks.

I.2 Literature Review

It is projected that machine learning (ML) and artificial intelligence (AI) will play major roles in 5G networks. For network operators, efficient radio resource management is essential. The use of substantial radio resources to forecast channel conditions in mobile networks has grown troublesome with the introduction of more contemporary technologies, techniques, and strategies. The process of predicting channel conditions can be automated to optimize resource usage. Ruzat et al. developed and assessed a machine learning-based technique for signal prediction to interference and noise ratio in mobile networks, which uses less radio resources. The study article focused only on managing radio resources and did not address the impact of radio radiation on human health. To anticipate SINR (Signal-to-Interference-and-Noise-Ratio), a machine learning-based method known as an Artificial Neural Network (ANN) is used in mobile networks to conserve radio resources. The majority of radio resource scheduling is done using sounding reference signals and estimated channel conditions, such as SINR (SRS). While preserving $R = 0.87$ accuracy, the proposed Non-Linear Auto-Regressive External/Exogenous (NARX)-based ANN seeks to decrease the rate of delivering SRS. Up to 4% of the spectrum can be saved in this way, increasing bandwidth effectiveness and reducing uplink power consumption. Search in Full Text [6].

Natalia et al. looked into the use of network slicing to deliver quality of service for various communication services across a shared network infrastructure. Network slicing was examined in the study, but no relation between electromagnetic radiation and human health was mentioned. Conducted a thorough assessment of the research on how deep learning is being utilized to get around various 5G challenges. The problem is that, in contrast to the recommended approach, the effort was primarily focused on reviewing work and provided no solutions to the identified problems with 5G technology [7].

Vila et al. looked at the relationship between RF and IF EMF exposure at work and the prevalence of brain cancers. The results suggest that exposure to RF electric and magnetic fields may contribute to the emergence and progression of brain tumors and warrant additional research. The research's weakness is that it is ambiguous and just considers the brain [8].

Verma looked at the negative effects of 5G radiation on a number of areas, including health, the environment, privacy, and thermal repercussions. The research has a weakness because it only performed a review exercise and didn't implement any fixes for the issues that were found [9]. The amount of scholarly literature on the impacts of 5G exposure in particular and EMF exposure in general is expanding quickly. Significant health hazards are supported by some research, but not by others. In 2011, the World Health Organization (WHO) and the International Agency for Research on Cancer (IARC) categorized electromagnetic fields with radiofrequency (EMF) as potentially carcinogenic to humans. Priority for EMF radiation evaluation has just been assigned by the IARC for the years 2020–2024 [10]. A growing number of scientists (as of December 18, 2019), including doctors and medical specialists, have signed an appeal against electromagnetic field (EMF) exposure, which they claim will worsen with the rollout of 5GA. The 5GA appeal was presented to the UN in 2015 and the EU in 2017, and as time goes on, more and more scientists will sign it. The signatories claim that due to the massive number of 5G transmitters—an estimated 10 to 20 billion connections—no one will be able to avoid exposure to continuous electromagnetic fields (EMF radiation) from self-driving cars, buses, surveillance cameras, home appliances, and other sources as wireless technology becomes more widely used [11]. According to the appeal, a plethora of scientific research have demonstrated the deleterious effects of electromagnetic field exposure, such as an elevated risk of cancer, genetic damage, learning and memory problems, neurological diseases, and more. The argument goes on to say that in addition to humans, the environment is also damaged.

Some experts believe that in this case, new exposure limits should be established to account for the unique aspects of exposure. Instead of choosing certain absorption rates based on energy, such limitations should be determined by the biological impacts of electromagnetic fields [12]. Because of its low potency, non-ionizing radiation from sources like mobile phones and 5G is commonly believed to be harmless. In the case of 5G, some of the scientists previously mentioned argue that the frequency to which everyone would be exposed due to the vast network of antennae and the predicted billions of simultaneous connections is the pulse 15.

Because 5G uses such a high level of pulsation, the goal of the technology is to achieve higher levels of pulsation by

utilizing higher frequencies that allow for such high levels of pulsation [13]. An analysis conducted in 2018 of more recently published, peer-reviewed publications on the physiological and biological consequences of radiofrequency electromagnetic fields—including 5G—supports the evidence already available on the effects of millimeter waves.

The review concludes that there is increasing evidence of the biological effects of radiofrequency electromagnetic fields (EMFs), even though some of the evidence is still preliminary or controversial. This suggests that high-frequency EMF may interact with biological systems on multiple levels and may have both oncological and non-oncological effects (mainly reproductive, metabolic, neurological, and microbiological). Additionally, the research indicates that the huge and growing density of wireless devices and antennas is causing major issues. In light of this, "...an international action plan for the construction of 5G networks has begun, with a forthcoming increase in devices and tiny cell density, as well as the future usage of millimeter waves, despite the biological impacts of 5G communication systems receiving very little attention." Conversely, millimeter waves have been shown to raise skin temperature, encourage cell proliferation, and quicken metabolic and inflammatory processes. According to the study's findings, more research is necessary to provide a more accurate and objective evaluation of the impacts of radiofrequency electromagnetic fields—or EMF—in general and millimeter waves in particular on human health.

II. NEW 5G BAND IN MM WAVE AND HEALTH

The public has strong opinions about the use of millimeter Wave bands (greater than 3.5 GHz). This is due to the fact that communications have never before used these frequencies. The biological consequences of mm-Waves have, in fact, been studied in the past, although not in relation to communications. According to reports, there were no harmful health effects in daily life when the safety standards were met. By 2024, the WHO hopes to have finished its evaluation of health concerns pertaining to radiofrequency radiation, including millimeter-waves [14]. The initial deployment of millimeter-wave base stations will be limited to high-data-traffic areas like airports, stadiums, and retail centers. The antennas will have a very low power output and be tiny (micro). As previously stated, these bands (high capacity) will only be utilized by short-range applications that require high speed rates. They won't be utilized inside of homes or other buildings, where 5G coverage is needed. Furthermore, they have a restricted ability to penetrate (high field attenuation). Sub-6 GHz frequencies (3.5 GHz and 700 MHz) will be used for 5G implementation most of the time [15].

III. Results

In simultaneous 4G or 3G network systems, the results of measuring human EMF exposure using PD and SAR in downlinks have been achieved. Umi and Uma are the two alternatives, as was previously mentioned. In two scenarios, 5G network effects are similar: According to the ISD, Umi reaches the summit after 100 meters, Uma reache the top after 250 meters due to its 500 m ISD, and the same is true for 4G and 3G. Figure 2 shows the results I obtained compared by results obtained by other authors.

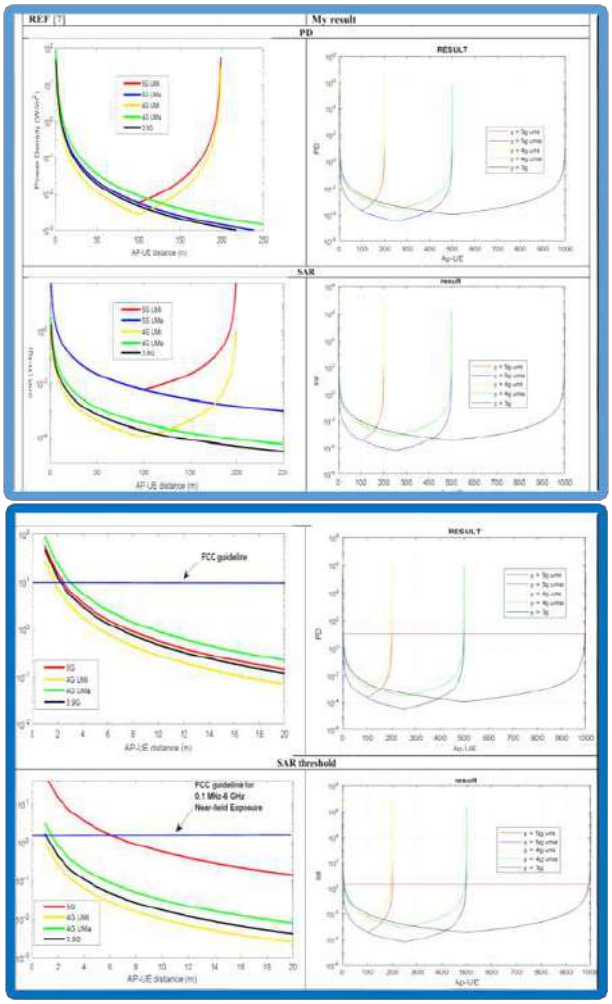

Figure 2. Comparison between others and my results.

Second, to ascertain which tissues are more affected by these specific frequencies, SAR and PD have been used for over 40 tissues at different frequencies. We discovered from the simulation that the PD technique had no adverse effects and produced the same outcome. According to alteration in response to frequency variations in the SAR, Different frequencies on Different Tissues, the most impacted breast fat levels are often the higher ones. Because of its 200-meter ISD, the consequences are the same in all circumstance. It comes back up to the peak at 100 meters. Figure 3 shows Tissues effect at 40 GHz, 20 GHz and 100 GHz.

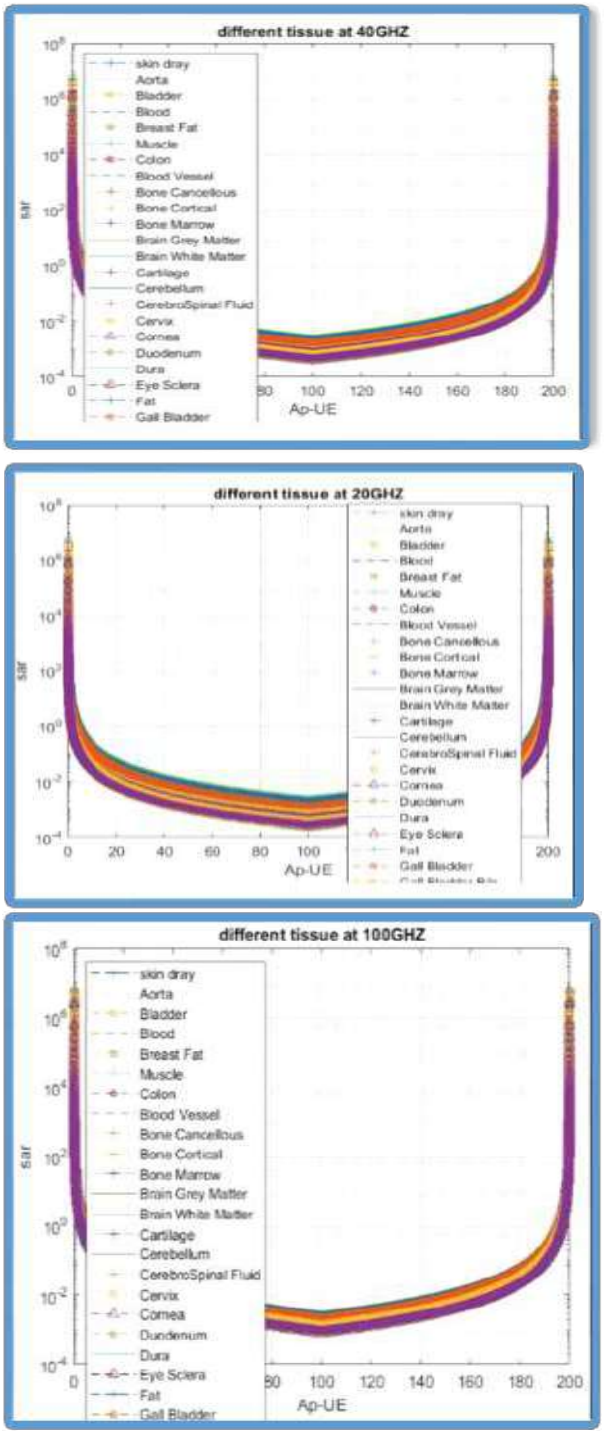

Figure 3. Tissues effect at 40 GHz, 20 GHz and 100 GHz

Figures 4 and 5 demonstrate the effect on tissues at 20 GHZ and 100 GHz

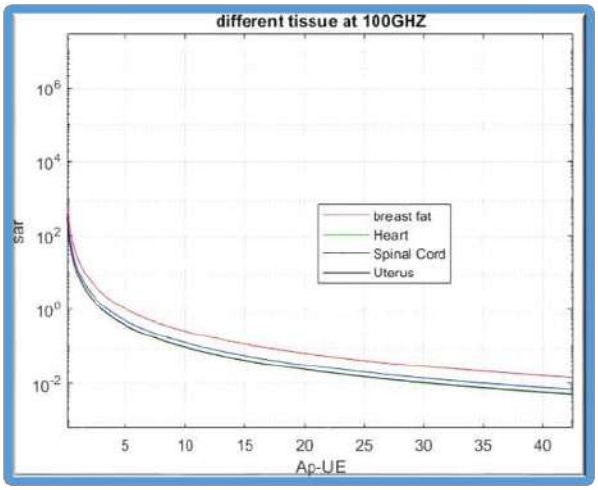

Figure 4. Tissues are not affected by zoom at 20 GHz

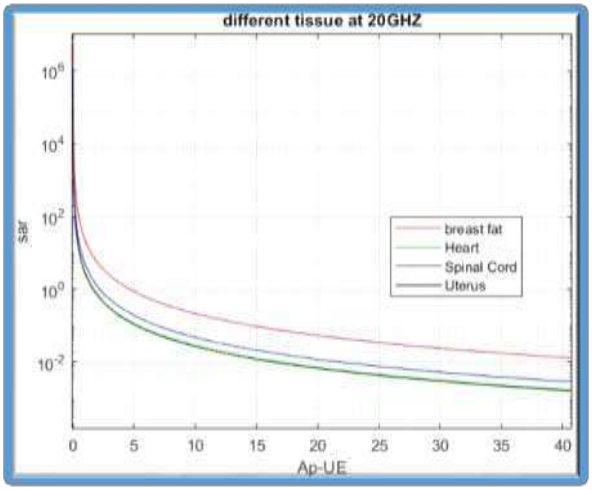

Figure 5. Tissues are not affected by zoom 100GHZ

Four categories are used to categorize tissues: Epithelial tissue refers to the cell sheets that coat the outside of the body. Connective tissue between the bones. It binds and safeguards the organs and cells that make up the body. The parts of the body are all interconnected and supported. Excitable muscle tissue that reacts to stimulation by contracting, to simulate movement. In order to produce the excitability of tissues that contain nerves also enables the transmission of electrochemical signals as nerve impulses from one area of the body to another. 53 body tissues were selected for this study's evaluation, and they were divided into different groups for the purpose of simulation.

III.1 The impact on various frequencies of tissues:

Breast fat, uterine muscle, spinal column nerves, and connective tissue in the heart. The selected frequencies have the greatest impact on breast fat in epithelial tissue. Furthermore, neural tissue is less influenced by the selected frequencies than epithelial tissue, as can be seen in the table

below.
Group 1:

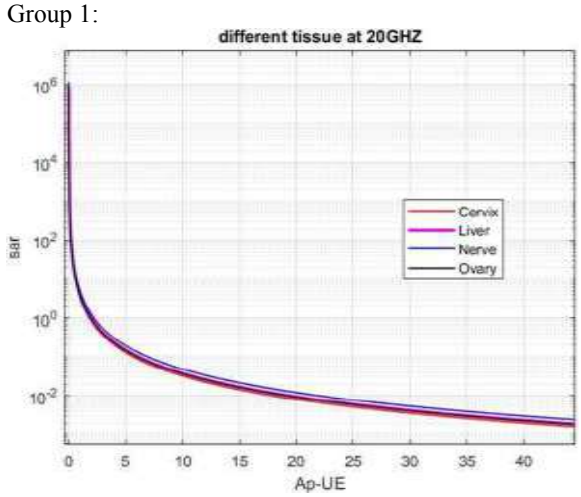

Figure 6: zoom out of the 20 GHz effect on tissues

The nerve is the tissue most impacted by the selected frequencies; as the table illustrates, nerve tissue is more effective than connective tissue.
The gallbladder is epithelial tissue, whereas the kidney is a connective tissue. Muscular and brain white matter both Contain nerve tissue.

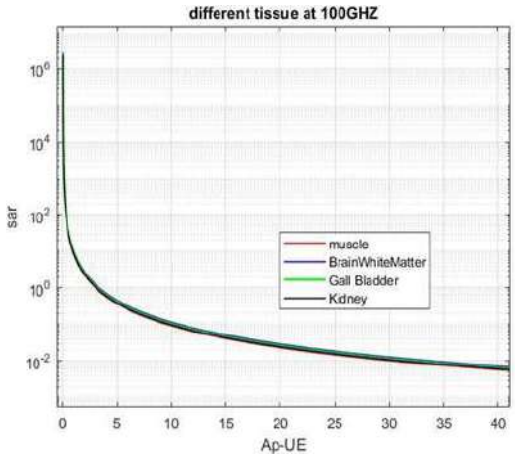

Figure 7: At 100 GHz, zoom out of the effect (group 3)

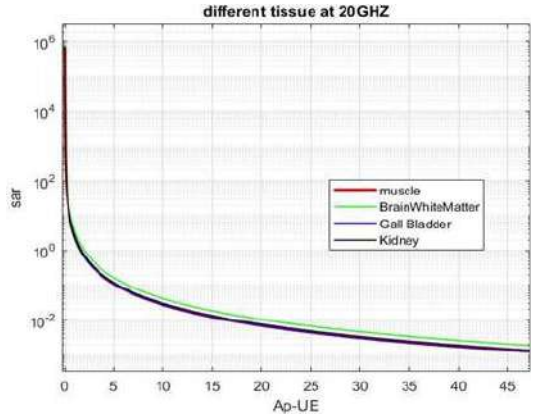

Figure 8: expand the view of the 20 GHz tissue effect

Table 1. Impact on the first tissue group

20GHZ	White matter in the brain			kidney
muscle	Gall bladder			
30 GHZ	White matter in the brain			kidney
bladder	gallstones		muscle	
40GHZ	White matter in the brain			kidney
bladder	gallstones		muscle	
60 GHZ	Brain white			
matter	bladder gallstones			kidney
muscle				
70 GHZ	Brain white			
matter	Gall bladder	kidney	muscle	
80GHZ	Brain			
white matter	Gall bladder	kidney	muscle	
100GHZ	Brain			
white matter	Gall bladder	kidney	muscle	

Table 2: Tissue parameters

Frequencies	Parameter	Tissue		
	Cerebellum	Pancreases		Gland
Duodenum				
20GHz	Conductivity	20.884	27.177	
27.177	29.735			
	Permittivity	24.444	31.597	31.597
34.123				
30GHz	Conductivity	28.947	38.115	
38.115	41.672			
	Permittivity	18.221	23.185	23.185
24.94				
40GHz	Conductivity	34.487	45.62	45.62
49.863				
	Permittivity	14.452	18.079	18.079
19.368				
60GHz	Conductivity	41.348	54.885	
54.885	59.975			
	Permittivity	10.448	12.656	12.656
13.449				
70GHz	Conductivity	43.613	57.933	
57.933	63.302			
	Permittivity	9.3166	11.125	11.125
11.778				
80GHz	Conductivity	45.43	60.37	60.37
65.964				
	Permittivity	8.489	10.006	10.006
10.557				
100GHz	Conductivity	48.194	64.066	
64.066	69.999			
	Permittivity	7.3768	8.5046	8.5046
8.918				

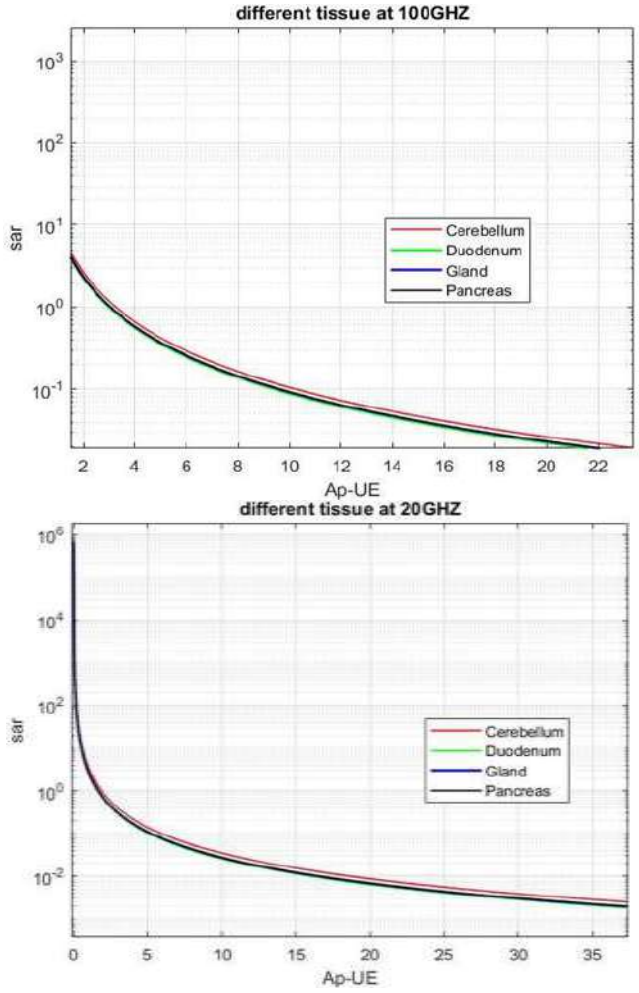

Figure 9: Zoom out of 100 GHz and 20 GHz effects on tissues (group 4)

The chosen frequencies have the greatest impact on the cerebellum, as shown in the table, whereas nerve tissue has the least impact (10).

III.2 Group3:

Stomach muscle tissue, prostate epithelial tissue, testicular connective tissue, and brain nerve tissue's gray matter.

Table 3: tissue parameter

Frequencies	Parameter	Tissue			
	Brain gray Matter	Prostate	Testis	stomach	
20GHz	Conductivity	22.732	27.447	27.447	29.735
	Permittivity	26.834	31.649	31.649	34.123
30GHz	Conductivity	31.755	38.4	38.4	41.672
	Permittivity	19.881	23.221	23.221	24.94
40GHz	Conductivity	37.952	45.916	49.863	
	Permittivity	15.666	18.107	18.107	19.368
60GHz	Conductivity	45.617	55.198	55.198	59.975
	Permittivity	11.188	12.675	12.675	13.449
70GHz	Conductivity	48.144	58.252	58.252	63.302
	Permittivity	9.9235	11.142	11.142	11.778
80GHz	Conductivity	50.169	60.695	60.695	65.964
	Permittivity	8.9985	10.021	10.021	10.557
100GHz	Conductivity	53.246	64.401	64.401	69.999
	Permittivity	7.7561	8.517	8.517	8.918

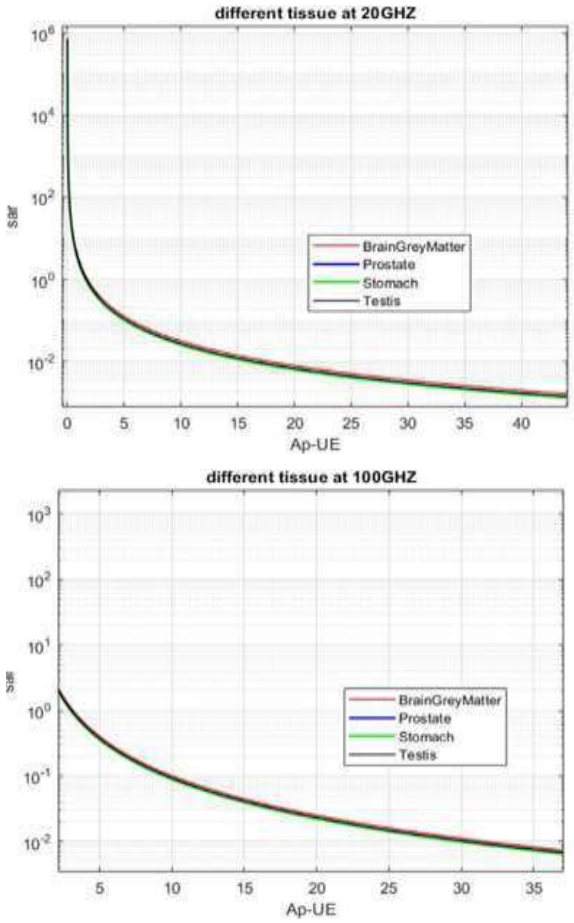

Figure 10: Zoom out of 20 GHz and 100 GHz effects on tissues.

The chosen frequencies have the most impact on the gray matter of the brain, as shown below in the table 4, whereas the nerve tissue has the least impact.

20GHZ	Brain gray matter	Prostate and Stomach	Testis
30 GHZ	Brain gray matter	Prostate and Stomach	Testis
40GHZ	Brain gray matter	Prostate and Stomach	Testis
60 GHZ	Brain gray matter	Prostate and Stomach	Testis
70 GHZ	Brain gray matter	Prostate and Stomach	Testis
80GHZ	Brain gray matter	Prostate and Stomach	Testis
100GHZ	Brain gray matter	Prostate and Stomach	Testis

The four primary groups of tissues are muscular, neural, epithelial, and connective tissues. It is found that the nerve tissues are the ones most affected by the chosen frequencies when contrasted with the other tissues under examination. Radiation in the same frequency range affects epithelia and connective tissue alike. Muscles are the least impacted tissues. Despite epithelia tissues, radiation has been demonstrated to work better on breast fat. You could make reference to the unnatural jump in which the breast fat protrudes from the body.

IV. Conclusions

The impacts of 5G frequencies, which include millimeter wave, on human health have been extensively studied in both clinical and scientific settings. 5G frequencies are a subset of a wider range of radio frequencies.

Research and meta-analyses of these clinical and scientific results have not turned up any proof—not even a suggestion—that exposures below the ICNIRP Guidelines' safety thresholds pose any known health risks to adults or children.

It's crucial to remember that 5G devices automatically reduce their transmission power to a level where an acceptable level of connectivity can still be kept. The network regulates the device's transmitted power. Downlinks greater than 20 GHz emphasize the significance of EMF exposure on many organs. After running the simulation, we found that the use of smaller cells and stronger electromagnetic beam directionality in 5G enhanced EMF exposure. The neuron, connective, epithelial, and muscular tissues were separated into five groups for this simulation. The specific absorption rate (SAR) and power density (PD) are calculated for over 40 tissues at different frequencies (20, 30, 40, 60, 70, 80, and 100 GHz). According to the results, the nerve tissues are most affected by the chosen frequencies, with connective tissues and epithelia tissue following suit.

References

[1] Safdar N. K.M., Arbab M.A., Salman A., Abadul H., Tariq K., and Muhammad T. “A Machine Learning Approach for 5G SINR Prediction”, International Journal of Electronics, 4(2), (2022), 1- 1

[2] Magnus M. “5G positioning using Machine Learning (ML). A Thesis presented to the Department of Electrical Engineering Linkoping University for the award of Master of Science, 2022

[3] Natalia Y., Yuliya G., Luis M. C., and Konstantin S. “An Analytical Model for 5G Network Resource Sharing with Flexible SLA-Oriented Slice Isolation”, International Journal of Summation Mathematics, 7(4), (2022),1-2

[4] Ruzat U., N. M., Arbab M.A., Salman A., Abadul H., Tariq K., and Muhammad T. “A Machine Learning Approach for 5G SINR Prediction”, International Journal of Electronics, 4(2), (2022), 1- 1

[5] Magnus M. “5G positioning using Machine Learning (ML). A Thesis presented to the Department of Electrical Engineering Linkoping

[6] AgostinoDi Ciaula,April 2018, Pages 367-375,International Journal of Hygiene and Environmental Health,Towards 5G communication systems: Are there health implications?

[7] ,https://doi.org/10.1016/j.ijheh.2018.01.011

[8] Natalia Y., Yuliya G., Luis M. C., and KonstantinS. “An Analytical Model for 5G Network Resource Sharing with Flexible SLA-Oriented Slice Isolation”, International Journal of Summation Mathematics, 7(4), (2020),1-19.

[9] Vila J, Michael C.T., Esther G.L., Jordi F., Joseph D. B., Laurel K., Lesley R., Geza B., Martine H.,Daniel K., Dave M, Marie E.P., Siegal S., Klans S., Brigitt S.,Joachim S., Jack S., Martie, VictorT., and Elisabeth C. “Occupational exposure to high-frequency electromagnetic fields and brain tumor risk in the INTEROCC study: An individualized assessment approach”, Environ Int, 8(119), (2018), 353-365.

[10] Verma S.C., Tejaswini T.M. and Devas P. “Harmful Effects of 5G Radiations: Review”. Proceedings of IRAJ International Conference, 24th March, 2019, Bengaluru, India,11(4), (2019), 71 -75.

[11] 5G Deployment: State of Play in Europe, USA and Asia, Policy Department for Economic, Scientific andQuality of Life Policies, Directorate-General for Internal Policies, European Parliament, June 2019.

[12] Di Ciaula A., Towards 5G communication systems: Are there health implications?, International Journal ofHygiene and Environmental Health, Volume 221, Issue 3, pp. 367-375, April 2018.

[13] Negreiro M., Towards a European gigabit society Connectivity targets and 5G, EPRS, European Parliament, June 2017.

[14] Russel C., 5 G wireless telecommunications expansion: Public health and environmental implications,Environmental Research, Volume 165, pp. 484-495, 2018.

[15] [14].Aydin D, Feychting M, Schuz J et al. Impact of random and systematic recall errors and selection bias in case- control studies on mobile phone use and brain tumors in adolescents (CEFALO study). Bioelectromagnetics 2011;32:396-407. doi: 10.1002/bem.20651.

[16] [15] Simko M, Mattsson MO. 5G Wireless Communication and Health Effects - A Pragmatic Review Based on Available Studies Regarding 6 to 100 GHz. Int J Envi- ron Res Public Health 2019;16:3406-29, doi:10.3390/ ijerph16183406

New expression for the resonant frequency of rectangular microstrip antenna using genetic algorithm and effective parameters

Tarek Fortaki*[1], Siham Benkouda[2], Ahmed Mahamdi[2], and Sami Bedra[1,3]

[1]LEA Laboratory, Electronics Department, University of Batna 2, Batna, Algeria
[2]LHS Laboratory, Electronics Department, University of Frères Mentouri - Constantine 1, Constantine, Algeria
[3]Industrial Engineering Department, University of Khenchela, Khenchela, Algeria
*corresponding author, E-mail: t.fortaki@univ-batna2.dz

Abstract

In this work, the cavity model for simple rectangular microstrip antenna is extended with some modifications to performing the resonant characteristics of the antenna. The cavity model in conjunction with the genetic algorithm is using for the design of rectangular microstrip antenna. Furthermore, the results present in this paper, are comparing with those presented elsewhere. Finally the effect of the different parameters of the rectangular antenna on the resonant characteristics is also investigated for fundamental and higher order modes.

1. Introduction

Microstrip antennas are becoming increasingly popular since they have small volume and a low-profile planar configuration. Easy mass production of such antennas using printed circuit technology leads to low fabrication cost. They are much easier to be integrated into microwave circuits on the same substrate [1]. Their main drawback is narrow bandwidth characteristics, which is considerably avoided by operating the antenna around the resonant frequency [2-14] or by generating new resonances.

In this study, resonant frequency of rectangular patch microstrip antenna is accurately determined via cavity analysis, using a simple effective permittivity and patch dimensions expressions including modal effects.

The aim of this work is to develop an accurate and efficient model of rectangular microstrip antenna, as well as to perform the analysis for rectangular microstrip antenna. The resonant frequency of this antenna can be determined from cavity model for various operational modes and structural parameters using proper equivalent model with effective structural parameters [15]. For this purpose, various expressions for effective patch dimensions L_{eff} ,W_{eff} and effective relative permittivity ε_{eff} are defined in the literature [4].

After obtaining the novel expression for the resonant frequency, we use this last in performing a parametrical study. In this parametrical study, the electrical and the geometrical parameters are both considered.

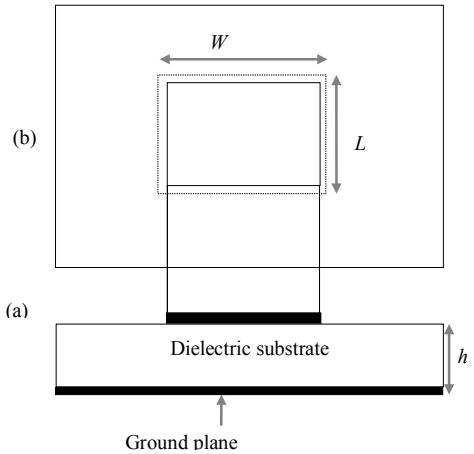

Figure 1: Geometry of a rectangular microstrip antenna.
a- Side view
b- Top view

2. Antenna configuration and design

The rectangular microstrip antenna structure is shown in figure 1. The resonant behavior of the antenna is independent of the feed so that the feed was not taken into account in the analysis.

To improve the accuracy of the magnetic wall cavity model, effective patch dimensions are used to include the modal effects. Hence, the modified formula is as follows:

$$f_c^{m,n} = \frac{0.15}{\sqrt{\varepsilon_{reff}}}\sqrt{\left(\frac{n}{L_{eff}}\right)^2 + \left(\frac{m}{W_{eff}}\right)^2}\ [\text{GHz}] \quad (1)$$

In equation (1), n and m define the propagating mode, while the other parameters are:

L_{eff} : Effective length of the patch.

W_{eff} : Effective width of the patch.

ε_{reff} : Effective relative permittivity of the substrate.

This last is used to account for the fact that small fraction of the field exists outside the dielectric substrate [4]. It is given by:

$$\varepsilon_{reff} = \left(\frac{\varepsilon_r + 1}{2}\right) + \left(\frac{\varepsilon_r + 1}{2}\right)\left(1 + 12\frac{h}{W}\right)^{\alpha_1} \qquad (2)$$

In equation (2), h is thickness of substrate, ε_r is the relative permittivity of dielectric medium. The effective dimensions of the radiating element are:

$$L_{eff} = L + 2\Delta L \qquad (3)$$

$$W_{eff} = W + 2\Delta W \qquad (4)$$

Note that in equations (3) and (4), the physical dimensions of the radiating element have been extended to account for the fringing fields. In equation (3), ΔL is defined as

$$\Delta L = \alpha_2 . h \left[\frac{\left(\varepsilon_{reff} + \alpha_3\right)\left(\frac{W}{L} + \alpha_4\right)}{\left(\varepsilon_{reff} + \alpha_5\right)\left(\frac{w}{h} + \alpha_6\right)}\right] \qquad (5)$$

The constants α_1, α_2, α_3, α_4, α_5 and α_6 given in the above equations are the coefficients to be determined by genetic algorithm.

3. Genetic algorithm (GA)

The GA is based on the evolution theory where weak species face extinction but strong ones survive and pass their genes to the next generation. However for the strong species to survive there is also a requirement for random injection of genes. As GA mainly manipulates matrices it is normally implemented using Matlab software. The step by step procedure of generating the software program is shown below.

Step 1: Each variable is assigned a number of binary digits so that the required accuracy of this variable is obtained in the final solution.

Step 2: All the variables in their binary form are grouped into a string which is called a chromosome.

Step 3: Matlab is used to select a fixed number of random chromosomes called a population out of all possible number of chromosomes that are present. This is called the current generation.

Step 4: Converting the digital value of each variable in a chromosome to an analogue value, the objective function f is evaluated and the relative fitness of each chromosome (Pi) is determined. This relative fitness is defined as:

$$f = \frac{1}{N}\sum_{L}\sum_{W}\sum_{\varepsilon_r}\sum_{h}\left[\frac{f_{me}(L,W,\varepsilon_r,h) - f_{ca}(L,W,\varepsilon_r,h)}{f_{me}(L,W,\varepsilon_r,h)}\right]^2 \qquad (6)$$

where f_{me} and f_{ca} are, respectively, the measured and calculated resonant frequency of rectangular microstrip antenna.

Step 5: The selective probability is determined by:

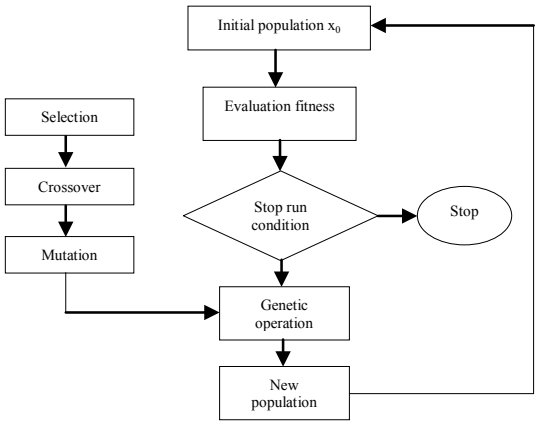

Figure 2: Flow chart of genetic algorithm.

$$P_{si} = \frac{eval_i[P_i]}{f} \qquad (7)$$

The cumulative probability of the chromosomes is given as:

$$q_i = \sum_{j=1}^{n} P_{sj} \qquad (8)$$

Then a random number 'r' is generated in the range 0 to 1. If qi-1≤ r ≤ qi then select Psi.

Step 6: Crossover is applied for random chromosomes between the parent and next generation to produce new off springs.

Step 7: The population is mutated by changing in a random way the value of the genes with the least significant bit having the highest probability of mutation and the most significant the least. The flowchart of GA operation is shown in figure 2. The next generation now becomes the parent generation and the above process is repeated until the genetic variation in the population is below a certain threshold. As the number of generations increases both the cross over rate and the mutation rate are gradually reduced.

The constants α_1, α_2, α_3, α_4, α_5 and α_6 given in the above equations are the coefficients to be determined by GA so as to minimize the following normalized errors (MQE):

$$\text{MQE} = \frac{1}{N}\sum_{i=1}^{n}\sum_{j=1}^{m}\left|\frac{f_{me} - f_{ca}}{f_{me}}\right| \qquad (9)$$

In the operation of optimization, the following parameters are used:

Maximum number of generations: 200
Population size: 20
Probability of 0 in initial population: 0.15
Probability of crossover: 0.5
Probability of mutation: 0.20
Optimization object: resonant frequency

The optimum values of the unknown coefficients shown in equations (2) and (5) are found to be:

Table 1: Validation of the new expression via comparison with experimental measurement.

W (*mm*)	*L* (*mm*)	*h* (*mm*)	ε_r	Resonant frequency (GHz)	
				Measured [15,16]	Our results
20.0	25.0	0.79	2.22	3.970	3.975
20.74	26.26	0.79	2.55	3.545	3.535
17.20	18.60	1.57	2.33	5.060	4.978
18.10	19.60	1.57	2.33	4.805	4.742
12.70	13.50	1.63	2.55	6.560	6.407

$$\alpha_1 = \alpha_2 = \alpha_5 = 0.5 \qquad (10)$$

$$\alpha_3 = 0.3\,,\ \alpha_4 = 0.25\,,\ \alpha_6 = 0.8 \qquad (11)$$

Using equations (10) and (11), the effective parameters of the modified magnetic wall cavity model are now fully defined.

4. Results and discussion

In order to demonstrate the appropriate of our suggestion, we compare our computed values of the resonant frequencies for the fundamental mode (TM01) of rectangular microstrip antenna with the experimental results reported by other scientists [15-16], all of which are given in table 1. It can be conclude that the new expression developed in this work can be very useful in the design of rectangular microstrip antenna.

Figure 3 shows the resonant frequency as a function of substrate thickness, for two different materials of dielectric substrate. Those isotropic materials are Parafin and Beryllium with relative permittivity 2.44 and 6.4, respectively. Our obtained values using genetic algorithm together with those generated from the curve fitting formula [17] both are reported in figure 3. The agreement between our numerical results and those of reference [17] is very good. It is clear from the results traced in figure 3 that when the thickness of the substrate increments, the resonant frequency decreases slowly.

Figure 4 depicts the influence of the relative dielectric constant of the dielectric substrate on the resonant frequency for the fundamental mode. The substrate has a thickness of h=1.6 mm. The numerical results are obtained for two patch sizes. The behavior of the resonant frequency is well expected since the resonant frequency is inversely proportional to the relative permittivity of the substrate as it is shown explicitly in equation (1).

Figure 5 shows the effect of the length of the rectangular patch on the resonant frequency for the fundamental mode for two different dielectric constants of the substrate and a fixed thickness equal to 1.6mm. The width of the patch is taken to be 10 mm. From the results of figure 5 it is observed that the length of the patch has a strong effect on the operating frequency for low as well as for high dielectric constant of the substrate. As an example, as the length of the rectangular patch increases from 5 mm to 27 mm, the resonant frequency decreases from 12 GHz to 4 GHz (see the curve of the Duroid substrate).

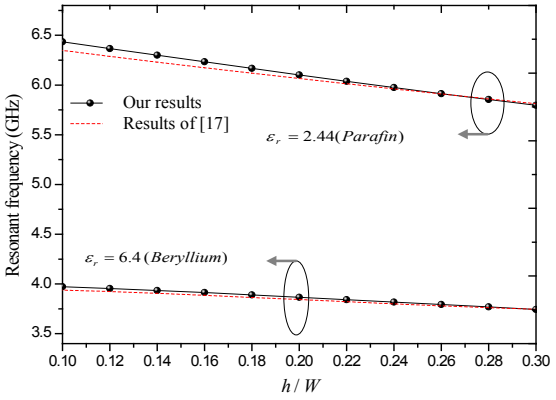

Figure 3: Resonant frequency as a function of the thickness of the substrate; L=10 mm.

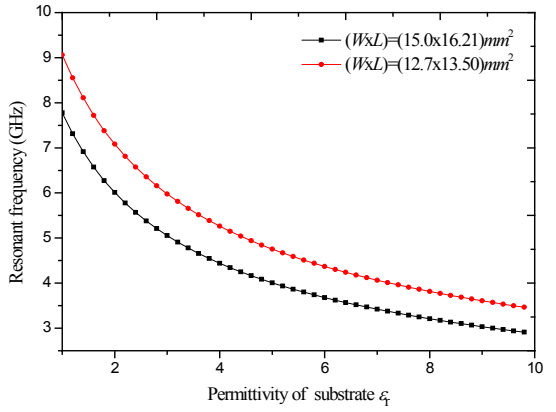

Figure 4: Resonant frequency as a function of the relative permittivity of the substrate; h=1.6 mm.

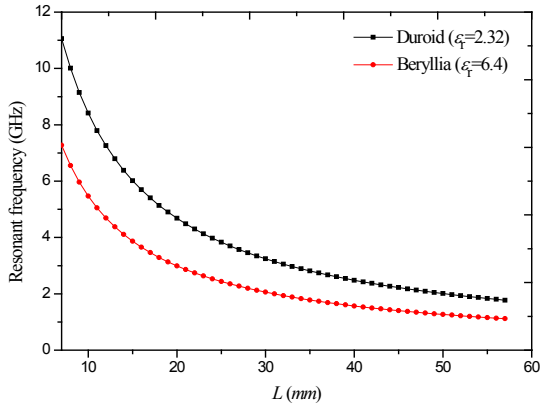

Figure 5: Resonant frequency as a function of the length of the rectangular patch; W=10 mm.

5. Conclusion

In this paper, a new expression has been derived based on cavity model in conjunction with genetic algorithms for a rectangular microstrip antenna. The results of the study obtained from implementing genetic algorithms enable us to conclude that the effectiveness of the cavity method based on optimization of antenna parameters strongly depends on the choice of the objective function or Fitness. The importance of this choice comes from the fact that this function constitutes the only link with the physical problem to be optimized with genetic algorithm. Computations have shown the effect of different parameters on the resonance characteristics of the rectangular antenna. These parameters include geometrical as well as electrical parameters of the antenna. The analysis presented here can be extended to study other parameters characterizing the rectangular patch antenna with various configurations.

References

[1] R. Bedra, S. Bedra, and T. Fortaki, Analysis of elliptical-disk microstrip patch printed on isotropic or anisotropic substrate materials, *International Journal of Microwave and Wireless Technologies* 8: 251-255, 2016.

[2] R. Bedra, S. Bedra, S. Benkouda, and T. Fortaki, Efficient full-wave analysis of resonant modes of circular microstrip antenna printed on isotropic or uniaxially anisotropic substrate, *Wireless Personal Communications* 81: 239-251, 2015.

[3] N. G. Alexopoulos and S. A. Maas, Characteristics of microstrip directional couplers on anisotropic substrates, *IEEE Trans. Microwave Theory Tech.* MTT-30: 1267–1270, 1982.

[4] N. G. Alexopoulos, Integrated circuit structures on anisotropic substrates, *IEEE Trans. Microwave Theory Tech.* MTT-33: 847–881, 1985.

[5] M. Behih, F. Bouttout, T. Fortaki, and C. Dumond, A Novel wideband and multi-band implantable antenna design for biomedical telemetry, The Applied Computational Electromagnetics Society Journal (ACES) 37: 441-457, 2022.

[6] M. Amir, H. Amar, T. Fortaki, S. Tebache, A. Hedir, H. Ghodbane, Open ended coaxial sensors with and without cavity for non-destructive applications, Engineering Research Express 4: pp. 035008, 2022.

[7] S. Bedra, R. Bedra, S. Benkouda, and T. Fortaki, Study of an inverted rectangular patch printed on anisotropic substrates, IETE Journal of Research 68: 1056-1063, 2022.

[8] S. Bedra, S. Benkouda, R. Bedra, and T. Fortaki, Characteristics of HTS inverted circular patches on anisotropic substrates, Journal of Computational Electronics 20: 892-899, 2021.

[9] S. Bedra, S. Benkouda, R. Bedra, and T. Fortaki, Inverted HTS rectangular patch antennas: Theoretical investigation, Physica C: Superconductivity and its Applications 580: pp. 1353802, 2021.

[10] A. S. Boughrara, S. Benkouda, A. Bouraiou, and T. Fortaki, Study of stacked high Tc superconducting circular disk microstrip antenna in multilayered substrate containing isotropic and/or uniaxial anisotropic materials, Advanced Electromagnetics 8: 1-5, 2019.

[11] A. Gadda, S. Bedra, C. Agaba, S. Benkouda, R. Bedra, and T. Fortaki, Computer-aided design of superconducting equilateral triangular patch on anisotropic substrates, Progress In Electromagnetics Research M 86: 203-211, 2019.

[12] S. Bedra, R. Bedra, S. Benkouda, and T. Fortaki, Analysis of HTS circular patch antennas including radome effects, International Journal of Microwave and Wireless Technologies 10: 843-850, 2018.

[13] Y. Bentrcia, S. Bouttout, S. Benkouda, and T. Fortaki, Spectral domain analysis of rectangular stacked patches printed on a substrate characterized by dielectric and magnetic anisotropy, Journal of Computational Electronics 17: 399-405, 2018.

[14] S. Bouttout, Y. Bentrcia, S. Benkouda, and T. Fortaki, Parametric study of stacked microstrip patch antenna with dissimilar substrates, Journal of Nano- and Electronic Physics 10: 1-4, 2018.

[15] K. Mehmet, A novel technique to calculate the bandwidth of rectangular microstrip antenna elements with thick substrates, *Microwave and Optical Technology Letters* 12: 60-64, 1996.

[16] K. Mehmet, A simple technique for the calculation of the bandwidth of rectangular microstrip antenna elements with various substrate thicknesses, *Microwave and Optical Technology Letters* 12: 16-20, 1996.

[17] W. C. Chew and Q. Liu, Resonance frequency of a rectangular microstrip patch, *IEEE Transactions on Antennas and Propagation* 36: 1045-1056, 1988.

Resonant Characteristics of a Superconducting Thin Film Resonator Using the Two-Fluid Model and Artificial Neural Networks

Siham Benkouda*[1], Tarek Fortaki[2], Abdelkrim Gadda[1], and Sami Bedra[2,3]

[1]LHS Laboratory, Electronics Department, University of Frères Mentouri - Constantine 1, Constantine, Algeria
[2]LEA Laboratory, Electronics Department, University of Batna 2, Batna, Algeria
[3]Industrial Engineering Department, University of Khenchela, Khenchela, Algeria
*corresponding author, E-mail: siham.benkouda@umc.edu.dz

Abstract

In this work, we are interested to predicted the resonant characteristics of superconducting thin film microstrip resonator. First we calculated the spectral Green's tensor in the representation (TM, TE). Using the moment's method, we have reduced the integral equation into a linear system. Galerkin's procedure in the vector Fourier transform domain in conjunction with Gorter-Casimir's theorem of two fluids and the London brothers equations have been used for the numerical computation of the resonant frequency and the bandwidth of a rectangular patch superconductor embedded in a single layer substrate. In order to minimize the computing time, a neural approach based on artificial neural networks is introduced into the modeling process. Finally, the effects of a superconductor patch on the characteristics of the antenna are presented.

1. Introduction

In aeronautical applications, aerospace, military, mobile and terrestrial communications systems, low weight, low cost and high performance are the main requirements, the microstrip antennas comply these requirements [1]. The main advantages of these antennas are low weight, volume and thickness, low cost, simplicity of manufacture, networking capability and the integration of discrete elements, and finally conformability facilitating implantation on any type of support [2 - 5]. However, this type of element has limitations, such as narrow bandwidth, low gain and the ability to resonate at a single frequency [6]. In recent years, high-temperature superconductors (HTS) have given new dimensions to the industrial development of microwave circuits, superconducting passive microwave components such as antennas, filters, transmission lines and phase shifters have shown significant superiority to the corresponding components made with normal conductors such as gold, silver and copper because of the advantages of superconductors [7 - 15]. The advantages of using superconducting materials at high critical microwave temperatures include: very low losses; which means reducing the attenuation and the noise level, very small dispersion up to frequencies of a few tens of GHz, miniaturization of the microwave devices; which allows a wide scale integration and reduction in signal propagation time in the circuits. High-temperature superconducting microstrip antennas have a high gain relative to conventional antennas [16 - 20]. A number of methods using different levels of approximation have been proposed and used to analyses microstrip antennas. These methods can generally be divided into two groups: simple analytical methods and rigorous numerical methods. Simple analytical methods can give a good intuitive explanation of antenna radiation properties. However, these methods do not consider rigorously the effects of surface waves. Exact mathematical formulations in rigorous methods involve extensive numerical procedures, resulting in round-off errors and may also need final experimental adjustments to the theoretical results. These methods also require high performance large-scale computer resources and a very large number of computations [21 - 32]. To overcome all these limitations, a model based on artificial neural networks (ANN) is presented in this paper to calculate the resonant frequencies and bandwidth immediately. ANN is used to model the relationship between the parameters of the microstrip antenna and the resonant frequencies obtained from the moments method (MoM). This relatively simple model allows designers to predict accurately the resonant frequencies for a given design without having to develop or run the MoM codes themselves.

2. Analysis method

The problem to be solved is illustrated in Fig. 1. We have a rectangular superconducting patch of length '*a*', width '*b*' and height '*R*' printed on a dielectric substrate isotropic of thickness '*d*' characterized by the permeability of the vacuum μ_0 and a permittivity $\varepsilon_0\varepsilon_r$. The ambient medium is air with constitutive parameters μ_0 and ε_0. Considering $e^{j\omega t}$ time variations and starting from the Maxwell equations presented in the Fourier domain, we can show that the transverse fields inside the j layer ($z_{j-1} \prec z \prec z_{j+1}$) can be written in terms of the longitudinal components $\widetilde{E}$ and $\widetilde{H}$ as [33]-[34].

$$\widetilde{E}(k_s,z)=\begin{bmatrix}\widetilde{E}_x(k_s,z)\\ \widetilde{E}_y(k_s,z)\end{bmatrix}=\overline{F}(k_s)\cdot\begin{bmatrix}\frac{1}{k_s}\frac{\partial\widetilde{E}_z(k_s,z)}{\partial z}\\ \frac{\omega\mu_0}{k_s}\widetilde{H}_z(k_s,z)\end{bmatrix}$$

The above equation can be written more compactly as follows:

$$\widetilde{E}(k_s,z)=\overline{F}(k_s)e(k_s,z) \quad (1)$$

$$\widetilde{H}(k_s,z)=\begin{bmatrix}\widetilde{H}_y(k_s,z)\\ -\widetilde{H}_x(k_s,z)\end{bmatrix}=\overline{F}(k_s)\cdot\begin{bmatrix}\frac{\omega\varepsilon_j}{k_s}\widetilde{H}_z(k_s,z)\\ \frac{1}{k_s}\frac{\partial\widetilde{H}_z(k_s,z)}{\partial z}\end{bmatrix}$$

The above equation can be written more compactly as follows:

$$\widetilde{H}(k_s,z)=\overline{F}(k_s)h(k_s,z) \quad (2)$$

e and h are, respectively, the transverse electric and magnetic fields in the (TM, TE) representation, and

$$\overline{F}(k_s)=\frac{1}{k_s}\begin{bmatrix}k_x & k_y\\ k_y & -k_x\end{bmatrix} \quad (3)$$

with $k_s^2=k_x^2+k_y^2$. Substituting the expressions of $\widetilde{E}$ and $\widetilde{H}$ [33]-[35] into (1) and (2), we get

$$\overline{e}(k_s,z)=\overline{A}e^{-ik_z z}+\overline{B}e^{ik_z z} \quad (4)$$

$$\overline{h}(k_s,z)=\overline{\overline{g}}(k_s)\cdot\left[\overline{A}e^{-ik_z z}-\overline{B}e^{ik_z z}\right] \quad (5)$$

In (4) and (5), A and B are two component unknown vectors and

$$\overline{\overline{g}}(k_s)=\mathrm{diag}\left[\frac{\omega\varepsilon}{k_z},\frac{k_z}{\omega\mu}\right] \quad (6)$$

Writing (4) and (5) $z=z_{j-1}$ and $z=z_j$ and by eliminating the unknowns A and B, we obtain the matrix form

$$\begin{bmatrix}\overline{e}_j(k_s,z_j^-)\\ \overline{h}_j(k_s,z_j^-)\end{bmatrix}=\overline{\overline{T}}_j\begin{bmatrix}\overline{e}_j(k_s,z_{j-1}^+)\\ \overline{h}_j(k_s,z_{j-1}^+)\end{bmatrix} \quad (7)$$

with

$$\overline{\overline{T}}_j=\begin{bmatrix}\overline{\overline{T}}_j^{11} & \overline{\overline{T}}_j^{12}\\ \overline{\overline{T}}_j^{21} & \overline{\overline{T}}_j^{22}\end{bmatrix}$$

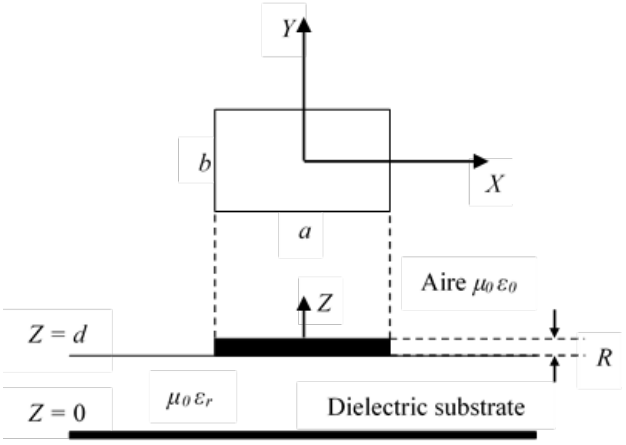

Figure 1: Geometrical structure of a superconducting rectangular microstrip patch.

$$\overline{\overline{T}}_j=\begin{bmatrix}\cos(k_{zj}d_j) & -i\cdot\overline{\overline{g}}^{-1}\cdot\sin(k_{zj}d_j)\\ -i\cdot\overline{\overline{g}}\cdot\sin(k_{zj}d_j) & \cos(k_{zj}d_j)\end{bmatrix} \quad (8)$$

Which combines e and h on the both sides of the j^{th} layer as input and output quantities. The matrix $\overline{\overline{T}}_j$ represents the j^{th} layer the (TM, TE) representation.

The boundary conditions for the considered structure resented in figure 1 in the spectral domain

$$\overline{e}_j(k_s,z_{j-1}^+)=\overline{0} \quad (9)$$

$$\begin{bmatrix}\overline{e}_2(k_s,z_1^+)\\ \overline{h}_2(k_s,z_1^+)\end{bmatrix}=\overline{\overline{T}}\begin{bmatrix}\overline{e}_1(k_s,z_0^+)\\ \overline{h}_1(k_s,z_0^+)\end{bmatrix}-\begin{bmatrix}\overline{0}\\ \overline{J}(Z_1)\end{bmatrix} \quad (10)$$

$$\overline{h}_2(k_s,z_1^+)=\overline{\overline{g}}_2(k_s)\cdot\overline{e}_2(k_s,z_1^+) \quad (11)$$

The transformed components of the tangential electric field are expressed as a function of the transformed current density components on the patch, as

$$\begin{bmatrix}\widetilde{E}_x\\ \widetilde{E}_y\end{bmatrix}=\begin{bmatrix}G_{xx} & G_{xy}\\ G_{yx} & G_{yy}\end{bmatrix}\cdot\begin{bmatrix}\widetilde{J}_x\\ \widetilde{J}_y\end{bmatrix} \quad (12)$$

To include the effect of the superconducting of the microstrip film, the dyadic Green's function is modified by considering a surface complex impedance Z_s, and is determinate by using the two-fluid model of Gorter and Casimir [35-37].

$$Z_s=\sqrt{\frac{i\omega\mu_0}{\sigma}} \quad (13)$$

If the thickness of the superconducting film R is less than three penetration depths, a better boundary condition is given by [37]

$$Z_s = \frac{1}{R \cdot \sigma} \tag{14}$$

Where the complex conductivity is given by [35] - [37]:

$$\sigma_1 = \sigma_n \left(\frac{T}{T_C}\right)^4 + \left(\left(1 - \left(\frac{T}{T_C}\right)^4\right) \Big/ \left(i\omega\mu_0\lambda_0^2\right)\right) \tag{15}$$

Using the complex resistive boundary condition, the characteristic matrix is determinate

$$\begin{bmatrix} \widetilde{E}_x \\ \widetilde{E}_y \end{bmatrix} = \begin{bmatrix} (G_{xx} - Z_s) & G_{xy} \\ G_{yx} & (G_{yy} - Z_s) \end{bmatrix} \cdot \begin{bmatrix} \widetilde{J}_x \\ \widetilde{J}_y \end{bmatrix} \tag{16}$$

The Galerkin moment method is implemented in the Fourier transform domain to reduce the integral equation to a matrix equation. The surface current J on the patch is expanded into a finite series of known basis functions J_{xn} and J_{ym}

$$J = \sum_{n=1}^{N} a_n \begin{bmatrix} J_{xn} \\ 0 \end{bmatrix} + \sum_{m=1}^{M} b_m \begin{bmatrix} 0 \\ J_{ym} \end{bmatrix} \tag{17}$$

Where a_n and b_m are the mode expansion coefficients to be sought, substituting the vector Fourier transforms, Next, the resulting equation is tested by the same set of basic functions that was used in the expansion of the patch current. Thus, the integral equation is discredited into the following matrix equation

$$\begin{bmatrix} (Z^1_{kn})_{N\times N} & (Z^2_{kn})_{N\times M} \\ (Z^3_{\ln})_{M\times N} & (Z^4_{\ln})_{M\times M} \end{bmatrix} \cdot \begin{bmatrix} (a_n)_{N\times 1} \\ (b_m)_{M\times 1} \end{bmatrix} = \begin{bmatrix} \overline{0} \\ \overline{0} \end{bmatrix} \tag{18}$$

$$Z^1_{kn} = \int_{-\infty}^{+\infty}\int_{-\infty}^{+\infty} (G_{xx} - Z_s)\widetilde{J}_{xn}(k_x, k_y)\widetilde{J}_{xk}(-k_x, -k_y)dk_x dk_y$$

$$Z^2_{kn} = \int_{-\infty}^{+\infty}\int_{-\infty}^{+\infty} G_{xy}\widetilde{J}_{ym}(k_x, k_y)\widetilde{J}_{xk}(-k_x, -k_y)dk_x dk_y$$

$$Z^3_{\ln} = \int_{-\infty}^{+\infty}\int_{-\infty}^{+\infty} G_{yx}\widetilde{J}_{xn}(k_x, k_y)\widetilde{J}_{yl}(-k_x, -k_y)dk_x dk_y$$

$$Z^4_{\ln} = \int_{-\infty}^{+\infty}\int_{-\infty}^{+\infty} (G_{yy} - Z_s)\widetilde{J}_{ym}(k_x, k_y)\widetilde{J}_{yl}(-k_x, -k_y)dk_x dk_y$$

The existence of non- trivial solution of (18) requires that

$$\mathrm{Det}[Z(f)] = 0 \tag{19}$$

Equation (19) is the characteristic equation for the complex resonant frequency of the generalized microstrip structure illustrated in Fig. 1. Where $\overline{Z}$ is the matrix in (18).

3. Artificial neural networks

Artificial neural network (ANNs) represents a promising modeling technique, especially for data sets having nonlinear relationships that are frequently encountered in engineering. In terms of model specification, artificial neural networks require no knowledge of the data source but, since they often contain many weights that must be estimated, they require large training sets. In addition, ANNs can combine and incorporate both literature-based and experimental data to solve problems [38-43].

There are many types of neural networks for various applications available in the literature [40]. In this work the multilayer perceptron (MLP) network is selected for the efficient calculation of Resonant Frequency and Bandwidth of rectangular microstrip antenna.

3.1. Multilayer Perceptron (MLP) networks

The multilayer perceptron (MLP) network is selected due to its simplest form and therefore most commonly used artificial neural network architectures have been updated for the calculation of the resonant frequency and bandwidth of microstrip antennas. MLP can be trained using many different learning [38 - 43], in our paper the standard back-propagation algorithm has been used for training.

As shown in Fig. 2, the MLP consists of an input layer, one or more hidden layers, and an output layer. Neurons in the input layer only act as buffers to neurons in the hidden layer. Each neuron in the hidden layer sums its input signals x_i after weighting them with the strengths of the respective connections w_{ji} from the input layer and computes its output y_j as a function of the sum, namely.

$$y_{ik} = f\left(\sum \mathrm{w}_{\mathrm{ji}} x_i\right) \tag{20}$$

Where f can be a simple threshold function or a sigmoid or hyperbolic tangent function [44]. The output of neurons in the output layer is computed similarly.

Training a network consists of adjusting weights of the network using the learning algorithm. A learning algorithm gives the change Δw_{ji} (k) in the weight of a connection between neurons i and j at time k. The weights are then updated according to the formula

$$W_0(k+1) = W_{ij}(k) + \lambda D_i P_j \tag{21}$$

3.2. Structures of the Neural Networks

In this work, Multilayer Perceptron (MLP) network is used in ANN model. MLP model is trained with backpropagation algorithm. The train and test data of the ANN were obtained from calculated with method (MoM) and a computer program using formulae given in Section 2. The data are in a matrix form consisting inputs and target values and arranged according to the definitions of the problems. The different network input and output parameters are shown in figure 3.

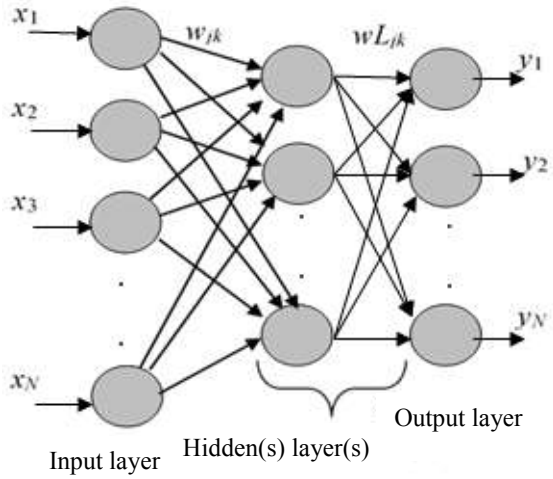

Figure 2: General form of multilayered perceptron.

In the MLP structure, input layer has the linear transfer function, the hidden and layers have the sigmoid function. Training an ANN with the use of a learning algorithm to compute the resonant frequencies and the bandwidth involves presenting it sequentially with different sets (*a, b, R, d,* ε_r*, T*) and corresponding measured values (*f, BW*)$_{measured}$. Differences between the target output (*f, BW*)$_{measured}$ and the actual output of the ANNs are evaluated by a learning algorithm. The adaptation is carried out after the presentation of each set (*a, b, R, d,* ε_r*, T*) until the calculation accuracy of the network is deemed satisfactory according to some criterion (for example, when the error between (*f, BW*)$_{measured}$ and the actual output for all the training set falls below a given threshold) or the maximum allowable number of epochs or generations is reached.
The ANN model developed here was trained with 795 samples and tested with 265 samples. Which has a configuration of 6 input neurons, 10 and 4 neurons in 2 hidden layers, and 2 outputs neurons with learning rate =0.1, goal = 3.6 10-6. With its optimized parameters. It is based on the results obtained by this model that we will study the different characteristics of the antenna (resonant frequency and bandwidth) as a function of its physical and geometrical parameters (*a, b, R, d,* ε_r*, T*), in the following section.

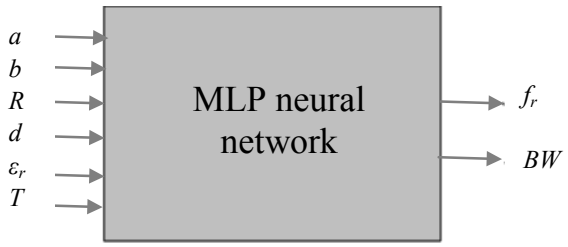

Figure 3: Neural model for predicting both resonant frequency and bandwidth of a microstrip superconducting resonator.

4. Numerical results and discussion

The patch dimension is *a*=l630µm, *b*=935µm and thickness *R*=350nm, using HTS materials YBCO with a critical temperature T_c of 89 K, a zero-temperature penetration depth of λ0=140nm and a normal state conductivity of σ = 106 S/m. The substrate used in this study was lanthanum aluminate (LaAIO3).

4.1. Validation of the proposed approach

In order to confirm the computation accuracy of the ANN model, our results are compared with [45] and [36]. Table 1 shows a good agreement between our results and those estimated by the models of [45] and [36].

Table 1: Comparison of Comparison of resonance frequencies with those of [42] and [43] for a simple superconducting patch microband structure.

T=50K	Resonant frequencies		
	***Calculated* [36]**	***Cavity model* [45]**	***Our results***
ε_r=11	41.041	41.638	41.930
ε_r=16	34.856	35.300	35.203
ε_r=23.81	28.671	28.937	28.768

4.2. Substrate thickness effect on the antenna characteristics.

The following graphs illustrate the simulation results of our ANN model. By varying the thickness of the substrate and fixing all the other parameters, the figures (Fig 4, Fig 5) represent the variation of the resonant frequency and the bandwidth as a function of the thickness of the substrate with the characteristics cited previously, formed on a substrate of relative permittivity ε_r = 23.81, from both figures it is concluded that:

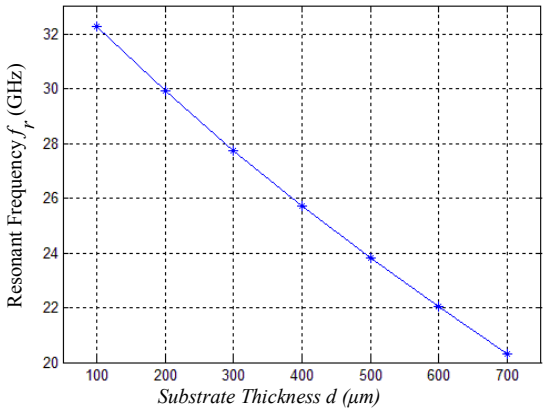

Figure 4: Resonance frequency of a rectangular superconducting patch microstrip antenna as a function of substrate thickness.

- The increase in the thickness of the dielectric substrate decreases with the resonance frequency, so it can be said that the latter is inversely proportional to the thickness of the dielectric substrate.

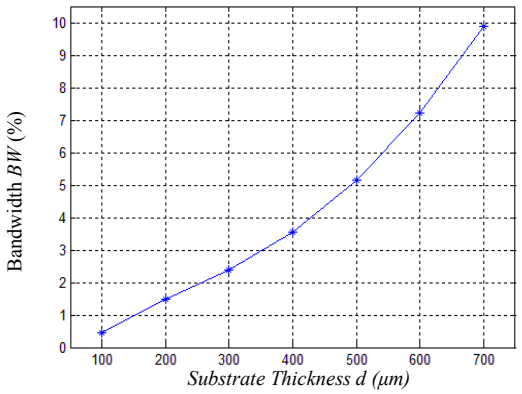

Figure 5: Bandwidth of a rectangular superconducting patch microstrip antenna as a function of substrate thickness.

- The increase in the thickness of the substrate causes the bandwidth to widen, so the bandwidth is proportional to the thickness of the substrate.

These behaviors are in agreement with those discovered by the case of a patch made from a perfect conductor.

4.3. Temperature effect on the antenna characteristics

The substrate used in this study was lanthanum aluminate (LaAIO3). which has a good lattice match with YBCO [46]. LaAIO3 have a relatively high dielectric constant for microwave and antenna applications, and the characteristics of the substrate often changes with temperature, this variation in the dielectric constant of LaAIO3 causes uncertainty and variation in the resonant frequency of microstrip antennas. The permittivity of LaAIO3 as a function of temperature is shown in Fig. 6 which it's given by [36]. Fig. 7 shows that the resonance frequency of an HTS antenna decreases progressively with the increase of the temperature. This decrease becomes more important for temperature values close to the critical temperature. Excellent agreements between our results and those measured by [45].

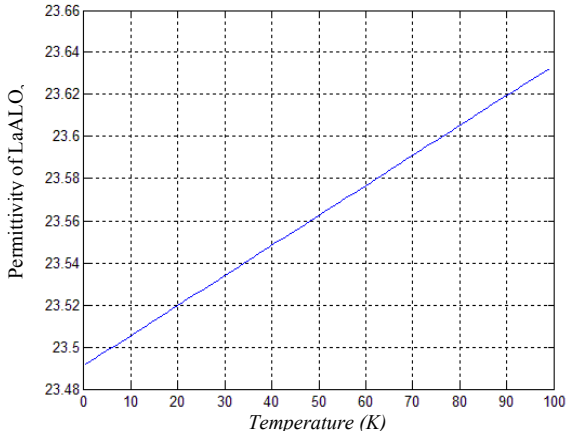

Figure 6: Permittivity of lanthanum aluminate (LaAIO3).

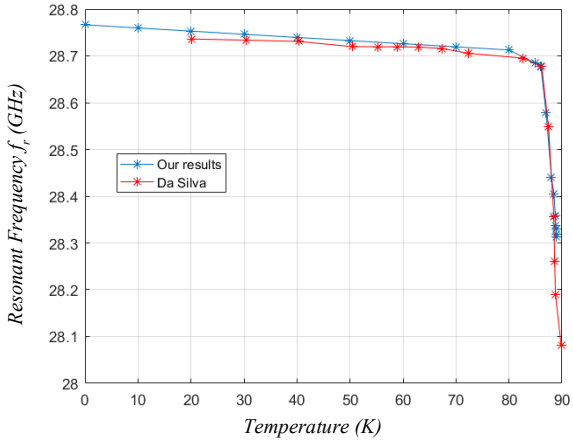

Figure 7: Resonant frequency for a microstrip superconducting patch antenna as a function of the operating temperature *T*.

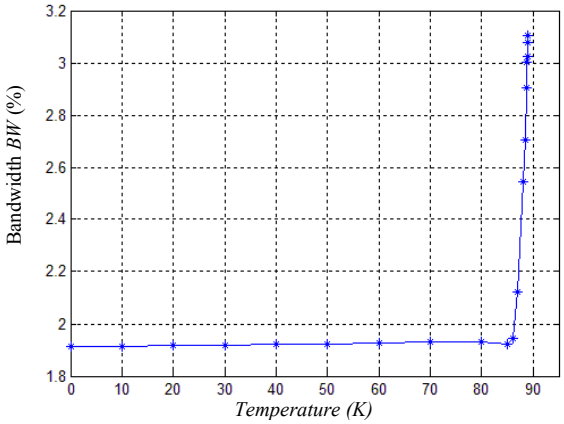

Figure 8: Bandwidth for HTS microstrip antenna as a function of the operating temperature *T*.

Fig. 8 shows that the bandwidth remains almost unchanged for $T<T_c$, but a large increase is obtained for temperatures close to the critical temperature. This completely different from that found by Silva et al. [36], while it is in very good agreement with that found experimentally by Richard et al. [45].

The sudden variations of the characteristics of the microstrip antenna with superconducting patch in the vicinity of the critical temperature are due to the disappearance of the superconducting phenomenon and the purely inductive effect of the electrons appears; therefore, the superconducting material becomes a normal conductor characterized by its actual conductivity 'σ' equal to the normal conductivity of the material 'σn'.

5. Conclusion

A rigorous full wave analysis of a rectangular microstrip patch using superconducting materials has been presented. The problem has been formulated in terms of integral equations using vector Fourier transforms. An efficient

technique has been used for determining the dyadic Green's functions. Galerkin's method has been used to solve the surface current density on the rectangular patch. In order to minimize the computing time, a neural model based on artificial neural networks has been constructed and introduced into the modeling process. The calculated results have been compared with those previously measured and available in various literatures, and excellent consistency has been found. From our work, we can confirm that the properties of the HTS antenna were stable at temperatures slightly lower than the critical temperature.

References

[1] C. A. Balanis, Antenna Theory, Analysis and Design, 3rd ed., New York: John Wiley & Sons Inc., 2005

[2] T. Fortaki, L. Djouane, F. Chebara, and A. Benghalia, Radiation of rectangular microstrip patch antenna covered with a dielectric layer, *Int. J. Electron.* 95: 989-998, 2008.

[3] D. Khedrouche, F. Bouttout, T. Fortaki, and A. Benghalia, Spectral-domain analysis of multilayer cylindrical-rectangular microstrip antennas, *Engng. Anal. Boundary Elem.* 33: 930-939, 2009.

[4] S. Benkouda and T. Fortaki, Resonance of rectangular microstrip patch over ground plane with rectangular aperture in the presence of high-permittivity dielectric layer below the aperture, *Proc. PIERS 2011*, Marrakech, Morocco, pp. 239-241, 2011.

[5] F. Zhao, T. T. Liu, and Z. P. Qian, A circularly polarized aperture stacked patch microstrip antenna for L band, *Progress in Electromagnetics Research C* 20: 95-109, 2011.

[6] S. Shekhawat, P. Sekra, D. Bhatnagar, V. K. Saxena, and J. S. Saini, Stacked arrangement of rectangular microstrip patches for circularly polarized broadband performance, *IEEE Antennas Wireless Propagat. Lett.* 9: 910-913, 2010.

[7] U. Mizutani, Introduction to the Electron Theory of Metals. England: Cambridge University Press, 2003.

[8] K. Fossheim and A. Sudbo, Superconductivity Physics and Application. New York: Wiley & Sons, 2004.

[9] A. Mourachkine, Room Temperature Superconductivity. England: Cambridge International Science Publishing, 2004.

[10] J. F. Seaux, "Conception, optimisation et test de dispositifs intégrant des matériaux en couche mince supraconducteurs ou ferroélectriques pour des applications de filtrage dans le domaine spatial," Doctoral Thesis, University of Limoges, April 2005.

[11] N. Sekiya, A. Kubota, A. Kondo, S. Hirano, A. Saito, and S. Ohshima, Broadband superconducting microstrip patch antenna using additional gap-coupled resonators, *Physica C* 445-448: 994-997, 2006.

[12] C. P. Poole, H. A. Farach, R. J. Creswick, and R. Prozorov, Superconductivity. London: Academic Press, Second edition, 2007.

[13] S. Benkouda, "Caractérisation d'un patch microbande supraconducteur dans une configuration substrat-superstrat. Effets du gap d'air sur la résonance de l'antenne supraconductrice ajustable," Magister Thesis, University of Batna, December 2008.

[14] T. Fortaki, M. Amir, S. Benkouda, and A. Benghalia, Study of high Tc superconducting microstrip antenna, *Proc. PIERS 2009*, Beijing, China, pp. 1405-1408, 2009.

[15] T. Fortaki, S. Benkouda, M. Amir, and A. Benghalia, "Air gap tuning effect on the resonant frequency and half-power bandwidth of superconducting microstrip patch, *Proc. PIERS 2009*, Beijing, China, pp. 1566-1570, 2009.

[16] M. A. Richard, K. B. Bhasin, and P. C. Claspy, Superconducting microstrip antennas: an experimental comparison of two feeding, *IEEE Trans. Antennas Propagat.* 41: 967-974, 1993.

[17] S. Liu and B. Guan, Wideband high-temperature superconducting microstrip antenna, *Electron. Lett.* 41, 2005.

[18] O. Barkat and A. Benghalia, Radiation and resonant frequency of superconducting annular ring microstrip antenna on uniaxial anisotropic media, *Journal of Infrared, Millimeter, and Terahertz Waves* 30: 1053-1066, 2009.

[19] F. Chebbara, S. Benkouda, and T. Fortaki, Fourier transform domain analysis of high Tc superconducting rectangular microstrip patch over ground plane with rectangular aperture, *Journal of Infrared, Millimeter, and Terahertz Waves* 31: 821-832, 2010.

[20] F. Benmeddour, C. Dumond, F. Benabdelaziz and F. Bouttout, Improving the performances of a high Tc superconducting circular microstrip antenna with mulailayered configuration and anisotropic dielectrics, *Progress In Electromagnetics Research C* 18: 169-183, 2011.

[21] P. K. Bhartia, V. S. Rao. and R. S. Tomar, Millimeter-Wave Microstrip and Printed Circuit Antennas, Artech House, Norwood, MA, 1991.

[22] M. Titaouine and F. Djahli, Simple and Efficient Approach for Arbitrary shaped Microstrip Antennas, *ITG Fachbericht* 178: 133-136, 2003.

[23] J. R. James, P. S. Hall, and C. Wood, Microstrip Antennas Theory and Design, Peter Peregrines Ltd, 1981.

[24] K. R. Carver and J. W. Mink, Microstrip Antenna Technology, *IEEE Transactions on Antennas and Propagation* AP-29: 2-24, 1981.

[25] Y. B. Gan, Vhee-Parng Chua, and Le-Wei Li, An Enhanced Cavity Model for Microstrip Antennas, *Microwave and optical Technology Letters* 40: 523-528, 2004.

[26] Y. T. Lo, D. Solomar, and W. F. Richard, Theory and experiment on microstrip antenna, *IEEE transactions on antennas Propagation* AP-27: 137-145, 1979.

[27] D.Sadiku and N.O.Mathew, Numerical techniques in electromagnetics", second edition, CRC Press, Boca Ration, London, New York, Washington, D.C, 2001.

[28] K.S.Yee, Numerical solution of initial boundary value problems involving Maxwell's equations in isotropic media, *IEEE,Trans on Antennas and propag*. 14: 302-307, 1966.

[29] D. R. Lynch and K. D. Paulsen, Time-Domain Integration of the Maxwell Equations on Finite Elements, *IEEE Transactions on Antennas and propagation* 38: 1933-1942, 1990.

[30] E. H. Newman and P. Tulyathan, Analysis of microstrip antennas using moment methods, *IEEE Trans. Antennas Propagat.* 29: 47-53, 1981.

[31] T. Itoh, Numerical techniques for microwave and millimeter-wave passive structures, A Wiley-Intercedence Publication, New York, Wiley, 1989.

[32] D.M. Pozar and S. M. Voda Arigorous analysis of a microstripline fed antenna, *IEEE Trans. Antennas Propagat.* AP-35: 1343-1350, 1987.

[33] D. M. Pozar Radiation and scattering from a microstrip patch on a uniaxial substrate, *IEEE Trans Antenna Propagat.* AP-35: 613-621, 1987.

[34] T. Fortaki and A. Benghalia, Rigorous Full-wave analysis of rectangular microstrip patches over ground planes with rectangular apertures in multilayered substrates that contain isotropic and uniaxial anisotropic materials, *Microwave and Optical Technology Letters* 41, 2004.

[35] Z. Cai and J. Bornemann, Generalized spectral- domain analysis for multilayered complex media and high-Tc superconductor applications, *IEEE Trans Microwave Theory Tech.* MTT-40: 2251-2257, 1992.

[36] S. G. da Silva, A. G. d'Assução, and J. R. S. Oliveira Analysis of high Tc superconducting microstrip antennas and arrays, *SBMO/IEEE MTT-S IMOC*, 1999.

[37] B. .G. Klopman and H. Rogala The propagation characteristics of wave-guiding structures with very thin superconductors; Application to coplanar wave- guide YBa2 CU307- x resonators, *IEEE Trans Microwave Theory Tech.* MTT-41: 781-791, 1993.

[38] C. Christodoulou and M. Georgiopoulos, Applications of Neural Networks in Electromagnetics, Norwood, MA: Artechhouse, 2001.

[39] S. Sagiroglu and K. Guney, Calculation of Resonant Frequency for an Equilateral Triangular Microstrip Antenna Using Artificial Neural Networks, *Microwave and Optical Technology Letters* 14, 89-93,1997.

[40] D. Karaboga, K. Guney, and S. Sagiroglu, Neural Computation of Resonant Frequency of Electrically Thin and Thick Rectangular Microstrip Antennas, *IEE Proc. Antennas Propag.* 146, 155-159, 1999.

[41] Q. J. Zhang and K. C. Gupta, Neural Networks for RF and Microwave Design, Artech House, Boston, MA, 2000.

[42] C. G. Christodoulou and M. Georgiopoulos, Application of Neural Networks in Electromagnetics, Artech House, MA, 2001.

[43] A. C. Maren, C. Harston and R. Pap, Handbook of Neural Computing Applications, Academic Press, London, 1990.

[44] K. Guney, and S. S. Gultekin, A comparative study of neural networks for input resistance computation of electrically thin and thick rectangular microstrip antennas, *Journal of Communications Technology and Electronics* 52, 483-492, 2007.

[45] M.A. Richard, K.B. Bhasin and P.C. Clapsy, Superconducting microstrip antennas: An experimental comparison of two feeding methods, *IEEE Trans Antennas Propagat.* AP-41: 967-974, 1993.

[46] J. D. Morrow, J. T. Williams, M. F. Davis, D. L. Licon, H. R. Rampersad, D. R. Jazdyk, X. Zhang, S. A. Long, and J. C. Wolfe, Circularly Polarized 20-GHz High-Temperature Superconducting Microstrip Antenna Array, *IEEE Transactions on Applied Superconductivity* 9: 4725-4732, 1999.

AES 2024, ROME - ITALY, 25 –28 JUNE 2024

Optimization of transient electromagnetic problems using discontinuous Galerkin methods

F. Wang[1*], T. Warburton[2], and N. Aage[1]

[1]Department of Civil and Mechanical Engineering, Technical University of Denmark, Denmark
[2]Department of Mathematics and the Program in Computational Modeling & Data Analytics Program, USA
[*]corresponding author: fwan@dtu.dk

Abstract: The study applies the discontinuous Galerkin finite element method (DG-FEM) to density-based topology optimization in transient electromagnetic problems. A discrete consistent adjoint method is employed to compute the objective sensitivity, while a reverse-time integration avoids storing forward-time solutions. The optimization approach is validated using a benchmark problem.

The discontinuous Galerkin finite element method (DG-FEM) [1] employs a space of basis and test functions resembling the finite element method but satisfies equations in a manner closer to the finite volume method. DG-FEM offers geometric flexibility, hp-adaptability, and an explicit semi-discrete form (locality), thereby outperforming finite difference, finite volume, and finite element methods for various types of problems. These characteristics render it computationally efficient and well-suited for addressing transient wave problems. Previously, only a limited number of studies have explored DG-FEM in design optimization, primarily focusing on shape and topology optimization for fluid problems [2, 3] and shape optimization of wave problems [4].

In this study, we investigate the application of DG-FEM in the density-based topology optimization of transient electromagnetic problems. The governing equations of the TM/Ez-polarized electromagnetic problems, with (H_x, H_y, E_z) as unknowns, are stated as

$$\varepsilon_r \frac{\partial E_Z}{\partial t} = c\left(-\frac{\partial H_x}{\partial y} + \frac{\partial H_y}{\partial x}\right),\ \mu_r \frac{\partial H_x}{\partial t} = -c\frac{\partial E_z}{\partial y},\ \mu_r \frac{\partial H_y}{\partial t} = c\frac{\partial E_z}{\partial x}, \tag{1}$$

where c is the light speed in a vacuum, ε_r and μ_r represent relative permittivity and permeability of the material.

We introduce nodal design variables to represent the material occupation in the domain. The material occupation in any location inside each element can be interpolated using the shape function. However, when nodal design variables are employed in higher-order elements, the interpolated design variables at a location within elements may exceed the design variable bounds of [0, 1], as illustrated in Fig. 1 (a) where the same Legendre polynomial basis is used to interpolate design variables as for the field quantities in DG-FEM. To address this issue, we propose employing a bivariate Bernstein-Bezier polynomial basis [5] to interpolate the material occupation inside each element. As depicted in Fig. 1 (b), the interpolated design variables are well-bounded by the design variable range of [0, 1]. Equation (1) is then solved using a weighted-adjusted DG-FEM [6] to handle wave propagation in heterogeneous media.

The optimization formulation for the transient electromagnetic problems can be formulated in a general form

$$\min_{\boldsymbol{\rho}} \quad G(t, \boldsymbol{\phi}), \qquad \boldsymbol{\phi} = \left[H_x, H_y, E_z\right],\ \mathbf{0} \le \boldsymbol{\rho} \le \mathbf{1},\ \ \varepsilon_r(x,y) = \rho(x,y)(\varepsilon - 1) + 1,\ \ \mu_r(x,y) = 1 \tag{2}$$

where $G(t, \boldsymbol{\phi})$ is a time-integrated function and ε is the relative permittivity of the material. The sensitivity of the objective with respect to design variables is obtained using a discrete, consistent adjoint method. To avoid the necessity of saving forward-time solutions, reverse-time integration solutions are utilized as the forward solutions in the adjoint sensitivity analysis.

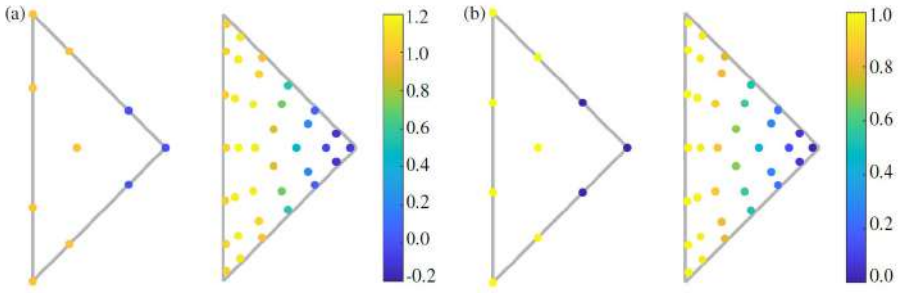

Figure 1. Nodal design variables (Left) and interpolated design variables (Right). (a) Legendre. (b) Bernstein.

The proposed approach is validated through the design of a SiO2 waveguide filter, where the objective is to minimize the magnitude of the Ez field along the target line denoted by the red line, as illustrated in Fig. 2 (a). The optimized design, along with the corresponding input (red line) and temporal response at the target (black line), are presented in Fig. 2 (b) and (c), respectively. It is evident that the recorded field at the target line has been significantly reduced.

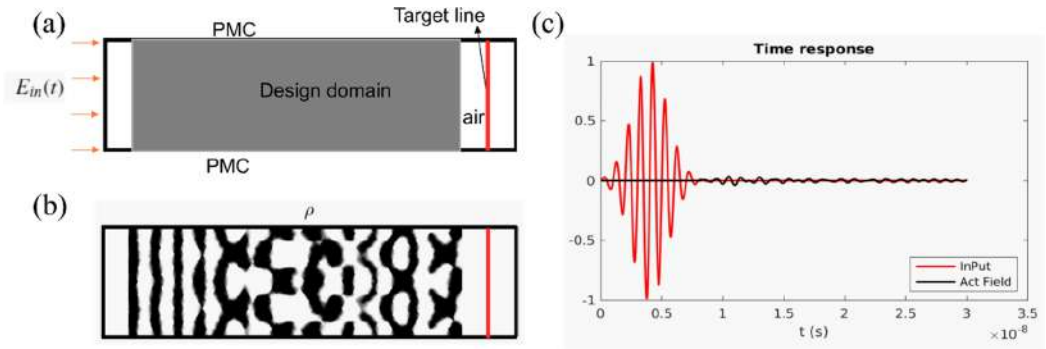

Figure 2. (a) Illustration of the filter design problem. (b) Optimized design. (c) Input (red line) and time response of the Ez field at the target line (black line).

Acknowledgments

We acknowledge the financial support from the Thomas B. Thrige Foundation through the project Topology Optimization and Additive Manufacturing for Radio Frequency Components.

References

1. Hesthaven, J. S., & Warburton, T. Nodal discontinuous Galerkin methods: algorithms, analysis, and applications. Springer Science & Business, 2007.
2. Wang, K., Yu, S., Wang, Z., Feng, R., & Liu, T. Adjoint-based airfoil optimization with adaptive isogeometric discontinuous Galerkin method. Computer Methods in Applied Mechanics and Engineering, 344, 602-625, 2019.
3. Papadopoulos, I. P. Numerical Analysis of a Discontinuous Galerkin Method for the Borrvall--Petersson Topology Optimization Problem. SIAM Journal on Numerical Analysis, 60(5), 2538-2564, 2022.
4. Wang, L., & Anderson, W. K. Adjoint-based shape optimization for electromagnetic problems using discontinuous Galerkin methods. AIAA journal, 49(6), 1302-1305, 2011.
5. Hungerbühler, R. and Garloff, J., Bounds for the Range of a Bivariate Polynomial over a Triangle. Reliable Computing, 4(1), pp.3-13 1998.
6. Chan, J., Hewett, R.J. and Warburton, T., Weight-adjusted discontinuous Galerkin methods: wave propagation in heterogeneous media. SIAM Journal on Scientific Computing, 39(6), A2935-A2961, 2017.

Electromagnetic interaction and coupling

AES 2024, ROME - ITALY, 25 –28 JUNE 2024

Enhanced Electromagnetic Interference Shielding of Self-Supporting and Ultrathin Ferrite-Decorated Carbon Nanotube Film

N. Cakmakci, and Y. Jeong*

Department of Materials Science and Engineering, Soongsil University, Seoul 06978, South Korea

*Corresponding author: yjeong@ssu.ac.kr

Abstract: Conventional EMI shielding materials need to be improved for new technologies. This study presents an ultrathin free-standing carbon nanotube film decorated with ferrite nanoparticles, demonstrating high electrical conductivity, good magnetic permeability, and enhanced shielding effectiveness. The film surpasses the commercial level and shielding effectiveness of copper in the same thickness.

Many advancements have been occurring in portable electronic devices and communication systems with the development of technology upon the demands of consumers. However, these innovations are accompanied by the issue of electromagnetic interference (EMI), recognized as a form of pollution due to its adverse impacts on human health, the environment, and various electronic infrastructures, including those in the medical and military[1]. Therefore, the development of high-performance EMI shielding materials possessing attributes such as electrical conductivity, permittivity, and magnetic permeability is imperative to mitigate the detrimental effects of EMI[2-6].

Metals have traditionally served as prevalent choices for EMI shielding due to their exceptional conductivity, but their high density and corrosive nature render them unsuitable for integration into next-generation devices[7]. Thus, efforts have been directed toward identifying lightweight alternatives with robust EMI shielding capabilities, such as MXenes and carbon nanotubes (CNTs), known for their high conductivities and low densities[3-6]. Despite the promising performance of MXenes as ultrathin EMI shielding materials, challenges persist in their fabrication processes and scalability, impeding their widespread adoption for everyday applications[3,4,8]. Another viable option exhibiting commendable EMI shielding efficacy is CNTs, often incorporated into rubber matrices to form thin film composites[5,6]. However, CNT/rubber composites encounter obstacles, including reduced electrical conductivity and mechanical integrity amidst adhesive chemical interactions[9].

Addressing these challenges, we present a novel solution involving the fabrication of an ultrathin and lightweight free-standing CNT film using the direct spinning method. The synthesized CNT film has a porous three-dimensional (3D) network structure, which can be confirmed by the SEM image in Figure 1a. The CNT film was decorated with ferrite (Fe_3O_4) nanoparticles (referred to as FCNT) to enhance its EMI shielding performance. The remarkable EMI shielding performance of the FCNT composite film can be attributed to the high conductivity of the CNT film and the superior magnetic properties conferred by the ferrite nanoparticles. Notably, the FCNT composite achieves an impressive shielding effectiveness (SE) of 94.7 dB with a thickness of 28 μm and a density of 2.06 g cm^{-3}, meeting commercial SE standards. Moreover, the FCNT composite film shows higher SE than the SE of Cu with the same thickness at the high-frequency range, as seen in Figure 1b. These findings underscore the considerable potential of the FCNT composite film as an ultrathin and low-density EMI shielding material suitable for large-scale production and widespread application.

This work was funded by the National Research Council of Science & Technology (NST) grant by the Korea

government (MSIT) (CRC22031-105) and the Institute of Civil Military Technology Cooperation funded by the Defense Acquisition Program Administration and Ministry of Trade, Industry and Energy of Korean government under grant No. 21-PD-CO-02.

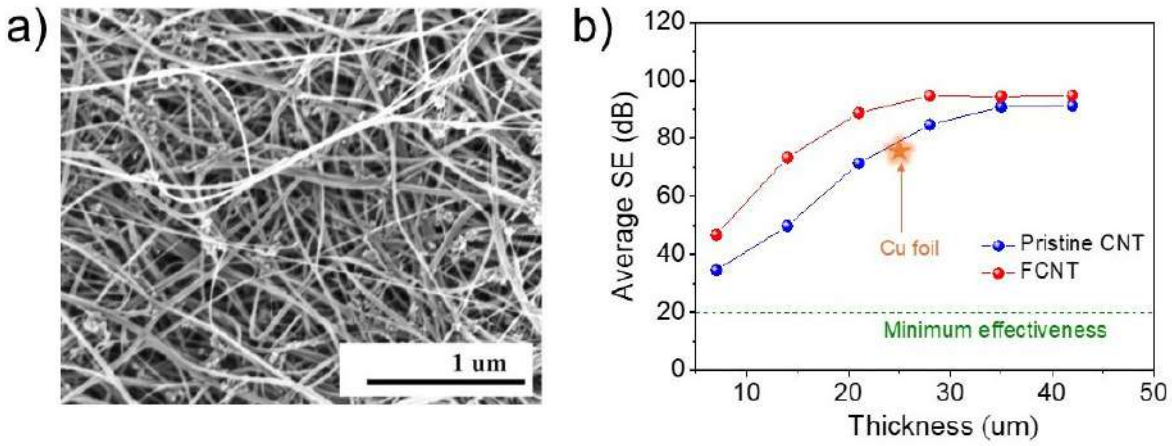

Figure 1. a) FE-SEM images of the CNT film, b) Average total SEs of pristine CNT film, and FCNT in different thickness.

References

1. Zhang, H. and S. Lin, "Research progress with membrane shielding materials for electromagnetic/radiation contamination," Membranes, Vol. 13, No. 3, 315, 2023.
2. Ahmad, H.S., T. Hussain, Y. Nawab, and H. Awais, "Graphene and Fe_2O_3 filled composites for mitigation of electromagnetic pollution and protection of electronic appliances," Compos. Sci. Technol., Vol. 240, 110097, 2023.
3. Iqbal, A., J. Kwon, M. K. Kim, and C. M. Koo, "MXenes for electromagnetic interference shielding: experimental and theoretical perspectives," Mater. Today Adv., Vol. 9, 100124, 2021.
4. Verma, R., P. Thakur, A. Chauhan, R. Jasrotia, and A. Thakur, "A review on MXene and its' composites for electromagnetic interference (EMI) shielding applications," Carbon, Vol. 208, 170–190, 2023.
5. Wang, Y., Z. Wei, L. Tan, Y. Li, L. Qin, and S. Li, "Review of polymer-based composites for electromagnetic shielding application," Molecules, Vol. 28, No. 15, 5628, 2023.
6. Joseph, T. M., H. J. Mariya, J. T. Haponiuk, S. Thomas, A. Esmaeili, and S. M. Sajadi, "Electromagnetic interference shielding effectiveness of natural and chlorobutyl rubber blend nanocomposite," J. Compos. Sci., Vol. 6, No. 8, 240, 2022.
7. Yao, B., X. Xu, H. Li, Z. Han, J. Hao, G. Yang, Z. Xie, Y. Chen, W. Liu, Q. Wang, H. Wang, "Soft liquid-metal/elastomer foam with compression-adjustable thermal conductivity and electromagnetic interference shielding," Chem. Eng. J., Vol. 410, 128288, 2021.
8. Zhu, M., C. Lu, and L. Liu, "Progress and challenges of emerging MXene based materials for thermoelectric applications," iScience, Vol. 26, 106718, 2023.
9. Chandra, R. B. J., B. Shivamurthy, S. D. Kulkarni, and M. S. Kumar, "Hybrid polymer composites for EMI shielding application-a review," Mater. Res. Express, Vol. 6, No. 8, 082008, 2019.

AES 2024, ROME - ITALY, 25 –28 JUNE 2024

Observation of tunable topological phases of polaritons in a cavity waveguide

Yan Meng[1,2,*], Zhen Gao[2,†]

[1] *School of Electrical Engineering and Intelligentization, Dongguan University of Technology, Dongguan, 523808, China*

[2] *Department of Electronic and Electrical Engineering, Southern University of Science and Technology, Shenzhen, 518055, China*

[*]presenting author: mengy@sustech.edu.cn

[†]corresponding author: gaoz@sustech.edu.cn

Abstract:

In this talk, we report the experimental demonstration of tunable topological polaritons within a cavity waveguide, achieved by modifying its width. This modification allows control over the photonic environment and the strength of light-matter interactions, enabling the realization of a topological phase transition without altering the material's lattice structure.

Summary:

The discovery of topological photonic states has significantly revolutionized our understanding of light manipulation, spawning wide applications in robust photonic devices such as topological waveguides, cavities, and lasers. Nevertheless, the manipulation of topological phases has been a daunting challenge, primarily due to the inherent preservation of the lattice structure. Recent progress in light-matter interactions has unveiled a novel mechanism for tuning topological polaritonic phases by modifying the surrounding photonic environment and light-matter interactions at the lattice sites, all without altering the lattice structure [1].

As shown in Fig. 1, to demonstrate the tunable topological phases of polaritons, we embed a dimerized chain of microwave helical resonators (MHRs) in a metallic cavity waveguide. The 1D dimerized chain of MHRs supports collective dipolar (dp) excitations (oscillating electric dipoles), which can be modeled as a prototypical 1D SSH model in the microwave regime [1]:

$$\mathcal{H}_{\mathrm{dp}} = \begin{pmatrix} \omega_0 & \Omega g_{k_x} \\ \Omega g_{k_x}^* & \omega_0 \end{pmatrix}. \tag{1}$$

When embedded within a metallic cavity waveguide, the dipolar excitations can couple with the fundamental photonic (ph) waveguide modes, upgrading the typical SU(2) SSH model (1D dimerized chain of MHRs) to a SU(3) polaritonic model (1D dimerized chain of MHRs embedded in a cavity waveguide) [2]:

$$\mathcal{H}_{\mathrm{pol}} = \begin{pmatrix} \omega_0 & \Omega g_{k_x} & i\xi_{k_x} e^{-i\chi k_x} \\ \Omega g_{k_x}^* & \omega_0 & i\xi_{k_x} e^{i\chi k_x} \\ -i\xi_{k_x} e^{i\chi k_x} & -i\xi_{k_x} e^{-i\chi k_x} & \omega_{k_x}^{\mathrm{ph}} \end{pmatrix}. \tag{2}$$

By embedding a 1D dimerized chain of MHRs in a metallic cavity waveguide, we report the first experimental observation of tunable topological polaritons by modifying only the surrounding photonic environment (light-matter interactions) without altering the lattice configuration. We experimentally demonstrate that the intrinsic band topology (Zak phase) and polaritonic band structure of the composite structure can be fundamentally tuned by changing the cavity waveguide width. Moreover, we experimentally identify three non-coincident critical points in the parameter space: when the polaritonic bandgap closes, when the Zak phase changes from nontrivial to trivial, and when the topological edge states begin to hybridize with the bulk states, verifying a new type of topological phase transition that includes three different critical transition points.

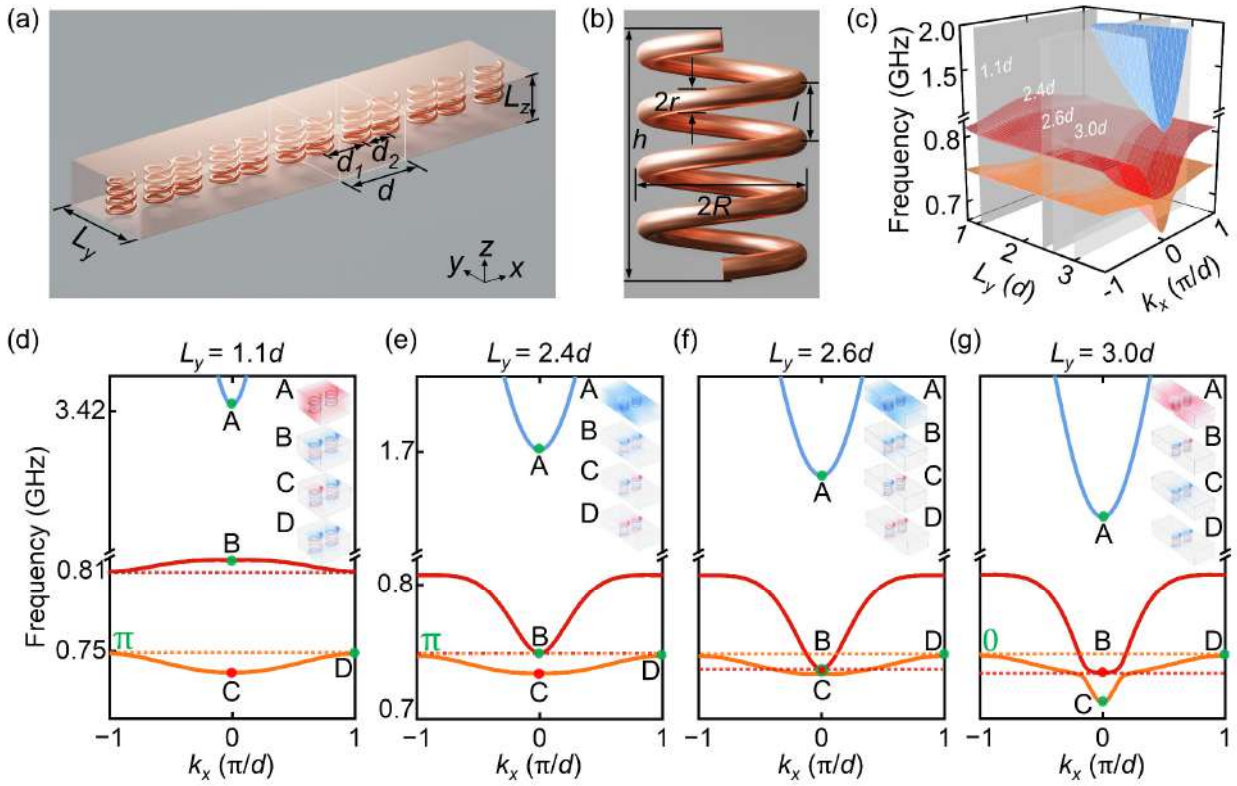

FIG. 1. Tunable topological phases of polaritons. (a) Schematic of the composite structure consisting of a 1D dimerized chain of MHRs embedded in a metallic cavity waveguide. (b) A single MHR is achieved by a copper wire with a diameter of $2r$, a helix diameter of $2R$, a helix height of h, and a helix axial intercept of l. (c) Simulated band structure diagram of the composite structure as a function of cavity waveguide width Ly and wavevector k_x. (d)-(g) Simulated band structures for different cavity waveguide widths $L_y = 1.1d$ (d), $2.4d$ (e), $2.6d$ (f), and $3.0d$ (g), respectively. Green letters π and 0 represent the Zak phases of the lowest polaritonic band ($\omega_{\mathrm{L}}^{\mathrm{pol}}$). Insets show the z-component of electric field (E_z) distributions of the eigenmodes at $k_x = 0$ (A,B,C) and $k_x = \pi/d$ (D).

Acknowledgements: Y.M. acknowledges support from the National Natural Science Foundation of China (Grant No. 12304484); the Basic and Applied Basic Research Foundation of Guangdong Province (Grant No. 2414050002552); and the Shenzhen Science and Technology Innovation Commission (Grant No. 202308073000209). Z. G. acknowledges support from the National Natural Science Foundation of China (Grant Nos. 62375118 and 12104211); the Shenzhen Science and Technology Innovation Commission (Grant No. 20220815111105001); and the Southern University of Science and Technology (SUSTech) (Grant Nos. Y01236148 and Y01236248).

References

1. C. A. Downing, T. J. Sturges, G. Weick, M. Stobi´nska, and L. Mart´ın-Moreno, Topological phases of polaritons in a cavity waveguide, Phys. Rev. Lett. **123**, 217401 (2019).

2. Zhao, Dong, Ziyao Wang, Linyun Yang, Yuxin Zhong, Xiang Xi, Zhenxiao Zhu, Maohua Gong, et al., Observation of tunable topological polaritons in a cavity waveguide, arXiv preprint arXiv:2401.10450 (2024).

Electric Near-Field Probe Calibration for PCB Emission Scanning (Invited)

H. Jia[1], F. Wan[1], J. Rossignol[2], V. Mordachev[3], G. Fontgalland[4], D-T. Do[4] and B. Ravelo[1]

[1]NUIST, Nanjing 210044, Jiangsu, China
[2]Université de Bourgogne, Dijon, France
[3]R&D Laboratory of EMC, BSUIR, Minsk, Belarus Country
[4]University of Mount Union (UMU), School of Engineering, Alliance, OH, USA
[*]Corresponding author: blaise.ravelo@yahoo.fr

Abstract: A electric (E) near-field (NF) probe modelling and calibration are investigated. The printed circuit board (PCB) EMC emission can be characterized following IEC-61967 standard uses the relevant E-NF probe. The analytical approach for calibrating such a probe for microstrip PCB is investigated. The calibration effectiveness is assessed with analytical, simulation and experimental investigation of EM radiation around 1-GHz.

1. Introduction: The EMC emission becomes electronic circuit designer's main concern. The NF scanning constitutes one of challenging techniques in EMC engineering [1-2]. Therefore, constant research work progress is necessary to reduce the EMC engineering cost and time spent particularly with the increase of PCB integration density [3]. Against this limit, EM simulation method [4] requires enormous effort to meet the standard compliances [5-6]. Moreover, standard [7] and miniature [8] NF probes were designed and implemented to improve the test facilities.

2. Description of NFS EMC Characterization: As NF scanning (NFS) test configuration, we explore in the present study the IEC-61967 standard, which is dedicated to PCB EMC emission characterization. Fig. 1 shows the test bench including a microstrip line (ML) with characteristic impedance Z_0=50-Ω and E-NF probe NFS system. The ML is connected to Port 1 of the vector network analyzer (VNA) and the other end is matched by a Z_0 load. The E-NF probe is connected to port 3.

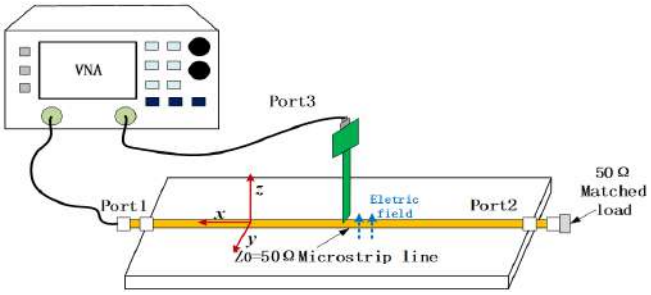

Fig. 1. E-NF probe test synoptic diagram.

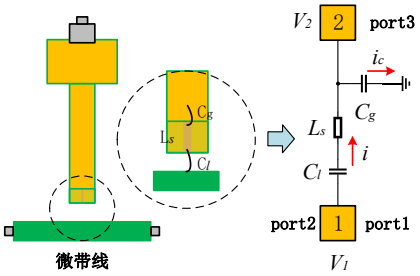

Fig. 2. Microstrip line-E-NF probe coupling model.

To calibrate the E-NF probe, we must consider the capacitive coupling between the ML and the NF probe as depicted by Fig. 2. In the proposed equivalent circuit, C_l plays the role of coupling capacitance between the microstrip line and the probe core line. The parallel capacitance between the core trace and the probe ground layer is C_g, which will significantly affect the transmission coefficient at high frequencies. The inductor L_s is the self-inductance of the core wiring. The induced current i is given by $i=C\cdot du/dt$ where u is the time-varying voltage between the probe tip and the microstrip line. The relationship between the output voltage of port 2 (V_2) and the input voltage of port 1 (V_1) versus frequency ω can be expressed as $V_2(\omega)/V_1(\omega) \propto 1/[1+C_g/C_l+L_sC_g\omega^2]$. In order to improve the low-frequency performance of the probe, C_l should be designed to be as large as possible and C_g should be reduced. Induced current will increase, and leakage current will decrease. At high frequencies, the effects of L_s and C_g become apparent. This means more current will flow to the ground plane through L_s and C_g. The actual power detected by the receiver will be lower. The effective area of the probe tip should be large, and the relative area between the ground plane and the probe tip should be small. Therefore, it is generally

recommended that the size of L_s be smaller. The following section describes the E-NF emission result.

3. Discussion on E-NF emission: The feasibility study of the E-NF calibration is performed with a proof-of-concept of 35 µm thick Cu-metallized ML with 40 mm×70 mm size designed on FR4 substrate having ε_r=4.5 and tan(δ)=0.1. The ML resonance peak is reached when its length approaches the value of quarter wavelength $\lambda/4$. A 4-layer monopole E-NF probe with 2-mm width and length was considered. The calibration test was carried out when the probe was placed 2 mm above the ML metallization plan. The measurement frequency span was from 0.1 GHz to 3 GHz by exciting the ML with 1 W input power AC voltage source.

Based on the configuration introduced in Fig. 1. the E-NF was extracted from S_{31}. The result of E-NF cartography along the scanning surface 60 mm 30 mm at the frequency 1 GHz is displayed in Fig. 3. One can see that the E-NF radiated varies up to 1 kV/m especially along the symmetric axis. The E-NF calibration was applied to more complex PCBs operating as active circuits. The scanned E-NF will be presented during the conference.

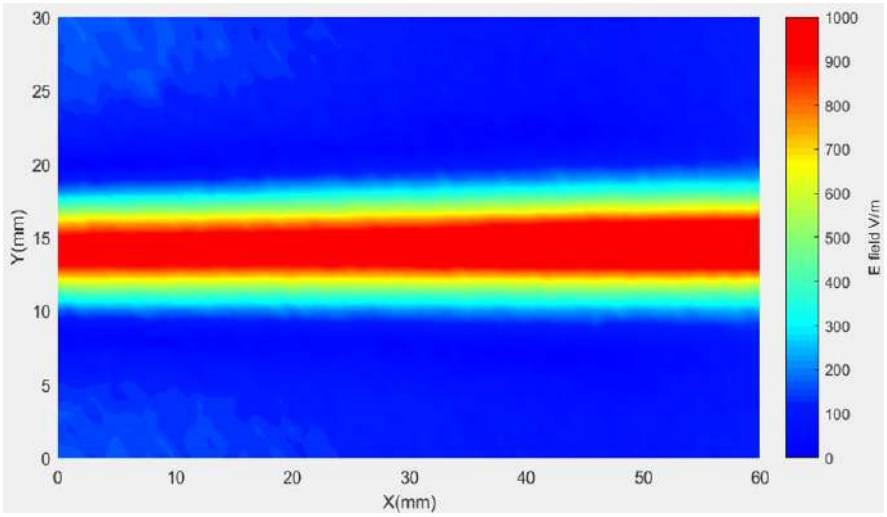

Fig. 3. E-NF magnitude cartography.

4. Conclusion: A study on H-NF probe calibration is reported. The analytical formulas for IEC-61967 standard are considered. The simulation and validation test with microstrip PCB is discussed. The E-NF calibration work is currently in progress for the challenging time-domain and transient EMC emission measurement of 6G PCB.

Acknowledgements: The work was supported in part by NSFC under Grants 62350610268 & 62371241 and in part by the National Key Research and Development Program of China under Grant 2022YFE0122700.

References

1. Liu, Y. et al., "Time-Domain Magnetic Dipole Model of PCB Near-Field Emission," IEEE Tran. EMC, vol. 58, no. 5, Oct. 2016, pp. 1561-1569.

2. Liu Y. and B. Ravelo, "Fully time-domain scanning of EM near-field radiated by RF circuits," PIER B, vol. 57, 2014, pp. 21-46.

3. M. Ramdani, et al., "The Electromagnetic Compatibility of Integrated Circuits-Past, Present, and Future," IEEE Trans. EMC, vol. 51, 1, pp. 2009,78-100.

4. Peng, X. et al., "Simulation-based electromagnetic radiation anti-interference measures and verification," Journal of Microwaves, vol. 30, no, S2, 2014, pp. 58-60.

5. Integrated Circuits-Measurement of electromagnetic emissions, 150 kHz to 1 GHz-Part 6: Measurement of conducted emissions-Magnetic probe method. 2002.

6. IEC, "Integrated circuits - Measurement of electromagnetic emissions - Part 1: General conditions and definitions," IEC 61967-1:2018, https://webstore.iec.ch/publication/59799

7. M. Kanda, "Standard probes for electromagnetic field measurements," IEEE Trans. AP, vol. 41, no. 10, 1993, pp. 1349-1364.

8. Mai-Khanh, N. et al, "An Integrated High-Precision Probe System in 0.18-µm CMOS for Near-Field Magnetic Measurements on Cryptographic LSIs," IEEE Sensors, vol. 13, no. 7, 2013, pp. 2675-2682.

AES 2024, ROME - ITALY, 25 –28 JUNE 2024

Role of Decoupling Techniques in MIMO Antenna Systems

Mohammed M. Bait-Suwailam[1,2]

[1] Communication and Information Research Center, Sultan Qaboos University, Oman

[2] Dept. of ECE, College of Engineering, Sultan Qaboos University, Oman
msuwailem@squ.edu.om

Abstract: Decoupling techniques in Multiple-Input Multiple-Output (MIMO) antenna systems play a crucial role in improving system performance. In MIMO systems, multi-antenna elements are quite often deployed for either transmission, reception or even both in order to increase channel capacity without requiring additional bandwidth or transmission power. However, a more challenging problem arise when placing multiple antenna elements in close proximity to each other. In fact, they can interfere with each other through a phenomenon known as mutual coupling. This interference can degrade the system's overall performance by altering signal transmission and reception characteristics. In order to mitigate these effects, decoupling techniques are employed. Such decoupling methods are generally categorized into two types: external and internal. For instance, external decoupling techniques involve the use of additional structures or other radiating/absorbing/reflecting elements outside the antenna array, while internal decoupling involves modifications within the antenna elements or array itself.

In this invited talk, a review of decoupling techniques for MIMO antenna systems is introduced with highlight of main MIMO performance metrics. Then, several use cases of designed and fabricated decoupling designs are presented and discussed. Additionally, the role of decoupling techniques in printed antenna systems is explored in context of electromagnetic waves nature in host planar substrates.

AES 2024, ROME - ITALY, 25 –28 JUNE 2024

Generalizing the Yagi-Uda Antenna: Multi-scale inverse design of disordered metamaterials for radiation pattern shaping

J. R. Capers[1*], L. D. Stanfield[1], J. R. Sambles[1], S. J. Boyes[2], A. W. Powell[1], A. P. Hibbins[1] and S. A. R. Horsley[1]

[1]Centre for Metamaterials Research and Innovation, University of Exeter, Stocker Road, Exeter, EX4 4Ql, United Kingdom
[2]DSTL Porton Down, Salisbury, Wiltshire, SP4 0JQ, United Kingdom
[*]corresponding author: j.capers@exeter.ac.uk

Abstract: We present, and experimentally test, a framework based on the coupled-dipole approximation for designing structures composed of a simple emitter with a passive disordered scattering structure of rods that is optimized to provide a desired radiation pattern. Our method enables the design and modelling of otherwise inaccessibly large scattering systems.

The traditional Yagi-Uda antenna [1] produces a highly directive beam from a simple dipolar source by placing rods around the driven element to either reflect or direct the radiation. In this work, we seek to conceptually generalize the Yagi-Uda antenna by asking whether, if the rods can be distributed anywhere in the plane around the emitter, greater control over the radiation pattern can be achieved. While the concept of parasitic arrays is not new, conventional design techniques provide little physical insight and often do not include coupling between array elements i.e. [2], causing performance to be degraded when elements are closely spaced.

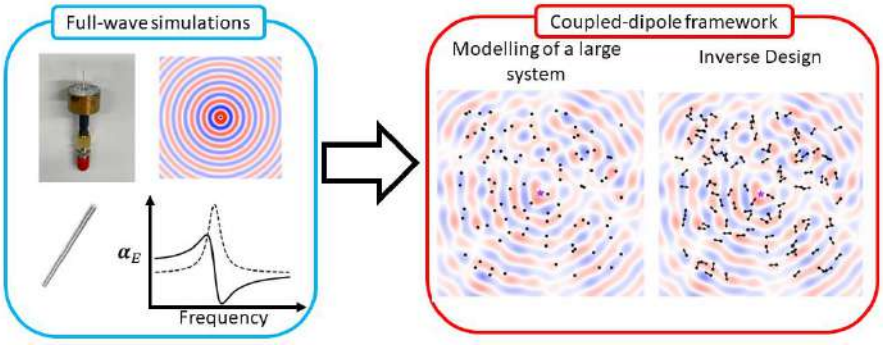

Figure 1 Our proposed solution is to numerically characterize the emitter (a sleeve antenna) and the scatterers (metal rods) using full-wave simulations, then to describe a large array of scatterers using the semi-analytic coupled-dipole approximation to enable the modelling and design of disordered arrays that produce the desired radiation pattern.

To address the modelling challenges, we have adopted a multi-scale approach, shown in Figure 1. The emitter, a sleeve antenna, and the scattering elements, metal rods with length corresponding to the half-wavelength resonance, are characterized individually using full-wave simulations. The fields from the emitter and the polarizability of the rods are then used in coupled-dipole code to model the scattering response of the system. Modelling the elements of the device independently means that the required simulations are small. The semi-analytic coupled-dipole approximation then allows for the modelling of very large parasitic arrays including all coupling effects. As a result, structures that are otherwise numerically inaccessible can be modelled. To then design devices with particular radiation patterns we utilize the adjoint method [3]. This technique is numerically

efficient and because it involves *analytically* finding the gradient of the figure of merit with respect to the positions of the scatterers, physical insight can be derived from it [3,4]. Our figure of merit is

$$F = \frac{1}{\sqrt{\int d\phi |E(\phi)|^2}\sqrt{\int d\phi\, |T(\phi)|^2}} \int d\phi |E(\phi)|T(\phi), \quad (1)$$

where $E(\phi)$ is the electric field in the plane of the emitter and $T(\phi)$ is the desired radiation pattern. Starting from a regular array of rods, our adjoint optimization iteratively adjusts the location of the rods to maximise the figure of merit. An example design is shown in Figure 2. Our technique allows for the control of the beam locations and widths simultaneously. While we focus on the particular problem of rods re-shaping the radiation from an emitter, our approach includes all of the physics of 3D vector electromagnetism and is flexible enough to be applicable to wavefront shaping, smart radio environments and radar cross-section manipulation.

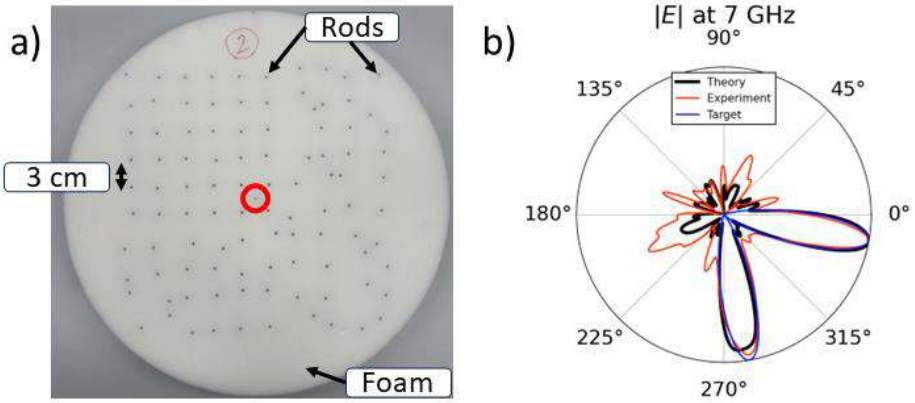

Figure 2 a) Designed device that has beams at the desired angles of $350°$ and $270°$, each with prescribed width of $15°$. The location of the emitter is indicated with a red circle. b) Measurements of the device operating at the desired working frequency of 7 GHz. The target radiation pattern is compared with the theoretically predicted radiation pattern from the coupled-dipole approximation and the experimental data.

We acknowledge financial support from the Engineering and Physical Sciences Research Council (EPSRC) of the United Kingdom, via the EPSRC Centre for Doctoral Training in Metamaterials (Grant No. EP/L015331/1). J.R.C also wishes to acknowledge financial support from Defence Science Technology Laboratory (DSTL). L. D. S. wishes to acknowledge financial support from Leonardo Ltd UK via the iCASE studentship grant EP/R511924/1. A.W.P. acknowledges financial support from the Royal Academy of Engineering under the Research Fellowship scheme. S.A.R.H acknowledges financial support from the Royal Society (URF\ R\ 211033).

References

1. Yagi, H., Uda, S., "Projector of the Sharpest beam of electric waves", Proceedings of the Imperial Academy Vol. 2, No. 2, 49-52, 1926.
2. Yang, F., Yang S., Chen Y., Qu, S., Hu J. "Synthesis of Sparse Antenna Arrays Subject to Constraint of Directivity via Iterative Convex Optimization" IEEE Antennas Wirel. Propag. Lett. Vol. 20, No. 8, 1498-1502, 2021
3. Capers, J. R., Boyes, S. J., Hibbins A. P., Horsley, S. A. R "Designing the collective non-local responses of metasurfaces", Commun. Phys. **4** (209) 2021
4. Capers, J. R., Stanfield, L. D., Sambles, J. R., Boyes, S. J., Powell, A. W., Hibbins A. P., Horsley, S. A. R "Multiscale design of large and irregular metamaterials", Phys. Rev. Applied **21** 014005 (2024)

AES 2024, ROME - ITALY, 25 –28 JUNE 2024

Spin wave amplification through Superradiance

E. X. R. Wang[1,2]

[1]The Hong Kong University of Science and Technology, China
[2]HKUST Shenzhen Research Institute, China
[*]corresponding author: phxwan@ust.hk

Abstract: Superradiance is a phenomenon of multiple facets that occurs in classical and quantum physics under extreme conditions. Here we present its manifestation in spin waves under an easily realized condition. We show that an interface between a current-free (normal) ferromagnetic (FM) region and a current-flow (pumped) FM region can be a spin wave supermirror whose reflection coefficient is larger than 1. The super-reflection is the consequence of current-induced spectrum inversion where phase and group velocities of spin waves are in the opposite directions. An incident spin wave activates a backward propagating refractive wave inside pumped FM region. The refractive spin wave re-enters the normal FM region to constructively interfere with the reflective wave. It appears that the pumped FM region coherently emits reflective waves, leading to a super-reflection. The process resembles superradiance of a spinning black hole through the Hawking radiation process, or Dicke superradiance of cavity photons inside population inverted media.

Metamaterials, metasurfaces, FSS and EBG

Broadband dispersion compensation with ultrathin multiresonant metasurfaces

Odysseas Tsilipakos[1*] and Thomas Koschny[2]

[1] Theoretical and Physical Chemistry Institute, National Hellenic Research Foundation, GR-11635 Athens, Greece
[2] Ames Laboratory–U.S. DOE and Department of Physics and Astronomy, Iowa State University, Ames, Iowa 50011, USA
[*]corresponding author: otsilipakos@eie.gr

Abstract: We propose multiresonant metasurfaces exhibiting a broadband and purely quadratic spectral phase to be utilized for dispersion compensation. The proposed metasurfaces require implementing a specific combination of Lorentzian resonances in the electric and magnetic surface conductivities. Our approach aspires to bring broadband dispersion engineering at ultrathin physical scales.

In recent years, metasurfaces (MSs) have been extensively studied for a myriad of applications. However, they have found limited use when it comes to broadband dispersion engineering and the temporal shaping of short pulses. This is because conventional, singly-resonant MSs are inherently narrowband and exhibit a specific spectral phase profile dictated by the resonance dispersion; for a single Lorentzian resonance centered at Ω it is of the form $\varphi(\omega) \propto \mathrm{atan}(\gamma(\omega - \Omega))$. The first example of a broadband, specifically-engineered spectral phase concerned a linear profile (spectrally-constant group delay), utilized to delay broadband pulses without distortion [1] and to perform achromatic wavefront manipulation (e.g., beam focusing and steering) [2,3]. However, a wider class of important applications requires a quadratic phase profile (linear group delay), namely, dispersion compensation, chirped pulse amplification, and more generally any application requiring control over the instantaneous frequency (chirp) and temporal duration of a broadband pulse through pulse chirping/de-chirping.

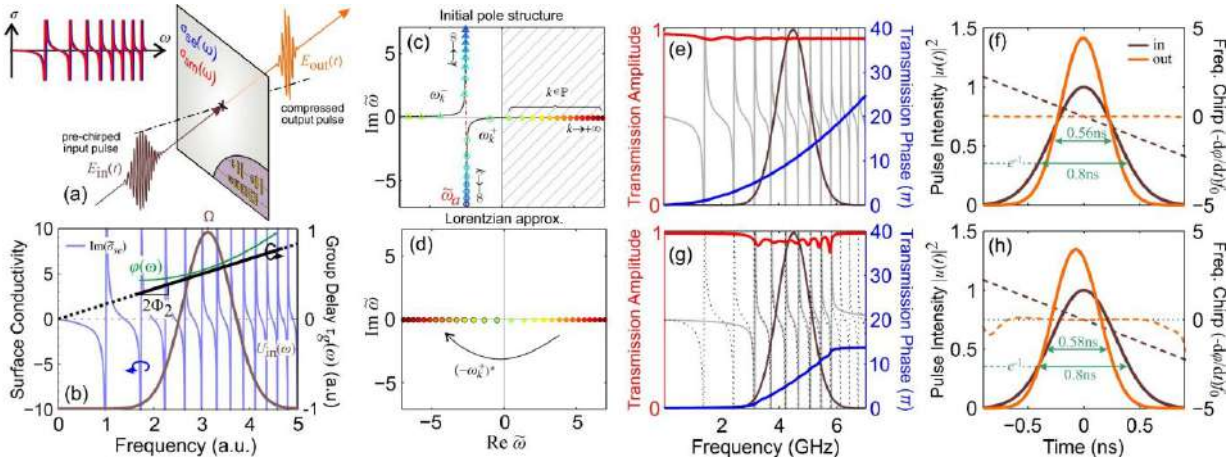

Figure 1: (a) Multiresonant metasurface with overlapping electric and magnetic surface conductivities for dispersion compensation in transmission. (b) The decreasing frequency spacing leads to positive group delay dispersion ($\Phi_2 > 0$). (c) Initial pole structure of required surface conductivity $\tilde{\sigma}_{se}(\omega)$. (d) Pole structure of the Lorentzian approximation $\tilde{\sigma}_{se}^{LA}(\omega)$. (e,f) Dispersion compensation example with an infinite Lorentzian resonance train. (g.h) The resonance train is truncated to seven resonances; the bandwidth becomes finite but the performance is not compromised.

Thus far, the approaches to dispersion compensation with MSs are either too narrowband or do not guarantee pulse integrity [4-6]. Here, we present a solution to this problem by constructing multiresonant MSs that implement

a purely quadratic phase profile which is both arbitrarily strong and (almost) arbitrarily broadband, as controlled by the spacing and number of the implemented resonances, respectively [7]. The main elements of our approach are illustrated in Fig. 1. A specific configuration of Lorentzian resonances in the electric and magnetic surface conductivities with decreasing(increasing) frequency spacing can lead to a purely quadratic phase $\varphi(\omega) = \Phi_2(\omega - \Omega)^2 + \Phi_1(\omega - \Omega) + \Phi_0]$ with positive(negative) group delay dispersion Φ_2 [Fig. 1(a),(b)].

In order to rigorously derive the required surface conductivities, we plug the desired transmission/reflection transfer function $H(\omega) = A\exp\{i\varphi(\omega)\}$ [$\varphi(\omega)$ is the quadratic phase and A allows for amplitude decay] in the expressions relating transmission/reflection plane-wave scattering coefficients with the surface conductivities of the MS [1]. The resulting prescription for the electric surface conductivity is found to be $\tilde{\sigma}_{se}(\omega) = -i\tan\{[\varphi(\omega) + i|\log A|]/2\}$. The poles of this complex function are depicted in Fig. 1(c). Subsequently, we keep only the poles with indices $k \in \mathbb{P}$ in Fig. 1(c) and complement them with their negative-conjugate counterparts [Fig. 1(d)] in order to end up with a Lorentzian approximation to the required conductivity [7]. The Lorentzian approximation $\tilde{\sigma}_{se}^{LA}(\omega)$ is (i) characterized by poles residing only in the lower complex half-plane (as required by causality) and (ii) possesses the correct spectral symmetry (real part: even; imaginary part: odd) so that it translates into a real function in the temporal domain, as required for physical response functions.

As can be seen in Fig. 1(e), implementing the Lorentzian approximation $\tilde{\sigma}_{se}^{LA}(\omega)$ the metasurface can exhibit a broadband quadratic spectral phase with a fairly flat amplitude. This can be used for dispersion compensation of chirped signals [Fig. 1(f)]. For operation in transmission(reflection) electric and magnetic conductivities have to be spectrally overlapping(interleaved). In the example of Fig. 1(e),(f), the output pulse is completely de-chirped and compressed by a factor of $\sqrt{2}$, as intended. In practice, the resonance trains need to be truncated. Figure 1(g) investigates this scenario keeping seven resonances. The compression is only slightly affected and the residual output chirp is negligible along the duration of the output pulse [Fig. 1(h)].

Acknowledgments

This work was funded by the Hellenic Foundation for Research and Innovation (H.F.R.I.) under the "2nd Call for H.F.R.I. Research Projects to support Post-doctoral Researchers" (Project Number: 916, PHOTOSURF).

References

1. Tsilipakos, O., Zhang, L., Kafesaki, M., Soukoulis, C. M. and Koschny, T., "Experimental implementation of achromatic multiresonant metasurface for broadband pulse delay," ACS Photon., Vol. 8, 1649-1655, 2021.
2. Fathnan, A. A., Liu, M., Powell, D. A., "Achromatic Huygens' Metalenses with Deeply Subwavelength Thickness," Adv. Optical Mater. Vol. 8, 2000754, 2020.
3. Tsilipakos, O., Kafesaki, M., Economou, E. N., Soukoulis, C. M. and Koschny, T., "Squeezing a prism into a surface: emulating bulk optics with achromatic metasurfaces," Adv. Opt. Mater., Vol. 8, 2000942, 2020.
4. Dastmalchi, B., Tassin, P., Koschny, T. and Soukoulis, C. M., "Strong group-velocity dispersion compensation with phase-engineered sheet metamaterials," Phys. Rev. B, Vol. 89, 115123, 2014.
5. Decker, M., Staude, I., Falkner, M., Dominguez, J., Neshev, D. N., Brener, I., Pertsch, T., Kivshar, Y. S., "High-efficiency dielectric Huygens' surfaces," Adv. Opt. Mater., Vol. 3, 813−820, 2015.
6. Divitt, S., Zhu, W., Zhang, C., Lezec, H. J. and Agrawal, A., "Ultrafast optical pulse shaping using dielectric metasurfaces," Science, Vol. 364, 890-894, 2019.
7. Tsilipakos O. and Koschny T., "Multiresonant metasurfaces for arbitrarily broad bandwidth pulse chirping and dispersion compensation," Phys. Rev. B, Vol. 107, 165408, 2023.

AES 2024, ROME - ITALY, 25 –28 JUNE 2024

Magnetic permeability investigation of AL800 ferrite by different methods

S. Rudys[1], C. Vollinger[2], J. Banys[3*], V. Kalendra[3]

[1]Antanas Gustaitis' Aviation Insitute, Vilnius Gediminas Technical University, Linkmenu str. 28-4, 08217 Vilnius, Lithuania
[2]CERN, Geneva, Switzerland
[3]Institute of Applied Electrodynamics and Telecommunications, Vilnius University, Sauletekio ave. 3, 10257 Vilnius, Lithuania
[*]corresponding author: juras.banys@ff.vu.lt

Abstract: The presence of anisotropy in the properties of materials provides challenges for characterization. We suggest extending the frequency range of the classic single-turn inductor method for disc with hole-shaped AL800 ferrite samples to GHz frequency range by using numerical methods, provided by Ansoft HFSS software.

A wide variety of magnetic materials such as ferrites, magneto-dielectrics, and multiferroics are used in various applications. The most popular class of magnetic materials are ferrites. Due to high magnetic permeability – ferrites are used in a wide range of applications - from conventional electronic equipment to fast kicker magnets in injection and extraction systems of circular accelerators [1]. Unfortunately, producers of the ferrites provide only basic information which is inadequate for precise magnetic permeability dependence on frequency or dependence on external field recovery, which is required for applications.

The measurements of the electromagnetic properties of materials consist of three main components: measurement equipment, device under test (DUT) with investigated material, and mathematical model. The model relates electrical values measured by the equipment and physical properties of the material, the latter being the goal of the measurement. The measurement method of magnetic permeability, based on single-turn inductor DUT [2], probably is the most popular due to the very simple mathematical model, hardware, and calibration.

Frequency dependence of the magnetic permeability of AL800 ferrite is presented in Fig.1, performing typical behavior of ferrites when 2 processes are assigned to spins and domain walls contribution. In addition, the third process is visible in the frequency range up to 2 GHz. On the frequencies higher than 2 GHz, we obtain resonance-like behavior of magnetic permeability. There are no physical reasons for such a steep increase of magnetic permeability. Thus, we can suppose, the model of the lumped inductor is not valid at high frequency. In this case, dimensions of the sample are comparable to the wavelength. The results of calculations of magnetic permeability using Ansoft HFSS software are presented in Fig.1 as blue and green dots on the relevant curves of magnetic permeability, obtained by single turn inductor method. The dielectric permittivity of the sample was measured earlier and was taken into account.

DUT as a microstrip line can be used for electric properties measurements [3]. Transverse electro-magnetic (TEM) wave propagates in the sample. In this case, the magnetic field is not circular. Field lines are straight, parallel to the strip, and perpendicular to the direction of propagation. Thus microstrip DUT is suitable for measurements of magnetic permeability tensor. Both electric and magnetic properties can be measured when connecting the microstrip to a two-port vector network analyser.

Experimental results using microstrip DUT with AL800 ferrite sample of magnetic permeability measurements are presented in Fig 2., as blue and green dots on the relevant curves (dark blue and red) of magnetic permeability for reference, obtained by single-turn inductor method. We are obtaining lower agreement with single-turn inductor measurements at lower frequencies (dark blue and red lines) than experimental results

in Fig. 1. Lower accuracy at low frequencies is caused due to reduced (approx. 3 times) sample volume under a magnetic field. Due to model complexity, microstrip model calculations were more time consuming than single turn inductor one -tens of minutes for calculation of the one point.

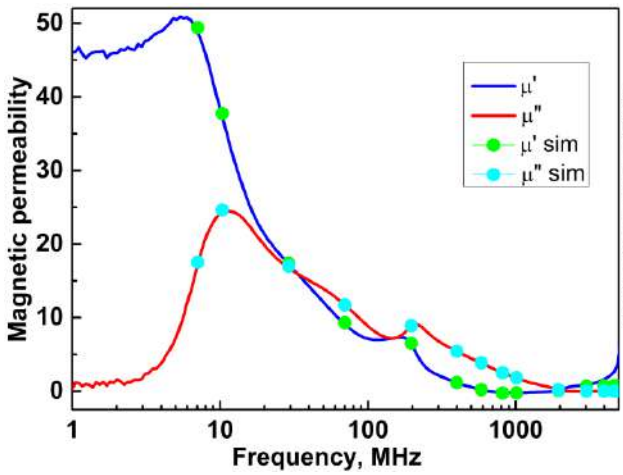

Fig. 1. Frequency dependence of the real (μ') and imaginary (μ") parts of magnetic permeability of AL-800 ferrite using a single-turn inductor method. Blue and green dots indicate the calculated values using the Ansoft HFSS EM simulation software. Measurements were performed at room temperature.

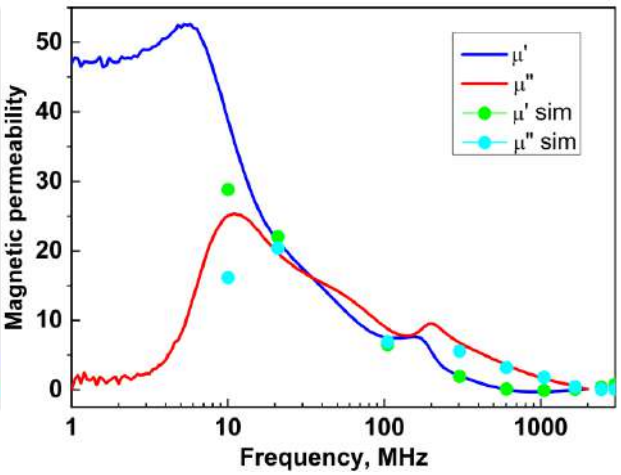

Fig. 2. Frequency dependence of the real (μ') and imaginary (μ") parts of magnetic permeability of AL-800 ferrite using a single-turn inductor setup. Blue and green dots indicate the calculated values using the Ansoft HFSS EM simulation software on microstrip setup.

The frequency range of single-turn inductor can be extended towards high frequency by using commercial electromagnetic simulation software. It is possible to measure the anisotropy of electromagnetic properties by using the suggested microstrip measurement setup and software for EM simulation. Using the optimization option in the commercial EM simulation software it is possible to find the electric and magnetic material properties of the samples in very complex shapes. Using numerical methods allows us to take into account the spurious factors arising at the connection of a measured sample to a metering circuit. Thus, it is possible to consider the EM simulation software as a powerful and universal tool for material properties measurements.

References

1. Harris, V. G. “Modern Microwave Ferrites,” IEEE Transactions on Magnetics, Vol. 48, No. 3, 1075-1104, 2012.
2. White, R. M. “Quantum Theory of Magnetism: Magnetic Properties of Materials”, Springer, Berlin, 2007.
3. Rudys, S., Ivanov, M., Banys J. Ansoft HFSS Software Application for the Dielectric and Magnetic Measurements of Ferroelectrics and Related Materials in Microwaves, Ferroelectrics, Vol 430, No. 1, 115-122, 2012.

Non-contact Bio-molecules Sensing via Exceptional Transitions on Non-Hermitian Metasurfaces

Hyunwoo Park[1], Sodam Jeong[1], Hyeji Son[1], Soojeong Baek[2] and Teun-Teun Kim[1*]

[1]University of Ulsan, Daehak-ro, Nam-gu, Ulsan, 93, Republic of Korea
[2]Korea Advanced Institute of Science and Technology (KAIST), Daehak-ro, Yuseong-gu, Daejeon, 291, Republic of Korea
[*]corresponding author: ttkim@ulsan.ac.kr

Abstract: We report the detection of trace amounts of amyloid-beta (Aβ) protein using non-Hermitian metasurfaces integrated with microfluidic channels. An abrupt phase transition in cross-polarized transmission, highly sensitive near the exceptional point, introduces a new approach to identifying conductive biomolecules.

Recent advances in non-Hermitian (NH) systems have revolutionized the study of optical phenomena, breaking down the conventional boundaries defined by Hermitian Hamiltonian descriptions. In particular, these NH systems are closely associated with known as NH degeneracy at points called exceptional points (EPs), where even very small changes can result in drastic optical responses. This makes them pivotal in developing highly sensitive photonic devices and sensors [1]. Metasurfaces, comprising two-dimensional arrays of engineered subwavelength structures, offer a promising approach for exploring EPs. By manipulating transmission properties with NH metasurfaces, phenomena such as the asymmetric transmission of circularly polarized light and abrupt phase transitions near EPs have been demonstrated, holding promise for applications in sensitive modulation and sensing [2]. Recently, our research has revealed that the Aβ protein, well-known as a dementia-inducing substance, exhibits its highest conductivity in the monomeric form before fibrillization proceeds, as determined through non-contact THz measurement [3]. However, detecting Aβ protein at extremely low molecular levels, below picomole concentrations, has been challenging in conventional optical systems. In this study, we present NH metasurfaces designed specifically for sensing conductive biomolecules. By utilizing the exceptional sensitivity to perturbations near EPs in NH metasurfaces, we identify slight fluctuations in Aβ protein concentrations at sub-picomolar levels, recognizing these changes as quantifiable phase shifts in cross-polarized transmission.

We designed NH metasurfaces comprising two split-ring resonators (SRRs) operating near EPs (Fig. 1a) [2]. A microfluidic channel was integrated for solution injection, allowing the solution to pass between adjacent meta-atoms. Fabrication involved UV lithography to pattern a metal layer, which was combined with polydimethylsiloxane (PDMS) to form microchannels, completing the microchip. Starting with the medium injected into the microfluidic channel using a pneumatic pump, the measurement range was from 1 zepto mol to 1 femto mol. Figure 1b shows the phase shift of circularly polarized light converted from LCP to RCP(T_{RL}) over the metasurfaces for each solute concentration. The observed phase change in cross-polarization transmission arises from the sensitivity of eigenvalues and eigenstates near EPs, with even slight changes causing rapid 2π phase jumps. The NH metasurface platform offers a robust framework for investigating conductive biomolecules, presenting a highly sensitive, non-contact optical sensing approach. This study highlights the potential of NH metasurfaces in enhancing detection capabilities across various applications in the terahertz frequency regime.

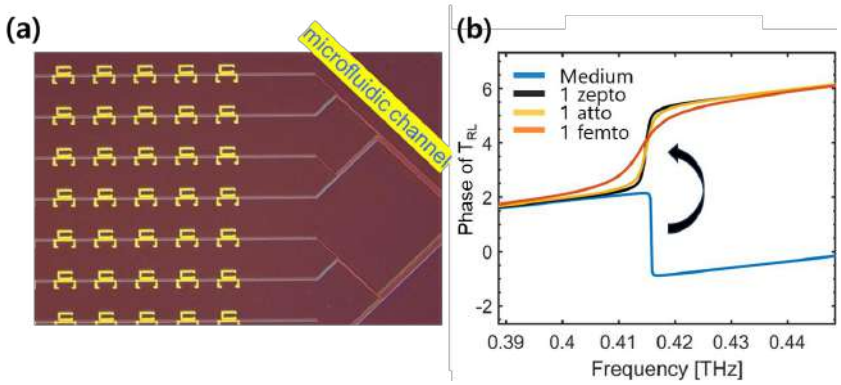

[Fig.1] (a) Optical microscopy images of microfluidic channel hybridized non-Hermitian metasurfaces. (b) Measured phase shift of T_{RL} with different Aβ protein concentrations.

Acknowledgments, This work was supported by National Research Foundation of Korea (NRF) through the government of Korea (NRF-2021R1C1C100631612)

References

1. W. Chen S *et al*., "Exceptional points enhance sensing in an optical microcavity," Nature, Vol. 548, 192-196, 2017.
2. S. H. Park *et al*., "Observation of an exceptional point in a non-Hermitian metasurface," Nanophotonics, Vol. 9, 1031-1039, 2020.
3. C. Heo *et al*., "Identifying Fibrillization State of A*β* Protein *via* Near-Field THz Conductance Measurement," ACS Nano, Vol. 14, 6548-6558, 2020.

Temporal metastructures enabling multi-mode generation and continuous spectrum radiation

D. Ramaccia[1*], L. Stefanini[1], A. Monti[1], M. Barbuto[2], S. Vellucci[2], M. Longhi[2], M. Karamirad[1], A. Toscano[1] and F. Bilotti[1]

[1] Dept. Of Industrial, Electronic and Mechanical Engineering, RomaTre University, Rome, Italy
[2] Dept. of Engineering, Niccolò Cusano university, Rome, Italy
[*]Corresponding author: davide.ramaccia@uniroma3.it

Abstract: With the advent of the temporal metamaterials, the time dimension has been exploited to unlock several time-equivalent scattering processes observed in space domain. In this contribution, we present our recent findings on the scattering effects emerging in time-varying metastructures, showing multi-mode generation and radiation of a continuous spatio-temporal spectrum.

In the last few years, the possibilities offered by metamaterials and metasurfaces have been further extended thanks to their modulation over time [1],[2]. This new degree of freedom enables the conceiving of a new class of scattering phenomena, characterized by a precise control of the temporal features of the electromagnetic waves [3]-[6], and consequently a new class of metadevices [7]-[11].

In this contribution, we present and discuss our recent results on the scattering process taking place within a guiding system when the boundary conditions are varied instantaneously, realizing a temporal interface for the guided mode [12], [13]. We analyze two relevant cases based on a parallel-plate waveguide (PPWG) system that allow generating a multi-mode propagation and the anomalous radiation process characterized by a continuous spatio-temporal spectrum of plane waves, respectively.

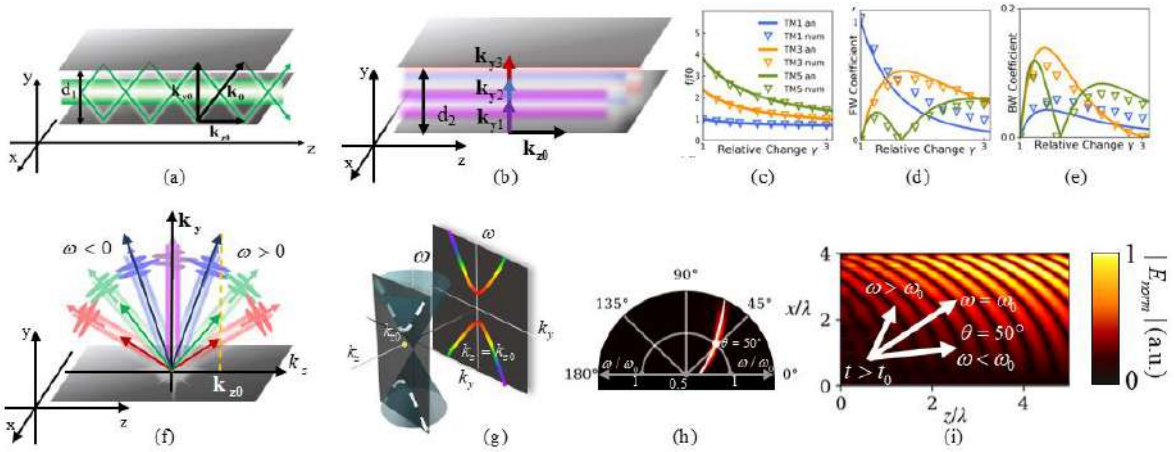

Figure 1: Scattering effects emerging from TV metastructures: (a) initial condition (t<t0) for a parallel plate waveguide; (b) boundary-induced temporal interface in a closed metastructure, scattering a discrete number of forward/backward propagating modes at different (results are reported in (c)-(e)); (f) boundary-induced temporal interface in a open metastructure, which scatters a continuous spectrum of plane waves sharing the same z-component of the propagating wavevector as shown on the light cone in (g); full-wave results of the frequency vs. propagation direction are in (h)-(i).

Figure 1(a)-(b) show a temporal interface realized by instantaneously switching the conductivity of the top plate to zero and placing a new plate at distance d_2. The effective medium perceived by the travelling wave changes and triggers the temporal interface, that generates a set of two opposite-propagating waves. The anomalous scattering response has been analytically described and numerically verified using an FDTD code, as shown in Figure 1c-e. It is clear that the change of the effective medium perceived by the wave performs in similar fashion to the changing of the actual material where the wave is propagating, simplifying the implementation of temporal metamaterials.

Figure 1(f) shows the case where the conductivity of the top plate is set instantaneously to zero, opening *de facto* the waveguide system. In this case, the wavevector matching between guided and radiated modes forces the excitation all the possible modes on the light cone sharing the same wavevector k_z (Figure 1(g)), realizing a polychromatic rainbow-like radiation generated by a simple monochromatic wave. Figure 2(h)-(i) report the amplitude of the E-field emerging from the PPWG after the temporal interface: most of the energy is coupled to the plane wave propagating along the direction θ_0 at the frequency ω_0 of the initial monochromatic wave. Plane waves at higher frequencies propagated at greater angles, whereas the ones at lower frequencies at smaller angles.

D.R. acknowledges the support of the Air Force Office of Scientific Research (AFOSR) through the grant FA8655-23-1-7065.

References

1. V. Pacheco-Peña, V. Pacheco-Peña, D. M. Solís, D. M. Solís, D. M. Solís, and N. Engheta, "Time-varying electromagnetic media: opinion," Optical Materials Express, vol. 12, no. 10, pp. 3829–3836, Oct. 2022.
2. E. Galiffi et al., "Photonics of time-varying media," Adv. Photonics, Vol. 4 No. 1, 2022.
3. A. Shaltout, A. Kildishev, and V. Shalaev, "Time-varying metasurfaces and Lorentz non-reciprocity," Opt Mater Express, vol. 5, no. 11, p. 2459, Nov. 2015.
4. D. Ramaccia, D. L. Sounas, A. Alù, A. Toscano, and F. Bilotti, "Doppler cloak restores invisibility to objects in relativistic motion," Phys Rev B, vol. 95, no. 7, p. 075113, Feb. 2017.
5. E. Galiffi, Y. T. Wang, Z. Lim, J. B. Pendry, A. Alù, and P. A. Huidobro, "Wood anomalies and surface-wave excitation with a time grating," Phys Rev Lett, vol. 125, no. 12, p. 127403, Sep. 2020.
6. H. Li and A. Alù, "Temporal switching to extend the bandwidth of thin absorbers," Optica, vol. 8, no. 1, p. 24, 2021.
7. D. Ramaccia, et al., "Nonreciprocity in antenna radiation induced by space-time varying metamaterial cloaks," IEEE Antennas Wirel Propag Lett, vol. 17, no. 11, pp. 1968–1972, Nov. 2018.
8. D. Ramaccia et al., "Electromagnetic Isolation Induced by Time-Varying Metasurfaces: Non-Reciprocal Bragg Grating," IEEE Antennas Wirel Propag Lett, Vol. 19, No.11, pp. 1886-1890, May 2020.
9. A. V. Marini, D. Ramaccia, A. Toscano, and F. Bilotti, "Metasurface-bounded open cavities supporting virtual absorption: free-space energy accumulation in lossless systems," Opt Lett, vol. 45, no. 11, pp. 3147–3150, May 2020.
10. A. V. Marini, D. Ramaccia, A. Toscano, and F. Bilotti, "Metasurface virtual absorbers: unveiling operative conditions through equivalent lumped circuit model," EPJ Applied Metamaterials, vol. 8, p. 3, Jan. 2021.
11. A. V. Marini, et al., "Perfect Matching of Reactive Loads Through Complex Frequencies: From Circuital Analysis to Experiments," IEEE Trans Antennas Propag, vol. 70, no. 10, pp. 9641–9651, Oct. 2022.
12. L. Stefanini, S. Yin, D. Ramaccia, A. Alù, A. Toscano, and F. Bilotti, "Temporal interfaces by instantaneously varying boundary conditions," Phys Rev B, vol. 106, no. 9, p. 094312, Sep. 2022.
13. L. Stefanini, D. Ramaccia, A. Toscano, and F. Bilotti, "Temporal rainbow scattering at boundary-induced time interfaces," Appl Phys Lett, vol. 122, no. 5, p. 051701, Jan. 2023.

Local Design of Phase-gradient Metasurfaces robust to Mutual Coupling and Fabrication Errors

D. Ramaccia[1*], L. Stefanini[1], A. Monti[1], M. Barbuto[2], S. Vellucci[2], M. Longhi[2], M. Karamirad[1], A. Toscano[1] and F. Bilotti[1]

[1] Dept. Of Industrial, Electronic and Mechanical Engineering, RomaTre University, Rome, Italy
[2] Dept. of Engineering, Niccolò Cusano university, Rome, Italy
[*]Corresponding author: davide.ramaccia@uniroma3.it

Abstract: Metasurfaces is undoubtedly one of the future disruptive technologies. Despite the current design methodologies are quite accurate, we demonstrate that the design may be affected by unpredictable deviations, that can be considered already during the design process by using a statistically corrected local design approach.

Phase-gradient metasurface is nowadays the primary technology for realizing novel antenna functionalities [1]-[3], metadomes for beam steering [4], grating lobe reduction [5] and enlarging the FoV [6], intelligent surfaces for the generation of composite vortices [7], and energy accumulation [8]-[9]. These metasurface-based devices are typically designed using conventional design methodologies together with optimization algorithms, completely overlooking the practical considerations of large-scale fabrication and deployment in real-world environments. Indeed, mutual coupling among MTS cells, fabrication defects, and the impact of mechanical and thermal stresses, are only some of the possible unpredictable deviations from the original design.

Starting from concept of electromagnetic roughness [10], [11], this contribution presents a novel statistical model for designing metasurface-based devices that exhibit resilience against unpredictable errors and defects. The model establishes a quantitative relationship between metasurface scattering performance and electromagnetic roughness, revealing that an average scattering gain loss is inevitable, as shown in Figure 1(a).

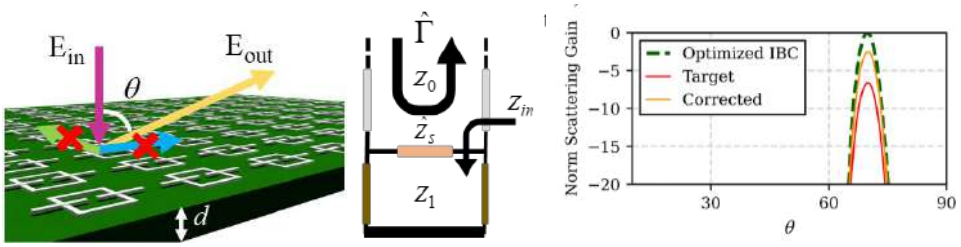

(a) (b) (c)

Figure 1: (a) Graphical representation of a reflective metasurface designed for achieving anomalous reflection. (b) Equivalent transmission line model of the metasurface illuminated by a normally incident plane wave; (c) Normalized scattering gain of the Optimized, Target, and Corrected by the proposed statistical model.

To address this issue, we propose a surface impedance transformation technique that enhances RIS robustness against unforeseen imperfections. Specifically, we describe the local input impedance Z_{in}, derived using the transmission line model in Figure 1(b), as if it were a random variable that considers the unpredictable deviation of the Local Input Impedance. Assuming a gaussian-like probability function of the deviations of the metasurface impedance Z_s, the random LII can be described by the following probability density function (pdf):

$$\mathrm{pdf}(\hat{Z}_{in}) = \frac{A}{1+(Z_{in}/Z_0)^2}\exp\left(\frac{\cos(2\,\mathrm{arccot}(Z_{in}/Z_0)-\varphi_0)}{\Delta\varphi^2}\right) \quad (1)$$

where A is a normalization constant and φ_0 is defined as $\varphi_0 = 2\,\mathrm{arccot}(Z_{in0}/Z_0)$, where Z_{in0} represents the target surface impedance that corresponds to the reflection phase φ_0.

To compensate this deviation from the desired target value, we define a transformation function for the input impedance that in turns affects the surface impedance Z_s. Here we identify a new value of input impedance Z'_{in0} such that its expected value is equal to Z_{in0}, i.e., the target value:

$$Z'_{in0} = \mathbb{E}\left\{\mathrm{pdf}(\hat{Z}_{in}, Z'_{in0})\right\}^{-1} = K(Z_{in0}) \quad (2)$$

Equation (2) introduces a novel design strategy for enhancing the statistical robustness of metasurfaces. Both target and corrected metasurfaces have been implemented and the corresponding performances have been numerically computed by using a CST Microwave Studio [12]. In Figure 1(c) we report the comparison of the scattering gains: the metasurface with the corrected surface reactance exhibits performances closer to the ideal scenario. It is worth highlighting that no optimization processes have been used in the full-wave simulations to achieve the results. More details on the design approach will be provided at the conference.

References

1. M. Barbuto *et al.*, “Metasurfaces 3.0: A New Paradigm for Enabling Smart Electromagnetic Environments,” IEEE Trans Antennas Propag, vol. 70, no. 10, pp. 8883–8897, Oct. 2022.
2. M. Barbuto *et al.*, "Intelligence Enabled by 2D Metastructures in Antennas and Wireless Propagation Systems," in IEEE Open Journal of Antennas and Propagation, vol. 3, pp. 135-153, 2022.
3. F. Bilotti *et. al*, “Reconfigurable intelligent surfaces as the key-enabling technology for smart electromagnetic environments, Advances in Physics: X, Vol.9, no. 1, pp. 1-47, 2024
4. L. Stefanini et al., “Multibeam Scanning Antenna System Based on Beamforming Metasurface for Fast 5G NR Initial Access,” IEEE Access, vol. 10, pp. 65982–65995, Jun. 2022.
5. D. Ramaccia et al., "Metasurface Dome for Above-the-Horizon Grating Lobes Reduction in 5G-NR Systems," in IEEE Antennas and Wireless Propagation Letters, vol. 21, no. 11, pp. 2176-2180, Nov. 2022
6. A. Monti et al., "Quadratic-Gradient Metasurface-Dome for Wide-Angle Beam-Steering Phased Array With Reduced Gain Loss at Broadside," in IEEE Transactions on Antennas and Propagation, vol. 71, no. 2, pp. 2022-2027, Feb. 2023.
7. M. Barbuto, A. Alù, F. Bilotti and A. Toscano, "Composite Vortex Manipulation as a Design Tool for Reflective Intelligent Surfaces," in IEEE Antennas and Wireless Propagation Letters, vol. 22, no. 10, pp. 2392-2396, Oct. 2023.
8. A. V. Marini, *et al.*, “Perfect Matching of Reactive Loads Through Complex Frequencies: From Circuital Analysis to Experiments,” IEEE Trans Antennas Propag, vol. 70, no. 10, pp. 9641–9651, Oct. 2022.
9. A. V. Marini, D. Ramaccia, A. Toscano, and F. Bilotti, “Metasurface-bounded open cavities supporting virtual absorption: free-space energy accumulation in lossless systems,” Opt Lett, vol. 45, no. 11, pp. 3147–3150, May 2020.
10. L. Stefanini, D. Ramaccia, A. Toscano, and F. Bilotti, “Scattering Gain Loss Bounds for Discretized Reconfigurable Intelligent Surfaces,” 2023 17th European Conference on Antennas and Propagation (EuCAP), pp. 1–4, Mar. 2023.
11. L. Stefanini, D. Ramaccia, A. Toscano, and F. Bilotti, “Characterization and compensation of RIS Scattering Gain Loss due to Electromagnetic Phase Roughness,” 2023 17th European Conference on Antennas and Propagation (EuCAP), pp. 1–4, Mar. 2023.
12. Dassault Systems Simulia, “CST Studio Suite,” https://www.3ds.com/products-services/simulia/products/cst-studio.

Wideband Microwave Metamaterials Energy Harvester

Mohammed M. Bait-Suwailam[1,2*], Hassan Al-Lawati[2], and Thamer Almoneef[3]

[1] Communication and Information Research Center, Sultan Qaboos University, Oman

[2] Dept. of ECE, College of Engineering, Sultan Qaboos University, Oman

[3] Dept. of EE, Prince Sattam bin Abdulaziz University, Saudi Arabia
[*] Corresponding author: msuwailem@squ.edu.om

Abstract: The design of a wideband metamaterials energy harvester for microwave applications is presented here. The developed electromagnetic harvester is based on the full power absorption that is collected across resistive loads. The simulation results show a wideband electromagnetic energy harvesting with wideband power absorption efficiency above 70%.

Recently, the field of radio frequency (RF) and microwave energy harvesting has been explored widely for utilizing such harvesters in many applications, including but not limited to radio frequency identification devices, low-power sensors, wireless power transfer, energy conversion enhancement, and flexible harvesters for healthcare applications [1]-[4].

In this work, we develop a wideband microwave electromagnetic energy harvester. The unit cell structure is based on an optimized H-shaped metallic resonator, which has not been proposed earlier. The resonant particles are made of conductive material, copper in this study. The proposed design contains an additional air spacer, which is an important parameter that is adopted in order to enhance the conversion efficiency and realize a wideband harvester. The results are presented using numerical full-wave simulation of Ansys HFSS.

Fig. 1 presents the unit cell of the proposed planar wideband metasurface electromagnetic energy harvester. The unit cell consists of a planar H-shaped resonant metallic surface with a cut gap, where energy is channeled and collected at a resistive load that is placed off-the center of the H-shaped resonator. The H-shaped resonator is printed on top of a Rogers RO6006 of size 20 x 20 mm^2, having a dielectric constant of ε_r = 6.15 and a thickness of 0.635 mm. The dimensions of the unit cell resonator has been optimized to enhance the matching impedance with free-space impedance over a wide frequency band. A metallic ground plate is placed at a standoff distance of d = 15 mm away from the developed metasurface unit cell (see Fig. 1).

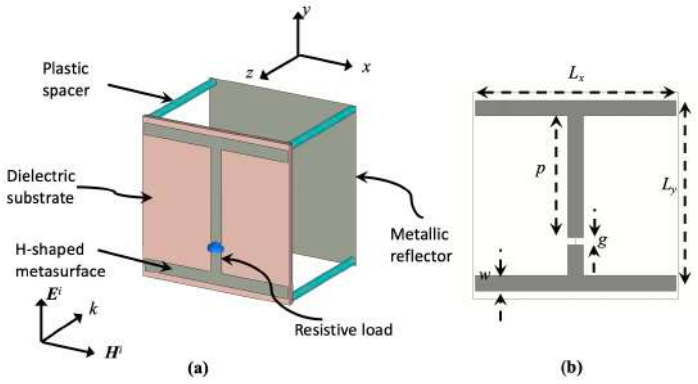

Fig. 1 (a) 3D view of the proposed H-shaped planar metasurface structure, and (b) top view showing the H-shaped resonator unit cell with its geometrical parameters. Note that grey area represents metallization.

Fig. 2(a) shows the numerical results of the reflection coefficient, magnitude of S_{11}, from the metasurface structure with periodic boundary conditions that was obtained using Ansys HFSS and compared with results from CST Microwave Studio. Strong agreement can be seen for the reflection coefficient below 3 GHz. A very minimal, yet negligible, discrepancy can be seen above 3 GHz, which is attributed mainly to the nature of the mesh scheme between the two simulators. Fig. 2(b) depicts the numerical results of the RF to AC conversion efficiency from the proposed wideband metasurface. As can be seen, very good agreement can be seen from the results that are obtained from the two numerical full-wave simulators. Based on the results, wideband energy harvesting was achieved, with a threshold level above 70% is considered in this study covering from nearly 1.5 GHz to 5 GHz.

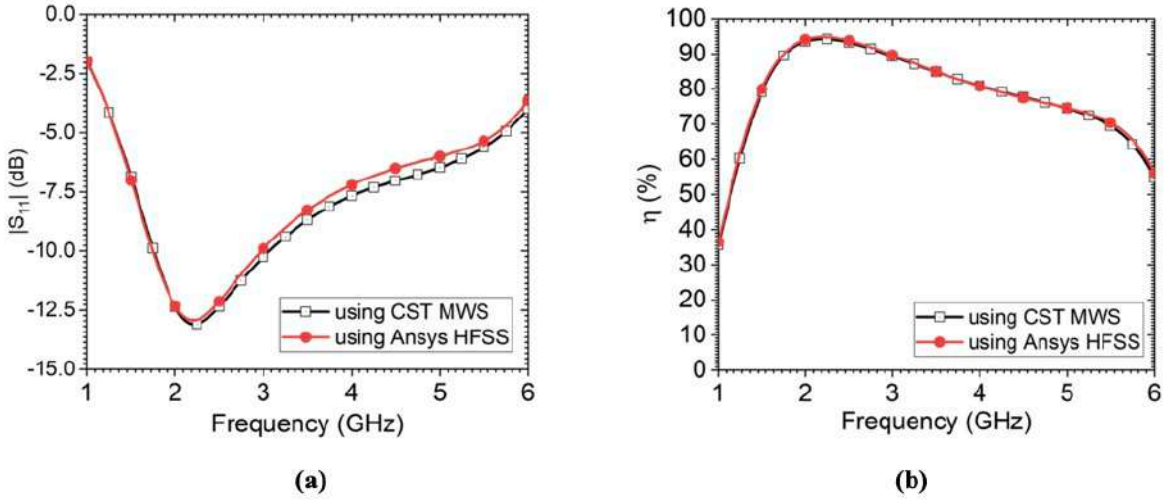

Fig. 2 (a) Numerical results of |S11| for the proposed metasurface in model shown in Fig. 1; (b) Numerical results of RF to AC conversion efficiency of the proposed wideband metasurface harvester. Note that a plastic support spacer with a dielectric constant of 2.7 and thickness of 15 mm and resistive load of 200 Ω were considered.

References

1. B., Yang, Y. and Cheng, C. ``Metamaterials-based enhanced energy harvesting: A review," Phys. B: Condens. Matter, vol. 438, 1–8, 2014.
2. Harouni, Z., Cirio, L., Osman, L., Gharsallah, A. and Picon, O. ``A dual circularly polarized 2.45-GHz rectenna for wireless power transmission," IEEE Antennas Wireless Propag. Lett., vol. 10, 306-309, 2011.
3. Khemar, A., Kacha, A., Takhedmit, H. and Abib, G. ``Design and experiments of a dual-band rectenna for ambient RF energy harvesting in urban environments," IET Microwaves Antennas and Propag., vol. 12, no. 1, 49-55, 2018.
4. Hawkes, A., Katko, A. and Cummer, S. ``Microwave metamaterial with integrated power harvesting functionality," Applied Physics Letters, vol. 103, no. 16, 163901-163901-3, 2013.

AES 2024, ROME - ITALY, 25 –28 JUNE 2024

Electromagnetic Routing using a 6-Port Topological Valley Junction

C. Johnson-Richards[1], A. Yakovlev[2], and V. Pacheco-Peña [1*]

[1] School of Mathematics, Statistics and Physics, Newcastle University, Newcastle Upon Tyne, NE1 7RU, United Kingdom.
[2] School of Engineering, Newcastle University, Newcastle Upon Tyne, NE1 7RU, United Kingdom.
victor.pacheco-pena@newcastle.ac.uk

Abstract: We design a 6-port junction using topological valley waveguides that exhibits equal power splitting between ports of the same valley type and extract a scattering matrix that enables the further design of linear computing devices.

Metamaterials and metasurfaces provide potential to manipulate light in space [1], [2] and time [3]–[7]. The use of metamaterials in computing with electromagnetic (EM) waves is especially interesting and has recently been reported in performing linear computing operations [8]–[11], providing the fundamental physics to design larger networks [12]. Topologically protected waveguides designed using valley photonic crystals (VPCs) that exhibit scattering protection from sharp bends [13] and discontinuities in the periodic lattice have increasingly attracted the attention of the scientific community as they offer low-loss compact solutions for photonic circuits [14]. VPC waveguides have been designed for linear logic-gates [15], and power splitting applications [16], [17].

In this communication, we present our efforts in designing a 6-port photonic VPC junction that exhibits equal power splitting at telecommunication frequencies between ports 2,4 and 6 (ports with the same valley type as the input port) with almost zero reflection to the input at port 1 [18]. This is achieved by designing a VPC waveguide with a hexagonal lattice. Then 6 VPC waveguides are joined at the center at 60º intervals. In so doing, spatial periodicity is maintained and a 6-port junction was realized. It will be shown how a scattering matrix that represent the transmitted/reflected signals through the junction can be calculated, similarly to [19]. The extraction of the scattering matrix is then exploited to design photonic devices for signal routing such as a wave director [19]. At the conference an analysis of the proposed 6-port VPC junction will be presented, this will include a numerical evaluation of equal power splitting, details of the scattering matrix extraction, and its efficacy in designing a wave director and further potential devices.

Acknowledgements

V.P.-P. and A. Y. would like to thank the support of the Leverhulme Trust under the Leverhulme Trust Research Project Grant scheme (No. RPG-2020-316 and RPG-2023-024). For the purpose of Open Access, the authors have applied a CC BY public copyright license to any Author Accepted Manuscript (AAM) version arising from this submission.

References

1. P. Rodríguez-Ulibarri, V. Pacheco-Peña, M. Navarro-Cía, A. E. Serebryannikov, and M. Beruete, “Experimental demonstration of deflection angle tuning in unidirectional fishnet metamaterials at millimeter-waves,” Appl. Phys. Lett., vol. 106, no. 6, p. 61109, Feb. 2015, doi: 10.1063/1.4908260/29173.
2. R. Geromel et al., “Compact Metasurface-Based Optical Pulse-Shaping Device,” Nano Lett., vol. 23, no. 8, pp. 3196–3201, 2023, doi: 10.1021/acs.nanolett.2c04980.
3. E. Galiffi et al., “Photonics of time-varying media,” Adv. Photonics, vol. 4, no. 1, pp. 1–32, 2022, doi: 10.1117/1.AP.4.1.014002.

4. V. Pacheco-Peña, M. Fink, and N. Engheta, “Temporal chirp, temporal lensing and temporal routing via space-time interfaces,” arXiv:2311.10855, Nov. 2023, Accessed: Mar. 13, 2024. [Online]. Available: https://arxiv.org/abs/2311.10855v1
5. V. Pacheco-Peña, D. M. Solís, and N. Engheta, “Time-varying electromagnetic media: opinion,” Opt. Mater. Express, Vol. 12, Issue 10, pp. 3829-3836, vol. 12, no. 10, pp. 3829–3836, Oct. 2022, doi: 10.1364/OME.471007.
6. V. Pacheco-Peña and N. Engheta, “Temporal aiming,” Light Sci. Appl., vol. 9, no. 1, pp. 1–12, 2020, doi: 10.1038/s41377-020-00360-1.
7. G. Castaldi, V. Pacheco-Peña, M. Moccia, N. Engheta, and V. Galdi, “Exploiting space-time duality in the synthesis of impedance transformers via temporal metamaterials,” Nanophotonics, vol. 10, no. 14, pp. 3687–3699, 2021, doi: 10.1515/nanoph-2021-0231.
8. V. Nikkhah, A. Pirmoradi, F. Ashtiani, B. Edwards, F. Aflatouni, and N. Engheta, “Inverse-designed low-index-contrast structures on a silicon photonics platform for vector–matrix multiplication,” Nat. Photonics 2024, pp. 1–8, Feb. 2024, doi: 10.1038/s41566-024-01394-2.
9. S. Sun et al., “Induced homomorphism: Kirchhoff’s law in photonics,” Nanophotonics, vol. 10, no. 6, pp. 1711–1721, 2021, doi: 10.1515/nanoph-2020-0655.
10. T. Knightley, A. Yakovlev, and V. Pacheco-Peña, “Neural Network Design of Multilayer Metamaterial for Temporal Differentiation,” Adv. Opt. Mater., vol. 11, no. 5, p. 2202351, 2023, doi: https://doi.org/10.1002/adom.202202351.
11. A. Ventisei, A. Yakovlev, and V. Pacheco-Peña, “Exploiting Petri Nets for Graphical Modelling of Electromagnetic Pulse Switching Operations,” Adv. Theory Simulations, vol. 5, no. 3, p. 2100429, Mar. 2022, doi: 10.1002/ADTS.202100429.
12. R. G. MacDonald, A. Yakovlev, and V. Pacheco-Peña, “Solving partial differential equations with waveguide-based metatronic networks,” arXiv:2401.00861, Dec. 2023.
13. J. K. Yang, Y. Hwang, and S. S. Oh, “Evolution of topological edge modes from honeycomb photonic crystals to triangular-lattice photonic crystals,” Phys. Rev. Res., vol. 3, no. 2, pp. 1–6, 2021, doi: 10.1103/PhysRevResearch.3.L022025.
14. Z. Qi et al., “Electrical tunable topological valley photonic crystals for on-chip optical communications in the telecom band,” Nanophotonics, vol. 11, no. 18, pp. 4273–4285, 2022, doi: 10.1515/nanoph-2022-0169.
15. M.-H. Chao, B. Cheng, Q.-S. Liu, W.-J. Zhang, Y. Xu, and G.-F. Song, “Novel optical XOR/OR logic gates based on topologically protected valley photonic crystals edges,” J. Opt., vol. 23, no. 11, p. 115002, Oct. 2021, doi: 10.1088/2040-8986/ac11ac.
16. P. Yang, P. Jiang, X. Guo, and L. Hou, “Topologically protected Mach – Zehnder interferometer Topologically protected Mach – Zehnder interferometer,” J. Opt., vol. 22, no. 10, p. 105001, Aug. 2020, doi: 10.1088/2040-8986/ABAC20.
17. R. Zheng et al., “Topological network transport in on-chip phononic crystals,” Phys. Rev. B, vol. 107, no. 24, p. 245122, 2023, doi: 10.1103/PhysRevB.107.245122.
18. C. Johnson-Richards, A. Yakovlev, and V. Pacheco-Peña, “Topological Valley Photonic Waveguides: Scattering matrix evaluation for linear computing,” Prep., 2024.
19. G. Lévêque et al., “Scattering-matrix approach for a quantitative evaluation of the topological protection in valley photonic crystals,” Phys. Rev. A, vol. 108, no. 4, p. 43505, Oct. 2023, doi: 10.1103/PhysRevA.108.043505.

The nanofabrication and unique properties of 3D metamaterials

Changzhi Gu*

Institute of Physics, Chinese Academy of Sciences, Beijing 100190, China
*corresponding author: czgu@iphy.ac.cn

Abstract: We develop the focused ion beam (FIB) stress-induced method for achieving 3D bidirectional micro-nano origami techniques, and realize flexible modulation of photons by utilizing origami metamaterials with metal and dielectric thin films. The research results have significantly enhanced the processing capacity of 3D nanostructures while providing valuable insights into efficient modulation and broad application possibilities for nanophotonics devices.

Summary

In the field of optics, three-dimensional (3D) metamaterials are the newly derived 3D meta-structures arrays. This arrangement ensures customizable manipulation abilities over physical properties while effectively reducing processing difficulties, which meets the demands of miniaturization, high efficiency, and multifunctionality in microdevice applications. Therefore, the fabrication and design of 3D metamaterials have garnered extensive attention recently within the field of nanophotonics, becoming one of the important cutting-edge research directions.

We have developed FIB stress induction technology and achieved the fabrication of bidirectional micro-nano structure origami, and further explored the deformation processes of two origami modes and revealed the origin and formation mechanism of stress. Firstly, using the stress induction method of FIB, the flexible and controllable 3D micro-nano bidirectional origamis are successfully achieved, and the relationship between ion dose and deformation degree was established. Then, concentrate on the bidirectional origami phenomenon, we studied the microscopic process of high-energy ion beam bombarding the target with Monte Carlo simulation, and obtained that the stress originates from atomic sputtering, and the deformation process corresponds to the change of sputtering amount. Finally, it was shown that the experimental results are consistent with our proposed FIB induced origami theory, in virtue of studying the processing of different materials and atomic force microscopy (AFM) measurement on the surface morphology.

The bidirectional folded 3D metamaterials with functions for photon spin angular momentum modulation were designed and prepared, achieving high circular dichroism (CD) values and all phase modulation while ensuring high efficiency. On the one hand, the relationship between the geometric configuration and CD value was determined by finite element method, and the bidirectional folded Al structure with high intrinsic chirality was designed. On this basis, using the finite difference time domain (FDTD) method and multi-level sub scattering theory, the surface current distributions and multipole moments scattering intensities of the optimal chiral structure at the strongest response position were analyzed, elucidating the electromagnetic coupling in the strong optical chirality. Finally, the chiral metamaterials obtained a CD value of 0.78 in measurements and achieved high purity photon spin resolution. On the other hand, by designing the SiN_x bidirectional folding configuration, the full transfer phase control of spin photons was obtained by using the folding angle variation. Moreover, the folded dielectric metalens was constructed by the gradient change of phase configuration, realizing the line focusing function at 1550 nm wavelength.

Acknowledgements

This work was supported by the National Key Research and Development Program of China under Grant No.

2022YFA1204100 and 2021YFA1400700, the National Natural Science Foundation of China under Grant Nos. 61888102, 11974386, 62174179, 12074420, U21A20140 and 61905274, the Strategic Priority Research Program of Chinese Academy of Sciences (CAS) under Grant Nos. XDB33000000 and XDB28000000

References

1. Zheng R., Pan R., Sun C., Du S., Jin A., Li C., Geng G., Gu C., Li J., "Bidirectional Origami Inspiring Versatile 3D Metasurface," Advanced Materials Technologies, 7, 2200373, 2022.

2. Zheng R., Pan R., Geng G., Jiang Q., Du S., Huang L., Gu C., Li J., "Active multiband varifocal metalenses based on orbital angular momentum division multiplexing," Nature Communications, 13, 4292, 2022.

3. Du S., Guo Y., Huang X., Sun C., Zhang Z., Hu L., Zheng R., Bai Q., Jin A., Yang H., Zhang Y., Li J., Gu C., "Strain lithography for two-dimensional materials by electron irradiation," Applied Physics Letters, 120, 093104, 2022.

4. Bai Q., Huang X., Guo Y., Du S., Sun C., Hu L., Zheng R., Yang Y., Jin A., Li J., Gu C., "Gap-Surface-Plasmon Induced Polarization Photoresponse for MoS_2–Based Photodetector," Nano Research, 16, 10272, 2023.

5. Liu, Z., S. Du, A. Cui, Z. Li, Y. Fan, et al., "High-Quality-Factor Mid-Infrared Toroidal Excitation in Folded 3D Metamaterials," Adv. Mater. 29, 1606298, 2017.

6. Yang, S., Z. Liu, S. Hu, A. Jin, H. Yang, et al., "Spin-Selective Transmission in Chiral Folded Metasurfaces," Nano Lett., 19, 3432-3439, 2019.

Nanophotonics, plasmonics and quantum optics

AES 2024, ROME - ITALY, 25 –28 JUNE 2024

Emission Line Selective Optical Manipulation Using Stimulated Recoil Force

T. Horai[1*], T. Wada[2], Y. Saito[1], M. Ashida[1], and H. Ishihara[1]

[1]Department of Materials Engineering Science, Osaka University, 1-3 Machikaneyama-cho, Toyonaka, Osaka, 560-8531, Japan

[2]Department of Physics and Electronics, Osaka Prefecture University, 1-1 Gakuen-cho, Naka-ku, Sakai, Osaka, 599-8531, Japan

[*]horai.t@opt.mp.es.osaka-u.ac.jp

Abstract: In this study, we propose an optical manipulation method to selectively target a particular emission line using the recoil force from induced light under inverted-occupation conditions. We evaluated this recoil force by using a four-level system and indicate the potential of the development of high-performance luminescent materials.

In the past, researchers have extensively studied optical manipulation using absorption and scattering of light. However, selective manipulation based on emission lines has not been possible. This study proposes a novel method for selectively manipulating nanoparticles based on their emission properties. When a particle is in an occupation inversion state, light that induces stimulated emission triggers luminescence, leading to the generation of a recoil force [1]. Unlike the typical absorbing optical force, which saturates at high-power input, the stimulated recoil force (SRF) significantly reduces saturation by facilitating a rapid transition of electrons from the excited state to the ground state, surpassing the rate of spontaneous emission. This phenomenon enables the generation of very strong forces. The focus of this paper is on nanodiamonds containing NV centers (NV-NDs). NV-NDs are known for their resistance to photobleaching and high biocompatibility, making them promising candidates for fluorescent markers in biosensing applications. However, during the synthesis of NV-NDs, nanodiamonds without NV centers (pristine-NDs) are also produced, posing a challenge for their selective sorting. Moreover, for applications where NV-NDs are used as fluorescent markers for single biomolecules, it is desirable for them to be smaller than 10 nm in size [2]. Therefore, this paper discusses the theoretical feasibility of sorting NV-NDs using the SRF.

In this theoretical demonstration, we evaluate the optical force using the general expression for the time-averaged optical force [3]:

$$\langle \mathbf{F} \rangle = \frac{1}{2} \Re \left[\sum_{\omega} \int \mathrm{d}\mathbf{r} \{ \nabla \mathbf{E}^{*}(\mathbf{r}, \omega) \} \cdot \mathbf{P}(\mathbf{r}, \omega) \right], \tag{1}$$

where $\mathbf{E}$ and $\mathbf{P}$ are the time-harmonic responses of the electric field and induced polarization, respectively, ω is the angular frequency of the incident light, and $\mathbf{r}$ is the particle position. We calculate the induced polarization by solving the density matrix equation for the material system, which includes the phenomenological relaxation constants, as $i\hbar(\partial\hat{\rho}/\partial t) = \left[\hat{H}, \hat{\rho}\right] - \hat{\Gamma}\hat{\rho}$, where $\hat{\rho}$, $\hat{H}$, and $\hat{\Gamma}$ denote the density matrix of the system, the total Hamiltonian represented as $\hat{H} = \hat{H}_0 + \hat{V}$ and the phenomenological dephasing constants, respectively. $\hat{H}_0$ represents the unperturbed component, and $\hat{V}$ represents the light-matter interaction energy, given by $\hat{V} = -\hat{\mu} \cdot \mathbf{E}(\mathbf{r}, t)$, where $\hat{\mu}$ denotes the dipole moment matrix. In this study, the off-diagonal components of the density matrix are expanded in a Fourier series to account for the nonlinear optical response.

We describe the calculation model of the NV-ND used in this study. We modeled the NV-ND as a four-level system with energy levels assumed to be $\hbar\Omega_{31} = 1.945$ eV, $\hbar\Omega_{41} = 2.010$ eV, $\hbar\Omega_{21} = \hbar\Omega_{43} = 0.065$ eV. We

set $\mu_{31} = 4.3$ D [4], corresponding to the zero-phonon transition, and $\mu_{32} = \mu_{41} = 8.6$ D. The dephasing constants between levels j and k were assumed to be $\gamma_{jk} = 10$ meV, considering room temperature in water. The population decay constants were set to be $\Gamma_{21} = \Gamma_{43} = 15$ meV [5], and $\Gamma_{31} = \Gamma_{32} = 29$ neV based on the fluorescence lifetime [6].

We propose a method for sorting NV-NDs and pristine-NDs using SRF. As shown in Fig. 1(a), the setup involves irradiating counter-propagating pump light (6 W) along the z-axis and manipulation light (6 W) along the positive z-axis in a capillary with an inner diameter of 1 μm. The beam waist radius by a focused beam is set to 2.5 μm. Importantly, the optical force of the pump light is canceled out. Consequently, pristine-NDs are transported in the direction of the manipulation light, while NV-NDs are transported in the opposite direction of the manipulation light due to SRF. Therefore, only the NV-NDs are transported in the negative z-axis direction in the capillary and are concentrated. For the evaluation of the optical force and the kinetic analysis, NV-NDs and pristine-NDs are assumed to be spheres with a diameter of 10 nm.

To evaluate the effectiveness of the assessed SRF in water at room temperature, we conducted kinetic simulations to separate NV-NDs and pristine-NDs. Figure 1(b) shows histograms of the final positions of NV-NDs and pristine-NDs after 10 minutes of laser exposure. (There were 50 of each ND present, and they were located at $z = 0$ at the start of laser irradiation.) This result suggests that SRF can be employed to selectively isolate NV-NDs with single defects even at room temperature.

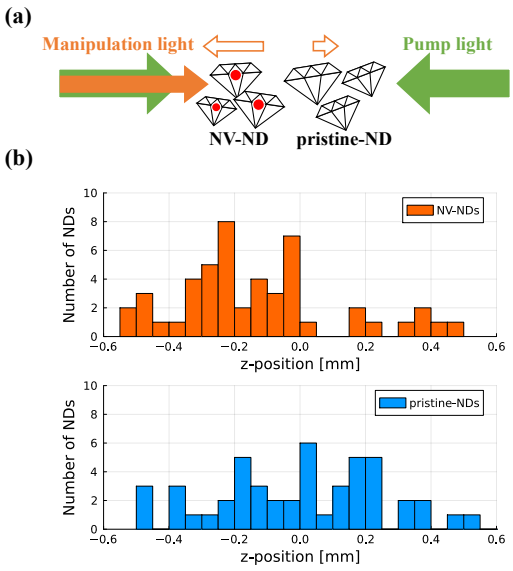

Figure 1. (a) Conceptual diagram of NV-NDs and pristine-NDs sorting method and (b) Histograms of NV-NDs and undoped-NDs after 10 minutes of laser exposure. There were 50 of each ND present, and they were located at $z = 0$ at the start of laser irradiation.

This technique is expected to have a significant impact on the field of nanophotonics by utilizing it, thanks to the high-quality NV-NDs that can be collected.

References

1. Kudo, T. and Ishihara, H., "Proposed nonlinear resonance laser technique for manipulating nanoparticles," Phys. Rev. Lett. 109, 087402 (2012).
2. Terada, D., Segawa, T. F., Shames, A. I., Onoda, S., Ohshima, T., Ōsawa, E., Igarashi, R., and Shirakawa, M., "Monodisperse five-nanometer-sized detonation nanodiamonds enriched in nitrogen-vacancy centers," ACS Nano 13, 6461 (2019).
3. Iida, T. and Ishihara, H., "Theory of resonant radiation force exerted on nanostructures by optical excitation of their quantum states: From microscopic to macroscopic descriptions," Phys. Rev. B 77, 245319 (2008).
4. Gali, A., "Ab initio theory of the nitrogen-vacancy center in diamond," Nanophotonics 8, 1907 (2019).
5. Ulbricht, R., Dong, S., Gali, A., Meng, S., and Loh, Z.-H., "Vibrational relaxation dynamics of the nitrogen-vacancy center in diamond," Phys. Rev. B 97, 220302 (2018).
6. Doherty, M. W., Manson, N. B., Delaney, P., Jelezko, F., Wrachtrup, J., and Hollenberg, L. C. L., "The nitrogen-vacancy colour centre in diamond," Phys, Rep. 528, 1 (2013).

Theoretical study of optical manipulation using electronic resonant light by controlling the triplet state populations

Y. Umekawa[1*], T. Horai[1], R. Bresolí-Obach[2], H. Ishihara[1,3]

[1]Department of Materials Engineering Science, Graduate School of Engineering Science, Osaka University

[2]Dept. of Appl. and Anal. Chem., Institut Químic de Sarrià, Universitat Ramon Llull

[3] Center for Quantum Information and Quantum Biology, Osaka Univ., Japan
*umekawa.y@opt.mp.es.osaka-u.ac.jp

Abstract: In recent research, Bresolí-Obach *et al.* experimentally demonstrated a new approach to control the optical force on polystyrene microparticles doped with phenalenone using chemical stimuli. This study theoretically explains a unique scheme of optical manipulation demonstrated in the above work by considering nonlinear optical response of a four-level electronic system.

In recent years, there has been considerable research interest in optical manipulation of nanoparticles, yet manipulating them at the nanometer scale remains challenging. Weak optical forces on nanomaterials make it difficult to overcome disturbances, such as thermal fluctuations. One promising approach to address this challenge is to use the optical resonance effect (ORE), which amplifies optical forces by irradiating light resonant with the transition energy of nanoparticles [1]. Previous studies have enhanced optical forces by tuning the physical conditions of the system. Interestingly, a recent experiment reported by Bresolí-Obach *et al.* successfully altered the optical force by chemical stimuli [2]. They achieved chemical control over the optical force by modulating the triplet lifetime using molecular oxygen for polystyrene micro-particles doped with phenalenone. Although the mechanism is well explained in Ref. [2], further development of this method is anticipated if we can theoretically reproduce these results based on the microscopic model.

In this study, we modeled phenalenone as a four-level system to theoretically validate these mechanisms. Figure 1(a) shows the conceptual diagram of phenalenone modeled as a four-level system. States $|1\rangle$ and $|3\rangle$ represent the ground and excited states of the singlet, respectively, while states $|2\rangle$ and $|4\rangle$ correspond to the ground and excited states of the triplet, respectively. Although the triplet lifetime is typically very long, molecular oxygen can efficiently quench this state. To achieve resonance force enhancement, a two-laser system was used: a 405 nm laser to excite phenalenone ($|1\rangle$ to $|3\rangle$) and a 488 nm laser responsible for the upper excited state optical resonant cycle ($|2\rangle$ to $|4\rangle$ to $|2\rangle$). Importantly, even at low excitation light intensities, a significant enhancement in optical force can be achieved if the lifetime of $|2\rangle$ is long.

We describe the theoretical calculations used in our analysis. To evaluate the optical force, we use the time-averaged force [2]:

$$\langle \mathbf{F} \rangle = \frac{1}{2} \mathrm{Re} \left[\sum_{\omega} \int_{V} \mathrm{d}\mathbf{r} \{ \nabla \mathbf{E}^{*}(\mathbf{r}, \omega) \} \cdot \mathbf{P}(\mathbf{r}, \omega) \right], \quad (1)$$

where **E** and **P** are the time-harmonic responses of the electric field and induced polarization, respectively. We calculate the expected value of polarization by solving the equation of motion of the density matrix by nonperturbative method to obtain the optical forces [3]. The equation of motion of the density matrix for the material system, which includes the phenomenological relaxation constants, is given by: $i\hbar(\partial\hat{\rho}/\partial t) = [\hat{H}, \hat{\rho}] - \hat{\Gamma}\hat{\rho}$, where $\hat{\rho}$, $\hat{H}$, and $\hat{\Gamma}$ denote the density matrix of the system, the total Hamiltonian represented as $\hat{H} = \hat{H}_0 + \hat{V}$ and the phenomenological dephasing constants, respectively. $\hat{H}_0$ represents the unperturbed component, and $\hat{V}$ represents the light-molecule interaction energy, given by $\hat{V} = -\hat{\mu} \cdot \mathbf{E}(\mathbf{r}, t)$, where $\hat{\mu}$ denotes the dipole moment matrix. By solving the equation of motion for the density matrix, we can obtain the expected value of the dipole moment $\vec{\mu}_{\mathrm{res}} = \mathrm{Tr}[\hat{\rho}\hat{\mu}]$.

Figure 1(b) shows the calculated relationship between optical force and excitation light intensity, varying the lifetime of $|2\rangle$ as shown in Fig. 1(a). (Note that in our theoretical calculations, the 488 nm laser was set as a plane wave with an intensity of 1 kW/cm^2.) The results indicate that a longer lifetime of $|2\rangle$ leads to higher optical pressure. This effect is attributed to an increased number of electrons participating in the optical resonance cycle of the upper excited state, which aligns with the trends observed in experiments. These results well reproduce the results of Ref. 2, suggesting the possibility of enhancing the degrees of freedom to control optical forces by chemical methods. This approach could significantly impact various research fields, including optics, biochemistry, and physical chemistry.

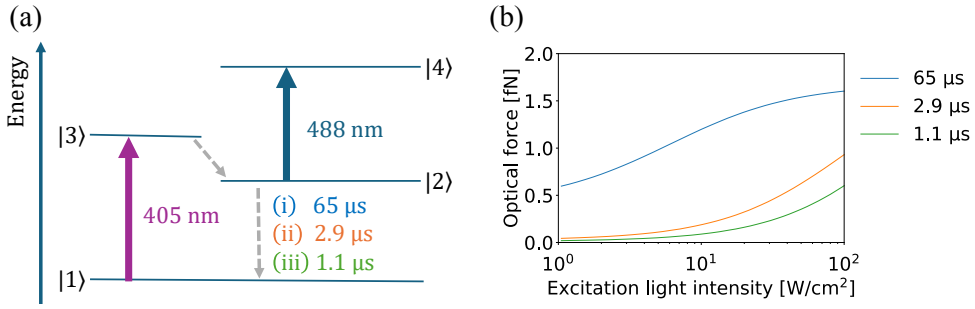

Figure 1. (a) Energy level diagram of phenalenone. (i) ~ (iii) show controlled lifetime of the state $|2\rangle$. (b) Calculated relationship between optical force and excitation light intensity, varying the lifetime

References

1. Iida, T. and H. Ishihara, "Theorical Study of the Optical Manipulation of Semiconductor Nanoparticles under an Excitonic Resonance Condition," Phys. Rev. Lett., Vol. 90, 057403, 2003.
2. Bresolí-Obach. R, S. Nonell, H. Masuhara and J. Hofkiens, "Chemical Control Over Optical Trapping Force at an Interface," Adv. Optical Mater., Vol. 10, 2200940, 2022.
3. Kudo, T. and H. Ishihara, "Proposed Nonlinear Resonance Laser Technique for Manipulating Nanoparticles," Phys. Rev. Lett., Vol. 109, 087402, 2012.

AES 2024, ROME - ITALY, 25 –28 JUNE 2024

Combined thermal and mechanical phenomena induced by the fluctuations of the electromagnetic field

J. R. Deop-Ruano[1]*, and A. Manjavacas[1]*

[1]Instituto de Óptica "Daza de Valdés" (IO-CSIC), Spain
*corresponding author: juan.deop@csic.es
*corresponding author: a.manjavacas@csic.es

Abstract: Casimir interactions and radiative heat transfer originate from the fluctuations of the electromagnetic field. In this work, we study the coupled transfer of momentum and energy in different nanoscale systems. We observe that the movement of the nanostructures allows us to control the heat transfer, and vice versa.

The fluctuations of the electromagnetic field drive the radiative heat transfer between material structures [1, 2]. Another intriguing phenomenon stemming from these fluctuations is the Casimir forces and torques experienced by neutral nanostructures, offering a pathway for the transfer of momentum at the nanoscale [3, 4]. Despite their shared physical origin, radiative heat transfer and Casimir interactions have traditionally been studied as independent phenomena. However, as evidenced in our study, Casimir interactions can significantly impact radiative heat transfer, and vice versa.

In this work [5], we analyze the concurrent exchange of energy and angular momentum within a pair of nanostructures with different temperatures, rotating around a shared axis (see Figure 1). Our work reveals that the rotation of these nanostructures can increase, decrease, or even reverse radiative heat transfer between them, compared to the transfer in the absence of rotation. These findings unveil the potential of rotating nanostructures for modulating radiative heat transfer.

Moreover, we study the propulsion of Janus-like nanostructures placed in an environment at a different temperature [6]. Janus nanostructures are characterized by two distinct sides with different material properties. Due to the difference in the emission of photons between the two sides, the structure spontaneously accelerates as it thermalizes with the environment. We comprehensively characterize the force and the associated motion of the structure as a function of its temperature and thickness, for different combinations of materials. In doing so, we prove the possibility of manipulating material structures using thermal radiation.

Our analysis is grounded in the framework of fluctuational electrodynamics, which we employ to derive analytical expressions for the forces, torques, and power exchanged between nanostructures. This study unravels intricate phenomena arising from the interplay between Casimir interactions and radiative heat transfer, opening avenues for leveraging moving nanostructures to control radiative heat transfer, as well as for utilizing thermal radiation for accelerating and manipulating nanostructures.

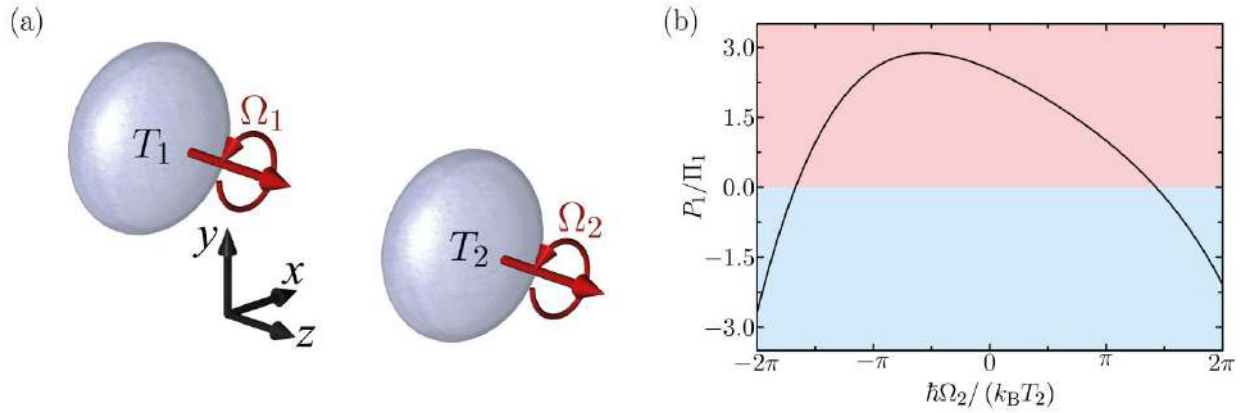

Figure 1. (a) Schematics of the system under consideration. (b) Power transferred between the nanostructures P_1, normalized to the power transferred in the absence of rotation Π_1, as a function of Ω_2 for $T_1 = 1.5T_2$, $\Omega_1 = \pi k_B T_2/\hbar$. The red (blue) background indicates positive (negative) values of the normalized power transferred.

References

1. Biehs, S.-A.; Messina, R.; Venkataram, P. S.; Rodriguez, A. W.; Cuevas, J. C.; and Ben-Abdallah, P., "Near-field radiative heat transfer in many-body systems", Rev. Mod. Phys., Vol. 93, 025009, 2021.
2. Manjavacas, A.; and García de Abajo, F. J., "Radiative heat transfer between neighboring particles", Phys. Rev. B, Vol. 86, 075466, 2012.
3. Pendry, J. B., J. Phys. Condens. Matter, "Shearing the vacuum-quantum friction", Vol. 9, 10301, 1997.
4. Sanders, S.; Kort-Kamp, W. J. M.; Dalvit, D. A. R.; and Manjavacas, A., "Nanoscale transfer of angular momentum mediated by the Casimir torque", Commun. Phys., Vol. 2, 1-7, 2019.
5. Deop-Ruano, J. R.; and Manjavacas, A., "Control of the radiative heat transfer in a pair of rotating nanostructures", Phys. Rev. Lett. Vol. 130, 133605, 2023.
6. Deop-Ruano, J. R.; García de Abajo, F. J.; and Manjavacas, A., "Thermal radiation forces on planar structures with asymmetric optical response", Submitted, 2024.

Efficient hot-carrier-generation supported by the localization of hybridized plasmon in Au nanoparticle arrays

S. Inoue[1*], T. Yokoyama[1], K. Sasaki[2], H. Misawa[2,3,4], and H. Ishihara[1,5]

[1] Graduate School of Engineering Science, Osaka Univ., Japan
[2] Research Institute for Electronic Science, Hokkaido Univ., Japan
[3] Center for Emergent Functional Matter Science, National Yang Ming Chiao Tung Univ., Taiwan
[4] Research Institute for interdisciplinary Science, Okayama Univ., Japan
[5] Center for Quantum Information and Quantum Biology, Osaka Univ., Japan
[*]corresponding author: inoue.s@opt.mp.es.osaka-u.ac.jp

Abstract: Hot-carrier-generation (HCG) via plasmons can boost photoelectric conversion. Our recent research introduced Au-nanoparticle-array/TiO_2/Au-film (ATA) structure, enhancing HCG through an antenna effect. In this study, we explore symmetry-breaking nanoparticle arrays on ATA, finding they can support antenna effect above, underscoring the importance of optimally exciting the localized modes of hybridized plasmon.

When light irradiates metallic nanoparticles (NPs), it induces collective excitation of electrons, leading to the generation of a strong electric field near the surface, a phenomenon known as Localized Surface Plasmon Resonance (LSPR). LSPR has garnered significant attention not only for shaping electromagnetic fields but also for its potential in photoelectric conversion. Plasmons can produce hot carriers (HCs), electrons more energetic than those in thermal equilibrium. These HCs can be readily injected into attached semiconductors beyond the Schottky barrier, facilitating photoelectric conversion [1]. The hot-carrier-generation (HCG) mechanism via plasmons holds promise for enhancing the performance of artificial photosynthesis [2] and solar cells [3]. Nevertheless, its efficiency remains inadequate, and numerous challenges persist.

Shi et al. proposed Au NPs/TiO_2/Au film (ATA) structures (Fig. 1) to explore HCG efficiency [4]. The incorporation of both the Au film and Au NPs leads to the creation of Fabry-Pérot “cavity” (FP cavity) modes, resulting in the splitting of absorbance peaks in the spectrum due to strong coupling between the plasmon and FP cavity modes. This strong modal coupling significantly boosts light absorption, thereby enhancing photoelectric conversion and water splitting when utilizing NPs as photoanodes.

Recently, we investigated ATA structures using ordered Au NPs arrays [5]. Experimental results indicated that as Au particle number density (PND) increases, absorbance spectra exhibit asymmetric peak-splitting behavior and the apparent quantum efficiency (AQE) of the photoelectric conversion markedly improves compared to the case without the Au film. Our theoretical analysis qualitatively explains these results, highlighting that the coherent coupling between plasmons, strengthened by the FP cavity effect, plays a pivotal role. Especially, the mechanism of AQE enhancement resembles an antenna effect, which is concentration of energy from the global NP sites to the local hot sites (NPs with significant damping and high injection efficiency). It underscores that a well-designed array of Au NPs significantly enhances the HCG.

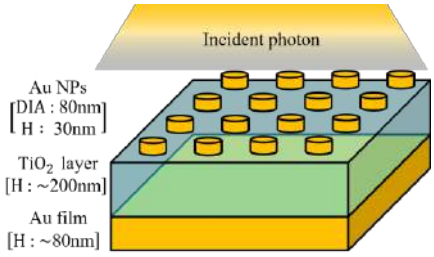

Fig.1: Schematic view of ATA structure.

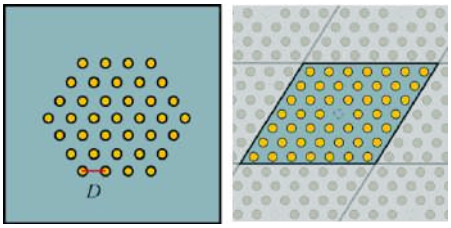

Fig.2: Cluster and point defects system.

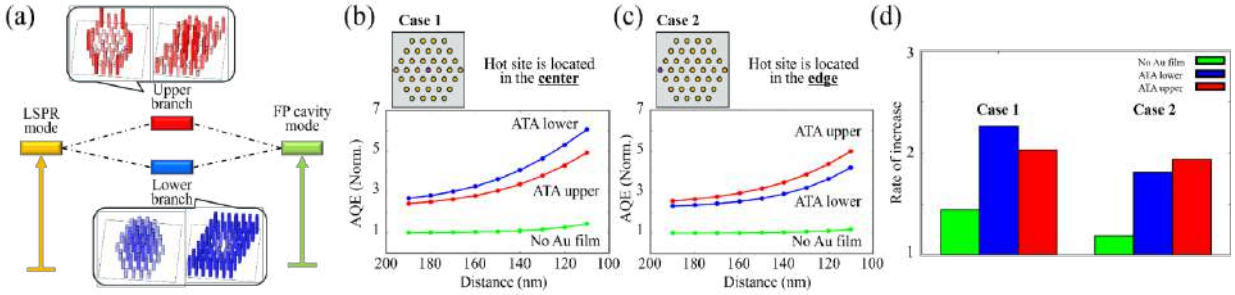

Fig.3: (a)Schematic energy diagram of ATA structure with symmetry-breaking NP arrays. The upper and lower branch states show different spatilal distributions. (b,c) NP-NP distance (D) dependence of AQE for the lower (blue) and the upper (red) modes of ATA, compared to the case without Au film (green) when the hot site is located in the center (b) and the edge (c) of the cluster [6]. AQE is normalized by the value at D=190 nm for green case. (d)Rate of increase of AQE from D = 190 to D = 110 in the case 1 and case 2. AQE is more elevated in case 1.

In this study, we examined symmetry-breaking NP arrays such as clusters of Au NPs and defects in periodic Au NPs (Fig. 2) within ATA structure. In such scenarios, the localized modes of hybridized plasmon are expected to form (Fig. 3a), prompting us to theoretically investigate their effect on AQE. In the case of hexagonal cluster, the plasmons induce a spatially nonuniform eigenmode owing to enhanced coherent coupling between plasmons as NP-NP distance (D) decreases. Edge- and center-localized modes of hybridized plasmons emerged at the upper and lower energy levels, respectively (Fig. 3a). This localization supports antenna effect (mentioned in [5]) at specific hot site locations, resulting in enhanced AQE (Fig. 3b.3c) [6]. Notably, as shown in Fig. 3d, case 1 proves more conducive to efficient HCG due to the presence of more bright sites near a hot site in terms of rate of increase. These findings underscore the importance of optimally exciting the localized modes of hybridized plasmon aligned with the spatial distribution of hot sites.

We introduce the spatial localization of hybridized plasmon modes through symmetry-breaking NP arrays within ATA structure. Coupled modes between FP cavity mode and hybridized plasmon show different behaviors in the lower and upper branches, resulting in the enhancement of HCG at specific hot site location. These results emphasize the critical role of selectively exciting optimal modes. Defects in periodic Au NPs offer practical advantages in terms of integrability, a topic we will discuss in further detail during the actual presentation.

References

1. Brongersma, M. L., N. J. Halas and P. Nordlander “Plasmon-induced hot carrier science and technology,” Nat. Nanotechnol., Vol. 10, 25–34, 2015.
2. Ueno, K., T. Oshikiri and H. Misawa, “Plasmon-Induced Water Splitting Using Metallic-Nanoparticle-Loaded Photocatalysts and Photoelectrodes,” Chem. Phys. Chem., Vol. 17, 199–215, 2016.
3. Ueno, K., T. Oshikiri, Q. Sun, X. Shi and H. Misawa, “Solid-State Plasmonic Solar Cells,” Chem. Rev., Vol. 118, 2955–2993, 2018.
4. Shi, X., K. Ueno, T. Oshikiri, Q. Sun, K. Sasaki and H. Misawa, “Enhanced water splitting under modal strong coupling conditions,” Nat. Nanotechnol., Vol. 13, 953-958, 2018.
5. Liu, Y., X. Shi, T. Yokoyama, S. Inoue, Y. Sunaba, T. Oshikiri, Q. Sun, M. Tamura, H. Ishihara, K. Sasaki and H. Misawa, “Quantum-Coherence-Enhanced Hot-Electron Injection under Modal Strong Coupling,” ACS Nano, Vol. 17, 8315-8323, 2023.
6. Inoue, S., T. Yokoyama, K. Sasaki, H. Misawa and H. Ishihara, “Scheme to Enhance Hot Carrier Generation Owing to the Localized Mode of Hybridized Plasmon in Gold Nanoparticle Arrays,” J. Phys. Chem. C, published online, 2024.

Superfluorescence-induced optical force in metallic nanofiber systems

H. Arahari[1*], H. Ishihara[1], and N. Yokoshi[2]

[1]Dept. of Materials Engineering Science, Osaka University, Toyonaka, Osaka, 560-8531, Japan
[2]Dept. of Physics and Electronics, Osaka Metropolitan University, Sakai, Osaka, 599-8531, Japan
[*]corresponding author: arahari.h@opt.mp.es.osaka-u.ac.jp

Abstract: Superfluorescence is a coherent luminescence phenomenon induced spontaneously by light-mediated interactions among emitters. We theoretically evaluated superfluorescence-induced optical forces enhanced by utilizing surface plasmon modes of Ag nanofibers and proposed optical manipulations reflecting its characteristics. This study leads to novel ordered optical manipulations by designing the emitter arrangement and environment.

Optical force, generated through the exchange of momentum between light and matter, finds applications across a wide range of fields, including molecular biology [1] and optomechanics [2]. Here, when we focus on luminescence-induced optical forces [3], we can propose optical manipulations reflecting luminescence characteristics and luminescence-induced order formation, greatly expanding the applications and degrees of freedom of optical manipulation. Specifically, our research targets superfluorescence - a spontaneous coherent luminescence phenomenon - and investigates the application of superfluorescence in generating optical forces. Superfluorescence, a quantum phenomenon predicted by Dicke [4], is the synchronized emission from densely packed excited particles, generating a cooperative pulsed radiation. This effect results from the exchange of photons among emitters, which exhibits directional and coherent emission, and its peak emission intensity is proportional to the square of the number of emitters (N^2). The properties of superfluorescence can be designed by controlling the emitters' spatial arrangement and environmental factors [5], making it promising as a new coherent light source.

We considered a situation in which more intense superfluorescence is generated by using surface plasmon modes propagating on metallic nanofibers to enhance the interaction between emitter nanoparticles. We evaluated the superfluorescence-induced optical forces when a total of N emitters was placed at two positions near the Ag nanofibers, as shown in Figure 1(a). The analysis explores how changes in the number and arrangement of emitters affect these forces, leading to new ways to study photoinduced ordering in emitter ensembles, such as the spontaneous coherence formation and directional emission of superfluorescence.

The Hamiltonian of the system consists of the N two-level emitters with the center-of-mass momentum, the emitted photons, and the dipole interaction between them. From the Hamiltonian, one can derive Heisenberg equations for the inter-emitter correlation and the population [5];

$$\frac{\partial}{\partial t}\langle\hat{\sigma}_i^+\hat{\sigma}_j^-\rangle = \mathrm{i}\big(\omega_i-\omega_j\big)\langle\hat{\sigma}_i^+\hat{\sigma}_j^-\rangle - \frac{\mathrm{i}}{\hbar\varepsilon_0}\big(1-2\langle\hat{\sigma}_i^+\hat{\sigma}_i^-\rangle\big)\sum_{m=1}^{N}\boldsymbol{d}_m\cdot\boldsymbol{G}^*\big(\boldsymbol{r}_m,\boldsymbol{r}_i,\omega_j\big)\cdot\boldsymbol{d}_i\langle\hat{\sigma}_m^+\hat{\sigma}_j^-\rangle$$

$$+\frac{\mathrm{i}}{\hbar\varepsilon_0}\big(1-2\langle\hat{\sigma}_j^+\hat{\sigma}_j^-\rangle\big)\sum_{m=1}^{N}\boldsymbol{d}_m\cdot\boldsymbol{G}\big(\boldsymbol{r}_j,\boldsymbol{r}_m,\omega_i\big)\cdot\boldsymbol{d}_j\langle\hat{\sigma}_i^+\hat{\sigma}_m^-\rangle. \qquad (1)$$

Here, $\boldsymbol{G}$ is expressed as the photon Green's function in the cylindrical coordinate [6]. $\hat{\sigma}_i^+$ ($\hat{\sigma}_i^-$) represents the raising (lowering) operators of the i-th emitter with the resonant frequency ω_i and the dipole moment $\boldsymbol{d}_i$. Within

the rotating wave approximation and the adiabatic approximation, the optical recoil force exerted on i-th emitter induced by superfluorescence is described as,

$$f_i = -\langle \nabla_{r_i} \hat{H} \rangle = -\frac{2}{\varepsilon_0} \sum_{m=1}^{N} \mathrm{Re}\left[\left(\nabla_{r_i} \boldsymbol{d_i} \cdot \boldsymbol{G}(\boldsymbol{r}_i, \boldsymbol{r}_m, \boldsymbol{\omega}_i) \cdot \boldsymbol{d}_m \right) \langle \hat{\sigma}_i^+ \hat{\sigma}_m^- \rangle \right]. \qquad (2)$$

We evaluated the optical forces $\boldsymbol{F}=\sum_{i=1,N/2} f_i$ on a cluster of emitters at each position, as shown in Figure 1(a). Figures 1 (b,c) indicate that the optical forces predominantly manifest in a direction orthogonal to the fiber axis (x-direction). Increasing the number of emitters at the same point, the peak of the optical forces is proportional to N^2 and the peak width is proportional to $1/N$. Thus, these forces reflect the characteristics of superfluorescence. Additionally, it has been found that the direction of optical forces can be controlled on the x-axis by increasing the number of emitters' positions. As shown in Fig. 1(c), these forces induce divergent motions among two groups of emitters along the fiber (z-direction). By affixing emitter nanoparticles onto the fiber or constraining the radial movement of emitters along the fiber through near-field effects, it is feasible to manipulate the emitters along the fiber, which leads to forming an ordered arrangement in which the superfluorescence occurs most strongly. In our presentation, we will discuss the mechanical dynamics of emitters under optical forces induced by superfluorescence in the vicinity of an Ag nanofiber.

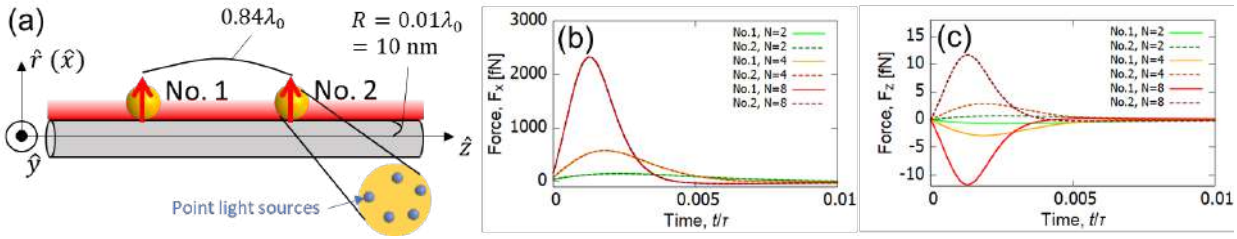

Fig 1. (a) Schematic picture of our assumed system. The two-level emitters are placed on an Ag nanofiber. The emission wavelength of the emitters is λ_0=1 μm and its radiative lifetime τ=0.1 ns. The radius of the Ag fiber is set to be R=0.01λ_0=10 nm. The radius of the emitters is 5 nm. The distance between emitters is 0.84λ_0, which is the condition that the radiation field is in phase and the emitters are most strongly correlated. The dipole directions of all the emitters are directed in the x-direction. (b,c) Dynamics of optical force exerted on the emitters in (a) x- and (b) z-direction.

References

1. S. Corsetti and K. Dholakia, "Optical Manipulation: Advances for Biophotonics in the 21st Century", J. Biomed. Opt. 26 (2021).
2. M. Aspelmeyer, T. J. Kippenberg, and F. Marquardt, "Cavity Optomechanics", Rev. Mod. Phys. 86, 1391 (2014).
3. H. Arahari, et al. "Luminescence-driven optomechanical system with micromechanical membranes." Optical Manipulation and Structured Materials Conference. 12606, 122-125, SPIE, 2023.
4. R. H. Dicke, "Coherence in Spontaneous Radiation Processes", Phys. Rev. 93, 99 (1954).
5. N. Yokoshi, et al., "Synchronization Dynamics in a Designed Open System", Phys. Rev. Lett. 118, 203601 (2017).
6. D. Dzsotjan, A. S. Sørensen, and M. Fleischhauer, Quantum Emitters Coupled to Surface Plasmons of a Nanowire: A Green's Function Approach, Phys. Rev. B 82, 075427 (2010).

AES 2024, ROME - ITALY, 25 –28 JUNE 2024

Antenna and interference effects in plasmon-assisted metal photoluminescence

Tigran V. Shahbazyan

Department of Physics, Jackson State University, Jackson, MS 39217 USA
shahbazyan@jsums.edu

Abstract: We present an analytical model for plasmonic enhancement of metal photoluminescence (MPL) in metal nanostructures. We find that the lineshape of MPL spectrum is determined by the interference between direct carrier recombination processes and those mediated by plasmonic antenna leading to a blueshift of MPL spectral band relative to scattering.

The origin of bright MPL from plasmonic nanostructures was suggested [1] to be due to excitation of the localized surface plasmon (LSP) by a recombining electron-hole pair [2] followed by the LSP radiative decay. This plasmonic antenna scenario has been confirmed by MPL measurements from single gold nanorods which revealed strong similarities between the MPL spectra and scattering spectra measured from the same structures [3-5]. At the same time, a persistent blueshift of MPL peak positions relative to LSP resonance in scattering spectra has been reported, which has not so far been explained.

We present an analytical model for MPL from plasmonic structures of arbitrary geometry with characteristic size is below the diffraction limit. For such systems, we derive an explicit expression for the MPL Purcell factor, which describes the plasmonic antenna effect, and trace the observed blueshift of MPL spectral band to destructive interference between the direct and antenna-assisted recombination processes. For frequencies w close to the LSP frequency w_n, we obtain the MPL Purcell:

$$\mathrm{F}(\omega) = \frac{2\pi \mathrm{c}^3}{\omega^3 V_\mathrm{m}} \frac{\varepsilon''(\omega)}{|\varepsilon(\omega) - \varepsilon'(\omega_n)|^2} \tag{1}$$

where $\varepsilon(\omega) = \varepsilon'(\omega) + i\varepsilon''(\omega)$ is metal dielectric function, c is speed of light, and V_m is metal volume. With such Purcell factor, we obtain the MPL enhancement factor relative to bulk MPL background as

$$M(\omega) = A_n \left| \frac{\varepsilon'(\omega_n) - 1}{\varepsilon(\omega) - \varepsilon'(\omega_n) - (2i\omega^3/3c^3)[\varepsilon(\omega) - 1]V_n} \right|^2 \tag{2}$$

where V_n is the effective system volume and the coefficient A_n depends on system geometry. The enhancement factor (2) can be used to describe the MPL spectra for systems of various shapes and sizes.

To illustrate our results, we present the MPL spectra for several gold nanostructures immersed in water by plotting Eq. (2) for a single LSP mode. In all calculations, we use the experimental gold dielectric function and, accordingly, the LSP wavelength range extends above 530 nm, which corresponds to the interband transitions onset in gold. Specifically, we choose the LSP peak positions at the wavelengths 620 nm, 670 nm, 710 nm and 750 nm, which are close to those measured in the MPL experiments [3-5]. We assume no particular shape but specify the overall nanostructure volume as $V_\mathrm{m} = L^3$, where L is the characteristic linear size. For gold structures, the optimal L lies in the interval between 20 nm and 60 nm, in which the MPL quenching is relatively weak while the LSP radiative damping is not too strong.

In Fig. 1, we plot the MPL enhancement factor (2) for general-shape gold nanostructures with L = 20 nm, in which the LSP resonance position can be tuned by varying the structure shape (e.g., by varying the aspect ratio of nanorods). The MPL enhancement factor exhibits nearly-Lorenzian resonances, whose amplitude increases with the wavelength, consistent with MPL quantum yield measurements [3-5].

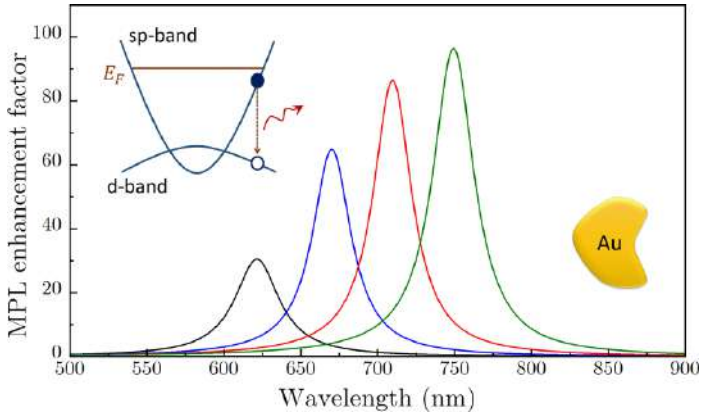

Figure 1. MPL enhancement factor for gold nanostructures with characteristic size 20 nm at various LSP wavelengths 620 nm, 670 nm, 710 nm and 750 nm. Inset: Schematics of interband transitions in gold.

In Fig. 2, we compare the MPL spectra for L = 40 nm gold nanostructures at same LSP wavelength values and the scattering spectra, which are both normalized to their maxima. A clear blueshift of the MPL spectral band relative to the LSP resonance in scattering spectra persists for all structures but is more pronounced for shorter wavelengths, consistent with the experiment [3-5]. This blueshift and the change in the resonance lineshape originate from the interference between the direct and LSP-mediated recombination processes, which is incorporated in the MPL enhancement factor (2).

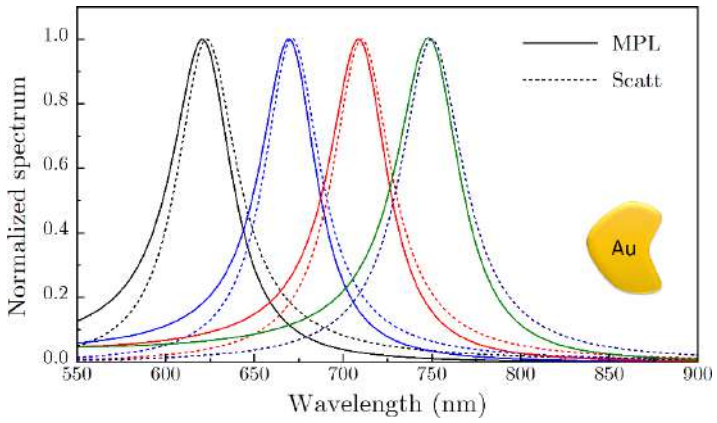

Figure 2. Normalized MPL and scattering spectra for gold nanostructures with characteristic size 40 nm at the same LSP wavelengths as in Fig. 1.

References

1. Dulkeith, E. *et al*., "Plasmon emission in photoexcited gold nanoparticles," Phys. Rev. B, Vol. 70, 205424 (2004).
2. Shahbazyan, T. V., I. E. Perakis, and J.-Y. Bigot, "Size-dependent surface plasmon dynamics in metal nanoparticles," Phys. Rev. Lett. Vol. 81, 3120, 1998.
3. Yorulmaz, M. *et al*., "Luminescence Quantum Yield of Single Gold Nanorods," Nano Lett. Vol. 12, 4385 (2012).
4. Fang, Y. *et al*., "Plasmon Emission Quantum Yield of Single Gold Nanorods as a Function of Aspect Ratio," ACS Nano Vol. 6, 7177, 2012.
5. Rao, W., Q. Li, Y. Wang, T. Li, and L. Wu, "Comparison of Photoluminescence Quantum Yield of Single Gold Nanobipyramids and Gold Nanorods," ACS Nano Vol. 9, 2783, 2015.

Plasmonic-enhanced Fabry-Pérot cavity for photocatalysis application

Ning Lyu[1,2*], Anjalie Edirisooriya[2], Zelio Fusco[2], Fiona Beck[2], Christin David[1,3]

[1] Institut für Festkörpertheorie und Optik, Friedrich-Schiller-Universität Jena, 07743 Jena, Germany
[2] School of Engineering, Australian National University, Canberra ACT2600, Australia
[3]Abbe Centre of Photonics, 07745 Jena, Germany
[*]corresponding author: ning.lyu@uni-jena.de

Abstract: In photocatalysis, selectivity in reaction pathways has a significant challenge. We concentrate on coupling nanoparticles on cavities to catalyze the N-demethylation reaction. This design, rooted in strong coupling, enables active-control over light-driven photocatalysis through tailored cavity configurations. Through the adjustment, we have achieved a 7-fold enhancement in yield.

Photocatalysis holds immense potential for harnessing clean energy through chemical processes [1]. This typically encompasses multistep electron transfer processes that culminate in the simultaneous generation of diverse products [2,3]. However, achieving an active selective conversion of a specific product remains a challenge. Thus, we first concentrated on a single-step reaction: the N-demethylation of Methylene blue (MB) driven by light with an effective wavelength range between 530 to 710nm [5]. Here, gold nanoparticles (Au NPs) exhibit a strong resonance, and provide active control when coupled with other resonances, such as in a Fabry-Pérot cavity [4].

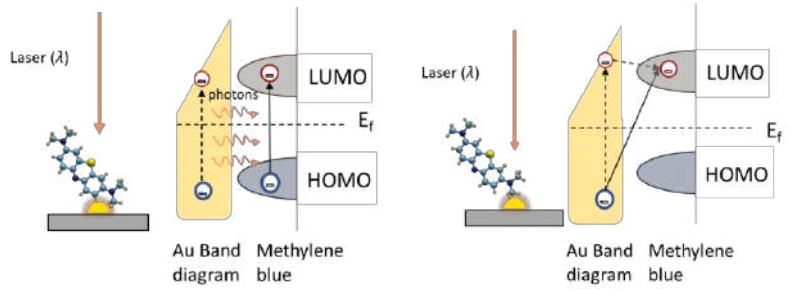

Figure 1: Localized Surface Plasmon Resonance (LSPR) band diagram for MB and gold nanoparticles showing the radiative decay (left) and non-radiative decay (right).

A thin layer of titanium dioxide (TiO2) was sputtered onto the surface of a metal mirror film. This interface displays a high reflectance, facilitating the occurrence of Fabry-Pérot (FP) resonances with a peak position determined by the TiO2 thickness. Additionally, Au nanoparticles were synthesized using an annealing process deposited onto the TiO2 layer. Coupling the Localized Surface Plasmon Resonance (LSPR, Fig. 1) with the constructive peak (‘switch on’) and destructive dip (‘switch off’) of the Fabry-Pérot resonance allows tailored designs for enhancing and suppressing photocatalysis, respectively.

Analysis of scanning electron microscope (SEM) images revealed that the interparticle gap of Au NPs is smaller than its size, indicating a non-negligible coupling between the Au nanoparticles (Fig.2). In simulations, utilizing a periodic model with averaged parameters proves inaccurate for describing this specific design. Consequently, we imported a 200×200nm^2 Atomic Force Microscopy (AFM) image into the model to describe the location and shape of nanoparticles and employed the Finite Element Method (FEM) to assess its optical performance.

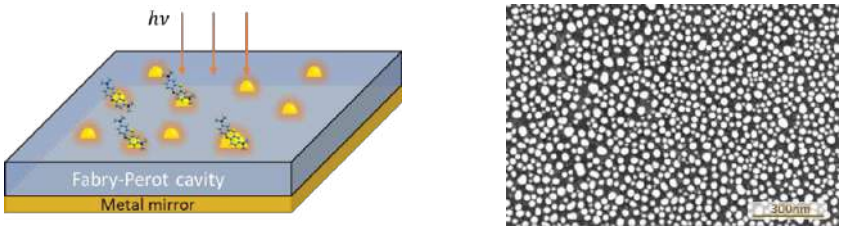

Figure 2: Configuration of plasmonic FP cavity showing random Au NPs on the TiO2 cavity with MB attached (left) and an SEM image of the gold nanoparticles with average radius r_{ave}=13nm and gap size g_{ave}=8nm (right).

The coupling of LSPR and FP resonances were characterized with a spectrophotometer, resulting in an absorption peak and dip in the absorption spectra of 'switch on/off' samples, respectively. With Ti metal mirror, the absorption doubles for the 'switch the resonance on' sample. Furthermore, to assess catalysis capability, surface-enhanced Raman spectroscopy was employed to monitor the progression of the MB N-demethylation reaction. The yield of the reaction is analyzed with the integration of the Raman peak of the reaction product. It was observed that the active design with enhanced absorption maintained a 7-fold enhancement in comparison to the low absorption 'switch off' sample over a 30s period (Fig. 3). Furthermore, Ti substrate exhibits instability during the annealing process at 500°C and forms a nanostructure at interface. Thus, the absorption peak is not only attributed to plasma resonance. To improve selectivity behavior, it is proposed to substitute Ti with a high-temperature-resistant material, such as Au.

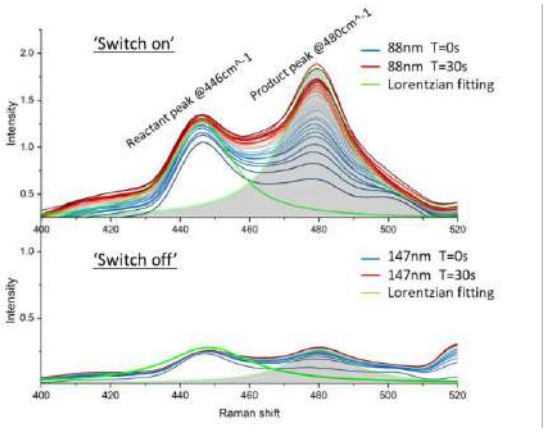

Figure 3: Temporal SERS results of 'switch on/off' samples in 30s; the product peak fits with Lorentzian curve.

Acknowledgements: The authors thank the German Research Foundation DFG (Deutsche Forschungsgemeinschaft) for financial support through the International Research Training Group IRTG 2675 and, additionally, the Australian National Fabrication Facility and TMOS for the support of experiments.

References

1. Y. Ma et al, Chemical Reviews, 114(19), 9987, (2014).
2. S. N. Habisreutinger et al, Angewandte Chemie International Edition, 52(29), 737, (2013).
3. J. L White, M. F. Baruch, J. E. Pander III, et al. Chemical Reviews, 115(23), 12888, (2015).
4. S. Zhao, Z. Fusco and F. J. Beck. Optica, 9(9), 1084-1039, (2022).
5. Z. Fusco., et al (2022). Journal of Materials Chemistry C, 10(19), 7511-7524.

AES 2024, ROME - ITALY, 25 –28 JUNE 2024

Plasmonic effects in composites fabricated by crystal growth techniques

P. Piotrowski,[1,2*] P. Paszke,[1,2] R. Nowaczyński,[2] H. Surma,[1] K. Sadecka,[1] N. Kongsuwan,[3,4] J. Toudert,[1] O. Hess,[5] D. A. Pawlak[1,2]

[1]Centre of Excellence ENSEMBLE[3] sp. z o.o., Wolczynska 133, 01-919 Warsaw, Poland
[2]Faculty of Chemistry, University of Warsaw, Pasteura 1, 02-093 Warsaw, Poland
[3]Quantum Technology Foundation (Thailand), 98 Soi Ari, Bangkok 10110, Thailand
[4]Thailand Center of Excellence in Physics, Ministry of Higher Education, Science, Research and Innovation, Bangkok 10400, Thailand
[5]School of Physics and CRANN Institute, Trinity College Dublin, Dublin 2, Ireland
[*] corresponding author: piotr.piotrowski@ensemble3.eu

Abstract: Optical effects that arise from introduction of plasmonic nanoparticles into volumetric systems will be presented, with a particular focus on glass and eutectic materials.

Plexcitonic systems combine plasmonic properties and excitonic emission which results in improved performance of the system by e.g. fast and intense luminescence, desirable in optoelectonic devices, ultrafast optical switches and quantum information science.

Here, we demonstrate optically active volumetric materials obtained with micro-pulling down method. By applying NanoParticle Direct Doping Method, nanocomposites with plasmonic properties are fabricated, which allows us to observe enhanced optical features. New generation of plasmonic materials are manufactured by NanoParticle-Direct Doping method developed in our laboratory. The possibility of direct introduction of plasmonic particles lets us easily dope glasses with NPs of various electromagnetic properties, thus tuning LSPR to enhance the targeted effects, e.g. PL of quantum dots.
Combining research on both fabrication and characterization of the novel materials with unusual electromagnetic properties may result in development of low-cost photonic devices with enhanced functionalities.

Acknowledgements
The authors thank the ENSEMBLE[3] Project carried within the International Research Agendas Programme (MAB/2020/14) of the Foundation for Polish Science co-financed by the European Union under the European Regional Development Fund and the Teaming Horizon 2020 programme of the European Commission (GA No. 857543) for supporting this work.

Optics and Photonics

AES 2024, ROME - ITALY, 25 –28 JUNE 2024

Fabry-Pérot and Friedrich-Wintgen bound states in the continuum in photonic triple-stub cavity

Y. Rezzouk[1], S. Khattou[1], M. El Ghafiani[1], M. Amrani[1], E.H. El Boudouti[1], A. Talbi[2] and B. Djafari-Rouhani[2*]

[1]Département de Physique, Faculté des Sciences, Université Mohammed I, Oujda, Morocco
[2]University of Lille, CNRS, Centrale Lille, Univ. Polytechnique Hauts-de-France, UMR 8520-IEMN, F-59000 Lille, France
[*]corresponding author: bahram.djafari-rouhani@univ-lille.fr

Abstract: We investigate theoretically and experimentally the existence of Fabry-Pérot (FP) and Friedrich-Wintgen (FW) bound states in the continuum (BICs) in a photonic triple-stub cavity. By slightly detuning from the BIC condition, the latter transforms to electromagnetic-induced transparency/reflection (EIT/EIR) or Fano resonances. Analytical findings are experimentally validated in the radio-frequency domain.

Bound states in the continuum (BICs) [1] are special kinds of resonant states with an infinite lifetime that remain confined in some parts of the system even though their frequencies lie in the radiative frequency range. Generally, BICs can occur through different mechanisms depending on their physical origin; among them are Fabry-Pérot (FP) BIC [2], and Friedrich-Wintgen (FW) BIC [3]. FP-BICs refer to destructive interference when two resonant cavities are spaced apart so that they are tuned to make the round-trip phase shift add up to an integer multiple of 2π. However, the FW-BIC is induced by the interaction of two modes within the same cavity. The resonances leading to FW-BIC have no separation and are coupled through the same radiation channel. The most notable feature of BICs is the occurrence of high-quality quasi-BICs in the transmittance spectrum. The quasi-BIC can appear in the shape of a Fano [4], electromagnetic-induced transparency (EIT) [5] or electromagnetic-induced reflection (EIR) [6] resonances.

The photonic stubbed structures featuring double stubs [7] have been intensively used to investigate EIT and Fano resonances as well as BICs. This cavity presents symmetric (S) and anti-symmetric (AS) modes that operate independently without interacting. In this communication [8], we propose a triple-stub cavity made up of a stub of length d_3 surrounded by two stubs of length d_2 and separated by segments of length d_1 (see Fig.1(a)). All the waveguides are made of coaxial cables with permittivity ε. We demonstrate that this cavity can display both FP-BIC and FW-BIC. When the cavity is inserted between two ports, we demonstrate theoretically and validate experimentally the existence of S-BIC and AS-BIC of FP-type under commensurability conditions between the lengths d_1, d_2 and d_3. In the following, we set d_1=1 as the unit of length. The S and AS-BICs may cross each other, giving rise to a two-times degenerate BIC (D-BIC). By breaking the symmetry of the cavity, AS-BIC and S-BIC can couple together and realize a FW-type BIC where one resonance remains with a zero width while the other broadens into a bright mode. By slightly detuning from the BIC condition, the latter transforms into either EIT, EIR or Fano resonances. All our analytical results, obtained from the Green's function method, have been confirmed experimentally in the radio-frequency domain using coaxial cables. Figure 1(b) shows the theoretical transmission intensity versus the dimensionless frequency $\Omega = \omega d_1 \sqrt{\varepsilon}/c$ (ω is the angular frequency and c the speed of light) and d_3 through the loss FP cavity (Fig. 1(a)). The corresponding experimental results, collected in Fig. 1(c), are in very good agreement with theory. Also, some transmission spectra are presented in Figs. 1 (d)-(f) at some selected values of d_3. The horizontal dotted line in panels (b)-(c) indicates the position of the AS-BIC, which is independent of d_3. Around Ω = 1, there

exists a symmetric resonance labeled S, which depends on d_3. One can observe a shrinking of the S-resonance as d_3 increases, which appears as a transparency window between two zeros (denoted by pink and white dotted points). This resonance disappears for d_3=0.5, giving rise to S-BIC. The crossing of the AS-BIC and S-BIC gives rise to D-BIC. For $d_3 > 0.5$, the S-resonance reappears when we shift slightly from the BIC position. The vertical arrows at $\Omega = 1$ indicates the position of the AS-BIC, which appears as a resonance with zero width, whatever the value of d_3. The S-resonance lying between two transmission zeros behaves as an EIT resonance. The electric field distributions associated with the AS-BIC and S-BIC at $\Omega = 1$ and for $d_3 = d_2$=0.5 are illustrated in Figs. 1(g) and (h). We can see that the BICs are tightly confined inside the cavity without emitting any external radiation. The electric field, with either anti-symmetric (Fig.1 (g)) or symmetric (Fig.1(h)) shape, vanishes at the junction points with the external leads.

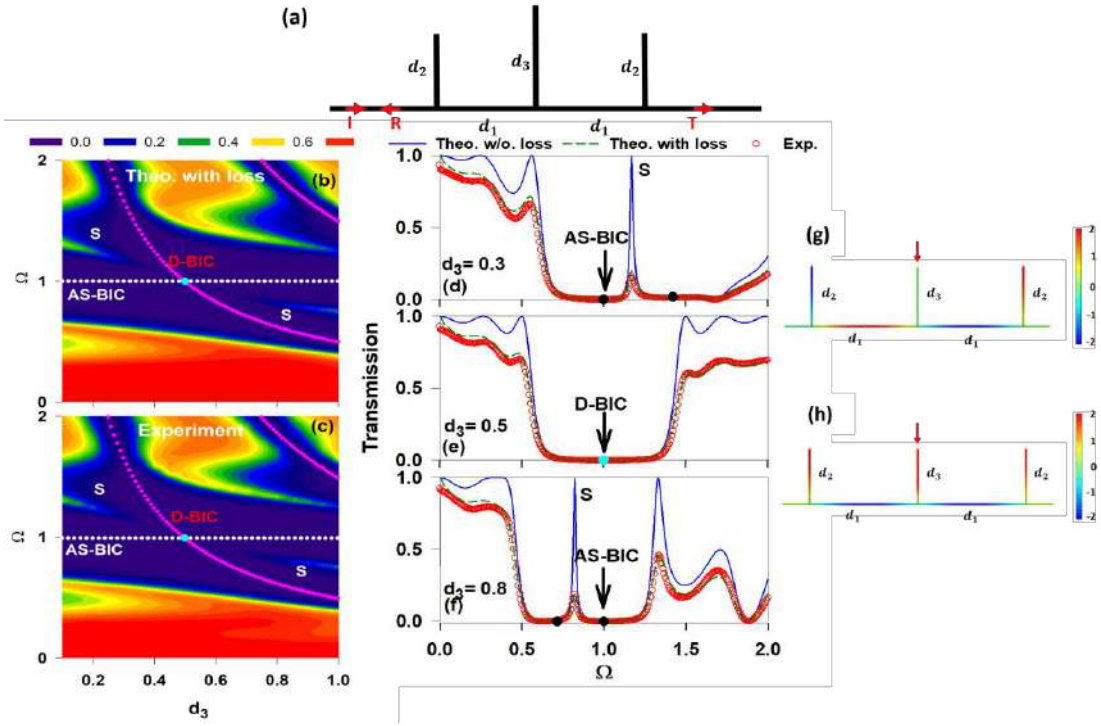

Figure 1: (a) Schematic of a symmetric triple-stub cavity. (b) Theoretical variation of the transmission magnitude in lossy system. (c) Experimental validation of the transmission magnitude. (d)--(f) Theoretical (blue and green curves) and experimental (red circles) transmission spectra for different values of d_3. (g) and (h) give the electric field map at $\Omega = 1$ and d_3= 0.5 of the AS-BIC (g) and the S-BIC (h). The red arrows in (g) and (h) indicate the excitation position.

References

1. J. von Neumann and E. P. Wigner, Z. Phys. **30**, 465-467, 1929.
2. D. C. Marinica, A. G. Borisov and S. V. Shabanov, Phys. Rev. Lett. **100**, 183902, 2008.
3. H. Friedrich, D. Wintgen, Phys. Rev. A **31**, 3964-3966, 1985.
4. U. Fano, Phys. Rev. **124**, 1866, 1961.
5. S. E. Harris, Phys. Today **50**, 36, 1997.
6. S.F. Mingaleev, A.E. Miroshnichenko and Y.S. Kivshar, Opt. Express **16**, 11647-11659, 2008.
7. A. Mouadili et al. J. Appl. Phys. **113**, 164101, 2013.
8. Y. Rezzouk et al. Submitted to Phys. Rev. B.

AES 2024, ROME - ITALY, 25 –28 JUNE 2024

Optical Coherence Tomography vs. X-ray imaging for biomedical applications

V.-F. Duma[1-3*] and R.-A. Erdelyi[1]

[1]Faculty of Electronics, Telecommunications, and Information Technology,
Polytechnic University of Timisoara, Bd. Vasile Parvan no. 2, Timisoara 300223, Romania
[2]Center of Research and Development for Mechatronics, National University of Science and Technology POLITEHNICA Bucharest, Splaiul Independentei 313, Sector 6, Bucharest, Romania
[3]3OM Optomechatronics Group, Faculty of Engineering, "Aurel Vlaicu" University of Arad, Str. Elena Dragoi no. 2, Arad 310177, Romania
[*]corresponding author: duma.virgil@osamember.org

Abstract: Optical Coherence Tomography (OCT) is compared to X-ray radiographies for the assessment capability of dental conditions, and it is used for optimizing the latter imaging technique, which is the gold standard for dentistry.

We report a series of studies we have performed regarding the comparison (and the possible synergy) of X-ray imaging and Optical Coherence Tomography (OCT), the latter a method based on low coherence laser interferometry. An in-house developed Swept Source (SS) OCT system with a center wavelength of 1310 nm was utilized. The two imaging methods are somehow contradictory regarding their parameters, as the former has high penetration depth but low resolution (when investigating living tissue, therefore with a limited radiation dose-according to the ALARA (as-low-as-possible radiation dose) protocol), while the latter has a low penetration depth (of around 1 mm) but a much better resolution – from 2 μm [1] to the most common 10 to 15 μm [2-5]. In contrast, X-ray radiographies are typically around 150 μm, with a performance of 75 μm for the considered field, of Dental Medicine, for which radiographies of different types (panoramic, intraoral, cone beam-CT (CBCT), and cephalometric) are the gold standard.

Thus, our first study [3] explored the entire range of medical conditions of the oral cavity (on patients in a clinical environment) and classified them according to the most appropriate imaging method for investigations: radiography or OCT. Three categories of conditions were pointed out: (i) those that must be investigated only with radiography, as they require high penetration depths and large Fields-of-View (FOV), including bone assessments; (ii) those that are best investigated with OCT, as they require high resolutions for a proper assessment, including metal crowns, enamel or dentine issues, and soft tissue; (iii) those for which a complementarity of X-ray imaging and OCT was demonstrated and that benefit from a blend of both methods – including orthodontics, periodontitis, as well as crown and filling adaptation. A special remark must be made regarding the capability to perform quantitative assessments/measurements, which we demonstrated that can be performed for all these conditions only using OCT (except for bone assessments and periodontitis, for which X-rays investigations are appropriate) [3]. For cavities, for example, which are the most common condition to be investigated, we show that using radiographies means errors of up to 50%; in contrast, OCT can provide precise results. Fig. 1 shows an example of such a comparative measurement.

This synergy of OCT and radiographies was further enhanced by developing, for the first time to our knowledge, and optimization method of dental X-ray imaging using the higher resolution method, OCT [4]. Essentially, the method consists on determining the optimal X-ray imaging parameters (anode voltage, current, exposure time, and radiation dose) by observing (*in vivo*) small conditions (for example cavities) using OCT and then performing (also ex vivo) radiographies with increasing parameters until the targeted medical conditions/sample details become visible (and therefore, can be investigated).

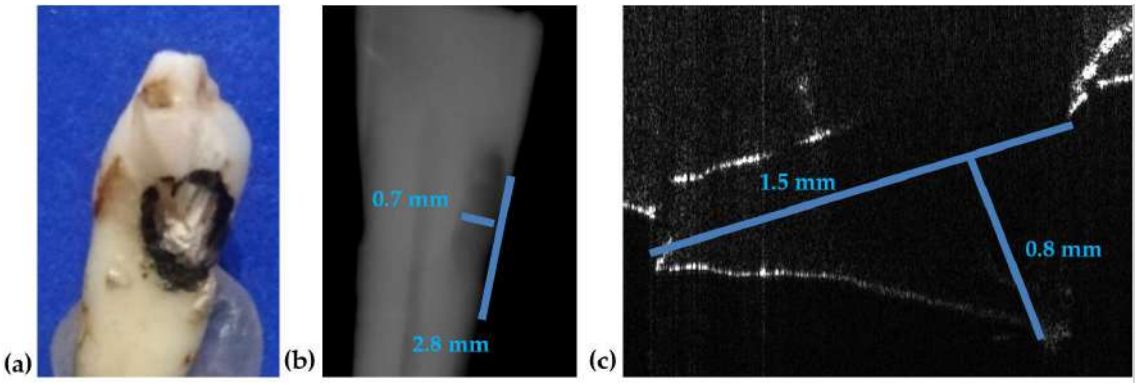

Fig. 1. **(a)** Incisive tooth with an area marked for OCT investigations; **(b)** a section cropped from the intraoral radiography with measurements of the cavity; **(c)** OCT B-scan where the depth and the length measurements of the cavity have been performed.

Fig. 2. Panoramic radiography obtained during the optimization process.

The method can be applied for panoramic and CBCT radiographies and it achieves a necessary trade-off between the necessity to increase resolution and to keep the radiation dose to a minimum. Figure 2 shows the final phase of the developed optimization process for a panoramic X-ray investigation. The method was then applied on patients, and it is in full development – including considering different types of modern X-ray units, for example Planmeca ProMax 3D Plus (Planmeca, Helsinki, Finland) and Gendex Oralix (Danaher Corporation, Washington DC, USA) in [4]. This direction of research is included in our (larger) project on comparing and investigating synergies of OCT with other imaging methods, including SEM, TEM, AFM, micro-CT, and confocal microscopy – with each method for different (classes of) applications, from biomedical to Non-Destructive Testing (NDT) for industry.

Acknowledgements: This work was supported by the Romanian IPCEI (Important Project of Common European Interest) on microelectronics, via Continental Automotive Romania.

References

1. Cogliati, A., Canavesi, C., Hayes, A., Tankam, P., Duma, V.-F., Santhanam, A., Thompson, K. P., Rolland, J. P., "MEMS-based handheld scanning probe with pre-shaped input signals for distortion-free images in Gabor-Domain Optical Coherence Microscopy," Optics Express, Vol. 24, No. 12, 13365-13374, 2016.
2. Drexler, W., Liu, M., Kumar, A., Kamali, T., Unterhuber, A., et al., "Optical coherence tomography today: speed, contrast, and multimodality," J. Biomed. Opt., Vol. 19, 071412, 2014.
3. Erdelyi, R.-A., Duma, V.-F., Sinescu, C., et al., "Dental Diagnosis and Treatment Assessments: Between X-rays Radiography and Optical Coherence Tomography," Materials, Vol. 13, No. 21, 4825, 2020.
4. Erdelyi, R.-A., Duma, V.-F., Sinescu, C., Dobre, G., Bradu, A., Podoleanu, A., "Optimization of X-ray Investigations in Dentistry using Optical Coherence Tomography," Sensors, Vol. 21, No. 13, 4554, 2021.

AES 2024, ROME - ITALY, 25 –28 JUNE 2024

Direct generation of terahertz cylindrical vector beams in nonlinear crystals

Seigo Ohno[1,2*], **Hiroaki Iwase**[1]

[1]Department of physics, Tohoku University, Japan

[2]Organization for Advanced Studies, Tohoku University, Japan
[*]corresponding author: seigo@tohoku.ac.jp

Abstract: A simple way to generate THz vector beams is proposed. We pay attention to the symmetry of nonlinear optical crystals. When the high-symmetry axis on which the THz-wave generation is forbidden is excited with focusing beam, the component deviated from the axis can contribute to generate a vortex beam.

In vector beams, the polarization direction is spatially distributed on the wavefront. Vector beams described in cylindrical coordinates are particularly characterized by the topological charge ℓ which is the winding number of the polarization direction relative to the beam center. The center has a dark singularity where the vector direction cannot be determined. Since the dark spot size is smaller than the diffraction limit of the beam, it is expected to be applied to super-resolution technology. Radial and azimuthal beams with $\ell = 1$ are also attracting attention because they respectively generate electric and magnetic fields oscillating in the propagation direction at a focal point when they are focused by a lens. In the THz region, significant devices to generate vector beam have been developed by some groups [1, 2]. These devices have commonly center symmetric pattern in the structure. In roughly speaking, this means that the topological nature in the structure is the origin of the topological nature in the generated vector beam. In our presenting method, the topological nature is prepared in an optical setup in which the in-plane component of the wavevector direction on the nonlinear crystal surface is rotating around the optical axis by focusing the incident beam as the concept given in Fig. 1[3]. The topological nature of deviated component from the optical axis can be projected on the generated THz beam of the polarization distribution around the optical axis if the optical axis is just corresponding to the forbidden direction of the THz wave generation due to the symmetry of the nonlinear crystal.

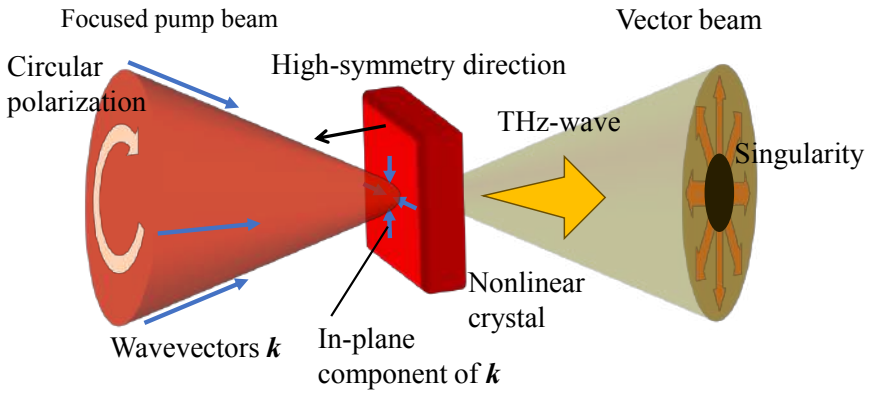

Fig.1 Concept of the presenting THz vector beam generation. The wavevector components deviated from the center in the focusing pump beam make the source of THz vector beam.

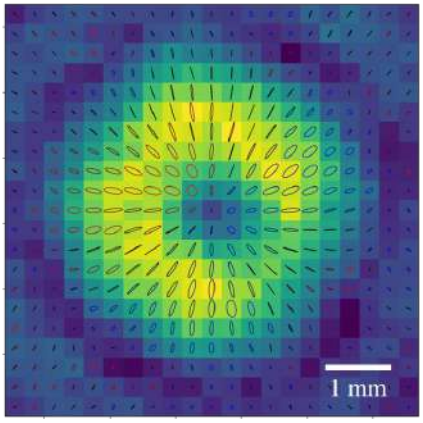

Fig.2 Experimentally observed polarization and intensity distribution at 0.5 THz. The color and the elliptical symbol of each pixels indicate the intensity of the terahertz wave and the polarization state at the corresponding position, respectively.

Based on this concept, we considered to utilize a ZnTe crystal for the THz vector beam generation. The nonlinear polarization excited by a circular polarized pump beam as the function of the incident direction in the polar coordinate is provided as

$$\begin{bmatrix} P_x \\ P_y \\ P_z \end{bmatrix} = -4d_{14}E_0^2 \begin{bmatrix} \sin\theta\cos\theta\sin\phi \\ \sin\theta\cos\theta\cos\phi \\ \sin^2\theta\sin\phi\cos\phi \end{bmatrix}, \qquad (1)$$

where d_{14} is second order nonlinear susceptibility. This formulation represents nonlinear polarizations around [111] and [100] directions distribute with the topological charge of $\ell = +1$ and -1, respectively.

We experimentally measured the polarization distribution when a circularly polarized pump pulse was focused on a (111)-cut ZnTe crystal with thickness of 0.5 mm. The result for 0.5 THz component is shown in Fig. 2. Since there is an intensity minimum at the center of the beam and the polarization is radially polarized, we can conclude the vector beam with $\ell = +1$ is directly generated from the ZnTe crystal. We believe this simple technique to generate a THz vector beam will contribute to wide applications of THz vector beams.

Acknowledgment

This work was partially supported by JST FOREST Program (JPMJFR2036) and KAKENHI (JP21H01018, JP22H01980, JP22H01253, 23K04567, and JP23K17885).

References

1. S. Winnerl, B. Zimmermann, F. Peter, H. Schneider, and M. Helm, “Terahertz bessel-gauss beams of radial and azimuthal polarization from microstructured photoconductive antennas,” Optics Express, Vol. 17, No. 3, 1571–1576, 2009.
2. R. Imai, N. Kanda, T. Higuchi, Z. Zheng, K. Konishi, and M. Kuwata-Gonokami, “Terahertz vector beam generation using segmented nonlinear optical crystals with threefold rotational symmetry,” Optics Express, Vol20, No. 20, 21896–21904, 2012.
3. H. Iwase and S. Ohno, “Direct generation of a terahertz vector beam from a ZnTe crystal excited by a focused circular polarized pulse,” Optics Express, Vol. 31, No. 16, 26923–26934, 2023.

AES 2024, ROME - ITALY, 25 –28 JUNE 2024

High-order terahertz Bessel beams with an orbital angular momentum

Katsuhiko Miyamoto[1,2*]

[1]Graduate School of Engineering, Chiba University, 1-33 Yayoi-cho, Inage-ku, Chiba 263-8522, Japan

[2]Molecular Chirality Research Center, Chiba University, 1-33 Yayoi-cho, Inage-ku, Chiba 263-8522, Japan

[*]corresponding author: k-miyamoto@faculty.chiba-u.jp

Abstract: We demonstrate a frequency tunable terahertz (THz) Bessel beam with an orbital angular momentum by employing the Tsurupica axicon lens in combination with the THz vortex source. THz Bessel beam output was tuned within the frequency range of 3-6 THz.

1. Introduction

Bessel beams, which are non-diffracting beams, consist of analytical solutions to the wave equation with unique properties such as self-healing wavefronts and deep depth of field than Gaussian beams [1]. Such beams are used in a variety of applications, including optical trapping, optical tweezer and high-resolution imaging [2]. In particular, the generation of Bessel beams in the terahertz (THz) region is expected to be applied to deep focal imaging and THz communications [3]. In previously, most studies have utilized a zero-order Bessel beam as the most basic form of beam.

In this presentation, we propose to generate high-order THz Bessel beams with an orbital angular momentum (OAM). OAM is characterized by a topological charge ℓ owing to its spiral wavefront, thereby enabling many kinds of applications in the visible, near-infrared and THz region. We demonstrate a tunable high-order THz Bessel beam with OAM in combination with the tunable THz vortex source based on a difference frequency generation [4] and the Tsurupica axicon lens which exhibits high transmission and low frequency dispersion in the THz region [5].

2. Tsurupica axicon lens

The most common way to generate a Bessel beam is with an axicon conical lens that can be used as a refractive optics. However, the axicon lens is typically designed for a specific THz frequency to depend on the absorption and frequency dispersion of the optical materials, and it inherently constrains the frequency tunability of the THz Bessel beam source. We developed a THz axicon lens formed of a polymeric material, dubbed Tsurupica, with a low frequency dispersion of refractive index and high transmittance [6]. Figure 1 shows the transmittance characteristics of Tsurupica polymer with a thickness of 2 mm and a comparison of Teflon polymer, a previously reported medium for axicon lens in the THz region. The axicon angle of the Tsurupica lens fabricated by mechanical polishing is 15 degrees. The average surface roughness of the flat side and conical side are less than 0.05μm and 0.3μm, respectively.

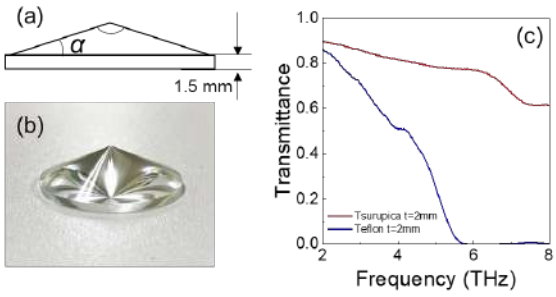

Fig. 1. (a) Illustration of the design; and (b) photograph of a Tsurupica axicon lens. (c) Transmittance of Tsurupica and Teflon with 2 mm thickness measured by FT-IR.

3. Experiments and results

Figure 2 shows an experimental setup for the generation of a high-order THz Bessel beam with OAM. A THz source consisted of a 1.5 μm dual-frequency picosecond laser (pulse width: ~8 ps, PRF: 1 MHz) pumped 4'-dimethylamino- N-methyl- 4-stilbazolium tosylate difference frequency generation (DAST-DFG) [10]. This setup generated a THz Laguerre-Gaussian (LG) mode with a topological charge $\ell = 1$ within the frequency region of 3 - 6 THz. The LG beam, upon passing through the Tsurupica axicon lens, transformed into a higher-order Bessel beam with multiple rings and OAM. The measurement system included a THz camera (NEC: IRV-T0831) and a room temperature detector (Gentec: THZ5B-BL).

The intensity distributions of 4 THz Bessel beams at the topological charge of $\ell = 0$ and 1 are summarized in Fig. 3. The generated first-order THz Bessel beam had a central dark core with multiple rings, indicating that they possess a helical wavefront and OAM originating from an on-axis phase singularity. The first-order Bessel beam had a non-diffraction property with a depth of focus exceeding 15 mm, which is approximately 10 times greater than that of the first-order LG beam.

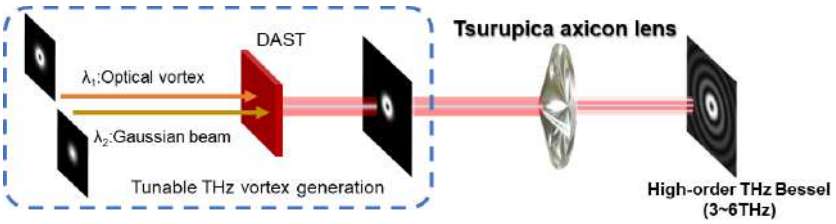

Fig.2 Schematic diagram of experimental setup for tunable THz Bessel beam generation

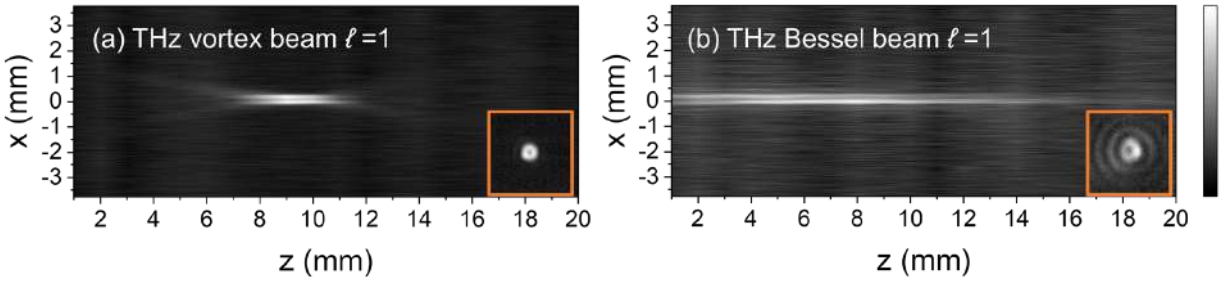

Fig.3 The propagation characteristics of the z-axis direction of (a) 1st-order LG and (b) Bessel beam at 4 THz, respectively.

4. Conclusion

We have successfully demonstrated the generation of a tunable high-order THz Bessel beam with OAM by employing a Tsurupica axicon lens in combination with a THz vortex source based on DAST-DFG. This system realized the generation of high-order THz Bessel beams within the THz frequency of 3 - 6 THz. Tunable THz Bessel beam with versatile OAM will allow the way towards novel advanced THz fundamental physics and technologies, such as OAM spectroscopy and communications systems, and so on.

References

1. J. Arlt and K. Dholakia, Opt. Commun. **177**, 297–301 (2000).
2. V. Garcés-Chávez, D. McGloin, H. Melville, W. Sibbett, and K. Dholakia, Nature **419**, 145–147 (2002).
3. Y. Monnai, D. Jahn, W. Withayachumnankul, M. Koch, and H. Shinoda, Appl. Phys. Lett. **106**, 021101 (2015).
4. K. Miyamoto, K. Sano, T. Miyakawa, H. Niinomi, K. Toyoda, A. Vallés, and T. Omatsu, Opt. Express **27**, 31840–31849 (2019).
5. K. Miyamoto, K. Suizu, T. Akiba, T. Omatsu, Appl. Phys. Lett. **104**, 261104 (2014).
6. K. Miyamoto, R. Nomura, S. Tsurumaru, and T. Omatsu, OSA Continum 1, 633-640 (2022).

AES 2024, ROME - ITALY, 25 –28 JUNE 2024

Large-area van der Waals heterostructures for photon harversting

M. C. Giordano[1*], M. Barelli[1], M. Gardella[1], G. Zambito[1], G. Ferrando[1], F. Buatier de Mongeot[1]

[1]Dipartimento di Fisica, Università di Genova, Via Dodecaneso 33, 16146 Genova, Italy
[*]corresponding author: maria.caterina.giordano@unige.it

Abstract: Large area stacking of van der Waals heterostructure arrays based on two-dimensional (2D) Transition Metal Dichalcogenide semiconductors (TMDs) is achieved by a novel physical deposition approach that also allows maskless confinement of 2D TMDs heterostructures onto flat-optics nanograting templates. The periodic nanoscale reshaping of the 2D semiconductor layers promote the excitation of Rayleigh Anomalies that are easily tunable over a broadband Visible and Near-Infrared by tailoring the illumination angle. Under this condition light propagation is effectively controlled promoting strong in-plane electromagnetic confinement, directional light scattering, and broadband photon absorption enhancement with strong impact in photoconversion applications.

Two-dimensional (2D) Transition Metal Dichalcogenide (TMD) semiconductors have attracted diffuse interest due to their exceptional optoelectronic properties and to the possibility to stack 2D layers in van der Waals heterostructures with strong potential in optoelectronic devices. However, the inherent low photon absorption of the atomic layers demands for novel light coupling schemes in view of photoconversion applications. There is also an urgent request to scale-up the lateral size of the 2D van der Waals (vdW) heterostructure devices, typically limited to micrometric flakes, and to engineer their shape at the nanoscale. Here the nanoscale reshaping of 2D vdW heterostructures based on TMDs layers is shown over large-area (cm^2 scale) demonstrating superior photon harvesting properties and opening new perspectives in photonics and energy conversion [1-4]. We show a flat-optics scheme based on large-area few-layers WS_2-MoS_2 heterostructures, endowed with type-II band alignment, and forming periodic nanogratings [5]. These nanopatterned layers can effectively steer the light propagation via Rayleigh Anomalies, promoting strong in-plane electromagnetic confinement and broadband omnidirectional photon absorption enhancement, with strong impact in photoconversion. A promising application deals with photo to chemical energy conversion that have been recently boosted in flat-optics few-layer MoS_2 lying onto flexible templates, opening new possibilities for large-scale energy storage. Additionally, this flat-optics configuration promotes directional light scattering properties enhanced in 2D TMD layers lying onto faceted nanogratings with the capability to steer light by controlling the local tilt of the nanofacets.

These large-area van der Waals heterostructures thus provide novel platforms with a strong potential towards real-world use of 2D TMDs layers in scalable nanophotonics, photoconversion and energy storage applications

References

1. C. Martella et al., Adv. Mater. 30, 1705615, **2018**.
2. M. Bhatnagar et al., Nanoscale, 12, 24385, **2020**.
3. M. Bhatnagar et al., ACS Appl. Mater. Interf., 13, 11, 13508, **2021**.
4. G. Ferrando et al., Nanoscale 15,4, 1953, **2023**.
5. M. Gardella et al., under review **2024**.

AES 2024, ROME - ITALY, 25 –28 JUNE 2024

Nanostructures for Photonic Functionalities and Medical Physics Applications

M.F. Pereira[1*], Humaira Zafar[1], V. Vaks[2], A. Ganguly[1] and G. Das[1]

[1]Department of Physics, Khalifa University, United Arab Emirates

[2]Institute for Physics of Microstructures, Russia
[*]corresponding author: mauro.pereira@ku.ac.ae

Abstract: In this talk we will summarize our recent theoretical and experimental studies of different types of nanostructures, including semiconductor superlattices, adiabatically bent superlattice-waveguides, nanocylinders and nanocones. We show their applications to THz spectroscopy-based medical diagnostics and new photonics functionalities.

In this talk we summarize our recent theoretical and experimental studies of different types of superlattices. We start with a summary of the predictive theory used to simulate giant control of THz nonlinearities and demonstrate its validity per direct comparison with experiments [1-4]. Next the same semiconductor superlattices are used for the detection of nitriles, showing potential as diagnostic method for cancer patients treated with chemotherapy. In the second part of the talk, we focus on compact and broadband adiabatically bent superlattice-waveguides with negligible insertion loss and ultra-low crosstalk.

Our approach is applicable to other waveguide geometries and integrated photonic platforms [5-8]. We conclude the talk discussing a low cost fabrication technique, delivering nanocylinders, truncated hexagon-based pyramids, circular pads on a conical base and nanocones with strong potential for a significant impact on biosensor applications [9].

References

1. M.F. Pereira et al, Sci Rep 10, 15950 (2020).
2. V. Vaks et al, Sci Rep 12, 18117 (2022).
3. M.F. Pereira, Nanomaterials 12, 1504 (2022).
4. Al-Ateqi, A., Pereira, M.F. , Opt Quant Electron 55, 1287 (2023).
5. Humaira Zafar et al, Opt. Express 31, 21389-21398 (2023).
6. H. Zafar et al, in IEEE Journal of Selected Topics in Quantum Electronics, vol. 29, no. 6: Photonic Signal Processing, pp. 1-9, Nov.-Dec. 2023, Art no. 4400109 .
7. Humaira Zafar et al, Opt. Express 30, 10087-10095 (2022).
8. Humaira Zafar et al, AIP Advances 10, 125214 (2020).
9. Ganguly, A., Zafar, H., Howells, C.T., Pereira, M.F. and Das, G. (2024), Small Struct., 5: 2300300.

Acknowledgements: The authors gratefully acknowledge support from the Khalifa University Internal Funding: CIRA-2021 (project code 8474000422) for M.F.P. and H.Z. and CIRA-2021 (project code: 8474000416) for A.G. and G.D.;

AES 2024, ROME - ITALY, 25 –28 JUNE 2024

Planarized Terahertz quantum cascade frequency combs with inverse-designed reflectors and integrated antennas for far field control

G.Scalari[1*], U. Senica[1], S. Gloor[1], P. Micheletti [1], D. Stark[1], M. Beck[1], and J.Faist[1]

[1]Institute for Quantum Electronics, Department of Physics, ETH Zürich, Zürich, Switzerland
[*]corresponding author: gscalari@ethz.ch

Abstract: We present a planarized THz QCL with an inverse-designed end facet reflector coupled to a surface-emitting patch array antenna, emitting combs of >800 GHz bandwidth at a central frequency of 2.9 THz. All the components have been optimized for octave-spanning spectral bandwidths between 2-4 THz and monolithically integrated on the same photonic chip.

There is a growing interest in THz photonics for telecommunications and sensing, as well as in fundamental studies. A variety of fundamental excitations in solid state systems lie in the THz range: quantum materials, including superconductors, novel magnetic and topological materials, graphene and its composites, and many others. THz radiation is as well widely used to control the dynamics and the states of quantum materials[1]
A prominent candidate as a source for telecommunications as well as for THz spectroscopy and material control is the THz quantum cascade laser[2]. Recent advances in the high temperature operation of these devices[3,4], combined with their frequency agility and the possibility to operate as frequency combs make them extremely appealing as key building blocks for THz photonics. THz QCLs can cover impressive bandwidths of more than an octave[5] and emit peak powers up to 1 W[6]. We recently introduced a new planarized platform[6] which allows the integration of active and passive components like waveguides, antennas[7] (see Fig.1(a,b)), splitters, high reflectivity and frequency selective mirrors to manipulate and shape in space and time THz radiation. Particularly, these lasers can as well operate as frequency combs, producing FM comb states spanning more than 1 THz or actively mode locked states to produce pulses of a few picosecond length , as shown in Fig.1(c,d) .

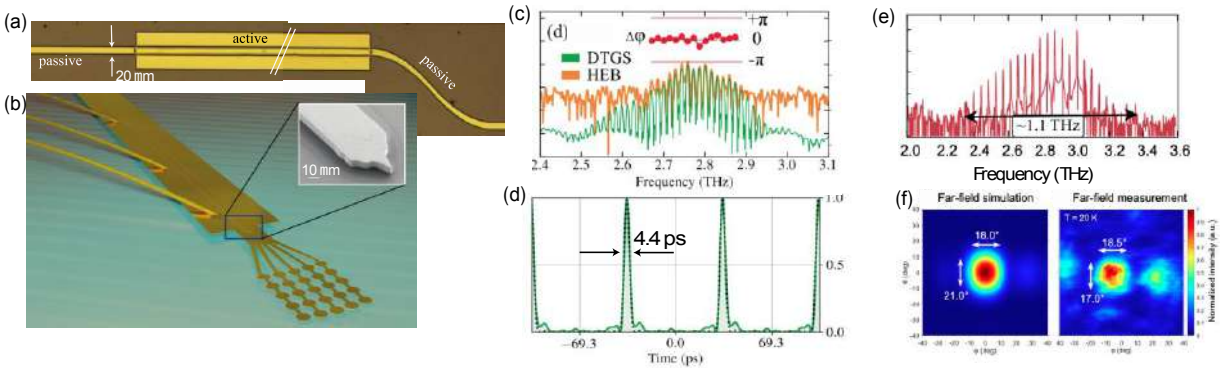

Figure 1. (a) Micrograph of an active laser with two passive waveguides abutted. (b). Cartoon picture of a device with an integrated antenna, in the inset is visible the dry-etched low reflectivity laser facet. (c)spectrum of an actively mode-locked planarized THz QCL. (d) reconstructed pulses emitted corresponding to spectrum in (c). (e) Spectral emission on an FM comb state spanning more than 1 THz. (f) Far-field emission profile of the antenna-coupled device with the 10% inverse-designed reflector.

The ultrafast dynamics of the QCL (ps lifetimes) makes them very appealing for creating pulse sequences that can eventually employed in coherent control of quantum systems. Interestingly, the optical resonator employed to confine the THz radiation is metallic, allowing to create structures well-below the diffraction limit in one or more directions. Such antennas can be integrated onto the chip thanks to the planarized approach (see Fig.1(b)). The reflectivity of the facet can be tailored via an inverse-design approach, allowing high power devices with front reflectivities of 10% and lower. We will show QCL frequency combs with improved power and far-field characteristics with measured devices showing a seven-fold improvement in slope efficiency compared to devices with a cleaved facet[8]. They feature peak powers of up to 13.5 mW with surface emission into a narrow beam with a divergence of (17.0^{o} x 18.5^{o}, Fig.1(f)) , while broadband fundamental and harmonic comb states spanning up to 800 GHz are observed.

References

1. Yang, C et al., *Terahertz control of many-body dynamics in quantum materials*. Nat Rev Mater 8, 518 (2023)
2. R Köhler et al., *Terahertz semiconductor heterostructure laser*, Nature 417 (6885), 156 (2002)
3. L. Bosco et al., *Thermoelectrically cooled THz quantum cascade laser operating up to 210 K*, Appl. Phys. Lett., 115, 010601 (2019)
4. A. Khalatapour et al., *Enhanced operating temperature in terahertz quantum cascade lasers based on direct phonon depopulation*, Applied Physics Letters 122 (16), 161101 (2023)
5. M. Rösch, G. Scalari, M. Beck, J. Faist, *Octave spanning semiconductor laser*, Nature Photonics, 9, 1 (2015)
6. L Li et al., *THz QCLs with >1 W output powers*, Electronics letters 50 (4), 309-311 (2014)
7. U Senica et al., *Planarized THz quantum cascade lasers for broadband coherent photonics*, Light: Science & Applications 11 (1), 347 (2022)
8. U. Senica et al., *Broadband surface-emitting THz laser frequency combs with inverse-designed integrated reflectors,* APL Photonics 8, 096101 (2023)

AES 2024, ROME - ITALY, 25 –28 JUNE 2024

Flexible holographic metasurfaces in the visible and mm-wave range

J. Xiao[1], T. Plaskocinski, M. Biabanifard [1], and A. Di Falco[1,*]

[1]School of Physics and Astronomy, University of St Andrews, North Haugh, KY16 9SS, St Andrews, UK
[*]corresponding author: adf10@st-andrews.ac.uk

Abstract: We present flexible holographic metasurfaces that show different images for different substrate shapes, and a self-calibrated curvature sensor.

Photonic metasurfaces realized on flexible and conformable substrates behave as electromagnetic skins that can transfer a tailored photonic response to any target substrate onto which they are applied. When enabled by digital holographic design approach, Flexible Holographic Metasurfaces (FHMs) retain all the advantages of their flat and rigid counterparts, while offering unique opportunities and challenges. For example, the photonic function can be marginally dependent on the substrate's shape [1,2], it can be completely decoupled from it [3], or the shape of the substrate can be encoded into the holographic design itself [4]. Flexible metasurfaces can be designed to exhibit epsilon-near-zero permittivity [5] or used for tunable lenses applications [6].

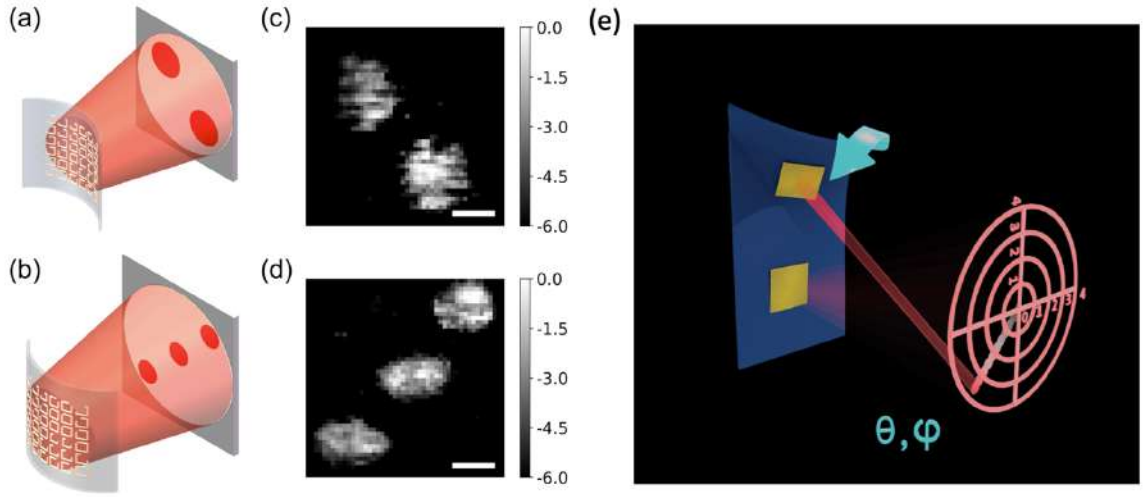

Figure 1 a),b) holographic metasurface bent with positive and negative radius of curvature; c), d) experimental images at 94GHz relative to panel a) and b), where the size bar is 1 cm [7]. (e) sketch of the working principle of the self calibrated sensor. [8]

Here, we report on our experimental demonstration of mechanically tunable, shape-dependent FHMs operating in the millimeter wavelength range (94 GHz) [7]. This adds a new degree of freedom to multiplex information in holographic metasurfaces. Specifically, we show that bending a FHM with different radii of curvature produces completely different images. The two independent holograms were encoded interleaving the phase profiles relative to two distinct images, as obtained from an iterative Gerchberg-Saxton algorithm, based on Rayleigh-Sommerfeld propagator. The fabrication of the FHMs was made photolithographically, using a dry film laminated on a thick polymeric substrate. The meta-atoms were based on metal-insulator-metal geometry, where

the top metallic layer was patterned with C-ring shapes, to produce the desired phase-only hologram. To demonstrate the correct functioning of the devices, we acquired images produced by the FHMs using a scanning head over an area of 10x10cm^2. Bending FHMs in specific configurations is relatively easy, when the substrate has dimension in the cm scales, and the operating wavelength is in the mm scale. At optical wavelengths, accurate positioning is more important. In the second part of this contribution, we introduce a flexible self-calibrating holographic curvature sensor that operates in the visible range. [8] The sensor is designed to detect any deformation in the target object. Unlike conventional methods, our sensor incorporates a holographic image with a reference scale and a cursor that indicates curvature, offering immediate readouts without mapping observable data onto substrate curvature. As shown in Figure 1e, the sensor comprises a two-dimensional scale and a dot as the curvature indicator. The dot displacement is proportional to angle changes as the substrate deforms. We provide details on the design, fabrication, and validation of the sensor, confirming the accuracy of self-calibration through independent angle measurements of reflected light from a uniform sensor area.

This research is supported by the European Research Council (ERC) under the European Union Horizon 2020 research and innovation program (Grant Agreement No. 819346).

References

1. Di Falco, A., Zhao, Y., Alu, A. “Optical metasurfaces with robust angular response on flexible substrates”, Appl. Phys. Lett. Vol. 99, 163110, 2011.
2. Burch, J., Wen, D. Chen, X. and Di Falco, A. "Conformable holographic metasurfaces," Scientific reports, Vol. 7, No. 1, 1-7, 2017.
3. Kamali, S. M., Arbabi, E., Arbabi, E., Horie, Y., and Faraon, A. "Highly tunable elastic dielectric metasurface lenses," Laser & Photonics Reviews, Vol. 10, No. 6, 1002-1008, 2016.
4. Burch, J., and Di Falco, A., “Surface topology specific metasurface holograms”, ACS Photonics 5, 1762-1766, 2018.
5. Li, X., Rizza, C., Schulz, S. A., Ciattoni, A., and Di Falco, A. "Conformable optical coatings with epsilon near zero response," APL Photonics, Vol. 4, No. 5, 2019.
6. Kim, J., Seong, J., Yang, Y., Moon, S.W., Badloe, T. and Rho, J., “Tunable metasurfaces towards versatile metalenses and metaholograms: a review”, Advanced Photonics, Vol. 4, No, 2, 024001-02400, 2022.
7. Xiao, J. Plaskocinski, T, Biabanifard, M., and Di Falco, A. "Shape Dependent Conformable Holographic Metasurfaces," Advanced Materials Technologies, Vol. 8, No. 10, 2202006, 2023.
8. Xiao, J. Plaskocinski, T, Biabanifard, M., and Di Falco, A. “Self-Calibrated Flexible Holographic Curvature Sensor”, Advanced Materials Technologies, 2301851, 2024.

Radar systems, target detection, localization, and tracking

An Intermodulation Radar for Sensing Applications

S. Pisa, P. Monsurrò, P. Tommasino, A. Trifiletti

Department of Information Engineering, Electronics and Telecommunications, Sapienza University of Rome, Italy
*corresponding author: stefano.pisa@uniroma1.it

Abstract: A nonlinear target to be used in intermodulation radar sensing applications has been studied. The target responses measured with an experimental setup and simulated with the MWO software were in good agreement. A Volterra series model of the target has been developed and compared with measurements.

An intermodulation radar utilizes its transmitting antenna to radiate two close in frequency tones towards the target antenna. If the target contains non-linear elements, intermodulation tones are produced. Of these, those of the third-order are close in frequency to the fundamental ones and therefore are re-radiated by the target antenna. The radar receiving antenna captures these signals and sends them towards the receiving section where they are measured [1]. Intermodulation radars have been used for the remote sensing of physiological activities by placing a nonlinear target on the thorax of a subject [2]. A focal point for this kind of applications is the realization of a nonlinear target that must generate strong intermodulation.

The non-linear target was realized by using an HSMS2850 Schottky diode with a reactive matching network [1]. This network was optimized with the MWO software, available inside the AWR design environment, in order to maximize the generation of third order intermodulation and to minimize the two tones reflection coefficient. The obtained circuit is shown in Fig. 1(a) while its physical realization on a Roger RO4003 30 mills substrate is reported in Fig. 1(b).

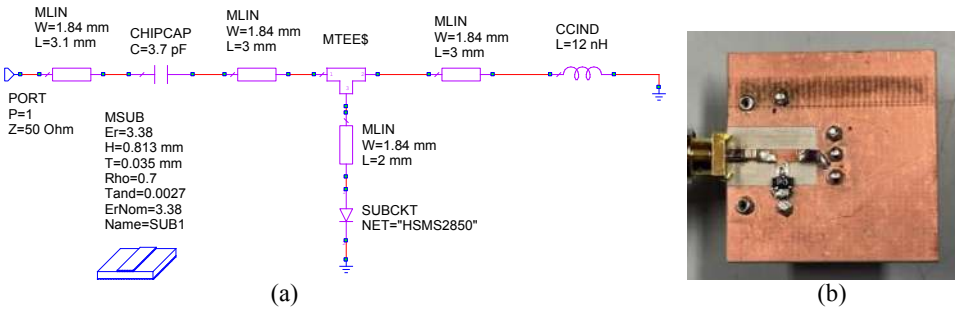

(a) (b)

Fig. 1 Scheme of the realized target (a) and its physical realization (b).

By using the experimental setup in Fig. 2(a) the target has been excited by applying two tones f_L=0.995 GHz and f_R=1.005 GHz with a power of 0 dBm. Fig. 2(b) reports the measured spectrum showing the presence of the left third order intermodulation products ($f_{IM3L} = 2f_L - f_R$ = 0.985 GHz) and of the right third order intermodulation product ($f_{IM3R} = 2f_R - f_L$ = 1.015 GHz). Moreover, the reflected f_L and f_R tones are also evidenced. The same graph shows the results obtained with the simulations performed with the MWO software which show a good agreement with measurements.

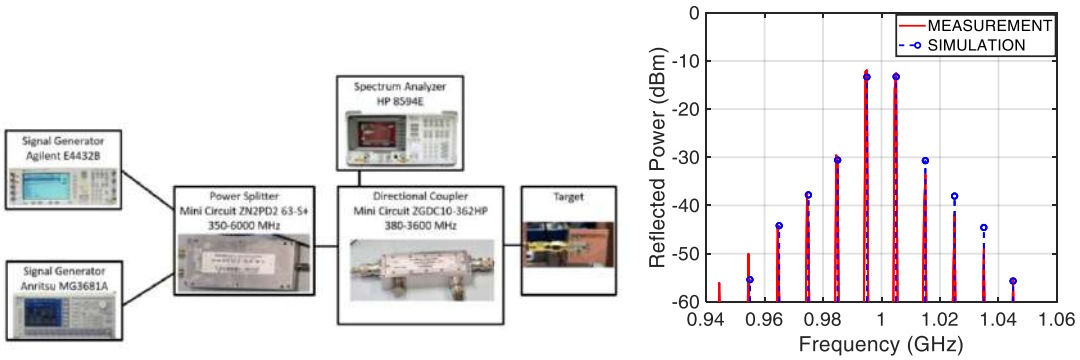

(a) (b)

Fig. 2 experimental setup (a) and measured and simulated target response.

Simulations have been performed to extract a Volterra model of the target. By using MWO software, the target has been excited employing 3 tones at 990, 1000, and 1010 MHz each with a power of 0 dBm. Then the target output y(n) has been imported in a matlab program and ordered in a vector Y of dimension N×1. Moreover, all the unknowns of the Volterra model have been ordered in a β vector of dimension L×1 with L≪N. Then, called X the matrix of input terms, delayed and multiplied together, of dimension N×L, it holds: $Y = X\,\beta$. The estimate of the Volterra parameters was obtained with least squares achieving: $\beta^* = (X^T X)^{-1} X^T Y$ [3]. The target response measured with the setup in Fig. 2(a) was reconstructed with the Volterra model and the obtained spectrum is reported in Fig 3 together with the measured one.

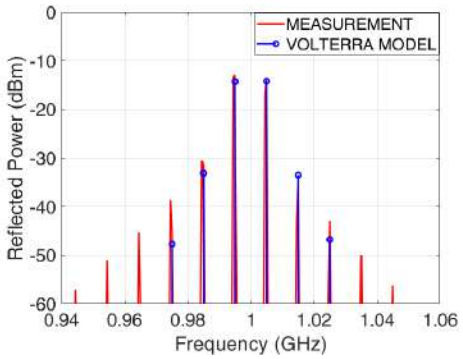

Fig. 3. MWO schematic (a) and plot of the original and fitted output responses (b).

The figure shows that the Volterra model is able to reconstruct the third order intermodulation produced by the target with a quite good accuracy and it is therefore suitable to be used for sensing and imaging applications of intermodulation radar.

References

1. S. Pisa, A. Trifiletti, P. Tommasino, P. Monsurrò, P. Tognolatti, G. Leuzzi, A. Di Carlofelice, E. Di Giampaolo, “An Intermodulation Radar for Non-Linear Target and Transceiver Detection,” Sensors 2024, 24, 1433.
2. A. Mishra, C. Li, “A review: recent progress in the design and development of nonlinear radars,” Remote Sens. vol 13, pp. 1-22 ,2021.
3. C. Bocciarelli *et al.*, "High-Accuracy Low-Cost Generalized Complex Pruned Volterra Models for Nonlinear Calibration," in *IEEE Transactions on Circuits and Systems I*, vol. 70, no. 9, pp. 3534-3544, Sept. 2023.

AES 2024, ROME - ITALY, 25 –28 JUNE 2024

A Drone Mounted Ground Probing Radar for the Characterization of the Buried Ice Deposits on Mars

O. Testa[1], S. Pisa[1], R. Cicchetti[1], A. Cicchetti[2], P. d'Atanasio[3], A. Zambotti[3]

[1]Department of Information Engineering, Electronics and Telecommunications, Sapienza University of Rome, Italy
[2]Istituto Nazionale di Astrofisica, Rome, Italy
[3]Italian National Agency for New Technologies, Energy and Sustainable Economic Development, Casaccia, Rome, Italy.
[*]corresponding author: Stefano.pisa@uniroma1.it

Abstract: A ground probing radar (GPR) to investigate the presence of water ice beneath the surface of Mars is presented. Measurements using the Time Domain Reflectometry (TDR) technique and simulations with the CST software highlighted the feasibility of the proposed GPR system.

A Ground Probing Radar (GPR) installed on a drone, can be used for the search of water ice in the first meters of depth of the Martian subsurface. Knowledge of the water ice location will enable on-site production of hydrogen and oxygen to power robotic missions or any future human exploration [1]. To obtain a range resolution of at least 15 cm in the medium (assuming a basaltic soil with relative dielectric permittivity of 9), a radar pulse duration of about 3 ns, and therefore a band of about 400 MHz, is necessary. Furthermore, the Radar must be able to operate up to a depth of about 5 meters so, to reduce the attenuation through the Mars ground and the antenna size, a center frequency of about 500 MHz has been used. To this end, the GPR should be equipped with a light and compact antenna suitable to operate between 300 MHz and 700 MHz. To meet these requirements, a planar antipodal Vivaldi antenna equipped with rectangular slots loaded with circular terminations has been designed so to improve antenna performance [2]. A prototype of this antenna has been realized on a cheap FR4 substrate [see Fig. 1(a)]. In the considered Ground Probing Radar the antenna is connected to a TDR system as depicted in Fig. 1(a). The frequency behavior of realized gain of the antenna prototype is reported in Fig. 1(b) showing a good agreement between measurements and numerical simulations.

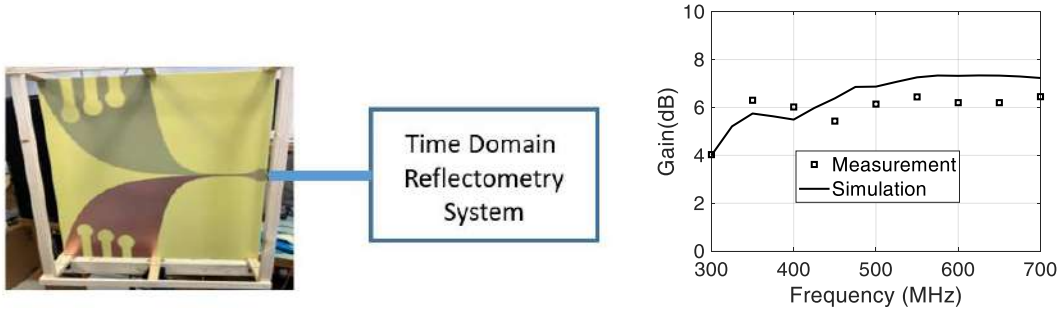

(a) (b)

Figure 1. Antenna prototype (a), and antenna realized gain (b).

A first set of measurements have been performed by placing the antenna in front of a metallic panel and measuring the pulse response for various antenna-panel distances. The pulses, with an initial frequency of 300 MHz and a final frequency of 700 MHz, were synthesized using the TDR option available on the Agilent E8363C network analyzer. The time-domain pulse responses for distances equal to 120 cm and 135 cm are

reported in Fig. 2. The first peak appearing in the antenna response, located at about 3.3 ns, is due to reflections at the antenna mouth, while the peaks at 13 ns and 15 ns are due to the metal panel reflections. Taking into account the time delay introduced by the antenna, the second peaks correspond to a distance of about 112 and 142 cm with errors of 8 cm and 7 cm, respectively. Therefore, the radar system equipped with the proposed antenna is suitable to measure a free-space target distance with errors less than about 10 cm.

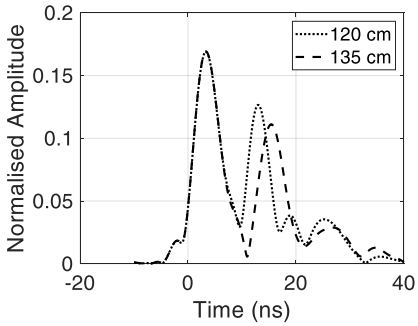

Figure 2. Antenna pulse response for 120 cm and 135 cm antenna-panel distances.

To test the ability of the proposed radar to operate on Mars surface, a typical scenario consisting of an ice layer (ε_r=3, σ= 0.0 S/m) of thickness wi=50 cm buried by basaltic rock (ε_r=9, σ= 0.01 S/m, wb=50 cm) has been investigated [see Fig. 3 (a)]. The GPR system was assumed to be placed 2 m away from the planet surface. The system response (at the antenna port) was obtained using the full-wave CST Studio Suite software [see Fig. 3(b)].

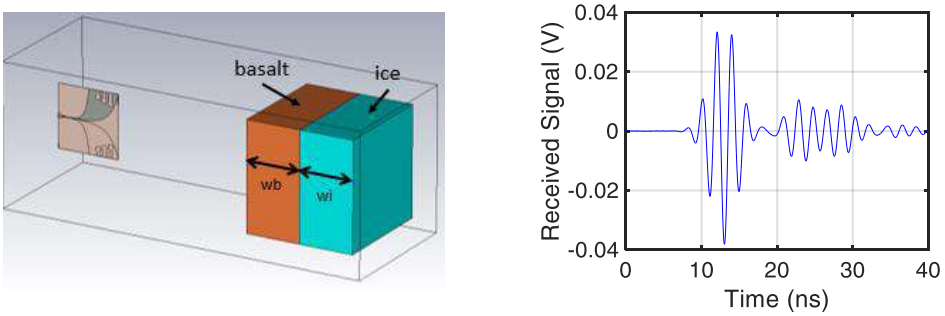

Figure 3. Investigated scenario (a), and plot of the pulse response at the antenna port (b)

The presence of the air-basalt, as well as basalt-ice reflections are well visible in the figure proving that the radar resolution is sufficient to discriminate typical Mars layers.

References

1. Picardi, G., J.J. Plaut, D. Biccari, et al., "Radar soundings of the subsurface of Mars," *Science*, vol. 310, No 5757, 1925-1928, 2015.
2. Pisa, S., F. Pastori, R. Cicchetti, E. Piuzzi, O. Testa, E. Pittella, A. Cicchetti, P. D'Atanasio, and A. Zambotti, "An Antipodal Vivaldi Antenna for a Drone-Mounted Ground Probing Radar," *PIERS M*, vol. 123, 53-61, 2024.

AES 2024, ROME - ITALY, 25 –28 JUNE 2024

Progress on Upgrading the HUSIR Radar for Deep-space Satellite Imaging

M. E. MacDonald*, D. L. Grimes, R. K. Lee, D. A. Gordon, M. D. Abouzahra and M. A. Schoenfeld

MIT Lincoln Laboratory, USA
*corresponding author: mmacdon@ll.mit.edu

Abstract: The Haystack Ultra-wideband Satellite Imaging Radar (HUSIR) is being upgraded to extend Inverse Synthetic Aperture Radar (ISAR) imagery of satellites at 3 cm resolution from low Earth to geosynchronous orbit. Progress on development of a new W-band (92 - 100 GHz) Gyro TWT transmitter, and upgraded receiver and feed subsystems, increasing peak transmit power from ~1 kW to ~50 kW is presented.

DISTRIBUTION STATEMENT A. Approved for public release. Distribution is unlimited.

This material is based upon work supported by the Department of the Air Force under Air Force Contract No. FA8702-15-D-0001. Any opinions, findings, conclusions or recommendations expressed in this material are those of the author(s) and do not necessarily reflect the views of the Department of the Air Force.

© 2024 Massachusetts Institute of Technology.

Delivered to the U.S. Government with Unlimited Rights, as defined in DFARS Part 252.227-7013 or 7014 (Feb 2014). Notwithstanding any copyright notice, U.S. Government rights in this work are defined by DFARS 252.227-7013 or DFARS 252.227-7014 as detailed above. Use of this work other than as specifically authorized by the U.S. Government may violate any copyrights that exist in this work.

Range Unlimited Coherent Lidar and Autonomous Self-Localization

O. Boyraz[1*], A. Atalar[1], C. J. Margison[1], M. M. Bayer[1], X. Li[1], O. B. Boyraz[1]

[1]University of California Irvine, USA
[*]corresponding author: oboyraz@uci.edu

Abstract: Current coherent lidar systems face limitations due to the coherence length of the laser, impacting measurement range and accuracy due to laser phase noise. Here, we present a novel coherent technology suitable for lidar and autonomous localization to achieve cm-level accuracies at distances up to 11km with 10 photons/point sensitivity.

1. Introduction

Positioning, navigation, and timing (PNT) systems, driven by GPS technology, are utilized across various sectors, from transportation to defense [1]. Emerging optical carrier-based localization systems offer chip-scale photonics alternatives for improved accuracy, particularly in GPS-denied environments. However, like RF-based approaches, many optical PNT systems require atomic clocks [2]. Concurrently, with recent advancements, coherent lidar technology has seen recent implementation in fields such as autonomous vehicles and satellite-based research [3], but faces limitations due to coherence length, impacting measurement range and accuracy due to laser phase noise [4]. In this paper, we introduce novel coherent-ranging technology to address coherence length limitations for long-range lidar measurements and provide means for autonomous self-localization opportunities for the remote receiver. Our approach enables operation beyond laser source coherence length, facilitating long-distance (>11km) ranging-based 3D imaging with high precision (σ = 1.25cm) at ~10pW received power levels. Additionally, it enables long-range (>1.8km), high-accuracy (σ <1cm), and high-resolution (~2cm) self-positioning.

2. Experimental Results and Discussion

Fig. 1a depicts the setup for 3D imaging beyond coherence length using a coherent lidar system. A CW laser at 1550nm is split into two branches: one acts as a local oscillator, and the other is modulated by a Mach-Zehnder modulator driven by four RF tones (510, 710, 890, and 950MHz). A 7.6km fiber simulates 11.4km of free space, followed by an EDFA to boost optical power.

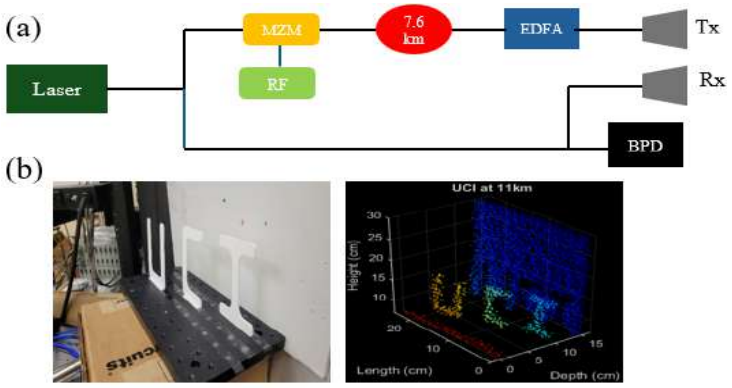

Figure 1: (s) Lidar architecture. (b) Imaging results of U, C, and I at 11.4km.

Echo from the target is collected by a receiver collimator in a bistatic setup, and heterodyne detection is performed at a balanced detector (BPD). Detailed theory and signal processing are discussed in our previous paper [5].

Fig. 1b shows imaging results with a 30cm-by-30cm target scene, revealing a resolution <3cm with an average

ranging error of σ = 1.25cm and received optical power at 10pW. The self-localization system utilizes a similar architecture, with independent free-running lasers on the Tx and Rx sides, each having <100kHz linewidth and 1064nm operation wavelength. Phase-locked RF tones at 500, 700, 890, and 950 MHz are utilized, with a 500kHz low-frequency signal mixed with 500MHz for coarse ranging. A ~1.2km fiber approximating 1.8km optical path length in free space is integrated to simulate long-distance light propagation.

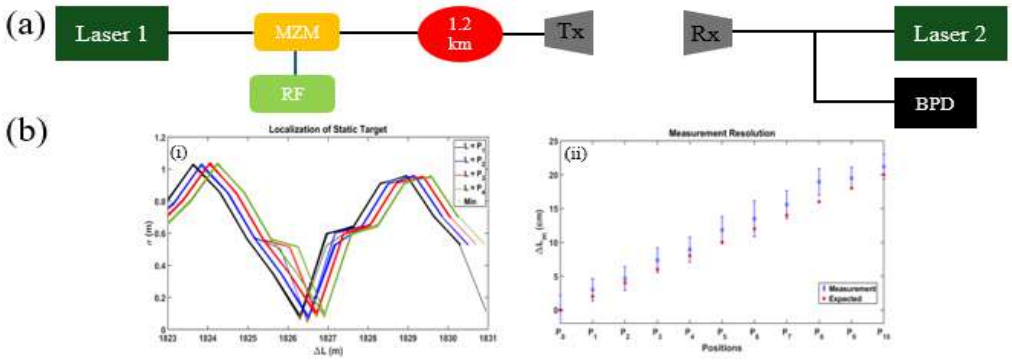

Figure 2: (s) O-CLAN architecture. (b) Ranging results (i) and measurement resolution (ii).

A motorized translational stage controls Rx side positioning. Measurements are taken at four locations, conducting 10 static target-ranging measurements at each location. Fig. 2b.i presents position triangulation results for 10 trials at each position (P1-P4), with yellow circles highlighting minimum standard deviation points. The average distances measured are 1826.30m, 1826.50m, 1826.71m, and 1827.91m, respectively. Fig. 2b.ii displays localization precision, with standard deviations of 10 trials at each position ranging from 0.9cm to 1.5cm at distances >1.8km. The measured distances fall within the precision range, demonstrating system's capability to resolve <2cm displacements at a range of ~2km. Detailed theory and signal processing are discussed in our previous paper [6].

3. Conclusion

Overall, we present the capabilities of the new coherent ranging methodology for long-distance precise 3D point cloud lidar imaging at distances >12x larger than the laser coherence length at very low received optical power levels. In addition, we show self-localization that can achieve high-resolution and high-precision photonic positioning over long distances (>1.8km) with <2cm localization precision, indicating to overcome limitations of traditional navigation methods, offering new opportunities for precise navigation and localization in challenging environments.

References

1. Simonsen K. et al., "LOCO GPSI: Preserve the GPS advantage for defense and security," PLANS 2004. Position Location and Navigation Symposium Monterey, CA, USA, 2004, pp. 598-603
2. Maheepala, M. *et al.*, "Light-based indoor positioning systems: A review," IEEE Sens. J., vol. 20, no. 8, pp. 3971–3995, 2020.
3. Hecht, J. "Lidar for self-driving cars," Opt. Photonics News 29(1), 26–33 (2018).
4. Zhou, Y. *et al*., (2023). Effects of a variable linewidth laser and variable linewidth shape laser on coherent FMCW LiDAR. Optics Continuum, 2(5), 1122-1136.
5. Mustafa Mert Bayer *et al*., "Single-shot ranging and velocimetry with a CW lidar far beyond the coherence length of the CW laser," Opt. Express **29**, 42343-42354 (2021)
6. Bayer M. M. *et al*., "Demonstration of Optical Clock-Free Localization and Navigation (CLAN)," in Journal of Lightwave Technology, vol. 41, no. 20, pp. 6457-6464, 15 Oct.15, 2023

Material Characterization and non-destructive testing

AES 2024, ROME - ITALY, 25 –28 JUNE 2024

Giant Magnetoimpedance Effect at GHz Frequencies in Amorphous Microwires

A. Zhukov[1,2,3,4], M. Ipatov[1], P. Corte-Leon[1,3], J. M. Blanco[2,3] and V. Zhukova[1,2,3*]

[1] Dept. Polymers and Advanced Materials, University of Basque Country, UPV/EHU, 20018 San Sebastian

[2] Dept. Appl. Phys., EIG, University of Basque Country, UPV/EHU, 20018 San Sebastian

[3] EHU Quantum Center, University of Basque Country, UPV/EHU, 20018 San Sebastian

[4]IKERBASQUE, Basque Foundation for Science, 48011 Bilbao, Spain

[*]corresponding author: valentina.zhukova@ehu.es

Abstract: Studies of the GMI effect of amorphous Co-Fe rich microwires reveal that they present GMI effect at GHz frequencies. We studied the correlation of magnetic anisotropy and GMI effect in Co-Fe rich microwires and observed that stress-annealing allows magnetic softening and improvement of frequency dependence of GMI ratio at high frequencies. Observed experimental dependences are discussed considering both different magnetic structure and the anisotropy in the bulk and near the surface and close analogy between giant magnetoimpedance and ferromagnetic resonance.

Studies of the Giant magnetoimpedance (GMI) effect have attracted considerable attention owing to one of the largest among the non-cryogenic effects sensitivity to applied magnetic field (up to 10 %/A/m) [1,2]. The GMI effect origin is attributed the penetration depth dependence of the AC current flowing through the magnetically soft conductor on applied magnetic field [1-3]. Commonly, the GMI effect is expressed in terms of the GMI ratio, $\Delta Z/Z$, given as:

$$\Delta Z/Z = [Z(H) - Z(H_{max})] / Z(H_{max}), \quad (1)$$

where H is the applied axial DC magnetic field and H_{max}- a maximum field typically of a few kA/m.

Typically the largest GMI effect ($\Delta Z/Z$ up to 650%) is observed in amorphous magnetic wires [1,2]. The $\Delta Z/Z(H)$ - dependence and maximum $\Delta Z/Z$ -value are determined by the type of magnetic anisotropy: in magnetic wires with circumferential easy axis a double-peak magnetic field dependence of the real component of wire impedance (and consequently of the GMI ratio) is observed. However, in magnetic wires with axial magnetic anisotropy a monotonic decay of the GMI ratio from H=0 is reported [2,3].

The development of novel industrial applications requires the GMI material miniaturization. Therefore, the tendency to reduce the magnetic wires diameter stimulated technological progress in the development of fabrication processes of thin wires [2]. It was predicted that, the diameter reduction must be associated with rising of the optimal GMI frequency range [3]. Indeed, the main prerequisite for the GMI effect observation is that the skin depth must be thinner that the wire radius.

Additionally, at high enough frequencies the domain walls are strongly damped. Therefore, only the magnetization rotation is responsible for the magnetic permeability variation upon external magnetic field at high frequencies [2]. Furthermore, at GHz frequencies range the link between the GMI and ferromagnetic resonance (FMR) is discussed [3].

The purpose of this paper is present last results on studies of the GMI effect at GHz frequencies.

Hysteresis loops have been determined by flux-metric method, as described elsewhere [2].

We measured magnetic field dependences of impedance, Z, and GMI ratio, $\Delta Z/Z$, for as-prepared samples and after heat treatments.

We used specially designed micro-strip sample holder. The sample holder was placed inside a sufficiently long solenoid that creates a homogeneous magnetic field, H. The sample impedance Z was measured using vector network analyzer from reflection coefficient S_{11}.

Magnetic field, H, dependence of real part, Z_1 of the longitudinal wire impedance Z_{zz} ($Z_{zz} = Z_1+iZ_2$), measured up to 4 GHz in $Co_{66}Cr_{3.5}Fe_{3.5}B_{16}Si_{11}$, $Co_{67}Fe_{3.85}Ni_{1.45}B_{11.5}Si_{14.5}Mo_{1.7}$ and $Co_{67.71}Fe_{4.28}Ni_{1.57}Si_{11.24}B_{12.4}Mo_{1.25}C_{1.55}$ microwires are shown in Fig.1. General features of these dependences is that the magnetic field of maximum shifts to the higher field region increasing the *f*. High enough magnetic field sensitivity, i.e. GMI effect till GHz- range frequencies should be also underlined.

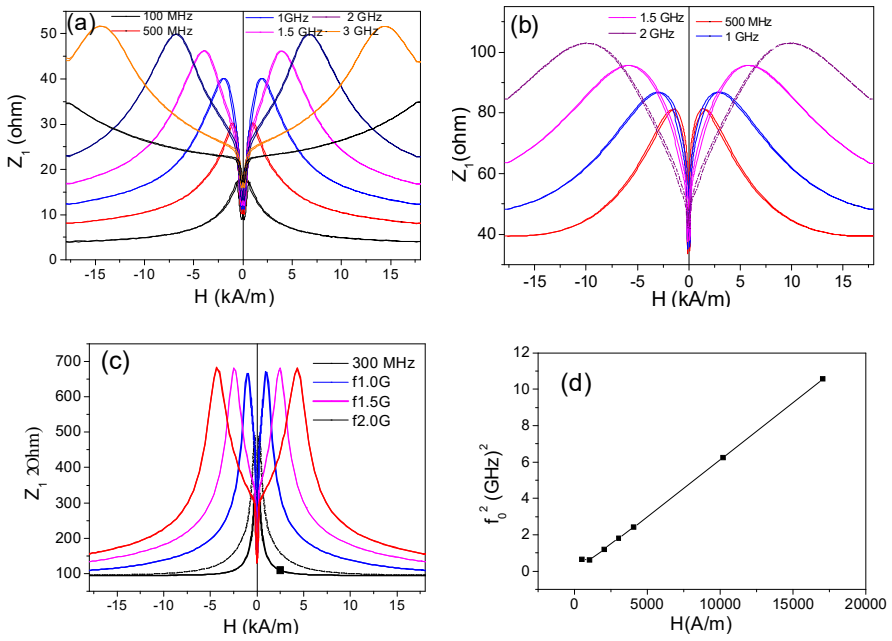

Fig.1. Z(H) dependence of $Co_{66}Cr_{3.5}Fe_{3.5}B_{16}Si_{11}$ (a) $Co_{67}Fe_{3.85}Ni_{1.45}B_{11.5}Si_{14.5}Mo_{1.7}$ (b) and $Co_{67.71}Fe_{4.28}Ni_{1.57}Si_{11.24}B_{12.4}Mo_{1.25}C_{1.55}$ (c) microwires measured at different frequencies and f_0^2(H) dependence plotted for $Co_{66}Cr_{3.5}Fe_{3.5}B_{16}Si_{11}$ microwire (d).

Usually the magnetic field of maximum, H_{max}, is attributed to the magnetic anisotropy field [2]. However, at elevated frequencies the magnetic field of Z_1 maximum, H_{max}, (1-10 kA/m) is much higher than the magnetic anisotropy field, observed in hysteresis loops (about 0.1 kA/m).

Previously GMI effect at elevated frequencies has been explained considering the fundamental link between ferromagnetic resonance, FMR, and GMI [3] Similarly to previous reports we plotted the dependence of the square of the frequency on H_{max} (Fig. 1c). The linear fit can be observed for high f and H_{max} –values. Consequently, from provided analysis we can deduce that some features of high frequency GMI effect can be described using FMR-like approximation.

References

1. Panina L.V. and Mohri, K. “Magneto-impedance effect in amorphous wires”, Appl Phys Lett. Vol. **65**, 1189-1191, 1994
2. Zhukov A., Ipatov M., Churyukanova M., Talaat A., Blanco J. M. and Zhukova V. “Trends in optimization of giant magnetoimpedance effect in amorphous and nanocrystalline materials”, J. Alloys Compound. Vol. 727, 887-901, 2017.
3. Zhukov A., Gonzalez-Legarreta L., Ipatov M., Corte-Leon P., Blanco J. M., and Zhukova V., “Giant magnetoimpedance effect at GHz frequencies in amorphous microwires”, AIP Advances Vol. 9, 125333, 2019.

AES 2024, ROME - ITALY, 25 –28 JUNE 2024

Temperature-dependent properties of amorphous oxide thin films for high-performance distributed Bragg reflectors

M. Magnozzi[1], S. Colace[1], S. Samandari[1], M. Granata[2], A. Amato[3], Michael Caminale[1], Christophe Michel[2], Gianluca Gemme[4], Laurent Pinard[2], Maurizio Canepa[1]

[1]OptMatLab, Dipartimento di Fisica, Università di Genova, Italy
[2]Laboratoire des Matériaux Avancés - IP2I, CNRS, Université de Lyon, Université Claude Bernard Lyon 1, F-69622 Villeurbanne, France
[3]Maastricht University, P.O. Box 616, 6200 MD Maastricht, The Netherlands
[4]Istituto Nazionale di Fisica Nucleare, Sezione di Genova, Italy
[*]corresponding author: magnozzi@fisica.unige.it

Abstract: Monitoring the evolution of thin films properties during thermal annealing is instrumental to enhance the performance of Bragg reflectors for different applications, ranging from radiative coolers to gravitational wave detectors. In situ analysis can provide access to the dynamics of amorphous materials when transitioning from 'disordered' amorphous to crystalline state.

Distributed Bragg Reflectors (DBR) are multilayered optical coatings widely used in many advanced optical and photonics applications, including lasers, solar cells, radiative coolers, sensors, and detectors for gravitational waves.

The DBRs are built by alternating two or more thin films with different refractive index; their appeal results from the possibility to finely tune their optical response, for example in terms of reflection and transmission of light, across the EM spectrum and in a way which is not achievable by means of a single, bulk material. Therefore, the properties of the thin films constituting the DBR play a key role in shaping the performance of the whole stack. These properties include thickness, refractive index, energy gap, and roughness[1,2], all parameters that have to be carefully optimized during the design of the DBR, and skillfully achieved during its fabrication. In this context, the characterization of both the DBRs and their constituent layers taken individually plays a key role to make sure that the actual DBRs perform according to their design. Crucially, characterization is important also to assess the evolution of thin films' properties following standard – and in some cases, mandatory – post-deposition treatments such as the thermal annealing. Despite the importance of post-deposition annealing, the evolution of structural and optical properties of amorphous thin films as a function of annealing temperature remains not well understood, and the available information typically rely on ex-post investigations, that is, without direct access to the dynamics of the annealing itself[3].

In this contribution, the dynamics of annealing of amorphous mixed-oxide thin films obtained by means of in situ spectroscopic ellipsometry will be presented[4]. The relevance of information provided by means of this analysis will be discussed, highlighting the insights made available by in situ analysis with respect to previously reported, ex-post investigations[3,5,6]. Indeed, in situ analysis of thermal annealing of thin films for high-performance DBR provides a convenient tool to identify the annealing parameters, such as the maximum temperature and the time duration, which result in the properties of the thin films composing the DBR being optimized. Switching from the applications to the fundamental science, the in situ analysis of the dynamics of the thermal annealing on amorphous thin films provides a rich playground, where the evolution of the atomic structure in amorphous materials can be probed up to the onset of crystallization.

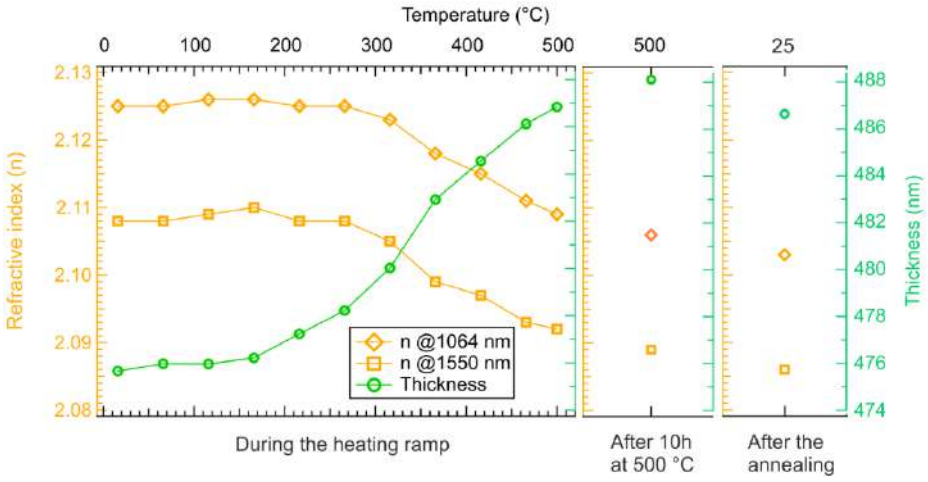

Fig. 1. Refractive index (orange markers) and thickness (green markers) of an amorphous mixed titania-tantala thin film measured in situ during the thermal annealing. In particular, the heating ramp is detailed (left graph), allowing to follow the evolution of refractive index and thickness as a function of the temperature. This kind of plots is instrumental to find the annealing parameters (such as maximum temperature and time duration) that yield the best-performing thin films constituting distributed Bragg reflectors (DBR) for different applications.

Acknowledgments

We gratefully acknowledge the project PRIN ERACLITO funded by the Italian Ministry of University and Research (MUR). This work was supported in part by the project Einstein Telescope Infrastructure Consortium (ETIC) (IR0000004) - MUR call n. 3264 PNRR, Miss. 4 - Comp. 2, Line 3.1.. We thank the Virgo Coating R&D collaboration for fruitful discussions. We thank Dr. Francesco Bisio for support in the setting of the heating cell and the development of related experimental methods.

References

1. Magnozzi, M. et al., “Optical properties of amorphous SiO_2-TiO_2 multi-nanolayered coatings for 1064-nm mirror technology”, *Opt. Mater.*, Vol. **75**, 94, 2018.
2. Amato, A. et al., “Optical properties of high-quality oxide coating materials used in gravitational-wave advanced detectors”, *J. Phys. Mater.*, **2**, 035004, 2019.
3. Amato, A. et al., “Effect of heating treatment and mixture on optical properties of coating materials used in gravitational-wave detectors”, *J. Vac. Sci. Technol. B* Vol. 37, 062913, 2019.
4. S. Colace et al., “Monitoring the evolution of optical coatings during thermal annealing with in situ spectroscopic ellipsometry”, *manuscript submitted.*
5. Magnozzi, M. et al., “Effects of mixing and annealing on the optical properties of TiO_2:Ta_2O_5 amorphous oxide coatings”, Optical Interference Coatings Conference OIC2022, Optica Technical Digest Series WB7 (2022)
6. Amato, A. et al., “Enhancing titania-tantala amorphous materials as high-index layers in Bragg reflectors of gravitational-wave detectors”, *ACS Appl. Opt. Mater.*, Vol **1**, 395, 2023.

AES 2024, ROME - ITALY, 25 –28 JUNE 2024

Development of Carbon Fiber Composites with Ferromagnetic Microwire Inclusions for Free Space Microwave Sensing

V. Zhukova[1], M. Ipatov[1], J. Malm[2], C. Johansson[2], R. B. Garcia-Etxabe[3], F. J.Vallejo[4], P. Olaskoaga[4] and A. Zhukov[1,5]

[1] Dept. Polymers and Advanced Materials, and Dept. Appl. Phys. University of Basque Country, UPV/EHU, 20018 San Sebastian

[2]RISE Research Institutes of Sweden, Digital Systems, Göteborg, Sweden

[3]GAIKER Technology Centre, Basque Research and Technology Alliance (BRTA), Spain

[4] Ideko Technology Centre, Elgoibar, Spain

[5]IKERBASQUE, Basque Foundation for Science, 48011 Bilbao, Spain

[*]corresponding author: arkadi.joukov@ehu.es

Abstract: This work focuses on free space microwave measurements of composites made from carbon fibers and ferromagnetic microwires inclusion focusing on the electromagnetic properties. We prepared and measured hysteresis loops and the magnetoimpedance effect of several glass-coated microwires and selected Co-rich microwires with better magnetic softness and higher magnetoimpedance effect. We observed that by using a low frequency modulating AC magnetic field allows to distinguish the microwave signals originated by ferromagnetic microwires inclusions from that generated by the carbon fibers. The location of carbon fibers near magnetic microwires has a critical effect on the response signals (scattering parameters S amplitude) obtained from such composites.

Glass-coated microwires prepared by the Taylor-Ulitovsky technique with diameters between 0.5 and 100 μm covered with thin, insulating, biocompatible and flexible glass-coating can present excellent magnetic softness, superior mechanical properties. Such features of glass-coated microwires allow development of new exciting applications in various magnetic sensors, as well as in smart composites with tunable magnetic permittivity [1,2].

One common challenge in composite materials is monitoring of stresses and temperature. Recently, stress dependencies of hysteresis loops and GMI effect have been proposed for the mechanical stresses monitoring in composites containing microwires inclusions [2].

In this paper, we present our latest results on studies of magnetic properties of glass-coated microwires and on our attempts to wireless health monitoring of composites containing both carbon fibers and ferromagnetic glass-coated microwires.

The composites containing both carbon fibers and Co-rich ferromagnetic glass-coated microwires were manufactured in the INFINITE EU project (Horizon Europe) at IDEKO's facilities (see Fig.1). For wireless measurements we used a free space microwave measurement setup (see Fig.2) consisting of two broadband horn antennas (1-17 GHz) fixed to the anechoic chamber and a vector network analyzer, previously employed for the characterization of the composites with magnetic wire inclusions [2]. Such setup allows to characterize composites of dimensions 20 x 20 cm^2.

Fig.1. Image of the carbon fiber composite with magnetic microwire inclusions (the vertical lighter fibres) with 5 mm spacing.

$Co_{64.6}Fe_{5.0}B_{16.0}Si_{11.0}Cr_{3.4}$ microwires (d=38 μm) microwires with better MI effect have been selected for the carbon fiber composite preparation.

The expected problem with composites containing conductive carbon fibers is that they can substantially interfere with the microwave signal from the magnetic microwire inclusions.

We proposed several solutions. Thus, in order to separate the microwave signal from ferromagnetic microwires, we used an external low frequency modulated magnetic field [2].

The other possibility is to separate the conductive carbon fibers from the magnetic microwires. Finally, use of magnetic microwires with better GMI performance can further increase the microwave response.

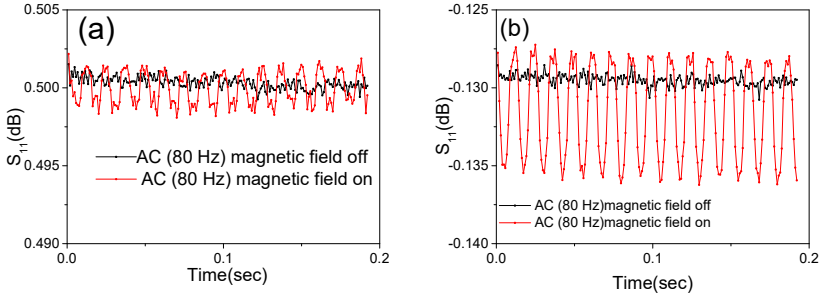

Fig.2. Effect of insulating plastic layer between the microwires and Carbon fibre composite on the S_{11} parameter. Measurements with plastic layer (a) and without plastic layer (b).

In Fig. 2a,b the microwave signals (S_{11} parameters) measured at 2 GHz are shown. As illustrated, the position of carbon fibers in vicinity of magnetic microwires critically affect the response signals obtained from such composites.

Thus, the presence of thin insulating plastic layer (30 μm thick) between the ordered microwires and carbon fiber composite can further increase the S_{11} parameters (see Fig.2b).

The aforementioned examples provide the routes for development of the composites made from the carbon fibers and magnetically soft amorphous glass-coated microwires inclusions.

References

1. . L. V. Panina, M. Ipatov, V. Zhukova, A. Zhukov, and J. Gonzalez, “Magnetic field effects in artificial dielectrics with arrays of magnetic wires at microwaves”, J. Appl. Phys. Vol. 109, 053901, 2011.
2. V. Zhukova, M. Ipatov, P. Corte-Leon, A. Gonzalez, A.García- Gómez, F. J. Vallejo, P. Olaskoaga, R. Garcia-Etxabe6, J.Malm, C. Johansson and A. Zhukov "Free Space Microwave Sensing of Carbon Fiber Composites With Ferromagnetic Microwire Inclusions," IEEE Sens. Lett., vol. 8, No. 1, 2500104, 2024, doi: 10.1109/LSENS.2023.3337071.